Première adaptation des amniotes au vol et phylogénie des avicéphales : l'apport de Coelurosauravus du Permien de Madagascar

Valentin Buffa

MUSEUM NATIONAL D'HISTOIRE NATURELLE

Ecole Doctorale Sciences de la nature et de l'Homme – ED 227

Année 2022 **N°attribué par la bibliothèque**

|_|_|_|_|_|_|_|_|_|_|_|_|_|

THESE

Pour obtenir le grade de

DOCTEUR DU MUSEUM NATIONAL D'HISTOIRE NATURELLE

Spécialité : Paléontologie

Présentée et soutenue publiquement par

Valentin Buffa

Le 29 novembre 2022

First flight adaptation in amniotes and avicephalan phylogeny: new insight from *Coelurosauravus* from the Permian of Madagascar

---

Sous la direction de **:**

Michel Laurin, Directeur de Recherche, CNRS

Jean-Sébastien Steyer, Chargé de Recherche, CNRS

JURY :

M. Fröbisch, Jörg	**Professor, Museum für Naturkunde and Humboldt-Universität zu Berlin, Allemagne**	**Rapporteur**
M. Scheyer, Torsten	**Privatdozent, University of Zurich, Palaeontological Institute and Museum, Suisse**	**Rapporteur**
Mme. Houssaye, Alexandra	**Directrice de Recherche, Centre national de la recherche scientifique, Paris, France**	**Examinatrice, Présidente du Jury**
Mme. Garcia, Géraldine	**Maîtresse de Conférence, Université de Poitiers, France**	**Examinatrice**
M. Laurin, Michel	**Directeur de Recherche, Centre national de la recherche scientifique, Paris, France**	**Co-directeur de thèse**
M. Steyer, Jean-Sébastien	**Chargé de Recherche, Centre national de la recherche scientifique, Paris, France**	**Co-directeur de thèse**
M. Cinnella, Paola	**Professeure, Sorbonne Université, Paris, France**	**Invitée**

Remerciements

Mes premiers remerciements s'adressent bien évidemment à mes deux co-directeurs de thèse Michel Laurin et Jean-Sébastien Steyer. Merci à tous les deux pour votre aide et votre soutien durant l'aventure qu'aura été cette thèse. Je joins également Paola Cinnella à ces remerciements, véritable co-encadrante de cette thèse bien qu'elle n'en ait pas l'étiquette. Merci de m'avoir permis de me plonger dans le monde merveilleux – et merveilleusement compliqué – de la dynamique des fluides, que j'espère continuer à explorer. Je n'oublie pas non plus Dino Frey, qui en plus de son accueil chaleureux au Muséum de Karlsruhe, m'a permis d'emprunter moultes spécimens, sans lesquels cette thèse n'aurait été que plus difficile. Merci à tous les quatre pour votre capacité à relire mes manuscrits plus vite que votre ombre !

Transitioning to English, I wish to express my warmest thanks to the members of my Ph.D. defense committee for their availability and for accepting to evaluate this manuscript. I look forward to meeting you all in person, and I wish you a nice reading of this dissertation!

Merci également aux différentes personnes de France et de Navarre qui m'ont donné accès à divers spécimens fossiles, tous plus beaux les uns que les autres : Dino Frey et Dennis Grabow (SMNK, Karlsruhe), Giuseppe Muscio et Paola Visentini (MFSN, Udine), Annalisa Aiello et Marco Valle (MCSNB, Bergame), Christina Lombardo (MPUM, Milan), Adam Pritchard (VMNH, Martinsville, Virginie), Nour-Eddine Jalil, Damien Germain et Salvador Baillon (MNHN, Paris). Merci à toutes les personnes qui ont pu rendre possible la réalisation de cette thèse : l'équipe administrative du CR2P (Angelina Bastos, Suzy Colas, Nadia Guerguadj, Sylvie Crasquin, Sylvain Charbonnier) ainsi que la direction de l'école doctorale 227. Merci également à toutes les personnes m'ayant aidé à photographier, préparer ou scanner mon matériel d'étude : Thomas Van de Kamp et Marcus Zuber (KIT, Karlsruhe), Florent Goussard, Nathalie Poulet, Colas Bouillet, Yohan Després, Séverin Morel, Lilian Cazes et Philippe Loubry (MNHN, Paris). Mention spéciale à Olivier Béthoux pour m'avoir transmis la passion du RTI et pour m'avoir prêté tout ce matériel (une valise bien remplie !) lors de mes visites de collection. Enfin, merci à Charlène Letenneur pour ses magnifiques reconstructions de *Coelurosauravus* qui viennent égayer ce manuscrit. Merci d'avoir supporté mes multiples commentaires, et au plaisir de retravailler ensemble !

Merci aussi à toutes les personnes avec qui j'ai pu échanger ou travailler durant mon passage au MNHN. Tout d'abord merci à Nour-Eddine Jalil et Peggy Vincent qui ont recueilli

le jeune stagiaire de Master que j'étais et ont continué à m'aider et à m'encourager jusqu'à la fin de ma thèse. Merci également à Jocelyn Falconnet, pour nos passionnantes discussions sur les diapsides Permiens, et la paléontologie en général. Merci à William Salaün, que j'ai eu la chance de co-encadrer durant son stage de Master 2 et qui m'a tout appris en CFD (et non l'inverse !). Merci enfin à tous les autres jeunes paléontologues du CR2P dont j'ai pu croiser la route : Les « Larbins » (Jordan et Alfred pour ne pas les nommer), Guillaume, Antoine, Mathieu, Marjorie, Thomas, Nicolas, Elvis, Vincent, Emile, Alison, Ana, Béatrice, Kévin, Jean, Laura, Thomas, Morgane, Marty et bien d'autres que j'oublie forcément mais qui ne comptent pas moins. Merci pour les bons moments passés avec vous tous !

Merci enfin à ma famille, mes amis, et à la foultitude de personnes formidables qui m'ont ouvert des portes, encouragé, soutenu et accompagné durant cette aventure. Je ne peux pas vous nommer tous ici, car à l'heure où j'écris ces lignes le dépôt de mon manuscrit de thèse est imminent… Mais c'est promis, je ne vous oublie pas, je pense à vous et on se revoit après ma soutenance !

Et enfin, à Juliette, merci du fond du cœur pour m'avoir accompagné, soutenu et supporté durant ces trois années. Sans toi, la thèse aurait été une épreuve, avec toi, ce fut une aventure. Merci pour tout.

Table of Contents

List of Tables

List of Figures

Résumé étendu

Les reptiles diapsides, représentés aujourd'hui par leur groupe apical Sauria, constituent le groupe d'amniotes actuels le plus diversifié et furent également les tétrapodes les plus remarquables durant toute l'Ère Mésozoïque. Comparativement, le registre fossile Permo-Triasique des diapsides non-sauriens, qui constituent les premiers diapsides, est relativement épars. Néanmoins, les diapsides non-sauriens montrent une disparité morphologique et écologique étonnante, incluant notamment des taxons terrestres, aquatiques, arboricoles et aériens, dont certains ont survécu à l'Extinction Permien-Trias (EPT) aux côtés des sauriens. Parmi les diapsides non-sauriens, les Weigeltisauridae du Permien tardif, premiers vertébrés planeurs connus, et les Drepanosauromorpha du Trias Supérieur, qui ressemblent à des caméléons, présentent parmi les plus extrêmes spécialisations liées à un habitat arboricole chez les tétrapodes. Ces deux groupes ont été regroupés dans le clade 'Avicephala', le plus ancien groupe de diapsides arboricoles et l'un des rares à avoir survécu à l'EPT. Cependant, la monophylie de ce clade reste controversée et demande à être réexaminée.

Toutefois, en tant que premiers diapsides spécialisés pour un mode de vie arboricole, l'étude des weigeltisauridés et des drépanosauromorphes, indépendamment de leurs relations phylogénétiques, devrait permettre de mieux comprendre l'adaptation à l'arboricolie chez les reptiles. Au sein des 'avicéphales', les weigeltisauridés, en raison de leurs grandes ailes membraneuses, semblent particulièrement performants pour naviguer dans le milieu discontinu et tridimensionnel que forment les canopées. Etant les premiers vertébrés planeurs connus, leur étude est primordiale pour comprendre l'évolution du vol chez les vertébrés. Pourtant, peu d'études se sont intéressées aux capacités de vol plané de ces reptiles, qui pourraient bien avoir été des parachutistes capables d'effectuer uniquement des descentes contrôlées, et non pas de véritables planeurs. Leur capacité à planer, pourtant quasi-unanimement acceptée, reste donc équivoque dans l'attente d'un examen quantitatif.

Cette thèse a ainsi pour objectif d'éclairer certains aspects de la paléobiologie et de l'évolution des weigeltisauridés et des drépanosauromorphes. Elle repose (1) sur un réexamen détaillé de spécimens fossiles provenant de diverses localités, (2) sur une réévaluation de l'arbre phylogénétique des diapsides Permo-Triasiques, et (3) sur une étude quantitative des performances de vol plané chez des reptiles actuels et éteints à l'aide de simulations numériques.

Dans un premier temps, la re-description détaillée de tous les spécimens attribués au weigeltisauridé *Coelurosauravus elivensis* du Permien supérieur de Madagascar a révélé plusieurs détails anatomiques jusqu'alors inconnus. Ces données ont permis de réaliser de nouvelles reconstructions de l'ensemble du squelette et des inférences morpho-fonctionnelles par analogie avec des reptiles actuels et éteints. Ces dernières soutiennent le mode de vie insectivore, arboricole et aérien précédemment proposé pour ce taxon. En particulier, les comparaisons avec des analogues actuels, à savoir le lézard volant *Draco* et les caméléons, suggèrent que *C. elivensis* aurait pu avoir un comportement de parade lorsqu'il était au sol, mais qu'il était aussi un planeur accompli, capable de contrôler l'extension et la cambrure de ses larges membranes alaires à l'aide de ses membres antérieurs. De plus, la re-description de *C. elivensis*, ainsi que l'examen par laminographie aux rayons X d'un spécimen de *Weigeltisaurus jaekeli* du Permien Supérieur Allemand, ont montré que les baguettes patagiales des weigeltisauridés étaient étroitement articulées avec les gastralia. Cela indique que l'aile de ces animaux s'étendait depuis la marge ventrale des flancs plutôt que depuis la marge dorsale, contrairement aux autres reptiles planeurs connus.

Dans un second temps, le réexamen détaillé de la plupart des spécimens de drépanosauromorphes du Trias Supérieur d'Italie a souligné de nombreuses différences anatomiques avec les weigeltisauridés, et a mis en évidence la présence de nombreux caractères typiques des archosauromorphes. Ces observations anatomiques ont été incluses dans une nouvelle matrice phylogénétique conçue pour résoudre les relations phylogénétiques des 'avicéphales' parmi les reptiles du Permo-Trias.

Les analyses phylogénétiques présentées dans ce manuscrit soutiennent l'hypothèse que les weigeltisauridés sont bien des diapsides non-sauriens, mais retrouvent les drépanosauromorphes comme groupe-frère des ptérosaures, formant un clade d'archosaures jusqu'ici inconnu. Ce résultat réduit le nombre de lignées de diapsides qui ont survécu à l'extinction massive du Permo-Trias, mais apporte surtout un nouvel éclairage sur l'évolution du vol battu chez les ptérosaures. En effet, plusieurs caractères que l'on pensait avoir évolué dans le contexte du vol battu sont en fait déjà présents chez les drépanosauromorphes et seraient donc mieux réinterprétés comme des exaptations dérivées d'une morphologie arboricole ancestrale. Cette nouvelle position systématique des drépanosauromorphes soutient donc l'hypothèse arboricole de l'origine des ptérosaures. En particulier, elle soulève la possibilité d'un ancêtre arboricole commun aux drépanosauromorphes et aux ptérosaures qui aurait été

capable de planer avec une membrane alaire, soulignant la nécessité d'une meilleure compréhension de cette locomotion particulière chez les reptiles de petite taille.

Enfin, l'examen détaillé des performances aérodynamiques du lézard volant actuel *Draco volans* au travers de simulations en dynamique des fluides numérique (CFD) et leur comparaison à des observations publiées, ont mis en évidence l'importance des changements de posture chez ce reptile qui lui permettent de contrôler son vol plané. L'étude de *C. elivensis* par ces mêmes méthodes confirme que ce reptile était en théorie capable de planer efficacement. En effet, les ailes de *C. elivensis* et *D. volans* permettent la création de tourbillons d'air dorsaux en vol, et donc de générer de la portance de façon similaire. Cependant, là où *D. volans* réalise une descente continue en planant, les trajectoires de vol plané simulées pour *C. elivensis* montrent une trajectoire phugoïde marquée par une grande oscillation. Cette trajectoire phugoïde aurait permis à *C. elivensis* d'effectuer une remontée passive au cours de son vol après une longue chute balistique initiale, et semble particulièrement propice pour les animaux plus grands comme *C. elivensis*. Enfin, nos simulations indiquent que *C. elivensis* aurait été capable de planer beaucoup plus efficacement dans une atmosphère plus dense comme celle qui régnait au Permien, ce qui suggère que l'atmosphère passée aurait pu permettre aux weigeltisauridés d'atteindre des tailles beaucoup plus grandes que les reptiles planeurs actuels.

Les résultats présentés au cours de cette thèse ont pour objectif d'approfondir notre compréhension de l'évolution du vol plané chez les reptiles et ouvrent de nombreuses perspectives pour des études futures. D'une part, il reste en effet encore bien des choses à étudier concernant l'anatomie de l'aile des weigeltisauridés, qui n'a aucun équivalent connu dans le règne animal. D'autre part, la nouvelle matrice de phylogénie construite durant cette thèse pourrait permettre d'étudier les relations de parenté d'autres reptiles énigmatiques, notamment des autres diapsides non-sauriens contemporains de *C. elivensis*, ou de tester d'autres hypothèses phylogénétiques concernant la composition des grands clades d'amniotes ou de sauropsides. De la même manière, la confrontation des résultats obtenus à des études similaires qui pourraient être menées avec d'autres matrices pourrait permettre de confirmer ou non les hypothèses phylogénétiques proposées dans cette thèse. Enfin, ce travail ouvre la porte à des études biomécaniques utilisant la dynamique des fluides numérique pour étudier le vol plané chez les tétrapodes fossiles. Au-delà de l'étude de *C. elivensis* présentée ici, il semble pertinent de prendre en compte la variabilité au sein des weigeltisauridés pour mieux comprendre leur paléobiologie.

Introduction

Reptiles, including birds, represent the most diverse group of extant amniotes, exceeding 20,000 described species, and have been the most abundant and diverse terrestrial vertebrates on Earth for much of the past 300 million years (Sues, 2019). As an icon of life from times long past, reptiles dominated terrestrial ecosystems throughout the Mesozoic Era, a time aptly called the "Age of Reptiles", and comprises the emblematic dinosaurs as well as several successful incursions into the marine and aerial realms (e.g., Weishampel et al., 2007; Motani, 2009; Witton, 2013). Nevertheless, much of the early evolutionary history of reptiles, especially with regards to their more modest late Paleozoic origins, remains poorly understood.

Today, reptiles are solely – or mostly, accounting for debates on turtle origins – represented by members of the Diapsida, the clade which includes all taxa with ancestrally two pairs of cranial temporal fenestrae (Gauthier and de Queiroz, 2020). In particular, lepidosaurs (today represented by lizards, snakes and the tuatara), and archosaurs (birds, crocodiles and their extinct relatives), form the crown-group Sauria, whose origin dates back to the late Permian Period, around 260 million years ago (Ezcurra et al., 2014). However, it is only during the Triassic Period that saurians, especially archosauromorphs (archosaur-line saurians), underwent their first major adaptive radiation and became dominant ecosystem components (e.g., Brusatte et al., 2011; Ezcurra et al., 2014, 2021; Bernardi et al., 2015; Ezcurra and Butler, 2018). The early evolutionary history of Sauria thus straddles the Permo-Triassic Mass Extinction (PTME), the most severe ecological crisis of the history of Life, (e.g., Erwin, 1990; Benton, 2003, Benton and Twitchett, 2003). In this context, the study of Permo-Triassic diversity, especially that of stem-saurian diapsids – those diapsids not included in the saurian crown group – is paramount to further our understanding of both the impact of the PTME on diapsids, as well as the early evolutionary history of crown-group reptiles.

During the late Paleozoic, reptiles, and to a stronger degree diapsids, were rather modest components of temnospondyl and synapsid-dominated ecosystems (Sahney et al., 2010). Nevertheless, stem-saurian diapsids show a surprisingly large morphological and ecological disparity, including well-recorded terrestrial, aquatic, arboreal and aerial taxa (Carroll, 1975, 1978, 1981; Gow, 1975; Currie, 1981; Reisz, 1981), and various groups survived the PTME alongside saurians (e.g., Ketchum and Barrett, 2004; Pritchard and Nesbitt, 2017). Among stem-saurian diapsids, the late Permian Weigeltisauridae, the oldest known gliding vertebrates,

and the chameleon-like Drepanosauromorpha from the Late Triassic show some of the most extreme specializations for an arboreal lifestyle in tetrapods (Frey et al., 1997; Schaumberg et al., 2007; Castiello et al., 2016; Pritchard et al., 2016, 2021). Both groups have been proposed to form the clade Avicephala (Senter, 2004; Pritchard et al., 2021), the earliest diapsid group of arboreal specialists, one of the few to survive the PTME, and the group under study in the present dissertation.

However, avicephalans have a complex taxonomic history. Indeed, whereas all recent studies recover weigeltisaurids as non-saurian diapsids (Ezcurra et al., 2014; Pritchard and Nesbitt, 2017; Schoch and Sues, 2018; Griffiths et al., 2021; Pritchard et al., 2021; Simões et al., 2022), drepanosauromorphs are alternatively recovered either as stem-saurian diapsids (Müller, 2004; Senter, 2004; Pritchard et al., 2016, 2021; Pritchard and Nesbitt, 2017) or archosauromorph saurians (Bennett, 2020; Sobral et al., 2020; Ford et al., 2021; Griffiths et al., 2021; Martínez et al., 2021; Simões et al., 2022) in the latest phylogenetic analyses. In addition, it has been suggested that Avicephala reflects convergent arboreal adaptations rather than actual phylogenetic relationships (Renesto and Binnelli, 2006; Renesto et al., 2010). Thus, there is no consensus regarding the monophyly of Avicephala. Nevertheless, as the earliest arboreal specialists, the study of weigeltisaurids and drepanosauromorphs, regardless of their phylogenetic relationships, provides a unique opportunity to further our understanding of arboreal adaptations in reptiles.

Life in the trees comes with a series of challenges for animals, such as moving around in a discontinuous three-dimensional habitat with substrates of varying width and compliance (Cartmill, 1974, 1985). Among those, the discontinuity of the arboreal realm imposes the need for an animal to safely move from one substrate to another, often at the risk of falling. As such, several vertebrates are capable of gap-crossing behaviors such as bridging gaps by brachiation, or taking to the air, either by jumping, gliding, or flying (Byrnes and Jayne, 2012; Graham and Socha, 2020). In some cases, such behaviors rely on strong morphological specializations that can be recognized in specimens of extinct animals (Fröbisch and Reisz, 2009; Simões et al., 2017).

Among avicephalans, specializations for gap crossing are best seen in weigeltisaurids, whose large patagial wings have long been considered as a spectacular case of gliding adaptation convergent with that of extant *Draco* agamid lizards (Schaumberg, 1976, 1986;

Carroll, 1978; Evans, 1982; Frey et al., 1997; Schaumberg et al., 2007). As the oldest known gliding vertebrates, the study of weigeltisaurid paleobiology is thus also paramount to our understanding of vertebrate flight. However, few studies have actually looked into the gliding capabilities of these reptiles. As the only assessment based on aerodynamics to date (McGuire and Dudley, 2011) suggested that they might be better considered as prachuters capable only of controlled but steep descent rather than actual efficient gliders, the gliding behavior of weigeltisaurids, advocated by all anatomical studies (Evans, 1982; Frey et al., 1997; Schaumberg et al., 2007; Pritchard et al., 2021), must be considered equivocal pending a quantitative examination.

Several fundamental questions arise from this short overview, namely: Are weigeltisaurids and drepanosauromorphs sister-groups, thus forming the clade Avicephala? If not, what are the phylogenetic affinities of both groups? What would then be the implications of avicephalan paraphyly on Permo-Triassic diapsid evolution? What do weigeltisaurids – and drepanosauromorphs for that matter – tell us about the origin and evolution of flight? Were weigeltisaurids even capable of true gliding flight?

The present dissertation aims to shed light on previously obscure aspects of weigeltisaurid and drepanosauromorph paleobiology and evolution, and to provide lines of evidence to answer the questions listed above. To this aim, this dissertation is organized – quite literally – from the ground up, starting from (1) a detailed reexamination of fossil specimens from various localities, housed in European Museum collections, then (2) a re-evaluation of the phylogenetic tree of Permo-Triassic diapsids and its implications for the evolution of flight in an arboreal context, and finally (3) a quantitative study of gliding performance in extant and extinct reptiles using numerical simulations.

In practical terms, the present dissertation is divided into six chapters:

Chapter 1—This chapter summarizes the diversity and evolution of reptiles during the late Paleozoic Era, spanning the first 60 Ma of their evolutionary history between their origin in the late Carboniferous some 320 million years ago, and the origin of Sauria around 260 million years ago at the end of the Permian. This sets the stage for the following chapters that will focus on Permo-Triassic diapsids and the early history of the saurian crown-group.

Chapters 2 and 3—Those chapters provide the two-part detailed anatomical re-description of the skull and postcranium of the weigeltisaurid *Coelurosauravus elivensis* Piveteau, 1926 from the late Permian Lower Sakamena Formation of southwestern Madagascar. The animal is entirely reconstructed in dorsal and lateral views for the first time, and several lines of evidence supporting the already commonly proposed arboreal and gliding lifestyle of this taxon are detailed.

Chapter 4—This chapter presents the development of a novel morphological phylogenetical matrix designed to resolve the nebulous phylogenetic relationships of avicephalans among Permo-Triassic reptiles. Much of this work relies on the detailed revision of character formulations to bridge the existing gap between early amniote and early diapsid phylogenies and hopefully provide a new perspective on Permo-Triassic diapsid phylogeny. As a case study, this chapter relies on a wealth of new anatomical data on drepanosauromorphs from the Late Triassic of Italy obtained from direct observations of the material. The resulting topology recovers drepanosauromorphs not as sister-group to weigeltisaurids, but to pterosaurs, thus shedding new light on the origin and evolutionary history of the acquisition of powered flight in the latter group.

Chapter 5—This chapter provides a detailed framework for the study of gliding flight in the extant agamid squamate *Draco volans* using Computational Fluid Dynamics (CFD), a set of numerical methods that simulate the flow of a fluid around a solid surface – in this case the flow of air around a gliding *Draco*. A systematic comparison of the aerodynamics of various postures is conducted using rigid-body models, complementing observed behavior in this taxon with simulated aerodynamic performances for the first time.

Chapter 6—This last chapter presents the application of the methodology outlined in the previous chapter to assess aerodynamic and gliding performances in the best-preserved weigeltisaurid *C. elivensis*. Weigeltisaurids are shown to have indeed been capable of true gliding flight, and adopted a flight behavior comprising a steep ballistic glide followed by a passive ‘phugoid’ climb-up that appears well suited for an oscillatory trajectory between trees. Weigeltisaurids were thus both the World’s first gliders, as well as the only known gliders to have experimented with this peculiar flight mode. In theory, *C. elivensis* appears capable of gliding as far as *D. volans*, but likely only at high atmospheric density, raising the question of the impact of changes in the Permian atmospheric composition on the origin of weigeltisaurids.

Chapter 1: Paleozoic origin of major reptile groups

> At the time of writing, the present chapter has been accepted for publication as an introductory review chapter, co-authored with M. Laurin (MNHN), for the next edition of the *Handbook of Zoology* on Reptilia, Volume 1 (ed. U. Joger, expected publication 2023, deGruyter, Berlin).

Introduction

Reptiles, including birds, dominated the ecosystems of the Mesozoic Era, a time aptly called the "Age of Reptiles", and represent the most speciose tetrapods of the extant biota, exceeding 20,000 described species. By comparison, the group had a more modest beginning in the temnospondyl and synapsid-dominated ecosystems of the Permo-Carboniferous (Sahney et al. 2010a). Nevertheless, early reptiles showed much morphological disparity, with well-recorded terrestrial, semi-aquatic and aerial taxa, and a size spectrum ranging from small 20-centimeter-long lizard-like forms to herbivorous giants exceeding three meters in length.

Hylonomus, the first known undisputable reptile (Carroll 1964; Müller & Reisz 2006) is known from the late Carboniferous (Bashkirian) of Nova Scotia, around 318 million years ago (Rygel et al. 2015). Its presence, and that of a putative synapsid in the same horizon (Carroll 1964), indicate that the divergence between sauropsids (or reptiles) and synapsids (mammals and their extinct relatives) had occurred by that time. The oldest known ichnofossils attributed to reptiles also come from the same horizon (Marchetti et al. 2020). In addition, morphological tip-dating (Ford & Benson 2020) and fossilized birth-death models (Didier & Laurin 2020) indicate an older divergence age between 322 and 340 Ma, which is coherent with the observed ghost lineage at the origin of amniotes (Reisz & Müller 2004; van Tuinen & Hadly 2004).

Our understanding of early reptile relationships is sparse compared to that of coeval synapsids, in part due to the much larger fossil record of the latter (see Angielczyk & Kammerer 2018), but recent advances in systematics and the advent of computerized phylogeny offer a better view of their beginnings. The goal of this chapter is thus to provide an overview of the fossil record and diversity of Paleozoic reptiles and of their evolutionary history leading to more recent major reptile groups.

Historical overview of early reptile phylogeny

Early works

Early workers typically lumped non-mammalian synapsids ('pelycosaurs') and some stem-amniotes such as diadectomorphs with reptiles (e.g. Goodrich 1916; Romer 1956). This 'reptile' group was typically divided into Anapsida, Synapsida and Diapsida based on the number of temporal fenestrae in the skull (Osborn 1903; Williston 1917), and anapsids were considered ancestral to both synapsids and diapsids (e.g. Carroll 1969a, 1988).

The advent of the Hennigian cladistic methodology cemented the basal synapsid-sauropsid dichotomy of amniotes (Gauthier et al. 1988a; Laurin & Reisz 1995; deBraga & Rieppel 1997) and provided a clear view of early synapsid relationships (see Reisz 1986). By contrast, the relationships of early reptiles remained poorly understood. This was further exacerbated as scientists endeavored to find the sister group of turtles, for which several reptilian taxa were chief contenders (reviewed in Lyson & Bever 2020; Schoch & Sues 2020).

Current status of early reptile phylogeny

Our knowledge of the early evolutionary history of reptiles drastically improved over the last century, and we now have a clearer view of early reptile relationships (Fig. 1). Amniotes are currently divided by a basal dichotomy into Sauropsida and Synapsida. Reptiles themselves are also divided into two major clades, the possibly extinct clade Parareptilia, and Eureptilia, the group which includes all or most extant reptiles, depending on the position of turtles (Tsuji & Müller 2009). These major clades can be diagnosed by series of skeletal characters, which have been repeatedly recovered in phylogenetical analyses (Table 1).

Parareptiles (meaning "next to reptiles") include several small early-diverging clades and the Procolophonia, a speciose parareptile clade that includes procolophonoids and pareiasaurs (Fig. 1), the largest parareptiles. However, the phylogenetic relationships between these small clades remain unclear (MacDougall et al. 2019a; Cisneros et al. 2021). The various

Table 1-1: Diagnostic skeletal characters for each major reptile clade. *Synapomorphies and typical parareptilian characters proposed for a parareptilian clade including mesosaurids as the first diverging group (see text).

Clade	Major skeletal synapomorphies	References
Sauropsida	1. presence of a suborbital opening in the palate; 2. presence of a large posttemporal fenestra in the occiput; 3. presence of a single coronoid in the lower jaw; 4. supinator process small and confluent with shaft of the humerus; 5. presence of a single pedal centrale	(Gauthier et al., 1988b; Laurin and Reisz, 1995; deBraga and Rieppel, 1997)
Parareptilia*	1. absence of a lacrimal-narinal contact; 2. absence of a caniniform tooth region; 3. absence of a subtemporal process of the jugal; 4. shorter postorbital region of the skull; 5. single embayment of the posterior margin of the skull roof; 6. absence of a supraglenoid foramen in the pectoral girdle	(Tsuji and Müller, 2009)
Eureptilia	1. the lack of a postorbital-supratemporal contact in the skull; 2. a narrow iliac blade; 3. a ventral constriction of the dorsal vertebral centra	(Müller and Reisz, 2006)
Diapsida	1. two temporal fenestrae in the skull, 2. a suborbital fenestra in the palate, 3. a contact between the paroccipital process of the opisthotic and the skull roof, 4. a mineralized sternum; 5. a high (0.7 to 0.9) radius/humerus length ratio	(Laurin, 1991)

synapomorphies proposed for the group (Table 1), are equivocal as they depend on the systematic position of mesosaurids, which have been considered either as early-diverging parareptiles (Gauthier et al. 1988b; Modesto 2006; MacDougall et al. 2018), or as the sister-group to all other sauropsids (Laurin & Reisz 1995; Laurin & Piñeiro 2017, 2018).

Eureptiles (or "true reptiles") can be divided into Captorhinidae, 'Protorothyrididae' and Diapsida (Fig. 1), the latter of which includes all or most extant reptiles. Captorhinidae, the first-diverging eureptiles, are known from a series of taxa from the Carboniferous to the Middle Permian, and the subfamily Moradisaurinae from the Late Permian. Lastly, diapsids diversified into Araeoscelidia and Neodiapsida, the latter of which includes a series of small clades with poorly-understood relationships and Sauria, the reptilian crown group (Fig. 1).

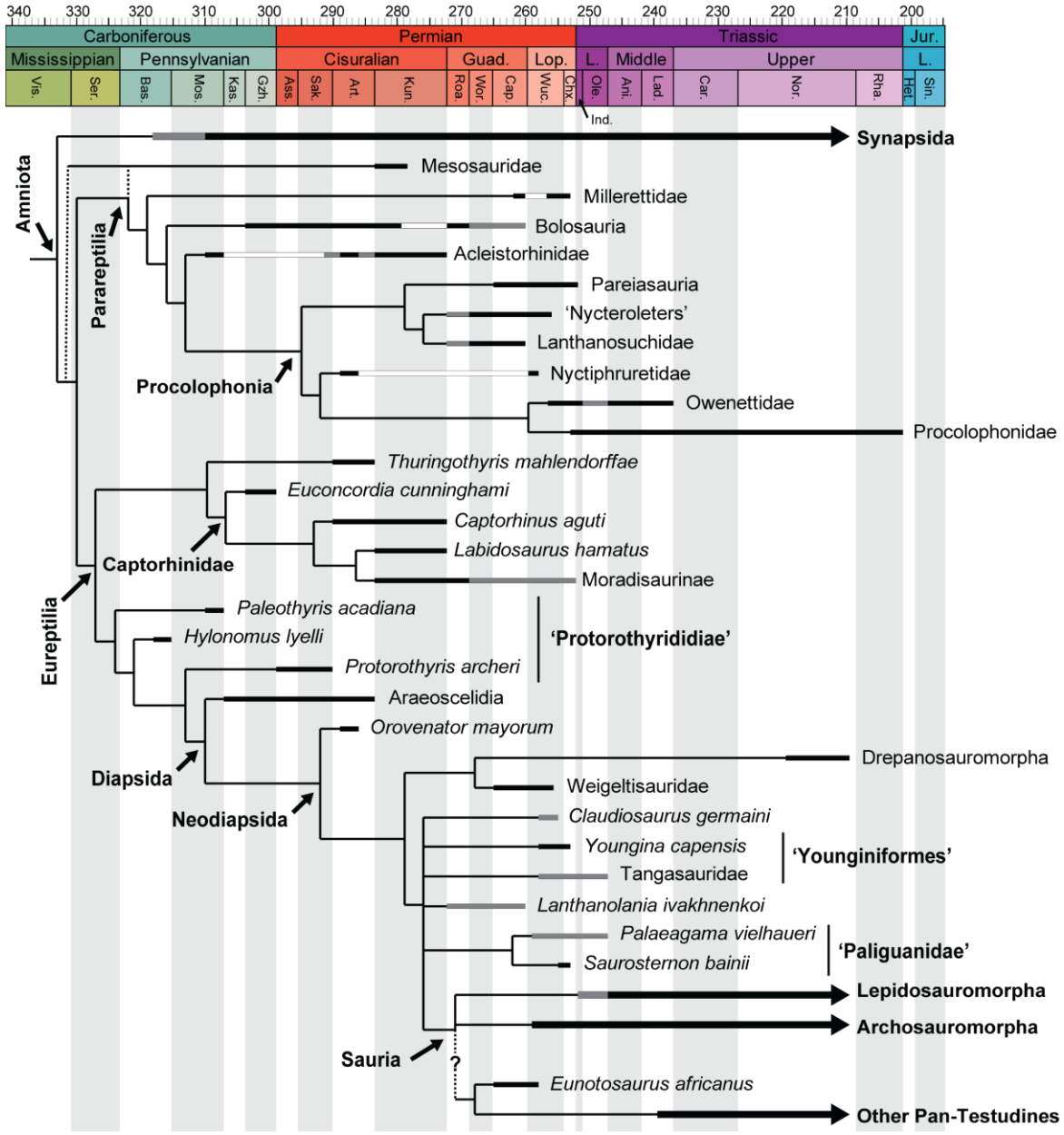

Figure 1-1: Simplified phylogeny of early reptiles mapped onto the Carboniferous-Early Jurassic stratigraphic chart (after Cohen et al. 2020). Topology based primarily on Tsuji and Müller (2009), MacDougall et al. (2019a) and Cisneros et al. (2021) for parareptiles, with Laurin and Piñeiro (2017) for one of the possible positions of mesosaurids, Modesto et al. (2018) for captorhinids, Müller and Reisz (2006) for 'protorothyridids', Evans (1988), Modesto and Reisz (2003), Ezcurra et al. (2014) and Pritchard et al. (2021) for early diapsids, and Bever et al. (2015) for the position of Pan-Testudines. Black bars indicate the stratigraphic distribution of each taxon, grey bars indicate uncertain ages or occurrences and white bars indicate gaps in fossil record; dotted lines indicate uncertain relationships. Internodal branch lengths constant for clarity. Abbreviations: Ani, Anisian; Art, Artinskian; Ass, Asselian; Bas, Bashkirian; Cap, Capitanian; Car, Carnian; Chx, Changhsingian; Gzh, Gzhelian; Het, Hettangian; Ind, Induan; Kas, Kasimovian, Kun, Kungurian; L, Lower; Lad, Ladinian; Mos, Moscovian; Nor, Norian; Ole, Olenekian; Rha, Rhaetian; Roa, Roadian; Sak, Sakmarian; Ser, Serpukhovian; Sin, Sinemurian; Vis, Visean; Wor, Wordian; Wuc, Wuchiapingian.

As a side note, as defined by Gauthier and de Queiroz (2020), Sauria comprises of the common ancestor of lepidosaurs and archosaurs and all of its descendants, and excludes turtles. The smallest clade including lepidosaurs, archosaurs and turtles would be Reptilia (Laurin and Reisz, 2020). While most studies now consider turtles as diapsid reptiles, their systematic position among the latter remains controversial (reviewed in Lyson & Bever 2020; Schoch & Sues 2020, but see Lichtig & Lucas 2021). Owing to this uncertainty, 'reptiles' are here considered as sauropsids while Sauria is here retained as the reptilian crown-group.

Recent challenges

The phylogenetic relationships described above represent the views expressed in a majority of recent studies, including two controversial points. However, several recent works have discussed the composition of Amniota (e.g. Berman 2013; Pardo et al. 2017; Klembara et al. 2020) and of Sauria (e.g. Ezcurra 2016; Scheyer et al. 2017; Simões et al. 2018), both of which are out of the scope of this chapter. Concerning 'traditional' early amniotes, Ford and Benson (2020) recently recovered the Varanopidae (previously considered as eupelycosaurian synapsids, Romer & Price 1940; Reisz 1986; Benson 2012), and parareptiles as successive sister-groups to neodiapsids (Fig. 2), echoing previously discussed inconsistencies in early amniote phylogeny (Laurin & Piñeiro 2017, 2018; MacDougall et al. 2018; Ford & Benson 2019).

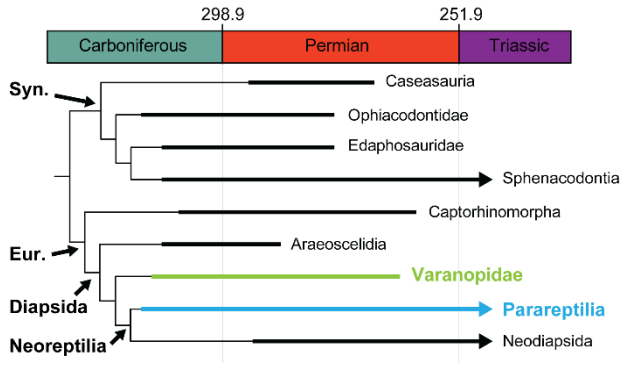

Figure 1-2: Simplified phylogeny of early amniotes illustrating the recent hypotheses placing the Varanopidae and Parareptilia inside Diapsida (see text). Black Bars indicate the stratigraphic distribution of each taxon. Abbreviations: Eur, Eureptilia; Syn, Synapsida.

Despite some counter-arguments (MacDougall et al. 2018; Maddin et al. 2020; Benoit et al. 2021), these hypotheses warrant discussion as they provide an alternative phylogeny of early amniotes after decades of relative stability. In particular, the removal of varanopids, which

have an extensive fossil record spanning from the Moscovian of North America to the Capitanian of South Africa (Maddin et al. 2020; Day & Rubidge 2020), from Synapsida would strongly impact our understanding of terrestrial ecosystems and synapsid faunal turnover in the Permian (Brocklehurst 2021). Lastly, these hypotheses pave the way for novel studies of character evolution in early amniotes (Ford & Benson 2020; Benoit et al. 2021).

The evolution of Paleozoic reptiles

The fossil record of Paleozoic reptiles is sparse compared with that of coeval temnospondyls and synapsids, which successively dominated the Carboniferous and Permian ecosystems (Sahney et al. 2010a; although see Brocklehurst 2021). However, parareptiles and captorhinids, due to their more robust skeleton, are represented by relatively abundant and complete remains (Verrière et al. 2016; MacDougall et al. 2017), allowing for a broad overview of the fossil record, diversity and evolution of Paleozoic reptiles.

Late Carboniferous

Reptiles appear in the fossil record in the Late Carboniferous, as attested by *Hylonomus* from the Bashkirian of Nova Scotia (Carroll 1964), and several slightly younger 'protorothyridids' (Carroll 1969b; Carroll & Baird 1972). Representatives of all major reptile clades are also present in this period (Table 2), with parareptiles appearing in the late Moscovian, diapsids in the Kasimovian, and captorhinids in the Gzhelian (Reisz 1981; Müller & Reisz 2005; Mann et al. 2019). As for other amniotes, it has been proposed that the collapse of rainforests in the late Moscovian-early Kasomovian drove the diversification of early reptiles through habitat reduction and increased endemism (Sahney et al. 2010b), and/or through increased dispersion in the more open habitats of the Gzhelian (Dunne et al. 2018; Brocklehurst et al. 2018).

All of these reptiles comprise small carnivorous forms (Fig. 3J-K) representing minor components of the temnospondyl-dominated ecosystem of the time, with one diapsid taxon also showing adaptations to a semi-aquatic lifestyle (deBraga & Reisz 1995). Synapsids overcame reptiles in diversity during the Gzhelian, with a two-to-one ratio of described species by the end

of the Carboniferous Period, and included some of the largest carnivores and herbivores of the time. However, this difference may be exacerbated by a preservation bias and phylogenetic uncertainty (Modesto et al. 2015; Brocklehurst 2021).

Table 1-2: Taxonomic diversity and Stratigraphic range of Paleozoic reptile groups (see text).

Taxon	Valid species	Stratigraphic range	Repartition
Mesosauridae	3 genera, 3 species	early Kungurian	Gondwana
Millerettidae	4 genera, 5 species	Capitanian -early Changhsingian	South Africa
Bolosauria	4 genera, 8 species	Gzhelian – early Capitanian	Laurasia
Acleistorhinidae	6 genera, 8 species	late Moscovian - Kungurian	Western Pangea
Lanthanosuchidae	3 genera, 5 species	Roadian - early Capitanian	Russia
'Nycteroleters'	5 genera, 7 species	Roadian - late Capitanian/early Wuchiapingian	Russia, North America, South Africa
Pareiasauria	> 15 genera, > 20 species	Capitanian - Changhsingian	Cosmopolitan
Owennettidae	5 genera, 6 species	Wuchiapingian - Ladinian	Cosmopolitan
Procolophonidae	> 30 genera, ~ 40 species	late Changhsingian - Rhaetian	Cosmopolitan
Captorhinomorpha	> 15 genera, > 20 species	Gzhelian - early Wuchiapingian (?Changhsingian)	Cosmopolitan
'Protorothyrididae'	6 genera, 8 species	late Bashkirian - Asselian/Sakmarian	Laurasia
Araeoscelidia	6 genera, 7 species	Kasimovian - Artinskian	
'Younginiformes'	6 genera, 6 species	Wuchiapingian - Early Triassic	Gondwana
Weigeltisauridae	4 genera, 5 species	late Capitanian - Wuchiapingian	Eastern Pangea
Drepanosauromorpha	8 genera, 10 species	late Carnian/early Norian - late Norian/early Rhaetian	Laurasia
Lepidosauromorpha	—	Early Triassic - present	Cosmopolitan
Archosauromorpha	—	Wuchiapingian - present	Cosmopolitan

Early Permian

The Asselian and Sakmarian stages of the Early Permian of Laurasia are populated mainly by bolosaurian parareptiles, small carnivorous captorhinids, araeoscelidians and the last 'protorothyridids' (Clark & Carroll 1973; Falconnet 2012, 2014; Brocklehurst 2017). Most taxa represent small predators, although araeoscelidians and bolosaurians both exhibit a strikingly gracile skeleton, with the latter also showing adaptations to high-fiber herbivory (Fig. 3C; Reisz 1981; Reisz & Sues 2000).

The following Artinskian and Kungurian stages show an increased diversification of reptiles in Laurasia. In particular, they record the evolution of high-fiber herbivory in captorhinids, with the appearance of omnivores in the Artinskian and that of moradisaurine herbivores with multiple tooth rows and propalinal jaws in the Kungurian (Fig. 3H-I; Brocklehurst 2017). This diversification is beautifully recorded in exceptional localities in the Artinskian of Laurasia, which also highlight the diversification of small parareptilian predators such as acleistorhinids and nyctiphruretids, and the first occurrence of occasional bipedality among bolosaurians (MacDougall et al. 2017, 2019b; Berman et al. 2021; Brocklehurst 2021). In contrast, the fossil record of diapsids is sparse in these stages, recording the last occurrence of araeoscelidians and only two occurrences of neodiapsids in the Artinskian (Reisz et al. 2011; Ford & Benson 2019; but see above).

The Gondwanan record of Early Permian reptiles mostly comprises mesosaurids (Fig. 3A). These aquatic animals are abundant in the early Kungurian of southern Africa and South America, and rank among the most extensively studied Paleozoic reptiles (e.g. Modesto 2006, 2010; Piñeiro et al. 2012; Silva et al. 2017), yet their systematic position remains uncertain (Fig. 1). However, barring mesosaurids, there are extremely few Gondwanan reptiles, with only a few occurrences reported in Brazil (Cisneros et al. 2020, 2021).

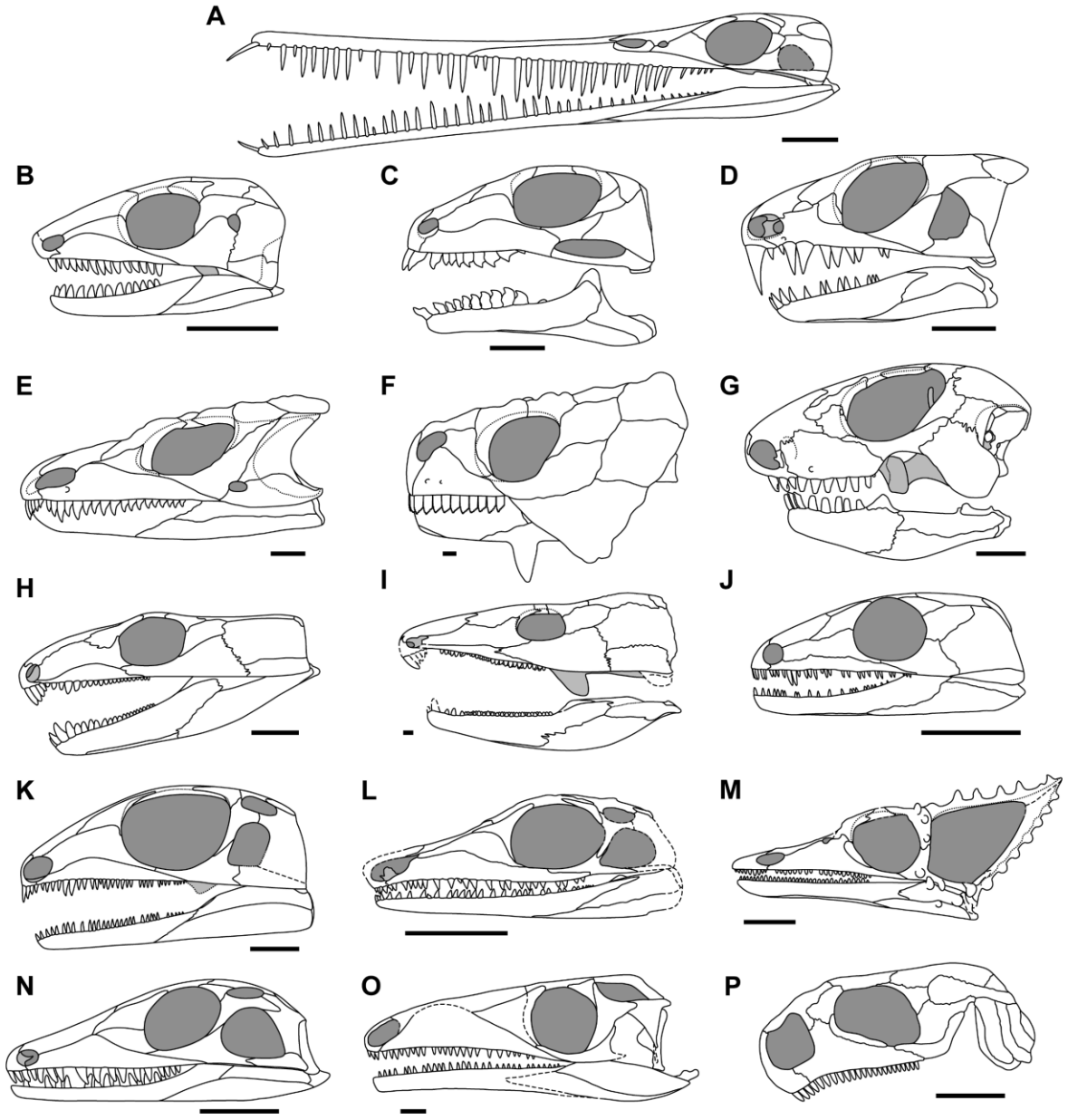

Figure 1-3: Line drawings of selected reptile skulls in left lateral view illustrating the disparity of the clade. (A) the mesosaur *Mesosaurus tenuidens* (redrawn and modified from Modesto, 2006 and Piñeiro et al., 2012a). (B) the bolosaurid *Belebey vegrandis* (redrawn from Reisz et al. 2007). (C) the millerettid *Milleretta rubidgei* (redrawn from Gow 1972). (D) the acleistorhinid *Colobomycter pholeter* (redrawn from MacDougall et al. 2017). (E) the 'nycteroleter' *Macroleter poezicus* (redrawn from Tsuji 2006). (F) the pareiasaur *Deltavjatia rossicus* (redrawn from Tsuji 2013). (G) the procolophonid *Progolophon trigoniceps* (redrawn from Carroll & Lindsay 1985). (H) the captorhinid *Captorhinus laticeps* (redrawn from Heaton 1979). (I) the captorhinid *Labidosaurikos meachami* (redrawn from Dodick & Modesto 1995). (J) the 'protorothyridid' *Paleothyris acadiana* (redrawn from Carroll 1969b). (K) the araeoscelid *Petrolacosaurus kansensis* (redrawn from Reisz 1981). (L) the putative varanopid *Orovenator mayorum* (redrawn from Ford & Benson 2019). (M) the neodiapsid *Weigeltisaurus jaekeli* (redrawn and modified from Bulanov & Sennikov 2015; Buffa et al. 2021). (N) the neodiapsid *Youngina capensis* (Carroll 1981). (O) the archosauromorph *Protorosaurus speneri* (redrawn from Gottmann-Quesada & Sander 2009). (P) the putative stem-turtle *Eunotosaurus africanus* (redrawn from Bever et al. 2015, mandible not reconstructed). Scale bars equal 1 cm.

The Early-Middle Permian transition witnessed the first extinction event of the Permian: Olson's Extinction (alternatively 'Olson's Gap' under different stratigraphic correlation schemes, see Reisz & Laurin 2001; Brocklehurst 2020). This interval records the beginning of the transition between the pelycosaur-dominated ecosystems of the Early Permian to the therapsid and parareptile-dominated ones of the Middle Permian (Sahney & Benton 2008; Brocklehurst et al. 2017; Brocklehurst 2020; Didier & Laurin 2021). While parareptiles do not show a decline in diversity or disparity during this interval, captorhinids seem to be severely affected, with extinction rates similar or higher than those of the end-Permian extinction event (Brocklehurst et al. 2015; Brocklehurst 2017).

Middle Permian

Following the transition to new ecosystems in the wake of Olson's Extinction, the Middle Permian is characterized by a progressive increase in diversity of reptiles, and an abundance of herbivorous taxa in general (Brocklehurst 2020; Brocklehurst & Benson 2021).

The diversity of parareptiles in the Roadian is only recorded in Laurasian deposits, in particular in the Mezen faunal assemblage of Russia (Olroyd & Sidor 2017; Sennikov & Golubev 2017; Schneider et al. 2020), which comprises some of the aquatic lanthanosuchids, and almost all known 'nycteroleters', the first reptiles with a tympanic middle-ear (Fig. 3E; Müller & Tsuji 2007). The parareptilian fossil record of the Wordian Ocher and Isheevo assemblages of Russia likely records the last occurrences of bolosaurians (Sennikov & Golubev 2017). Similarly, the fossil record of eureptiles seems to be relatively poor in the early Middle Permian, and there are no occurrences that are well-constrained within the Roadian-Wordian interval in Gondwana (Brocklehurst 2017; Cisneros et al. 2020).

In contrast, the Gondwanan record of reptiles is abundant in the Capitanian, indicating that several groups attained a cosmopolitan distribution. Among those are the large-sized moradisaurine captorhinids (Brocklehurst et al. 2015; Brocklehurst 2017), and pareiasaurs, the first known giant armored megaherbivores, which appeared at the beginning of the Capitanian (Fig. 3.F; Lee 1997a; Day & Rubidge 2020). The first millerettid parareptiles and the putative stem-turtle *Eunotosaurus* were also present in southern Africa by that stage (Fig. 3.B, P; Day & Rubidge 2020; Day & Smith 2020).

The Middle Permian fossil record of diapsids is extremely sparse (although see above), with only a single definitive occurrence of a neodiapsid reported from the Mezen faunal assemblage of Russia (Modesto & Reisz 2003; Ezcurra et al. 2014), and the first gliding weigeltisaurids reported from the younger Sundyr assemblage (late Capitanian, Sennikov & Golubev 2017). In light of this poor fossil record, previous studies have suggested that the first neodiapsids diversified in upland environments with a low preservation potential, leading to a poor understanding of the evolution of the group in the Early-Middle Permian (Bulanov & Sennikov 2010; Reisz et al. 2011).

The Middle-Late Permian transition is marked by a relatively poorly understood second extinction event. It records the extinction of dinocephalian therapsids, which may have favored dicynodonts (Sahney & Benton 2008), and that of several reptilian taxa such as the putative stem-turtle *Eunotosaurus* (Day & Rubidge 2021).

Late Permian

Reptiles appear to reach their maximum Paleozoic diversity and disparity in the Late Permian, with millerettids, pareiasaurs and moradisaurine captorhinids reaching their maximum diversity. Several new taxa also appear in the Wuchiapingian, such as procolophonoid parareptiles, various neodiapsids and crown-group reptiles. Procolophonoidea is the second major parareptilian group (Fig. 3F), and the only one to survive the Permo-Triassic mass extinction, which appeared to have a relatively minor effect on their diversity (Botha et al. 2007).

Neodiapsids are much better represented in the Lopingian (Fig. 1), with numerous occurrences from Laurasia and Gondwana indicating a large distribution of the group (Bulanov & Sennikov 2010; Ezcurra et al. 2014). Stem-saurian diapsids flourished in the Lopingian with the appearance and diversification of several taxa such as the terrestrial to semi-aquatic ‘paliguanids’ and ‘younginiforms’, the enigmatic semi-aquatic *Claudiosaurus*, or the chamaeleon-like arboreal and gliding weigeltisaurids (Fig. 3L-N; Gow 1975; Carroll 1981; Currie 1981; Pritchard et al. 2021; Buffa et al. 2021). Among those, at least the ‘younginiforms’ are known to extend into the Early Triassic (Harris & Carroll 1977; Ketchum & Barrett 2004). Furthermore, the Late Triassic arboreal drepanosauromorphs have recently been recovered as

stem-saurian reptiles closely related to the gliding weigeltisaurids, which implies a ghost-lineage from the Cisuralian to the Middle Triassic (Fig. 1; Senter 2004; Pritchard & Nesbitt 2017; Pritchard et al. 2021).

In contrast, Paleozoic crown-group reptiles remain poorly known, represented by several putative occurrences of incomplete specimens and a single well-known taxon, the early archosauromorph *Protorosaurus speneri* from the middle Wuchiapingian of Germany and England (Ezcurra et al. 2014). These animals are thus considered to have remained minor components of Permian ecosystems (Ezcurra & Butler 2018).

Triassic

The Permo-Triassic mass extinction had a profound impact on reptilian diversity, with only procolophonid parareptiles, some 'younginiforms' and crown-group reptiles extending beyond this boundary (Fig. 1). While 'younginiforms' are not known beyond the Early Triassic, procolophonoid and saurian reptiles diversified during this Period. The Triassic procolophonids were highly diverse and over 40 species are currently recognized (Cisneros & Ruta 2010). Some possess molariform, bicuspid teeth suggestive of high-fiber herbivory or durophagy (Reisz & Sues 2000) and exhibit sharp cranial spikes and frills (Fig. 2G). The group declined during the Late Triassic and became extinct at the end of the Rhaetian (Ruta et al. 2011; MacDougall et al. 2019b).

The origin of Sauria

Crown-group reptiles thus appear in the fossil record in the Late Permian, and can be diagnosed by a series of characters (see Laurin 1991). Among those, two have long been suggested as key characters to understand the origin of the group: the tympanic ear and the hooked fifth metatarsal.

The temporal skull bones are tightly sutured in early reptiles (despite a gradual loosening of the squamosal-quadrate contact in neodiapsids; Fig. 3) and the skull lacks a temporal emargination, indicating that a tympanum is absent (Sobral et al. 2016). The stapes is also a

robust bone bracing the skull in most of those taxa. In contrast, most known lepidosauromorphs and archosauromorphs show a tympanic middle-ear, with a robust, bracing paroccipital process instead of the slender stapes, and with a quadrate crest that likely housed the tympanum (Evans 2016; Sobral & Müller 2016). Several parareptiles acquired an analogous ear in which the tympanum was supported by an emargination of the quadratojugal and squamosal (Fig. 3), indicating that a tympanic middle-ear appeared at least twice in the evolutionary history of reptiles, in parareptiles and saurian diapsids (Müller & Tsuji 2007; Sobral et al. 2016).

Early reptiles show a progressively more strongly integrated foot, ranging from the broadly divergent digits of captorhinids to the slightly overlapping ones of diapsids (Heaton & Reisz 1986; Lee 1997b). All stem-saurians retain a straight, rod-like fifth metatarsal, although several neodiapsids lack a distal tarsal five and show a strong outer process as is typical in saurian reptiles (Goodrich 1942; Harris & Carroll 1977). Nearly all early saurian reptiles show a hooked fifth metatarsal which functions as an analogue to the heel bone of mammals and is typically considered a synapomorphy of the group (Robinson 1975; Laurin 1991; Lee 1997b; Borsuk-Białynicka 2018).

As a side note, while extant turtles possess a tympanic ear, early turtles did not (Sobral et al. 2016). Moreover, Joyce et al. (2013) cast doubt on the homology between the ‘hooked element’ in the pes of turtles and the fifth metatarsal of other saurians. As most studies recover turtles as diapsid reptiles (but see Lichtig & Lucas 2021), this would indicate that both characters described above had a much more complex evolutionary history. Nevertheless, both remain reliable for phylogenetic reconstruction and are paramount to our understanding of the ecology and functional morphology of early crown-group reptiles.

Conclusion

Parareptilia, Eureptilia and Diapsida, appear in the fossil record in the late Carboniferous. The first reptiles were small predators representing minor components of the temnospondyl-dominated ecosystems of the time. Small herbivores, occasional bipeds and semi-aquatic taxa were already present in the Early Permian, and the Middle Permian saw the appearance of large sized cosmopolitan megaherbivores. This diversification continued into the Late Permian, with the appearance of several terrestrial, semi-aquatic, arboreal and gliding taxa.

Furthermore, the Late Permian records the appearance of crown-group reptiles, and the evolution of several key characters that are paramount to our understanding of the evolution of extant faunas. Lastly, previous ideas about early amniote phylogeny have recently been challenged, thus paving the way for future studies of the evolution of these poorly-known animals.

Chapter 2: A new cranial reconstruction of *Coelurosauravus elivensis* Piveteau, 1926 (Diapsida, Weigeltisauridae) and its implications on the paleoecology of the first gliding vertebrates

The present chapter has been published as a research article (Buffa et al., 2021) in the *Journal of Vertebrate Paleontology*, co-authored with E. Frey (SMNK), J.-S. Steyer (MNHN), and M. Laurin (MNHN).

Abstract—The cranial skeleton of the enigmatic gliding neodiapsid reptile *Coelurosauravus elivensis* (Lower Sakamena Formation, Lopingian, Southwestern Madagascar) is re-described in detail. All previously referred specimens are re-examined under both direct observations and Reflectance Transformation Imaging. Their exquisite preservation yields detailed three-dimensional information on the outline of individual bones and their osteological relationships, which are missing in the Laurasian remains. In contrast to previous studies, the ontogenetic maturity of all specimens is re-affirmed. Previously unidentified elements of the palate, braincase and mandible are described, and a novel reconstruction is proposed, including the first palatal reconstruction in a weigeltisaurid reptile. *C. elivensis* has the smallest skull of all weigeltisaurids and differs from other species in its facial ornamentation, parietosquamosal frill and larger anterior maxillary dentition. We also provide extensive comparisons with contemporaneous reptiles, possibly closely related taxa and more recent analogs, as well as a preliminary discussion of the functional anatomy of the peculiar cranial morphology of weigeltisaurids. The cranial skeleton is a truss construction with large orbits and temporal fenestrae. By analogy with extant chamaeleonids, the elongate parietosquamosal frill is associated with an increase in length and diameter of the temporal jaw adductors, resulting in an increased gape and/or bite force and speed. Additionally, the spikes and frills of weigeltisaurids most likely served as a display and defensive structure.

Introduction

Diapsids were the most conspicuous components of tetrapod diversity during the Mesozoic Era. Despite being rare elements of the preceding late Paleozoic fossil record (Modesto and Reisz, 2003; Reisz et al., 2011; Sues, 2019), early diapsids show a conspicuous morphological disparity, with well-recorded terrestrial, semi-aquatic and aerial taxa (Carroll, 1975, 1978, 1981; Gow, 1975; Currie, 1981). Among those, the Lopingian Weigeltisauridae were the first amniotes to use aerial gliding locomotion (Carroll, 1978; Evans, 1982; Bulanov and Sennikov, 2015a-c) and are a key group to understand the range of alternative adaptations for gliding flight in amniotes.

Weigeltisaurids include several taxa known from either Laurasia or Gondwana (Bulanov and Sennikov, 2015a-c): *Weigeltisaurus jaekeli* (Weigelt, 1930a) (Lopingian, Germany and England), *Coelurosauravus elivensis* Piveteau, 1926 (Lopingian, Madagascar), *Glaurung schneideri* Bulanov and Sennikov, 2015c (Lopingian, Germany), *Rautiania alexandri* Bulanov and Sennikov, 2006 (Lopingian, Russia) and *Rautiania minichi* Bulanov and Sennikov, 2006 (Lopingian, Russia). *Wapitisaurus problematicus* Brinkman, 1988 (Early Triassic, Canada), known from a poorly preserved skull, has been interpreted as a weigeltisaurid but this attribution is doubtful (Bulanov and Sennikov, 2010). Therefore, this taxon will not be further considered here, pending its systematic revision.

The peculiar cranial anatomy of weigeltisaurids has been subject to a lot of attention since the description of *Coelurosauravus* (Piveteau, 1926), and there have been numerous controversies on their cranial osteology (Carroll, 1978; Evans, 1982; Evans and Haubold, 1987; Schaumberg et al., 2007). However, recent studies by Bulanov and Sennikov (2015a-c) and the discovery of numerous isolated three-dimensional weigeltisaurid remains in the Permian of Russia (Bulanov and Sennikov, 2006, 2010, 2014) have led to a better understanding of the comparative anatomy within the group.

Historically, weigeltisaurids were first informally considered as pterosaurs (Weigelt, 1930a:626), and have since been considered as dinosaur relatives (Boule, 1910; Piveteau, 1926), rhynchocephalians (Weigelt, 1930a), early ("pelycosaur-grade") synapsids (Kuhn, 1939) or stem-saurians (Huene, 1956; Carroll, 1978; Evans and Haubold, 1987; Laurin, 1991). Recent phylogenetic analyses, however, recover weigeltisaurids as close relatives of saurians

(e.g., Ezcurra et al., 2014; Schoch and Sues, 2018a; Pritchard and Sues, 2019; Sobral et al., 2020) with some recovering a close relationship to either drepanosauromorphs (Merck, 2003; Senter, 2004; Pritchard et al., in press) or 'paliguanids' (Müller, 2004).

However, previous descriptions lack comparisons to a broad array of taxa and a phylogenetic context. The anatomy of weigeltisaurids is unique in many aspects, and detailed comparisons with contemporaneous reptiles, potentially closely related taxa, and both extinct and extant analogs is paramount to better understand the morphology, paleoecology and evolution of these enigmatic gliding reptiles. This study aims at describing novel details on the skull of weigeltisaurids, with a focus on the material of *Coelurosauravus* from the Lopingian of Madagascar.

Institutional Abbreviations—**MNHN**, Muséum national d'Histoire naturelle, Paris, France; **SMNK**, Staatliches Museum für Naturkunde Karlsruhe, Karlsruhe, Germany; **SSWG**, Sektion Geologie, Ernst-Moritz-Arndt Universität, Griefswald, Germany.

Geological background

Age and Provenance—All specimens described here come from the upper beds of the Lower Sakamena Formation (southwestern Madagascar), currently considered as Wuchiapingian in age (Piveteau, 1926; Currie, 1981; Hankel, 1994; Lucas, 2017). These specimens were collected in 1907-1908 by J.-M. Colcanap, a captain of the French colonial infantry, and are among the first vertebrate remains to be collected from this formation. The exact locality is unknown, but it is likely in the vicinity of Mount Eliva, near the upstream portion of the Sakamena River. A comprehensive review of the first excavations of Colcanap and the provenance of this material is currently underway by the lead author (VB, unpubl. data). Therefore, a geological section cannot be presented at the current state of investigation.

Most studies agree on the continental nature of these deposits (e.g., Besairie, 1972; Smith, 2000). During the Lopingian, the faunal and floral community preserved in the Lower Sakamena Formation inhabited a wetland area in a roughly North-South running rift valley under a temperate, warm and humid climate, with seasonal rainfalls and possible monsoons (Besairie, 1973; Wescott and Diggens, 1998; Smith, 2000).

Preservation—All specimens referred to *C. elivensis* are preserved in very fine-grained nodules formed by concentric precipitation around the entire trunk region (Fig. 1, Supplemental Data 1), as described for other Malagasy Permian reptiles (Smith, 2000). These nodules are split along their greatest diameter mostly along the coronal plane of the skeleton, each half of the split nodule exposing either the ventral or dorsal aspect. All specimens consist of skeletal remains preserved in connection, but most of the bones have been eroded, possibly further removed by etching (Fig. 1). Thus, only the external mold of the bones is preserved. The nodular matrix has a light brown color, but in some cases, the external molds of the bones are dark grey, likely evidence of recent bone removal.

Figure 2-1: *Coelurosauravus elivensis* Piveteau, 1926 (Madagascar, Lopingian), lectotype MNHN.F.MAP325a. Dorsal surface of individual preserved as a natural external mold. Scale bar equals 5 cm.

Despite missing bone, the material from Madagascar bears information on the 3D outline of individual bones and their anatomical arrangement. Anatomical details were observed using silicone casts (1 µm resolution). The study of this material thus brings key 3D anatomical information, which is absent in the compacted specimens from western Europe (*Glaurung*, *Weigeltisaurus*, Frey et al., 1997; Schaumberg et al., 2007; Bulanov and Sennikov, 2015b-c)

and in the isolated bones from eastern Europe (*Rautiania*, Bulanov and Sennikov, 2006, 2010), where the anatomical arrangement is missing.

Table 2-1 Denominations and identifications of previously published specimens referred to the genera *Coelurosauravus* and *Weigeltisaurus* with preserved cranial remains.

Specimen denomination	Identification	Material examined	Remarks
MNHN.F.MAP325a	*Coelurosauravus elivensis* (Lectotype)	MNHN.F.MAP325a	Patrimonial number 1908-11-21a
MNHN.F.MAP317a-b	*Coelurosauravus elivensis* (Paralectotype)	MNHN.F.MAP317a-b	Patrimonial number 1908-11-22a-b
MNHN.F.MAP327a-b	*Coelurosaravus elivensis*	MNHN.F.MAP327a-b	Patrimonial number 1908-5-2
SSWG 113/7	*Weigeltisaurus jaekeli* (Holotype)	SMNK-PAL 34899a (cast)	-
Ellrich specimen	*Weigeltisaurus* sp.	SMNK-PAL 2882	Counterpart in anonymous private collection
Wolfsberg specimen	*Weigeltisaurus* sp.	SMNK-PAL 34910 (cast)	Specimens in Munk private collection, currently being transferred to the Naturkundemuseum im Ottoneum, Kassel

Material and Methods

Material—All specimens previously referred to *Coelurosauravus elivensis* were examined. Original specimens or high-fidelity epoxy resin casts of specimens previously referred to *Weigeltisaurus* were also studied for comparative purposes (Table 1).

Taxonomic Remarks—Most European weigeltisaurid specimens have previously been attributed to *Coelurosauravus*, with *Weigeltisaurus* being considered a subjective junior synonym at the time (Evans and Haubold, 1987). More recently, *Coelurosauravus* was restricted to the specimens from Madagascar (Bulanov and Sennikov, 2015a) and *Weigeltisaurus* was re-established as a valid taxon, based on SSWG 113/7, the holotype of *Weigeltisaurus jaekeli* (Bulanov and Sennikov, 2015b). Bulanov and Sennikov (2015b:1110) also tentatively and informally refer all German specimens to *Weigeltisaurus* sp. (explicitly not

to the species *Weigeltisaurus jaekeli*) with evidence only being given for the Ellrich specimen SMNK-PAL 2882. However, there was no mention of the British specimen, which thus remains of unclear attribution. All German and British material lacking cranial material can not be identified more precisely than to Weigeltisauridae because most diagnostic characters are cranial. Furthermore, as was argued by Haubold and Schaumberg (1985:194), *Gracilisaurus ottoi* Weigelt, 1930b, considered as a junior subjective synonym of *Weigeltisaurus jaekeli* by Evans and Haubold (1987), instead has priority provided both taxa are synonyms (Weigelt, 1930a:675, 1930b:279). A re-examination of *G. ottoi* is thus needed to reassess this synonymy.

Because of this uncertainty, and in accordance with Schaumberg et al. (2007; Table 1), we restrict the use of the species name *Weigeltisaurus jaekeli* to the holotype only. All other German and British specimens are referred to by their collection numbers and housing institution name or locality reference. In addition, previous studies refer to the *C. elivensis* material using patrimonial numbers, although the MNHN collections have more recent MNHN.F.MAP designations for the Malagasy Permian collection. We favor the latter and provide correspondence with the previously used patrimonial numbers (Table 1). Lastly, in the absence of articulated material from eastern Europe, we refer to individual specimens in open nomenclature as *Rautiania* sp. following the use of Bulanov and Sennikov (2010).

Reflectance Transformation Imaging (RTI)—The individual bones are often jumbled and thus difficult to identify in the Malagasy material. RTI is a method that computes a single ‘interactive specimen’ on which the illumination can be oriented at will (Hammer et al., 2002). This method was used in order to compensate for the nature of preservation of the specimens, using a custom-made portable light dome (an updated version of that used in Béthoux et al., 2016; Cui et al., 2018). Sets of 54 photographs under different LED sources were compiled using the RTIBuilder software. The resulting RTI files provided in Supplemental Data 1 can be opened using the software RTIViewer (both softwares are freely available at www.culturalheritageimaging.org). As a result, this study is one of the first usages of RTI to study fossil vertebrate specimens.

Systematic Paleontology

NEODIAPSIDA Benton, 1985 sensu Reisz, Modesto and Scott, 2011

WEIGELTISAURIDAE Kuhn, 1939

COELUROSAURAVUS ELIVENSIS Piveteau, 1926

Daedalosaurus madagascariensis Carroll, 1978:149, figs. 5-7.

Lectotype—MNHN.F.MAP325a (Fig. 1), external mold of the dorsal surface of a partially preserved specimen (Piveteau, 1926:pl.17-1; Carroll, 1978:fig. 2; Evans, 1982:fig. 16B; Evans and Haubold, 1987:figs. 3B, 13C, 16B, D, 17; Bulanov and Sennikov, 2015a:pl.5-1b).

Paralectotype—MNHN.F.MAP317a-b (part and counterpart), external mold of the ventral surface of a partially preserved specimen preserved on two slabs (Piveteau, 1926:pl.17-3; Carroll, 1978:fig. 3; Evans, 1982:figs. 15-16A; Evans and Haubold, 1987:figs. 3A, 13A-B; Bulanov and Sennikov, 2015a:pl.5-2).

Referred Material—MNHN.F.MAP327a-b, external mold of a sub-complete specimen preserved on two slabs (Carroll, 1978:figs. 5-7; Evans, 1982:figs. 14, 17-18; Evans and Haubold, 1987: figs. 4-5, 12, 14-15A, 21).

Type Horizon—Top of the Lower Sakamena Formation, Lopingian.

Type Locality—Sakamena River, upstream region, exact location unknown, Southwestern Madagascar.

Emended Diagnosis (Modified from Evans and Haubold, 1987)—Maxillary teeth with symmetrical apices; anterior maxillary teeth significantly larger than mid-/posterior teeth; anterior and dorsal jugal processes subequal (shared with *Rautiania*); ornamented dorsal jugal process; parietal posttemporal process uniform in width (shared with *Glaurung*); tubercles on parietal posttemporal process (shared with *Glaurung*).

Remarks—Piveteau (1926) first described this taxon based on both MNHN.F.MAP325a and MNHN.F.MAP317a without designating a holotype. Carroll (1978) later designated MNHN.F.MAP325a as the "type" (Carroll, 1978:144), which was later considered as the holotype by Evans (1982) and Evans and Haubold (1987). Following the designation of Carroll (1978) among the two syntypes of Piveteau (1926), and in accordance with the International Code of Zoological Nomenclature (ICZN, 1999, article 74.5), MNHN.F.MAP325a is here considered as the lectotype of *Coelurosauravus elivensis*. In addition, MNHN.F.MAP317b, counterpart of the paralectotype MNHN.F.MAP317a first described by Piveteau (1926) is also considered as a paralectotype.

We do not follow the diagnosis of Evans and Haubold (1987), which was erected for an assemblage of both *Coelurosauravus* and *Weigeltisaurus* specimens, the latter at that time having been considered as a junior subjective synonym of the former. This diagnosis would be better adapted for the family Weigeltisauridae, which is currently under review by the authors.

Osteological redescription

The material of *Coelurosauravus* allows for an almost complete examination of the skull (Fig. 2). The individual bones and sutures are hard to identify in the lectotype due to late diagenetic compression, but are readily visible in the similarly preserved MNHN.F.MAP317b (Figs. 3, 4A-B). In addition, MNHN.F.MAP317a preserves several slightly compressed bones of the palate and braincase that previously had not been identified (Fig. 4C-D). MNHN.F.MAP327b shows several exquisitely preserved bones, with a portion of the right side of the skull roof preserved in natural arrangement in internal view, and other scattered bones from the left side, palate and posterior skull bones (Fig. 5). Due to its exquisite preservation, this specimen has played a key role in previous studies and reconstructions of the skull of *Coelurosauravus* (Bulanov and Sennikov, 2015a:414).

Our detailed examination of all known specimens of *Coelurosauravus* resulted in a new reconstruction of the skull for this taxon (Fig. 2). Most of our interpretations agree with those of Bulanov and Sennikov (2015a:fig. 3) but some significant differences are discussed below.

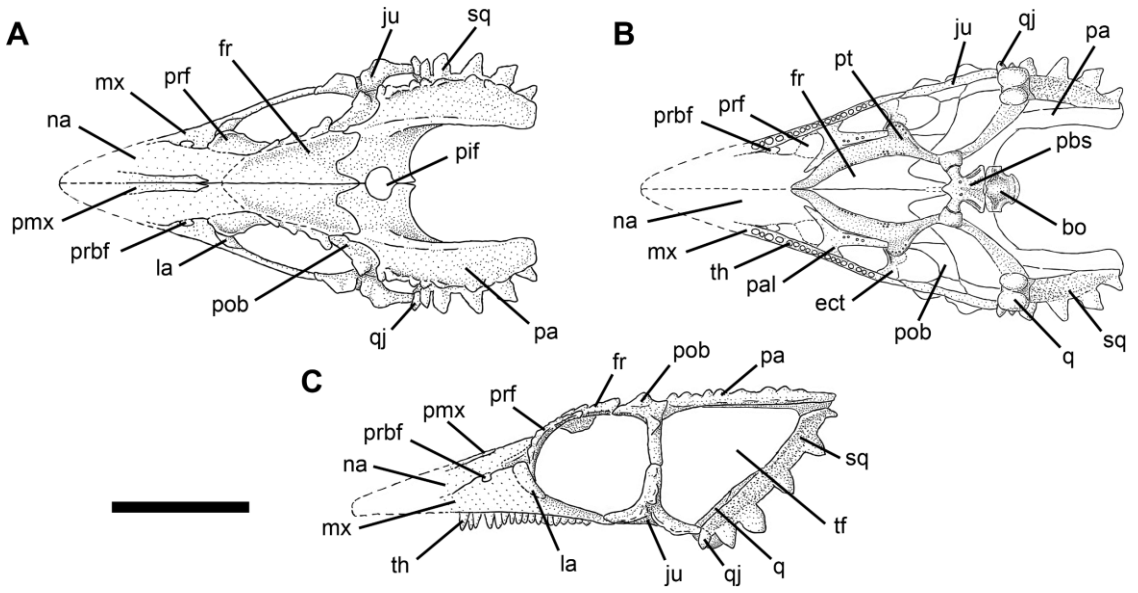

Figure 2-2: *Coelurosauravus elivensis* Piveteau, 1926 (Madagascar, Lopingian), skull reconstruction based on all referred specimens. Poorly known or unpreserved elements outlined by dashed lines. **A**, dorsal view; **B**, ventral view; **C**, left lateral view. **Abbreviations**: **bo**, basioccipital; **ect**, ectopterygoid; **pif**, pineal foramen; **fr**, frontal; **ju**, jugal; la, lacrimal; **mx**, maxilla; **na**, nasal; **pa**, parietal; **pal**, palatine; **pbs**, parabasisphenoid; **pif**, pineal foramen; **pmx**, premaxilla; **pob**, postorbital; **prf**, prefrontal; **prbf**, preorbital fenestra; **pt**, pterygoid; **q**, quadrate; **qj**, quadratojugal; **sq**, squamosal; **tf**, temporal fenestra; **th**, tooth. Scale bar equals 1 cm.

Ontogenetic Stage of Specimens

Bulanov and Sennikov (2015a:422) commented on the small size of all *Coelurosauravus* skulls compared to other weigleltisaurids, and interpreted these specimens as "juveniles". The reconstructed skull length for *Coelurosauravus* is indeed just ca. 35 mm (Table 2), which is about half of the relative size of that of the *Weigeltisaurus* holotype, *Glaurung*, and *Rautiania* (ca. 60 mm, Table 2; Bulanov and Sennikov, 2010, 2015a-c), and is also significantly smaller than that of the Ellrich specimen (ca. 50 mm, Table 2). Their hypothesis is also supported by the tubercular parietal ornamentation of *Coelurosauravus*, which, in *Rautiania*, is characteristic of immature individuals, while mature ones bear parietal spikes (Bulanov and Sennikov, 2015a).

Table 2-2: Skull measurements of weigeltisaurids. *measurements based on reconstructions; [1]measurements from Bulanov and Sennikov (2015b).

Measurements (mm)	*Coelurosauravus* (Fig. 1)	*Weigeltisaurus* (holotype)	Ellrich specimen SMNK-PAL 2882
Total skull length	35.63*	57.33	50.78
Basal skull length	27.96*	42[1]	32.85
Postorbital skull height	10.43*	-	-
Skull width (quadrate articulation)	17.96*	-	-
Orbit diameter	8.44*	11.7[1]	9.96
Parietal total length	14.74*	-	23.02
Parietal main body length	5.65*	-	6.49
Interparietal suture length	3.82*	-	4.47
Posttemporal process length	9.09*	18[1]	16.53
Pineal foramen diameter	2.14*	-	2.75
Humerus length	29.9*	34.51	26.11
Measurements (mm)	MNHN.F.MAP325a	MNHN.F.MAP317a-b	MNHN.F.MAP327a-b
Total skull length	-	-	-
Basal skull length	-	-	-
Postorbital skull height	-	-	-
Skull width (quadrate articulation)	-	-	-
Orbit diameter	-	8.34	8.86
Parietal total length	16.21	15.92	14.65
Parietal main body length	5.56	4.96	5.53
Interparietal suture length	-	4.25	3.85
Posttemporal process length	10.65	10.96	9.12
Pineal foramen diameter	-	2.43	2.04
Humerus length	29.04	30.62	30.05

However, our detailed examination of the *Coelurosauravus* specimens and the evaluation of commonly used size-independent criteria to assess ontogenetic maturity in extinct reptiles (recently reviewed in Griffin et al., 2021) do not show any evidence of immaturity. The cranial bones of all *Coelurosauravus* specimens are well-ossified and bear well-defined processes (Figs. 3-5), identical to those of individuals of other weigeltisaurids taxa considered mature by Bulanov and Sennikov (2006, 2010, 2015a-c). In extant saurians, the ossification of cranial bones increases during postnatal ontogeny (e.g. Rieppel, 1992; Maisano, 2002). Thus, completely ossified bones are indicative of maturity (Evans, 2008; Griffin et al., 2021).

The postcranium conforms well with this evaluation. The neurocentral sutures are closed on all specimens, the long bones bear well-ossified epiphyses and processes in all specimens, and all carpal and tarsal bones are present and well-ossified (Fig. 1; Carroll, 1978; Evans and Haubold, 1987). This matches the *Weigeltisaurus* and *Rautiania* specimens considered mature by Bulanov and Sennikov (2010, 2015b). Although the timing of the appearance of these features is variable among extant and extinct saurians (Griffin et al., 2021 and references therein), these characters are commonly used as indicators of morphological maturity in extinct reptiles, in particular in coeval stem-saurians from the Lopingian of Madagascar (Currie, 1981; Currie and Carroll, 1984; Caldwell, 1995).

Conversely, the presence of large orbits and pineal foramen, which are seen in *Coelurosauravus* (Fig. 2), are commonly used as criteria indicating skeletal immaturity (Bhullar, 2012; Griffin et al., 2021). However, as both structures are also present in the larger Ellrich specimen (Table 2) and in the more mature individuals of *Rautiania* (Bulanov and Sennikov, 2006), we do not consider them as indicative of immaturity in weigeltisaurids, at least with regard to currently known specimens.

The parietal posttemporal processes of the lectotype and paralectotype are unornamented, while those of MNHN.F.MAP327b – the *Coelurosauravus* specimen with the shortest parietal bone (Table 2) – bear low tubercles on the medial and lateral margins of the posttemporal process. In extant reptiles, the timing of the appearance of cranial dermal ornamentation is highly variable, appearing at embryonic stages in crocodilians (Vickaryous and Hall, 2008) and chamaeleonids (Rieppel, 1993a), but much later during postnatal development in some other squamates (Evans, 2008; Glynne et al., 2020). The use of this

character to assess maturity is thus highly clade-specific, and this seems to be the case for extinct reptiles as well (Griffin et al., 2021). However, the sculpturing of dermal bones – regardless of the sculpturing type and timing of appearance – generally increases with age in tetrapods (Vickaryous and Hall, 2008; Witzmann et al., 2010; Buffrénil et al., 2015, 2016). Thus, despite the difference in size, we agree with Bulanov and Sennikov (2015a) that the ornamentation of MNHN.F.MAP327b indicates a more mature ontogenetic stage than the slightly larger specimens of *Coelurosauravus*. We agree with Bulanov and Sennikov (2015a) that this minor variability may reflect asynchronous osteogenesis in different individuals due to various unknown factors, or simply individual variation rather than subtle interspecific variation. Furthermore, the minor differences in frill length are not correlated to those of the humeral length, which conforms with slight intraspecific variations (Table 2). Substantial intraspecific variation in skull shape and size, especially concerning cranial crests, has similarly been reported in chamaeleonid (Measey et al., 2009; da Silva and Tolley, 2013) and phrynosomatid squamates (Powell et al., 2017).

Lastly, Bulanov and Sennikov (2015a) argue that the tubercular parietal ornamentation indicates an immature stage in *Coelurosauravus*, although they consider the same type of ornamentation as plesiomorphic for weigeltisaurids based on the mature specimen of *Glaurung* (Buanov and Sennikov, 2015c). Based on the size-independent criteria described above, we consider that mature individuals of *Coelurosauravus* bore tubercular parietal ornamentation instead of spikes, as in *Glaurung*. Interspecific differences in cranial ornamentation are very common in more recent reptiles such as ceratopsian dinosaurs (Sampson et al., 1997; Dodson et al., 2007) and squamates (Evans, 2008, and references therein), exemplified by chamaeleonids (Rieppel, 1981, 1987; Bickel and Losos, 2002; Anderson and Higham, 2013) and phrynosomatids (Jenkins and Tanner, 1968; Presch, 1969; Powell et al., 2017).

In summary, we disagree with Bulanov and Sennikov (2015a) in considering all *Coelurosauravus* specimens as immature individuals. Instead, we consider them morphologically mature and comparable to other known weigeltisaurid specimens based on various size-independent criteria. Our interpretation suggests that the total skull length varies between weigeltisaurid taxa, with *Coelurosauravus* having the smallest skull of all members of the group.

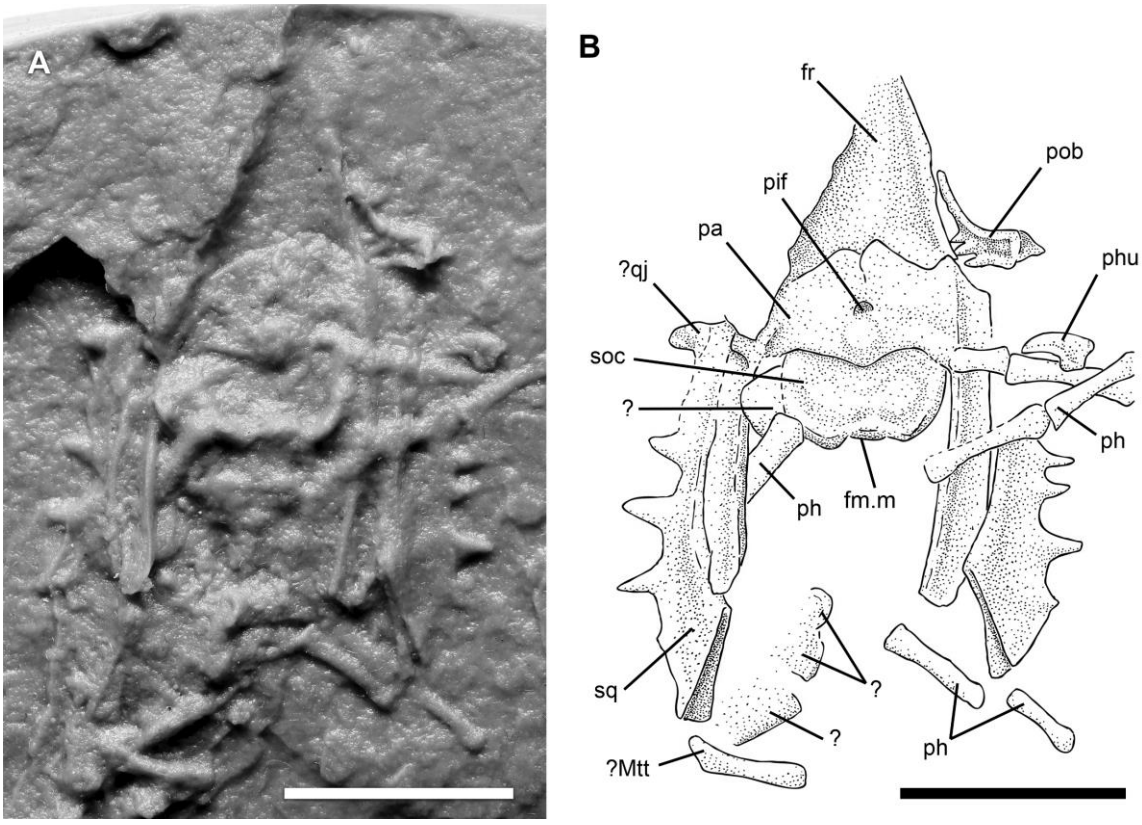

Figure 2-3: *Coelurosauravus elivensis* Piveteau, 1926 (Madagascar, Lopingian), lectotype MNHN.F.MAP325a, skull. **A**, silicone cast of dorsal surface of individual preserved as a natural external mold; **B**, interpretative drawing of **A**. **Abbreviations**: **fm.m**, dorsal margin of foramen magnum; **fr**, frontal; **Mtt**, metatarsal; **pa**, parietal; **ph**, phalange; **phu**, ungual phalange; **pif**, pineal foramen; **pob**, postorbital; **qj**, quadratojugal; **soc**, supraoccipital; **sq**, squamosal. Scale bars equal 1 cm.

Skull Roof

All specimens show the ornamented frill typical of weigeltisaurids. The parietal and squamosal bones are indeed at least three times as long as wide and form a frill posterior to the skull (Figs. 3-4). The quadratojugal also makes a small contribution to the anteroventral portion of the frill (Fig. 2). As reconstructed, the frill of weigeltisaurids thus encompasses the entire posterior skull roof and temporal regions (Fig. 2; Bulanov and Sennikov, 2015a-b). This morphology is very reminiscent of the parietosquamosal frill of ceratopsian dinosaurs (e.g., Sampson et al., 1997; Dodson et al., 2007) which occupies the same regions, well visible in lateral view. In contrast, the parietal crests or roofed helmets of crested squamates typically only involves the posterior skull roof while the temporal region is not involved, especially its ventral portion. This morphology is best exemplified by chamaeleonids (Rieppel, 1981, 1987;

Rieppel and Crumly, 1997; Anderson and Higham, 2013). As such, the cranial frill of weigeltisaurids will hereafter be termed 'parietosquamosal frill' in analogy to ceratopsians. We stress that this does not indicate homology of the weigeltisaurids and ceratopsian frills, but only topological similarities.

As in all weigeltisaurids, the *Coelurosauravus* specimens show sharp spikes on the circumorbital bones, as well as prominent spikes on the squamosal. Based on computed tomography, Bulanov and Sennikov (2010) described these spikes as hollow and vascularized and postulated that they derived from osteoderms that fused to the dermal bones of the skull. However, no trace of this fusion can be seen, casting doubt on this interpretation (Bulanov and Sennikov, 2010:pl. 9). We note that although fusion of putative osteoderms to the skull bones is rare in reptiles (Vickaryous and Sire, 2009), small dermal ossifications typically fuse to the frill of ceratopsians during ontogeny (Samson et al., 1997; Dodson et al., 2007; Horner and Goodwin, 2006, 2008), and this could have been also the case in weigeltisaurids.

Rostrum—Bulanov and Sennikov (2015a:fig. 3A) reconstructed *Coelurosauravus* with a very slender rostrum, accentuated by a laterally concave maxilla and a broad postorbital region in dorsal view. However, the anterior extent of the rostrum is missing in all specimens, and the maxilla of MNHN.F.MAP327a is only visible in medial view (Fig. 5) so a definite outline of the rostrum cannot be ascertained. What is preserved of the nasal is rectangular and does not suggest a transversally constricted rostrum. Thus, we reconstruct *Coelurosauravus* with a gradually tapering rostrum, as is typical of contemporaneous diapsids such as *Claudiosaurus* or *Youngina* (Gow, 1975; Carroll, 1981), and similar to the skull reconstruction of *Rautiania* (Bulanov and Sennikov, 2006:fig. 1). The general outline and length of the rostrum in our reconstruction (Fig. 2) is inferred from the proportions of the more complete *Weigeltisaurus* holotype and the Ellrich specimen (SMNK-PAL 34899a, SMNK-PAL 2882, VB pers. obs.)

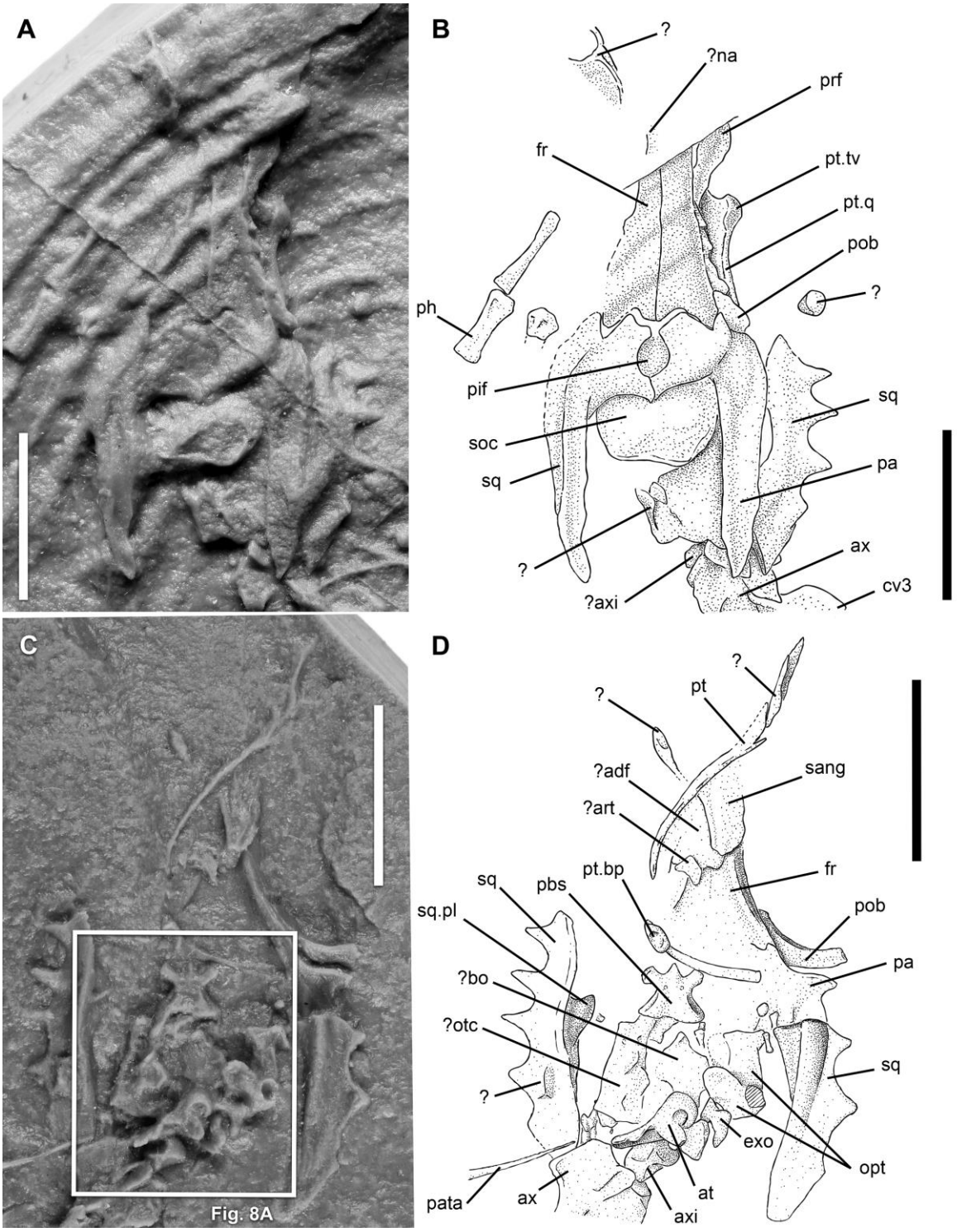
A
B
?
?na
prf
fr
pt.tv
pt.q
pob
?
ph
pif
sq
soc
sq
pa
?
ax
?axi
cv3
C
Fig. 8A
D
?
?
pt
?adf
sang
?art
fr
pt.bp
sq
pbs
sq.pl
pob
pa
?bo
?otc
sq
?
exo
opt
pata
ax
at
axi

← Figure 2-4: *Coelurosauravus elivensis* Piveteau, 1926 (Madagascar, Lopingian), paralectotype MNHN.F.MAP317a-b, skull. **A**, silicone cast of MNHN.F.MAP317b, dorsal surface of individual preserved as a natural external mold; **B**, interpretative drawing of **A**; **C**, silicone cast of MNHN.F.MAP317a, ventral surface of individual preserved as a natural external mold; **D**, interpretative drawing of **C**. **Abbreviations**: **adf**, adductor fossa; **art**, articular; **at**, atlantal centrum; **ax**, axis; **axi**, axial intercentrum; **bo**, basioccipital; **cv3**, third cervical vertebra; **exo**, exoccipital; **fr**, frontal; **na**, nasal; **opt**, opisthotic; **otc**, otic capsule elements; **pa**, parietal; **pata**, patagial spar; **pbs**, parabasisphenoid; **pif**, pineal foramen; **ph**, phalange; **pob**, postorbital; **prf**, prefrontal; **pt**, pterygoid; **pt.bp**, pterygoid basicranial process; **pt.q**, pterygoid quadrate ramus; **pt.tv**, pterygoid, transverse flange; **sang**, surangular; **soc**, supraoccipital; **sq**, squamosal; **sq.pl**, squamosal posterior lamina. Scale bars equal 1 cm.

Premaxilla—The supranarial process of the right premaxilla is preserved in MNHN.F.MAP327b (Fig. 5). Owing to the preservation of the neighboring skull bones, this process is presumably preserved close to its natural position. It is about six times as long as wide. It deeply incises the nasal posteromedially, contributing substantially to the anterior skull roof, which is typical of weigeltisaurids. It has a wedge-shaped posterior end (contra Bulanov and Sennikov, 2015a:417), identical to that of *Rautiania* (Bulanov and Sennikov, 2010), the *Weigeltisaurus* holotype (Bulanov and Sennikov, 2015b) and the Ellrich specimen (VB, per. obs.; Pritchard et al., in press). The rest of the bone is missing. Therefore, the entire outline of the bone cannot be reconstructed.

All stem-saurians possess a slender supranarial process emerging dorsally from the premaxilla. This might be a synapomorphy of diapsids (deBraga and Reisz, 1995). However, the length of this process is highly variable, being short in some taxa (e.g., *Petrolacosaurus*, Reisz, 1981) and elongate in others, generally in those taxa with an elongate snout (e.g., *Youngina*, Gow, 1975). Some early saurians also show a complete reduction of the supranarial process, such as the gliding kuehneosaurids (Robinson, 1962; Evans, 2009) or some archosauromorphs (Dilkes, 1998; Flynn et al., 2010).

Maxilla—The left maxilla is preserved in medial view in MNHN.F.MAP327b (Fig. 6). It is about three times as long as high and likely represents the longest bone in the snout (Figs. 2, 6). It tapers in height anteriorly but its anterior portion is missing. It is thus impossible to describe the participation of this bone to the naris.

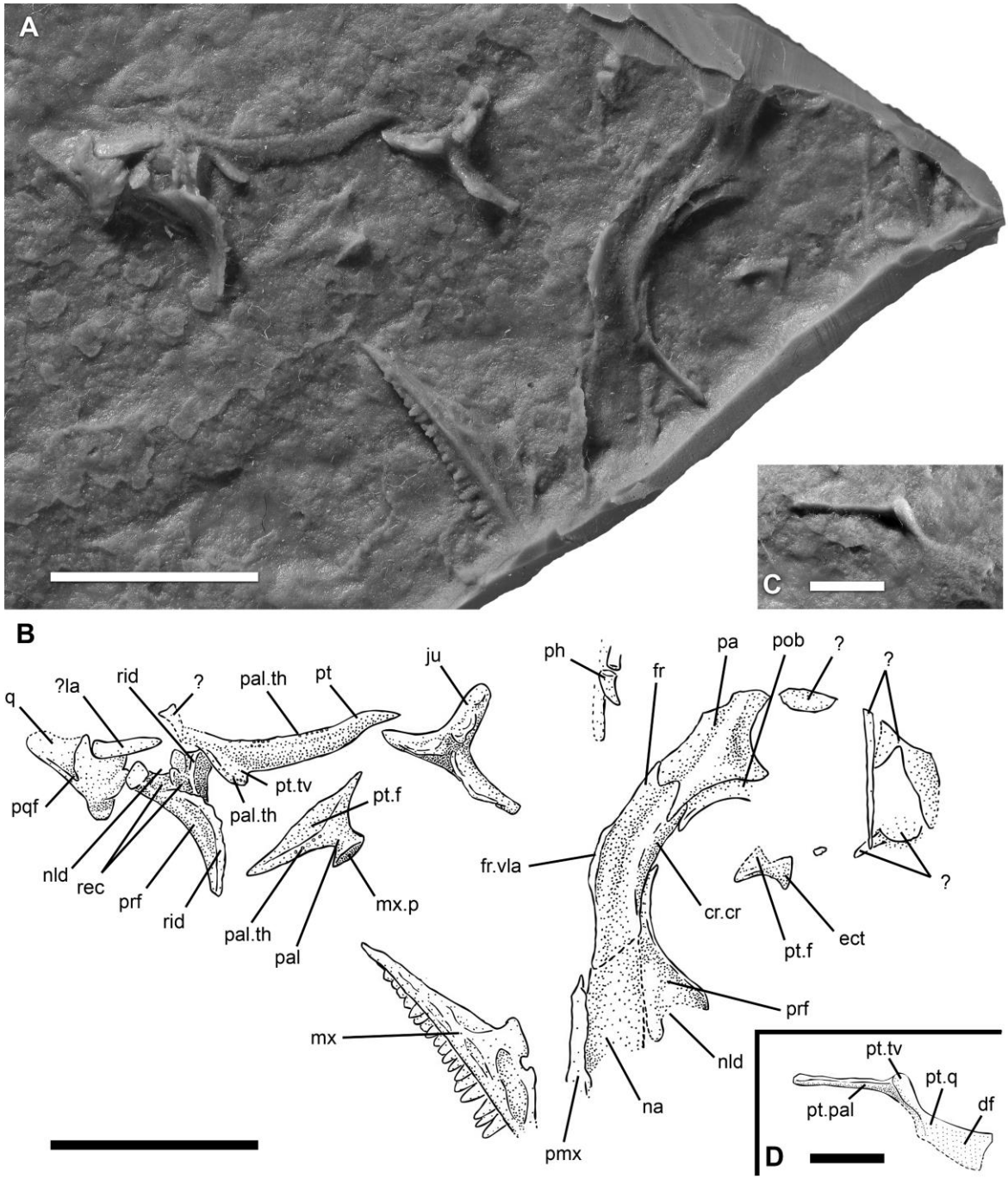

Figure 2-5: *Coelurosauravus elivensis* Piveteau, 1926 (Madagascar, Lopingian), MNHN.F.MAP327b, cranial remains preserved mostly in ventral (internal) view. **A**, silicone cast of individual preserved as a natural external mold; **B**, interpretative drawing of **A**; **C**, disarticulated right pterygoid, cropped out from **A**; **D**, interpretative drawing of **C**. **Abbreviations**: **cr.cr**, crista cranii; **df**, dorsal flange of quadrate ramus of pterygoid; **ect**, ectopterygoid; **fr**, frontal; **fr.vla**, frontal ventral lamina; **ju**, jugal; **la**, lacrimal; **mx**, maxilla; **na**, nasal; **nld**, nasolacrimal duct; **pa**, parietal; **pal**, palatine; **pal.th**, palatal tooth; **ph**, phalange; **pmx**, premaxilla; **pob**, postorbital; **pqf**, paraquadrate foramen; **prf**, prefrontal; **pt**, pterygoid; **pt.pal**, pterygoid palatal process; **pt.f**, pterygoid facet; **pt.q**, pterygoid quadrate ramus; **pt.tv**, pterygoid transverse flange; **q**, quadrate; **rec**, recess; **rid**, ridge. Scale bars equal 1 cm (**A**, **B**), and 5 mm (**C**, **D**).

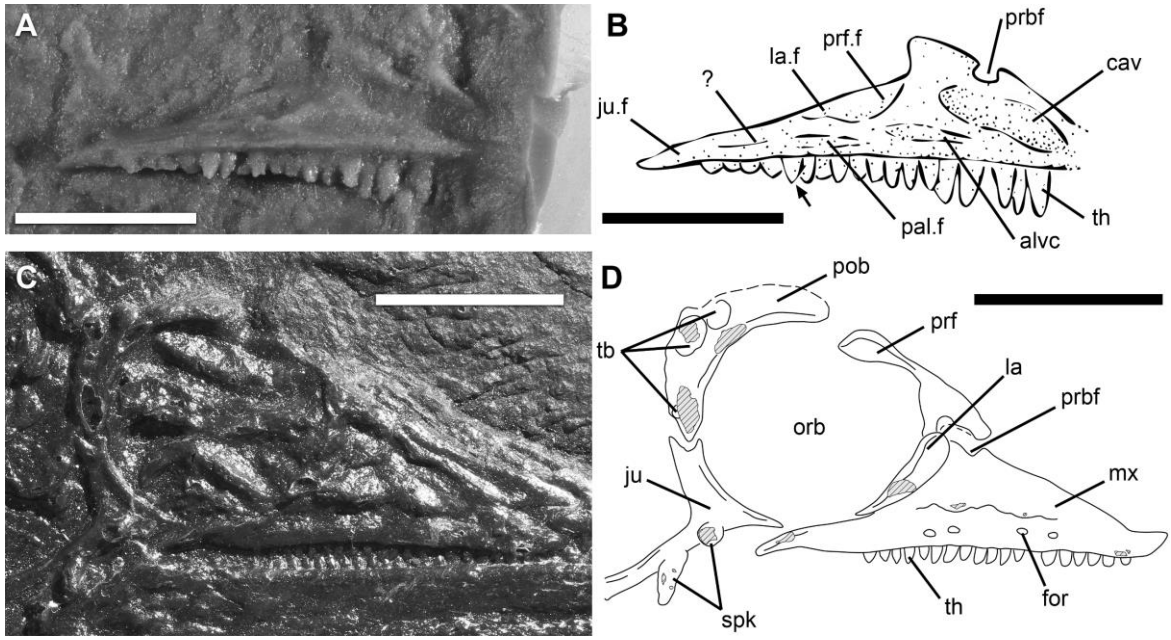

Figure 2-6: Close-up views of weigeltisaurids specimens. **A**, *Coelurosauravus elivensis* Piveteau, 1926 (Madagascar, Lopingian), MNHN.F.MAP327b, medial surface of left maxilla, individual preserved as a natural external mold; **B**, interpretative drawing of **A**; **C**, *Weigeltisaurus jaekeli* (Weigelt, 1930a) (Germany, Lopingian), SMNK-PAL 34899a, cast of holotype SSWG 113/7, photograph of right anterior region in lateral view; **D**, interpretative drawing of the circumorbital bones of **C**. **Abbreviations**: **alvc**, alveolar canal; **cav**, cavity; **for**, foramen; **ju**, jugal; **ju.f**, jugal facet; **la**, lacrimal; **la.f**, lacrimal facet; **mx**, maxilla; **orb**, orbit; **pal.f**, palatine facet; **pob**, postorbital; **prbf**, preorbital fenestra; **prf**, prefrontal; **prf.f**, prefrontal facet; **spk**, spike; **tb**, tubercle; **th**, tooth. Arrow indicates preserved tooth 14. Scale bars equal 5 mm (**A**, **B**), and 1 cm (**C**, **D**).

The maxilla gradually increases in height posteriorly up to the highest part of the maxillary dorsal lamina, at about the anteroposterior midpoint of the bone. This lamina abutted the nasal and prefrontal, and it is incised by a small preorbital fenestra (sensu Bulanov and Sennikov, 2015a:420), as is typical in weigeltisaurids (Bulanov and Sennikov, 2015a-b). As clearly seen in MNHN.F.MAP327b, this fenestra deeply incises the maxilla, which forms its entire anterior, ventral and posterior margins. In contrast, both the maxilla and nasal contribute equally to the anterior and posterior margins of the preorbital fenestra in the *Weigeltisaurus* holotype (Fig. 6C-D; Bulanov and Sennikov, 2015b). The dorsal margin of the maxilla between the naris and preorbital fenestra is straight and oriented anteroventrally, as in the *Weigeltisaurus* holotype (Fig. 6C-D) and the Ellrich specimen (VB, pers. obs.). In contrast this margin is rounded and longitudinally shorter in both *Rautiania* morphotypes (Bulanov and Sennikov, 2006), which might be a synapomorphy of this taxon.

The dorsal lamina of the maxilla is low and expands only slightly above the alveolar portion in early eureptiles and araeoscelidians (e.g., Heaton, 1979; Reisz, 1981). However, it is at least 1.5 times higher than the alveolar portion in most early neodiapsids (e.g., *Acerosodontosaurus, Youngina*, Gow, 1975; Currie, 1980). The latter condition is also prevalent in early archosauromorphs (e.g., *Prolacerta*, *Protorosaurus*, Modesto and Sues, 2004; Gottmann-Quesada and Sander, 2009) and some early lepidosauromorphs (*Gephyrosaurus*, *Sophineta*, Evans, 1980; Evans and Borsuk-Białynicka, 2009). In some taxa with a high dorsal lamina of the maxilla, this lamina is longitudinally shortened so that it is roughly as high as long in lateral view. This is the case in *Claudiosaurus* (Carroll, 1981) and some early lepidosauromorphs (e.g., *Fraxinisaura*, *Marmoretta*, Evans, 1991; Schoch and Sues, 2018b).

The posterior margin of the dorsal lamina of the maxilla of MNHN.F.MAP327a is concave as in other weigeltisaurids (Fig. 6C-D; Bulanov and Sennikov, 2015b) and bears continuous suture facets for the lacrimal and prefrontal bones (Fig. 6). It merged continuously with the suborbital process, which forms a straight posteroventrally oriented dorsal margin. The suborbital process extends posteriorly, contributing broadly to the anteroventral orbital margin in MNHN.F.MAP327b, which is typical for weigeltisaurids (Fig. 6; Bulanov and Sennikov, 2015b). Posteriorly, this process bears a dorsal articular surface for the jugal (Fig. 6). The maxilla is generally excluded from the anteroventral orbital margin in early neodiapsids and saurians by a lacrimojugal and/or a prefrontojugal contact (e.g., Carroll, 1981; Gottmann-Quesada and Sander, 2009). In particular, this appears to be the case in drepanosauromorphs (Renesto et al., 2010). In contrast, the maxilla participates in the anteroventral orbital margin in kuehneosaurids (Robinson, 1962), early lepidosauromorphs (*Marmoretta*, *Sophineta*, Waldman and Evans, 1994; Evans and Borsuk-Białynicka, 2009), rhyncocephalians (*Diphydontosaurus*, *Gephyrosaurus*; Evans, 1980; Whiteside, 1986) but not in squamates (*Eichstaettisaurus*, *Huehuecuetzpalli*, Reynoso 1998; Simões et al., 2017 and see Evans, 2008).

The medial surface of the dorsal lamina bears a deep concavity situated ventral to the preorbital foramen, extending anteroventrally to the limit of the preserved portion of the bone (Fig. 6). Its position is similar to the nasal gland cavity described in lepidosauromorphs, although the latter seems much shallower (e.g. Evans, 2008; Evans & Borsuk-Białynicka 2009). As was argued by Bulanov and Sennikov (2015a:420), this cavity of MNHN.F.MAP327b is in

continuity with the lacrimal and prefrontal suture facets, and more probably housed the nasolacrimal duct. This interpretation conforms to the reconstructed pathway of the nasolacrimal duct in *Orovenator* (Ford and Benson, 2019:fig. 5). Such a cavity could not be identified on the Ellrich specimen (VB, pers. obs.; Pritchard et al., in press), the only western European specimen which preserves the maxilla in medial view. The maxilla of MNHN.F.MAP327b also bears a slender shallow cavity just dorsal to the alveolar shelf, which is situated vertical to the apex of the dorsal lamina (Fig. 6). This cavity probably housed the dorsal alveolar canal, although no foramina are visible. More posteriorly, the alveolar shelf bears a shallow rhomboidal suture facet for the palatine (Fig. 6). According to Bulanov and Sennikov (2015a:420), this suggests that the choanae of *Coelurosauravus* were longitudinally elongate and protruded posteriorly as in *Youngina*. Evans and Haubold (1987:fig. 21) interpreted an elongate recess positioned posteriorly between the jugal facet and the alveolar margin as the suture facet for the ectopterygoid (Fig. 6). However, owing to the width of the ectopterygoid, this surface is too close to that for the palatine (Fig. 2). We thus reconstruct the ectopterygoid more posteriorly, and it is possible that it also contacted the jugal. This conforms well with the length of the pterygoid bone and the position of the transverse flange (Fig. 2). We are, however, unable to anatomically identify the surface described by Evans and Haubold (1987).

The alveolar shelf of *Coelurosauravus* is horizontal, transversely wide, and its dorsal and ventral margins taper posteriorly (Fig. 6). There are 18 incompletely preserved teeth and two empty alveoli. The teeth are arranged in a densely packed row, as in all weigeltisaurids (Bulanov and Sennikov, 2006, 2015b). The tooth count is similar to that estimated for *Rautiania minichi* and the *Weigeltisaurus* holotype (Bulanov and Sennikov, 2006, 2015b), but significantly less than the 30 teeth estimated for *Rautiania alexandri* (Bulanov and Sennikov, 2006).

Bulanov and Sennikov (2015a:420) considered that the apices of the posterior teeth are not reproduced in latex casts. We were unable to observe the bottom of the tooth cavities as they are deeply encased in the matrix. However, based on the complete rendering of some teeth on both Bulanov and Sennikov's (2015a:pl. 5) cast and ours (Fig. 6), we think that at least some cavities are empty, such as that of preserved tooth 14. The preserved teeth of MNHN.F.MAP327b thus seem to gradually decrease in height posteriorly. In contrast, the

anterior teeth are not significantly larger than the more posterior ones in the *Weigeltisaurus* holotype (Fig. 6), the Ellrich specimen (VB pers. obs.; Pritchard et al., in press), or in both *Rautiania* morphotypes (Bulanov and Sennikov, 2006). The posteriormost portion of the maxilla is edentulous.

There are no caniniform teeth in the maxilla of MNHN.F.MAP327b, and their absence is considered as a synapomorphy of neodiapsids (Laurin, 1991). The teeth all bear conical and sharply pointed crowns without carinae. The few completely preserved apices are roughly vertical (Fig. 6), while those of the *Weigeltisaurus* holotype (Fig. 6) and the Ellrich specimen (VB pers. obs.; Pritchard et al., in press) are slightly recurved. The teeth of MNHN.F.MAP327b are roughly circular in cross-section. In contrast, *Rautiania*, exhibits labiolingually compressed mid-posterior teeth (Bulanov and Sennikov, 2006, 2010) while the posterior teeth of *Glaurung* are labiolingually compressed with slightly mesiodistally expanded apices (Bulanov and Sennikov, 2015c).

There is no lingual shelf covering the base of the teeth on MNHN.F.MAP327b (Fig. 6). Following recent definitions, this suggests a pleurodont dentition whereby “the teeth are attached to the lingual surface of the labial wall of the jaw” (LeBlanc et al., 2020:1), resulting in an asymmetric tooth attachment (Jenkins et al., 2017; Bertin et al., 2018; LeBlanc et al., 2020). This agrees with previous descriptions of weigeltisaurids including *Coelurosauravus* (Carroll, 1978; Evans and Haubold, 1987).

Pleurodonty is often used to suggest lepidosauromorph affinities (e.g., Schoch and Sues, 2018b; Cavicchini et al., 2020). Based on recent definitions (see above), pleurodonty appears to be rare outside lepidosauria, being only reported in early captorhinomorphs (LeBlanc and Reisz, 2015), some thalattosaurians (Druckenmiller et al., 2020), a few sauropterygians (Chun et al., 2016; de Miguel Chaves et al., 2018) and the enigmatic neodiapsid *Claudiosaurus* (Carroll, 1981). A ‘subpleurodont’ dentition has also been reported in *Palaeagama* although no criteria were given (Carroll, 1975).

Lacrimal—Among weigeltisaurids, the lacrimal has only been tentatively identified as a badly crushed element in the *Weigeltisaurus* holotype (Bulanov and Sennikov, 2015b:fig. 1). However, we instead interpret the lacrimal of this specimen as a crescentic element just posterior to the maxilla and ventral to the prefrontal (Fig. 6C-D). It forms the ventral half of the

anterior orbital margin, but hardly extends onto the snout anteriorly, being restricted anteriorly by the prefrontal and maxilla. This element was previously figured and tentatively identified as prefrontal fragments or the lacrimal by Evans and Haubold (1987:fig. 2). As a result, the lacrimal of the *Weigeltisaurus* holotype is much better defined than reconstructed by Bulanov and Sennikov (2015b:fig. 2).

Our new interpretation of the lacrimal in the *Weigeltisaurus* holotype results in a tentative identification of the lacrimal in *Coelurosauravus* (Fig. 5). Bulanov and Sennikov (2015a:420) identified a slender bone lying near the right prefrontal, pterygoid and quadrate as a broken off and displaced pterygoid quadrate ramus. Owing to the excellent preservation of the neighboring skull bones and the close proximity of this bone and the right prefrontal, we find this interpretation unlikely. Instead, we interpret this bone as a slightly rotated right lacrimal, visible in lateral view (Fig. 5).

The bone lies upside-down relative to the corresponding contact facets on the right prefrontal. The dorsal portion is broad and rounded, its ventral one tapers to a point posteroventrally. The orbital margin of the lacrimal is slightly more robust. There is virtually no facial expansion so that the lacrimal fitted between the prefrontal and maxilla and formed the anterior orbital margin. Presumably, it also formed the lateral wall of the lacrimal foramen.

Strong reduction of the lacrimal bone is uncommon among early diapsids (e.g., *Petrolacosaurus*, *Youngina*, Gow, 1975; Reisz, 1981) and archosauromorphs (e.g., *Prolacerta*, *Protorosaurus*; Modesto and Sues, 2004; Gottmann-Quesada and Sander, 2009). In contrast, the lacrimal of lepidosauromorphs underwent a reduction early in their evolutionary history (Evans, 2003, 2008). This bone is reduced or absent in most of the earliest taxa known from the Triassic (e.g., *Clevosaurus*, *Diphydontosaurus*, *Megachirella*, *Sophineta*; Whiteside, 1986; Fraser, 1988; Evans and Borsuk-Białynicka, 2009; Simões et al., 2018).

Nasal—The posterior portion of the right nasal is present in situ in ventral view in MNHN.F.MAP327b but is absent on the other *Coelurosauravus* specimens. The preserved fragment is elongate and quadrangular with a roughly constant width (Fig. 5). Bulanov and Sennikov (2015a:417, pl. 5) identified a bone fragment lying between the right nasal and prefrontal on MNHN.F.MAP327b as the broken off lateral margin of the nasal, bearing the dorsal margin of the preorbital fenestra. However, a break of the nasal appears unlikely to us

considering the good preservation of the neighboring bones, and we alternatively identify this structure as the anterior portion of the right prefrontal. Its shape is thus similar to the better-preserved left prefrontal, and it contributes to the nasolacrimal duct (Fig. 5). The lateral margin of the nasal is obscured and there is neither a trace of the margin of the preorbital fenestra nor of the low anterolateral crest described for the *Weigeltisaurus* holotype (Bulanov and Sennikov, 2015b).

The suture between the nasal and frontal is very hard to identify and has only been tentatively followed through RTI photographs (Fig. 5). What is visible indicates a serrated anteromedially oriented suture, suggesting that both nasals were probably separated posteromedially by the adjoined anterior processes of the frontals, contrary to the reconstruction of Bulanov and Sennikov (2015a:fig. 3).

Prefrontal—Both prefrontals are preserved in MNHN.F.MAP327b. The right one is visible in ventromedial view in connection with the neighboring bones. The left one is displaced but exquisitely preserved and visible in lateral and posterolateral views (Fig. 5). The posterodorsal portion of the right prefrontal is also preserved in situ in MNHN.F.MAP317b (Fig. 4). The prefrontal expands anteriorly onto the posterior snout, and posterodorsally, forming roughly the anterodorsal quarter of the dorsal orbital margins (Fig. 2).

The posterodorsal process of the prefrontal braces the frontal laterally and extends posteriorly over a third of the orbit length (Figs. 4-5), as on the *Weigeltisaurus* holotype (Fig. 7) and the Ellrich specimen (VB, pers. obs.; Pritchard et al., in press). The dorsal portion of the bone is dorsoventrally thin and extends laterally, bearing a sharp and faintly ornamented ridge (Fig. 5).

Excluding the ornamented ridge, the dorsal and facial portions of the bone gradually merge into each other. The facial portion of the bone extends ventrally over at least half of the height of the orbit. It expands anteroventrally and bears an inverted V-shaped recess with the apex meeting the anterior extent of the lateral ornamented ridge. As was argued by Bulanov and Sennikov (2015a:419), this recess is deeply incised laterally and formed the medial wall of the posterior portion of the posterior portion of the nasolacrimal duct (Fig. 5). Both dorsal and ventral margins of this V-shaped cavity meet the dorsal lamina of the maxilla, with the ventral one thickening into a ventral footplate-like process abutting on the latter bone (Fig. 5). The

dorsal margin bears a low, sharp longitudinal ridge for the reception of the dorsal lamina of the maxilla. Presumably, this V-shaped recess was partially covered laterally by the lacrimal (Fig. 2).

Frontal—The frontal is preserved on all specimens. It is preserved on both sides in MNHN.F.MAP317b, where it is visible in dorsal view, although it is unclear whether the anteriormost portion is preserved or not (Figs. 4). We were indeed unable to trace the nasofrontal suture reported by Evans and Haubold (1987:fig. 3) on this specimen, even using RTI photographs. Additionally, both bones are poorly preserved on the lectotype MNHN.F.MAP325a (Fig. 3), and the right frontal is preserved in ventral view on MNHN.F.MAP327b, lying in connection with the neighboring bones of the skull roof (Fig. 5).

The frontal is elongate and triangular, about three times as long as its minimum length width. The lateral margins of both frontals gradually diverge posteriorly, each bone reaching its maximum width posterior to the orbit (Figs. 2-4). Each bone extends across the entire orbital region. Its suture with the nasal is only tentatively identified on MNHN.F.MAP327b (see above, Fig. 5). The frontal broadly contributes to the mid-dorsal orbital margin, separating the prefrontal and the postorbital (Fig. 2). As seen on MNHN.F.AMP317b, the orbital margin of each frontal bears a faint ornamentation similar to that of the left prefrontal of MNHN.F.MAP327b (see above, Figs. 4-5). Posteriorly, the frontoparietal suture is coarsely sinusoidal (‘zigzagged’ according to Bulanov and Sennikov, 2015a:417), as is best seen in MNHN.F.MAP317b (Fig. 4). The posterior margin of each frontal is incised at mid-width by the anteromedial process of the parietal, dividing the posterior quarter of the frontals into a posteromedial and a posterolateral process.

As is seen in MNHN.F.MAP327b, the cranial crests of the frontal ventrally reinforce the orbital margin and are continuous with the robust orbital margin of the prefrontal (Fig. 5). Medially, the frontal bears a ventrally projecting lamina that Bulanov and Sennikov (2015a) considered diagnostic of the genus (Fig. 5B, reconstructed in lateral view on Fig. 2C). This lamina differs from the subolfactory processes of squamates, which extend ventromedially from the lateral portion of the frontal (e.g., Gauthier et al., 2012). Presumably, this lamina provided bony support for the interorbital septum in *Coelurosauravus*. We were unable to identify a similar structure on the *Weigeltisaurus* holotype (SMNK cast of SSWG 113/7, VB, pers. obs.)

or the Ellrich specimen (VB, pers. obs.). However, it might have been obliterated by late diagenetic compression of the German material.

Postfrontal—We follow Bulanov and Sennikov (2015a:423) in identifying the only bone in the posterolateral corner of the orbit as the postorbital due to its ventral contact with the jugal, which is typical for early amniotes (e.g., Romer, 1956). Consequently, we concur with Bulanov and Sennikov (2015a-c) that the postfrontal bone is absent as a discrete element in weigeltisaurids. Determination of whether this bone was lost or became fused to the postorbital is impossible based on the known material and is out of the scope of this study.

Among eureptiles, the loss of a distinct postfrontal is only reported among saurian taxa (turtles, some archosauromrophs and lepidosauromorphs; Lee, 1995; Conrad, 2008; Nesbitt, 2011), with the proterochampsian archosauriforms providing the earliest appearance of this character in the Middle-Late Triassic (Nesbitt, 2011). As such, the loss of a distinct postfrontal in weigeltisaurids represents the earliest occurrence of this feature in sauropsids.

Postorbital—The right postorbital is partially preserved in dorsal view and lies adjacent to the neighboring bones in the lectotype and MNHN.F.MAP317b (Figs. 3-4). The bone is complete and better preserved in MNHN.F.MAP327a-b, where it lies in connection with the left parietal, far away from the other cranial elements (Figs. 5, 7).

The postorbital has an inverted L-shape and forms the dorsal half of the posterior orbital margin and a small portion of the skull roof (Figs. 2), which is also the case in the *Weigeltisaurus* holotype (Fig. 6C-D) and the Ellrich specimen (VB pers. obs.). It is thus biradiate and lacks the posterior process that is present in the triradiate postorbital of all other stem-saurians where this region is known (e.g., Carroll, 1975, 1981; Gow, 1975; Currie, 1980, 1981; Reisz, 1981). As a result, the supratemporal bar is absent in weigeltisaurids, although an incipient postorbital posterior process contributing to the dorsal margin of the temporal fenestra has been reported in *Glaurung* (Bulanov and Sennikov, 2015c, but see discussion below).

The dorsomedial process of the postorbital is preserved on all *Coelurosauravus* specimens (Figs. 3-5, 7). It is subtriangular with a convex posterior margin and contributes to the skull roof and the posterodorsal orbital margin. Anteriorly, the dorsomedial process is acuminate and contacts the posterolateral process of the frontal. It underlies the frontal and thus occupies a similar position to the postfrontal of other amniotes (e.g., Romer, 1956). The

dorsomedial and ventral processes of the postorbital merge at a roughly right angle, as is the case on the *Weigeltisaurus* holotype (Fig. 6C-D) and in *Rautiania* (Bulanov and Sennikov, 2015b). This angled portion fits into the recess in the anterolateral margin of the parietal (Figs. 2, 4, 7).

The ventral process of the postorbital is slender and vertical (Figs. 5, 7). It is elongate and abuts on the dorsal process of the jugal ventrally. It forms the dorsal portion of the posterior orbital margin and the anterior margin of the temporal fenestra (see below). In contrast, the ventral process of the postorbital is acuminate and incises the dorsal process of the jugal on the *Weigeltisaurus* holotype (Fig. 6C-D). The postorbital of MNHN.F.MAP327a-b bears two robust spikes, one on the dorsomedial process, near its meeting point with the ventral process, and a larger one on the dorsal portion of the ventral process (Fig. 7A). The external surface of the postorbital of MNHN.F.MAP317b is smooth while that of the lectotype bears three slender tooth-like dorsal projections (Fig. 3). The *Weigeltisaurus* holotype bears a third low ventral tubercle just dorsal to the postorbitojugal suture (Fig. 6C-D; Bulanov and Sennikov, 2015b).

Jugal—The left jugal is visible in lateral view in MNHN.F.MAP327b. It lies disarticulated from the other skull bones (Fig. 5). This bone is triradiate, with subequal anterior and dorsal processes and a 1.3 times longer posterior process. This morphology is similar to that of *Rautiania* (Bulanov and Sennikov, 2015a:fig. 2N) but contrasts with the reduced anterior process of the *Weigeltisaurus* holotype (Fig. 6C-D) and the Ellrich specimen (Pritchard et al., in press).

As reconstructed, the anterior process of the jugal of *Coelurosauravus* extends anteriorly ventral to the orbit over almost half the orbital length (Fig. 2). This process is acuminate and bears a ventral suture facet for the maxilla anteriorly. The dorsal process of the jugal is vertical and ends bluntly, abutting on the ventral process of the postorbital and forming the ventral portion of the postorbital bar. It does not interdigitate with the ventral process of the postorbital, in contrast to the *Weigeltisaurus* holotype where the ventral process of the postorbital fits in a recess on the dorsal process of the jugal (Fig. 6C-D). The posterior process of the jugal is the thinnest and longest, forming most of the ventral margin of the temporal fenestra and the temporal region of the skull. It ends bluntly and presumably contacts the quadratojugal, completing the infratemporal bar.

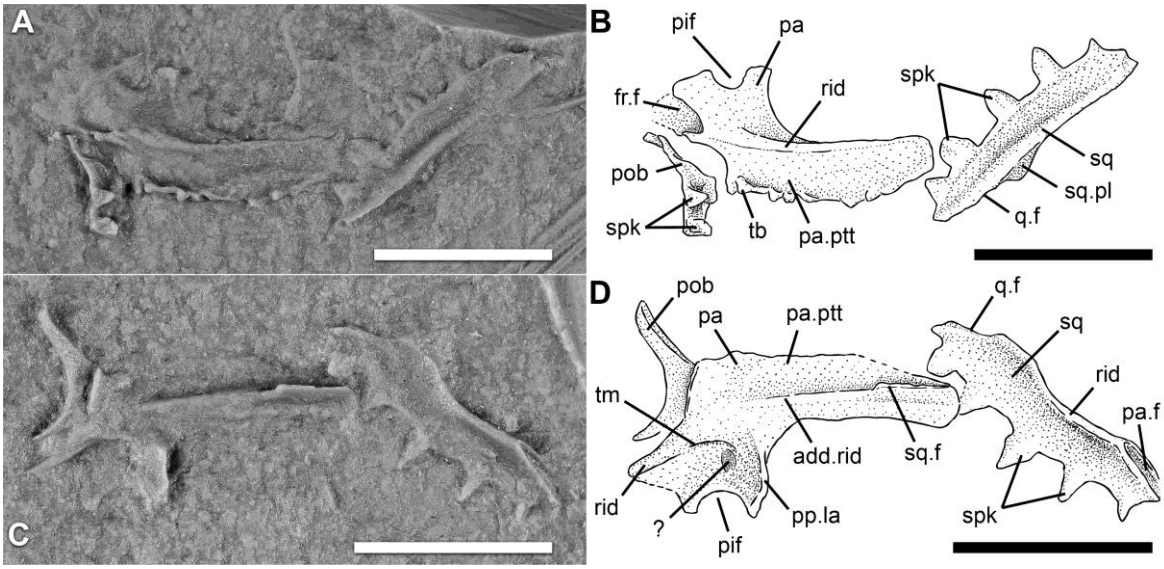

Figure 2-7: *Coelurosauravus elivensis* Piveteau, 1926 (Madagascar, Lopingian), MNHN.F.MAP327a-b, parietosquamosal frill, left half. **A**, silicone cast of MNHN.F.MAP327b, dorsal surface of individual preserved as a natural external mold; **B**, interpretative drawing of **A**; **C**, silicone cast of MNHN.F.MAP327a, ventral surface of individual preserved as a natural external mold; **D**, interpretative drawing of **C**. **Abbreviations**: **add.rid**, ridge for origin of the adductor musculature; **fr.f**, frontal facet; **pa**, parietal; **pa.f**, parietal facet; **pa.ptt**, parietal posttemporal process; **pif**, pineal foramen; **pob**, postorbital; **pp.la**, postparietal lamina; **q.f**, quadrate facet; **rid**, ridge; **spk**, spikes; **sq**, squamosal; **sq.f**, squamosal facet; **sq.pl**, squamosal posterior lamina; **tb**, tubercles; **tm**, attachment point of taenia marginalis. Scale bars equal 1 cm.

The jugal of MNHN.F.MAP327b is ornamented. Each process of the bone bears a sharp spike with an elongate base, the main axis of which radiates from the center of the bone (Fig. 5). In addition, the dorsal process bears a small knob-like protrusion near its tip. The external surface of the dorsal process of the jugal is devoid of such ornamentation in *Rautiania* (Bulanov and Sennikov, 2015a:fig. 2N) and the *Weigeltisaurus* holotype (Fig. 6C-D).

Parietal—The parietal is preserved in all specimens. This bone is hatchet-shaped in dorsal view and contributes to the dorsal portion of the parietosquamosal frill (Fig. 2). Both parietals are preserved in situ in the lectotype and MNHN.F.MAP317a-b (Figs. 3-4). The anterior portion of the right parietal of MNHN.F.MAP327b lies in connection with the neighboring skull bones, while the left one is displaced but perfectly preserved in ventral and dorsal views, lying near the left postorbital and squamosal (Fig. 7).

The parietal of *Coelurosauravus* bears a broad, horizontal and greatly elongate posttemporal process that extends the skull table posteriorly, forming a quarter of the total skull length (Table 2). This process forms the dorsolateral margin of the parietosquamosal frill, which

is typical of weigeltisaurids (Fig. 7; Bulanov and Sennikov, 2006, 2010, 2015a-c). The posttemporal process extends posteriorly from the posterolateral margin of each parietal, forming a deep posteromedial recess in the occipital part of the skull. The postorbital wedges into a deep recess at the junction between the main body of the parietal and the posttemporal process (Fig. 7).

The posttemporal process is a dorsoventrally thin sheet of bone. It is straight and maintains a constant width before tapering to a blunt end in its posterior quarter (Fig. 7). Among weigeltisaurids, this morphology is most similar to that of *Glaurung* (Bulanov and Sennikov, 2015c). In contrast, the posttemporal processes of both *Rautiania* morphotypes and the *Weigeltisaurus* holotype (Bulanov and Sennikov, 2006, 2015a-b), and of the Ellrich specimen (VB, pers. obs.; Pritchard et al., in press) show some degree of medial curvature and gradually decrease in width posteriorly.

As seen in MNHN.F.MAP327b, the dorsal margin of the posttemporal process is concave between the raised medial and lateral margins, which extend anteriorly onto the skull roof and bear small tubercles creating an irregular crenulated surface (Fig. 7A). The medial margin is supported by a sharp ridge that extends to the anterior margin of the bone, delimiting the anteromedial extent of the posttemporal process (Fig. 7A-B). The posttemporal process of the lectotype and MNHN.F.MAP317a-b is thinner and smooth, which could be attributed to individual variation (see above, Figs. 3-4). The parietal ornamentation of MNHN.F.MAP327a-b is similar to that of *Glaurung* (Bulanov and Sennikov, 2015c). In contrast, *Rautiania*, the *Weigeltisaurus* holotype (Bulanov and Sennikov, 2010, 2015b) and the Ellrich specimen (Pritchard et al., in press) all bear prominent dorsolaterally oriented, spikes on the lateral margin of the posttemporal process.

The body of the parietal forms the posterior portion of the skull roof. It bears a broad and convex anterior process incising the middle of the posterior margin of the frontal, forming a coarsely sinusoidal suture (Fig. 4). In contrast, the frontoparietal suture is usually U-shaped in Permo-Triassic reptiles, with the anteromedial process of the parietal extending medial to the frontal (e.g., Carroll, 1981; Reisz, 1981; Gottmann-Quesada and Sander, 2009; Evans, 1980, 2009). In *Coelurosauravus*, the bone also bears a pointed anterolateral process partially separating the frontal from the postorbital (Fig. 5). The medial margin of the bone is marked by

a deep incision in all *Coelurosauravus* specimens, indicating an extremely large pineal foramen occupying at least half of the interparietal suture (Fig. 7). The surface of the bone immediately posterior to the pineal foramen sharply turns dorsally.

Ventrally, the parietal bears several ridges (Fig. 7C-D). The posterior margin of the bone extends in a sharp transverse ventral postparietal lamina (Fig. 7D). This lamina may have served for the articulation with the supraoccipital, or alternatively as the origin area of the nuchal muscles. Although we found no trace of a postparietal, this lamina could also have served for the articulation with this bone. Paired posparietals indeed seem to be preserved in the Ellrich specimen (VB, pers. obs.; Pritchard et al., in press). The anterolateral margin of the parietal is also sharply turned ventrally at a right angle, continuing anteromedially as a ridge, forming the postorbital sutural facet. A sharp medial ridge extends longitudinally over the ventral surface of the posttemporal process (Fig. 7B). This ridge likely served as the origin area of the external adductor musculature by analogy with the jaw musculature of crested chamaeleonids (see discussion below). This ridge becomes gradually sharper posteriorly before transforming into a sharp ventral lamina in its posterior third. This lamina served as the articulation flange to accommodate the squamosal (Fig. 7D). A shallower parasagittal ridge extends from the anterior end of the adductor ridge to the level of the posterior margin of the pineal foramen (Fig. 7). The size, orientation and position relative to the pineal foramen conforms well with similar ridges identified as the point of attachment of the cartilaginous taenia marginalis in other early reptiles (Reisz, 1981; Ford and Benson, 2019). As the taenia marginalis connects the otic capsule to the braincase in reptiles (Romer, 1956), this ridge likely delimited the lateral wall of the neurocranium. A small ovate depression lies between the attachment point of the taenia marginalis and the pineal foramen (Fig. 7D). This depression might be linked to the midbrain, which is roofed by the parietal in reptiles (e.g. Fabbri et al., 2017), but we were unable to assess its homology. Alternatively, this structure might result from a concretion in the nodular matrix that is indistinguishable from the parietal bone on the specimens due to the lack of bone matter.

Squamosal—The left squamosal is preserved in ventral and dorsal views in MNHN.F.MAP327a-b, lying near the left postorbital and parietal (Fig. 7). Both squamosals are preserved in situ in the lectotype and MNHN.F.MAP317a-b (Figs. 3-5).

As in all weigeltisaurids, the squamosal, forms the ventrolateral margin of the parietosquamosal frill and is vastly different from the tetra- or triradiate bone of other early diapsids (e.g., Reisz, 1981). The squamosal is at least four times as long as wide, and is roughly straight on all *Coelurosauravus* specimens (Figs. 2-6, 7). In contrast, this bone is dorsally curved in *Rautiania*, the *Weigeltisaurus* holotype (Bulanov and Sennikov, 2010, 2015b) and the Ellrich specimen (Pritchard et al., in press). The squamosal of *Glaurung* shows sharply angled dorsal and ventral portions (Schaumberg et al., 2007; Bulanov and Sennikov, 2015c).

As is best seen in MNHN.F.MAP317a, the squamosal is slightly broader anteroventrally than posterodorsally and bears broad suture surfaces for the quadratoquadratojugal complex (Fig. 7). The squamosal also bears an anteroposteriorly thin posteromedial lamina (Figs. 4, 7). It fitted into the corresponding suture line on posterior surface of the quadrate. In addition, the main body of the squamosal extends ventrolaterally and fits into a facet on the lateral surface of the quadrate. As such, the squamosal braced the quadrate laterally and posteriorly. The quadrate is also braced laterally and posteriorly in early reptiles, including araeoscelidians (Reisz, 1981), but the posterior lamina is lost in most other neodiapsids in which the quadrate is only braced laterally (Gow, 1975; Currie, 1981).

The squamosal of MNHN.F.MAP327a-b and MNHN.F.MAP317a-b bears five spikes (Fig. 7), which may be the usual number in *Coelurosauravus*. This is also the number reported for *Rautiania* (Bulanov and Sennikov, 2010). The number of spikes for the *Weigeltisaurus* holotype is seven or eight (SMNK-PAL 34899a, VB, pers. obs.). The morphology of those spines shows strong intraspecific variability in *Coelurosauravus*. On the lectotype and the better preserved MNHN.F.MAP327a-b, the anterior spikes are stout with the width of the base and height being subequal. Furthermore, the spikes are more closely packed than the more widely spaced, sharper and more slender posterior ones, which are 1.2 times longer than wide (Figs. 3, 7). In contrast, MNHN.F.MAP317a-b shows the opposite pattern, with the anterior spikes being sharper than the posterior ones (Fig. 4). In *Coelurosauravus*, as in *Rautiania* and the *Weigeltisaurus* holotype, the spikes extend to the posterodorsal margin of the bone, while the dorsal portion of the bone surface is smooth in *Glaurung* (Bulanov and Sennikov, 2015c).

Quadratojugal—Based on articulated material of *Rautiania*, Bulanov and Sennikov (2010) describe the quadratojugal of weigeltisaurids as a very small bone lacking both dorsal

and anterior processes but bearing a spike on its external surface, similar to those of the squamosal. The quadratojugal was previously undescribed for *Coelurosauravus* (Bulanov and Sennikov, 2015a). We tentatively interpret a slightly displaced spike anterior to the left squamosal of the lectotype as a quadratojugal spike (Fig. 3). As preserved, this spike is not oriented in the same plane as any of the spikes from the left and right squamosals, suggesting that it is part of a distinct bone or element. The relationship of the quadratojugal to the quadrate is reconstructed based on well-preserved material of *Rautiania* (Fig. 2; Bulanov and Sennikov, 2010:fig. 1, pl. 9).

The anterior process of the quadratojugal is elongate in stem-saurians such as araeoscelidians or *Youngina* (Gow, 1975; Reisz, 1981), forming up to half of the infratemporal bar (ITB) although it is reduced in *Claudiosaurus* (Carroll, 1981) and weigeltisaurids (Bulanov and Sennikov, 2010). In contrast, the anterior process of the quadratojugal is often reduced in saurians regardless of the completeness of the ITB, rarely extending beyond a third of the ITB in early archosauriforms (e.g. Nesbitt, 2011; Ezcurra, 2016).

The dorsal process of the quadratojugal is very small in weigeltisaurids (Bulanov and Sennikov, 2010) and in stem-saurians such as *Petrolacosaurus* or *Claudiosaurus* (Carroll, 1981; Reisz, 1981) and possibly *Youngina* (Gow, 1975, but see Gardner, pers. comm. in Pritchard, 2015). This process is similarly small in early lepidosauromorphs (e.g., *Gephyrosaurus*, *Sophineta*, Evans, 1980; Evans and Borsuk-Białynicka, 2009). In kuehneosaurids the quadratojugal is absent (Evans, 2009). In contrast, the dorsal process of the quadratojugal is often well developed in archosauromorphs (Müller, 2003).

Quadrate—The left quadrate is preserved in posteromedial view on MNHN.F.MAP327b (Fig. 5). It is small and vertically oriented. The posterior margin of the bone is straight, expanding into a thin dorsal process. The pterygoid ramus expands anteriorly to an unknown extent, as its anterior portion is missing. The dorsomedial surface of the bone is marked by a deep excavation, presumably the suture line for the squamosal and pterygoid. The posteroventral portion of this excavation forms a notch, which we interpret as the posterior paraquadrate foramen due to its similarity to that described for *Rautiania* (Fig. 5; Bulanov and Sennikov, 2010). Ventrally, the bone bears two articular condyles. Both condyles are separated

by a deep sulcus, with the lateral one extending twice as much ventrally as the medial one (Fig. 5).

The quadrate of most saurians has a concave posterior margin, a lateral tympanic crest (Laurin, 1991), and an expanded, slightly convex, dorsal head (e.g., Evans, 1991; Simões et al., 2018; Pritchard and Sues, 2019). That of *Paliguana* and lepidosauromorphs also bears a lateral tympanic conch (Carroll, 1975; Evans, 2003). The quadrate morphology of weigeltisaurids thus conforms well with that of stem-saurians in lacking a tympanic crest and conch, and having a slender dorsal head (e.g., *Hovasaurus*, *Petrolacosaurus*, *Youngina*, Gow, 1975; Currie, 1981; Reisz, 1981).

Palate

The palate is only partially preserved in MNHN.F.MAP317a-b and MNHN.F.MAP327b (Figs. 4-5). We here provide the first reconstruction of the palate of *Coelurosauravus*, which is also the first palatal reconstruction of any weigeltisaurid (Fig. 2B). In all specimens the bones are disarticulated and displaced. There is no trace of the vomers in any of the preserved specimens. As reconstructed, the palate shows a large interpterygoid vacuity and large paired suborbital fenestrae and subtemporal fossae (Fig. 2B).

Palatine—The left palatine is exposed in ventral view in MNHN.F.MAP327b, lying close to the left pterygoid (Fig. 5). The bone is asymmetrical, with the medial margin three times as long as the lateral margin. Both anterior and posterior margins are deeply embayed, separating the palatal surface and maxillary process by a short, robust neck.

The medial portion of the bone reaches its maximum length and minimum thickness (i.e. dorsoventral height) at its medial margin. The entire ventromedial margin of the bone bears a deep longitudinal facet for the palatal process of the pterygoid. This facet gradually increases in transverse width posteriorly, reaching its maximum width level with the maxillary process before gradually tapering to a point posteriorly (Fig. 5). The pterygoid facet is framed laterally by a ridge, marking a step-like increase in the thickness of the palatine. This ridge bears an anteromedially oriented row of at least four palatal teeth posterior to the maxillary process (Fig. 5). These teeth are very small, less than 2 mm in diameter. As reconstructed, the palatine

contacted the ectopterygoid posterolaterally (Fig. 2B), although this contact may be artificial, as we are unable to identify a contact area on either the lateral surface of the palatine or the medial surface of the ectopterygoid.

The asymmetrical anterior margin of the bone is concave with the vomerine process extending at least three times further anteriorly than the maxillary process. It thus forms the posterior and posteromedial margins of the choana (Fig. 2). The posterior margin of the palatine is similarly asymmetrical, forming the anterior and anteromedial margins of a posteriorly widening suborbital fenestra. Laterally, the maxillary process expands rapidly and bears an elongate suture facet for the maxilla.

Suborbital Fenestra—The presence of a suborbital fenestra has long been considered a synapomorphy of diapsid reptiles (Laurin and Reisz, 1995; deBraga and Rieppel, 1997). Its outline can be reconstructed in *Coelurosauravus* based on the margins of the neighboring bones (Fig. 2B). This fenestra is subtriangular and gradually widens posteriorly. Its medial margin is oriented parasagittally and its lateral one anterolaterally. The suborbital fenestra ends bluntly anteriorly, which contrasts to the anteriorly pointed suborbital fenestra of rhyncocephalians (Evans, 1980; Whiteside, 1986; Fraser, 1988).

Diapsids show a trend of an enlargement of the posterior portion of the suborbital fenestra. The fenestra of araeoscelidians is long and narrow, as in *Claudiosaurus* (Carroll, 1981; Reisz, 1981). That of younginiforms broadens slightly posteriorly although it lacks a posterior transverse expansion as the palatine retains a longitudinally oriented lateral margin (Gow, 1975; Carroll, 1981). The proportions of the suborbital fenestra are highly variable in early saurians (e.g. Ezcurra, 2016), although some show a posteriorly widened fenestra reminiscent of that of weigeltisaurids (e.g. *Marmoretta*, *Prolacerta*, Evans, 1991; Waldman and Evans, 1994; Modesto and Sues, 2004). A posteriorly expanded suborbital fenestra could support affinities with younginiforms or saurians.

Pterygoid—Both pterygoids are preserved in MNHN.F.MAP327b. The left one lies in ventral view near the left palatine while the right one, exposed in dorsolateral view lies isolated at some distance to the other cranial remains (Fig. 5). Both pterygoids are partially preserved in MNHN.F.MAP317a-b (Fig. 4), but to a larger extend than previously reported by Bulanov

and Sennikov (2015a). The right one lies anteriorly, overlying the frontals in ventral view, while the left lies just anterior to the parabasisphenoid.

The entire left palatal ramus is preserved in MNHN.F.MAP327b. It is elongate, thin and crescentic in ventral view, tapering gradually anteriorly before ending in an anterior wedge-shaped extremity. The concave medial margin suggests an elongate interpterygoid vacuity and a contact between both pterygoids restricted to the anterior wedge-shaped terminus of the bone (Fig. 2B). As is evident in both MNHN.F.MAP327b and MNHN.F.MAP317a, the pterygoid indeed bears a slender elongate facet in its anterior extremity. More posteriorly, as seen in MNHN.F.MAP327b, the lateral margin merges smoothly with the transverse flange described below. As is best visible in the posterior region of the original slab, the palatal ramus bears several palatal teeth arranged in two, tightly packed longitudinal rows on the medial side of the bone (Fig. 5).

The transverse flange is visible in all specimens. As best seen on the well preserved left pterygoid of MNHN.F.MAP327b (Fig. 5), this flange extends anteroventrolaterally from the posterolateral corner of the bone and merges smoothly with the palatal ramus. The lateral margin of the flange is slightly thickened posteriorly and bears a single row of palatal teeth similar in size to those of the palatal ramus (Fig. 5). As is visible on the right pterygoids of MNHN.F.MAP327b and MNHN.F.MAP317b, the dorsal surface of the transverse flange is slightly convex (Figs. 4-5).

The basicranial process of the pterygoid is preserved on the left pterygoid of MNHN.F.MAP317a and is identified based on its proximity to the parabasisphenoid and the close fit in size between the recess on the pterygoid and the basipterygoid processes of the latter bone (Fig. 4). It is visible in medial aspect, lying near the parabasisphenoid. The basicranial process is a robust, knob-like expansion at the meeting point of the palatal, transverse and quadrate processes of the pterygoid (Figs. 2-3). It bears a deep concave surface that encompasses the neighboring right basipterygoid process of the parabasisphenoid.

The quadrate ramus is preserved on the right pterygoid of MNHN.F.MAP327b, and on the left pterygoid of MNHN.F.MAP317a (Figs. 4-5). It is anteroposteriorly long and dorsoventrally thin. The quadrate ramus of the right pterygoid of MNHN.F.MAP327b gradually

expands dorsoventrally into a high dorsal flange. As the medial margin of the bone is unpreserved, we cannot say whether an arcuate flange was present (Fig. 5C-D).

Ectopterygoid—We agree with the identification of the left ectopterygoid of MNHN.F.MAP327b by Bulanov and Sennikov (2015a:422). Based on our interpretation of the pterygoid facet (see below), the bone is preserved in ventral view and lies near in the articulated skull roof portion (Fig. 5).

Similar to the palatine, the anterior and posterior margins of the bone are strongly concave, such that the bone consists of a robust short neck and expanded medial and lateral portions. However, in contrast to the palatine, both parts are of similar size and proportions (Fig. 5). The bone thus forms the posterior and posteromedial margins of the suborbital fenestra, and the anterior and anteromedial margins of the subtemporal fossa (Fig. 2). The lateral portion is very similar to that of the palatine. It is robust and bears an elongate lateral margin for the articulation with the external skull bones. It is unclear if this contact was restricted to the jugal or extended over the maxilla. The ectopterygoid lateral contact is restricted to the jugal in most early diapsids (Currie, 1980, 1981; Reisz, 1981). This is also the case in most saurians (Camp, 1945; Evans and Borsuk-Białynicka, 2009; Flynn et al., 2010) although it extends over the maxilla in several groups (Evans, 1980; Spielmann et al., 2008).

A sharp ridge extends anteromedially from the posterior margin of the lateral articular facet of the bone to its anteromedial extremity. Posterior to this ridge, the medial portion of the bone bears a recess, presumably to accommodate the transverse flange of the pterygoid. As reconstructed, the ectopterygoid contacted the palatine anteriorly (Fig. 2B), although we were unable to identify any facet on either bone.

Braincase

Of the braincase bones, only the parabasisphenoid and a potential basioccipital condyle were previously identified in MNHN.F.MAP317a (Bulanov and Sennikov, 2015a:422). However, our detailed examination of the specimen results in a new interpretation of this region (Figs. 4, 8).

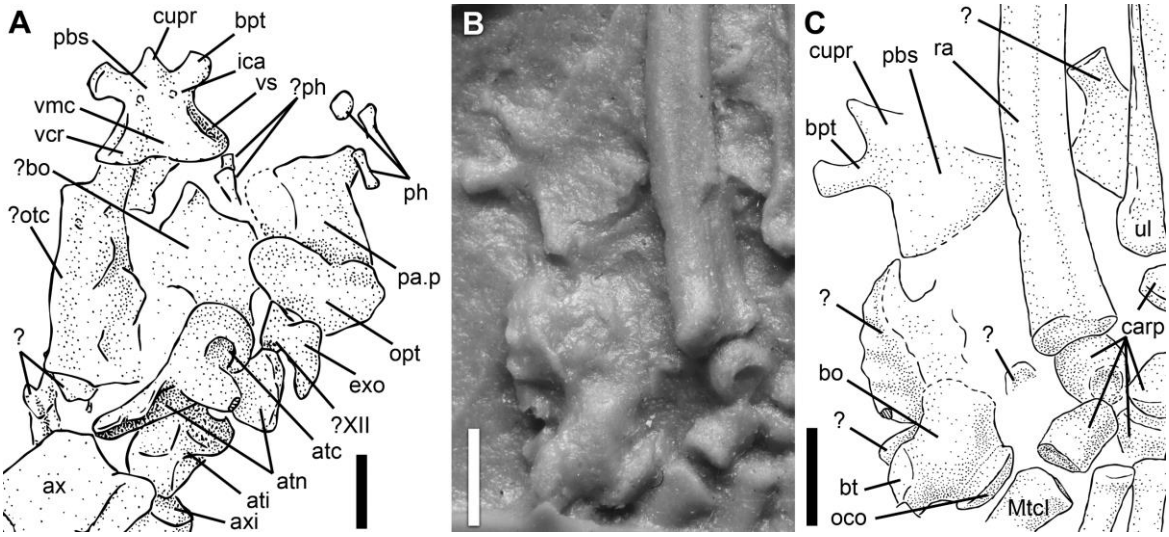

Figure 2-8: *Coelurosauravus elivensis* Piveteau, 1926 (Madagascar, Lopingian), braincase and postcranial elements mostly in ventral view. **A**, close up view of paralectotype MNHN.F.MAP317a, as indicated in Fig. 4C. **B**, disarticulated elements in MNHN.F.MAP327a, silicone cast of individual preserved as a natural external mold; **C**, interpretative drawing of **B**. **Abbreviations**: **atc**, atlantal centrum; **atn**, atlantal neural arch; **ax**, axis; **axi**, axial intercentrum; **bo**, basioccipital; **bpt**, basipterygoid process; **carp**, carpal elements; **cupr**, cultriform process of parasphenoid; **exo**, exoccipital; **ica**, foramen for internal carotid artery; **Mtc**, metacarpal; **oco**, occipital condyle; **opt**, opisthotic; **otc**, otic capsule elements; **pa.p**, paroccipital process; **pbs**, parabasisphenoid; **ph**, phalange; **ra**, radius; **ul**, ulna; **vcr**, ventrolateral crest; **vmc**, ventromedial concavity; **vs**, vidian sulcus; **XII**, foramen for hypoglossal nerve (CN XII). Scale bars equal 2 mm.

Parabasisphenoid—The parabasisphenoid of MNHN.F.MAP317a is well preserved and lies near its anatomical position (Fig. 8). Additionally, we interpret a flat triangular bone near the right carpus of MNHN.F.MAP327a as the parabasisphenoid due to its similar shape to that of MNHN.F.MAP317a (Fig. 8). This bone was previously identified as an atlantal neural arch by Carroll (1978:fig. 6). In both specimens, the basisphenoid and parasphenoid bones are indistinguishable.

The parabasisphenoid is edentulous on both *Coelurosauravus* specimens, as in *Youngina* and almost all saurians (Gardner et al., 2010; Matsumoto and Evans, 2017). In contrast the parabasisphenoid of most stem-saurians is denticulated (*Claudiosaurus*, *Lanthanolania*, *Petrolacosaurus*, Carroll, 1981; Reisz, 1981; Modesto and Reisz, 2003), which is also the case in kuehneosaurids (Evans, 2009) and the early lepidosauromorph *Fraxinisaura* (Schoch and Sues, 2018b).

The cultriform process appears very reduced in both *Coelurosauravus* specimens and is slightly shorter than the basipterygoid processes (Fig. 8). However, this may be an artefact of

preservation, suggesting that it was slightly anterodorsally oriented and its anterior portion was encased in the matrix of the lost counterpart block. A strongly reduced cultriform process indeed only occurs in some parareptiles but has otherwise not been described for other early amniotes (e.g., Carroll and Lindsay, 1985).

The main body of the bone forms an equilateral triangle, one corner of which points anteriorly. The basipterygoid processes extend anterolaterally and slightly ventrally from the base of the cultriform process (Fig. 8). They consist of a slightly elongate and constricted neck with a circular cross-section and an expanded convex head with an ovate articular surface facing anterolaterally (Fig. 8).

The parabasiphenoid of MNHN.F.MAP317a bears a pair of small foramina housing the internal carotid artery on its ventral surface, medial to the base of the basipterygoid processes (Fig. 8A). These foramina are not covered ventrally by the ventrolateral crests as is otherwise common among early diapsids (Müller et al., 2011; Ford and Benson, 2019). The ventrolateral crests are robust and low, extending posterolaterally along the lateral sides of the ventral surface of the bone but not meeting anteriorly. Instead, they remain separate. They delimit a deep ventrolateral trough on each side of the bone, presumably the vidian sulci (Fig. 8A), but these do not extend ventrolaterally as a thin lamina to floor this canal, as is the case in most early reptiles (Müller et al., 2011). Based on other criteria, we consider MNHN.F.MAP317a-b as morphologically mature (see above), suggesting that the lack of contribution to the floor of the vidian sulcus does not indicate an immature ontogenetic stage and an incomplete ossification. The extent of these crests and their contribution to the floor of the vidian sulcus seem to be slightly variable in saurian reptiles as well, both inter- and intra-specifically (e.g. Evans, 1980, 1986, 2009). Conversely, a similar morphology is found in most early synapsids excluding varanopids (Ford and Benson, 2019).

The posteroventral surface of the bone is concave between the ventrolateral crests in both *Coelurosauravus* specimens (Fig. 8). The posterior margin of the parabasisphenoid is roughly straight, with a slightly concave medial portion. There is no trace of posterolateral processes. Most early diapsids exhibit either short (e.g., *Claudiosaurus*, *Petrolacosaurus*, Carroll, 1981; Reisz, 1981) or elongate posterolateral processes of the parasphenoid (e.g., *Thadeosaurus*, *Youngina*, Currie and Carroll, 1984; Gardner et al., 2010).

Supraoccipital—The supraoccipital is visible in MNHN.F.MAP317b, but is best preserved in the lectotype (Figs. 3-4). It is a quadrangular bone, occupying the space between the medial margins of the posttemporal processes of the parietal. It articulated with the parietal anteriorly, possibly abutting the postparietal lamina of the parietal (Fig. 7), with the exoccipitals posteroventrally, as well as with the bones of the otic capsule, although the articulations with the latter bones are not visible on any of the specimens. The entire dorsal surface of the bone is concave on both specimens and framed by slightly elevated lateral and posterior margins. There is no trace of the dorsal sagittal ridge described for some other early diapsids (e.g., *Hovasaurus*, *Petrolacosaurus*, Currie, 1981; Reisz, 1981), although this might be due to late diagenetic compression (Figs. 3-4). The anterolateral processes, if present, are not visible on any *Coelurosauravus* specimen. The posteroventral margin of the supraoccipital is slightly elevated relative to the dorsal surface of the bone. Its median portion is concave, forming the dorsal margin of the foramen magnum medially.

Exoccipital—We identify a small crescentic bone lying near the basioccipital and the atlantal centrum in MNHN.F.MAP317a as the left exoccipital, visible in posterior view (Fig. 8A). The braincase experienced diagenetic compression but very slight displacement of the individual bones. According to our interpretation, the concave medial margin of the bone represents the left lateral margin of the foramen magnum, as in all early diapsids (Evans, 1986; Gardner et al., 2010; Sobral and Müller, 2019). The exoccipital was thus not fused to the neighboring elements in contrast to some early reptiles (e.g., *Prolacerta*, *Youngina*, Evans, 1986, 1987; Gardner et al., 2010). The exoccipitals form the lateral margins of the foramen magnum.

The dorsal portion of the exoccipital expands dorsally and dorsomedially, forming a broad contact with the supraoccipital medially and opisthotic laterally. Ventrally, the bone bears as a robust pillar-like expansion that abuts on the basioccipital. The extent of the exoccipitals over the dorsal and ventral margins of the foramen magnum is unknown due to the disarticulation of the material. A recess in the medial margin of the exoccipital lateral to the foramen magnum might represent the foramen for the passage of the hypoglossal nerve (CN XII; Fig. 8A).

Basioccipital—The basioccipital lies near the carpus and the parabasisphenoid of MNHN.F.MAP327a (Fig. 8B-C). It is oriented ventrolaterally and is visible in right ventrolateral view. Despite being figured by Carroll (1978:fig. 6), this bone was previously unidentified. It is a small quadrangular bone with a convex ventral surface. Its anterolateral margins bear robust, low basal tubera (Fig. 8B-C) with lunate suture facets for the articulation with the parabasisphenoid. More posteriorly, the basioccipital is strongly constricted before expanding into a rounded projection forming the ventral portion of the occipital condyle (Fig. 8B-C). As is visible in posterior view, the occipital portion of the basioccipital is dorsoventrally narrow and presumably only formed the ventral portion of the condyle.

Bulanov and Sennikov (2015a:422, pl. 5) identified a circular bone on MNHN.F.MAP317a as the basioccipital, forming the entire occipital condyle. However, this structure does not conform to the basioccipital of MNHN.F.MAP327a. We instead consider the large circular pit of this element as a deep notochordal pit, and interpret this bone as a vertebral centrum, presumably that of the atlas based on its short length and position. Although the atlantal centrum is pierced by a notochordal pit in most stem-saurians, suggesting a large pit in posterior view (Vaughn, 1955; Carroll, 1981; Reisz, 1981), descriptions of the posterior surface of the atlas centrum are scarce in early diapsids, in part due to the fusion of this element to the axis in many taxa (Romer, 1956). However, the atlantal centrum of MNHN.F.MAP317a conforms well to that of captorhinids (Peabody, 1952; Sumida, 1990) and varanopids (Campione and Reisz, 2011), which also bears a deep nothochordal pit in posterior view. The atlantal centrum of MNHN.F.MAP317a partially obscures a plate-like bone lying just posterior to the parabasisphenoid, which may represent the basioccipital (Fig. 8A).

Otic Capsule—Several fragments in MNHN.F.MAP317a may belong to the otic capsule. An elongate rectangular structure in contact with the posterolateral portion of the parabasisphenoid bears a complex system of ridges and is pierced by at least one foramen. This structure may accommodate semicircular canals. However, it is too poorly preserved to be anatomically identified with certainty.

A large element lying immediately anterior to the left exoccipital is interpreted as the opisthotic based on its position and our identification of the paroccipital process (Fig. 8A). We identify the paroccipital process based on its length, shape and blunt terminus, suggesting a

contact with the dermal skull roof, as in several early diapsids (Evans, 1986; Flynn et al., 2010; Sobral and Müller, 2019). However, we are unable to identify its area of contact. In contrast, the paroccipital ends freely in *Claudiosaurus* and *Hovasaurus* (Carroll, 1981; Currie, 1981). The paroccipital process of MNHN.F.MAP317a is rectangular and thin, which conforms well with that of several archosauromorphs, where this process is anteroposteriorly flattened (Flynn et al., 2010; Sobral and Müller, 2019). Based on the position of the proximal portion of the bone, this comparison suggests that the opisthotic is visible in anterior view (Fig. 8A). The proximal portion of the bone is only identified thanks to its relation to the paroccipital process. We were unable to identify structures unequivocally.

Mandible

We interpret previously unidentified bones in MNHN.F.MAP317a as the posterior portion of the right mandibular ramus (Fig. 4), which is transversely crushed and visible in dorsolabial view. The preserved bones correspond to the surangular and possibly the articular.

Surangular—We interpret the largest of the two elements as the posterior portion of the right surangular, visible in labial view (Fig. 4). This identification is based on the subtle irregular sculpturing of the bone, its blunt, irregular posterior extremity, and its smooth and slightly concave margin on the right. In these aspects, this bone conforms well to the posterior portion of the surangular of the *Weigeltisaurus* holotype, which is of similar shape, also shows a very subtle sculpturing on its labial surface, and bears a smooth, concave dorsal margin forming the labial wall of the adductor fossa (VB, pers. obs.; Bulanov and Sennokov, 2015b). Based on this identification, the dorsal margin of the surangular of MNHN.F.MAP317a faces to the right side of the animal, indicating that the bone is the right surangular in lateral view (Fig. 4).

The dorsal surface of the bone expands medially to form a shelf overhanging the adductor fossa, as in *Weigeltisaurus* (Bulanov and Sennikov, 2015b) and *Rautiania*, although the dorsal shelf almost closes the adductor fossa in dorsal view in the latter (Bulanov and Sennikov, 2010). Similar surangular dorsomedial shelves have been considered as a synapomorphy of varanopids (Ford and Benson, 2019, 2020), and have been described for *Acerosodontosaurus* and *Hovasaururs* (Currie, 1980, 1981). The irregular ventral margin of the

bone may indicate breakage, or the articular surface for the angular, which is not preserved on the specimen (Fig. 4). There is no trace of the posterior surangular spikes reported in *Rautiania* and *Weigeltisaurus* (Bulanov and Sennikov, 2010, 2015b).

?Articular—A small crescentic element lies near the posterior margin of the surangular. Based on its position relative to the surangular and thus the adductor fossa, we tentatively identify this element as a portion of the articular bone, forming the posteriormost portion of the mandibular ramus (Fig. 4). The posterior surface of the element is concave, although the articular cotyles for the quadratoarticular articulation cannot be identified. We were able to identify neither the retroarticular process, which is prominent in *Rautiania* and the *Weigeltisaurus* holotype (Bulanov and Sennikov, 2010, 2015b), nor the dorsal and medial processes described for *Rautiania* and the *Weigeltisaurus* holotype (Bulanov and Sennikov, 2010, 2015b).

Discussion

A detailed analysis of the phylogenetic position of weigeltisaurids among Permo-Triassic reptiles is out of the scope of this study, pending a re-description of the weigeltisaurid postcranium, which is currently under study by the authors. However, the reexamination of the cranial material of *Coelurosauravus elivensis* provided here and its comparison with other weigeltisaurids allows for a discussion of the morphology and functional anatomy of the skull of these enigmatic animals.

Cranial Reconstruction

Our reconstruction of the skull of *Coelurosauravus* resembles that of Bulanov and Sennikov (2015a:fig. 3A) although we highlight subtle differences. It allows for new comparisons within weigeltisaurids, focusing on peculiarities such as the large skull openings, the parietosquamosal frill, and putative muscle attachment areas.

The dermal bones of the skull are very light and hollow in weigeltisaurids, which Bulanov and Sennikov (2010) interpret as an adaptation to their aerial lifestyle. However, the

truss-like skull structure of weigeltisaurids (Fig. 2) presumably housed large eyeballs and temporal muscles (as discussed below) which, in addition to the frill and ornamentation, might have added to the skull weight. As bone matter is not preserved in the Malagasy material, we focus here on the macrostructural aspects of the skull.

Preorbital Fenestra—Weigeltisaurids possess a small preorbital fenestra enclosed between the nasal and maxilla and excluded from the lacrimal (Figs. 2, 6; Bulanov and Sennikov, 2015a-b). Apertures anterior to the orbit have not been reported in stem-saurians with the possible exception of drepanosauromorphs (Calzavara et al., 1980 but see Renesto, 1994), but have been extensively studied in saurians (Witmer, 1995, 1997 and references therein). Yet, neither the function nor the homology of this structure in weigeltisaurids has been discussed.

Antorbital openings are present in a wide range of unrelated taxa (e.g., mesosaurid and thalattosaurian reptiles; Rieppel et al., 2005; Modesto, 2006; Piñeiro et al., 2012) but are better known in archosauriforms (Nesbitt, 2011). In archosauriforms, the antorbital fenestra is typically formed by the maxilla and lacrimal, and houses the pathways of the paranasal air sinus and that for the nasolacrimal duct more dorsomedially (Witmer, 1995, 1997). As described above (see "maxilla" section), the nasolacrimal duct of weigeltisaurids passes ventral to the preorbital fenestra, differentiating the latter from the antorbital fenestra of archosauriformes. In addition, the preorbital fenestra of weigeltisaurids is formed solely by the maxilla and nasal, in contrast to the condition in archosauriforms and other non-archosauriform reptiles where other bones contribute to the antorbital openings (Rieppel et al., 2005; Modesto, 2006; Piñeiro et al., 2012).

The weigeltisaurid preorbital fenestra is thus distinct from the antorbital openings of other reptiles, at least in its topography. On the *Weigeltisaurus* holotype, this fenestra lies dorsal to the supralabial row of foramina for the maxillary branch of the trigeminal nerve (Fig. 6C-D). It is thus likely not derived from this innervation. The lack of extant homologues prevents us from identifying a possible function.

Orbit—Bulanov and Sennikov (2015a:fig. 3A) reconstructed *Coelurosauravus* with a very broad postorbital region, due to the lateral expansion of the frontal, postorbital and parietal bones. As a result, that study depicted this taxon with large, laterally positioned and

anterolaterally oriented orbits. In contrast, we reconstruct *Coelurosauravus* with a much more slender postorbital region (Fig. 2A). While we concur with the reconstruction of the parietal and postorbital bones based on MNHN.F.MAP327a-b, we found evidence of enlarged posterolateral processes of the frontals neither in the lectotype nor in MNHN.F.MAP317b (Figs. 3-4). The frontal of MNHN.F.MAP327b is preserved in ventral view. What is visible of the lateral margin of the bone does not indicate such enlarged processes. Thus, we disagree with Bulanov and Sennikov's (2015a) reconstruction of the frontal of *Coelurosauravus*. In our reconstruction, the orbits of *Coelurosauravus* are oriented laterally instead of anterolaterally as they suggested. However, we concur with Bulanov and Sennikov (2015a) that the orbits of *Coelurosauravus* are positioned on the lateral face of the skull, in contrast to the more dorsolaterally positioned orbits of *Youngina* (Gow, 1975).

The orbits are very large in *Coelurosauravus*, forming roughly a third of the reconstructed basal skull length (tip of rostrum to occipital condyle; Fig. 2, Table 2). This 1/3 ratio of the orbit also occurs on the *Weigeltisaurus* holotype (28%, Bulanov and Sennikov, 2015b:1104) and the Ellrich specimen (30%, Table 2), and is also reconstructed for *Rautiania* (Bulanov and Sennikov, 2010:pl. 9). In *Glaurung*, the orbits are much smaller, occupying only 24% of the basal skull length (Bulanov and Sennikov, 2015c).

Pineal Foramen—Forming approximately 56% of the length of interparietal suture, the pineal foramen of *Coelurosauravus* is very large (Fig. 2; Table 2), suggesting a fully functional parietal eye (Edinger, 1955; Gundy and Wurst, 1976). This is also the case in the Ellrich specimen (62%, Table 2) and on the reconstruction of *Rautiania* of Bulanov and Sennikov (2006:fig.1). Although the relative size of the pineal foramen of weigeltisaurids shows a slight variability (see above), it is significantly larger than that of coeval diapsids such as *Youngina* (ca. 28% of interparietal suture length, BP/1/3859, VB pers. obs.), *Claudiosaurus* (ca. 31%, Carroll, 1981:fig. 15) and *Hovasaurus* (ca. 35%, MNHN.F.MAP373, VB pers. obs.).

Temporal Fenestration—Temporal fenestration has long been used in the classification of amniotes based on the presence or absence of an infratemporal fenestra (ITF) and a supratemporal fenestra (STF) (e.g., Osborn, 1903). In anatomically diapsid skulls, the ITF is typically bordered by the postorbital, jugal, quadratojugal and squamosal while the STF is bordered by the postorbital, parietal and squamosal (Reisz, 1981). However, several

phylogenetic studies have questioned the universality of these characters (e.g., Müller, 2003; Laurin and Piñeiro, 2017, 2018; MacDougall et al., 2018; Ford and Benson, 2020).

The possession of both an ITF and an STF is probably plesiomorphic in diapsids (Müller, 2003). However, the temporal fenestration is subjected to a very high degree of plasticity in reptiles (e.g. Piñeiro et al., 2012; Werneburg, 2019; Ford and Besnon, 2020), as exemplified by the loss of the ITF in *Araeoscelis* (Reisz et al., 1984) and the multiple convergent losses and reacquisitions of the ITB in later diapsids (e.g., *Claudiosaurus*, sauropterygians, squamates, archosauromorphs, Müller, 2003; Curtis et al., 2011). However, the preservation of the supratemporal bar (STB) appears much more conservative (Rieppel, 1984a, 1993b; Werneburg, 2019).

A short posterodorsal process of the postorbital underlying the parietal and forming the anterodorsal margin of the temporal fenestra was reported in *Glaurung* (Bulanov and Sennikov, 2015c). Bulanov and Sennikov (2015c:1363) consider this process as homologous to that of other diapsids, although its relationships to the parietal and sole temporal fenestra are more similar to that found in edaphosaurian synapsids, where the posterior process of the postorbital abuts the lateral margin of the parietal (e.g., Romer and Price, 1940; Modesto, 1995). Under that interpretation, the temporal fenestra of weigeltisaurids would result from the dorsal expansion of the ITF and the loss of contact between the postorbital and squamosal. Whether weigeltisaurids underwent a prior reduction of the STF is unknown, but the temporal morphology and the continuous postorbitoparietal contact suggest its absence in *Glaurung* (Bulanov and Sennikov, 2015c:fig. 2). Alternatively, the postorbital posterior process described by Bulanov and Sennikov (2015c) might be a misinterpreted bone fragment of unknown anatomical attribution, owing to the poor preservation of the badly crushed specimen.

Additionally, the quadratojugal of weigeltisaurids is very small, with reduced anterior and dorsal processes (see description above). The ITB of weigeltisaurids is thus formed mostly by the posterior process of the jugal (Fig. 2). We note that in those stem-saurians with a complete ITB, the latter is formed by subequal contributions of the jugal and quadratojugal (Gow, 1975; Reisz, 1981; Reisz et al., 1984), but is mostly formed by the jugal in saurians with a complete ITB (e.g., archosauromorphs, rhyncocephalians, borioteiioid squamates, Whiteside, 1986; Evans and Jones, 2010; Nesbitt, 2011; Simões et al., 2016). As the absence of a complete

ITB may be plesiomorphic for saurians, previous studies argue that the morphology in saurians with a complete ITB is indicative of a secondarily acquired diapsid condition (i.e. a reappearance of the ITB) in the context of bite force enhancement and/or skull stabilization (e.g., Müller, 2003; Curtis et al., 2011; Simoes et al., 2016). The morphology of the weigeltisaurid ITB may thus suggests a similar reacquisition, indicating more crownward saurian affinities for weigeltisaurids. However, a convergent acquisition of this morphology from a fully diapsid skull by posterior extension of the jugal and reduction of the quadratojugal is also possible.

Ornamentation—The weigeltisaurid skull is ornamented, even in the very small Wolfsberg specimen (Schaumberg, 1976, 1982, 1986). This ornamentation covers the circumorbital, temporal and posterior mandibular bones and comprises both elongate spikes and smaller tubercles (Fig. 2; Bulanov and Sennikov, 2015a-c).

Based on computed tomography, Bulanov and Sennikov (2010) interpreted the circumorbital and frill spikes of *Rautiania* as hollow osteoderms that have fused to the underlying bone. However, the small tubercles on the posttemporal processes of *Coelurosauravus* and *Glaurung* have not been examined. By analogy with pachycephalosaurian dinosaurs, the spikes of weigeltisaurids may be of osteodermal origin, but the smaller tubercles could alternatively be protrusions of the bones (Goodwin and Evans, 2016). Similarly, micro-CT and histological data show that the tubercles of extant chamaeleonids consist of regionalized outgrowths of the bones (Prötzel et al., 2018). Further studies focusing on the microstructure or histology of the ornamentation of weigeltisaurids are needed to assess their homology.

Parietosquamosal Frill—All known weigeltisaurids specimens with articulated skulls show a conspicuous parietosquamosal frill (Schaumberg et al., 2007; Bulanov and Sennikov, 2015a-c). Even the small-sized Wolfsberg specimen exhibits this peculiar morphology (Schaumberg, 1976, 1982, 1986). In addition, the fossiliferous Russian deposits have failed to yield remains lacking a frill, despite numerous specimens being recovered (Bulanov and Sennikov, 2006, 2010, 2014, 2015c). It is thus likely that all weigeltisaurid individuals bore ornamented frills regardless of their ontogenetic stage, and that the presence of this structure is not sexually dimorphic, although this cannot be ascertained in light of the rarity of articulated cranial remains (seven specimens preserve articulated skull portions). Similarly, the casque of

chamaeleonids forms at very early ontogenetic stages (e.g., Rieppel, 1993a), and its presence is not sexually dimorphic, although males show a relatively larger and more ornamented casque in some taxa (Stuart-Fox et al., 2006; Stuart-Fox, 2013). In ceratopsians, even the smallest known individuals have a parietosquamosal frill (Goodwin et al., 2006; Horner and Goodwin, 2006).

Jaw Adductor Musculature

The parietosquamosal frill of weigeltisaurids is formed by the elongation of the parietal and squamosal (Fig. 2). A similar morphology occurs in the casque of chamaeleonid squamates and frill of ceratopsian dinosaurs, which have been proposed as analogs for weigeltisaurids (Weigelt, 1930a; Huene, 1930; Schaumberg et al., 2007). This elongation has been linked to changes (observed in chamaeleonids, only inferred in ceratopsians) in the jaw adductor musculature, especially that inserting in the STF (Haas, 1955; Ostrom, 1964, 1966; Rieppel, 1981, 1987; Maiorino et al., 2017).

The excellent preservation of the *Coelurosauravus* skull allows for a preliminary discussion on the adductor musculature of weigeltisaurids. The adductor musculature of extant reptiles includes several muscles, with the m. adductor mandibulae A2 being dominant (Diogo et al., 2018; = "m. adductor mandibulae externus" of other authors e.g., Romer, 1956; Haas, 1973; Abdala and Morro, 2003; Holliday and Witmer, 2007). This muscle is divided in three portions: superficialis (A2-S), medialis (A2-M), and profundus (A2-P).

An origin area of the A2-S could not be identified unequivocally in *Coelurosaravus*. This muscle typically originates from the medial margin of the STB in extant lepidosaurians (Haas, 1973) and from the medial surface of the quadratojugal in crocodilians (Schumacher, 1973; Holliday, 2009). However, these structures are absent or reduced in weigeltisaurids (see above). It is possible that the A2-S covered the A2-M laterally as in geckos (Haas, 1973; Rieppel, 1984b), or that it had a fleshy origin leaving no trace on the bones (Bryant and Seymour, 1990). Alternatively, the A2-S originates on the squamosal in birds (Holliday and Witmer, 2007; Holliday, 2009). Owing to the slightly concave dorsal surface of the squamosal (Fig. 7), this may also have been the case in *Coelurosauravus*, although we found no insertion rugosity for bundles of Sharpey fibers. In addition, as proposed for those saurians with a complete ITB (see

above), the presence of a complete ITB in weigeltisaurids prevented the expansion of the A2-S over the labial surface of the mandible (Rieppel and Gronowski, 1981; Simões et al., 2016). This is further supported by the presence of elongate spikes on the posterior lateral surface of the mandible in *Rautiana* and on the *Weigeltisaurus* holotype (Bulanov and Sennikov, 2010, 2015b). Consequently, the A2-S insertion was mostly limited to the dorsal margin of the mandible, possibly to the surangular dorsomedial shelf.

The A2-M and A2-P differ greatly among extant reptiles. The A2-M is typically large in lepidosaurs and may occupy a shallow fossa on the posteromedian margin of the STF, while the A2-P is smaller (Haas, 1973). In contrast, the A2-M is small and less differentiated in extant archosaurs while the A2-P is large and typically originates from the posteromedian margin of the STF (Schumacher, 1973; Holliday, 2009). As weigeltisaurids are generally considered as stem-saurians (Müller, 2004; Simões et al., 2018; Pritchard and Sues, 2019), their general muscular pattern cannot be confidently inferred. However, the parasagittal ridge on the ventral surface of the posttemporal process of the parietal of *Coelurosauravus* almost certainly served as the origin of the adductor musculature (Fig. 7). Thus, a large A2-M and/or A2-P probably originated from the dorsal margin of the single temporal fenestra of weigeltisaurids. The origin surface of those adductor muscles also possibly extended onto the slightly concave anterodorsal margin of the squamosal.

Given our interpretation is correct, the adductor muscles thus had a very long surface of origin lateral to the posttemporal adductor ridge (Fig.7). Owing to the size of the identified area of origin and its position relative to the mandible, those muscles not only had long fibers, resulting in a rapid jaw adduction and likely a wide gape, but also a large diameter, resulting in an increased adduction power (Herrel et al., 1999, 2001; Huyghe et al., 2009).

Interestingly, the reacquisition of a complete ITB has been correlated with an increased bite force in sphenodontians and archosauromorphs by strengthening the skull against strains during feeding (e.g., Müller, 2003; Curtis et al., 2011). The presence of a complete ITB thus conforms well to the increased muscle mass and size described above, although further phylogenetic analyses will confirm whether the presence of a complete ITB in weigeltisaurids results from a reacquisition, or was present ancestrally.

Figure 2-9: *Coelurosauravus elivensis* Piveteau, 1926 (Madagascar, Lopingian), life reconstruction of the head, body hidden by *Glossopteris* leaves (found associated with *C. elivensis* in the fossil assemblage). The colors are based on extant chamaeleonids squamates. Illustration by Charlène Letenneur (MNHN).

Paleoecology of Weigeltisaurids

Weigeltisaurid paleoecology has been repeatedly discussed, mostly concerning their aerial lifestyle by comparison to the agamid *Draco* and the gliding kuehneosaurids (Carroll, 1978; Evans and Haubold, 1987; Frey et al., 1997). In contrast, their peculiar cranial morphology has been considerably less addressed (Schaumberg et al., 2007; Bulanov and Sennikov, 2015a-c). Based mostly on their postcranial anatomy, weigeltisaurids have been considered insectivorous arboreal and gliding reptiles, an interpretation followed here. Referring to the crested skulls, to arboreality or gliding capability, we suggest that ceratopsian dinosaurs, chamaeleonid squamates and the gliding agamid *Draco* may be well-suited to reconstruct the paleoecology of weigeltisaurids (e.g. Weigelt, 1930a; Schaumberg et al., 2007). Based on their spiky ornamentation, phrynosomatid iguanids could also serve as good analogues for weigeltisaurids.

By applying the principle of actualism (e.g. Vorobyeva, 2007), we thus provide elements to reconstruct the paleoecology of *Coelurosauravus* and other weigeltisaurids based on their cranium (Fig. 9). However, as the functional interpretation of a structure in the fossil

record is notoriously difficult (Gould, 1974; Benton, 2010; Knell and Sampson, 2011; Padian and Horner, 2011, 2014; Hone et al., 2012; Mendelson and Shaw, 2012, 2013; Hone and Naish, 2013), and in light of the scarcity of weigeltisaurids specimens and that of their recent analogues, we stress that the interpretations discussed below remain speculative.

Biting and Diet—As discussed above, the elongation of the parietosquamosal frill of weigeltisaurids may be correlated with an increase in size of the m. adductor mandibulae A2, in particular its medialis and/or profundus sections, as observed in chamaeleonids (Rieppel, 1981, 1987).

Chamaeleonids are known to consume relatively large prey compared to other lizards, due to their ballistic tongue (e.g. Herrel et al., 2000), and to their relatively high bite force resulting from their large adductor musculature (Vanhooydonck et al., 2007; Measey et al., 2013; da Silva et al., 2016; Dollion et al., 2017). Similarly, an increase in bite force has been linked to an increase in head height and thus in the size of the adductor musculature in several extant squamates, allowing for the consumption of large and/or hard preys (Herrel et al., 1999, 2001; Verwaijen et al., 2002). The large jaw adductor musculature in weigeltisaurids may generate a relatively strong bite force and a rapid jaw adduction (snapping), even if they lack a well-developed coronoid process for the insertion of the jaw adductor muscles (Bulanov and Sennikov, 2010, 2015b).

Previous studies have proposed an insectivorous diet for weigeltisaurids based on their dentition (Carroll, 1978; Bulanov and Sennikov, 2015a-c). We concur that the simple conical teeth of *Coelurosauravus* seem well suited for piercing arthropod integuments (e.g. Evans and Sanson, 1998). However, variation in crown shape has been reported in weigeltisaurids, with *Glaurung* and *Rautiania* showing labiolingually flattened teeth with a slight apical mesiodistal expansion (Bulanov and Sennikov, 2006; 2015c). Bulanov and Sennikov (2015c) argued that these differences could indicate differences in trophic specialization, but this is hard to ascertain in light of the lack of associated prey items (e.g. insects), and the wide range of food sources exploited by extant squamates, including vegetation (Bels et al., 2019, and references therein). These differences in tooth morphology could also be linked to the size of the frill and bite force. However, as the relationships between these structures are not well understood in extant taxa

(e.g. chamaeleonids), they will not be discussed further here (Measey et al., 2009, 2011, 2013; da Silva et al., 2016; Dollion et al., 2017).

Display Structures—Extant squamates undertake stereotypical displays to signal conspecifics – males and females – and to deter predators (Carpenter and Ferguson, 1977; Greene, 1987). For example, chamaeleonids undertake lateral displays using their casque to appear larger (Kelso and Verrell, 2002; Stuart-Fox, 2013), and phrynosomatids, which exhibit a spiky ornamentation reminiscent of that of weigeltisaurids, assumes a chin-down posture to position their horn vertically to deter predators (Bergmann and Berk, 2012). By analogy, similar display behaviors have been proposed for ceratopsian dinosaurs (e.g., Maiorino et al., 2017).

The elongate and ornamented parietosquamosal frill of weigeltisaurids may have functioned as a display structure as well (Fig. 9). Previous studies have suggested that the frill was mobile, and could be extended for courtship and/or to deter predators (Schaumberg et al., 2007). However, we concur with Bulanov and Sennikov (2015b) that the frill was rigid due to constricting joints. Weigelt (1930a) also proposed that the spines could mimic surrounding coniferous branches to serve as camouflage (Weigelt, 1930a). However, this is highly hypothetical since camouflage is highly dependent on coloration (Stevens and Merilaita, 2009; Cuthill, 2019), which is unknown in weigeltisaurids.

Additionally, many squamates show intraspecific aggressive behavior (Carpenter and Ferguson, 1977). Chamaeleonids may fight through biting and horn thrusts, in which case individuals with a larger casque generally win (Stuart-Fox et al., 2006; Stuart-Fox, 2013). These fights can lead to injury, but it is unclear whether the casque protected the neck and occipital region of the head. For many authors, the horns of ceratopsians were likely used in sexual combat or defense against predators, during which the frill prevented injuries caused by horn thrusts, thus protecting the temporal muscles and the neck (Farlow and Dodson, 1975, Farke, 2004, 2014; Farke et al., 2009, 2010; Krauss et al., 2010 but see Tanke and Rothschild, 2010). Their horns are indeed composed of solid bone, giving them sufficient resistance to be used as weapons (Sampson et al., 1997; Horner and Goodwin, 2008). Secondarily possible functions such as thermoregulation have also been proposed as potential exaptations of the frill (e.g., Barrick et al. 1998).

While there is no basis to infer aggressive behavior in weigeltisaurids, this would add evolutionary advantage on an increased bite force. Their frill and ornamentation, highly reminiscent of those of chamaeleonid squamates and ceratopsian dinosaurs (Fig. 9), could thus have served as a defense mechanism, to deter small predators or conspecifics and/or to protect the temporal muscles and the neck during male to male combats. We note, however, that gliding flight escape was likely a more efficient defensive mechanism, at least against predators, as in *Draco* (Greene, 1987).

Conclusion

The detailed re-description of all known specimens of *Coelurosauravus elivensis* highlights several hitherto unknown anatomical details. We interpret several bones on MNHN.F.MAP317a as portions of the palate and braincase, which were previously undescribed in weigeltisaurids. This allows for the first reconstruction of the palate of *C. elivensis* and as such the first palatal reconstruction for weigeltisaurids. *C. elivensis* differs from all other known weigeltisaurids in its large anterior marginal dentition and cranial ornamentation, particularly in its parietosquamosal frill. Our detailed osteological re-description of the cranium and comparisons with other weigeltisaurids and other reptiles provide a background that should be useful in future phylogenetic and biomechanical analyses. Elucidating the systematic position of weigeltisaurids is out of the scope of this paper, but a phylogenetic analysis is currently under work by the authors. However, the novel anatomical data allow for a discussion on the functional anatomy of the unique cranial morphology of *C. elivensis* and other weigeltisaurids. Our data support the insectivorous, arboreal and aerial lifestyle suggested by previous works. In analogy with extant chamaeleonids and more tentatively ceratopsian dinosaurs, we suggest that the elongation of the parietosquamosal frill, the loss of the upper temporal bar and the enlargement of the temporal fenestra are linked with a size increase of the external jaw adductor musculature, resulting in an increased gape, bite force and jaw adduction speed. Additionally, the ornamentation of the frill and orbital series likely served as display structures for intraspecific communication and/or for deterring predators.

Chapter 3: The postcranial skeleton of the gliding reptile *Coelurosauravus elivensis* Piveteau, 1926 (Diapsida, Weigeltisauridae) from the late Permian of Madagascar

> The present chapter has been published as a research article (Buffa et al., 2022) in the *Journal of Vertebrate Paleontology*, co-authored with E. Frey (SMNK), J.-S. Steyer (MNHN), and M. Laurin (MNHN).

Abstract—The postcranial skeleton of the gliding neodiapsid reptile *Coelurosauravus elivensis* (Lower Sakamena Formation, late? Permian, southwestern Madagascar) is re-described in detail based on all previously referred specimens. The exquisite preservation of the material provides three-dimensional details of the individual bones, which are missing in the Laurasian weigeltisaurid material. A new skeletal reconstruction of *C. elivensis* is proposed including the first reconstruction of a weigeltisaurid reptile in lateral view. The re-examination of the material highlights interspecific differences in the postcranium of weigeltisaurids, in particular in the trunk and patagial spars. These animals have long been considered as arboreal and gliding reptiles. However, new information on the postcranium of *C. elivensis* reveals strong similarities with both extant and extinct quadrupeds specialized for a clinging arboreal lifestyle. Additionally, the presence of an additional phalanx in the fifth digit of the manus is now attested for all weigeltisaurids where this region is preserved. We suggest that this morphology could have allowed weigeltisaurids to grasp their patagium as observed in the extant gliding agamid *Draco*. Weigeltisaurids are thus the earliest known gliding vertebrates and some of the first tetrapods with an obligatory arboreal lifestyle, but also represent the only known vertebrates with a hyperphalangy aligned with a gliding apparatus.

Introduction

Despite their sparse late Paleozoic fossil record, early diapsids show a surprisingly large morphological disparity (Sues, 2019). Several terrestrial, semi-aquatic and arboreal taxa had indeed appeared by the end of the Permian (Carroll, 1975, 1978, 1981; Gow, 1975; Currie, 1981a). Among those, the late Permian Weigeltisauridae are the earliest known gliding tetrapods (Carroll, 1978; Evans, 1982; Bulanov and Sennikov, 2015a–c; Buffa et al., 2021), and their study is paramount to understand the evolution of gliding flight in amniotes.

Weigeltisauridae include several taxa known from Laurasia and Gondwana (Bulanov and Sennikov, 2015a–c): *Weigeltisaurus jaekeli* (Weigelt, 1930) (Lopingian, Germany and England); *Coelurosauravus elivensis* Piveteau, 1926 (Capitanian–Lopingian?, Madagascar); *Glaurung schneideri* Bulanov and Sennikov, 2015c (Lopingian, Germany); *Rautiania alexandri* Bulanov and Sennikov, 2006 (Capitanian–Lopingian?, Russia); and *Rautiania minichi* Bulanov and Sennikov, 2006 (Capitanian–Lopingian?, Russia). *Wapitisaurus problematicus* Brinkman, 1988 (Early Triassic, Canada) was described as a weigeltisaurid, but its cranial morphology does not conform to recent descriptions, notably in lacking a large temporal fenestra (TMP 86.153.14, VB, pers. obs.; Brinkman, 1988). Following recent studies (Bulanov and Sennikov, 2010; Buffa et al., 2021), we will thus not consider this taxon as a weigeltisaurid, pending the systematic revision of the sole, poorly known specimen.

Weigeltisaurids have been considered pterosaurs (Weigelt, 1930:626), dinosaur relatives (Boule, 1910; Piveteau, 1926), rhynchocephalians (Weigelt, 1930), early ("pelycosaur-grade") synapsids (Kuhn, 1939) or stem-saurians (Huene, 1956; Carroll, 1978; Evans and Haubold, 1987; Laurin, 1991). Today, all recent phylogenetical analyses recover weigeltisaurids as stem-saurians (e.g. Ezcurra et al., 2014; Schoch and Sues, 2018; Pritchard and Sues, 2019; Sobral et al., 2020; Griffiths et al., 2021), possibly closely related to drepanosauromorphs (Merck, 2003; Senter, 2004; Pritchard et al., 2021) or 'paliguanids' (Müller, 2004).

The anatomy of weigeltisaurids is unique with respect to their arboreal and aerial lifestyle. While the cranium has recently received a lot of attention (Bulanov and Sennikov, 2006, 2010, 2015a–c; Schaumberg et al., 2007; Buffa et al., 2021; Pritchard et al., 2021), their postcranium remains poorly understood (Frey et al., 1997; Schaumberg et al., 2007; Bulanov

and Sennikov, 2010; Pritchard et al., 2021). The present study aims to describe novel postcranial details of *Coelurosauravus* from the Lopingian? of Madagascar, which has not been revised recently (Carroll, 1978; Evans, 1982; Evans and Haubold, 1987).

Institutional Abbreviations—**GM**, Geiseltalmuseum, Martin-Luther-Universität, Halle, Germany; **MNHN**, Muséum national d'Histoire naturelle, Paris, France; **SMNK**, Staatliches Museum für Naturkunde Karlsruhe, Karlsruhe, Germany; **SSWG**, Sektion Geologie, Ernst-Moritz-Arndt Universität, Griefswald, Germany; **TMP**, Tyrell Museum of Paleontology, Drumheller, Canada; **TWCMS**, Sunderland Museum, Tyne and Wear County Museums, Sunderland, England.

Material and Methods

Material—We examined all specimens previously referred to *Coelurosauravus elivensis* (Carroll, 1978; Bulanov and Sennikov, 2015a; Buffa et al., 2021). For comparison, we also examined original specimens or high-fidelity epoxy resin casts previously referred to *Weigeltisaurus*. The complete list of the studied material is provided in Table 1.

Geological Background—All known specimens of *Coelurosauravus elivensis* come from the upper beds of the Lower Sakamena Formation (southwestern Madagascar), which is commonly considered of Wuchiapingian age (e.g. Piveteau, 1926; Currie, 1981a; Hankel, 1994; Lucas, 2017). However, recent reinvestigations (Smith, 2020) and a possible Capitanian age for the Russian taxa (Sennikov and Golubev, 2017) suggest that the age of the Lower Sakamena Formation is poorly constrained and could extend from late Guadalupian to late Lopingian (possibly Capitanian to Changhsingian). All specimens are preserved in fine-grained nodular concretions. The remains are mostly preserved as external molds, showing skeletal imprints largely in connection. Most bones have been eroded and possibly further removed by etching or using acid so that only their external molds are preserved. A more comprehensive review of the first excavations led by J.-M. Colcanap in southwestern Madagascar during the early 20th century is underway by VB.

Table 3-1: Denominations and identifications of previously published specimens referred to the genera *Coelurosauravus* and *Weigeltisaurus*.

Specimen denomination	Identification	Material examined	Remarks
MNHN.F.MAP325a	*Coelurosauravus elivensis* (Lectotype)	MNHN.F.MAP325a	Patrimonial number 1908-11-21a
MNHN.F.MAP317a & b	*Coelurosauravus elivensis* (Paralectotype)	MNHN.F.MAP317a-b	Patrimonial number 1908-11-22a & b
MNHN.F.MAP327a & b	*Coelurosaravus elivensis*	MNHN.F.MAP327a-b	Patrimonial number 1908-5-2
SSWG 113/7	*Weigeltisaurus jaekeli* (Holotype)	SMNK-PAL 34899a (cast)	-
Ellrich specimen	*Weigeltisaurus* sp.	SMNK-PAL 2882	Counterpart in unknown private collection
GM 1462	*Weigeltisaurus* sp.	SMNK-PAL 34899b (cast)	-
Bodental specimen	*Weigeltisaurus* sp.	SMNK-PAL 34866 (cast) & 34866b (original)	Main slab in Bürger private collection
Wolfsberg specimen	*Weigeltisaurus* sp.	SMNK-PAL 34910 (cast)	Specimens in Munk private collection, currently being transferred to the Naturkundemuseum im Ottoneum, Kassel
Bahaus specimen	*Weigeltisaurus* sp.	-	Specimen in Simon private collection
Eppelton specimen	?*Weigeltisaurus* sp.	TWCMS B5937 (photographs)	-

Taxonomic Remarks—Buffa et al. (2021) provide an overview of current challenges and uncertainties in weigeltisaurid taxonomy. We follow their taxonomic framework (Table 1), summarized as follows: (1) The more recent MNHN.F.MAP inventory numbers for the MNHN specimens (including *Coelurosauravus elivensis*). (2) *Weigeltisaurus jaekeli* is exclusively used for the holotype specimen. (3) All other Western European specimens are referred to by their collection numbers, housing institution or locality reference. (4) All specimens from Eastern Europe are referred to as *Rautiania* sp. except for type specimens following Bulanov and Sennikov (2010).

According to this framework, SMNK-PAL 2882 is referred to as 'the Ellrich specimen' (Table 1) in contrast to Pritchard et al.'s (2021) recent referral of this specimen to *Weigeltisaurus jaekeli*. This should not be taken as a disagreement with Pritchard et al.'s (2021) reexamination of this specimen, but as the result of a more cautious consideration of the species *W. jaekeli* itself. As stated by Buffa et al. (2021), this standpoint highlights the need for reexamination of this species' diagnosis in light of other Western European specimens, especially since such a revision may result in *W. jaekeli* being recovered as a junior synonym of *Gracilisaurus ottoi* (see Haubold and Shaumberg, 1985).

Reflectance Transformation Imaging (RTI)—By computing a single 'interactive specimen', on which the illumination can be reoriented, RTI can help identify individual bones on jumbled specimens (Hammer et al., 2002). We use this method to compensate for the nature of preservation of the specimens using the same custom-made portable light dome as Buffa et al. (2021, an updated version of that used by Béthoux et al., 2016; Cui et al., 2018). Sets of 54 photographs under different LED sources were compiled using the RTIBuilder software. The resulting RTI files provided in Supplemental Data (Figs. S1–S3) can be opened using the software RTIViewer (both software packages are freely available at www.culturalheritageimaging.org).

Systematic paleontology

NEODIAPSIDA Benton, 1985 sensu Reisz, Modesto and Scott, 2011a

WEIGELTISAURIDAE Kuhn, 1939

COELUROSAURAVUS ELIVENSIS Piveteau, 1926

v*1926 *Coelurosauravus elivensis* (gen. nov, sp. nov.); Piveteau, 1926:173–177, pl. 17.1, 17.3.

v1977 "Institut de Paléontologie, Paris, no. 1908-5-2"; Carroll, 1977:385, fig. 14.

v1978 *Coelurosauravus elivensis* Piveteau, 1926; Carroll, 1978:144–149, figs. 1–4.

v1978 *Daedalosaurus madagascariensis* (gen. nov., sp. nov.); Carroll, 1978:149–159, figs. 5–7.

v1982 *Coelurosauravus elivensis* Piveteau, 1926; Evans, 1982:111–116, figs. 14–19.

v1987 *Coelurosauravus elivnensis* Piveteau, 1926; Evans and Haubold, 1987:275–302, figs. 3–5, 12–17, 21.

v2015 *Coelurosauravus elivensis* Piveteau, 1926; Bulanov and Sennikov, 2015a:413–423, figs. 1, 2, pl. 5.

v2021 *Coelurosauravus elivensis* Piveteau, 1926; Buffa et al., 2021:1–25, figs. 1, 3–8.

Lectotype—External mold of the dorsal surface of a partially preserved skeleton, MNHN.F.MAP325a (Piveteau, 1926:pl. 17.1; Carroll, 1978:fig. 2; Evans, 1982:fig. 16B; Evans and Haubold, 1987:figs. 3B, 13C, 16B, 16D, 17; Bulanov and Sennikov, 2015a:pl. 5.1b; Buffa et al., 2021:figs. 1, 3). See Buffa et al. (2021) for discussion of the type material.

Paralectotype—External mold of the ventral surface of a partially preserved skeleton, MNHN.F.MAP317a, b, preserved on two slabs (part and counterpart) (Piveteau, 1926:pl. 17.3; Carroll, 1978:fig. 3; Evans, 1982:figs. 15, 16A; Evans and Haubold, 1987:figs. 3A, 13A, 13B; Bulanov and Sennikov, 2015a:pl. 5.2; Buffa et al., 2021:figs. 4, 8A).

Referred Material—External mold of a sub-complete skeleton, MNHN.F.MAP327a, b, preserved on two slabs (part and counterpart) (Carroll, 1978:figs. 5–7; Evans, 1982:figs. 14, 17, 18; Evans and Haubold, 1987: figs. 4, 5, 12, 14, 15A, 21; Buffa et al., 2021: figs. 5, 6A, 7, 8B, 8C).

Type Horizon—Top of the lower Sakamena Formation, late? Permian (?Capitanian–Lopingian).

Type Locality—Sakamena River, upstream region, exact location unknown, southwestern Madagascar.

Emended Diagnosis—Maxillary teeth with symmetrical apices; anterior maxillary teeth significantly larger than mid-/posterior teeth; anterior and dorsal jugal processes subequal (shared with *Rautiania*); ornamented dorsal jugal process; parietal posttemporal process not tapering in width (shared with *Glaurung*); ornamental tubercles on parietal posttemporal

process (shared with *Glaurung*); patagial spars regularly positioned throughout the wing (modified from Buffa et al., 2021).

Remarks—*Coelurosauravus* possesses 23 presacral vertebrae, including five cervicals and 18 dorsals. This contrasts with the 21 presacral vertebrae including eight cervicals and 13 dorsals of the Ellrich specimen. However, as no other weigeltisaurid specimen preserves a complete presacral vertebral column, we refrain from polarizing this character state in weigeltisaurids and provisionally exclude it from the diagnosis of *Coelurosauravus*, pending the discovery of additional weigeltisaurid specimens preserving this feature.

Osteological redescription

The material of *Coelurosauravus* permits an almost complete examination of the postcranial skeleton. In the lectotype, the individual bone imprints (hereafter 'bones' for simplicity) are badly preserved due to late diagenetic compression and disarticulation, but the specimen comprises most of the skeletal elements between the skull and mid-length of the tail (Figs. 1, 2). The paralectotype specimens show well-preserved individual bones still mostly in connection between the skull and last presacral, but the sacral and caudal vertebrae are missing, as are both hindlimbs (Figs. 3, 4). Lastly, MNHN.F.MAP327a, b is the best preserved and one of the most complete weigeltisaurid specimens to date. The main slab preserves most of the skeleton, with the individual lying on its left side although the trunk region is mostly covered by the patagial spars (Figs. 5, 6). The counter slab preserves a large portion of the mid-posterior tail with the vertebrae lying in connection (Fig. 7).

Buffa et al. (2021) previously noted the ontogenetic maturity of all *Coelurosauravus* specimens based on size-independent criteria (recently reviewed in Griffin et al., 2021). This is in contrast to the view of Bulanov and Sennikov (2015a:422), who considered all specimens as 'juveniles.' As noted by Buffa et al. (2021), the postcranium shows closed neurocentral sutures, fused scapula and coracoid and well-ossified long bones, carpals and tarsals (see below). All of these characters are commonly used as indicators of morphological maturity in extinct reptiles, such as the coeval stem-saurians from the late Permian of Madagascar (Currie, 1981a; Currie

and Carroll, 1984; Caldwell, 1995). The postcranium thus conforms with the evaluation of Buffa et al. (2021) of the ontogenetic maturity of all *Coelurosauravus* specimens.

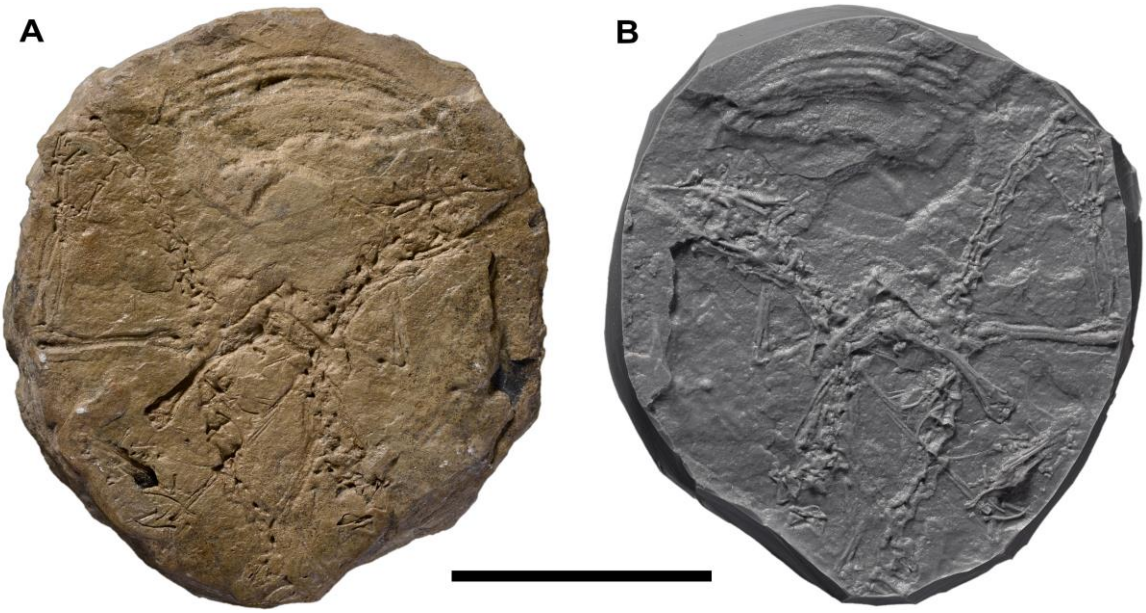

Figure 3-1: *Coelurosauravus elivensis* Piveteau, 1926 (Madagascar, late? Permian), lectotype MNHN.F.MAP325a. **A**, dorsal surface of individual preserved as a natural external mold; **B**, silicone cast of **A**. Scale bar equals 5 cm.

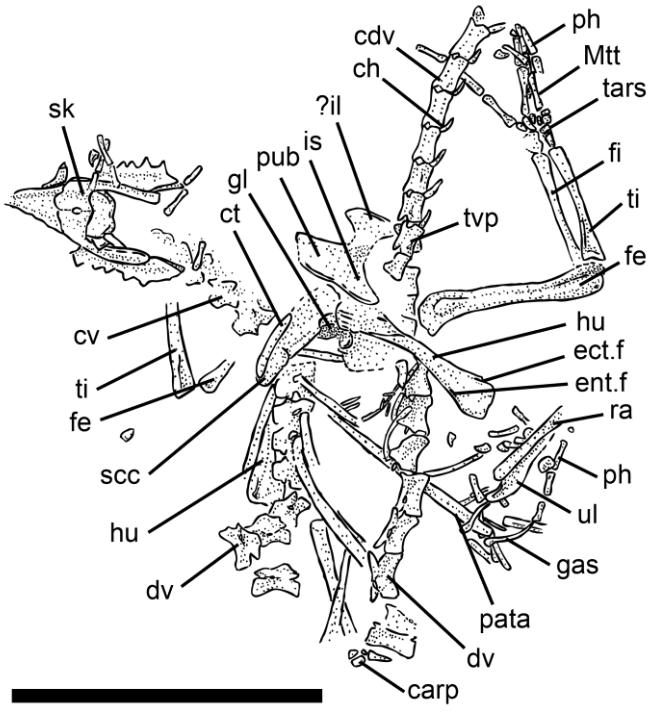

Figure 3-2: *Coelurosauravus elivensis* Piveteau, 1926 (Madagascar, late? Permian), lectotype MNHN.F.MAP325a. Interpretative drawing of dorsal surface of individual preserved as a natural external mold. **Abbreviations**: **carp**, carpal elements; **ch**, chevron; **cv**, cervical vertebra; **ct**, cleithrum; **dv**, dorsal vertebra; **ect.f**, ectepicondylar foramen; **ent.f**, entepicondylar foramen; **fe**, femur; **fi**, fibula; **gas**, gastralia; **gl**, glenoid; **hu**, humerus; **il**, ilium; **is**, ischium; **Mtt**, metatarsus; **pata**, patagial spar; **ph**, phalanx; **pub**, pubis; **ra**, radius; **scc**, scapulocoracoid; **sk**, skull; **tars**, tarsal elements; **ti**, tibia; **ul**, ulna. Scale bar equals 5 cm.

Vertebral Column

All *Coelurosauravus* specimens preserve portions of the vertebral column, with the vertebrae lying mostly in connection. The presacral series is best preserved in the paralectotypes (Figs. 3, 4), and is less well preserved in the lectotype (Figs. 1, 2) and MNHN.F.MAP327a (Figs. 5, 6). The latter specimen also preserves partial sacral vertebrae. The caudal vertebrae are best preserved in MNHN.F.MAP327a, b (Figs. 5–7). The anterior portion of the tail is also preserved in the lectotype (Figs. 1, 2). For all specimens, the presacrals will be numbered cranial to caudal, starting with the atlas (presacral 1).

As is visible on the slightly displaced presacral and caudal vertebrae of MNHN.F.MAP327a (Figs. 5, 6, 8A, 8B), the vertebrae are all deeply amphicoelous, possibly notochordal as is typical in stem-saurians (Carroll, 1975, 1981; Gow, 1975; Currie, 1980, 1981a) including other weigeltisaurids (Evans, 1982). In most archosauromorphs, the notochordal canal is closed (Gow, 1975; Nesbitt et al., 2015; Pritchard et al., 2015). The centra of all vertebrae are long and low (between two or three times as long as high; Fig. 8). In contrast, the centra of other early diapsids are only slightly longer than high (Carroll, 1975, 1981; Gow, 1975; Currie, 1980, 1981a). The neural arches of *Coelurosauravus* are slender with the zygapophyses close to the median line, as is typical in neodiapsids but in contrast to the swollen morphology typical of early eureptiles and araeoscelidians (Sumida, 1990; Sumida and Modesto, 2001). None of the vertebrae show the mammillary processes present in araeoscelidians (Vaughn, 1955), *Hovasaurus* (Currie, 1981a) and some early archosauromorphs (Gow, 1975; Gottmann-Quesada and Sander, 2009).

Several vertebrae of *Coelurosauravus* bear sharp laminae extending between anatomical landmarks such as the rib facets or zygapophyses. The description of these structures follows the nomenclature of Wilson (1999).

Figure 3-3: *Coelurosauravus elivensis* Piveteau, 1926 (Madagascar, late? Permian), paralectotypes MNHN.F.MAP317a, b. **A**, MNHN.F.MAP317b, dorsal surface of individual preserved as a natural mold; **B**, silicone cast of **A**; **C**, MNHN.F.MAP317a, ventral surface of individual preserved as a natural mold; **D**, silicone cast of **C**. Scale bar equals 5 cm.

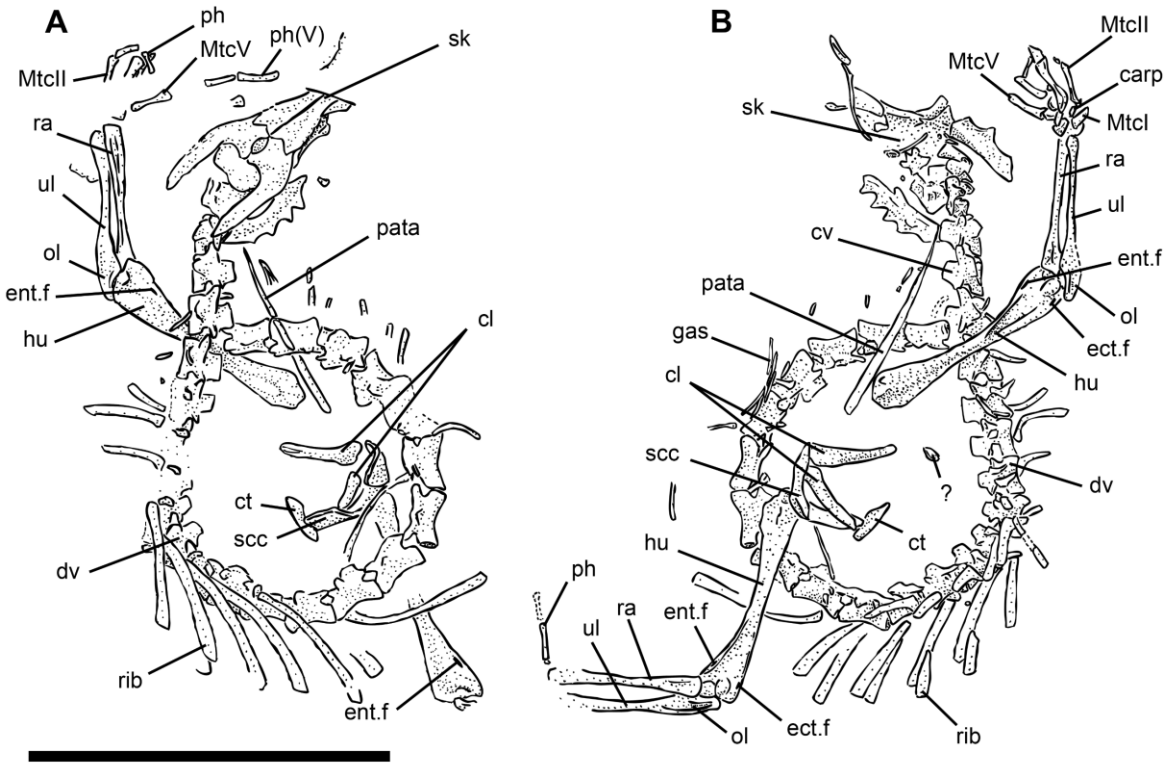

Figure 3-4: *Coelurosauravus elivensis* Piveteau, 1926 (Madagascar, late? Permian), paralectotypes MNHN.F.MAP317a, b. **A**, interpretative drawing of MNHN.F.MAP317b, dorsal surface of individual preserved as a natural mold; **B**, interpretative drawing of MNHN.F.MAP317b, dorsal surface of individual preserved as a natural mold. **Abbreviations**: **carp**, carpal elements; **cl**, clavicle; **ct**, cleithrum; **cv**, cervical vertebra; **dv**, dorsal vertebra; **ect.f**, ectepicondylar foramen; **ent.f**, entepicondylar foramen; **gas**, gastralia; **hu**, humerus; **Mtc**, metacarpal; **ol**, olecranon process of ulna; **pata**, patagial spar; **ph**, phalanx (digit number in brackets when known); **ra**, radius; **scc**, scapulocoracoid; **sk**, skull; **ul**, ulna. Scale bar equals 5 cm.

Presacral Count—The anterior-most two vertebrae preserved on MNHN.F.MAP327a lie anterior to the pectoral girdle on MNHN.F.MAP327a (Figs. 5, 6, 8A, 8B). Owing to the slight anterior displacement of the vertebrae and lateral rotation of the pectoral girdle, we identify the first preserved vertebrae as the last cervical, and the second one as the first dorsal. In addition, these vertebrae show a transition from a ventrally turned and pointed transverse process to a horizontal and blunt one (Figs. 8A, 8B). This transition occurs between presacrals 5 and 6 in the complete presacral column of MNHN.F.MAP317a (Figs. 3, 4). A similar transition is also seen on the lectotype (Figs. 1, 2). According to our interpretation, *Coelurosauravus* thus possesses five cervical vertebrae. Lastly, we suggest that MNHN.F.MAP317a, b preserves the entire presacral series (Figs. 3, 4), indicating that *Coelurosauravus* has 18 dorsal vertebrae. This conforms well to the distance between pectoral

and pelvic girdles in MNHN.F.MAP327a (see dorsal vertebrae below). Thus, including the five cervicals and 18 dorsals, the presacral vertebral column of *Coelurosauravus* consists of 23 presacral vertebrae.

In contrast, eight cervicals and thirteen dorsals were reported in the Ellrich specimen (Frey et al., 1997; Müller et al., 2010; Pritchard et al., 2021). Similarly, Schaumberg (1976, 1986) reports at least six or seven cervicals in the Wolfsberg specimen. Thus, there appears to be hitherto unreported variability in the number of presacral vertebrae in weigeltisaurids.

The total presacral count of weigeltisaurids is low compared with other stem-saurians: 28 to 29 in *Araeoscelis*, 26 in *Petrolacosaurus*, 25 in *Hovasaurus* and likely in *Thadeosaurus*, at least 24 in *Youngina*, and 24 in *Claudiosaurus* (Carroll, 1981; Currie, 1981a; Reisz, 1981; Currie and Carroll, 1984; Reisz et al., 1984; Smith and Evans, 1996). Müller et al. (2010) suggested that the plesiomorphic state for diapsids was 26 presacrals including 6 cervicals and 20 dorsals. The presacral count is similarly high in drepanosauromorphs: 31 in *Megalancosaurus*, 24 in *Vallesaurus* and at least 27 in *Drepanosaurus* (Renesto et al., 2010).

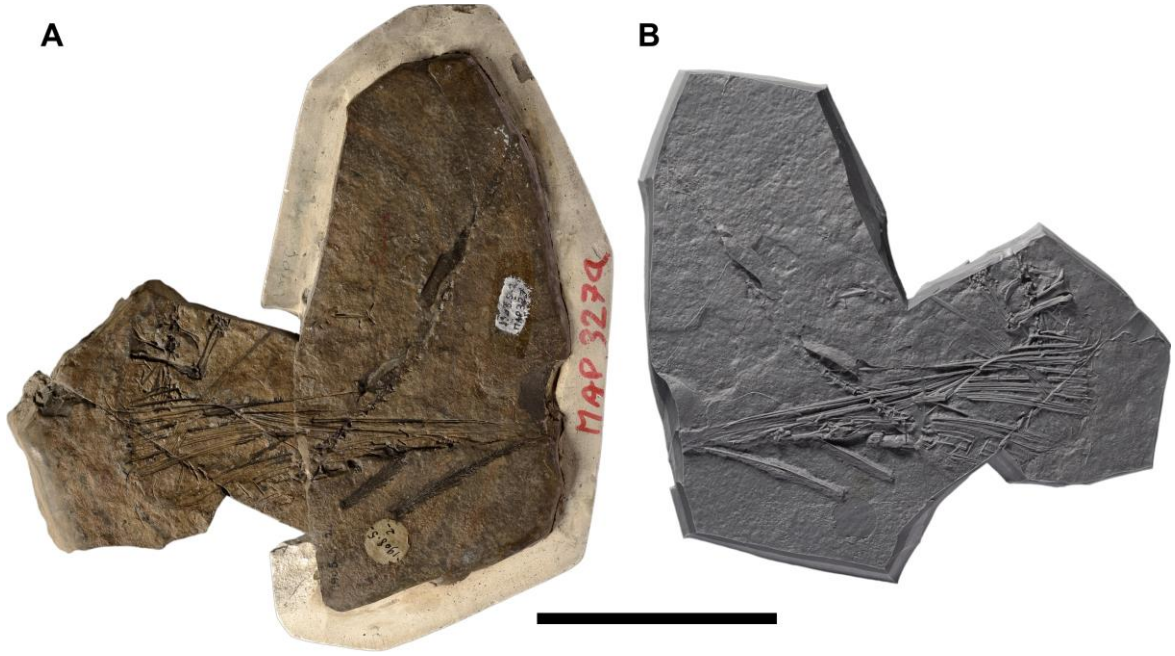

Figure 3-5: *Coelurosauravus elivensis* Piveteau, 1926 (Madagascar, late? Permian) MNHN.F.MAP327a. **A**, right lateral surface of individual preserved as a natural external mold; **B**, silicone cast of **A**. Scale bar equals 10 cm.

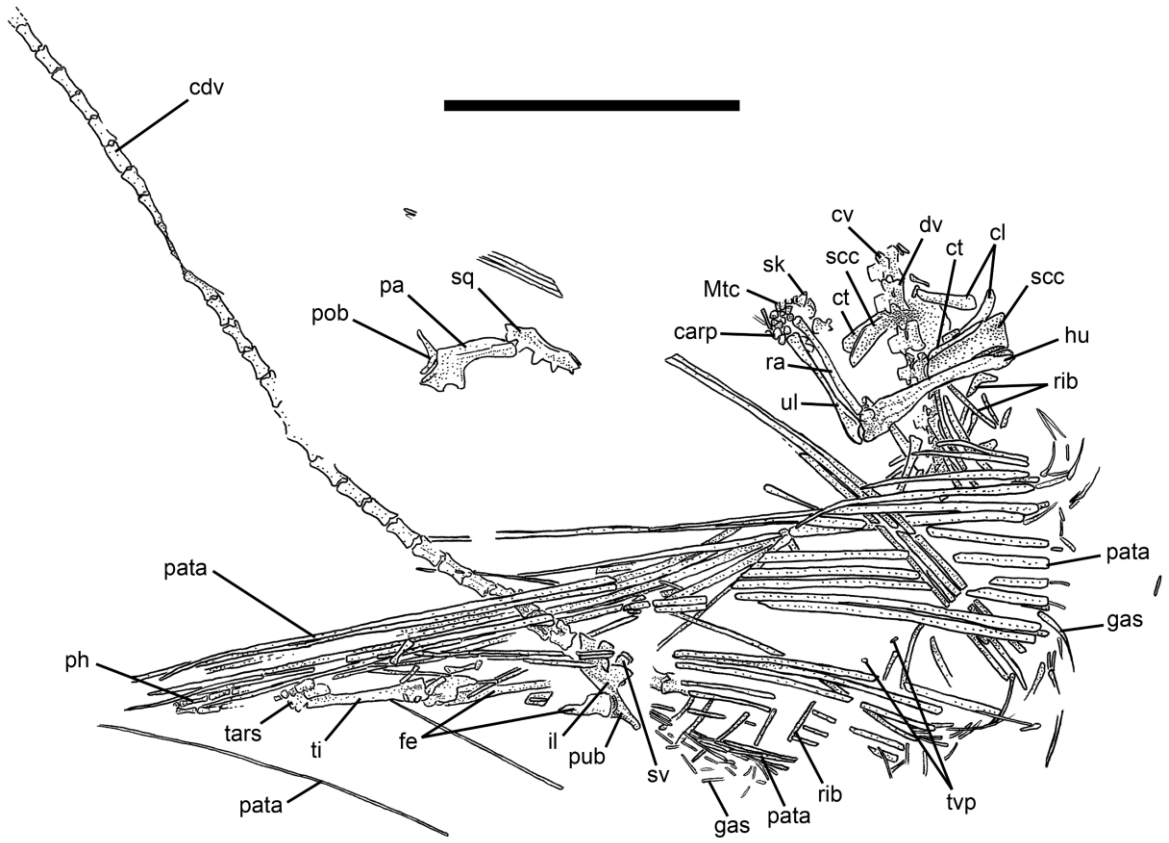

Figure 3-6: *Coelurosauravus elivensis* Piveteau, 1926 (Madagascar, late? Permian) MNHN.F.MAP327a. Interpretative drawing of right lateral surface of individual preserved as a natural external mold. **Abbreviations**: **carp**, carpal elements; **cdv**, caudal vertebra; **cl**, clavicle; **ct**, cleithrum; **cv**, cervical vertebra; **dv**, dorsal vertebra; **fe**, femur; **gas**, gastralia; **hu**, humerus; **il**, ilium; **Mtc**, metacarpus; **pa**, parietal; **pata**, patagial spar; **ph**, phalanx; **pob**, postorbital; **pub**, pubis; **ra**, radius; **scc**, scapulocoracoid; **sk**, skull elements; **sq**, squamosal; **sv**, sacral vertebra; **tars**, tarsal elements; **ti**, tibia; **tvp**, transverse process of dorsal vertebra; **ul**, ulna. Scale bar equals 10 cm.

Atlas-Axis Complex—Most of the bones of the atlas-axis complex are preserved in ventral view in MNHN.F.MAP317a (Figs. 3, 4, 8C, 8D). The bones are slightly disarticulated but lie roughly in their anatomical position relative to the skull and post-axial cervicals. According to our interpretation, the preserved elements consist of the atlantal centrum, intercentrum and paired neural arches, the axis, and the axial intercentrum (Figs. 8C–8E). It is unclear whether or not there was a proatlas.

Bulanov and Sennikov (2015a) interpreted a circular element close to the braincase of MNHN.F.MAP317a as the occipital condyle, formed entirely by the basioccipital. However, as this does not conform to the better-preserved basioccipital of MNHN.F.MAP327a (Buffa et al.,

2021), we identify this element as an atlantal vertebral centrum in posteroventral view based on its position relative to the braincase and neck of the animal (Figs. 8C, 8D). The dorsal margin of the bone is hidden under the right atlantal neural arch. The ventral margin of the atlantal centrum is rounded, suggesting that it is sub-circular in outline. The bone was not fused with the axial intercentrum, as in some early amniotes *Acerosodontosaurus*, *Hovasaurus* and most early archosauromorphs (Gow, 1972, 1975; Currie, 1980, 1981a; Sumida et al., 1992; Dilkes, 1998; deBraga, 2003; Campione and Reisz, 2011; Miedema et al., 2020) but unlike some allokotosaurian archosauromorphs and most lepidosauromorphs (Hoffstetter and Gasc, 1969; Nesbitt et al., 2015; O'Brien et al., 2018).

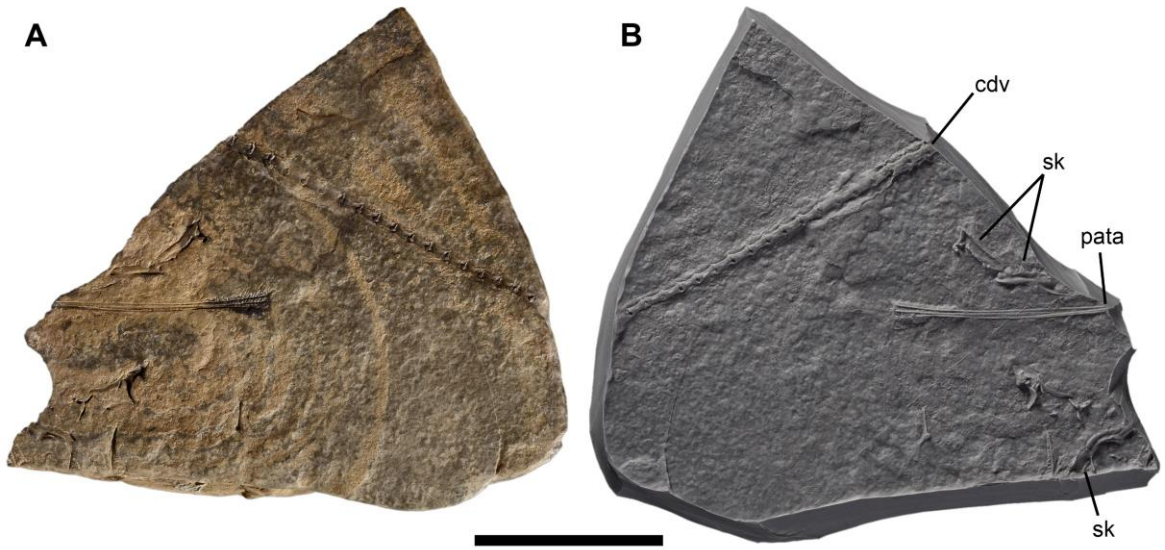

Figure 3-7: *Coelurosauravus elivensis* Piveteau, 1926 (Madagascar, late? Permian) MNHN.F.MAP327b. **A**, left lateral surface of individual preserved as a natural external mold; **B**, silicone cast of **A**. **Abbreviations**: **cdv**, caudal vertebra; **pata**, patagial spar; **sk**, skull elements. Scale bar equals 10 cm.

The posterior margin of the atlantal centrum is mostly occupied by a large, circular notochordal pit. Such a pit is also present in captorhinids (Peabody, 1952; Sumida, 1990) and varanopids (Campione and Reisz, 2011). This was certainly also the case in most stem-saurians with a notochordal atlantal centrum (Vaughn, 1955; Carroll, 1981; Reisz, 1981), although the posterior surface of the atlantal centrum is rarely described. The atlantal centrum of *Coelurosauravus* is short and ring-like in anterior or posterior view, as is typical in early amniotes (Romer, 1956; Sumida, 1990; Sumida et al., 1992).

The contralateral atlantal neural arches are unfused. The right neural arch is almost complete and visible in posterior view, whereas the left is broken and only its neural spine is visible (Figs. 8C, 8D). We were unable to identify the neurocentral suture between the appressed atlantal centrum and right neural arch, although it might have been present in the unpreserved anterior portions of the bones. The atlantal neural arch is composed of a ventral process that articulated with the anterior portion of the atlantal centrum, as in most early amniotes (Romer, 1956; Sumida et al., 1992), and of a slender posterior process projecting posterodorsally that articulated with the axis. The posterior process is narrow and bears the neural spine as well as a small but distinct postzygapophysis (Figs. 8C–8E). There is no trace of an atlantal rib or of a corresponding articular facet on the atlantal neural arch, suggesting that this rib was absent in *Coelurosauravus*, as is the case in *Claudiosaurus* and *Hovasaurus* (Carroll, 1981; Currie, 1981a), but in contrast to the condition in early reptiles (Reisz, 1981; Sumida, 1990).

In MNHN.F.MAP317a, a short, slightly posteriorly concave plate overlies the atlantal centrum (Figs. 8C, 8D). This element likely does not represent the median process of the neural arch because it lacks the robust articular facet for the atlas described for all early amniotes (Currie, 1980; Reisz, 1981; Sumida et al., 1992; Campione and Reisz, 2011). This plate may represent a distinct element, possibly a displaced proatlas.

The atlantal intercentrum lies just posterior to the atlantal centrum and is visible in ventral view (Figs. 8C, 8D). It is about half the length of the axis and the succeeding vertebrae, but is two times longer than the atlantlal centrum. The bone tapers slightly posteriorly so that its anterior surface is slightly wider than its posterior one, which is further emphasized by a ventrolateral constriction at midlength (Figs. 8C, 8D). The ventral surface of the bone is beveled anteriorly and posteriorly, forming a X-shaped arrangement of ridges, giving the intercentrum a wide V-shaped outline in lateral view (Fig. 8E). The beveled anteroventral surface is smoothly convex, merging with the anterior surface of the bone. The posteroventral surface is steeply beveled and represents the contact surface for the anterodorsal portion of axial intercentrum. Owing to the shape and size of the atlantal intercentrum, we suggest that it contacted the atlantal centrum dorsally and articulated with the axial intercentrum posteriorly (Figs. 8E). The bone thus excluded the atlantal centrum from the ventral margin of the cervical column, as in some early amniotes where the atlantal centrum and axial intercentrum are distinct (Gow, 1972;

Sumida et al., 1992; deBraga, 2003; Campione and Reisz, 2011), araeoscelidians (Vaughn, 1955, Reisz, 1981) and early neodiapsids (Currie, 1980, 1981a).

The axis is almost identical to the succeeding cervical vertebrae, described below (Fig. 8). Its centrum is amphicoelous, long and low, about three times as long as high. Its ventral margin is horizontal in lateral view and lacks a midventral ridge or keel. This ridge is present in most early diapsids (Vaughn, 1955; Currie, 1981a; Currie and Carroll, 1984). Both anterior and posterior margins are angled anterodorsally, as in araeoscelidians (e.g. Reisz, 1981).

The neural arch of the axis bears a pair of transverse processes, two pairs of zygapophyses, and the neural spine. The transverse processes are triangular in dorsal aspect. They extend laterally at right angle to the neural arch before angling ventrally. They are prolonged posteriorly by a low posterior centrodiapophyseal lamina. Such a lamina is also present in *Petrolacosaurus* (Reisz, 1981). As suggested by the poorly preserved remains of the axial rib (Figs. 8C, 8D), the diapophysis must have been positioned on the lateral apex of the transverse process, whereas the parapophysis was likely positioned near the anterior margin of the centrum.

The zygapophyses extend anteriorly and posteriorly at right angle from the neural arch, delimiting the vertebral foramen on either side. The prezygapophyses bear dorsolaterally facing articular facets for the postzygapophyses of the atlantal neural arch. In contrast, the prezygapophyses of the succeeding vertebrae are oriented anterodorsally and bear dorsomedially facing articular facets (Fig. 8). The neural arch is subtly excavated between the zygapophyses at the base of the neural spine, although not to the degree of the third cervical (see below). The neural spine is approximately 1.5 times the height of the centrum and roughly rectangular in lateral aspect. In contrast to the anterodorsally expanded axial neural spine of araeoscelidians and tanystropheids (Vaughn, 1955; Reisz, 1981; Nosotti, 2007: Miedema et al., 2020), its dorsal margin is anteroventrally angled, most markedly in its anterior portion, where it is angled ca. 30° to the horizontal. The posterior margin of the neural spine is subtly concave in lateral view and is thickened ventrally, where it merges with the neural arch (Figs. 8C–8E).

The axial intercentrum is small compared to the atlantal one and is visible in ventrolateral view. What is preserved suggests that it was crescentic and articulated with the beveled posteroventral surface of the atlantal intercentrum.

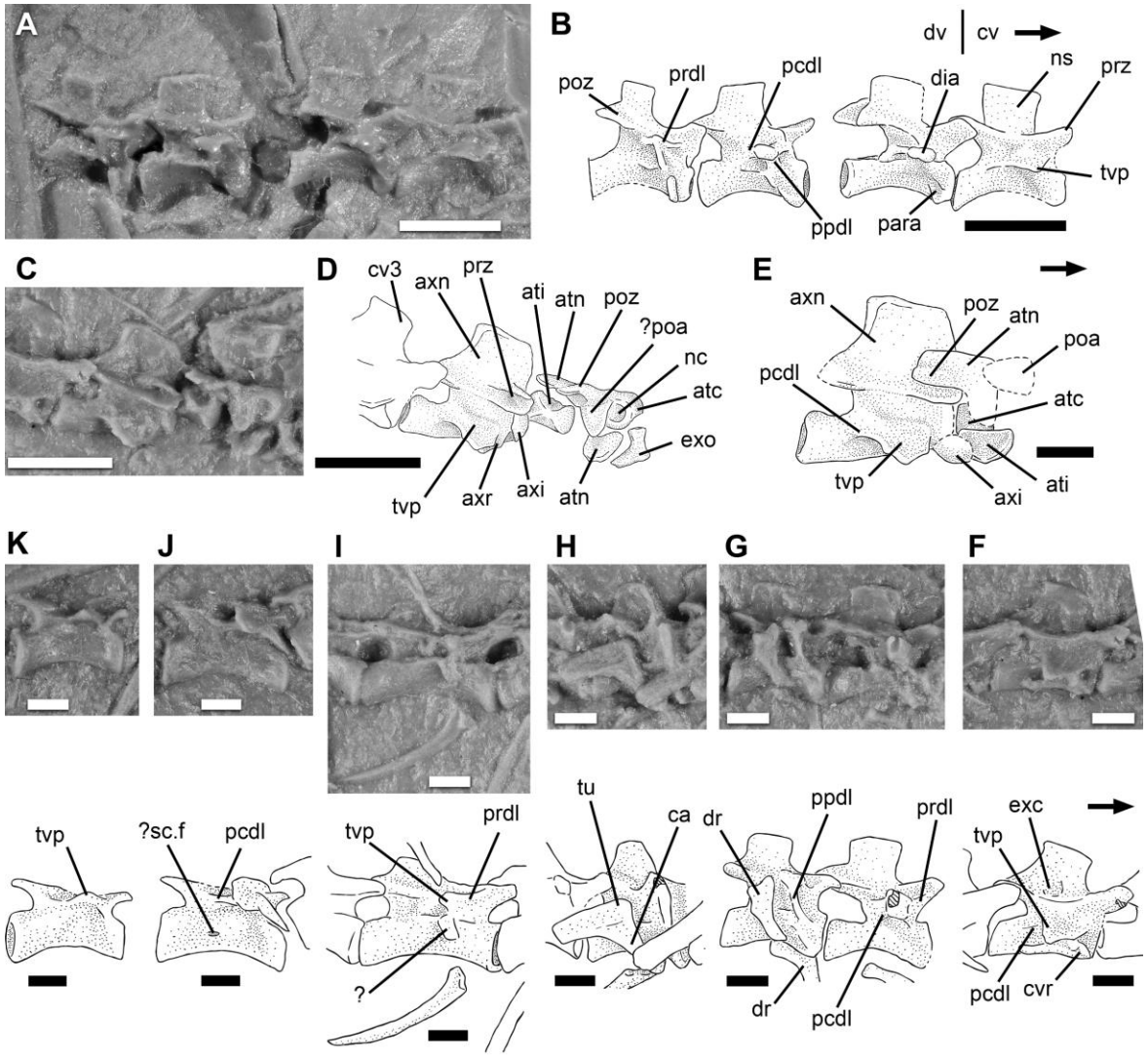

Figure 3-8: *Coelurosauravus elivensis* Piveteau, 1926 (Madagascar, late? Permian), presacral vertebrae. **A**, **B**, last cervicals and first dorsals of MNHN.F.MAP327a in right lateral view, silicone cast (**A**) and interpretative drawing (**B**) of individual preserved as a natural external mold; **C**–**E**, atlas-axis complex of paralectotype MNHN.F.MAP317a in right lateral view, silicone cast (**C**), interpretative drawing (**D**) and reconstruction (**E**) of individual preserved as a natural external mold; **F**–**K**, presacral vertebrae of paralectotype MNHN.F.MAP317a in right lateral view, silicone cast and interpretative drawing of cervical 3 (**F**) and dorsals 2 and 3 (**G**), 6 (**H**), 10 (**I**), 16 (**J**), 18 (**K**). **Abbreviations**: **atc**, atlantal centrum; **ati**, atlantal intercentrum; **atn**, atlantal neural arch; **axi**, axial intercentrum; **axn**, axial neural spine; **axr**, axial rib; **ca**, capitulum; **cv**, cervical vertebra; **cvr**, cervical rib; **dia**, diapophysis; **dr**, dorsal rib; **dv**, dorsal vertebra; **exc**, excavation; **exo**, exoccipital; **nc**, notochordal canal; **ns**, neural spine; **para**, parapophysis; **pcdl**, posterior centrodiapophyseal lamina; **poa**, proatlas; **poz**, postzygapophysis; **ppdl**, paradiapophyseal lamina; **prdl**, prezygodiapophyseal lamina; **prz**, prezygodiapophysis; **sc.f**, subcentral foramen; **tu**, tuberculum; **tvp**, transverse process. Arrows indicate anterior direction. Scale bars equal 5 mm (**A**–**E**) and 2 mm (**F**–**K**).

Post-axial Cervical Vertebrae—As discussed above, *Coelurosaruavus* has three post-axial cervical vertebrae, all of which are preserved in MNHN.F.MAP317a, b (Figs. 3, 4). Only the posterior-most cervical is preserved in MNHN.F.MAP327a (Figs. 8A, 8B). The outline of at least three poorly preserved cervicals is preserved in the lectotype (Figs. 1, 2).

As is best visible in MNHN.F.MAP317a, b, the post-axial cervicals are all similar to the axis (Fig. 8F). The centra gradually increase in length along the series. They are all slightly longer than those of the anterior-most dorsals but around 1.3 times shorter than the mid-posterior dorsals (Table 2), as is the case in the Ellrich specimen (Pritchard et al., 2021). Similarly, elongate cervical centra occur in araeoscelidians (Reisz, 1981; Reisz et al., 1984), drepanosauromorphs (Renesto et al., 2010) and several early archosauromorphs (Gow, 1975; Gottmann-Quesada and Sander, 2009; Nesbitt et al., 2015; Pritchard et al., 2015). The centra only show a slight ventrolateral constriction and lack the midventral ridge or keel typically present in early reptiles (Vaughn, 1955; Currie, 1980, 1981a; Reisz, 1981). The anterior and posterior margins of each cervical centrum are slightly angled anterodorsally (ca. 15° to the vertical), as described for the axis. A similar angulation was reported in araeoscelidians. The cervicals of *Coelurosauravus* thus differ strongly from those of drepanosauromorphs, their putative sister group (Pritchard et al., 2021), which have heterocoelous centra, anteriorly displaced neural arches, and posteroventrally projecting hypapophyses (Renesto and Fraser, 2003; Renesto et al., 2010).

All centra are closely appressed, lacking the beveling typical of intercentral articulations, which appear absent in all specimens. Cervical intercentra are present in almost all stem-saurian diapsids (Vaughn, 1955; Carroll, 1981; Currie, 1981a; Reisz, 1981), although they are absent in drepanosauromorphs (Renesto et al., 2010) and several early archosauromorphs (Nosotti, 2007; Gottmann-Quesada and Sander, 2009; Nesbitt et al., 2015).

As is seen in MNHN.F.MAP317a, b, the transverse processes are triangular in dorsal aspect, pointing posterolaterally. In contrast to those of the axis, they are straight and not turned ventrally (Fig. 8F). The posterior centrodiapophyseal lamina is more subtle on the third cervical than on the axis (Fig. 8F) and is absent in the posteriorly following cervicals. As in the axis, the diapophysis occupied the lateral extremity of the transverse process whereas the parapophysis was positioned near the anterior margin of the centrum.

Presacral vertebra	Centrum length (mm)
Cervical 1 (= atlas)	0.80*
Cervical 2 (= axis)	5.31
Cervical 3	5.52
Cervical 4	5.62
Cervical 5	5.98
Dorsal 1	5.50
Dorsal 2	5.17
Dorsal 3	5.23
Dorsal 4	5.63
Dorsal 5	5.43*
Dorsal 6	5.01
Dorsal 7	5.41
Dorsal 8	5.60
Dorsal 9	6.84
Dorsal 10	7.15
Dorsal 11	7.47
Dorsal 12	7.50
Dorsal 13	7.30
Dorsal 14	7.19
Dorsal 15	7.07
Dorsal 16	7.04
Dorsal 17	6.69
Dorsal 18	5.99

Table 3-2: Presacral centrum length of paralectotype MNHN.F.MAP317a, b. '*' indicates approximate measurements due to incomplete preservation.

The neural arch of the third cervical of MNHN.F.MAP317a, b bears a shallow excavation between the zygapophyses lateral to the base of the neural spine (Fig. 8F). In the axis and the other post-axial cervicals, this excavation is much shallower (Figs. 3, 4, 8). Similar excavations were reported in araeoscelidians (Vaughn, 1955; Reisz, 1984) and some archosauromorphs (Nesbitt et al., 2015). The neural spines of the post-axial cervicals are all rectangular in lateral aspect and gradually increase in anteroposterior length throughout the column with the posterior-most being roughly the size of the axial neural spine. They are relatively low, around 1.5 times the height of the centum, in contrast to the very low cervical neural spines of araeoscelidians (Vaughn, 1955), and the triangular neural spines of the *Weigeltisaurus* holotype (Evans and Haubold, 1987; Bulanov and Sennikov, 2015b). As seen in MNHN.F.MAP317a, b, the neural spine of the third cervical vertebra is strongly inclined ventrally (ca. 25° to the horizontal), as in the axis (Fig. 8F). A similar inclination is present in the anterior-most post-axial cervicals of several archosauromorphs (Gottmann-Quesada and Sander, 2009; Nesbitt et al., 2015). The posterior cervical neural spines have a more horizontal dorsal margin (Figs. 3, 4, 8A, 8B, 8F).

The cervical vertebrae of all *Coelurosauravus* specimens are associated with short ribs, in contrast to the prominent long and slender cervical ribs typical of archosauromorphs (Gow, 1975; Nesbitt et al., 2015), and the absence of ribs in the drepanosauromorphs *Megalancosaurus* and *Vallesaurus* (Renesto et al., 2010). The ribs of the third cervical of MNHN.F.MAP317a, b are the only ones preserved in their anatomical position and are oriented parasagittally (Fig. 8F). The ribs of the following cervicals are all preserved in a more posteroventral orientation, but do not appear to lie in connection with the respective vertebrae (Figs. 3, 4). Thus, the orientation of the cervical ribs remains unclear in *Coelurosauravus*. None of the articular ends of the cervical ribs are sufficiently preserved to identify them as holo- or dichocephalous or to reliably assess the presence of an accessory process. This process was reported in araeoscelidians, *Claudiosaurus* and archosauromorphs (Carroll, 1981; Reisz, 1981; Benton, 1985).

Dorsal Vertebrae—As mentioned above, we reconstruct *Coelurosauravus* with 18 dorsal vertebrae, all of which are preserved in connection in the paralectotypes (Figs. 3, 4). The dorsal series is partially preserved and separated in two portions in the lectotype (Figs. 1, 2), and most of the vertebrae are covered by the patagial spars on MNHN.F.MAP327a so that only the extremities of some transverse processes of the mid-posterior dorsals are visible (Figs. 5, 6).

As measured on the best-preserved vertebral column of the paralectotypes, the dorsal vertebrae show incipient regionalization (Table 2). The centra of dorsals one to eight (the anterior half of the dorsal column) are all slightly shorter (ca. 0.9 times) than the post-axial cervicals. They vary in length, dorsal four being the longest of this series, and dorsal six the shortest. Dorsals 10 to 16 are the longest presacral vertebrae, with a maximum central length attained for dorsals 11 to 13 (Table 2). The posterior-most two centra show a rapid decrease in length, which is also visible in the lectotype (Fig. 3). This rapid length reduction in the two posterior-most presacrals is typical in early amniotes (e.g. Reisz et al., 2011b), and further supports a count of 18 dorsal vertebrae, which yields a total of 23 presacrals in *Coelurosauravus*.

As seen in the paralectotypes, the dorsal centra all have strongly concave ventral margins in lateral view, contrary to the straighter ventral margins of the cervical centra (Fig. 8).

There is no trace of a midventral ridge or keel on any dorsal vertebra, as in other weigeltisaurids (Pritchard et al., 2021) and *Claudiosaurus* (Carroll, 1981), but in contrast to most early diapsids (Vaughn, 1955; Carroll, 1975, 1981; Currie, 1980, 1981a). The anterior and posterior surfaces of the centra are vertical throughout the dorsal column contrary to the anterodorsally inclined surfaces of the cervicals. Subcentral foramina seem mostly absent, but might be represented by a small pit on dorsal 21 (Fig. 8J). Subcentral foramina are evident in most dorsals of other early neodiapsids from Madagascar (Currie, 1980, 1981a; Carroll, 1981).

As for the cervical series, the dorsal centra of MNHN.F.MAP317a, b are closely appressed and lack any articular facet for intercentra, suggesting that intercentra were absent. Dorsal intercentra are present in all other early diapsids, but are absent in drepanosauromorphs (Renesto et al., 2010) and in several archosauromorphs (Nosotti, 2007; Gottmann-Quesada and Sander, 2009; Nesbitt et al., 2015).

As noted above, the transverse processes are rectangular, contrary to the triangular ones of the cervicals. As seen on the paralectotypes, the diapophysis is located on the transverse process, while the parapophysis is invariably present on the anterodorsal corner of the centrum (Figs. 8G–8K). The transverse processes of *Coelurosauravus* extend lateral to the neural arch, as in other weigeltisaurids (Evans, 1982), although not to the level of some early archosauromorphs (Gow, 1975; Gottmann-Quesada and Sander, 2009; Nesbitt et al., 2015). In contrast, the transverse processes of other neodiapsids barely extend lateral to the neural arch and are hardly visible in dorsal view (Currie, 1980, 1981a; Carroll, 1981).

As best seen in MNHN.F.MAP327a, the transverse processes of the first two dorsals end bluntly in an anteroposteriorly oriented facet bearing the diapophysis (Figs. 8A, 8B). On both vertebrae, the transverse processes are reinforced by low paradiapophyseal laminae extending anteroventrally from the diapophysis to the parapophysis, and posterior centrodiapophyseal laminae, as in the anterior cervicals. The second dorsal also shows a low prezygodiapophyseal lamina extending anterodorsally from the diapophysis (Figs. 8A, 8B). These laminae are also present on the first two dorsals of the paralectotypes, although partially obscured by rib fragments (Fig. 8G). As is seen in the paralectotypes and MNHN.F.MAP327a, the transverse processes of dorsals three to eight are much shorter anteroposteriorly. The prezygodiapophyseal, paradiapophyseal and posterior centrodiapophyseal laminae are

invariably present and sharper than in the first dorsals (Figs. 8G, 8H). The posterior dorsals are not as well preserved, but the laminae are clearly less marked. As is seen in dorsal 10 (Fig. 8I), the paradiapophyseal lamina is absent whereas the prezygodiapophyseal lamina remains. This is also the case in the successive vertebrae (Figs. 8J, 8K). The posterior centrodiapophyseal lamina is absent in dorsal 10 (Fig. 8I) but present in the posterior dorsals (Figs. 8J, 8K).

All of these laminae are absent in coeval neodiaspsids such as *Hovasaurus* (Currie, 1981a) and *Thadeosaurus* (MNHN.F.MAP360a, b, VB, pers. obs.), although *Acerosodontosaurus* shows sharp prezygodiapophyseal laminae in its dorsal vertebrae (MNHN.F.MAP359, VB, pers. obs.). Posterior centrodiapophyseal laminae are also present in *Petrolacosaurus* (Reisz, 1981). These laminae are, however, prevalent in early archosauromorphs (Ezcurra et al., 2014).

We were unable to detect significant variations in the orientation of the zygapophyses, but as most are obscured by rib fragments on the paralectotypes, a substantial variability in their orientation cannot be excluded. We found no trace of excavation of neural arches at the base of the neural spine of any dorsal vertebra (Fig. 8), contrary to the situation in araeoscelidians (Vaughn, 1955) and several early archosauromorphs (Nesbitt et al., 2015; Spiekman, 2018), where excavations at the base of the neural spine are present at least in the anterior dorsals.

There is, however, substantial variability in the size and shape of the neural spines (Fig. 8). The first dorsals bear low (subequal to the centrum height), rectangular neural spines with a slight increase in length along their dorsal terminus, forming concave anterior and posterior margins (Figs. 8A, 8B, 8G). The succeeding vertebrae show slightly dorsally tapering neural spines in lateral aspect with a slightly (ca. 30°) anteroventrally angled anterior margin (Fig. 8H). As seen in MNHN.F.MAP317b, the neural spines of the succeeding longer vertebrae are mostly unpreserved and their dimensions remain unknown (Figs. 8I–8K). Overall, the neural spines of *Coelurosauravus* are all subequal or longer than high in lateral view, as in *Claudiosaurus*, *Kenyasaurus* and *Saurosternon*, but in contrast to the higher-than-long spines of *Acerosodontosaurus*, *Hovasaurus*, *Thadeosaurus* and *Youngina* (Currie, 1981a, 1981b) or drepanosauromorphs (Renesto et al., 2010). They lack a transverse expansion at their dorsal terminus, as described for *Hovasaurus* (Currie, 1981a). We found no trace of the additional intervertebral articulations described by Currie (1981b) for ‘younginiforms’, nor of the

zygosphenial joint of *Saurosternon* and some saurians (Hoffstetter and Gasc, 1969; Carroll, 1975).

Most of the dorsal ribs are incompletely preserved on the *Coelurosauravus* specimens. As is best seen on the paralectotypes (Figs. 3, 4), the more anterior dorsal ribs are slender and only slightly longer than the cervical ribs. They are strongly dichocephalous and L-shaped, with the capitulum extending at roughly a right angle to the main axis of the rib (Fig. 8H). This conforms to the position of the corresponding costal facets on the vertebrae. The ribs gradually increase in size in the more posterior vertebrae, reaching a maximum size in the mid-dorsal region (dorsals 10–16; Figs. 3, 4), but remain dichocephalous. The rib of dorsal 10 is most likely incomplete and thus does not correspond to the associated costal facets (Fig. 8I). The ribs of the posterior dorsals are poorly preserved in all specimens. What is preserved suggests that they rapidly decrease in size, becoming subequal to the anterior dorsal ribs and more strongly curved. They appear to be holocephalous, although their preservation precludes a definite statement. In contrast to drepanosauromorphs (Renesto et al., 2010) and some archosauromorphs (Spielmann et al., 2008; Nesbitt et al., 2015), none of the dorsal ribs are fused with the neural arches.

Sacral Vertebrae—The sacral vertebrae are only partially visible in right lateral aspect in MNHN.F.MAP327a because they are overlain by the iliac blade (Figs. 9A, 9B). One vertebra bears a laterally extended rib that is visible near the middle of the dorsal margin of the iliac blade and is therefore confidently identified as a sacral due to its position. The preceding vertebra is partially hidden below the anterodorsal margin of the iliac blade, but bears an expanded rib as well, which is partially visible anterior to the iliac blade (Figs. 9A, 9B). Lastly, owing to the length of the iliac blade and its slight postmortem rotation ventrally relative to the vertebral column, we consider the vertebra close to the posterior portion of the iliac blade as a sacral vertebra as well (Fig. 9). Its rib cannot be identified because the vertebra is obscured by patagial spars and the iliac blade. According to our interpretation, there are three sacral vertebrae in *Coelurosauravus*. In contrast, Carroll (1978:fig. 6) only identified the posterior-most two sacrals of MNHN.F.MAP327a. However, three sacrals were also reported in *Rautiania* (Bulanov and Sennikov, 2010), and this number was thus likely typical for weigeltisaurids. Only two sacrals were previously reported in the Eppelton specimen (Evans, 1982), but the preservation of this specimen precludes a definite statement (TWCMS B5937.1, VB, pers. obs.) *Megalancosaurus* also possesses three sacrals, although only two are reported

for other drepanosauromorphs (Renesto et al., 2010). In contrast, all known stem-saurians, and most Permo–Triassic saurians possess two sacral vertebrae (Gow, 1975; Reisz, 1981; Nesbitt et al., 2015). Owing to the length of the iliac blade and the position of the sacral neural spines, the sacral vertebrae appear to have been some of the shortest in the column.

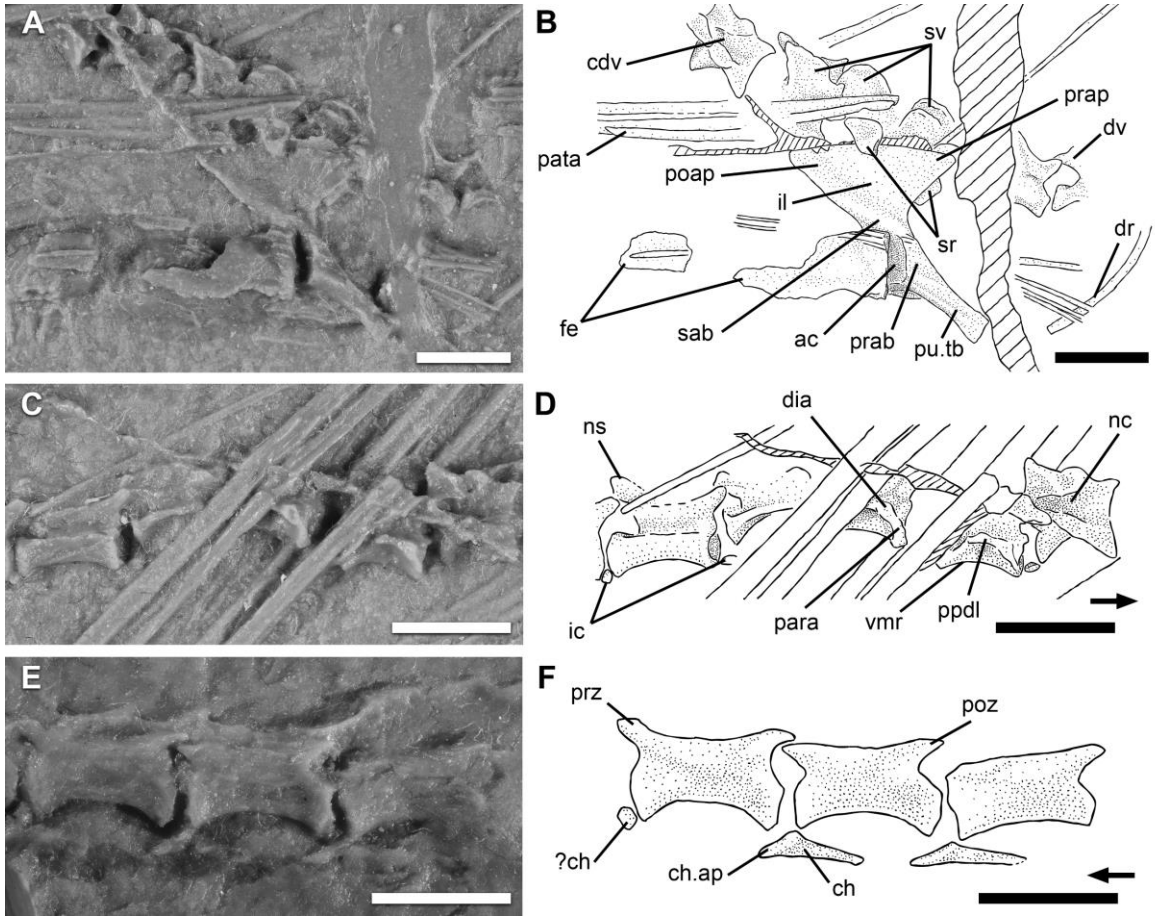

Figure 3-9: *Coelurosauravus elivensis* Piveteau, 1926 (Madagascar, late? Permian), MNHN.F.MAP327a, b, right pelvis, sacral and caudal vertebrae in right lateral view, individual preserved as a natural external mold. **A**, **B**, sacrum and right pelvis of MNHN.F.MAP327a, right lateral view; **C**, **D**, caudals 1 to 5 of MNHN.F.MAP327a, right lateral view; **E**, **F**, caudals 13 to 15 of MNHN.FMAP327b, left lateral view. Silicone casts (**A**, **C**, **E**) and interpretive drawings (**B**, **D**, **F**). **Abbreviations**: **ac**, acetabulum; **cdv**, caudal vertebra; **ch**, chevron; **ch.ap**, anterior process of chevron; **dia**, diapophysis; **dr**, dorsal rib; **fe**, femur; **ic**, intercentrum; **il**, ilium; **nc**, notochordal canal; **ns**, neural spine; **para**, parapophysis; **pata**, patagial spar; **poap**, postacetabular process of iliac blade; **poz**, postzygapophysis; **ppdl**, paradiapophyseal lamina; **prab**, preacetabular buttress; **prap**, preacetabular process of iliac blade; **prz**, prezygapophysis; **pu.tb**, pubic tubercle; **sab**, supraacetabular buttress; **sr**, sacral rib; **sv**, sacral vertebra; **vmr**, ventromedian ridge. Arrows indicate anterior direction. Dashed areas indicate breaks. Scale bars equal 5 mm.

The sacral ribs are too poorly preserved to yield anatomical details. Based on the length of the iliac blade it is likely that the ribs of the sacrals from anterior to posterior were oriented

posterolaterally, laterally and anterolaterally respectively, as is the case in *Rautiania* (Bulanov and Sennikov, 2010).

Caudal Vertebrae—MNHN.F.MAP327a preserves the 29 immediately postsacral caudal vertebrae, with caudals 11 to 29 being also preserved in the counterpart (MNHN.F.MAP327b, Figs. 5–7). A string of at least nine anterior caudal vertebrae is also preserved in the lectotype (Figs. 1, 2). As seen in MNHN.F.MAP327a, b, the anterior-most three caudals are only two-thirds as long as the succeeding ones (Table 3, Figs. 9C, 9D). Caudals 4 to 8 show a rapid increase in centrum length, whereas the successive caudals show no further significant variation in length.

The centra of the anterior-most three caudals of MNHN.F.MAP327a show a strong ventrolateral constriction (Figs. 9C, 9D). Their ventral margins are slightly concave in lateral view and bear a ventromedian ridge. Their neural arches are similar to those of the presacrals, but the neural spines are not preserved in any of the specimens. The transverse process of the anterior-most caudal is poorly preserved, but the following two show longitudinally expanded transverse processes (Figs. 9C, 9D). The diapophysis and parapophysis are indeed convergent and linked by a paradiapophyseal lamina, forming a L-shaped articular surface with the main axis oriented horizontally. This is reminiscent of the morphology of the sacral and first caudal vertebrae of the Eppelton specimen (Evans, 1982), and suggests the presence of caudal ribs, although they are not visible on MNHN.F.MAP327a. The first three caudals of the lectotype are poorly preserved but conform to the morphology of MNHN.F.MAP327a (Figs. 1, 2).

The successive caudals show a trend of simplification along the vertebral column. The more anterior caudals show a strong ventrolateral constriction, which gradually recedes and is absent in the more posterior caudals, suggesting a gradual decrease in width of the centra posteriorly along the series. Early neodiapsids typically show a transition from a medial ridge to a sagittal canal framed by a pair of longitudinal ridges (Carroll, 1981; Currie, 1981a), but the preservation of the caudals prevents such an observation in *Coelurosauravus*. As seen in the lectotype, the transverse processes rapidly shorten along the proximal portion of the tail, as do the neural spines (Figs. 1, 2). Both appear to be absent from the fifth or sixth caudal posteriorly. The transverse processes are straight, extending at right angle from the neural arch on the lectotype. This contrasts with the posteriorly curved transverse processes of araeoscelidians

(Reisz, 1981). The caudal neural spines are all low and triangular, shorter than the centrum and positioned at level with the postzygapophyses (Figs. 1, 2, 9C, 9D). As seen in MNHN.F.MAP327a, b, the zygapophyses remain well-developed throughout the preserved portion of the tail and articulate with those of the neighboring caudals (Figs. 9E, 9F), as in the Eppelton and Ellrich specimens (Evans, 1982; Pritchard et al., 2021). We found no trace of an autotomic septum in any of the vertebrae of MNHN.F.MAP327a or the lectotype.

Haemal arches are preserved in lateral view in the lectotype and MNHN.F.MAP327a, b and appear to have been present throughout most of the preserved portion of the tail, although small intercentra are present between the anterior-most caudals instead (Figs. 9C–9D). The proximal portion of each haemal arch articulates between succeeding centra, as in most early diapsids, but in contrast to drepanosauromorphs, where the haemal arches are fused to the centra (Renesto et al., 2010). The first haemal arches are visible in the lectotype, showing a slight posteroventral curvature and a shallowly convex ventral margin (Figs. 1, 2). The haemal arches associated with caudals 13 to 29 are preserved in MNHN.F.MAP327b. They differ from those preserved in the lectotype in their proximal portion, which bears an anterior acuminate process (Figs. 9E, 9F). The transition thus occurs between the ninth and thirteenth caudals, but this region is poorly preserved on all *Coelurosauravus* specimens. All haemal arches gradually taper in width in lateral aspect. This morphology is consistent with that described for the Eppelton and Ellrich specimens (Evans, 1982; Pritchard et al., 2021).

Gastralia

Thin splint-like bones are visible in the abdominal region of all *Coelurosauravus* specimens, but are best preserved in MNHN.F.MAP327a (Figs. 5, 6, 10, S1). Based on their morphology, anatomical position and arrangement described below, we confidently identify these bones as gastralia.

The organization of the gastral basket is unclear because the trunk of MNHN.F.MAP327a is only visible in lateral view and has undergone slight diagenetic compression (Figs. 5, 6). However, the anterior region is better preserved and shows that the gastralia were organized into a series of transverse rows, the first two of which are visible on the specimen (Fig. 10A). Each row consists of at least two thin splint-like elements, which will

be numbered from medial to lateral. In contrast, only a single long curved element was described in the Ellrich specimen (Pritchard et al., 2021). Similarly, we were unable to identify more than one gastralium per row in the gastral basket of the Eppelton and Wolfsberg specimens, although this may be due to preservation (TWCMS B5937, cast SMNK-PAL 34910, VB, pers. obs.).

Table 3-3: Selected measurements of MNHN.F.MAP327a, b. '*' indicates approximate measurements due to incomplete preservation. Chord length is measured along the line linking the proximal and distal ends of each patagial, and is thus independent from the curvature of each element.

Caudal vertebra	Centrum length (mm)	Patagial	Absolute length (mm)	Chord length (mm)
Caudal 1	3.39*	Patagial 1	15.80	15.47
Caudal 2	3.51	Patagial 2	20.26	19.41
Caudal 3	3.35*	Patagial 3	28.97	28.81
Caudal 4	3.85*	Patagial 4	42.40	41.74
Caudal 5	4.20	Patagial 5	60.83	60.71
Caudal 6	4.61	Patagial 6	86.53	86.20
Caudal 7	4.90	Patagial 7	105.97*	105.76*
Caudal 8	5.10	Patagial 8	153.405	152.32
Caudal 9	5.24	Patagial 9	163.755*	162.84*
Caudal 10	5.03	Patagial 10	> 53.37	> 53.32
Caudal 11	5.03	Patagial 11	119.51*	118.21*
Caudal 12	4.99	Patagial 12	118.77*	117.56*
Caudal 13	5.20	Patagial 13	130.91*	129.84*
Caudal 14	5.15	Patagial 14	135.73*	133.74*
Caudal 15	5.11	Patagial 15	> 16.53	> 16.53
Caudal 16	4.99	Patagial 16	131.64*	130.11*
Caudal 17	5.14	Patagial 17	> 56.73	> 56.36
Caudal 18	5.20	Patagial 18	> 49.86	> 49.56
Caudal 19	4.99	Patagial 19	73.38	73.20
Caudal 20	5.02	Patagial 20	> 39.99	> 39.66
Caudal 21	5.20	Patagial 21	> 37.38	> 37.22
Caudal 22	5.02	Patagial 22	> 50.59	> 50.15
Caudal 23	5.04	Patagial 23	> 12.95	> 12.95
Caudal 24	5.13	Patagial 24	> 12.93	> 12.93
Caudal 25	4.93	Patagial 25	> 11.15	> 11.15
Caudal 26	4.80	Patagial 26	> 10.97	> 10.97
Caudal 27	4.74	Patagial 27	> 11.60	> 11.60
Caudal 28	4.87	Patagial 28	> 15.709	> 15.709
Caudal 29	-	Patagial 29	> 6.162	> 6.162

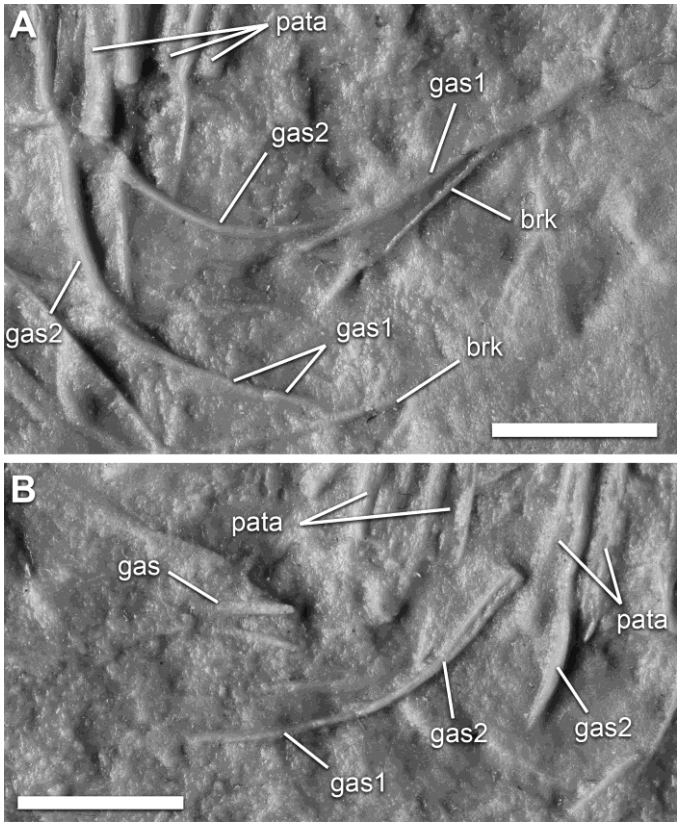

Figure 3-10: *Coelurosauravus elivensis* Piveteau, 1926 (Madagascar, late? Permian), MNHN.F.MAP327a, b, gastralia, silicone cast individual preserved as a natural external mold. **A**, gastalial rows 1 and 2 in right anterolateral view; **B**, mid-posterior gastralial row in right lateral view. **Abbreviations**: **brk**, break; **gas**, gastralia; **pata**, patagium. Scale bars equal 5 mm.

Gastralium 1 is the thinnest and is almost straight (Fig. 10). Its median portion is obscured in all visible gastral rows on MNHN.F.MAP327a. Therefore, it remains unclear if it corresponds to a pair of medial gastralia fused into a chevron-like element, as is the case in early neodiapsids (Carroll, 1981; Currie, 1981a) and in the most anterior gastral row in later saurians (e.g. Claessens, 2004), or if it is indeed the medial-most element. Gastralium 1 bears an anterodorsal facet for gastralium 2 in its lateral portion. Gastralium 2 is nearly 1.5 times longer and shows a strong curvature (Fig. 10). Its lateral end is strongly expanded (about 1.5 times the breadth of the corpus) and forms a knob. This knob is closely associated with a patagial spar in several places of the trunk in MNHN.F.MAP327a, suggesting these elements were articulated.

The trunk of MNHN.F.MAP327a has collapsed due to diagenetic compression, so the orientation of the gastral rows is uncertain. As preserved, the anterior-most rows appear to be posterolaterally oriented (Fig. 10A), suggesting these rows were organized in a series of anteriorly oriented chevrons spanning the width of the abdomen (as described by Witzmann,

2007). This is the typical organization in reptiles (e.g. Carroll, 1981; Claessens, 2004). However, the mid-posterior gastralia, while isolated, are all oriented anterolaterally (Fig. 10B), suggesting the gastral rows formed wide posteriorly oriented chevrons (as described by Witzmann, 2007) in contrast to the more anterior ones. A similar difference in orientation is seen in the Ellrich specimen (Pritchard et al., 2021). However, it is also possible that these gastralia formed roughly transverse rows as in the gastral basket of the Eppelton specimen (Evans, 1982) or the Wolfsberg specimen (SMNK cast, VB, pers. obs.; Schaumberg, 1976).

Pritchard et al. (2021) recently proposed that the patagial spars of weigeltisaurids could be modified gastralia, as is suggested by their close association with the gastralia in the Ellrich specimen, which is similar to that of MNHN.F.MAP327a. Under that interpretation, each transverse gastral row would comprise three elements in *Coelurosauravus*, which is the typical number in early diapsids (Carroll, 1981; Currie, 1981a). *Sphenodon* and extant crocodilians have a similar number (e.g. Günther, 1867; Howes and Swinnerton, 1901; Vickaryous and Hall, 2008) whereas dinosaurs and pterosaurs have at most two gastralia on either side (Claessens, 2004; Claessens et al., 2009).

While Pritchard et al.'s (2021) interpretation remains plausible, we stress that more data are needed to assess the homology between the patagials of weigeltisaurid and the lateral gastralia of other reptiles, such as histological thin-sections. Thus, we retain the patagial spars and gastralia as distinct, potentially non-homologous elements in the following description.

Patagial Spars

Patagial spars (hereafter "patagials", following Pritchard et al., 2021:47) forming the bony support of the patagium, have long been recognized as diagnostic of weigeltisaurids (Frey et al., 1997; Schaumberg et al., 2007; Pritchard et al., 2021). Isolated spars are visible on the lectotype and paralectotypes, but MNHN.F.MAP327a appears to show a complete patagial skeleton and will thus serve as the basis for the following description (Figs. 5, 6).

MNHN.F.MAP327a shows at least 29 spars on the right side, with patagials 13 to 16 lying rotated anteriorly (Figs. 5, 6). Pritchard et al. (2021) reported the same number in this specimen and counted at least 24 patagials in the Ellrich specimen. The distal extremities of the

patagials from the left side are visible in the specimen, but their proximal portions are obscured. As is visible on the right side, the patagials are roughly regularly spaced throughout the patagium (Figs. 5, 6). This is in stark contrast to the "bundles" described for the Ellrich specimen (Frey et al., 1997:1451), suggesting a different organization of the patagial support. The individual spars are long and thin in MNHN.F.MAP327a. They maintain a roughly constant width for at least half to two-thirds of their length before tapering distally. Each patagial bears a longitudinal groove in its proximal and middle portions, and they were likely biconcave in cross-section, as described by Schaumberg et al. (2007).

Patagials 1 to 9 rapidly increase in length, with patagial 9 being the longest in the patagium (Table 3). Patagials 10 to 14 are incomplete distally, but what is preserved suggests a gradual decrease in length along the series. Between patagials 15 and 22, only patagials 16 and 19 are sub-complete distally, but the preserved patagial portions suggest a slightly more rapid decrease in length as concluded from the thickness at the distal breaks. The proximal portions of the more posterior patagials are missing so their length cannot be assessed. Patagials 1 to 10 show an increase in thickness and the following ones become gradually thinner along the wing. All this conforms well with the patagial series of the Ellrich specimen (Pritchard et al., 2021).

Patagials 1 and 2, the shortest in the patagium (Table 3), are oriented anterolaterally so that their distal portion lies anterior to their proximal one when the wing is deployed (Figs. 5, 6). They are sigmoidal, curving anteriorly in their proximal half and posteriorly in their distal half. In contrast, the anterior patagials of the Ellrich specimen are nearly straight (Pritchard et al., 2021). Patagials 3 to 8 of MNHN.F.MAP327a do not show such a sigmoidal curvature, although patagials 1 through 4 and 8 are posteriorly curved distally (Figs. 5, 6). Except for patagials 19, 23 and 24, none of the more posterior patagials show a complete distal end. Thus, it remains unclear whether or not they were curved distally.

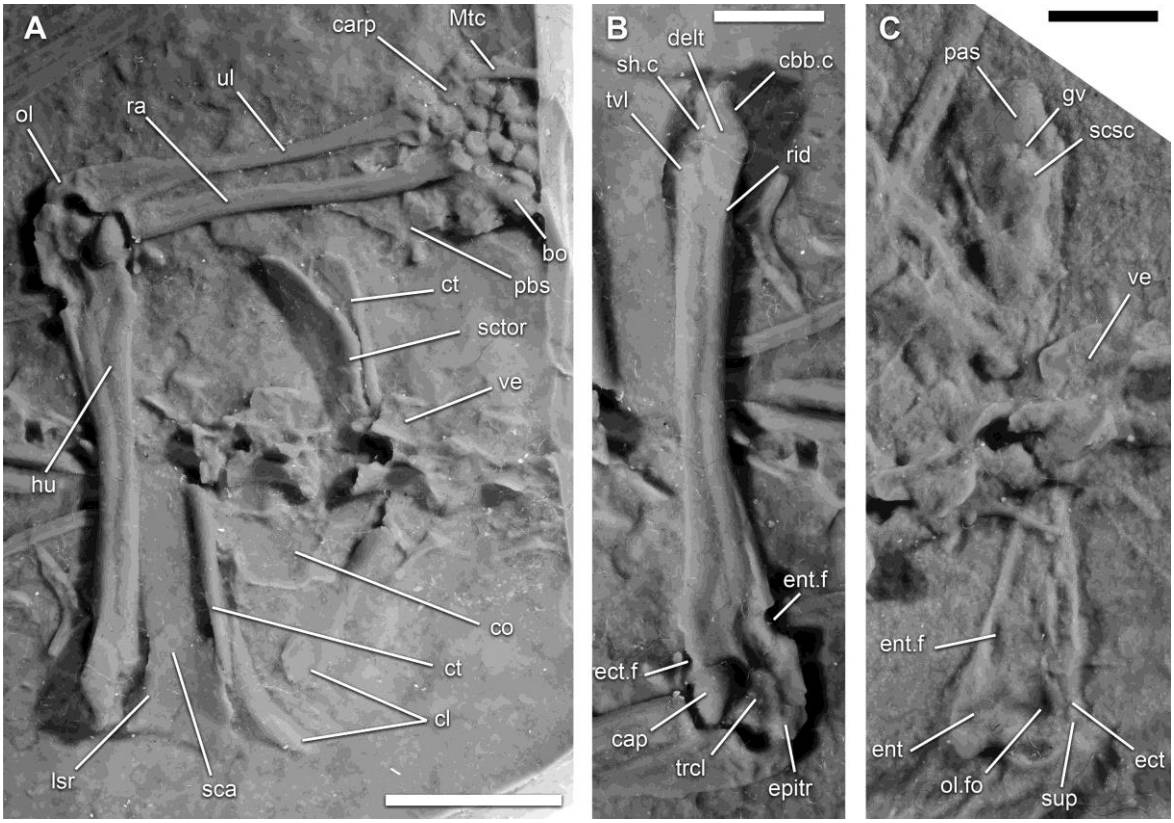

Figure 3-11: *Coelurosauravus elivensis* Piveteau, 1926 (Madagascar, late? Permian), forelimb, silicone casts of individuals preserved as natural external molds. **A**, pectoral girdle and right forelimb of MNHN.F.MAP in right lateral view; **B**, humerus of **A** in ventral view; **C**, humerus of paralectotype MNHN.F.MAP317b in dorsal view. **Abbreviations**: **bo**, basioccipital; **cap**, capitulum; **carp**, carpal elements; **cbb.c**, cavity for M. coracobrachialis brevis; **cl**, clavicle; **co**, coracoid plate; **ct**, cleithrum; **hu**, humerus; **delt**, deltopectoral crest; **ect**, ectepicondyle; **ect.f**, ectepicondylar foramen; **ent**, entepicondyle; **ent.f**, entepicondylar foramen; **epitr**, crest for M. epitrochleoanconaeus; **gv**, groove; **lsr**, lateral scapular ridge; **Mtc**, metacarpal; **ol**, olecranon process of ulna; **ol.f**, olecranon fossa; **pas**, proximal articular surface; **pbs**, parabasisphenoid; **ra**, radius; **rid**, ridge; **sca**, scapular blade; **scsc**, crest for M. subcoracoscapularis; **sctor**, scapular torus; **sh.c**, cavity for M. scapulohumeralis; **ul**, ulna; **trcl**, trochlea; **tvl**, transverse humeral line; **ve**, vertebra. Scale bars equal 1 cm (**A**) and 5 mm (**B**, **C**).

Pectoral Gridle

The pectoral gridle is preserved in all *Coelurosauravus* specimens. It is visible in right lateral view in the lectotype but is badly weathered (Figs. 1, 2). The individual bones are slightly disarticulated in the paralectotypes, allowing for the description of the articular surfaces (Figs. 3, 4). The pectoral girdle is exquisitely preserved in MNHN.F.MAP327a. This specimen will thus serve as the basis for the following description (Figs. 5, 6, 11A). The elements are

preserved in connection, and the pectoral girdle is slightly angled relative to the transverse plane in a way that the right side is visible in lateral view and the left in medial view (Fig. 11A).

The pectoral girdle of MNHN.F.MAP327a comprises both scapulocoracoids, clavicles and cleithra (Fig. 11A). There is no trace of the interclavicle (contra Evans and Haubold, 1987:fig. 14), which is also not visible in the paralectotypes despite all the other bones being present. Owing to the otherwise exquisite preservation of all other bones that remain roughly in anatomical position, we propose this element was reduced or missing in *Coelurosauravus*. In contrast, the interclavicle is prominent in all early diapsids (Carroll, 1975; 1981; Gow, 1975; Currie, 1981a). Among diapsid reptiles, the loss of the interclavicle was only reported in limbless squamates (Conrad, 2008; Gauthier et al., 2012) and dinosaurs (Nesbitt, 2011, but see Vickaryous and Hall, 2010; Tschopp and Mateus, 2013).

None of the *Coelurosauravus* specimens preserves an ossified sternum, which is otherwise present in *Araeoscelis* and common among 'younginiforms' and 'paliguanids' (Vaughn, 1955; Carroll, 1975; Currie, 1981a; Zanon, 1990). However, as indicated by Carroll (1978), the empty space between the posterior margin of the scapulocoracoid and the anterior-most row of gastralia in MNHN.F.MAP327a suggests that a broad cartilaginous sternum was likely present in *Coelurosauravus* (Figs. 5, 6).

Scapulocoracoid—The scapula and coracoid are fused in MNHN.F.MAP327a without any discernable suture (Fig. 11), as is the case in the lectotype and paralectotype (Figs. 1–4). This has been proposed as indicating maturity in diapsid reptiles (Currie and Carroll, 1984; Griffin et al., 2021) and thus suggests a mature age of the *Coelurosauravus* specimens (see Buffa et al., 2021 for a more detailed assessment based on the skull).

The scapular blade extends vertically as a rectangular plate and is about three times as high as it is wide (Fig. 11). Dorsally, it extends roughly to the level of the vertebral column (Fig. 11) in contrast to the shorter scapular blades of *Claudiosaurus* and *Hovasaurus* (Carroll, 1981; Currie, 1981a) and the extremely tall and narrow blades of drepanosauromorphs (Renesto et al., 2010; Castiello et al., 2016). As is visible in medial view on the left side of MNHN.F.MAP327a, the scapular blade is reinforced anteriorly by a low scapular torus (sensu Pawley and Warren, 2006), and the blade becomes gradually thinner dorsally in longitudinal direction (Fig. 11). Its anterior margin is roughly vertical in contrast to the strongly convex

anterodorsal margin of the scapular blade of araeoscelidians (Vaughn, 1955; Reisz, 1981), and the concave one of drepanosauromorphs (Renesto et al., 2010; Castiello et al., 2016) and several archosauromorphs (Dilkes, 1998; Spielmann et al., 2008; Nesbitt et al., 2015). The dorsal surface of the blade forms a rugose margin suggesting the presence of a cartilaginous suprascapula. The anterior margin of the scapular blade bears a thin articular surface for the cleithrum.

The scapular blade progressively becomes transversely and longitudinally broader just dorsal to the glenoid and its contact with the coracoid portion of the scapulocoracoid. The posterior margin of the scapular blade is prolonged by a low-but-robust lateral supraglenoid ridge dorsal to the glenoid (Fig. 11). There is neither a supraglenoid buttress nor a supraglenoid foramen, as is typical in neodiapsids (deBraga and Rieppel, 1997) but in contrast to araeoscelidians (Vaughn, 1955; Reisz, 1981).

As is visible on MNHN.F.MAP327a and MNHN.F.MAP317a, b, the coracoid and scapular portions of the scapulocoracoid meet at slightly more than a right angle (Fig. 11). The coracoid plate extends medially to the sagittal plane of the animal. It does not protrude anterior to the scapular blade, and its posterior extent is not visible in any specimen. From what is preserved we conclude that it extended for a short distance posterior to the glenoid. The posteromedial portion coracoid of MNHN.F.MAP317b appears turned dorsally, although this is likely due to diagenetic compression (Figs. 3, 4).

The glenoid is poorly preserved in all specimens. Two triangular protrusions, the scapular and coracoidal contributions to the glenoid articulation, are exposed in the vicinity of the humeral head in the lectotype (Figs. 1, 2). The glenoid of *Coelurosauravus* had the ‘screw-shaped’ morphology typical of early tetrapods (Romer, 1956).

Cleithrum—Cleithra are visible in all specimens, but are best preserved in MNHN.F.MAP327a (Fig. 11). The bone comprises a slender cleithral shaft, extending ventrally from the dorsal region of the scapular blade to the level of the top of the lateral supraglenoid ridge. As visible in both MNHN.F.MAP327a and the lectotype, the bone fans slightly dorsally over the top of the scapular blade. The posterior margin of the cleithral shaft bears a long articular surface that meets the anterior margin of the scapular blade along most of its height.

Paired cleithra were described in araeoscelidians, *Acerosodontosaurus* and *Hovasaurus* (Currie, 1980, 1981a; Reisz, 1981) but were considered absent in most other stem-saurians. As the cleithrum is liable to be unpreserved or misinterpreted (e.g. as a cervical rib, Romer and Price, 1940:114), we suggest that its absence in *Youngina* (Gow, 1975) is equivocal. On the contrary, as indicated by numerous specimens, we follow Carroll (1981) in considering this bone absent in *Claudiosaurus*.

Clavicles—The clavicles are visible in dorsal and lateral views on MNHN.F.MAP327a and MNHN.F.MAP317a and in posteroventral view in MNHN.F.MAP317b (Figs. 3, 4H).

As seen in MNHN.F.MAP327a, the clavicles are composed of a dorsal portion that covered the cleithrum and a ventral one that articulates with the anterior margin of the scapular blade. Part of the ventral portion of the clavicle extends medially along the anterior margin of the coracoid plate (Fig. 11). Both portions merge smoothly into each other at an obtuse angle of about 120°.

The dorsal process of the clavicle gradually tapers towards its terminus. It is convex anteriorly, but its posterior surface bears an elongate articular surface for the cleithrum and scapulocoracoid, as is visible in MNHN.F.MAP317b (Fig. 2). On the contrary, the ventral process of the clavicle becomes gradually broader medially. At the same time, it gradually decreases in height medially and possibly forms an articular surface for the interclavicle, although we were unable to identify a corresponding sutural surface. The subtle, gradual expansion of the ventral process of the clavicle conforms well with that of other neodiapsids (e.g. Currie, 1981a), but lacks the broader expansion typical of early reptiles and araeoscelidians (Holmes, 1977; Reisz, 1981).

Forelimb

Elements of the forelimb are preserved in all specimens. The description of the long bones follows the terminology of Romer (1922) and considers that the humerus is oriented perpendicular to the sagittal plane of the animal, with the lower arm set at a right angle to the humerus, pointing downwards. The orientation axes of the individual bones are thus consistent with previous studies on stem-saurian reptiles (e.g. Carroll, 1981; Currie, 1981a). The long bones are slightly disarticulated in the lectotype (Figs. 1, 2) but are mostly complete and lie in

connection with each other on both sides in the paralectotypes (Figs. 3, 4). The right forelimb is exquisitely preserved in MNHN.F.MAP327a and lies in connection with the pectoral girdle (Figs. 5, 6, 11).

Humerus—The humerus is the longest bone in the forelimb (Fig. 11). It has the tetrahedral shape typical of all early tetrapods (Romer, 1922), with the epiphyses twisted almost at right angle to each other. As is seen in all specimens, the humerus of *Coelurosauravus* is gracile, with the epiphyses only slightly enlarged relative to the diaphysis. Among early diapsids, this morphology is typical for weigeltisaurids (Evans and Haubold, 1987; Bulanov and Sennikov, 2010; Pritchard et al., 2021), and araeoscelidians (Vaughn, 1955; Reisz, 1981; Reisz et al., 1984). In contrast, other early neodiapsids possess greatly enlarged humeral heads (Carroll, 1975, 1981; Currie, 1980, 1981a), as do most early archosauromorphs (Gottmann-Quesada and Sander, 2009; Nesbitt et al., 2015). As seen in all *Coelurosauravus* specimens, the humerus is nearly straight with both epiphyses aligned in the proximodistal axis of the bone (Fig. 11). This is also the case in the *Weigeltisaurus* holotype (Evans and Haubold, 1987), but contrasts with the strongly curved humerus of *Rautiania* (Bulanov and Sennikov, 2010).

The humerus is preserved either in dorsal or ventral view in all specimens (Figs. 1–4, 11). Thus, the proximal epiphysis is only partially visible. The proximal epiphysis of MNHN.F.MAP327a is partially visible in ventral view (Fig. 11B). It bears a robust deltopectoral crest extending ventrally from the proximal articulation over the length of the epiphysis. This crest delimits deep anteroproximal and posteroproximal concavities on the proximal epiphysis and is prolonged distally by a low longitudinal ridge separating the ventral and posterior surfaces of the bone. The anteroproximal cavity is delimited ventrally by a sharp transverse ridge (transverse humeral line of Romer, 1922:555). The dimensions of this cavity suggest an extensive insertion for the M. scapulohumeralis. The posteroproximal cavity probably represents the broad proximal insertion pit of the M. coracobrachialis brevis (Holmes, 1977). MNHN.F.MAP317b exposes the proximal epiphyses of both humeri in dorsal view (Fig. 11C). The robust humeral head comprises of a smooth, ovate condyle. It is oriented dorsoventrally as in *Rautiania* (Bulanov and Sennikov, 2010). More distally, the proximal epiphysis bears a strong tuber on its dorsal surface, separated from the humeral head by an anteroposteriorly oriented groove. Based on its position relative to the articular head, this conforms well with the insertion of the M. subcoracoscapularis described for *Captorhinus*

(Holmes, 1977). Kuehneosaurids also show a prominent insertion area for the M. subcoracoscapularis (Colbert, 1970).

All preserved humeri bear longitudinal grooves on their dorsal and ventral surfaces, likely due to slight diagenetic compression. This indicates that the bone structure was fragile, more so than that of the exceptionally preserved vertebrae, suggesting it was mostly hollow with thin cortical walls.

The distal epiphysis is about twice as wide as the diaphysis. As is seen in all specimens, the ectepicondyle is small and does not extend beyond the posterior margin of the diaphysis (Fig. 11). As is best seen in MNHN.F.MAP317a, the supinator process is slender and extends distally parallel to the main axis of the bone, forming the anterior wall of the ectepicondylar foramen (Figs. 3, 4). This foramen appears open in the lectotype and MNHN.F.MAP327a because the supinator process is obscured or broken distally (Fig. 11), but was presumably closed in these specimens prior to the fracture, as in the paralectotypes (Figs. 3, 4). An enclosed ectepicondylar foramen was also described for *Rautiania* (Bulanov and Sennikov, 2010). In contrast, this foramen is not enclosed by the supinator process in the *Weigeltisaurus* holotype (Evans and Haubold, 1987).

As seen in all *Coelurosauravus* specimens, the entepicondyle extends slightly posteriorly beyond the distal margin of the diaphysis and distal to the trochlea (Fig. 11) as in *Rautiania* (Bulanov and Sennikov, 2010). The entepicondyle is roughly triangular, meeting the diaphysis at an obtuse angle (ca. 160°), unlike the robust and rectangular entepicondyle of *Hovasaurus* and *Thadeosaurus* (Carroll, 1981; Currie, 1981a). An entepicondylar foramen is visible in all *Coelurosauravus* specimens on the proximal portion of the entepicondyle as in *Rautiania* (Bulanov and Sennikov, 2010). The capitellum consists of a robust ovate condyle that articulated with the proximal epiphysis of the radius. The trochlea of the distal epiphysis is subtle and rounded distally. The capitellum and trochlea are well ossified and prominent in comparison to those of *Youngina* (BP/1/3859, VB, pers. obs.) or contemporaneous neodiapsids (Currie, 1980, 1981a; Carroll, 1981). Such a morphology is also present in *Rautiania* (Bulanov and Sennikov, 2010) and is reminiscent of early reptiles (Holmes, 1977; Reisz, 1981) or putative arboreal reptiles such as drepanosauromorphs (Pritchard et al., 2016). As best seen in MNHN.F.MAP327a, the ventral surface of the entepicondyle posterior to the trochlea forms a

low crest, suggesting a strong origin point of the M. epitrochleoanconaeus (Fig. 11B; Holmes, 1977). This appears to be the case in *Rautiania* as well (Bulanov and Sennikov, 2010:fig. 4). The dorsal surface of the distal epiphysis is broken and weathered on both the lectotype and MNHN.F.MAP317b. What is preserved in MNHN.F.MAP317b suggests that there was a deep olecranon fossa framed on either side by low epicondylar ridges.

Radius—The radius is visible in all specimens but is best preserved in MNHN.F.MAP327a, where the bone is seen in posterior view. The radius is an elongate and gracile bone with a cylindrical shaft. The bone is slightly sigmoidal, and the distal epiphysis appears to be inclined anterodistally (Fig. 11). There is no trace of the strong twisting observed in other neodiapsids (*Claudiosaurus*, *Hovasaurus*, Carroll, 1981; Currie, 1981a). The radius of other weigeltisaurids was described as straight in the *Weigeltisaurus* holotype and the Ellrich specimen (Pritchard et al., 2021), but we think that a slight inclination of the distal epiphysis may have been obliterated by diagenetic compression. Both epiphyses are only slightly expanded relative to the diaphysis.

The proximal epiphysis of the radius is best preserved in MNHN.F.MAP317a (Figs. 3, 4). Its proximal surface is strongly concave to accommodate the prominent capitellum of the humerus. As is best seen in the paralectotypes (Figs. 3, 4), the radius bears a slight lateral lip reminiscent of a tiny olecranon ("posterior lip" of Carroll, 1981:330). This structure is obscured by the ulna in MNHN.F.MAP327a (Fig. 11). This lip was otherwise recognized in *Hovasaurus* and *Thadeosaurus* (Carroll, 1981; Currie, 1981a). Pritchard et al. (2021) described a radioulnar articulation in the Ellrich specimen. However, we were unable to identify an articular facet on either bone in any *Coelurosauravus* specimen. Owing to the slight rotation of these bones, we think that the presence of this articulation is equivocal (see below). The proximal epiphysis becomes gradually more slender and continues into the diaphysis.

The distal epiphysis is best preserved in MNHN.F.MAP327a (Fig. 11B). Its distal surface is slightly concave and oriented anterodistally. It shows an anteroposterior constriction slightly lateral to the longitudinal axis of the bone, dividing the distal articular surface into a broad medial surface and a small lateral surface (Figs. 11C, 12). This lateral surface is roughly four times smaller than the medial one. It served for the articulation with the intermedium whereas the medial one served for the articulation with the radiale.

Ulna—The ulna is preserved in similar manner as the radius in the *Coelurosauravus* material. It is an elongate, gracile bone with a cylindrical shaft and is slightly sigmoidal in posterior view. Both epiphyses are expanded relative to the diaphysis, reaching up to twice the width of the shaft in posterior aspect.

The proximal epiphysis bears a well-developed olecranon delimited medially by a deeply concave sigmoid notch (Fig. 11). This process is also seen in the *Weigeltisaurus* holotype and the Ellrich specimen (Evans and Haubold, 1987; Pritchard et al., 2021). As is seen in MNHN.F.MAP327a, the olecranon and sigmoid notch are reinforced by a prominent ridge running along the posterior surface of the bone. The posterior surface of the olecranon bears subtle pits, suggesting that the olecranon served as the insertion of a robust tendon for the M. triceps medialis (Holmes, 1977).

The distal epiphysis of the ulna is best preserved in posterior view in MNHN.F.MAP327a but is broken in two parts distally (Fig. 11A). According to the outline of the less well-preserved ulnae of the paralectotypes (Figs. 3, 4), the distal epiphysis of the ulna was slightly broader than the diaphysis and presumably articulated with both the intermedium and ulnare. It also articulated with the neighboring pisiform, as in all amniotes (Romer, 1956) but this articular surface is obscured in all specimens.

Manus

Elements of the manus are preserved in all specimens, although none of them are complete. The carpal elements are best preserved in MNHN.F.MAP327a, where they are seen in ventral view (Figs. 12, S2). This specimen will thus serve as the basis of the following description.

Our re-examination of the carpus resulted in a novel interpretation of the individual elements, which slightly differs from that of Carroll (1978:fig. 6) and Evans and Haubold (1987:fig. 15A). The carpus of *Coelurosauravus* comprises 11 bones, which is the standard number in early amniotes (Romer, 1956), and includes the radiale, intermedium, ulnare, pisiform, two centralia and five distal carpals. Carpal elements are also present in the

paralectotypes but are mostly obscured and hard to identify (Figs. 3, 4). Some are also completely disarticulated and unidentifiable on the lectotype (Figs. 1, 2).

None of the digits are preserved in the left manus, but preservation permits examination of the metacarpals (Fig. 12). The digits of the right hand of the paralectotype is slightly more complete (Figs. 3, 4). The digit that lies closest to the skull shows three phalanges in connection, none of which being the ungual. This digit likely represents digit V (see below). The manus has thus rotated relative to the forearm because this digit now lies medial to the others.

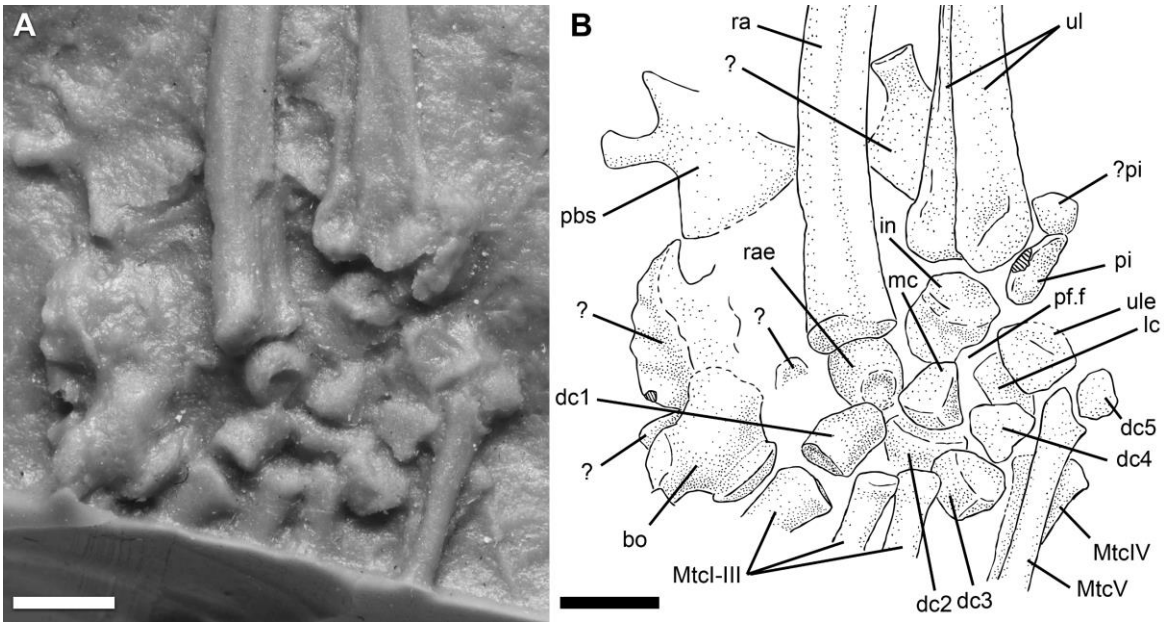

Figure 3-12: *Coelurosauravus elivensis* Piveteau, 1926 (Madagascar, late? Permian), MNHN.F.MAP327a, carpus, ventral view. **A**, silicone cast of individual preserved as a natural external mold; **B**, interpretative drawing of **A**. **Abbreviations**: **dc**, distal carpal; **in**, intermedium; **lc**, lateral centrale; **mc**, medial centrale; **Mtc**, metacarpal; **pbs**, parabasisphenoid; **pf.f**, perforating foramen; **pi**, pisiform; **ra**, radius; **rae**, radiale; **ul**, ulna; **ule**, ulnare. Scale bars equal 2 mm.

Radiale—The radiale is a small, rounded bone lying in proximoventral view close to the articular surface of the distal epiphysis of the radius (Fig. 12). The ventral surface of the bone bears a deep recess with a circular outline. Owing to its size and position relative to the other carpals, this bone likely articulated with the distomedial articular surface of the radius and the intermedium proximally, the medial centrale laterally and distal carpal 1 distally. It may have articulated with distal carpal 2 as well, although this cannot be ascertained because both bones are partially obscured and the individual elements slightly displaced. In araeoscelidians

(Reisz, 1981) and early neodiapsids (Carroll, 1981; Currie, 1981a), the radiale is excluded from an articulation with distal carpal 1 by the medial centrale.

Intermedium—We identify a small bone lying just distal to the ulna as the intermedium, which is visible in proximoventral view (Fig. 12). Evans and Haubold (1987) only described the ventral surface of this element, and Carroll (1978) identified this element as the lateral centrale. According to its broad proximal surface, the bone likely articulated with the distolateral articular facet of the radius and distomedial portion of the ulna proximally. The long medial margin of the bone suggests that it articulated with the radiale medially (see above). The lateral surface of the intermedium bears a low incisura, indicating its contribution to the perforating foramen. As in most early amniotes, the intermedium likely formed the median half of the perforating foramen and articulated with the medial margin of the ulnare. However, we failed to identify a corresponding incisura on the ulnare (see below). Based on its position and the size of the neighboring elements, the intermedium likely articulated with both centralia distally. This conforms with the contacts reconstructed by Evans and Haubold (1987).

Ulnare—As described by Carroll (1978) and Evans and Haubold (1987), the ulnare is a rectangular element, which is visible in ventral view, lying slightly distal to the intermedium and pisiform in MNHN.F.MAP327a (Fig. 12). The ventral surface of the bone is shallowly concave and bears a low ridge near its center. Owing to its slight displacement and the lack of an identifiable incisura for the perforating foramen, it is difficult to say whether or not the ulnare has rotated. Therefore, the reconstruction of its contacts with the neighboring bones is somewhat speculative. The shape of the carpal elements is compatible with the typical carpal articulation in early amniotes (Romer, 1956), suggesting the ulnare may have contacted the ulna, intermedium and pisiform proximally, the lateral centrale medially, and distal carpal 5 distally. Based on the size of the lateral centrale, it is possible that it articulated with distal carpal 4 as well, although this cannot be ascertained. This configuration would conform with the contacts proposed by Evans and Haubold (1987).

Pisiform—We follow Carroll (1978) and Evans and Haubold (1987) in their identification of the pisiform in MNHN.F.MAP327a, which is visible in proximoventral view (Fig. 12). This carpal lies distolateral to the ulna close to its anatomical position. Based on its position relative to the neighboring elements, it articulated with the ulna proximally and the

ulnare medially, as is typical in early amniotes (Romer, 1956). A small sub-rectangular structure lies proximal to the pisiform, lateral to the distal head of the ulna. It may correspond to a broken-off portion of the pisiform, although this remains tentative because the pisiform would then be unusually large compared to other amniotes (Romer, 1956).

Medial Centrale—The medial centrale is a small polygonal element visible in distoventral view in MNHN.F.MAP327a (Fig. 12). It is keystone-shaped, with its distal margin being wider than its proximal one. Based on its position and the articular surfaces on the neighboring elements, the medial centrale likely articulated with the radiale, intermedium and lateral centrale proximally, and distal carpals 1 and 2 distally. Whether or not it articulated with distal carpal 3 cannot be ascertained because of the disarticulation of the bones in MNHN.F.MAP327a. Contrary to Evans and Haubold (1987), we suggest no contact between the medial centrale and distal carpal 4. Both *Hovasaurus* and *Thadeosaurus* have a wide medial centrale that contacts distal carpal 4 (Carroll, 1981; Currie, 1981a).

Lateral Centrale—We follow Evans and Haubold (1987) in their identification of the lateral centrale of MNHN.F.MAP327a (Fig. 12). This rectangular element is seen in ventral aspect but is partially obscured by the ulnare and distal carpal 3. It is unclear whether or not this element has rotated, making the reconstruction of its articulations difficult. As the shape of the carpal elements is compatible with the typical carpal articulation in early amniotes (see ulnare above), the lateral centrale may have articulated with the intermedium and ulnare proximally, the medial centrale medially and distal carpal 4 distally.

Distal Carpals—All five distal carpals are preserved in MNHN.F.MAP327a (Fig. 12). Our interpretation follows that of Carroll (1978). Distal carpal 1 is seen in ventral view. It is a robust cylindrical bone that articulated with the radiale proximally, distal carpal 2 laterally and metacarpal I distally (Fig. 12). Because of its slender distal terminus, a distal contact with metacarpal II seems unlikely.

Following Carroll (1978), we consider a broad, mostly obscured element as distal carpal 2 (Fig. 12) and not as fused distal carpals 2 and 3 as reported by Evans and Haubold (1987). Distal carpal 2 articulated with the medial centrale proximally, distal carpals 1 medially, distal carpal 3 laterally and metacarpal II distally. Contacts with the radiale proximomedially and metacarpal III distolaterally are equivocal because these elements are slightly displaced and

partially unpreserved. Distal carpal 2 was likely excluded from a contact with metacarpal III by the large distal carpal 3.

Evans and Haubold (1987) identified the large subcircular element lying lateral to metacarpal III as distal carpal 4 because of its large size as is typical in most early amniotes (Romer, 1956). However, we concur with Carroll (1978) in identifying this bone as distal carpal 3 instead based on its close location to distal carpal 2 and metacarpal III (Fig. 12). The size and robustness of distal carpal 3 conforms well with that of the less well-preserved carpus of the *Weigeltisaurus* holotype (SMNK cast of SSWG 113/7, VB, pers. obs.). This bone likely articulated with the lateral centrale proximally, distal carpals 2 medially, distal carpal 4 laterally and metacarpals III and IV distally. A contact between distal carpal 3 and the medial centrale is equivocal because these two bones are only partially preserved.

Distal carpal 4 is a relatively small subtriangular element compared to distal carpal 3 (Fig. 12), at most as large as distal carpal 3. In contrast, distal carpal 4 is typically the largest of the series in early amniotes (Romer, 1956). Based on the articular facets of the bone, distal carpal 4 articulated with the ulnare proximally, the lateral centrale proximomedially, distal carpals 3 medially, distal carpal 5 laterally, and metacarpal IV distally.

Distal carpal 5 is sub-rectangular and the smallest of the series. Distal carpal 5 thus articulated with the ulnare proximally, distal carpal 4 medially, and metacarpal V distally.

Metacarpals—The proximal portions of the metacarpals are preserved in MNHN.F.MAP327a, but the rest of the bones are not preserved in this specimen (Fig. 12). The right manus of the paralectotypes is the most complete of any specimen, but its metacarpal I is also partially preserved (Figs. 3, 4). Metacarpal III is the longest in the series, as is the case in the *Weigeltisaurus* holotype and *Rautiania* (Evans and Haubold, 1987; Bulanov and Sennikov, 2010). In contrast, the longest in the series is typically metacarpal IV in early amniotes (Romer, 1956). Owing to the preservation of the paralectotypes and MNHN.F.MAP327a, it remains unclear whether or not the metacarpals overlapped each other proximally. Such an overlap is described for the *Weigeltisaurus* holotype (Evans and Haubold, 1987).

As seen in MNHN.F.MAP327a, metacarpal I bears a slightly expanded proximal extremity relative to the shaft, which bears a shallowly concave articular facet for distal carpal 1 (Fig. 12). Metacarpals II and III are visible mostly in ventrolateral view (Fig. 12). Their

proximal articular surfaces are slightly concave to accommodate the respective distal carpals. Metacarpal III is more robust than the other metacarpals, as seen on MNHN.F.MAP317a, b (Fig. 4). The head of metacarpal IV is 1.2 times wider than that of metacarpal I in MNHN.F.MAP327a (Fig. 12). As for metacarpals II and III, metacarpal V is mostly visible in ventrolateral view. It bears a prominent proximolateral process that frames the entire lateral margin of distal carpal 5.

Phalanges—All *Coelurosauravus* specimens preserve portions of the phalangeal series. The non-ungual phalanges are all long slender bones with slightly expanded extremities (Figs. 1–4). Digit V of the right manus of the paralectotypes is the only reasonably complete digit (Figs. 3, 4). It shows two phalanges in connection with the space for the missing first phalanx between this series and metacarpal V. The most distal phalanx is the longest, and identified as the penultimate by comparison with the long penultimate phalanx in digit V of *Rautiania* (Bulanov and Sennikov, 2010). The ungual phalanx is missing, indicating that digit V of *Coelurosauravus* comprised four phalanges as in other weigeltisaurids (Evans and Haubold, 1987; Bulanov and Sennikov, 2010; Pritchard et al., 2021). In contrast, all Permo–Carboniferous diapsids have three phalanges in digit V (Romer, 1956).

Ungual phalanges are preserved in the lectotype and MNHN.F.MAP327b. They are all recurved and sharply pointed with the distal tip of the claw extending roughly to the level of the strong flexor tubercle. These bones all bear lateral longitudinal carinae.

Pelvic Girdle

The right pelvis is well-preserved in lateral view in MNHN.F.MAP327a (Figs. 9A, 9B). It is partially obscured by the femoral head so that only portions of the ilium and pubis are visible. The left puboischiatic plate is visible in medial view in the lectotype (Figs. 1, 2), as suggested by Carroll (1978) based on its shape and position relative to the sacral region. This plate is badly weathered with a triangular pubic portion pointing anteroventrally and a trapezoidal ischiatic portion pointing posteriorly (Figs. 1, 2). An even more weathered triangular structure expands dorsally from this puboischiatic plate, which might represent the ilium. However, this identification remains tentative. The pelvis is missing in the paralectotype (Figs. 3, 4).

Provided that our identification of the pelvic girdle of the lectotype is correct, the putative puboischiatic plate shows no trace of a thyroid fenestra (Figs. 1, 2). This fenestra is also absent in the puboischiadic plates of other weigeltisaurids (Evans, 1982).

Ilium—The outline of the ilium seems to be partially preserved on the lectotype, although this identification remains tentative (see above; Figs. 1, 2). The bone is otherwise preserved in lateral view in MNHN.F.MAP327a (Figs. 9A, 9B). It is a thin dorsoventrally compressed bone. The pubic peduncle bears an anteroventrally oriented surface for the pubis as indicated by the low groove separating both bones. Nothing can be said about the ischiatic peduncle.

A robust, posterodorsally oriented supraacetabular buttress borders the acetabular cavity (Figs. 9A, 9B). A similarly robust supraacetabular buttress is present in *Claudiosaurus* and 'younginiforms' (Carroll, 1981; Currie, 1980, 1981a). This supraacetabular buttress is most massive in its middle portion, immediately dorsal to the acetabulum. Anteriorly, it merges into the pubic peduncle and is aligned with the preacetabular buttress of the pubis (Figs. 9A, 9B). More posteriorly, the supraacetabular buttress forms the posteroventral margin of the iliac blade and gradually decreases in transverse thickness, fading into the iliac blade posterodorsally.

The iliac blade is triangular in lateral aspect, flaring dorsally and with roughly symmetrical preacetabular and postacetabular processes, the latter being only slightly longer (Figs. 9A, 9B). The antero- and posteroventral margins of the iliac blade thus diverge anterodorsally and posterodorsally whereas its dorsal margin runs roughly horizontally. This morphology is similar to other weigeltisaurids (Evans, 1982; Pritchard et al., 2021), but we found no trace of the dorsal embayment reported by Pritchard et al. (2021) for the Ellrich specimen. In contrast, the iliac blade of other stem-saurians is typically lanceolate in lateral aspect and lacks a preacetabular process, as in *Hovasaurus* or *Thadeosaurus* (Carroll, 1981; Currie, 1981a), or only bears a small preacetabular tuber as in *Acerosodontosaurus* (Currie, 1980). However, a similar but smaller preacetabular process is present in several archosauromorphs (Nesbitt et al., 2015; Pritchard and Sues, 2019). Provided our interpretation of the pelvic girdle of the lectotype is correct, the postacetabular process did not extend posterior to the ischium in *Coelurosauravus* (Figs. 1, 2). This would contrast with the situation in other stem-saurians, where the postacetabular process of the iliac blade extends beyond the

posterior margin of the ischium (Currie, 1980, 1981a; Carroll, 1981). Fine striations radiate dorsally across the lateral surface of the iliac blade in MNHN.F.MAP327a (Figs. 9A, 9B). They presumably mark the attachment area of the thigh musculature (Romer, 1922).

Pubis—Little of the pubis is visible in MNHN.F.MAP327a (Figs. 9A, 9B). As described by Carroll (1978), the most conspicuous part of the bone is the prominent, anteroventrally oriented pubic tubercle, which ends with a concavity presumably housing the iliopubic ligament (Romer, 1922). A robust ridge extends from the preacetabular buttress of the pubis to this concavity. Anteriorly, the preacetabular buttress delimits a broad posteriorly facing surface for the contribution of the pubis to the acetabulum. In *Acerosodontosaurus*, *Hovasaurus* and *Thadeosaurus* the pubis barely contributes to the acetabulum, and none of these taxa have a preacetabular buttress (Currie, 1980, 1981a; Carroll, 1981). Lastly, the anterodorsal margin of the pubis of MNHN.F.MAP327a lacks the short flange present in 'younginiforms' (Currie, 1980, 1981a; Carroll, 1981).

Ischium—Provided our interpretation of the pelvic girdle of the lectotype is correct, the ischium is preserved in medial view (Figs. 1, 2). The bone is short and trapezoidal in lateral aspect, being slightly anteroposteriorly longer than the ischium. The medial surface of the ischium is shallowly concave.

Hindlimb

The lectotype preserves elements of both hindlimbs, with both femora lying perpendicular to the long axis of the body and the knees bent in a way that the forelegs and pes extend posteromedially along the vertebral column of the tail of the animal (Figs. 1, 2). The left hindlimb underlies the broken-off trunk of the animal and is mostly obscured, but the right one is almost complete. Despite being weathered, the individual bones remain mostly in anatomical position. Elements of the hindlimbs in MNHN.F.MAP327a are more poorly preserved. They extend posteriorly from the pelvic region and are oriented posteroventrally with respect to the tail (Figs. 5, 6). There is no trace of the hindlimbs in the paralectotypes (Figs. 3, 4).

As for the forelimb, we follow the terminology of Romer (1922) for the description. For the sake of clarity, the femora are described as if oriented perpendicular to the sagittal plane,

with the foreleg bent ventrally roughly at a right angle. This is consistent with previous descriptions of weigeltisaurids including *Coelurosauravus* (Carroll, 1978; Evans and Haubold, 1987).

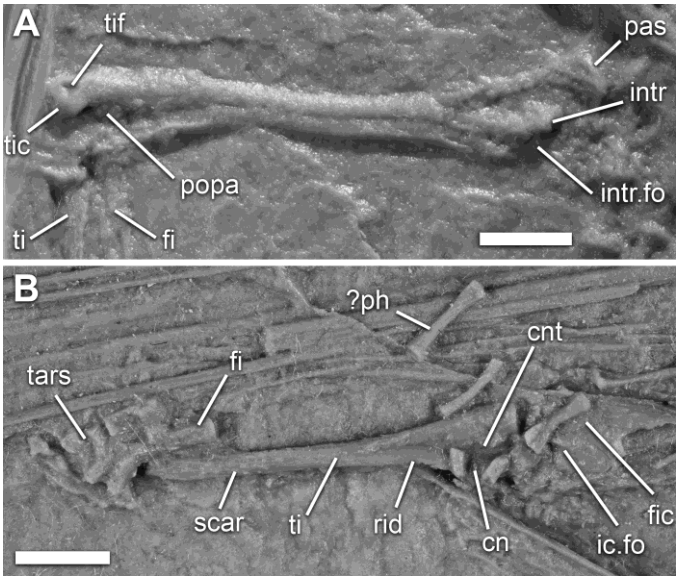

Figure 3-13: *Coelurosauravus elivensis* Piveteau, 1926 (Madagascar, late? Permian), hindlimb, silicone casts of individuals preserved as natural external molds. **A**, right femur of lectotype MNHN.F.MAP325a in anteroventral view; **B**, right tibia and partial fibula and tarsus of MNHN.F.MAP327a in posterodorsal view. **Abbreviations**: **cn**, cnemial crest; **cnt**, cnemial trough; **fi**, fibula; **fic**, fibular condyle; **ic.fo**, intercondylar fossa; **intr**, internal trochanter; **intr.fo**, intertrochanteric fossa; **pas**, proximal articular surface; **ph**, phalanx; **popa**, popliteal area; **rid**, ridge; **tars**, tarsal elements; **ti**, tibia; **tic**, tibial condyle; **tif**, tibial fossa. Scale bars equal 5 mm

Femur—The right femur is subcomplete and visible in anteroventral view on the lectotype (Fig. 13). The left one is also preserved in anteroventral view, but only its distal epiphysis is exposed (Figs. 1, 2). Both femora are also partially preserved in MNHN.F.MAP327a but overlie each other (Figs. 5, 6). The diaphysis of the left femur is seen between the broken-off epiphyses of the right one.

As is best visible in the lectotype, the femur is a long and slender bone, being slightly longer than the humerus (Figs. 1, 2, 13). It consists of a cylindrical diaphysis with epiphyses that are about twice as wide as the shaft. In anterior view, the bone shows a slight sigmoidal curvature (Fig. 13) as is typical for early diapsids (Benton, 1985).

The proximal epiphysis is diagenetically compressed in the lectotype (Fig. 13). The femoral head is rounded in anteroventral view. As described by Carroll (1978), the low internal trochanter is visible distoventral to the femoral head, framing a mostly obscured intertrochanteric fossa. It does not extend proximally to the level of the proximal articulation,

as in the Ellrich specimen (Pritchard et al., 2021). Nothing can be said about the poorly preserved proximal surface of the right femur of MNHN.F.MAP327a (Figs. 9A, 9B).

The diaphysis is best preserved in the lectotype (Fig. 13). It is cylindrical and shows a slightly larger diameter than the humeral shaft (Figs. 1, 2). There is no trace of a fourth trochanter or an adductor crest which are typically present in early reptiles (Holmes, 2003), or of the thin linea aspera described for araeoscelidians (Vaughn, 1955; Reisz, 1981).

The distal epiphysis is visible in anteroventral view in the lectotype (Fig. 13A). Based on the position of the hindlimb relative to the pelvis and our identification of the shallow intercondylar fossa, it is also visible in posterodorsal view in MNHN.F.MAP327a (Fig. 13B). The tibial condyle is preserved on both sides of the lectotype. It is rounded in outline and forms a low anteroventral crest slightly offset from the bone (Fig. 13). Dorsal to this crest, the tibial condyle bears a low, triangular tibial fossa on its posterior surface. The slightly concave popliteal area is partially visible in the lectotype (Fig. 13). The fibular condyle is mostly obscured by tarsal elements in MNHN.F.MAP327a, but its outline suggests that it is rounded (Fig. 13B). What is visible in this specimen suggests that the tibial and fibular condyles extended posteriorly to the same level. This is typical for early neodiapsids (Carroll, 1975, 1981; Gow, 1975; Currie, 1980, 1981a). In contrast, in early amniotes, including araeoscelidians, the fibular condyle extends distal to the tibial one (Reisz, 1981; Holmes, 2003). Pritchard et al. (2021), described the latter morphology in the more poorly preserved Ellrich specimen, contrasting with the femur of *Coelurosauravus*.

As is seen in MNHN.F.MAP327a, the posterior and dorsal surfaces of the distal epiphyses bear short longitudinal striations, which likely mark the insertions areas of the flexor and extensor musculature respectively.

Tibia—The tibia is exquisitely preserved in lateral view on the right side of MNHN.F.MAP327a (Fig. 13B). Both tibiae are also preserved in connection with the femur in the lectotype, where they are visible in medial view (Figs. 1, 2, 13). The tibia is a long and slender bone with a slender distal epiphysis but a highly expanded proximal one reaching up to three times the width of the shaft. As is best seen in the lectotype, the bone is slightly curved, with a shallowly concave posterior margin and a convex anterior one.

As is best seen in MNHN.F.MAP327a, the proximal epiphysis rapidly expands from the diaphysis (Fig. 13B). It bears a prominent cnemial crest anteriorly, which is separated from the proximal epiphysis by a deep cnemial trough (sensu Pawley and Warren, 2006). The anteroproximal portion of the cnemial crest is obscured by tarsal elements, so it is impossible to say whether or not a cnemial tuber was present (Fig. 13B). A prominent cnemial crest is typically present in early reptiles (Holmes, 2003), including araeoscelidians (Vaughn, 1955; Reisz, 1981), but this structure is generally considered absent in early neodiapsids (Ford and Benson, 2020: character 282), although it was also described in some early saurians (e.g., Nesbitt et al., 2015).

As is seen in MNHN.F.MAP327a, a low ridge runs along the anterior surface of the bone as a continuation of the cnemial crest (Fig. 13B). The diaphysis thus appears mediolaterally compressed. Most of the lateral surface of the bone bears short pits and scars, suggesting the insertion area of the extensor musculature of the tarsus. These scars extend distally to the base of the distal epiphysis (Fig. 13B).

The distal epiphysis is poorly preserved in both specimens. As is seen in the lectotype, it is only barely expanded relative to the diaphysis and rounded in medial view (Figs. 1, 2, 14). It articulates distally with the astragalus, but the distal surface of the bone is missing. It is thus unclear whether or not it showed a “stepped” outline, as described for the Ellrich specimen (Pritchard et al., 2021:44).

Fibula—The right fibula is visible in medial view in the lectotype. It is poorly preserved, with a mostly collapsed medial surface (Figs. 1, 2). Only the distal portion of the right fibula is seen in MNHN.F.MAP327a, lying among the tarsal elements (Fig. 13B).

As is visible in the lectotype, the distal anterior margin of the bone is weakly concave (Figs. 1, 2). However, because the proximal epiphysis of the bone is obscured, it remains unclear whether or not the bone was arcuate as in early reptiles (Holmes, 2003) or sigmoidal as in early neodiapsids (Carroll, 1981; Currie, 1981a). Little can be said about the medial surface of the diaphysis because it is compacted. The distal epiphysis is slightly expanded with respect to the diaphysis and accommodates the adjacent astragalus and calcaneus (Figs. 1, 2, 14).

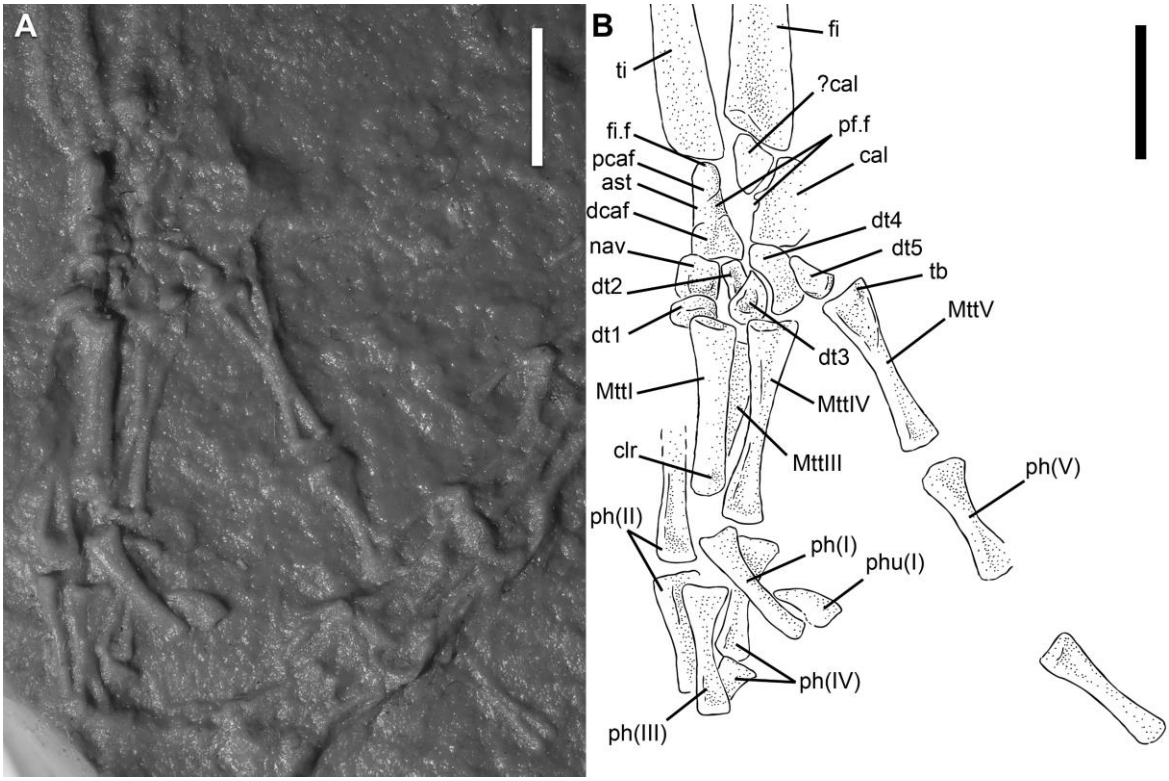

Figure 3-14: *Coelurosauravus elivensis* Piveteau, 1926 (Madagascar, late? Permian), lectotype MNHN.F.MAP325a, right foot, dorsal view, individual preserved as a natural external mold. **A**, silicone cast; **B**, interpretative drawing of **A**. **Abbreviations**: **ast**, astragalus; **cal**, calcaneus; **clr**, contralateral ridge; **dcaf**, distal calcaneal facet of astragalus; **dt**, distal tarsal; **fi**, fibula; **fi.f**, fibular facet; **Mtt**, metatarsal; **nav**, navicular; **pcaf**, proximal calcaneal facet of astragalus; **pf.f**, perforating foramen; **ph**, phalanx (digit number in brackets); **phu**, ungual phalanx (digit number in brackets); **tb**, tubercle; **ti**, tibia. Scale bars equal 5 mm.

Pes

The right pes is completely preserved in the lectotype and is visible in ventral view, including the proximal portions of several digits (Figs. 14, S3). Disarticulated tarsals, metatarsals and phalanges are also preserved in MNHN.F.MAP327a, although the individual bones are impossible to distinguish (Fig. 13B). Carroll (1978:fig. 2) and Evans and Haubold (1987:fig. 17A) proposed various interpretations of the tarsus of the lectotype, but both illustrated a proximolateral expansion of the astragalus. Careful examination of the cast and original specimen indeed shows a polygonal structure proximolateral to the astragalus (Fig. 14), but it is located too far from the latter to be a part of it. It remains unclear if this element is a portion of the calcaneus or just a concretion.

Astragalus—The astragalus of the lectotype lies distal to the tibia. It has slightly rotated from its anatomical orientation, and is now visible in lateral view (Fig. 14). The overall shape of the bone and its articular surface for the tibia thus remain unknown. In lateral view, the bone shows a gradual increase in thickness, with its distal margin being twice as thick as its proximal one. The bone bears a short proximolaterally oriented articular facet for the fibula (Fig. 14).

The entire lateral surface of the astragalus served as an articular surface for the calcaneus (Fig. 14). However, this surface is interrupted near its mid-height by an incisura forming the medial wall of the foramen for the perforating artery. This foramen forms a ventrodistally running groove separating the calcaneal articulation into proximal and distal facets that are subequal in height. This morphology is typical in early neodiapsids (Brinkman, 1979; Carroll, 1981; Currie, 1981a). In contrast, the proximal facet is roughly twice as wide as the distal one in araeoscelidians (Vaughn, 1955; Reisz, 1981). The proximal calcaneal facet is slightly convex whereas the distal one is concave and oriented distolaterally, corresponding to the respective facets of the calcaneus (Fig. 14).

Because the astragalus of the lectotype is only visible in lateral view, its distal articulations with the other bones are hard to reconstruct. However, based on the very slight displacement of the bones and the morphology of distal tarsal 4 (see below), the astragalus of *Coelurosauravus* likely articulated with the navicular and distal tarsals 2 and 4 distally.

Calcaneus—The calcaneus is the least well-preserved tarsal, visible in ventral view in the lectotype (Fig. 14). Its ventral surface seems slightly concave, but this may be due to slight diagenetic compression. As stated above, the proximal extent of the bone is unclear due to a small, indeterminate structure just distal to the fibula that may be a fragment of the calcaneus.

The medial margin of the bone bears a shallow incisura, forming the lateral margin of the perforating foramen (Fig. 14). As for the astragalus, this foramen divides the astragalar contact in proximal and distal portions. Whereas the proximal extent of the bone remains uncertain, the distal articular facet is slightly proximomedially oriented, which conforms well with the corresponding facet on the astragalus. The distal margin of the bone is transversely short relative to the preserved lateral extent of the bone. It articulated with distal carpals 4 and 5 along its entire length.

As is seen in ventral view, the calcaneus shows its greatest thickness at its medial margin, which is also indicated by the calcaneal facets of the astragalus (Fig. 14). The bone then gradually tapers laterally. Carroll (1978:fig. 2) recognized a large lateral expansion, which was not identified by Evans and Haubold (1987:fig. 17A). Although the lateral extent of the bone is unpreserved, it certainly extended beyond the level of its distal margin (Fig. 14).

Navicular—The navicular (following Piñeiro et al., 2016, the 'centrale' or 'lateral centrale' of other authors) lies distal to the medial portion of the astragalus in the lectotype (Fig. 14). It is an almost quadratic bone in ventral view. Owing to its shape, the bone bears subequal articular facets for the astragalus proximally, distal tarsal 2 laterally, and distal tarsal 1 distally. It thus overhangs distal tarsal 1 and is excluded from distal tarsal 3 by the contact between the astragalus and distal tarsal 2.

A bone of similar shape and position was identified as distal tarsal 1 in the *Weigeltisaurus* holotype by Evans and Haubold (1987:fig. 11). We suggest that this element corresponds to the navicular, with distal tarsal 1 missing (SMNK cast of SSWG 113/7, VB, pers. obs.). We interpret the element identified as the navicular by Evans and Haubold (1987:fig.11) as the distal calcaneal articular surface of the astragalus, which is here visible in medial view. This conforms well with the morphology of the astragalus of *Coelurosauravus*, which is preserved in a similar view (see above).

Distal Tarsals—All five distal tarsals are visible in ventral view in the lectotype (Fig. 14). Each one shows a strongly concave dorsal surface, although this may be due to diagenetic compression.

Distal tarsal 1 lies between the navicular and metatarsal II in the lectotype (Fig. 14). It is a proximodistally compressed bone, at least twice as wide as it is long. It is the widest of all distal tarsals. The bone articulated with metatarsal I, but it is unclear whether or not it also articulated with metatarsal II because the latter bone is missing.

Distal tarsal 2 is the transversely thinnest in the series (Fig. 14). It is rectangular in dorsal aspect and its distal portion is obscured by distal tarsal 3. As described above, it articulated with the astragalus proximally, thereby excluding distal tarsal 3 from the navicular. Owing to its width, distal tarsal 2 articulated with metatarsal II only.

Distal tarsal 3 is teardrop-shaped, with its tapered end pointing proximally (Fig. 14). It is overhung proximally by distal tarsal 4, which excludes the bone from the astragalus. Owing to the shape of the proximal surface of metatarsal IV, it appears that distal tarsal 3 articulated with both metacarpals III and IV.

Distal tarsal 4 is the proximodistally longest in the series (Fig. 14). It is very slender, being roughly twice as long as it is wide. The bone bears a strong proximomedial process that overhangs distal tarsal 3 and articulates with the astragalus. Lateral to the astragalar contact, the proximal margin of the bone articulates with the calcaneus. The lateral margin of the bone is slightly convex and provides the articulation for distal tarsal 5.

Distal tarsal 5 is the smallest of the series (Fig. 14). It is subtriangular in dorsal aspect, points proximomedially and has a short proximal contact with the calcaneus.

Owing to our interpretation of the navicular of the *Weigeltisaurus* holotype, the tarsals of *Coelurosauravus* and *Weigeltisaurus* conform well with one another.

Metatarsals—The metatarsal series is partially preserved in the lectotype (Fig. 14). As identified by Evans and Haubold (1987), the digits are slightly jumbled so that metatarsals I, IV and V are visible, while metatarsal II is missing and metatarsal III is partially visible between metatarsals I and IV. All preserved metatarsals have long and slender shafts with slightly expanded proximal and distal articular extremities.

Metatarsal I has an almost flat proximal articular surface for distal tarsal 1. Its distal terminus has a quadrangular extremity, framed proximally by a pair of contralateral ridges. Metatarsal IV is only slightly longer than metatarsal I. As described above, its wide proximal extremity likely articulated with distal tarsals 3 and 4. The distal end of the bone is convex in ventral view, lacking the quadrangular extremity and contralateral ridges of metatarsal I. Metatarsal V is subequal in length to metatarsal I, but its overall morphology is more similar to that of metatarsal IV. It is not hooked, in contrast to most saurian reptiles (Lee, 1997) and lacks the outer (poterolateral) process that is present in other early neodiapsids (Robinson, 1975; Brinkman, 1979; Borsuk-Bialynicka, 2018). The fifth metatarsal of the lectotype also bears a proximolateral tubercle, just distal to its proximal articulation.

Phalanges—The digits are only partially preserved in the lectotype, but preservation allows for a minimal count of the phalanges of each digit (Fig. 14). Elements of all digits are preserved. These include both phalanges of digit I, the second of which being the ungual, at least two of digit II, one of digit III, and two of digits IV and V respectively (Fig. 14). Several disarticulated phalanges are also visible in MNHN.F.MAP327a, although none can be assigned to a given digit (Fig. 13B).

The non-ungual phalanges of the pes are roughly identical in shape to those of the manus, consisting of slender shafts with slightly expanded extremities (Fig. 14). A disarticulated distal digit comprising four bones including the ungual suggests that the penultimate phalanx was substantially longer than the antepenultimate.

Discussion

A reappraisal of the phylogenetic position of weigeltisaurids is currently under study by the authors, and is outside the scope of this paper. However, the detailed re-description of the postcranial skeleton of *Coelurosauravus elivensis* provided here allows for a discussion of the anatomy, functional morphology and paleoecology of these enigmatic gliding reptiles.

Skeletal Reconstruction

The material available for *Coelurosauravus* allows for an almost complete reconstruction of the skeleton of this reptile (Fig. 15). We focus here on the postcranial skeleton of *Coelurosauravus*, as the skull reconstruction has already been provided by Buffa et al. (2021). The mandible, poorly preserved in all *Coelurosauravus* specimens, is reconstructed following the proportions of that of the *Weigeltisaurus* holotype (Bulanov and Sennikov, 2015b).

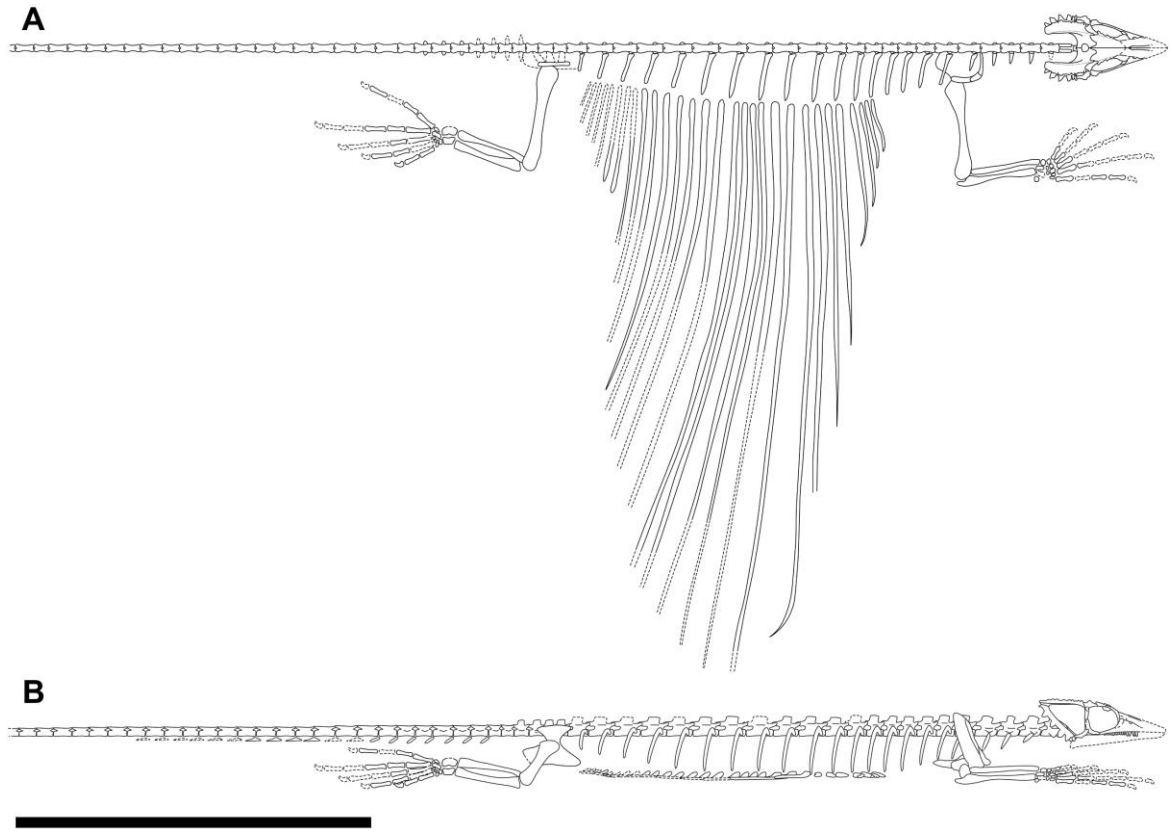

Figure 3-15: *Coelurosauravus elivensis* Piveteau, 1926 (Madagascar, late? Permian), skeletal reconstruction in dorsal (**A**) and right lateral (**B**) view based on all referred specimens. Poorly known or unpreserved elements outlined by dashed lines and reconstructed from the Ellrich specimen (Pritchard et al., 2021). Skull reconstruction based on Buffa et al. (2021); outline of trunk in dorsal view based in part on the Eppelton specimen (TWCMS B5937, VB, pers. obs.); elements from the left side not figured; gastral basket too incomplete to be accurately reconstructed (see text). Scale bar equals 10 cm.

The reconstruction of the presacral vertebral column is based on the complete series preserved in the paralectotypes (Figs. 3, 4, 8), whereas the outline of the trunk is based on the partial Eppleton specimen, which is preserved mostly in dorsal view (TWCMS B5937, VB, pers. obs.; Evans, 1982). The latter specimen was also used by Pritchard et al. (2021) for their reconstruction of the Ellrich specimen. The rest of the vertebral column is mostly based on MNHN.F.MAP327a, although the tail of this specimen is incomplete and includes only the first 29 vertebrae (Figs. 5–7). Given a vertebral count of 50 to 70 among early amniotes (Romer, 1956), the tail of *Coelurosauravus* was much longer than what is preserved. The girdles and limbs are reconstructed based on all known specimens. The manual and pedal digits, which are fragmentary in all *Coelurosauravus* specimens, are reconstructed based on the complete series of the Ellrich specimen (Pritchard et al., 2021). Several patagials are incompletely preserved in

MNHN.F.MAP327a. Their extent was reconstructed by following the outline of the wing reconstructed from the few complete elements (Fig. 15).

Carroll (1978) provided the first and only skeletal reconstruction of *Coelurosauravus elivensis* to date. However, this reconstruction assumes that the wing was supported by the trunk ribs as in the extant agamid *Draco* and the Late Triassic kuehneosaurids. For a long time, this was a commonly accepted interpretation (Evans, 1982; Evans and Haubold, 1987, but see Schaumberg, 1976, 1986). All of the more recent reconstructions are based on the German material, particularly the Ellrich specimen (Frey et al., 1997; Schaumberg et al., 2007; Pritchard et al., 2021), and do not reflect the anatomy of *Coelurosauravus* from Madagascar. We thus provide a revised reconstruction of this taxon in dorsal view, as well as the first skeletal reconstruction of a weigeltisaurid in lateral view (Fig. 15).

According to our reconstruction, *Coelurosauravus* is a gracile reptile of ca. 180 mm in snout-vent length, and at least 320 mm in total length including the preserved portion of the tail (Fig. 15). Based on the length of the longest patagials (Table 3) and the width of the trunk preserved at this level in the Eppelton specimen (TWCMS B5937, VB, pers. obs.), this animal had a wingspan of ca. 350 mm (Fig. 15). These values differ slightly from those provided by Evans (1982), but this probably reflects differences in the reconstruction and interpretation of the patagials. *Coelurosauravus* had a dorsoventrally compressed body. Both limbs are long and lender, with large autopodia. Based on our reconstruction, the forelimb is ca. 80 mm in length, with the manus being ca. 33 mm long. The hindlimb is slightly longer, measuring ca. 90 mm with a 40 mm long pes.

Our reconstruction broadly conforms to that of Pritchard et al. (2021) for the Ellrich specimen but with some significant differences, such as in the proportions of the skull, neck and trunk, or the arrangement of the patagials. Based on direct observation of those specimens, we interpret these differences as interspecific differences between *Coelurosauravus elivensis* and *Weigeltisaurus jaekeli* (or at least the Ellrich specimen) rather than differences in interpretation.

Remarks on the Homology of Patagials

As summarized by Pritchard et al. (2021), early workers interpreted the patagials as true ribs, and consequently reconstructed the wing as derived from the dorsal half of the trunk (Carroll, 1978; Evans, 1982). The interpretation of the patagials as dermal ossification by Schaumberg (1976, 1986) and Frey et al. (1997) invalidated these reconstructions although the anchoring of the patagials, and consequently of the wing skeleton, to the rest of the body remained unknown. Based mostly on the Ellrich specimen, Pritchard et al. (2021) recently suggested that the base of the patagials was closely associated with the gastral basket, and thus emerged from the ventral half of the flanks. Our observations of MNHN.F.MAP327a confirm this interpretation and indicate a possible articulation between each patagial and the lateral-most element of each transverse gastral row (Figs. 10, 15).

The exact nature of the patagial ossifications, however, remains unclear. Based on previous works, it may be proposed that the patagials are: (1) neomorph ossifications with no known homologue; (2) intramembranous ossification from the laterally expanded myosepta of the trunk wall musculature; (3) lateral gastralia. We concur with Pritchard et al.'s (2021) assessment that these structures may be homologues of lateral gastralia. This interpretation indeed conforms best with the putative articulation between patagials and gastralia described above because similar articulations are present between adjacent gastralia in other reptiles (Claessens, 2004). Further studies are needed to confirm this hypothesis.

Paleoecology of Weigeltisaurids

Weigeltisaurids have long been considered as arboreal and gliding reptiles (Carroll, 1978; Evans, 1982; Evans and Haubold, 1987; Frey et al., 1997; Schaumberg et al., 2007; Bulanov and Sennikov, 2010; Buffa et al., 2021; Pritchard et al., 2021), an interpretation followed here. Yet, the exquisite preservation of the *Coelurosauravus* material re-described above provides an opportunity to further discuss the functional morphology of the postcranial skeleton and lifestyle of these enigmatic animals.

Inferring the function of a given structure in the fossil record and reconstructing the paleoecology of extinct organisms is notoriously difficult (e.g. Gould, 1974; Benton, 2010;

Padian and Horner, 2011; Hone and Faulkes, 2014). This is particularly true for weigeltisaurids in light of the scarcity of specimens and their phylogenetical distance to recent analogues (Buffa et al., 2021). As a result, the interpretations discussed here must remain speculative.

Figure 3-16: *Coelurosauravus elivensis* Piveteau, 1926 (Madagascar, late? Permian), life reconstruction. Individuals clinging to *Glossopteris* trunk (Glossopteris leaves are associated with *C. elivensis* in the fossil assemblage) (Left), and gliding while grasping its wing (Right). The colors are based on the extant agamid *Draco* and chamaeleonid squamates. Illustration by Charlène Letenneur (MNHN).

Arboreality—Weigelt (1930) and Huene (1930) first identified the arboreal lifestyle of weigeltisaurids by analogy with extant chamaeleonids mainly based on cranial similarities. The patagial skeleton was only recognized in later studies. As all extant gliding tetrapods are exclusively arboreal (Dudley et al., 2007; Socha et al., 2015), every study since then has accepted an obligatory arboreal life style of weigeltisaurids. However, they hardly consider the presence of non-patagial features, which are indicative of arboreality. Only Bulanov and Sennikov (2010) discuss the forelimb of *Rautiania* in the context of climbing. This is particularly surprising, as the patagium of weigeltisaurids would severely hinder terrestrial

locomotion (Bulanov and Sennikov, 2010), making weigeltisaurids some of the earliest known amniotes with an obligatory arboreal lifestyle, and among the first ones to be described from the Paleozoic in the literature.

For quadrupedal animals, locomotion in an arboreal habitat is subject to various challenges that include (1) moving up and down on inclined, vertical or overhanging surfaces, (2) bridging distances between branches, and (3) moving in a three-dimensional environment on substrates of variable width and compliance (Cartmill, 1974, 1985).

(1) Moving on inclined or vertical and often narrow and irregular surfaces requires generating traction to counteract the weight of the animal and prevent pitching in order to minimize the risk of falling (Cartmill, 1974, 1985). Traction is generated at the contact points or surfaces between animal and substrate. In medium- to large-sized quadrupeds (> 100 mm), traction is generated by interlocking the claws into the surface irregularities of the substrate (clinging), or by encircling the substrate with supporting appendages or the entire body (grasping; Cartmill, 1974, 1985; Hildebrand and Goslow, 2001; Fröbisch and Reisz, 2009). A third mechanism (adhesion), implies the generation of capillary or van der Waals forces though adhesive surfaces (Cartmill, 1985; Labonte et al., 2016). This mechanism is common in small-sized animals (< 100 mm; Fröbisch and Reisz, 2009), and is represented in larger animals by gekkotans (up to 200 g; Russell et al., 2019). In the latter, the presence of large adhesive surfaces implies prominent specializations of the autopodia such as the dorsal flexion of the penultimate phalanges, eventual reduction of other phalanges including unguals, and presence of paraphalanges (summarized in Russell and Bauer, 2008). As there is no evidence for such specializations in the large-sized weigeltisaurids (> 250 g, Evans, 1982), it seems unlikely that these reptiles clung to trees through adhesion.

As identified by Fröbisch and Reisz (2009), claw-based clinging is characterized by an elongation of the penultimate phalanges, whereas autopodial grasping is characterized by an elongation of the proximal ones. All known weigeltisaurid autopodia show conspicuous elongation of the penultimate phalanges (Figs. 3, 4, 14; Evans, 1982; Evans and Haubold, 1987; Bulanov and Sennikov, 2010; Pritchard et al., 2021), suggesting that as arboreal quadrupeds, weigeltisaurids likely used clinging to generate traction (Fig. 16). This is strongly supported by the sharp, laterally compressed and strongly recurved ungual phalanges of weigeltisaurids

(Bulanov and Sennikov, 2010; Pritchard et al., 2021), which have long been considered typical of clinging arboreal taxa (Arnold, 1998; Zani, 2000; Tulli et al., 2009; D'Amore et al., 2018). Such claws are commonly used to infer an arboreal lifestyle in extinct and extant taxa (Feduccia, 1993; Spielmann et al., 2005, 2006; Fröbisch and Reisz, 2009; Birn-Jeffrey et al., 2012; Simões et al., 2015, 2017; Jenkins et al., 2020).

Among clinging arboreal quadrupeds, pitching during arboreal locomotion is avoided by keeping the body, and thus the center of gravity, close to the substrate (Cartmill, 1974, 1985; Higham and Jayne, 2004; Lammers and Zurcher, 2011; Schmidt and Fischer, 2011). These taxa thus typically show a dorsoventrally compressed body. Such a flat body outline is seen in many extant and extinct arboreal squamates (e.g. Arnold, 1998; Simões et al., 2017) such as the gliding agamid *Draco* (Hoffstetter and Gasc, 1969) and the putative arboreal varanopid *Ascendonanus* from the Middle Permian of Germany (Spindler et al., 2018). The dorsoventrally compressed body of *Coelurosauravus* (Fig. 15) could allow for a locomotion on inclined surfaces and is thus suggestive of an arboreal lifestyle (Fig. 16).

Extant arboreal limbed squamates, further counterbalance pitching through active stiffening of the trunk (Grinham and Norman, 2020). These taxa typically exhibit an elongate preacetabular process of the ilium compared to closely related terrestrial forms (e.g. Tinius et al., 2018). This process serves as the origin of the M. quadratus lumborum (Russell and Bauer, 2008), a dorsoflexor muscle that stiffens the posterior part of the trunk and thus provides bracing against gravitational forces during arboreal or bipedal locomotion (Borsuk-Białynicka, 2008; Grinham and Norman, 2020; Paparella et al., 2020). Provided weigeltisaurids had a similar muscular arrangement, their prominent preacetabular process suggests a similar active pitching control during arboreal locomotion.

In addition, arboreal quadrupeds typically use their forelimbs to generate traction during locomotion (Arnold, 1998). In such taxa, the forelimbs approximate the hindlimbs in length. This is seen in various squamates (Arnold, 1998), including extinct taxa (Evans and Barbadillo, 1998; Simões et al., 2015, 2017), and the Permian varanopid *Ascendonanus* (Spindler et al., 2018). This morphology would provide more symmetrical attachment points anterior and posterior to the center of gravity, which would further help in keeping the body of the animal close to the substrate (Arnold, 1998; Alexander, 2013), and would increase reach to bridge gaps.

In weigeltisaurids, the forelimb is ca. 90% the length of the hindlimb, which is consistent with those taxa that use the forelimbs significantly during arboreal locomotion (Fig. 16).

Lastly, most of the propulsion is generated during the retraction phase of the hindlimb in quadrupedal climbers (Zaaf et al., 1999; Anzai et al., 2014). These taxa thus typically show a larger area of origin for the hindlimb retractor muscles than for the protractor muscles (Tinius et al., 2018). In contrast, the large preacetabular process of the ilium in weigeltisaurids could have served as a broad origin area for the hindlimb protractors, suggesting a faster and more powerful protraction during locomotion (Hutchinson, 2001; Russell and Bauer, 2008). As noted by Tinius et al. (2018), an increase in hindlimb protractor origin area could be linked to frequent controlled arboreal head-down descent in extant squamates, suggesting a similar behavior for weigeltisaurids. However, given that gliding is a rather energically cheap locomotion (e.g. Socha et al., 2015), it may have been cheaper than frequent arboreal descent. It is thus likely that the protractor muscles were involved during other movements, possibly allowing for a faster arboreal ascent, or were also active during gliding (see below).

(2) In an arboreal habitat, the substrate is discontinuous (Cartmill, 1985). To compensate such discontinuities, extant arboreal tetrapods show a variety of gap-crossing behaviors such as swinging (exclusively in graspers), jumping, gliding or flying (Cartmill, 1974, 1985; Graham and Socha, 2020). Evidently, the patagia of weigeltisaurids would have allowed them to cross large gaps by gliding similar to extant arboreal gliders (Graham and Socha, 2020). As argued by Pritchard et al. (2021), the patagia of weigeltisaurids are inserted more ventrally than in *Draco* and are thus likely attached below the center of gravity of the animal (Fig. 15). This low-wing configuration would offer maneuverability but less stability (Frey et al., 2003). However, the large wingspan of weigeltisaurids could have allowed for a dihedral position of the patagia, which would have stabilized flight and thus effectively counterbalanced this trade-off (Frey et al., 2003). Such a wing conformation would have provided both a stable long-distance flight combined with optional maneuverability when necessary.

Lastly, the tail has been identified as a key component of locomotion in arboreal habitats (Gillis and Higham, 2016). Indeed, numerous extant arboreal quadrupeds, namely reptiles, use their tail for balance while climbing (Jusufi et al., 2008; Fleming and Bateman, 2012), turning or crossing gaps (Higham et al., 2001; Larson and Stern, 2006), jumping (Gillis et al., 2009;

Kuo et al., 2012; Libby et al., 2012) or falling (Jusufi et al., 2008, 2010, 2011). In the case of *Draco*, tail stiffness is muscularly controlled and serves to direct the gliding course (John, 1971; Clark et al., 2021). The tail of weigeltisaurids is long and slender with short neural and haemal spines (Fig. 9; Evans, 1982). As argued for coelurosaurian dinosaurs, which show a similar morphology of the tail skeleton, this may indicate a reduction of the caudofemoral musculature and suggest a decoupling of the tail and hindlimb. This decoupling would allow the tail to act as a stabilizer (Persons and Currie, 2012; Persons et al., 2013; Pittman et al., 2013).

(3) There is little to no evidence to support a discussion regarding the diameter and compliance of the substrates favored by weigeltisaurids, or to assess the density of foliage or branches in the late Permian forest ecosystems where these reptiles lived. Most extant arboreal squamates have slender bodies enabling them to walk on narrow substrates and move around obstructions (Arnold, 1998). While the dorsoventrally compressed body of weigeltisaurids seems consistent with such environments, one must account for the patagia of these animals. Their large span, especially compared to *Draco*, would physically have hindered locomotion with lateral body undulations, even when folded back (Fig. 16).

Gliding—The gliding locomotion of weigeltisaurids has long been consensual (Schaumberg, 1976, 1986; Carroll, 1978; Evans, 1982; Evans and Haubold, 1987; Frey et al., 1997), and is not challenged here. However, little is known on the gliding performance of these animals. McGuire and Dudley (2011) suggested that weigeltisaurids were too big to be efficient gliders by comparison with the extant agamid *Draco*. However, the patagia of weigeltisaurids is unique in terms of shape and high aspect ratio (Fig. 15; Evans, 1982), low-wing configuration with the option for a dihedral configuration during flight (Fig. 15; Pritchard et al., 2021), and supporting structures (Schaumberg, 1976, 1986; Frey et al., 1997; Schaumberg et al., 2007; Pritchard et al., 2021). All of these factors may have increased the gliding capacity of weigeltisaurids although this cannot be ascertained without studying the aerodynamic performance of these animals.

At present, it is unclear how the wing of weigeltisaurids was extended during flight. Schaumberg et al. (2007), based on their reconstruction of the patagium very close to the forelimb, suggested a tendinous connection between the scapula and anterior-most patagial. According to that interpretation, the wing could be extended by a sharp protraction of the

forelimb and could be further stabilized by filling the lungs with air to inflate the ribcage (Schaumberg et al., 2007). While there is no basis to discuss the benefits of inspiration during gliding in the available material, it is apparent that the anterior margin of the patagium is positioned at a distance to the forelimb in MNHN.F.MAP327a, likely due to the presence of a cartilaginous sternum (Figs. 5, 6). Such a gap would have been difficult to bridge by a tendon while maintaining an efficient angle of attack. Furthermore, extension of the patagia through protraction of the forelimb is unlikely because it would cause accidental openings of the patagia during limb-based locomotion.

In *Draco*, the patagia are first extended by the contraction of the iliocostal and intercostal musculature (Colbert, 1967; John, 1970; Russell and Dijkstra, 2001) and can be further expanded by interlocking the claws in the scales on the anterior dorsal surface of the patagia (Dehling, 2017). This is permitted by the long arms of this squamate and by a postaxial abduction of the manus. As indicated by Dehling (2017), such an abduction appears possible in weigeltisaurids as well, as shown by the position of the right manus of the Ellrich specimen (Pritchard et al., 2021). Furthermore, as exemplified by *Coelurosauravus* (Fig. 15), the forelimb could likely extend across the proximal half of the leading edge of the wing. Provided our reconstruction of the digits is correct, they could reach the level of the fifth patagial, which incidentally corresponds to the first patagial without distal curvature (Fig. 15). In *Draco*, the aspect ratio of the patagia is much lower than in weigeltisaurids. Thus, the forelimb spans the entire leading edge, and grasps the almost straight first rib, forming the transverse leading edge of the wing. Based on the similarities between *Draco* and *Coelurosauravus*, we suggest that weigeltisaurids were able to grasp, extend, hold, and to a certain degree manipulate the patagia during gliding flight, even if they could not reach the distal end of the leading edge (Fig. 16).

Interestingly, weigeltisaurids have an additional phalanx in manual digit V, as reported in *Rautiania*, *Weigeltisaurus* (Bulanov and Sennikov, 2010; Pritchard et al., 2021), and now in *Coelurosauravus* (Figs. 3, 4, 15). Their manual phalangeal formula is thus 2/3/4/5/4 instead of the plesiomorphic 2/3/4/5/3 formula of amniotes (Romer, 1956). This is surprising in light of the extreme rarity of such occurrences of hyperphalangy in terrestrial amniotes (Greer, 1992; Russell and Bauer, 2008). Similar cases of hyperphalangy have been reported in a few gekkotan genera (Russell and Bauer, 1990, 2008), and a similar morphology can be attained in anurans by the addition of an intercalary bone between the penultimate and ungual phalanges (Greene,

1981; Paukstis and Brown, 1990; Manzano et al., 2007). However, in both cases, such hyperphalangy evolved in the context of an increase in adhesive surface, which is unlikely to have been the case in weigeltisaurids because of their larger size (see above).

However, the digit morphology of weigletisaurids follows the pattern known in extant tetrapods in adding a phalanx to digit V, the lateral-most digit (Greer, 1992; Fedak and Hall, 2004). This additional phalanx would increase the reach of the hand significantly in weigeltisaurids (Greer, 1992), which Bulanov and Sennikov (2010) interpreted as an adaptation to arboreal lifestyle that would have a negative effect on terrestrial locomotion.

We further suggest that the increase in reach by the lateral-most manual digit could facilitate the grasping of the leading edge of the wing and thus could have helped in controlling the expansion, tension, orientation and camber of the large patagia of weigeltisaurids. According to this interpretation, weigeltisaurids would represent the first known tetrapods to have evolved hyperphalangy in the context of aerial locomotion (Fedak and Hall, 2004).

The hindlimbs are involved during gliding in most extant gliding reptiles. They are often abducted, positioned at or slightly below the coronal plane of the animal, and bent at the knees so that the forelegs are oriented posteromedially (Emerson and Koehl, 1990; McGuire, 2003; Dehling, 2017). This posture has been proposed to increase stability (Emerson and Koehl, 1990). A similar behavior has been inferred for extinct paravians, which may have employed a biplane gliding apparatus (Longrich, 2006; Chatterjee and Templin, 2007, but see Padian and Dial, 2005; Dececchi and Larsson, 2011). As seen in MNHN.F.MAP327a, weigeltisaurids appear to have been capable of an extensive hind limb abduction (Figs. 5, 6). This is further supported by the triangular iliac blade of these animals, which would have provided a large origin area for the iliofemoral abductor muscle (Hutchinson, 2001; Russell and Bauer, 2008). The hind limbs of the *Coelurosauravus* lectotype also show a bended posture similar to that employed by extant gliders (Figs. 1, 2; Emerson and Koehl, 1990). Weigeltisaurids thus likely employed a gliding posture similar to that of the extant agamid *Draco* (Fig. 16).

Lastly, evidence from in situ forests suggests that late Pennsylvanian forests, while taxonomically and vertically heterogenous, had rather open canopy strata with spatially separated arborescent taxa resulting in little crown overlap (reviewed in DiMichele and Falcon-Lang, 2011, but see Opluštil et al., 2009, 2014). In contrast, Cisularian forests show evidence

of denser communities, suggestive of more continuous canopy strata (Gulbranson et al., 2012; Wang et al., 2012; Luthardt et al., 2016), although less dense forests also occurred (Gulbranson et al., 2012; Opluštil et al., 2021). It could thus be argued that selective pressure for an aerial locomotion in a continuous canopy was minimal prior to the Cisularian, but this assumption requires further paleoecological studies, especially with respect to canopy density and continuity. However, such change in forest structure could explain why no gliders have been reported prior to weigeltisaurids although several arboreal or scansorial amniotes have been described from Pennsylvanian and Cisularian deposits (Spindler et al., 2018; Mann et al. 2021).

Conclusion

The detailed re-description of the postcranial skeleton of all known specimens of *Coelurosauravus elivensis* reveals hitherto unknown anatomical details. *C. elivensis* has a shorter neck and longer trunk than the weigeltisaurids from Western Europe (at least the Ellrich specimen). The re-examination of the osteology of these specimens yields new information for future phylogenetic and biomechanical analyses of weigeltisaurids. Weigeltisaurids have long been considered as arboreal, mostly in relation to their assumed gliding capacities, but this has only barely been discussed with respect to the non-patagial postcranium. However, the long, gracile and dorsoventrally compressed body of weigeltisaurids, as well as their almost equally long fore- and hindlimbs with elongate autopodia strongly support a clinging arboreal lifestyle for these animals.

Additionally, we describe a fourth phalanx in the fifth manual digit of *C. elivensis*, making it the third weigeltisaurid taxon showing this apomorphy. This supernumerary phalanx has previously been interpreted as feature to increase reach during tree climbing. We further suggest that the longer reach of digit V of the weigeltisaurid manus aligned with an apparent abduction ability, would have allowed these animals to grasp the leading edge of their patagia at the midpoint of their leading edges. The extant agamid *Draco*, which controls the expansion, orientation and camber of its wing in part through such a grasp, supports this assumption. The likely derivation of the patagial spars from the gastralia basket resulting in an attachment of the

patagium below the center of gravity would have increased the maneuverability by destabilizing the flight. Stable flight could have been brought about by the dihedral angling of the patagia with the help of the arms. Thus, we suggest that weigeltisaurids were both the first known gliding tetrapods with an adjustable flight apparatus and among the first with an anatomically supported obligatory arboreal lifestyle. Furthermore, weigeltisaurid appear to represent the only known animals to have evolved hyperphalangy in the context of both climbing and gliding.

Chapter 4: Triassic chamaeleon-like reptiles support arboreal origin of pterosaurs

> At the time of writing, the present chapter is very close to submission as a research article co-authored with E. Frey (SMNK), J.-S. Steyer (MNHN), and M. Laurin (MNHN).

Abstract—The Triassic Period witnessed the diversification of most major Mesozoic and extant reptile groups, including pterosaurs, the first vertebrates capable of powered flight. Yet, Triassic ecosystems were also populated by small, poorly known sauropsids that are critical in elucidating the early evolution of Mesozoic reptiles. Here, we provide new anatomical information on several specimens of the Late Triassic Drepanosauromorpha, a group of small chameleon-like scansorial reptiles from Laurasia, and present phylogenetic analyses of Permo-Triassic diapsids based on a new morphological dataset. Our analyses recover drepanosauromorphs and pterosaurs forming the hitherto unrecognized clade A clade nov.. Clade A and Lagerpetidae are united in the clade Pterosauromorpha, which in turn forms the sister-taxon to Dinosauromorpha. The recovery of Drepanosauromorpha as Triassic archosaurs drastically reduces the ghost lineage at the base of this group and reduces the number of diapsid lineages that survived the Permo-Triassic Mass Extinction. Most importantly, drepanosauromorphs share a number of unique derived characters with pterosaurs, some of which were previously thought to have evolved in the context of powered flight. These characters are best reinterpreted as exaptations, derived from an ancestral arboreal morphology. Drepanosauromorphs thus illuminate the sequence of acquisition of character states leading to pterosaurian powered flight and support the hypothesis that pterosaurs originated from scansorial reptiles. The wide paleogeographic distribution of Clade A suggests that this group underwent a rapid radiation into the arboreal realm, paving the way for the takeoff of pterosaurs that later ruled the Mesozoic skies.

Introduction

The Triassic Period witnessed the rapid diversification of crown-group reptiles and has long been recognized as a pivotal time for the evolution of life on land (Padian, 1986; Fraser and Sues, 1997, 2010; Sues and Fraser, 2010; Chen and Benton, 2012; Benton, 2016). Archosauromorpha and their crown group Archosauria underwent an adaptive radiation during this time interval and rapidly became the dominant component of terrestrial ecosystems, with most well-known Mesozoic reptile groups such as pseudosuchians, dinosaurs and pterosaurs being highly diverse by the end of the Triassic (Brusatte et al., 2011; Sookias et al., 2012; Nesbitt et al., 2013; Ezcurra et al., 2014, 2021; Bernardi et al., 2015; Foth et al., 2016, 2021; Ezcurra and Butler, 2018). Yet, much of the early evolutionary history of these groups remains unclear due to both the completeness of the fossil record and large morphological gaps resulting from the rapid radiation of Triassic archosaurs. This is chiefly exemplified by pterosaurs, the first vertebrates capable of powered flight, whose origins remain one of the more nebulous questions in vertebrate paleontology (Benton, 1999; Hone and Benton, 2007; Witton, 2013; Baron, 2021). However, terrestrial Triassic ecosystems were also populated by enigmatic taxa, which have recently proved to be critical in elucidating the early evolutionary history of some of the major Mesozoic reptile groups (Dzik, 2003; Nesbitt et al., 2010, 2017; Langer et al., 2013; Kammerer et al. 2020; Müller and Garcia, 2020; Norman et al., 2022), and pterosaurs in particular (Ezcurra et al., 2020; Foffa et al., 2022; Kellner et al., 2022).

Drepanosauromorpha, a group of small, less than 500 mm long reptiles from the Late Triassic of Laurasia, are among the most peculiar Triassic diapsids. These bizarre reptiles combine a bird-like head, barrel shaped trunk and laterally compressed tail. Some taxa also exhibit a hooked prehensile tail and opposable digits (Renesto et al., 2010; Castiello et al., 2016; Pritchard et al., 2016; Pritchard and Nesbitt, 2017). The highly specialized anatomy of these reptiles suggests that they were efficient arboreal climbers (Calzavara et al., 1980; Renesto, 1994a, 2000; Renesto and Binelli, 2006; Castiello et al., 2016; Pritchard and Nesbitt, 2017) or scansorial hook-and-pull diggers (Renesto, 1994b; Pritchard et al., 2016; Gonçalves and Sidor, 2019; Jenkins et al., 2020), although some authors have argued in favor of a more fossorial (Pinna, 1984, 1986; Jenkins et al., 2020), aquatic (Berman and Reisz, 1992; Colbert and Olsen, 2001) or gliding (Ruben, 1998; Geist and Fedduccia, 2000) lifestyle for some taxa.

Given their unique anatomy, the phylogenetic relationships of drepanosauromorphs remain unclear. This is further exacerbated by the nature of preservation of most of the available specimens, comprising either fully articulated but badly crushed specimens or three-dimensional but isolated bones. Only very few specimens are preserved both in articulation and in three dimensions (Renesto et al., 2010; Pritchard et al., 2016; Pritchard and Nesbitt, 2017). Drepanosauromorphs were first described as lepidosauromorphs (Pinna, 1980, 1984; Berman and Reisz, 1992) before being more consistently considered as archosauromorphs (generally as 'protorosaurians'; Renesto, 1994a, 2000; Alifanov and Kurochkin, 2011), as recovered by several phylogenetic analyses (Evans, 1988; Benton and Allen, 1997; Dilkes, 1998; Rieppel et al., 2003; Renesto et al., 2010; Bennett, 2013). Some authors also suggested affinities to 'thecodont' archosauriforms (Calzavara et al., 1980), pterosaurs (Renesto and Binelli, 2006) or birds (Feduccia and Wild, 1993; Fedducia, 1996; Geist and Feduccia, 2000). However, later analyses yielded little or no support for these latter hypotheses (see Renesto et al., 2010).

Recent studies focusing on drepanosauromorph relationships consistently recover them as non-saurian diapsids (Pritchard et al., 2016; Pritchard and Nesbitt, 2017, see also Müller, 2004), possibly representing the sister-group to the late Permian weigeltisaurid gliding reptiles, forming the clade Avicephala (Merck, 2003; Senter, 2004; Pritchard et al., 2021). However, other broad-scale studies fail to recover such topologies and instead recover drepanosauromorphs as archosauromorphs (Bennett, 2020; Sobral et al., 2020; Ford et al., 2021; Griffiths et al., 2021; Martínez et al., 2021; Simões et al., 2022). Finally, the monophyly of Avicephala is still debated (Renesto and Binelli, 2006; Renesto et al., 2010), and ought to be reassessed, especially in light of recent detailed redescriptions of late Permian weigeltisaurid material (Bulanov and Sennikov, 2015a, 2015b; Buffa et al., 2021, 2022; Pritchard et al., 2021).

Here, we provide new anatomical information on several drepanosauromorphs based on direct observations, Reflectance Transformation Imaging and re-examination of published segmented Computed Tomography (CT) data, which form the base of a new morphological phylogenetic dataset designed to reassess the phylogenetic relationships of avicephalans among Permo-Triassic diapsids. We recover a topology that is markedly different from published studies in supporting archosaurian affinities for drepanosauromorphs for the first time and suggesting a close relationship between drepanosauromorphs and pterosaurs, casting light on the early evolution of flight in the latter taxa.

Methods

Material examined

We re-examined all specimens currently referred to *Megalancosaurus preonensis* (holotype MFSN 1769a, b; MPUM 6008; MPUM 8437a, b) as well as the holotype specimens of *Drepanosaurus unguicaudatus* (MCSNB 5728), *Vallesaurus cenensis* (MCSNB 4751) and *Vallesaurus zorzinensis* (MCSNB 11342) housed in the Museo "Caffi" di Scienze Naturali Bergamo, Bergamo, Italy (MCSNB) and the Museo Friulano di Scienze Naturali, Udine, Italy (MFSN). We also studied the STL models segmented from the CT data of the holotype and only known specimen of *Avicranium renestoi* (AMNH FARB 30834, courtesy A. Pritchard), housed in the American Museum of Natural History, New York, USA.

All other material studied either through first-hand observations of specimens, published segmented CT data or photographs in order to build the phylogenetic dataset are listed in Appendix 1.

Reflectance Transformation Imaging (RTI)

Most Italian drepanosauromorphs specimens are articulated but badly crushed and distorted (Fig. 1). RTI is a method that computes a single 'interactive specimen' on which the illumination can be oriented at will (Hammer et al., 2002). We use this method to compensate for the nature of preservation of the specimens using the same custom-made portable ca. 300 mm diameter automated light dome as was used in Buffa et al. (2021, 2022, an updated version of that used by Béthoux et al., 2016). Sets of 54 photographs under different LED sources were compiled using the RTIBuilder software under a Highlight Based (HSH) Filter using a black hemisphere placed close to the area of interest as an illumination reference.

We compiled RTI files of regions of interest for all specimens of *M. preonensis* and *V. cenensis* (see Supplemental Data), but did not do so for *D. unguicaudatus* to avoid damaging the specimen by placing the light dome on the surface of the very large slab. The resulting RTI files provided in the Supplementary Material can be opened using the software RTIViewer (both software packages are freely available at www.culturalheritageimaging.org).

Morphological dataset

We compiled a broad taxon and character dataset designed to reassess the phylogenetic relationships of Avicephala, the clade comprising Weigeltisauridae and Drepanosauromorpha, and possibly the enigmatic reptile *Longisquama insignis* (Senter, 2004; Pritchard et al., 2021). All sufficiently preserved avicephalans are thus included in our dataset, comprising the weigeltisaurids *Coelurosauravus elivensis*, *Rautiania* sp. and *Weigeltisaurus jaekeli*, the drepanosauromorphs *Avicranium renestoi*, *Dolabrosaurus aquatilis*, *Drepanosaurus unguicaudatus*, *Megalancosaurus preonensis* and *Vallesaurus cenensis*, as well as *Longisquama insignis*.

Given the competing hypotheses regarding the systematic position of drepanosauromorphs (summarized in Renesto et al., 2010; Pritchard and Nesbitt, 2017), our taxon sample comprises well-known representatives of non-saurian diapsids, lepidosauromorphs (including the kuehneosaurid *Icarosaurus*, sister group of drepanosauromorphs as per Müller, 2004), and archosauromorphs (including Triassic pterosaurs and lagerpetids, their sister-group as per Ezcurra et al., 2020). Furthermore, given the repeated recovery of avicephalans as early-diverging neodiapsids (Merck, 2003; Müller, 2004; Senter, 2004; Pritchard et al., 2016, 2021; Pritchard and Nesbitt, 2017), and the possible placement of both varanopids and parareptiles among early diapsids as well (Laurin and Piñeiro, 2017; Ford and Benson, 2019, 2020, see also Simões et al., 2022), we increased our taxon sample stemward to better assess character and taxon evolution at the base of the diapsid tree. We thus include two iconic anamniotic tetrapods, *Seymouria* and *Limnoscelis*, and several well-known permo-carboniferous synapsids, varanopids, parareptiles, captorhinids and ‘protorothyridids’ in our dataset (see Appendix 1 for the complete taxon list).

We compiled a list of 407 morphological characters to reflect our broad taxon sample. Our character sample comprises 303 characters taken from previous phylogenetic analyses (Schoch and Sues, 2018; Ezcurra et al., 2020; Ford and Benson, 2020; Griffiths et al., 2021; Pritchard et al., 2021; Spiekman et al., 2021; Simões et al., 2022), 90 similarly compiled characters that were modified to fit our dataset, and 14 new characters. Of the total of 407 characters, 84 multistate characters represent morphological series, whereby a given state is intermediate between the preceding and following ones. The latter were considered additive given previous studies have shown that ordering such characters gives more reliable results than

when not doing so, even if minor ordering errors are made (Rineau et al., 2015, 2018, see Appendix 2 for the complete character list). All characters are equally weighted.

Parsimony analyses

Analysis 1—Our first analysis includes all taxa and characters from our dataset with the exception of *Longisquama insignis* and *Scleromochlus taylori*. The partial skeleton of the holotype and only known skeletal specimen of *L. insignis* is indeed poorly preserved and is only superficially described (Sharov, 1970; Haubold and Buffetaut, 1987; Unwin, 2000). We thus initially exclude *L. insignis* in accordance with Pritchard et al. (2021). In contrast, *S. taylori* is known from several specimens comprising subcomplete skeletons, and has been subject to several detailed descriptions (Padian, 1984; Sereno, 1991; Benton, 1999; Bennett, 2020; Foffa et al., 2022). However, the preservation state of the material has led to contradictory interpretations of various skeletal elements such as the tarsus (Sereno, 1991; Benton, 1999; Bennett, 2020; Foffa et al., 2022). Therefore, we initially exclude this taxon as well in accordance with previous studies (Nesbitt et al., 2017; Ezcurra et al., 2020). The aim of analysis 1 is thus to assess the phylogenetic status of Avicephala sensu Pritchard et al. (2021, i.e. excluding *L. insignis*) by avoiding uncertainties stemming from highly incomplete or anatomically controversial Operational Taxonomic Units (OTUs). As a secondary objective, this analysis also aims to cast light onto the origin of Pterosauria. Analysis 1 thus employs 80 OTUs.

Analysis 2—Both *L. insignis* and *S. taylori* are included in the taxon sample of analysis 2, which is otherwise identical to analysis 1. Analysis 2 thus features 82 OTUs.

We also conducted a series of three constrained analyses (analyses C1, C2 and C3) to assess the differences in tree length, resolution and overall topology while imposing the recovery of Drepanosauromorpha among a specific portion of the diapsid tree, namely: non-saurian Neodiapsida for analysis C1 (which could recover Avicephala), non-archosauriform Archosauromorpha crownward to the late Permian *Protorosaurus* (i.e. Triassic archosauromorphs) for analysis C2, and non-archosaurian Archosauriformes for analysis C3. To this aim, we employ simplified trees as backbone topologies:

C1 = (*Petrolacosaurus kansensis*, (*Drepanosaurus unguicaudatus*, (*Clevosaurus hudsoni*, *Protorosaurus speneri*, *Euparkeria capensis*)))

C2 = (*Petrolacosaurus kansensis*, (*Protorosaurus speneri*, (*Drepanosaurus unguicaudatus*, (*Euparkeria capensis*, *Eoraptor lunensis*))))

C3 = (*Petrolacosaurus kansensis*, (*Mesosuchus browni*, *Prolacerta broomi*, (*Drepanosaurus unguicaudatus*, (*Batrachotomus kupferzellensis*, *Eoraptor lunensis*))))

All analyses were conducted in PAUP* v4.0a (Swofford, 2003) under maximum parsimony. We employ a heuristic search algorithm with 1000 random additional sequence replicates and a Tree Bisection and Reconnection (TBR) branch swapping algorithm (reconnection limit = 8). Branches are collapsed if they lack transformations under all optimizations (i.e. maximum length = 0). We quantified branch support through Bremer support values and a Bootstrap resampling analysis with 1000 replicated heuristic searches, themselves with 10 random additional sequence replicates. *Seymouria* was designated as the outgroup.

Systematic paleontology

Archosauria Cope, 1869 [Gauthier and Padian, 2020]

Pterosauromorpha Kuhn-Schnyder and Rieber, 1986 [Andres and Padian, 2020]

Clade A clade nov. [this study]

Definition—The least inclusive clade containing *Megalancosaurus preonensis* Calzavara, Muschio and Wild, 1980 and *Pterodactylus antiquus* (Sömmerring 1812) but not *Lagerpeton chanarensis* Romer, 1971.

Diagnosis—Numbers represent character states recovered as unambiguous synapomorphies (see Appendices 2, 5): Basipterygoid process of parabasisphenoid long, with hemispherical articular facets (162:1); cervical centrum extends markedly beyond posterior margin of postzygapophysis (226:1); cervical centrum tapering posteriorly, anterior surface

much wider than posterior one (227:1); cervical neural arch substantially broader than centrum (232:1); cervical prezygapophyses with subvertical articular surfaces (234:1); three sacral vertebrae (266:1); glenoid fossa mainly lateral, facing more laterally than posteriorly and without posteriorly prominent supraglenoid lip in lateral view (291:0); capitellum and trochlea strongly developed as distinct ball-shaped structures (313:0); preacetabular process of iliac blade anteroposteriorly long and extending beyond anterior margin of pubic peduncle (349:3); iliac supra-acetabular buttress absent (352:0); pubic apron absent (353:0); penultimate phalanges of pes significantly longer than preceding phalanges or metacarpals (405:1); pedal unguals with well-developed ventral tubercle (407:1).

Remarks specific to the present manuscript—The main result of this study is the recovery of a hitherto unrecognized clade (Clade A here) uniting drepanosauromorphs and pterosaurs among ornithodiran archosaurs. However, we refrain from naming this clade here to avoid confusion regarding priority and taxonomic authority. In the meantime, we will use only the vernacular term ‘acrobatosaurs’ to describe the representatives of Clade A.

Comparative anatomy

The unique morphology of drepanosauromorphs can be almost entirely reconstructed based on the subcomplete or complete specimens from Italy and North America. Our detailed re-examination of this material led to emended interpretations of anatomical details of several specimens (see rationale details in Appendix 3), which have significant implications of the phylogenetic position of drepanosauromorphs and unexpected implications for the origins of pterosaurs.

The drepanosauromorph skull is known from *A. renestoi* (New Mexico, USA) and *M. preonensis* and *V. cenensis* (Italy; Fig. 1). Their dermal skull anatomy conforms exceedingly well to that of archosauromorphs in showing a distinct subnarial process of the premaxilla, a concave posterior margin of the ascending process of the maxilla, and a long anterior process of the jugal excluding the maxilla from the orbit. All these characters have already been recognized as diagnostic for archosauromorphs (Appendix 3). In addition, *M. preonensis* lacks

an antorbital fenestra (Fig. 1b, i), a long-held synapomorphy of archosauriforms (Benton, 1985; Gauthier et al., 1988; Juul, 1994), and *V. cenensis* has a pineal foramen (Fig. 1d), which is considered absent in all archosaurs and most non-proterosuchid archosauriforms (Nesbitt, 2011). Both character states thus suggest that drepanosauromorphs are not archosauriforms.

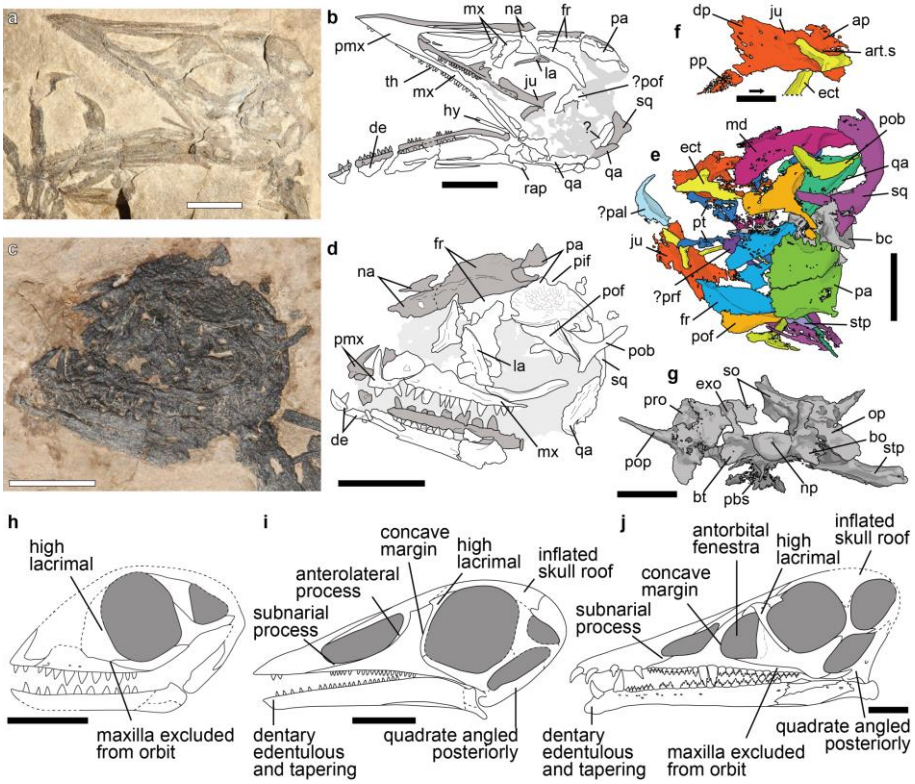

Figure 4-1: Cranial anatomy of the drepanosauromorphs *Megalancosaurus preonensis*, *Vallesaurus cenensis* (Norian, Italy) and *Avicranium renestoi* (Norian, New Mexico, USA), and the pterosaur *Eudimorphodon ranzii* (Norian, Italy). **a**, **b**, *M. preonensis*, photograph and interpretive drawing of subcomplete skull of holotype MFSN 1769b in left lateral view. **c**, **d**, *V. cenensis*, photograph and interpretive drawing of subcomplete skull of holotype MCSNB 4751 in left lateral view. **e**-**g**, *A renestoi*, surface models of holotype AMNH FARB 3083, interpretive drawing of skull in dorsal view (**e**), left jugal in medial view (**f**), subcomplete braincase in posterior view (**g**). **h**-**j**, skull reconstructions of *V. cenensis* (modified from Renesto and Binelli, 2006) (**h**), *M. preonensis* (modified from Renesto and Dalla Vecchia, 2005) (**i**), and *E. ranzii* (redrawn from Wild, 1979) (**j**) in left lateral view. Arrow indicates anterior direction. **ap**, anterior process; **art.s**, articular surface; **bc**, braincase; **bo**, basioccipital; **bt**, basal tuberosities; **de**, dentary; **dp**, dorsal process; **ect**, ectopterygoid; **exo**, exoccipital; **fr**, frontal; **hy**, hyoid; **ju**, jugal; **la**, lacrimal; **md**, postdentary complex of mandible; **mx**, maxilla; **na**, nasal; **np**, notochordal pit; **op**, opisthotic; **pa**, parietal; **pal**, palatine; **pbs**, parabasisphenoid; **pif**, pineal foramen; **pmx**, premaxilla; **pob**, postorbital; **pof**, postfrontal; **pop**, paroccipital process; **pp**, posterior process; **prf**, prefrontal; **pro**, prootic; **pt**, pterygoid; **qa**, quadrate; **rap**, retroarticular process; **so**, supraoccipital; **sq**, squamosal; **stp**, stapes; **th**, teeth. Scale bars, 5 mm (**a**-**d**, **f**-**i**), 10 mm (**e**, **j**).

However, drepanosauromorphs (at least *M. preonensis*) have a very high skull, a laterally exposed nasal with an anterolateral process, and a high lacrimal forming most of the anterior orbital margin (Fig. 1h, i). This combination of characters is only known in Permo-Triassic archosaurs (Nesbitt, 2011; Ezcurra, 2016). In addition, as previously noted (Renesto, 2000; Renesto and Dalla Vecchia, 2005; Pritchard and Nesbitt, 2017), drepanosauromorphs show a strongly inflated parietal skull roof and a posterodorsally inclined quadrate (Fig. 1h, i), a combination of characters unique to pterosaurs among Permo-Triassic diapsids (Fig. 1j; Dalla Vecchia, 2013, 2014). Lastly, the lack of posterior emargination in the quadrate of drepanosauromorphs, which is otherwise prevalent in saurian diapsids (Laurin, 1991; Evans, 2016; Sobral and Müller, 2016), has been used to suggest a very stemward position for this group (Pritchard and Nesbitt, 2017; Pritchard et al., 2021). However, the quadrates of *M. preonensis* and *V. cenensis* (and possibly *A. renestoi*, Fig. 1e, see Appendix 3) are very similar to those of Triassic pterosaurs in shape and orientation (Prondvai and Ősi, 2011; Dalla Vecchia, 2014), indicating that the straight posterior margin of the quadrate of drepanosauromorphs could also result from the strong posterodorsal inclination of the bone linked with an inflated skull roof.

The only known drepanosauromorph braincase is that of *A. renestoi* from New Mexico (Fig. 1g), which exhibits several characters interpreted as plesiomorphies by Pritchard and Nesbitt (2017). We concur with Pritchard and Nesbitt (2017) that the paroccipital process of the opisthotic of *A. renestoi* does not reach the squamosal nor the quadrate laterally and that the stapes of this taxon is the most robust of any Triassic diapsid (Fig. 1g). Both morphologies are unknown in saurian diapsids but present in some non-saurian diapsids (Carroll, 1981; Currie, 1981; Reisz, 1981). However, based on our examination of this specimen, we suspect that it is morphologically immature (Appendix 3). This suggests that some of the other plesiomorphies proposed by Pritchard and Nesbitt (2017), namely the short basal tuberosities of the basioccipital and deep notochordal pit on the occipital condyle, may instead result from incomplete ossification. If our interpretation is correct, *A. renestoi* is more plausibly interpreted as a crown-reptile, contrary to previous suggestions. Lastly, as was noted by Pritchard and Nesbitt (2017), the braincase of *A. renestoi* is verticalized (Fig. 1g), a feature otherwise only reported in allokotosaurs and archosauriforms (Gower and Sennikov, 1996; Nesbitt, 2011; Ezcurra, 2016).

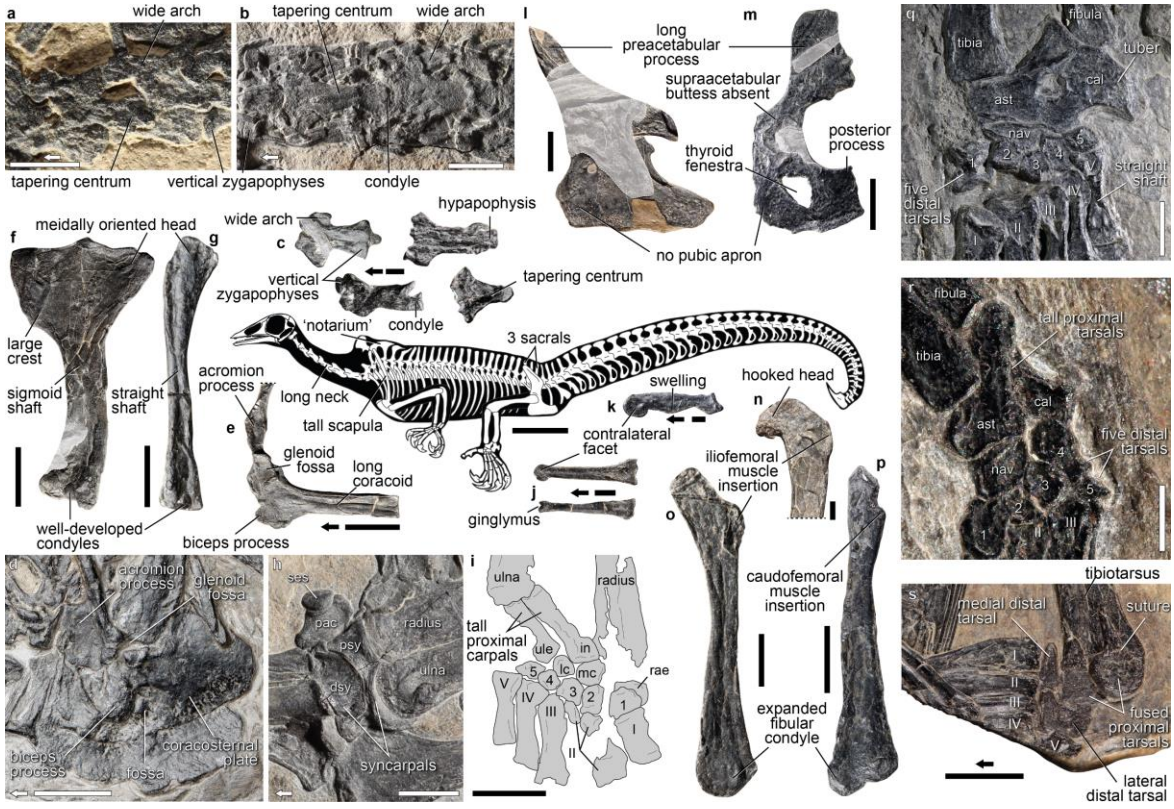

Figure 4-2: Postcranial anatomy of the drepanosauromorphs *Drepanosaurus unguicaudatus*, *Megalancosaurus preonensis*, *Vallesaurus cenensis*, and *Vallesaurus zorzinensis* and the pterosaurs *Eudimorphodon ranzii* and *Peteinosaurus zambelli* (Norian, Italy). a, *V. cenensis*, holotype MCSNB 4751, axis and first cervical in ventral view. **b**, *E. ranzii*, holotype MCSNB 2888, cervicals 3 and 4 in ventral view. **c**, *M. preonensis*, MPUM 6008, cervicals 1-4 (numbered from first preserved) in dorsal (top left), ventrolateral (bottom left, reversed) and ventral (top and bottom right) view. **d**, pectoral girdle of same in left lateral view. **e**, *E. ranzii*, holotype MCSNB 2888, left scapulocoracoid in lateral view. **f**, right humerus of same in ventral view. **g**, *M. preonensis*, MPUM 6008, left humerus in anterodorsal view. **h**, *E. ranzii*, holotype MCSNB 2888, left carpus in dorsal view. **i**, *M. preonensis*, MPUM 8473a, left carpus in ventral view. **j**, *E. ranzii*, holotype MCSNB 2888, manual penultimate phalanges, left digit III in left lateral view (top), right digit I in dorsal view (bottom). **k**, *D. unguicaudatus*, holotype MCSNB 5728, manual penultimate phalanx of left digit IV in left lateral view. **l**, *P. zambelli*, MCSNB 3496, partially disarticulated pelvis in left lateral view. **m**, *D. unguicaudatus*, holotype MCSNB 5728, right pelvis in lateral view (reversed). **n**, *P. zambelli*, MCSNB 3496, proximal portion of left femur in anterolateral view. **o**, *V. zorzinensis*, holotype MCNSB 11342, left femur in posterior view. **p**, *D. unguicaudatus*, holotype MCSNB 5728, right femur in anterior view. **q**, left tarsus of same in dorsal view. **r**, *M. preonensis*, MPUM 8473a, left tarsus in mostly dorsal view. **s**, *P. zambelli*, MCSNB 3496, right tarsus in dorsal view (reversed). Skeletal reconstruction of *Megalancosaurus* modified from Castiello et al. (2016). Arrows indicates anterior direction. **ast**, astragalus, **cal**, calcaneus, **dsy**, distal syncarpal, **in**, intermedium, **lc**, lateral centrale, **mc**, medial centrale, **nav**, navicular, **pac**, preaxial carpal, **psy**, proximal syncarpal, **ses**, sesamoid, **ule**, ulnare. Arabic numbers describe distal carpals/tarsals, roman numbers describe metapodials. Scale bars, 2 mm (**a**, **c**, **i-k**, **n**, **o**, **r**), 5 mm (**b**, **d**, **i**, **h**, **l**, **q**, **s**), 10 mm (**e**, **f**, **m**, **p**), 20 mm (reconstruction).

No drepanosauromorph mandible is sufficiently preserved to address the presence of an external mandibular fenestra (Fig. 1, see Appendix 3), a diagnostic character of archosauriforms and their immediate sister-group (Pinheiro et al., 2016, 2020). However, the lower jaw of *M. preonensis* lacks a distinct coronoid bone (see Appendix 3), a condition that occurs in a few Triassic archosauromorphs (Spiekman et al., 2021) but is more frequent in archosaurs (Bona et al., 2022). Lastly, all drepanosauromorphs lack teeth in the anterior portion of the dentary as is the case in some allokotosaurs and pterosauromorphs (Fig. 1h-j; Sues, 2003; Spielmann et al., 2008; Ezcurra et al., 2020).

Previous studies have noted that the procoelous and heterocoelous cervical vertebrae of drepanosauromorphs share a number of additional unique similarities with those of Triassic pterosaurs (Fig. 2a-c, Appendix 3; Dalla Vecchia and Cau, 2015). The dorsal vertebrae bear very high neural spines with the anterior ones fusing into a notarium-like structure reminiscent of that of some birds and pterodactyloid pterosaurs (Fig. 2; Aires et al., 2021, 2022). There is no trace of a notochordal canal nor of intercentra throughout the presacral column as is typical in archosauromorphs (Ezcurra, 2016), nor of gastralia, which are only absent in a few Triassic archosaur taxa (Nesbitt, 2011). The sacrum comprises three sacral vertebrae in all drepanosauromorphs where this region is known (Fig. 2; see Appendix 3). This is also the case in weigeltisaurids (Bulanov and Sennikov, 2010; Buffa et al., 2022) and several Triassic archosaurs (Nesbitt, 2011). Lastly, the laterally compressed tail of drepanosauromorphs is autapomorphic, most notably in the terminal tail hook of drepanosaurids, which is unknown in any other reptile (Fig. 2; Renesto et al., 2010).

The scapulocoracoid of all drepanosauromorphs shows an extremely high scapular blade framed anteriorly by a marked and dorsally positioned acromion process (Fig. 2d). That of *M. preonensis* shows a marked tuberosity for the biceps musculature on the coracoid (Appendix 3). These features are exclusively present in archosaurs among Triassic diapsids (Nesbitt, 2011; Ezcurra, 2016). An ossified sternum is distinctly present in *M. preonensis* (Fig. 2d) and other drepanosaurids (Harris and Downs, 2002), as is also the case in non-saurian diapsids (Carroll, 1975; Currie, 1981) and some archosaurs (pterosaurs, dinosaurs; Bradley et al., 2019).

The humeral heads of drepanosauromorphs are set at a low angle to each other and the bone lacks an entepicondylar foramen, as is typical in archosauromorphs (Ezcurra, 2016). The

humeral head is medially expanded and asymmetric at least in *M. preonensis* (Fig. 2g), similar to proterochampsians and archosaurs (Ezcurra, 2016). The capitellum and trochlea are highly developed and form rounded condyles, as in early diapsids and pterosaurs (Fig. 2f, g; Reisz, 1981; Dalla Vecchia, 2014; Buffa et al., 2022). Whereas *V. cenensis* retains the plesiomorphic manual phalangeal formula of 2-3-4-5-3, all other drepanosauromorphs show reduced manual digits (e.g. 2-2-2-3-3 for *M. preonensis*, ?2-2-2-2-2 for *D. unguicaudatus*; Renesto et al., 2010), which is reminiscent of the reduction of digit V in ornithodirans and IV and V in dinosaurs (Barta et al., 2018). Lastly, the distal phalanges of drepanosauromorphs are similar to those of pterosaurs in the presence of large rounded contralateral facets forming a distal ginglymus (Fig. 2j, k; see also Dalla Vecchia and Cau, 2015).

All drepanosauromorphs have a high, anterodorsally expanded iliac blade reminiscent of the anterior expansion common in archosauromorphs, especially in archosaurs (Nesbitt, 2011; Pritchard and Sues, 2019). At least in *D. unguicaudatus*, the pelvic girdle shows paired thyroid fenestrae contrary to the median thyroid fenestra of early saurians and the continuous puboischiatic plate of archosaurs (Fig. 2m; Nesbitt, 2011; Pritchard and Sues, 2019). No drepanosauromorph shows any trace of a pubic apron, which is typically present in azhendohsaurids and archosauriforms (Ezcurra, 2016) except pterosaurs (Wellnhofer, 1978). *V. cenensis* and *V. zorzinensis* both show a marked trochanteric insertion area for the iliofemoral musculature, reminiscent of the anterior trochanter of archosaurs (Fig. 2n, o; Appendix 2; Hutchinson, 2001a). Given this interpretation, it is possible that the trochanter, which is visible in *D. unguicaudatus* and *M. preonensis* (Fig. 2p) is homologous to the archosauriform fourth trochanter rather than to the plesiomorphic internal trochanter, although this remains equivocal (Appendix 3).

The tarsus of *D. unguicaudatus* and *M. preonensis* show a distinct distal tarsal 5 and a straight metatarsal V (Fig. 2q, r), which are considered fused in all saurians, forming a hook-shaped metatarsal (Joyce et al., 2013; Diaz and Trainor, 2015; Borsuk-Białynicka, 2018). All Italian drepanosauromorphs have a distinct navicular, which articulated with the tibia, a condition typical of non-archosauriform archosauromorphs (Gower, 1996). Proximally, the calcaneus of *D. unguicaudatus*, *Do. aquatilis*, and *M. preonensis* exhibit a robust calcaneal tuber, a typical feature of archosauromorphs (Fig. 2q; Benton, 1985; Nesbitt, 2011). This tuber also has a strongly concave ventral margin as in allokotosaurians and several archosauriforms (Ezcurra, 2016). Lastly, the pedal ungual phalanges of all drepanosauromorphs have strong

ventral flexor tubers, similar to allokotosaurians and Triassic pterosaurs (Spielmann et al., 2008; Dalla Vecchia, 2014; Nesbitt et al., 2015).

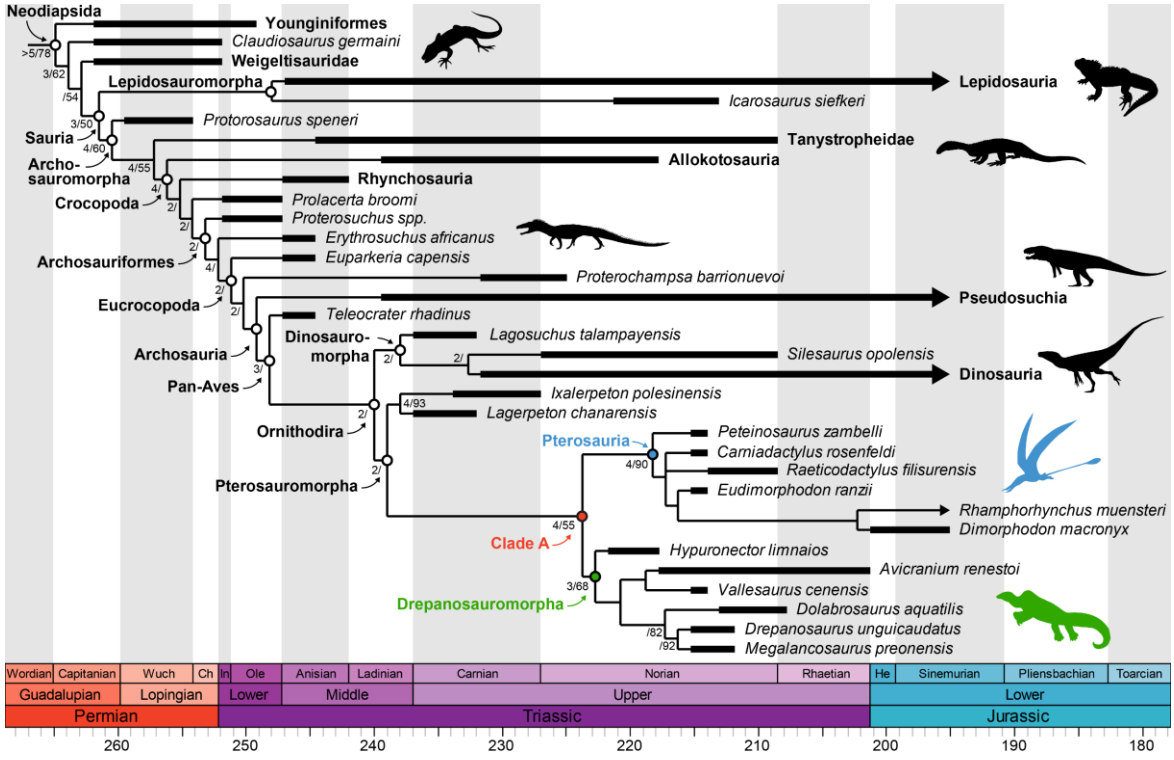

Figure 4-3: Time-calibrated simplified strict consensus tree (4 MPTs; L = 2700 steps; CI = 0.1965; RI = 0.6181) of Analysis 1 focused on Neodiapsida. Node label: Bremer value (when > 1)/Bootstrap (when > 50%). Black bars indicate stratigraphic distribution of taxa (ages given in Supplementary Material). Internal branch length minimally 1 Ma for clarity. Silhouettes (top to bottom, *Youngina*, *Sphenodon*, *Prolacerta*, *Proterosuchus*, *Postosuchus*, *Herrerasaurus*, *Rhamphorhynchus*, *Drepanosaurus*) from PhyloPic database (public domain). **Ch**, Changhsingian; **He**, Hettangian; **In**, Induan; **Ole**, Olenekian; **Wuch**, Wuchiapingian.

Discussion

Phylogenetic analyses

Our phylogenetic analyses recover a topology that is broadly congruent with most recent studies (Ezcurra et al., 2020; Ford and Benson, 2020; Pritchard et al., 2021; Spiekman et al., 2021) regarding amniotes and Permo-Triassic diapsids (Fig. 3, presented in detail in Appendices 4, 5). However, we recover drepanosauromorphs and pterosaurs as sister-groups among ornithodirans, forming the previously unrecognized clade Clade A clade nov. Clade A, together with Lagerpetidae, form the clade Pterosauromorpha, the sister-taxon to Dinosauromorpha. When the enigmatic taxon *S. taylori* is included (Analysis 2), it is recovered

as the sister-taxon to all other pterosauromorphs (see Appendix 4), as in recent studies (Ezcurra et al., 2020, discussed in Foffa et al., 2022).

However, drepanosauromorphs lack an antorbital fenestra, a hallmark of archosaurian reptiles (Fig. 1; Witmer, 1997; Pinheiro et al., 2016, 2020) and share a series of anatomical characters that have been considered plesiomorphic for all crown-group reptiles, notably in the braincase (discussed in Appendix 3) and the tarsus. Indeed, at least in the late-diverging *D. unguicaudatus* and *M. preonensis*, the tarsus has a complete series of five distal tarsals (Fig. 2q, r). In contrast, all crown-group diapsids, including the earliest representatives from the late Permian (Gottmann-Quesada and Sander, 2009) have a hooked fifth metatarsal, likely resulting from the fusion of the latter to distal tarsal 5 (Joyce et al., 2013; Diaz and Trainor, 2015; Borsuk-Białynicka, 2018). Thus, the occurrence of this morphology in Late Triassic diapsids is highly problematic. Moreover, eucrocopodan archosauriforms typically have dorsoventrally compressed proximal tarsals that share a concavoconvex articulation, and no distinct navicular bone (Sereno, 1991; Nesbitt, 2011; Ezcurra, 2016), contrary to the condition in drepanosauromorphs (Fig. 2q, r). The morphology of the proximal tarsals thus appears problematic if drepanosauromorphs are considered archosaurian reptiles.

While archosaurian phylogeny has historically relied heavily upon the evolution of the tarsus (summarized in Sereno, 1991), it has also been noted that it characterizes the evolution of the group in a context of cursorial terrestrial locomotion (Bennett, 1996, 2013, 2020). Our understanding of early archosaurian evolutionary history is thus at least partially shaped by the need for effective and stable terrestrial locomotion. Such locomotion can be considered mostly bidimensional, whereby the weight of the animal, the propulsion force exerted during locomotion, and the ground reaction force are transferred vertically into the ground through the limbs (Carrano, 1998; Hildebrand and Goslow, 2001). In contrast, in an arboreal habitat, where locomotion occurs in a three-dimensional space, forces must be exerted to the substrate in many directions (Cartmill, 1985; Preuschoft, 2002). As a result, animals typically show an increase in limb mobility (Hildebrand and Goslow, 2001; Higham and Jayne, 2004; Fischer et al., 2010). It would thus be expected that the selective pressures exerted on an arboreal archosaur would differ from that of cursorial taxa.

The lack of extant or extinct quadrupedal (i.e. non-flying) arboreal ornithodirans precludes a direct comparison between drepanosauromorphs and other bird-line archosaurs.

However, as seen in chameleons (arguably the best analogues for most drepanosauromorphs; Renesto, 1994a, 2000), a fully arboreal locomotion can have an impact on mesopodial morphology. Chameleons indeed possess tarsal elements that fail to ossify ancestrally in Sauria, such as distal tarsal 5, and exhibit discrete proximal tarsals, which are ancestrally fused in chamaeleonids (Diaz and Trainor, 2015). Incidentally, this would also be the case for drepanosauromorphs if they are considered archosaurs. The peculiar tarsal morphology of chameleons has been attributed to changes in selective pressure due to an increased diversity of force vectors acting on the autopod (Diaz and Trainor, 2015). Similar changes have also been reported for small arboreal mammals, such as the silky anteater *Cyclopes* (Wood Jones, 1953), which is often considered a good analogue for *Drepanosaurus* (Renesto, 1994b; Pritchard et al., 2016). Provided drepanosauromorphs are archosaurs, it is thus possible that their peculiar tarsus is not plesiomorphic but apomorphic. Further supporting this point, constrained phylogenetic analyses require 5 additional steps to recover drepanosauromorphs among non-saurian diapsids, 6 steps to recover them as non-archosauriform archosauromorphs, and 8 steps to recover them as non-archosaurian archosauriforms (Appendix 4). It is thus more parsimonious the refer Drepanosauromorphs to pterosauromorph archosaurs, forming the new clade Clade A together with pterosaurs (Fig. 3).

Evolutionary implications

The implications of this new phylogenetic position of drepanosauromorphs are twofold. First, because we do not recover an avicephalan clade grouping drepanosauromorphs and weigeltisaurids at the base of the diapsid tree, there is little evidence of stem-saurian diapsids surviving into the Late Triassic (see Appendix 4 for a discussion on *L. insignis*). As a consequence, the number of diapsid lineages surviving the Permo-Triassic Mass Extinction is reduced from three to two (Fig. 3) comprising Younginiformes (here recovered monophyletic, Fig. 3; Harris and Carroll, 1977; Ketchum and Barrett, 2004) and Sauria (Ezcurra et al., 2014). In addition, the position of drepanosauromorphs among other Late Triassic archosaurs drastically reduces the ghost lineage at the base of the group (Fig. 3), which would have extended at least to Late Permian if they were to be considered non-saurian diapsids, and to the Early Permian if they were recovered in a basal position among this group (see Senter, 2004; Pritchard and Nesbitt, 2017; Pritchard et al., 2021).

Second, drepanosauromorphs provide new information regarding the origin of pterosaurs. These reptiles are best-preserved in the Calcare di Zorino and Dolomia di Forni Formations, which are considered late middle Norian to late Norian in age (ca. 215 Ma, Alaunian 3-Sevatian 1, See Appendix 1). Incidentally, these formations also yielded the oldest known undisputed pterosaurs (Dalla Vecchia, 2006, 2013, 2014; Renesto, 2006; Barrett et al., 2008) Older North American drepanosauromorph remains, namely *H. limnaios* from the Ewin Creek and Nursery Members of the Lockatong Formation of New Jersey or isolated remains from the *Placerias* Quarry of the Bluewater Creek Formation of Arizona have been considered of late Carnian age (Renesto et al., 2009). However, the occurrences of *H. limnaios* are now estimated as late Lacian (late early Norian) through eccentricity cycles (ca. 221 Ma, Kent et al., 2017), and the *Placerias* Quarry is now also well-constrained as late Lacian by U-Pb geochronology (ca. 219 Ma, Ramezani et al., 2014). Thus, the oldest drepanosauromorphs are late early Norian in age, predating the earliest pterosaurs by about 5 million years (Fig. 3). Given the first lagerpetids (both stratigraphically and phylogenetically) date back to the Ladinian-early Carnian (see Appendix 1; Ezcurra et al., 2017; Müller et al., 2018; Kammerer et al., 2020), the ghost lineage separating ‘acrobatosaurs’ and lagerpetids is reduced to at least ca. 13 Ma. However, it remains unclear whether ‘acrobatosaurs’ originated in Laurasia or Gondwana. Nevertheless, the occurrences of drepanosauromorphs indicate that ‘acrobatosaurs’ were already widespread throughout western Laurasia in the late Alaunian (late early Norian), foreshadowing the Pangean distribution achieved by pterosaurs in the late Norian (Jenkins et al., 2001; Dalla Vecchia, 2013; Martínez et al., 2022).

Arboreal origin of Pterosauria

Most non-archosaurian archosauriforms as well as the first crocodile- and bird-line archosaurs are considered as terrestrial quadrupeds, while more crownward Triassic ornithodirans are cursorial bipeds (Kubo and Kubo, 2012; Grinham et al., 2019; Pintore et al., 2021). Interestingly, lagerpetids have recently been considered scansorial based on the strong curvature of their manual claws (Ezcurra et al., 2020, although not *S. taylori*, see Foffa et al. 2022). Moreover, an arboreal origin of pterosaurs has often been proposed (Wild, 1984; Unwin, 1988; Bennett, 1997, although see Padian, 1983, 1984, 1985 for a terrestrial hypothesis), and that most authors agree early pterosaurs were competent, if not habitual, climbers (Clark et al.,

1998; Witton, 2013, 2015; Mazin and Pouech, 2020). In this context, the intermediate systematic position of drepanosauromorphs (Fig. 3), whose arboreal or scansorial habits have been repeatedly noted (Calzavara et al., 1980; Renesto, 1994a, 2000; Renesto and Binelli, 2006; Castiello et al., 2016; Pritchard and Nesbitt, 2017), casts light onto the diversification of 'acrobatosaurs' in an arboreal habitat prior to the evolution of powered flight in pterosaurs.

A number of characters considered unique to pterosaurs, some of which are thought to have been acquired in the context of the acquisition of powered flight, are already present in drepanosauromorphs. All 'acrobatosaurs' have a high skull with large orbits and an inflated parietal region (Fig. 1; Pritchard and Nesbitt, 2017). Both features have been correlated to an increased brain capacity linked to three-dimensional vision in pterosaurs and birds and interpreted as adaptations to locomotion in a three-dimensional environment, either in tree crowns or through the air (Sustaita et al., 2013; Witmer et al., 2003). Apart from 'acrobatosaurs', no other Triassic saurian shows such drastic adaptations (Pritchard and Nesbitt, 2017). 'Acrobatosaurs' share numerous unique derived characters on the cervical vertebrae including a long heterocoelous centrum extending posterior to a very robust neural arch that bears vertically oriented zygapophyses (Fig. 2a-c; Dalla Vecchia and Cau, 2015). This morphology likely reduced lateral movement of the neck, which prevented torsion by a zygapophyseal lock while retaining the capacity for raising and lowering the head, which has been considered as an adaptation to an arboreal habitat (Renesto, 2000; Renesto and Fraser, 2003). Additionally, Dalla Vecchia and Cau (2015) report on possible pneumatic foramina in isolated cervical vertebrae of drepanosauromorphs, which resemble the pneumatic foramina found in Triassic pterosaurs (Butler et al., 2009). If this interpretation is correct, it provides evidence that pneumaticity, a prerequisite for powered flight, was already present in the common ancestor to all 'acrobatosaurs'.

Given the modifications of the forelimb of pterosaurs with respect to powered flight, only few comparisons can be made with the drepanosauromorph forelimb, especially with respect to the carpus (Fig. 2h, i). Yet, the presence of an ossified sternum and closely articulating or fused clavicles at least in *D. ungicaudatus* and *M. preonensis* (Fig. 2d, see Appendix 3) conforms with the idea that these elements (as well as the interclavicle) fuse to form the large sternal plate of pterosaurs (Wild, 1993). While further studies are needed to understand the role of the sternum in drepanosauromorphs, it likely provided a large origin area for the pectoral adductor musculature and allowed for powerful and rapid adduction of the

humerus (Castiello et al., 2016). Thus, it appears likely that the use of reinforced pectoral adductors in locomotion was already present in ‘acrobatosaurs’ prior to the evolution of powered flight in pterosaurs. In addition, ‘acrobatosaurs’ are the only Triassic archosauromorphs with well-ossified and distinct capitellum and trochlea on the humerus for the articulation with the lower arm bones (Fig. 2; Pritchard et al., 2016). This suggests that the strong elbow joint of pterosaurs first appeared in the context of an arboreal rather than aerial locomotion.

‘Acrobatosaurs’ are the only Triassic archosaurs without a pubic apron (Fig. 2), and this has been considered a reversal to the plesiomorphic diapsid condition in pterosaurs (Nesbitt, 2011; Ezcurra, 2016). As a result, ‘acrobatosaurs’ likely had a flatter body surface and lower attachment angle of the femoral adductors with respect to the horizontal plane, contrary to all other archosaurs (Hutchinson, 2001a, b). In addition, all ‘acrobatosaurs’ lack a supraacetabular buttress (Fig. 2m, n), which would allow for the abduction of the femur above the horizontal plane (Unwin, 1988; Bennett, 1997; Chatterjee and Templin, 2004; although see Padian, 1983). The pelvis construction of ‘acrobatosaurs’ thus allows for the wide range of femoral mobility required for climbing. Provided our identification of an ‘anterior trochanter-like’ muscle insertion in *V. cenensis* and *V. zorzinensis* is correct (Fig. 2o), all ‘acrobatosaurs’ share a sharp, proximally positioned insertion for the abductor iliofemoral musculature (Hutchinson, 2001a), which complements our interpretation of the pelvis regarding femoral abduction. Lastly, the manus and pes of all ‘acrobatosaurs’ have long penultimate and sharp ungual phalanges bearing a prominent flexor tubercle. This conjunction of characters, which is absent in most Permo-Triassic archosauromorphs,is also present in Triassic pterosaurs (Dalla Vecchia, 2014). These features have been considered an arboreal adaptation in amniotes (Zani, 2000; Fröbisch and Reisz, 2009; Tulli et l., 2009; Birn-Jeffrey et al., 2012; Simões et al., 2017; D’Amore et al., 2018), further supporting the arboreal origin of pterosaurs.

Given most characters shared by drepanosauromorphs and pterosaurs appear linked to arboreality, it could be argued that the clade Clade A reflects convergence for an arboreal lifestyle in drepanosauromorphs and pterosaurs rather than a close phylogenetic relationship. However, we argue that the large number of diagnostic characters for ‘acrobatosaurs’ such as modifications of the skull, axial skeleton and pectoral girdle (Figs. 1, 2), the high branch support values recovered in our phylogenetic analysis (Fig. 3), as well as a congruence in the stratigraphic and paleogeographic occurrences of both taxa strongly suggest that

drepanosauromorphs and pterosaurs are sister taxa forming the clade Clade A. In this context, it appears plausible that some characters previously thought to have appeared in conjunction with powered flight in pterosaurs are best reinterpreted as exaptations, derived from an ancestral arboreal or scansorial adaptation. Clade A thus represent the first archosaurs to specialize for an arboreal lifestyle, with trilophosaurid archosauromorphs being the only other Triassic taxa showing arboreal adaptations (Spielmann et al., 2005, 2006). It could further be argued that 'acrobatosaurs' represent the first adaptative radiation of archosauromorphs in the arboreal habitat, although further quantitative studies are needed to confirm this hypothesis.

'Proto-pterosaur' perspectives

Drepanosauromorphs form with pterosaurs the new clade Clade A, and demonstrate that the early evolution of pterosaur-line archosaurs was much more complex than previously suggested. Numerous anatomical characters previously thought to have appeared in conjunction with powered flight in pterosaurs were in fact already present in the common ancestor to all 'acrobatosaurs', casting light on the arboreal origin of flight in Triassic archosaurs. Nevertheless, even though drepanosauromorphs illuminate important aspects of the early evolution of pterosauromorphs, there is still much uncertainty regarding the evolutionary history along the 'acrobatosaur' stem after its divergence from the cursorial and possible scansorial lagerpetids in the early Carnian.

At this stage, it is worth mentioning that gliding flight through the use of a patagial membrane has been hypothesized for at least two drepanosauromorphs, *H. limnaios* and *M. preonensis* based on limb proportions (Ruben, 1998; Renesto et al., 2010). Further studies refuted this hypothesis in *M. preonensis* (Renesto, 2000), but both controlled descent and gliding appear plausible in *H. limnaios* although no direct evidence of a patagium has been found (Renesto et al., 2010). Such a patagial membrane is a prerequisite key innovation (sensu Miller et al., 2022) for pterosaurian flight, and has been a key component of all 'proto-pterosaur' scenarios (Wild, 1984; Bennett, 1997; Witton, 2013; Koroljov, 2017). While they are by no means direct pterosaur 'ancestors', drepanosauromorphs such as *H. limnaios* may suggest that a patagium was already present in the common ancestor to all 'acrobatosaurs'. However, we note that the subsequent reduction of this membrane in other drepanosaurids (as implied by our

topology, Fig. 3) is unlikely and absent in extant taxa (Dudley et al., 2007), and stress that this possibility requires further studies and fossil discoveries.

Foreword to chapters 5 and 6

The next two chapters delve into the application of Computational Fluid Dynamics (CFD) to the study of gliding locomotion in tetrapods. While this exciting field of research has gathered a lot of attention in recent years, it is still far from a widespread topic in the community of vertebrate paleontologists. Moreover, it requires some knowledge of fluid dynamics as well as computer sciences, two disciplines paleontologists rarely specialize in.

Speaking from a beginner's experience, CFD paleobiological studies are subject to a steep learning curve. Thankfully, the rise of these methods in paleobiology has prompted the recent publication of reviews tailored for paleontologists with a penchant for biomechanics. I have thus taken the liberty to compile here a handful of these works that were of a great help to me during this thesis, and that may be of help to a reader without a biomechanical background.

Regarding fluid dynamics, biologists and paleontologists both typically look to Vogel (1996) for an accessible synthesis. Koehl (2011) also provides a concise introduction to the aerodynamic concepts tackled in this thesis. Regarding the application of CFD to Paleontology, Rahman (2017, 2020) and Hebdon et al. (2020) provide synthetic hands-on approaches, while Gibson et al. (2021) offer a more strong-armed theorical synthesis. There are also numerous aerodynamical textbooks available, but these works were written with biologists in mind, and are thus of easier access to paleontologists.

Hopefully, the reader will find them as useful as I have.

Chapter 5: Influence of posture during gliding flight in the flying lizard *Draco volans*

> At the time of writing, the present chapter is very close to submission as a research article co-authored with W. Salaün (IDA) and P. Cinnella (IDA).

Abstract— The aerodynamic and gliding performances of the flying lizard *Draco volans* are studied here using a Computational Fluid Dynamics model. The systematic study of the aerodynamics of several postural changes, namely wing extension, increased body camber, and limb positioning, provides hitherto unappreciated information regarding gliding flight in this emblematic animal. *D. volans* generates large whirl-shaped vortices above its wings during gliding that produce the necessary pressure differences to generate lift, allowing it to cover, in theory, dozens of meters with minimal effort. Furthermore, we demonstrate that the traditional arms-first representation of these reptiles is not aerodynamically viable, which conforms to the absence of such postures in recorded glides. This detailed study will facilitate future comparisons of gliding in other taxa, including extinct gliders for which similar modeling approaches are among the only methods available for the study of gliding flight.

Introduction

Life in the trees comes with a series of challenges for animals, including moving in a three-dimensional environment with inclined surfaces and substrates of variable width and compliance (Cartmill, 1974, 1985; Preuschoft, 2002). In addition, arboreal habitats are discontinuous, making it a necessity for animals to employ gap-crossing behaviors in order to move around between branches and trees (Byrnes and Jayne, 2012; Graham and Socha, 2020). In this context, several vertebrate and invertebrate taxa are capable of aerial gliding locomotion, allowing them to move efficiently in a three-dimensional environment (Norberg, 1990; Dudley et al., 2007; Alexander, 2015). During gliding flight, an animal indeed performs a controlled descent by converting gravitational potential energy to aerodynamic work, which results in net horizontal movement (Dudley et al., 2007; Socha et al., 2015).

Among arboreal reptiles, the agamid flying lizards of the genus *Draco*, representing around 45 species endemic to South-East Asia (McGuire and Heang, 2001), are undoubtedly the most specialized gliders. These gracile squamates show a suite of extreme anatomical specializations to gliding locomotion, including a broad patagium spanning the entire length of the body as well as a pair of hyoid folds that serve as canards to increase stability in flight (Colbert, 1967; Russel and Dijkstra, 2001; McGuire and Dudley, 2011). The patagium of *Draco* is supported by five to seven ribs depending on the species (Inger, 1983; Musters, 1983), which can be extended laterally through muscular contraction and active manual handling to increase the area of the lift-generating surface (Colbert, 1967; John, 1970; Russel and Dijkstra, 2001; Dehling, 2017).

The gliding prowess of *Draco* was recognized early on, but for a long time, our understanding of the aerodynamics of gliding flight in these reptiles remained obscured by their cryptic lifestyle and limitations of experimental setups (Colbert, 1967; McGuire, 2003; McGuire and Dudley, 2005, 2011), including the known tendency of reptiles to 'underperform' in experimental conditions (Losos et al., 2002). New information has come to light recently from both direct observations (Khandelwal and Hedrick, 2020, 2022) and wind-tunnel experiments (Clark et al., 2021), highlighting the importance of body posture during gliding (Clark et al., 2021; Khandelwal and Hedrick 2022). However, there has been no attempt to address the aerodynamic performances of *Draco* through numerical simulations.

We thus provide here the first quantitative study of gliding flight in *Draco* using Computational Fluid Dynamics (CFD) in an effort to complement published experimental results and further our understanding of the gliding behavior of this emblematic animal.

Materials and Methods

Specimen data

All of the three-dimensional models (hereafter 'geometries' to avoid confusion with the mesh and numerical models described below) used in this study derive from the *Draco volans* specimen LSUMZ herp 81750 housed in the Louisiana State Museum of Natural History (LSUMZ), Baton-Rouge, Lousiana, USA. This specimen was CT-scanned in the University of Florida Nanoscale Research facility (70 kV, 200 µA, voxel size 0.063 mm) and is accessible on the MorphoSource 2.0 repository (http://n2t.net/ark:/87602/m4/M77362). All vertical slices were converted from 16 bits to 8 bits using ImageJ v.2.1.0 to save storage space. The dataset thus comprises 1862 vertical slices with a resolution of 351x800 pixels and a voxel size of 0.063 mm. The slices were then imported into the 3D segmentation software Mimics v.21.0 (Materialise, Leuven, Belgium), and three-dimensional surface models of the skin and skeleton of the specimen were generated in individual masks using the threshold tool for given grey levels, and exported as STL files (Figure 1a).

Using CT-scanned specimens for CFD analyses

While geometries generated by segmented CT-scan data provide a reliable representation of the original specimen, they are generally highly irregular, formed by a very high number of vertices and numerous intersecting faces (Figure 1a). Thus, they cannot directly be used for CFD analyses without risking aberrant meshing and calculation results, and inducing high temporal and storage costs. Various processing steps are required to use a CT-scan-derived geometry for CFD, which is then referred to as image- based CFD (Kuhlmann et al., 2022).

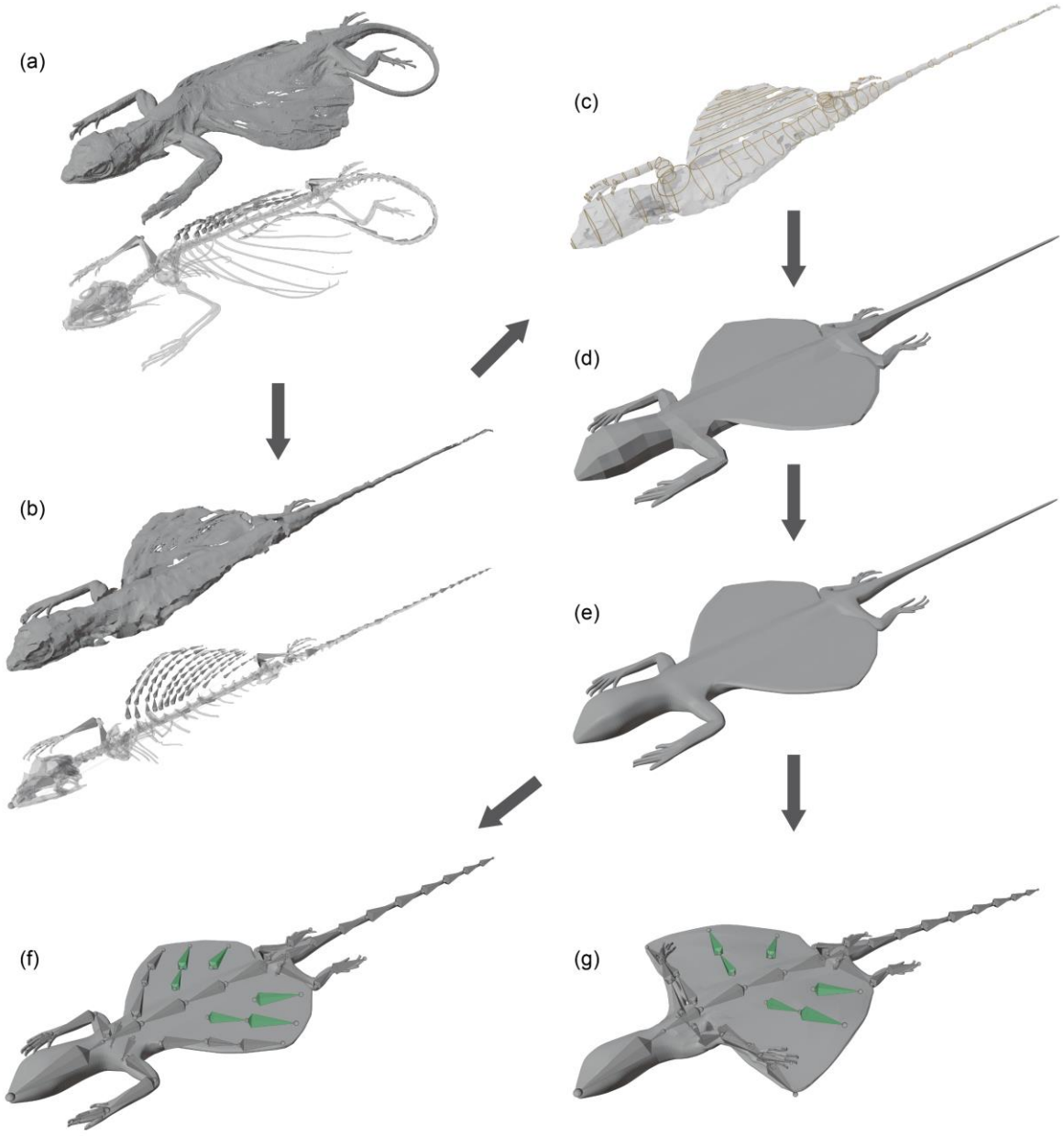

Figure 5-1: Main steps of the workflow employed to correct CT-scan-derived models for use in CFD analyses: (**a**) segmented skin and skeleton surface models parented to preliminary armature mimicking the right side of the skeleton; (**b**) lower-resolution surface models of (**a**) repositioned by moving the armature bones to mimic a standard resting pose; (**c**) series of vertical eight-vertices circles positioned along each part of the segmented skin model; (**d**) coarse surface model resulting from symmetrizing the circles of (**c**) to recreate the left-side elements, generating faces to link adjacent circles, and manually joining each part; (**e**) smooth surface model of (**d**) with applied triangulate and subsurface modifiers; (**f**) P0 geometry with parented armature; (**g**) P2 geometry obtained by moving the armature bones. Green bones in the posterior wing indicate dependency to the rotation applied to the leading-edge bones.

Furthermore, most specimens available for image-based CFD are museum or university collection specimens, which rarely comprise freshly dead specimens and are almost never

preserved in 'standard' postures used for biomechanical analyses unless they were sacrificed and fixed for this express purpose (e.g. McGuire, 2003; Zhao et al., 2019). Indeed, as preserved, LSUMZ herp 81750 does not lie in a standard pose as its wing and tail are partially folded under the body (Figure 1a), so it is necessary to reconstruct the symmetry of the animal along the longitudinal axis.

Lastly, collection specimens may show some degradation. For example, LSUMZ herp 81750 shows traces of desiccation and bears several holes in the patagium (Figure 1a, b). Given these holes are located on the lift-generating surface, it is expected that their presence would have been detrimental to a live animal, and are thus not desired for a study of gliding performance.

Several methods have been proposed to reliably reconstruct and retrodeform digitized vertebrate specimens (Lautenschlager, 2016a, b; Rahman and Lautenschlager, 2016; Brassey et al., 2016; Bishop et al., 2021; DeVries et al., 2022). However, those stem from paleontological studies, which generally focus on skeletal and whole-body (i.e. modeling the body by simple shapes) reconstructions rather than fleshed-out ones. Fleshed-out reconstructions (e.g. 3D slicing, Henderson, 1999), or more generally artistic reconstructions (e.g. Steyer et al., 2010) are often avoided in biomechanical studies since they are subject to artistic interpretations regarding soft tissue volume (Brassey, 2016; Lautenschlager, 2016a). By comparison, there have been little to no studies on the retrodeformation and life reconstruction of natural history collection specimens, which are subject to similar preservation issues despite showing extensive data on soft tissue volume, as shown by LSUMZ herp 81750.

Fleshed-out reconstructions are a prerequisite to biomechanical image-based CFD analyses. However, few CFD biomechanical analyses provide a detailed explanation of how the 3D models used were constructed, and those that do are either not based on CT-scan data (e.g. Kogan et al., 2015; Zhao et al., 2019), or are not based on natural history collection specimens (e.g. Inthavong et al., 2009; Provini and Van Wassenbergh, 2018).

As we are not aware of any other published workflow allowing for some degree of standardization in the construction of geometries derived from CT-scanned natural history collection specimens for image-based CFD analyses, we provide here a list of steps retracing our construction of a smooth, symmetrical 3D fleshed-out model of specimen LSUMZ herp 81750 of *Draco volans*. Given the focus of our study is to assess the impact of posture on the

aerodynamics of gliding flight in this reptile, we also retrace our construction of a skeletal armature that can be used to easily change the pose of this 3D model.

In essence, this workflow represents a compound list of steps inspired by proposed workflows for 'armature-retrodeformation' (sensu DeVries et al., 2022; see also Garwood and Dunlop, 2014), whole-body reconstruction (specifically inspired by Allen et al., 2009; most recently Bishop et al., 2021) and image-based CFD (Kuhlmann et al., 2022).

Proposed workflow—(1) As preserved, LSUMZ herp 81750 does not lie in a standard resting pose (Figure 1a). It is thus necessary to reconstruct the symmetry of the animal along the longitudinal axis. We thus imported the 3D surface models resulting from the segmentation of LSUMZ herp 81750 into the opensource 3D modeling software Blender v.2.90.1.

First, we reduced the number of faces in the mesh using the built-in 'Decimate' modifier used in collapse mode with a ratio of 0.025, meaning only 2.5% of the original faces are kept. This decimation affects the mesh to some degree (e.g. loss of the scalation pattern, but has little impact on the overall shape of the mesh (Figure 1a, b). However, it allows for a much easier further processing.

Then, we divided the original geometry into anatomical parts (distinct 'meshes' in Blender): trunk, limbs, wing, and tail that could be reworked independently. We then created an approximate skeletal armature for individual parts and repositioned the animal in a commonly represented resting pose (Figure 1b), here similar to McGuire (2003:fig. 1). This was done for only one of each paired elements, which were then symmetrized for consistency

(2) The segmented 3D surface models of LSUMZ herp 81750 are highly irregular and comprise numerous intersecting faces. Furthermore, LSUMZ herp 81750 shows traces of desiccation and bears several holes in the patagium (Figure 1a, b).

In order to palliate both issues, we generated series of vertical circles of eight vertices along the body, limbs and wings and arranged individual vertices to fit to the outline of the specimen (Figure 1c). We then generated surface meshes for each anatomical part by automatically forming faces between the corresponding vertices of adjacent circles (Figure 1d). The arms, legs, wings and tails were then manually attached to the body by generating faces between corresponding vertices.

Steps (1) and (2) are very similar to steps discussed in the context of other biomechanical numerical analyses (e.g. Allen et al., 2009; Bishop et al., 2021; DeVries et al., 2022). Step (2) is especially important as the generation of easily-manipulable octogonal circles allows for some degree of standardization in the construction of the numerical models. However, contrary to paleontological studies that lack soft tissue data and thus thrive to keep all octagonal circles of similar shape, the vertices of all circles were here manually moved to closely fit to the skin of the animal. The positioning of the individual vertices, however, is highly subjective and dependent on operator judgment (see also Hutchinson et al., 2011).

(3) The resulting geometry is much simpler than the original segmented one and can be easily manipulated. In counterpart, it is quite angular, contrasting with the smoother outline of the original specimen (Figure 1a, d). We thus applied the following modifications to the newly generated surface models (through the 'Subsurface' and 'Triangulate' Modifiers in Blender): (a) doubling of the number of all vertices, thus dividing each existing face into four equal faces; (b) additional doubling of the wing vertices; (c) further dividing all faces from a square to two triangles while conserving bilateral symmetry. Triangular faces, being simpler polygons, indeed save computation time compared to squared faces. The resulting mesh is thus smooth, as required for CFD analyses (Figure 1e).

(4) We then created an armature composed of individual segments ('bones' in Blender), and parented it to the geometry using the 'Automatic Weights' parenting option in Blender to link each bone to the neighboring vertices of the geometry in order to mimic the skeleton of the original specimen (Figure 1e). By rotating the bones of this skeletal armature, it is possible to mimic postures observed in live *Draco volans* individuals while retaining the integrity of the overall 3D model (Figure 1e, f). Given the various parts of the wing of *Draco* are linked by muscular, elastin and collagen fibers, we applied a 'Copy Rotation' bone constraint to the posterior rows of bone in each wing and adjusted its influence to mimic the movement of the leading-edge row with some degree of inertia (influence 0.6, 0.1, and 0.3 for the median and lateral row two bones and row tree bone respectively).

However, the resulting geometry is still rather complex. Thus, we manually corrected the automatic weight allocation of the armature bones to the geometry (in Blender's 'Weight Paint' mode) to prevent aberrant deformation of selected vertices. This step, while very time-

consuming, is particularly important for CFD analyses, as aberrant deformations can have severe repercussions on the meshing and analyses steps of the CFD analyses.

The resulting geometry is thus symmetrical, smooth and comprises only a single- layer outline of the specimen formed by numerous adjoined triangular faces (186 944 faces) that closely follows the morphology of the original specimen. It is also parented to a skeletal armature whose influence on the geometry was manually adjusted to allow for the repositioning of the model to mimic postures observed in the living animal.

Limitations— An important point to consider is that this geometry is entirely smooth and rigid, and thus does not reproduce the scalation or the flexibility of the wing of live *Draco* specimens, which are involved in gliding (Russell and Dijkstra, 2001; Khandelwal and Hedrick, 2022). Nevertheless, this geometry should save considerable computational time, and can be considered roughly identical to live *Draco* specimens from a morphological standpoint following previous studies on gliding vertebrates (e.g. Zhao et al., 2019).

Another point is that our geometry is not entirely symmetrical. Whereas the limbs and wings were symmetrized for consistency, the body, head and tail of the animal were simply retrodeformed so that the vertebral column was oriented along the sagittal axis (Figure 1). We made no attempt to symmetrize these parts, and on the contrary thrived to fit the skin of the animal independently on each site to better reflect the actual morphology of the animal. While not actually a limitation since all bilateral animals are minutely asymmetric, this is expected to incur asymmetrical calculation results and is thus an important point to consider.

Finally, while parenting the geometry to an armature provides an easy manner of generating postures, it does not appear to conserve internal volume (see Mass Estimation below). This is expected as any change in the geometry is obtained by reducing or increasing the size of given faces, which in turn impacts the internal volume of the geometry. In live animals, although some degree of elasticity is present, much of the postural changes are permitted by skin folds, which are not accounted for here. The internal volume, and thus the mass, of a live animal are constant regardless of its posture. Thus, when using such geometries, it is paramount that an estimation of the difference in volume is conducted as a sensitivity analysis. When possible, we also advocate that the geometry closest to the original specimen should be used as a basis for volumetric and mass estimation as it reflects the actual volume of the specimen prior to deformation.

Table 5-1: Summary of the morphological features of the postural geometries ('PX', see text) used for CFD analyses

	P0	P1	P1a	P2	P2a	P3	P3a
Fully extended wing	no	yes	yes	yes	yes	yes	yes
Degree of body camber	none	none	none	low	low	high	high
Arms along the leading edge	no	no	yes	no	yes	no	yes

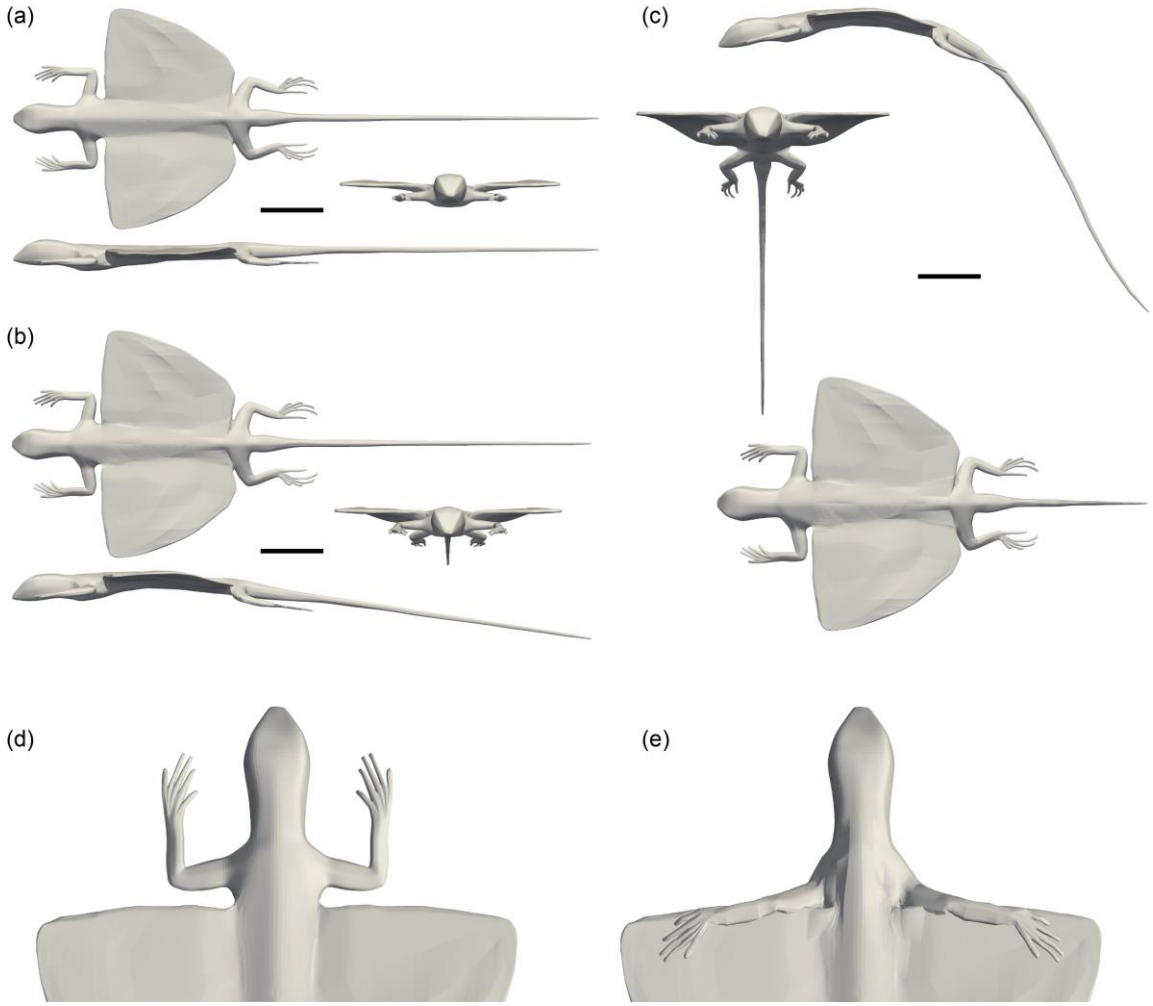

Figure 5-2: Selected geometries used for CFD analyses in dorsal, anterior and left lateral views: (**a**) P1, no camber geometry; (**b**) P2, low camber geometry; (**c**) P3, high camber geometry; (**d**) close-up view of P1 geometry with arms flexed at the elbow and hands pointing anteriorly ('arms-first'); (**e**) close-up view of arms oriented transversely and resting above the leading edge of the wing ('arms-transverse'). Scale bars equal 2 cm.

Three-dimensional geometries

We generated seven rigid-body postures using the geometry generated from the CT-scan data of the *Draco volans* specimen LSUMZ herp 81750 (Figure 2).

Posture P0 corresponds to the 'resting posture' of the animal with the wing being only partially open as preserved in the original specimen (Figure 1d). Posture P1 is identical to P0 but with the wing extended (by manually rotating the armature bones around the vertical axis) so that the leading edge is roughly perpendicular to the main axis of the body (Figure 2a). This posture is referred here as the 'standard gliding posture' as it is commonly used to depict *Draco* in the literature (Colbert, 1967; Russell and Dijkstra, 2001; McGuire, 2003). Posture P2 derives from P1 but with the anterior trunk and head, and the posterior trunk and tail angled ca. 7 relative to the horizontal, creating a low camber (Figure 2b). Posture P3 is similar to P2 but with a ca. 15 angulation of anterior and posterior trunk relative to the horizontal (Figure 2c). In addition, the tail of P3 was set at ca. 60 to the horizontal to mimic the very strong angulation observed in living *Draco* individuals during gliding flight. Table 1 summarizes the morphological features of each postural geometry.

In addition, given the recent description of the 'composite wing' of *Draco*, whereby the animal positions its forelimbs along the leading edge of the wings and interlocks his claws between enlarged scales on the dorsal surface of the patagium (Dehling, 2017), we generated three geometries, P1a, P2a, and P3a (hereafter 'arms-transverse' geometries), differentiated respectively from P1, P2, and P3 (hereafter 'arms-first' geometries) by the posterior rotation of the shoulder, and extension of the elbow and wrist so that the arm follows the leading edge of the wing and the digits mimic the interlocking of the claws over the patagium (Figure 2e). All of these rigid-body posture geometries were exported in STL format. Key measurements of the resting (P0) and standard gliding (P1) postures are given in Table 2.

Measurements—The mass *m* of a geometry was estimated under P0 and P1 postures by measuring the volume of the geometry prior to smoothing (Figure 1d) and multiplying it by a density value of 1000 $kg.m^{-3}$, similar to the volumetric mass estimation methodology described by Allen et al. (2009). The estimated mass for P0 and P1 postures were 7.25 g and 8.29 g respectively (Table 2). Both estimations fall well within the range of mass known for *Draco volans* (between 2 g and 13 g, Russell and Dijkstra, 2001; mean value of 8.475 g in Myhrvold et al., 2015; see Mori and Hikida, 1992 for a slightly lower but comparable range).

	P0	P1
Snout-vent length (mm)	75.7	75.7
Total length *l* (mm)	186	186
Wingspan *s* (mm)	56	70
Root chord *rc* (mm)	40.1	39.9
Tip chord *tc* (mm)	2.93	8.37
Mean chord *mc* (mm)	28.4	31.7
Reference point *R*–rostrum distance (mm)	37.9	38.7
Planform area *A* (cm^2)	18.41	23.87
Total area A_{tot} (cm^2)	22.37	31.05
Aspect ratio *AR*	1.31	2.05
Mass *m* (g)	7.25	8.29*
Wing loading *WL* (N/m^2)	38.63	29.80

Table 5-2: Key measurements of *Draco volans* geometries representing resting (P0) and standard gliding (P1) postures. Abbreviations: *mc* is the mean value of 10 regularly spaced chords along the width of the wing, *rc* and *tc*; *R* taken at 25% of *mc*; *AR* equals s^2/A; *WL* equals *mg/A* using *m* of P0 for both geometries, with *g* of 9.81 m/s^2. * indicates overestimated measurement (see text).

As mentioned above, the difference in mass results from the fact that our workflow does not maintain a constant volume when the geometry is deformed using the armature. Thus, the volume and mass of P1 are likely overestimated due to the extension of the wing. As P0 is a direct reproduction of the original specimen, we thus consider *m* as 7.25 g for all subsequent analyses.

We measured the planform area *A* (the area of the wings and trunk, 'total wing area' of McGuire, 2003) and total area A_{tot} by isolating the upper surface cells of each geometry (i.e. removing the lower surface cells to exclude volume information) and projecting them on the horizontal plane in Paraview v.5.9.0. We then validated those measurements in dorsal view using the area measurement tool of ImageJ v.2.1.0. We use the planform area *A* as the reference area for all our geometries following common practice for airplane-like biological models (Koehl et al., 2011). P0 and P1 have a *A* of 18.41 cm^2 and 23.87 cm^2 respectively, both of which fall well within the range of planform area for *Draco volans* (Mori and Hikida, 1992:fig. 2f; compare Russell and Dijkstra, 2001:fig. 2b and 2d for similar measurements).

The aspect ratio *AR* is a dimensionless measurement of the slenderness of the wing defined as s^2/A where *s* is the wingspan and *A* the planform area. We calculate an *AR* of 1.31 for P0 and 2.05 for P1 (Table 2). Induced drag generation (drag created through lift generation) decreases with *AR* (Anderson, 2017), which conforms to the expectation that P1 is more efficient for gliding than P0.

Given a mass of 7.25 g for both P0 and P1, the wing loading *WL* of these geometries are of 38.63 N/m^2 and 29.80 N/m^2 (or 3.94 kg/m^3 and 3.04 kg/m^3) respectively. Both values are within the range of *WL* reported by Mori and Hikida (1992) for *D. volans*. Surprisingly, these values are much higher than those reported by McGuire and Dudley (2005) for *Draco* species of similar mass (*D. uinquefasciatus*: *m*, 6.5 g and *WL*, 10.5 N/m^2; *D. formosus*: *m*, 8.8 g and *WL*, 14.1 N/m^2), and even surpass that of the largest measured species (*D. fimbriatus*: *m*, 18.7 g and *WL*, 23.5 N/m^2). Yet, they are comparable to those reported by Colbert (1967) for *D. maculatus* (*D. whiteaheadi* in Colbert, 1967). As our mass and planform area measurements fall within the known range for *D. volans*, we are unsure why our *WL* differ from those reported for McGuire and Dudley (2005) (they might result from different reference area calculations), and thus refrain from comparing absolute values of *WL* here.

Nevertheless, the higher *WL* calculated for P0 compared to P1 indicates P0 has a lower gliding performance, as gliding distance decreases with wing loading in *Draco* (Shine et al, 1998; McGuire, 2003; McGuire and Dudley, 2005, 2011). This highlights the need for flying lizards to keep their wing extended in flight, and conforms with observed gliding behavior (Dehling, 2017; Khandelwal and Hedrick, 2020, 2022).

Computational Fluid Dynamics (CFD)

Glide paths in gliding animals can be divided in three phases: the take-off, mid-glide, and landing phases (Khandelwal and Hedrick, 2020). McGuire and Dudley (2005) report that *Draco* lizards attained equilibrium gliding during mid-glide phase in about half of their glide trials (consisting of lizards gliding between two vertical poles). Equilibrium gliding occurs when the aerodynamic forces counteract weight so that the animal glides in a straight path at a fixed glide angle and velocity (Norberg, 1990; Koehl et al., 2011; Socha et al., 2015). However, Khandelwal and Hedrick (2020) have argued that such glides rarely occur in nature as *Draco* lizards typically maneuver between trees, following much more complex glide paths.

Nevertheless, the findings of McGuire and Dudley (2005) indicate steady-state aerodynamics are relevant to the study of gliding in the mid-glide phase in *Draco* provided there are no obstacles in its path. This is essentially identical to a wind tunnel or CFD setup where a *Draco* geometry is immersed in an incoming laminar airflow. Moreover, as equilibrium gliding

implies a constant glide angle, it can be described using static simulations rather than dynamic ones which incorporate motion but are very computationally demanding.

It is further necessary to estimate a priori the flow regime (laminar, transitional, turbulent) of the air around a gliding *Draco*. Fluid flow regime is dictated by the dimensionless Reynolds number *Re*, defined as the ratio between inertial and viscous forces:

$$Re = \frac{\rho U_\infty l}{\mu} \quad (1)$$

Where ρ is the density of the fluid (kg/m^3), U_∞ is the characteristic velocity (m/s) (usually corresponding to the flight velocity, or freestream velocity in a reference frame attached to the object), l is the characteristic dimension of the object (m), and μ is the dynamic viscosity of the fluid (kg/m·s).

Given the standard values of density (1.2 kg/m^3) and dynamic viscosity (1.8 x 10^{-5} kg/m·s) of air at 15 C at sea level, and as *Draco* lizards, ranging from 15 to 40 cm in length (60 to 150 mm in SVL, McGuire, 2003, and considering a SVL:total lengh ratio of 2.5 as in Table 2), have been reported to glide at speeds ranging between about 3 and 10 m/s (McGuire and Dudley, 2005), these reptiles are estimated to glide in a range of *Re* of 10^4 to 10^5. This range is typical of vertebrate gliders and flyers and is indicative of transitional to turbulent flows. These flows are characterized by some degree of chaotic behavior in the flow layers (Norberg, 1990; Vogel, 1994; Anderson, 2017), and cannot be described by numerically solving the instantaneous Navier-Stokes equations (representing the conservation of mass and momentum), the most commonly used way to predict fluid flow, because of the huge computational burden of solving all of the flow scales. However, time-averaged approaches relying on the Reynolds Averaged Navier- Stokes (RANS) equations allow for much more affordable and reasonably accurate representation of turbulent flows.

Lastly, given the gliding speeds of *Draco* are very small compared to the speed of sound (i.e. the Mach number is very close to 0), the flow of air is taken as incompressible, meaning we assume a constant air density (Anderson, 2017).

Thus, in this study, we examine gliding in *Draco* during mid-glide based on steady- state RANS simulations of incompressible flows. All CFD analyses (hereafter 'cases') were conducted using the open-source software OpenFOAM v.2012 on a Gnu/Linux Debian 9

workstation (Intel(R) Xeon(R) CPU X5650, 2.67GHz, 12 cores, 24 Go Ram). All cases were run in parallel on six processors.

In the following points, we describe the setup for a single case, illustrated by that of *Draco volans* in a resting pose (P0 geometry) set at an angle of attack of 0 relative to an incoming flow flowing at a constant velocity of 5 m/s.

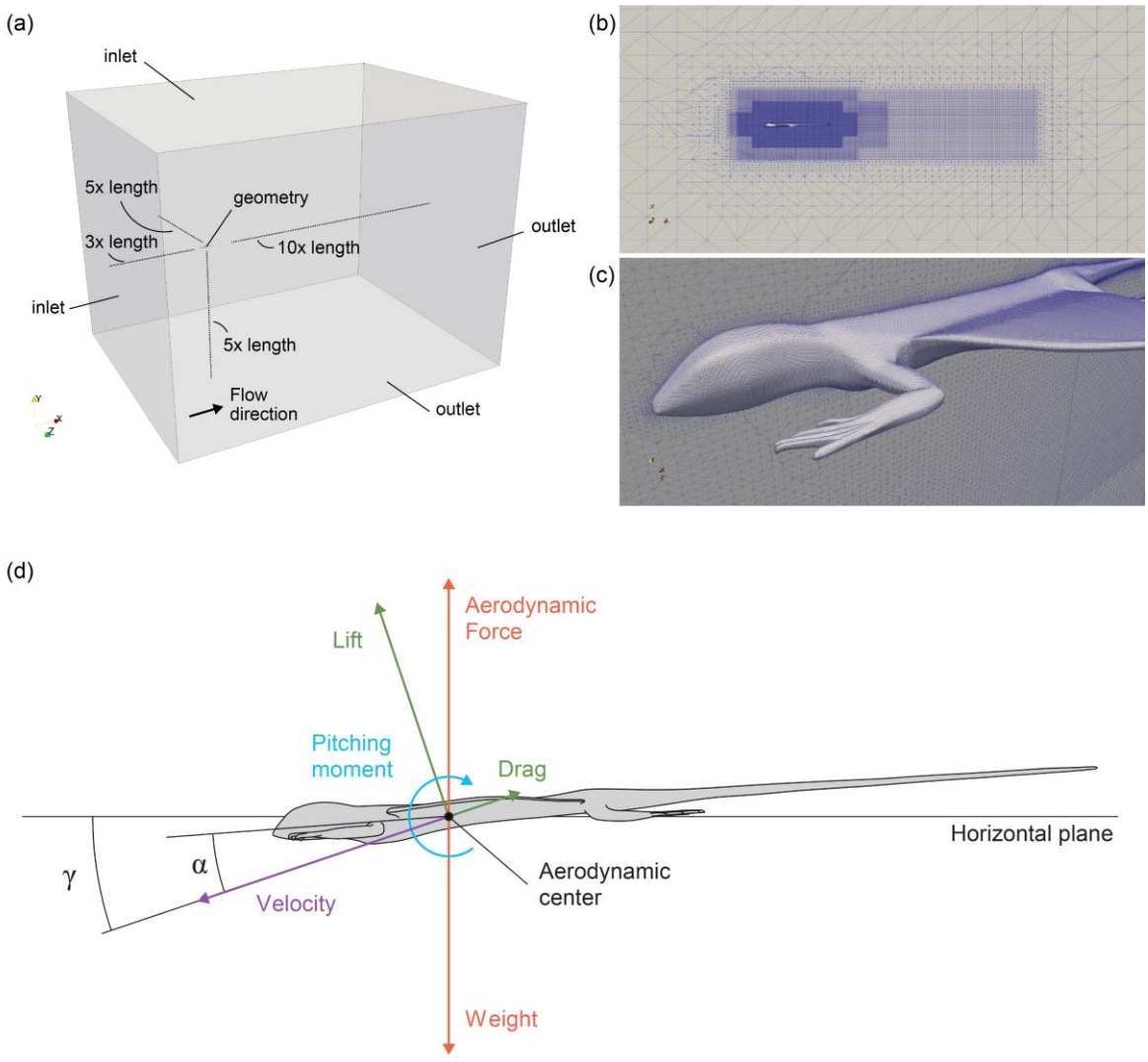

Figure 5-3: Overview of computational domain and mesh: (**a**) computational domain in oblique view illustrating the position of the geometry relative to the incoming airflow; (**b**) detail of the mesh on the sagittal plane (Z = 0), illustrating the Refinement Box around the geometry; (**c**) close-up oblique view of (**b**) illustrating the refinement layers and the discretization of the geometry; (**d**) free-body diagram of gliding *D. volans* illustrating glide angle γ, angle of attack α, forces and pitching moment.

Computational domain—We set up a rectangular (2.6x2x2 m) computational domain extending three times the length of our *Draco volans* geometry upstream, ten times downstream,

and five times on each side of the geometry in the vertical and transverse planes (Figure 3a). These relative dimensions conform well with that of previous biomechanical studies in which they are sufficient to capture fluid movement in the wake of the object of interest (e.g. Rahman, 2017, 2020).

Mesh generation—We discretize the computational domain using the snappyHexMesh mesh generation utility of OpenFOAM, which returns a mesh composed of a series of hexahedral and split-hexahedral cells. The snappyHexMesh utility employs an immersed boundary algorithm that first immerses the geometry in a starting mesh composed of a regular series of hexahedral cells before iteratively refining the mesh inside a designated area (the refinement box) set up according to the dimensions of the geometry (Figure 3b). The mesh is further divided in refinement layers inside the refinement box, where cells are split in gradually smaller cells closer to the geometry (Figure 3c). All cells entirely located inside the geometry are then removed as they are useless for external flows, and all cells crossing the geometry are cut along the boundary to exclude the portion inside the geometry as well, finally leading to a body-fitted unstructured mesh (Figure 3c).

We here employ a refinement box extending four times the length of our *Draco* geometry downstream and half this length in all other directions for all cases (Figure 3b) except for those derived from postures P3 and P3a where the refinement box extends the length of the *Draco* geometry downwards to encompass the strongly downturned tail.

Given the resolution and overall quality of the mesh has a direct impact on calculation results and time, we conducted a set of sensitivity analyses with varying parameters. Thus, all parameters, including those used to generate the mesh for all of the analyses, are described below.

Turbulence model—We employ RANS equations (which express conservation of time- averaged mass and momentum) in conjunction with the $k - \omega$ SST (Shear-Stress Transport) turbulence model in order to predict fluid flow (Menter, 1994). The $k - \omega$ SST model is widely used and considered very reliable, because of its satisfactory accuracy over a wide range of flow configurations, showing good agreement with experimental data (Wilcox, 2006).

Numerical solver—The governing equations of fluid flow are solved by using the Semi-Implicit Method for Pressure Linked Equations (SIMPLE) algorithm, one of the most commonly

used algorithms for incompressible, steady-state Navier-Stokes simulations (Patankar, 1980). The convective terms in the equations are approximated using a bounded second-order accurate upwind scheme and the viscous terms by a second-order Gauss scheme.

Boundary and initial conditions—The upstream and top faces of the rectangular domain relative to our *Draco* geometry were designated as the inlet (i.e. the inflow). At those boundaries, the freestream velocity (equal to the flight velocity) is assigned along with the inflow angle. The latter can be modified to simulate different angles of attack. We chose an inlet turbulence intensity I of 5% and a turbulence length scale l_t (m) of 7% of the characteristic length l. These terms are used to determine the inflow boundary conditions for the turbulent variables k and ω (see Wilcox, 2006 for equations). The downstream and bottom faces were designated as the outlet (i.e. outflow) (Figure 3a), where a zero-gradient condition was imposed. Lastly, a no-slip boundary condition was applied to our *Draco* geometry to constrain velocity to zero at the boundary with the geometry.

For incompressible flow, the pressure difference, rather than its absolute value, has an impact on fluid flow. We thus prescribe a reference pressure P of 0 for simplicity. Flow velocity and angle of attack are the only case-dependent initial conditions.

Cases—We conducted simulations of gliding flight for *Draco volans* (hereafter 'cases'), each with a specific setup of characteristic velocity, posture, and angle of attack. 77 cases were simulated at an unidirectional horizontal flow velocity of 5 m/s, one for each of the seven postures (P0, P1, P1a, P2, P2a, P3, P3a) set at selected angles of attack (-20°, -10°, -8°, -5°, 0°, 5°, 8°, 10 ° 15°, 20° and 25°). Additional cases were set up for sensitivity analyses (detailed below).

Under a SIMPLE solver, the designated timestep has no impact on the numerical results, provided that the number of iterations run by the solver is sufficient for the values of the returned parameters to converge over time to the steady-state solution. Here, we employ distinct timesteps for all cases, tailored to allow convergence but minimize computational cost, ranging from 140 to 900 steps depending on the velocity, posture and angle of attack used for each case.

Postprocessing—Aerodynamic performances rely on the Drag force D (N), oriented parallel to the incoming flow direction, and the Lift force L (N), oriented perpendicular to the flow (Figure 3d). In aerodynamics, these forces are typically described using the dimensionless lift and drag coefficients C_L and C_D, defined as:

$$C_D = \frac{2D}{\rho U^2 A}$$
$$C_L = \frac{2L}{\rho U^2 A} \quad (2)$$

In addition, the pitching moment M (N·m), describing torque along the pitching axis of the body, is also typically described using the dimensionless pithching moment coefficient C_M, defined as:

$$C_M = \frac{2M}{\rho U^2 A \cdot mc} \quad (3)$$

We use the open source software Paraview v.5.9.0 for visualization and postprocessing. The computation of streamlines (see below) relies of a point source forming a sphere of a 5 cm radius centered in the sagittal plane of the animal immediately behind the wing (7 cm from the rostrum) and at the mid-height of the animal (-2 mm from the coronal plane). The 100 computed streamlines all pass through this sphere, thus capturing the flow immediately around the geometry.

Sensitivity analyses

Given the degree of subjectivity in constructing the geometry of *Draco volans* and selecting the parameters for the meshing process, we conducted several sensitivity analyses to assess the influence of both aspects of calculation results. We thus ran 49 additional cases for three reconstructed geometries and four meshes at an unidirectional horizontal flow velocity of 5 m/s set at selected angles of attack (-20° , -10° , -5° , 0°, 5°, 10, 20°).

In addition, we conducted sensitivity analyses to determine whether the Reynolds number Re (calculated for different flow velocities) had a significant influence on calculation results as well. We thus ran 22 additional cases for two flow velocities for a single geometry set at selected angles of attack (-20°, -10°, -8°, -5°, 0°, 5°, 8°, 10°, 15°, 20° and 25°).

Table 5-3: Parameters used to generate meshed using the snappyHexMesh mesh generation utility of OpenFOAM and resulting calculation information for a standard case of a resting pose (P0) geometry set at an angle or attack α of 20 relative to a flow with a characteristic velocity U∞ of 5 m/s. Local (opposed to global) refers to a single processor when the calculation is run in parallel. ∗ indicates aberrant value.

	M0	M1	M2	M3 (final mesh)
Maximum number of local cells	100 000	500 000	500 000	500 000
Maximum number of global cells	2 000 000	2 000 000	3 000 000	3 000 000
Minimum number of cells to refine	10	6	6	6
Refinement surface levels (min max)	(5 6)	(6 7)	(8 8)	(9 9)
Refinement region levels (min max)	(10^{15} 4)	(10^{15} 4)	(10^{15} 6)	(10^{15} 6)
Number of surface layers	1	10	10	20
Expansion ratio	1	1	1	1.15
Thickness of layer furthest from wall	0.3	0.3	0.3	0.03
Minimum overall layer thickness	0.1	0.1	0.1	0.01
Meshing time (s)	77.56	146.92	1572.06	1108.78
Number of cells	472 958	586 125	4 371 878	5 164 204
Maximum aspect ratio	29.70	17.69	19.55	5.18
Calculation time (s)	837	1181	8343	9940
Average y^+	6.51	5.45	2.34	1.58

Mesh independence—As described above, we use the snappyHexMesh mesh generation utility of OpenFOAM. This utility employs a large number of parameters, some of which were selected to fit the requirements of our study (see OpenFOAM user Guide for more information, www.openfoam.org). Thus, we conducted a set of cases to assess the impact of selected parameters of mesh generation on the calculation results and computational cost.

The snappyHexMesh parameters for the coarser mesh M0 were taken from the built in OpenFOAM tutorial motorBike. We then modified selected parameters to generate a series of four meshes, noted M0 to M3, by progressively increasing the refinement in the near-wall region (Table 3).

The dimensionless wall distance y^+ is commonly used in CFD analyses to describe the maximum height of a boundary-layer cell that allows for a reliable characterization of fluid flow in this layer. Typically, y^+ is taken at $y^+ \leq 5$, but ideally closer to $y^+ = 1$ so that the height of the first layer of cells off the wall lies within the viscous-sublayer of the boundary layer region (detailed in Wilcox, 2006).

Figure 5-4: Geometries used in sensitivity analyses to assess the impact of geometry construction: (**a**) bulkier P0 geometry; (**b**) preferred P0 geometry; (**c**) thinner P0 geometry.

Geometry construction—As described above, the construction of the geometry involves the placement of vertices along the outline of the segmented surface files (step 2, Figure 1c). It is thus arguably the step involving the highest degree of subjectivity and margin of error as (a), the original specimen was only broadly symmetrized in step (1) and is dependent on operator judgment; (b), the original specimen was damaged, preventing a reliable placing of vertices in some areas; (c) all vertices were manually placed along the skin of the specimen, and it is highly unlikely a repeated construction would be identical.

To compensate this uncertainty in reconstruction, we automatically generated two additional geometries, one slightly bulkier, the other slightly thinner (Figure 4), using the Shrink/Fatten tool in Blender to move all vertices 0.05 mm outwards or inwards along their normal vectors (i.e. in the direction perpendicular to the surface). The postural geometry P0 was used as a basis for this analysis as it is directly obtained from the mesh generation without deformation from the armature skeleton.

Our rationale was that these new geometries mimic the construction of the geometry by a user with a tendency to put vertices slightly too far or too close to the specimen respectively. Given the number of vertices is not homogeneous throughout the geometry (e.g. there are relatively more vertices in the digits than in the body), this methodology can lead to exaggerated results, as seen in the unnaturally thin digits of the thinner model. Nevertheless, this provides a framework to compare the influence of vertices positioning during the geometry construction on the CFD results.

In addition, our mass estimations indicate slight differences in volume for our different geometries (Table 2), and it is unclear whether this difference impacts the calculation results. By generating a slightly bulkier P0 mesh (estimated mass 8.57 g), we thus also encompass the

mass (and volume) difference between P0 and P1. Thus, we expect the slight volume difference observed to fall inside the margin of error of geometry generation.

Velocity and Reynolds number—Gliding velocities ranging from around 3 to 8 m/s have been reported for various *Draco* species (McGuire and Dudley, 2005). Excluding variation in size (which does compensate for increased speed regarding *Re*, see equation 1), the speed at which an individual glides varies both during the different phases of a glide, as well as between glides (Khandelwal and Hedrick, 2020). We thus expect that these reptiles can operate at slightly different Reynolds numbers.

As described above, *Re* varies proportionally to the characteristic velocity U_∞ and the characteristic dimension l of *Draco* (Equation 1). In order to test the influence of *Re* on aerodynamic parameters, we conducted cases at a characteristic velocity of either 5 m/s or 10 m/s. The doubling in velocity allows for a direct assessment of the influence of gliding speed on the aerodynamics of *Draco*, but also indirectly describes the aerodynamics of two lizards gliding at 5 m/s, with one being twice the size (in total length) as the other, which are then dynamically scaled (Koehl et al., 2011). Both cases are indeed numerically comparable with regards to Reynolds number (Equation 1).

Given these analyses reflect gliding flight, they are all based on a gliding posture geometry with no camber (P1), the least deformed geometry relative to the original specimen that reflects an actual flight posture in *Draco* (Dehling, 2017).

Trajectory simulations

Using the C_D and C_L values returned by the CFD analyses, we compute 2D trajectory simulations by resolving equations of motion through time, following recent studies (Dyke et al., 2013). The following equations are solved for each time step:

$$V = \sqrt{V_x^2 + V_y^2} \tag{4}$$

$$L = 1/2 \cdot \rho V^2 A C_L \tag{5}$$

$$D = 1/2 \cdot \rho V^2 A C_D \tag{6}$$

$$\gamma = \arctan(V_y/V_x) \quad (7)$$

$$F_x = L\sin(\gamma) - D\cos(\gamma) \quad (8)$$

$$F_y = L\cos(\gamma) + D\sin(\gamma) \quad (9)$$

$$a_x = F_x/m \quad (10)$$

$$a_y = (F_y/m) - g \quad (11)$$

Were V is the total glide velocity (m/s), V_x is the horizontal glide velocity (m/s), V_y is the vertical glide velocity (m/s), γ is the glide angle, F_x and F_y are the horizontal and vertical aerodynamic forces (N) respectively, a_x and a_y are the horizontal and vertical accelerations (m/s^2) respectively, and g is the gravitational acceleration (taken at 9.81 m/s^2).

For each time step Δt of 0.01 s, the velocity for the following time step is determined by:

$$V_x(t + \Delta t) = V_x(t) + a_x\Delta t \quad (12)$$

$$V_y(t + \Delta t) = V_y(t) - a_y\Delta t \quad (13)$$

And the location for the following time step is determined by:

$$X(t + \Delta t) = X(t) + V_x\Delta t \quad (14)$$

$$Y(t + \Delta t) = Y(t) - V_y\Delta t \quad (15)$$

Where t is the time (s) and X and Y are the horizontal and vertical locations (m) respectively.

We compute two sets of simulations, starting from two different heights. First, we compute gliding trajectories from a height of 5 m in order to compare those results to those of Clark et al. (2021), as well as the recorded glides of Khandelwal and Hendrick (2022: max observed take-off height 4 to 5 m) and Khandelwal and Hendrick (2020: mean take-off height 7.4 m). However, as these heights are constrained by limitation of the vertical position of camera height (Khandelwal and Hendrick, 2022), they likely represent only a portion of the actual take-off heights in *Draco*. We thus also compute gliding simulations from a height of 30 m, an estimate of tropical rainforest canopy height worldwide (although the Indo-Malayan rainforest inhabited by *Draco* are typically tens of meters higher, Dudley and DeVries, 1990), and more importantly a height within the range observed perch heights in *Draco* (Inger, 1983). All glides started with

an initial horizontal velocity $V_x(0)$ of 2.5 m/s and no vertical initial velocity (i.e., a strictly horizontal jump), as done by Clark et al. (2021).

The animal is here kept at a fixed angle of attack and posture throughout the glide, as done by Clark et al. (2021). While this is a gross oversimplification of the actual gliding behavior of *Draco*, which actively controls its glide trajectory (Dehling, 2017; Khandelwal and Hedrick, 2020, 2022), it allows for a systematic assessment of posture on gliding performance. Furthermore, we neglect here the take-off and landing phases of a glide trajectory, assuming the mid-glide phase occurs from the instant the animal leaves the support to the instant it touches the ground. Again, this is a gross oversimplification (Dehling, 2017; Khandelwal and Hedrick, 2020, 2022), but as the mid-glide phase is the only one where steady-state conditions have been reported (McGuire and Dudley, 2005), it is the only phase for which our CFD results are applicable.

For each posture, the angle of attack for the gliding simulation was determined as the one which maximizes the lift-to-drag ratio C_L/C_D. This value $(C_L/C_D)_{max}$ is indeed a standard measure of gliding performance, corresponding to a glide angle γ (the angle between *Draco* and the ground, Figure 3d) which maximizes the horizontal distance of a glide (Emerson and Koehl, 1990; Koehl et al., 2011). In short, these simulations thus permit the assessment of the impact on posture on maximum gliding distance.

Results

Sensitivity analyses

Mesh independence— The cases for mesh refinements M0, M1, M2, and M3 mostly yield very similar C_D and C_L values (Figure 5a). However, meshes M0 and M1 yield slightly higher C_D and C_L for high angles of attack (AoA) (C_D: 0.39 and 0.38; C_L: 0.87 and 0.86 respectively at 20°) compared to M2 and M3 (C_D: 0.34 and 0.35; C_L: 0.73 and 0.74 resp. at 20°). Regarding C_M, the M3 cases generally return the highest values (0°: -0.0026; 25°: -0.023), with M1 and M2 cases returning subequal or slightly lower values (0°: -0.0024 and -0.0031; 20°: -0.023 and -0.025 resp.) (Figure 5b). However, M0 cases yield much lower C_M values (0°: -0.0068; 20°: -0.024).

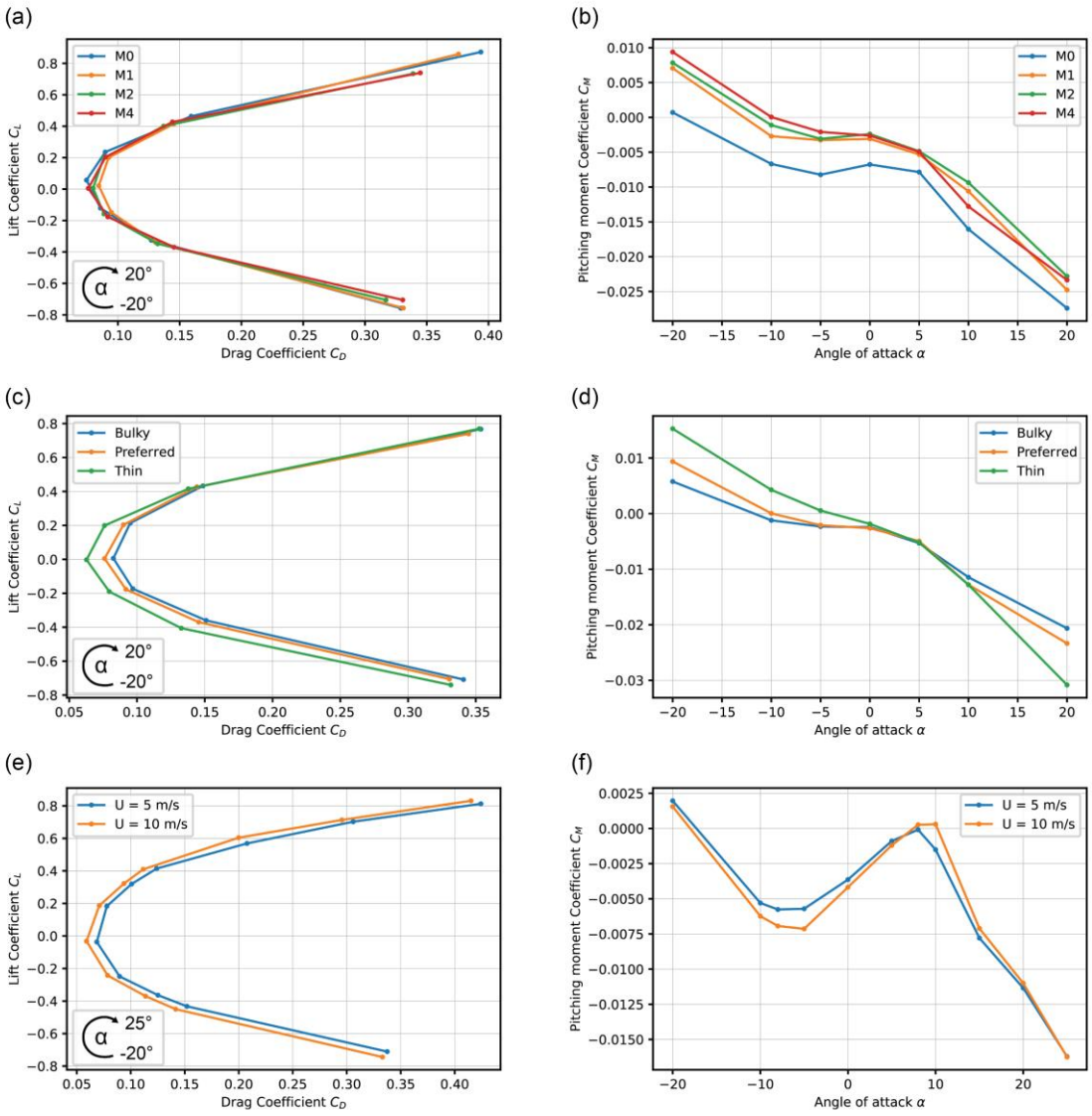

Figure 5-5: Results from sensitivity analyses regarding: the mesh generation parameters (**a**, **b**), the construction of the geometry (**c**, **d**), and velocity *U* (**e**, **f**). Left column, lift and drag coefficients under varying angles of attack *α*; Right column, pitching moment coefficient against angle of attack. *U* equals 5 m/s, Mesh is M4, and geometry follows preferred case unless otherwise noted. (**a**-**d**), cases using P0 geometry; (**e**, **f**) cases using P1 geometry.

These results indicate mesh refinement has an impact on pitching moment, which is highly underestimated by coarser meshes, and to a lesser degree on Lift and Drag, which are slightly overestimated by coarser meshes at high angles of attack. However, given the small differences in aerodynamic parameters between M2 and M3 (especially C_D and C_L where the differences are mostly < 5%), we consider our CFD results to be mesh independent, meaning the mesh

resolution does not significantly affect the computational results. Further refinement could further reduce this margin, but at a larger computational cost, and is thus not attempted here.

Regarding y^+, M2 and M3 yield values ≤ 5, with those of M3 very close to 1 (≈ 1.58 at 20°, Table 3). This indicates finer meshes provide a better prediction of fluid flow in the boundary layer. Based on these sensitivity analyses, as well as induced calculation times (Table 3), we elect to use our finest mesh refinement M3 for all subsequent cases.

Geometry construction—C_D increases with thickness for low AoAs (thin: 0.063; peferred: 0.076; bulky: 0.083 resp. at 0°). Indeed, the bulkier geometry offers a larger surface for frictional forces. In contrast, the thickness of the geometry has little influence on C_L, and thus on Lift for all angles of attack (Figure 5c). As a consequence, the bulkier geometry is expected to reach a shorter flight range than the thinner one.

The slope of C_M decreases with geometry thickness (Figure 5d) so that the C_M values are much lower at high negative AoAs and much higher at high positive AoAs for the bulkier geometry compared to the preferred and thinner ones (-20°: 0.0153, 0.0094 and 0.0058; 20°: -0.0308, -0.0233 and -0.0206 resp.). As a result, a C_M of 0 is attained for an AoA of about -11° for the bulkier geometry, -10° for the preferred one, and -5° for the thinner one.

The negative slope of C_M indicates that all geometries are longitudinally stable (e.g., the negative C_M at high AoAs induces a nose-down pitching that counteracts the upwards orientation of the animal, see e.g. Koehl et al., 2011). The stable fixed points (where C_M equals 0 and the C_M slope is negative) represent AoAs where the geometry experiences no pitching moment and is able to passively conterbalance perturbation (Koehl et al., 2011). Our analysis thus indicates bulkier geometries are stable relative to pitching at higher negative AoAs than thinner ones (Figure 5d). Lastly, the difference in C_M for high negative and positive AoAs indicates that thinner geometries generate stronger pitching moments due to the stronger suction induced next to the leading edge. As a consequence, bulkier geometries are more stable for these ranges os AoAs.

As expected, our preferred geometry always yields intermediate values between the bulkier and thinner one for all aerodynamic coefficients (Figure 5), meaning it is always included in the estimated margin of error induced by manually constructing the geometry. Thus, all subsequent cases employ geometries derived from it.

Velocity, size and Reynolds number—C_L values are very similar for cases at a velocity of 5 m/s or 10 m/s, which corresponds to a doubling of the Reynolds number (Figure 5e). The C_D values decrease slightly when *Re* increases (5 m/s: 0.424; 10 m/s: 0.415 resp. at 25°), due to the reduced relative importance of viscous friction (Anderson, 2017).

Regarding pitching moment, cases at 10 m/s recover lower C_M at low negative AoAs (-10° to 0°) and higher at low positive angles of attack (8° to 15°) compared to cases at 5 m/s (e.g. 0.0069 against 0.0058 at -5°). In contrast, all cases show similar values for high negative and positive AoAs (Figure 5f). In addition, while case for both velocities show a first stable fixed point at around -17°, the upwards sloping for low positive AoAs yields a C_M of 0 only for cases at 10 m/s, corresponding to an unstable fixed point near 8° and a stable one near 10° (Figure 5f). Despite those minute differences in C_M at low AoAs, the values are very similar overall for all cases, indicating there is very little effect of *Re* on stability in *Draco* for the range tested here.

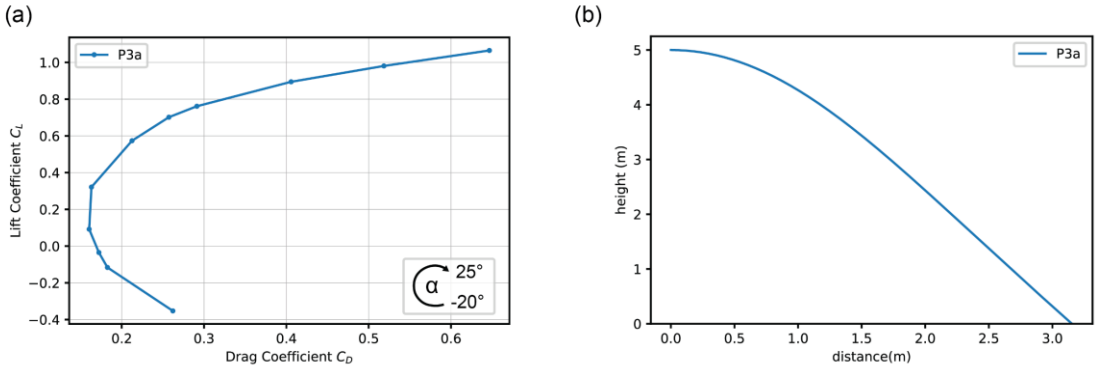

Figure 5-6: Aerodynamic and gliding performances for a *Draco* P3a geometry: (**a**) lift and drag coefficients under varying angles of attack α at a constant flow velocity U of 5 m/s; (**b**) trajectory simulation, gliding at a fixed α of 0 after jumping from a 5 m perch at an initial horizontal speed $V_h(0)$ of 2.5 m/s.

Validation

The present study relies on an entirely numerical approach to assess the gliding performances of *Draco volans*. Despite some degree of confidence being provided by sensitivity analyses, it is desirable to validate our computational setting by confronting our results to experimental data.

Studies on gliding flight in *Draco* are rare, and most rely on direct observations of live animals (McGuire and Dudley, 2005; Khandelwal and Hedrick, 2020, 2022) where aerodynamic

coefficients are calculated from recorded glide trajectories rather than directly measured. However, Clark et al. (2021) conducted wind-tunnel experiments based on 3D-printed geometries of two *Draco* species, including *D. maculatus* which is comparable in size and mass to our geometry (total length *l*: 197 mm; *m*: 5.9 g). Given the geometry used by Clark et al. (2021:fig. 3) is highly cambered and has the forelimbs positioned along the leading edge of the wing, we compare the results of Clark et al. (2021) to cases under a P3a geometry and a flow velocity of 5 m/s (Figure 6).

Comparisons of C_D and C_L (Figure 6a) to that reported by Clark et al. (2021) are hampered by the use of different reference areas *A*: the projected area of the wing and trunk here, but the area of the frontal surface of the geometry in Clark et al. (2021). Nevertheless, accounting for differences between natural conditions and computational models, as well as interspecific variability, our C_D of 0.65 and C_L of 1.06 recovered for a P3a geometry at an AoA of 25° are comparable to the mean values (C_D = 0.51; C_L = 1.43) calculated for live *D. dussumieri* at a mean AoA of 25.4° reported by Khandelwal et al. (2022) (a slightly larger species than *D. volans*, max SVL = 97 mm, Seekar et al., 2013).

As a second means of validation, we simulate the glide trajectory for a *Draco* P3a rigid-body geometry jumping from a 5 m perch at a horizontal speed of 2.5 m/s and gliding at an fixed angle of attack of 0°. These are the same initial conditions as those employed by Clark et al. (2021). Under those conditions, we estimate a gliding distance of 3.16 m for our P3a geometry (Figure 6b), which is slightly less than the 3.64 m reported by Clark et al. (2021) for a similar model of *D. maculatus* with a rigid tail. However, this difference is expected given ou geometry has a slightly larger mass, and thus wing loading (Table 2), both values being negatively correlated with glide distance in *Draco* (McGuire, 2003; McGuire and Dudley, 2005, 2011). Further supporting this point, the much larger model of *D. fimbriatus* of Clark et al. (2021) yielded a much shorter 2.93 m distance.

Thus, accounting for significant differences in experimental settings, our computational models conforms to the experimental wind-tunnel results obtained by Clark et al. (2021), and with some caution to the direct observations of Khandelwal and Hedrick (2022). It can thus be reliably applied to the study of gliding locomotion in *Draco*.

Table 5-4: Summary of the aerodynamic and gliding performances for all postures.

	P0	P1	P1a	P2	P2a	P3	P3a
$(CL/CD)_{max}$	2.96	3.34	2.93	3.73	3.25	2.93	2.73
AoA_{max}	10°	10°	10°	8°	5°	10°	8°
$Distance_{5m}$ (m)	3.45	3.44	3.44	3.72	3.41	4.33	4.14
$Time_{5m}$ (s)	1.11	1.01	1.11	1.13	1.01	1.21	1.20
Average $velocity_{5m}$ (m/s)	5.63	5.66	5.63	5.66	5.65	5.54	5.53
$Distance_{30m}$ (m)	62.61	68.61	61.90	86.07	66.46	74.99	68.92
$Time_{30m}$ (s)	7.17	7.56	7.10	10.05	7.33	10.69	9.66
Average $velocity_{30m}$ (m/s)	10.05	10.31	10.05	9.34	10.37	7.67	7.91

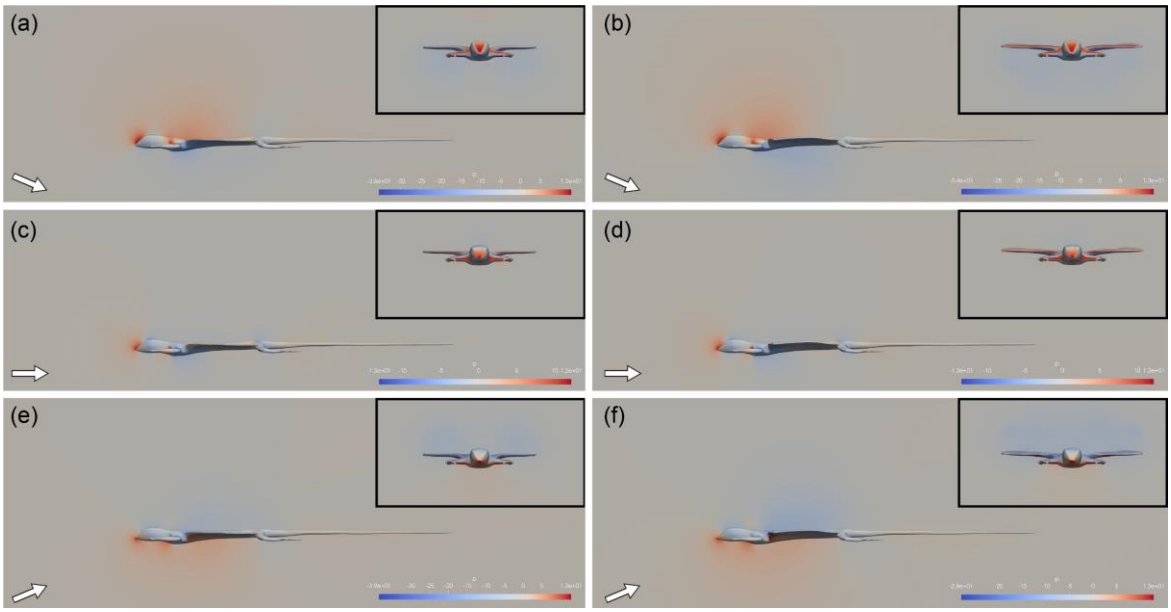

Figure 5-7: Pressure field around *Draco* geometries in lateral (sagittal plane) and anterior views (transverse plane immediately behind the wings) for P0 (left) and P1 (right) geometries for different angles of attack α: (**a**, **b**) α = -20°; (**c**, **d**) α = 0°; (**e**, **f**) α = 20°. Arrows indicate incoming airflow direction. Grey indicates initial value P = 0 Pa; U = 5 m/s), blue indicates lower values, red indicates higher values.

Influence of posture

Previous studies have shown that *Draco*'s gliding behavior relies on active control of its posture (Dehling, 2017; Khandelwal and Hedrick, 2022). Here, we assess the impact of three postural changes, namely the extension of the wing, the degree of camber of the body, and the positioning of the forelimb, on the aerodynamic performances of our seven *Draco volans* geometries (Table 4).

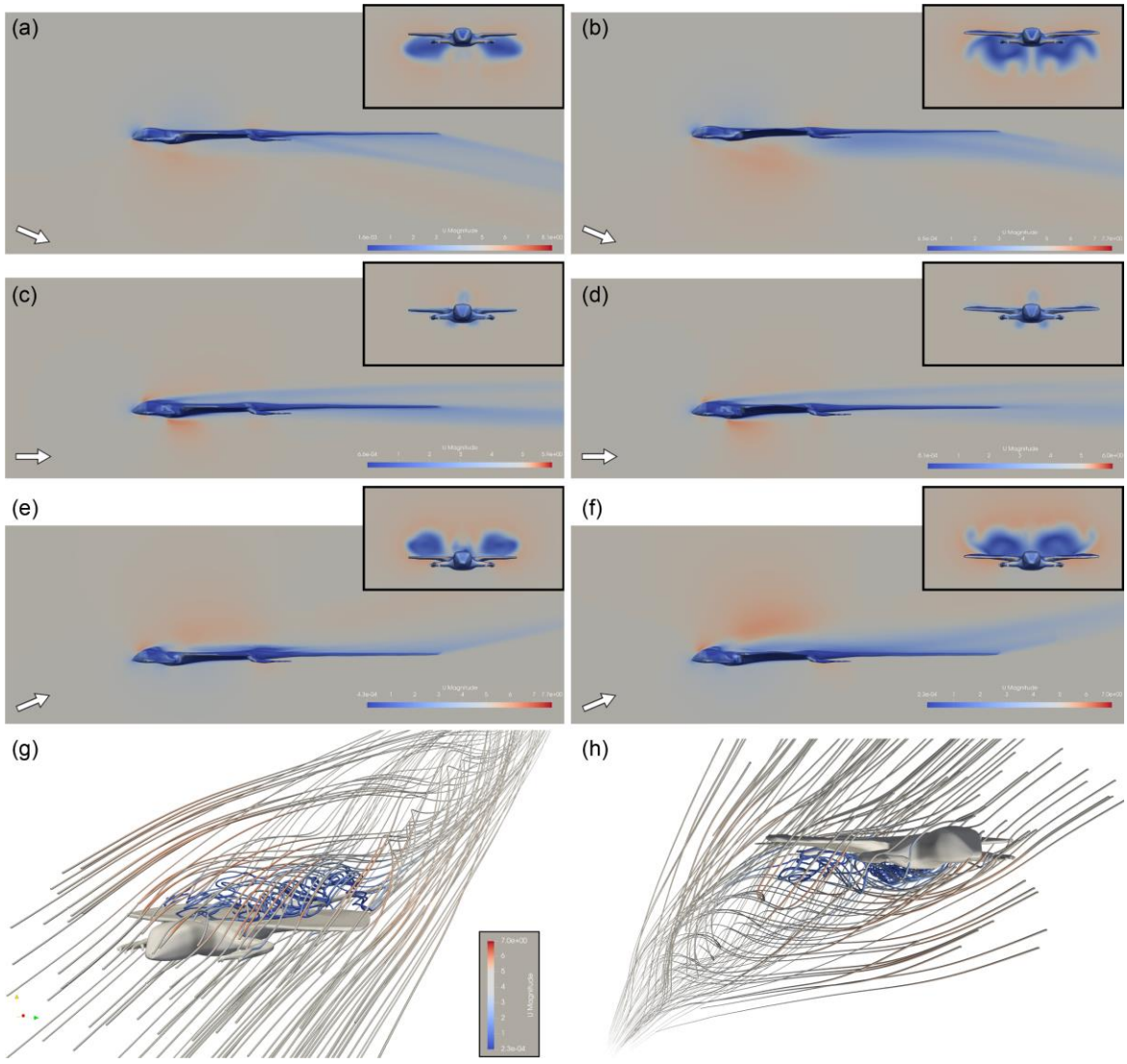

Figure 5-8: Velocity field around *Draco* geometries for different angles of attack α: (**a-f**) scalar fields in lateral (sagittal plane) and anterior views (transverse plane immediately behind the wings) for P0 (left) and P1 (right) geometries; (**g**, **h**) oblique view of streamlines representing the velocity field. (**a**, **b**, **h**) α = -20°; (**c**, **d**) α = 0°; (**e-g**) α = 20°. Arrows indicate incoming airflow direction. Grey indicates initial value P = 0 Pa; U = 5 m/s), blue indicates lower values, red indicates higher values.

Wing extension—As expected, for both P0 and P1, the surface facing the fluid flow (or frontal surface) is always subject to an increase in pressure due to the incoming airflow (Figure 7), and this overpressure is displaced dorsally for negative AoAs and ventrally for positive ones. Whereas there is little development of a pressure difference more posteriorly for an AoA of 0°, a slight underpressure develops below the wing for negative AoAs, and a stronger one is present over the upper surface of the wing for high positive AoAs (Figure 7). These pressure differences cover a larger area for P1 geometries due to the expansion of the wing.

Regarding velocity, regions of lesser speed can be seen running parasagittaly over the head and under the flanks of the animal at an AoA of 0° (best seen in anterior view, Figure 8c, d). The differences in velocity are much more prominent for high negative and positive AoAs where regions of lesser velocity form under the wing for negative AoAs and over its upper surface for positive ones. These regions correspond to the underpressure regions noted above, and are characterized by large vortices (Figure 8g, h). As seen in the scalar fields, these vorticies occupy a much larger area for the P1 geometry, which generates larger pressure differences due to the deployed wings and thus, larger trailing vortices.

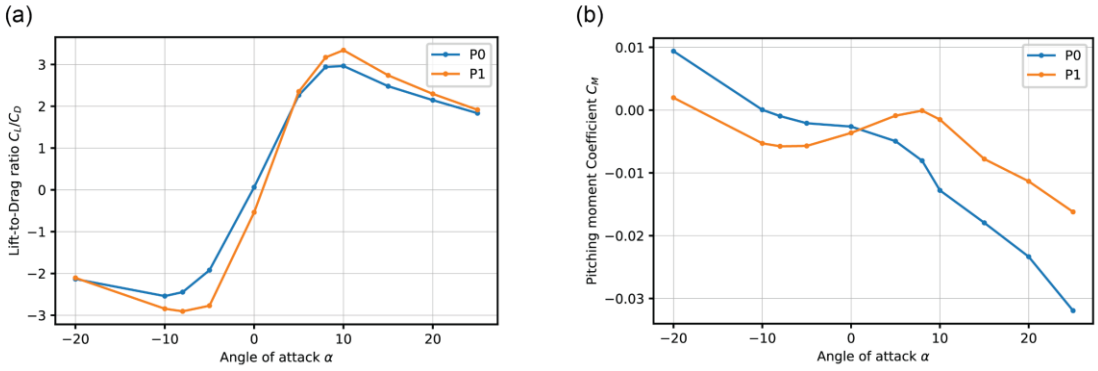

Figure 5-9: Comparison of gliding performances for *Draco* P0 and P1 postural geometries: (**a**) lift-to-drag ratio C_L/C_D under varying angles of attack α; (**b**) pitching moment coefficient against angle of attack.

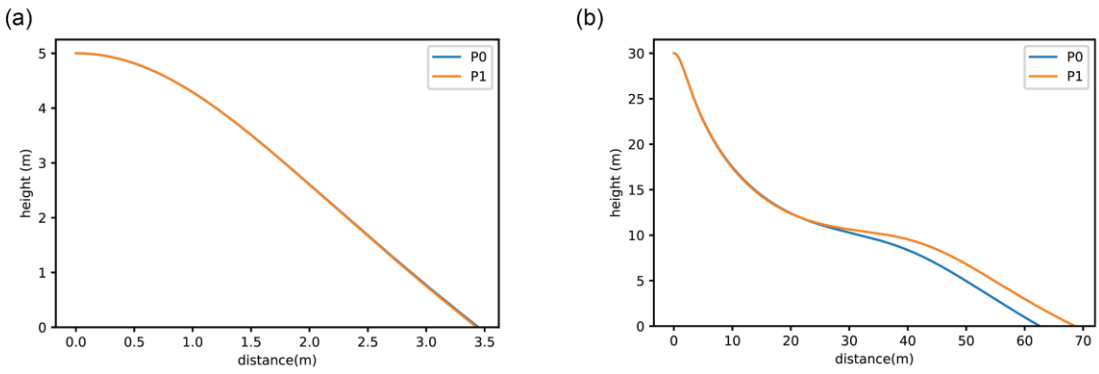

Figure 5-10: Trajectory simulation, gliding at fixed angle of attack α of 10° which maximizes the lift-to-drag ratio C_L/C_D after jumping from a 5 m (**a**) or 30 m (**b**) perch at an initial horizontal velocity $V_h(0)$ of 2.5 m/s.

Since the P0 and P1 geometries have different wing areas A (Table 2), which are involved in the calculation of their respective C_D and C_L (see Equation 2), there is little point in comparing their actual values. However, wing area is not a factor in the lift-to-drag ratio C_L/C_D (see Equation 2), a standard measure to describe gliding performance. The C_L/C_D ratio is proportional

to the horizontal distance covered by a glider, and its maximal value $(C_L/C_D)_{max}$ (which corresponds to a given AoA) characterizes a glide angle γ (the angle between *Draco* and the ground) which maximizes horizontal distance of a glide (Emerson and Koehl, 1990; Koehl et al., 2011). A lower $(C_L/C_D)_{max}$ indicates a steeper gliding angle, and consequently a shorter maximal horizontal distance.

The C_L/C_D ratio varies in a similar way for both P0 and P1 but the amplitude of values is smaller for P0 (Figure 9a). Both geometries thus reach their $(C_L/C_D)_{max}$ for an AoA of 10°, but that of P0 is lower than that of P1 (2.96 and 3.34 resp.). The simulated gliding trajectories from a jump of 5 m for a fixed AoA of 10° are nearly identical for the P0 and P1 postures, both gliding for about 3.45 m in 1.11 s, making for an average gliding speed of 3.43 m/s (Table 4). As for the P3a trajectory computed above, these results conform to that of Clark et al. (2021). In contrast, for a jump from 30 m P1 covers a longer horizontal distance (68.61 m) than P0 (62.61 m) and glides over a slightly longer time (P0: 7.17 s; P1: 7.56 s, Table 4, Figure 10b). These measures indicate an overall glide speed of 8.73 m/s for P0 and 9.08 m/s for P1.

As expected based on $(C_L/C_D)_{max}$, the gliding simulations for a 30 m jump show that a *Draco* with an expanded wing has a higher gliding performance (taken as maximal horizontal distance) than one with partially folded wings. For both geometries, the trajectory can be divided in (1), a ballistic phase (from heights 30 m to 15 m) where the weight is very large compared to aerodynamic force; (2) a mid-glide phase (heights 12 m to 10 m) of shallow slope, where the aerodynamic force largely counteracts weight; (3) a shallow descent phase (heights 10 m to 0 m) where the aerodynamic force only partially counteracts weight, increasing again the descent rate (Figure 10b). Note that these phases are only qualitative divisions, and should not be compared to the standard glide phases described by Khandelwal and Hendrick (2020).

The P0 and P1 geometries show nearly identical gliding behaviors during phase (1), but phases (2) and (3) cover a significantly longer horizontal distance and have a lower slope for P1 than for P0, indicating a stronger lift generation and weight compensation, and resulting in a longer glide.

Similarly to C_L and C_D, C_M also depends on the wing area A (see Equation 3). However, as A is constant, this does not change the stable fixed points, which occur for an AoA of about -18° for the P1 geometry and -10° for P0 (Figure 9b). In addition, the negative slope is much

stronger for P0 than P1 cases, indicating that a posture with extended wings generates les pitching moment overall, and is thus more stable.

Interestingly, for P1, the slope of C_M against AoA is positive for low AoAs (-5° to 8°) (Figure 9b). Whereas a negative C_M slope indicates stability in pitching (i.e. the pitching moment passively conteracts the angulation of the body due to AoA), a positive slope indicates instability in pitching (i.e. the pitching moment adds to the body angulation) (Koehl et al., 2011). This slope reaches a local maximum ($C_M = -8.6 \cdot 10^{-6}$) for an AOA of 8° which corresponds to an unstable fixed point. No such inversion in slope is present for P0, although the negative slope is significantly shallower also for low AoAs (Figure 9b).

In short, a *Draco* lizard with a partially folded wing is relatively stable in pitching for all AoAs while a *Draco* with expanded wings is stable for high negative and positive angles of attack (more so than for folded wings), but unstable for low AoAs.

Body camber—The pressure and velocity fields behave in a similar manner for geometries P2 and P3 as for P0 and P1 with regards to AoA (Figures 11, 12). However, the size of the underpressure and low velocity regions are much larger in P2, and even more so in P3, such that the vortices are larger, more developed and cover a broader area with increased camber.

As a side note, some cases show a bilaterally asymmetrical solution (e.g. Figures 11f, 12f). Since the timestep is tailored to reach a steady-state solution, we interpret this asymmetry as the result of the asymmetry of the original specimen, which was translated onto the geometry (see above).

In addition, the strong lowering of the tail in posture P3 creates a long region of lower pressure and velocity that is always located above its upper surface regardless of AoA (Figures 11, 12). Thus, the lowering of the tail indices further vortices in the wake of the animal, likely generating more drag. In addition, as this region of lesser pressure and velocity is present whether an underpressure or overpressure is present above the wing, it appears the role of the tail in drag generation is decoupled from body angulation.

The aerodynamic coefficients of the P1, P2, and P3 cases show that C_L markedly increases with camber (Figure 13a), which conforms to the larger areas of underpressure and lower velocity observed (Figures 11, 12). This is particularly striking for high negative AoAs (-0.40

and -0.71 resp. at -20°) whereas for high positive AoAs the increase is much smaller (1.04 and 0.81 resp. at 25°).

C_D also increases with camber (Figure 13a), although P1 has a higher value than P2 and P3 at high negative AoAs (0.34, 0.28, and 0.29 resp. at -20°). The increase in C_D with camber is particularly striking at high positive AoAs (P1: 0.42; P2: 0.50; P3: 0.63 at 25°). As for C_L, this increase in C_D conforms with the strong pressure and velocity differences observed and their induced vortices (Figures 11, 12).

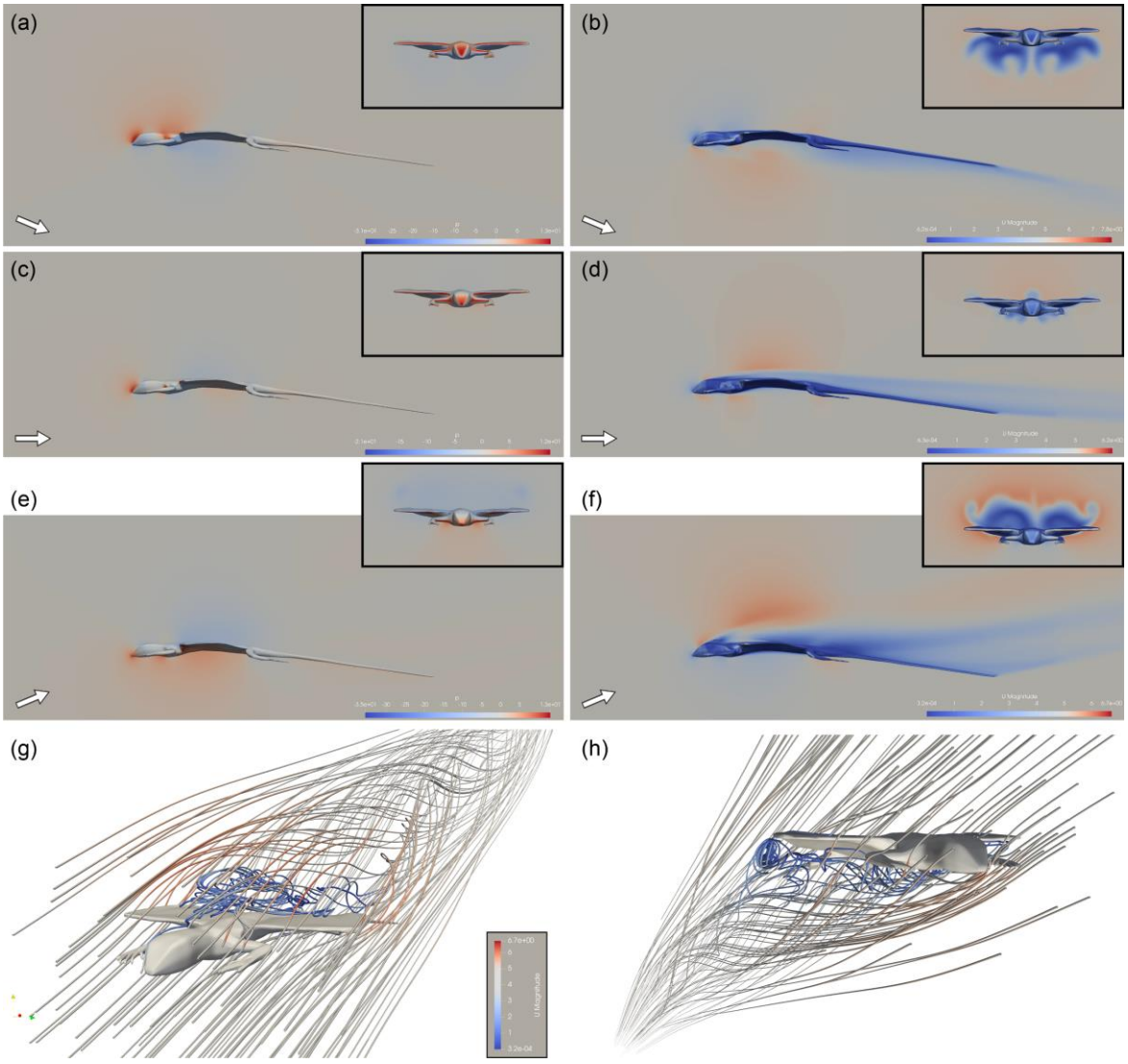

Figure 5-11: Pressure (**a**, **c**, **e**) and velocity (**b**, **d**, **f**-**h**) fields around a *Draco* P2 geometry for different angles of attack α: (**a**-**f**) scalar fields in lateral (sagittal plane) and anterior views (transverse plane immediately behind the wings); (**g**, **h**) oblique view of streamlines representing the velocity field. (**a**, **b**, **h**) α = -20°; (**c**, **d**) α = 0°; (**e**-**g**) α = 20°. Arrows indicate incoming airflow direction. Grey indicates initial value P = 0 Pa; U = 5 m/s), blue indicates lower values, red indicates higher values.

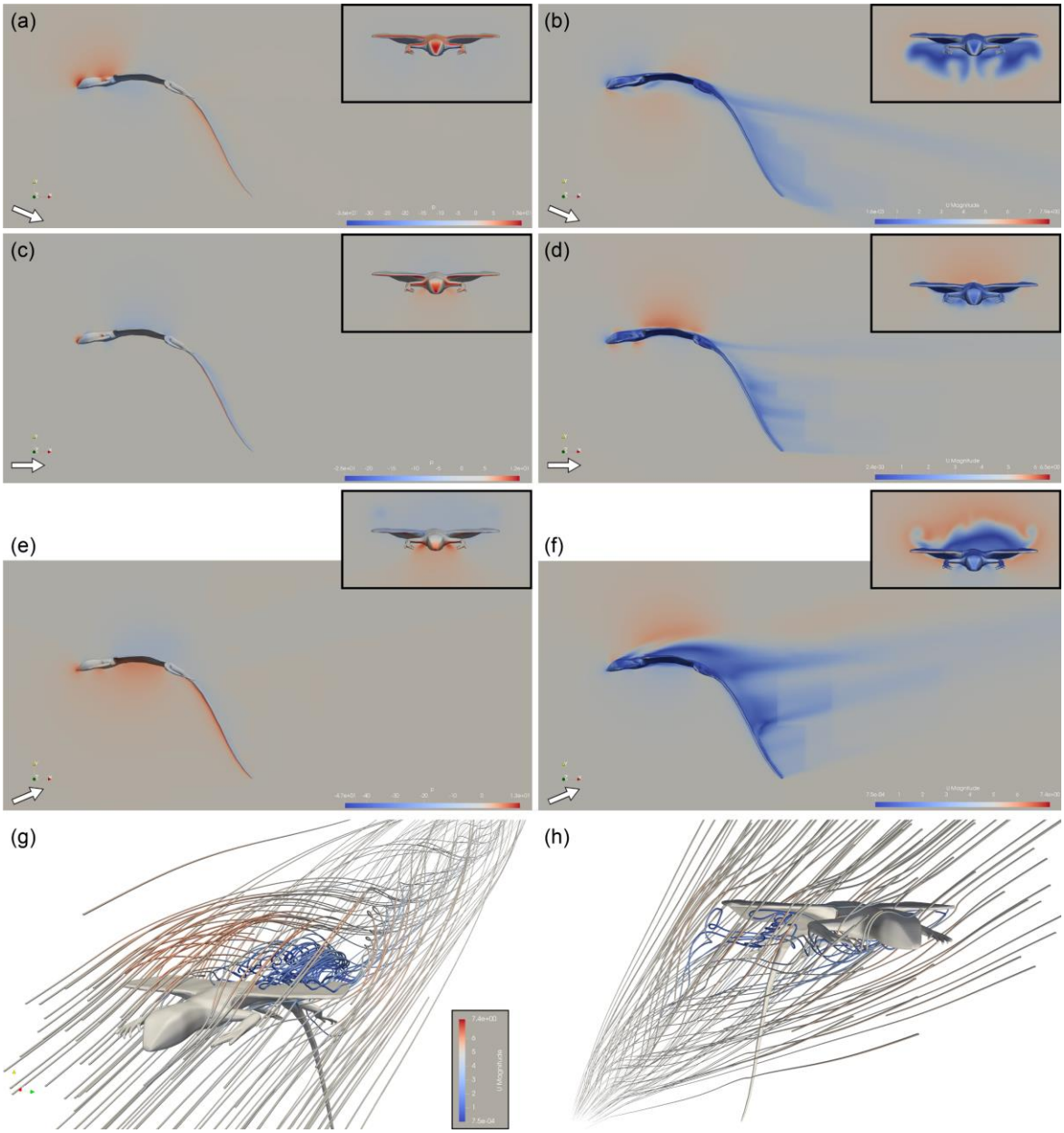

Figure 5-12: Pressure (**a**, **c**, **e**) and velocity (**b**, **d**, **f**-**h**) fields around a *Draco* P3 geometry for different angles of attack α: (**a**-**f**) scalar fields in lateral (sagittal plane) and anterior views (transverse plane immediately behind the wings); (**g**, **h**) oblique view of streamlines representing the velocity field. (**a**, **b**, **h**) α = -20°; (**c**, **d**) α = 0°; (**e**-**g**) α = 20°. Arrows indicate incoming airflow direction. Grey indicates initial value P = 0 Pa; U = 5 m/s), blue indicates lower values, red indicates higher values.

The lift-to-drag ratio C_L/C_D increases markedly with camber for negative AoAs, but the values are more similar for positive AoAs (Figure 13c). There does not appear to be a correlation between the value of $(C_L/C_D)_{max}$ and camber. Indeed, as mentioned above, P1 reaches a $(C_L/C_D)_{max}$ of 3.34 at 10° whereas P2 reaches a $(C_L/C_D)_{max}$ of 3.73 at 8°, and P3 a $(C_L/C_D)_{max}$ of 2.93 at 10°. Given the higher $(C_L/C_D)_{max}$ of P2, we expect this geometry to cover a greater

distance than all others. For a 5 m jump, this does not appear the case. Indeed, while, P2 covers a distance of 3.72 m, more than P0, P1, P1a or P2a, P3 and P3a cover longer distances of 4.33 and 4.14 respectively (Table 4).

However, when jumping from a 30 m perch, P2 indeed produces a longer glide 86.07 m in 10.05 s) with P3 falling slightly shorter (74.99 m in 10.69 s), and P1 even more 68.61 m in 7.56 s) (Figure 14). Interestingly, the average velocity was highest for P1 (10.31 m/s) and higher for P2 (9.34 m/s) than P3 (7.67 m/s), and thus does not appear directly correlated to gliding distance.

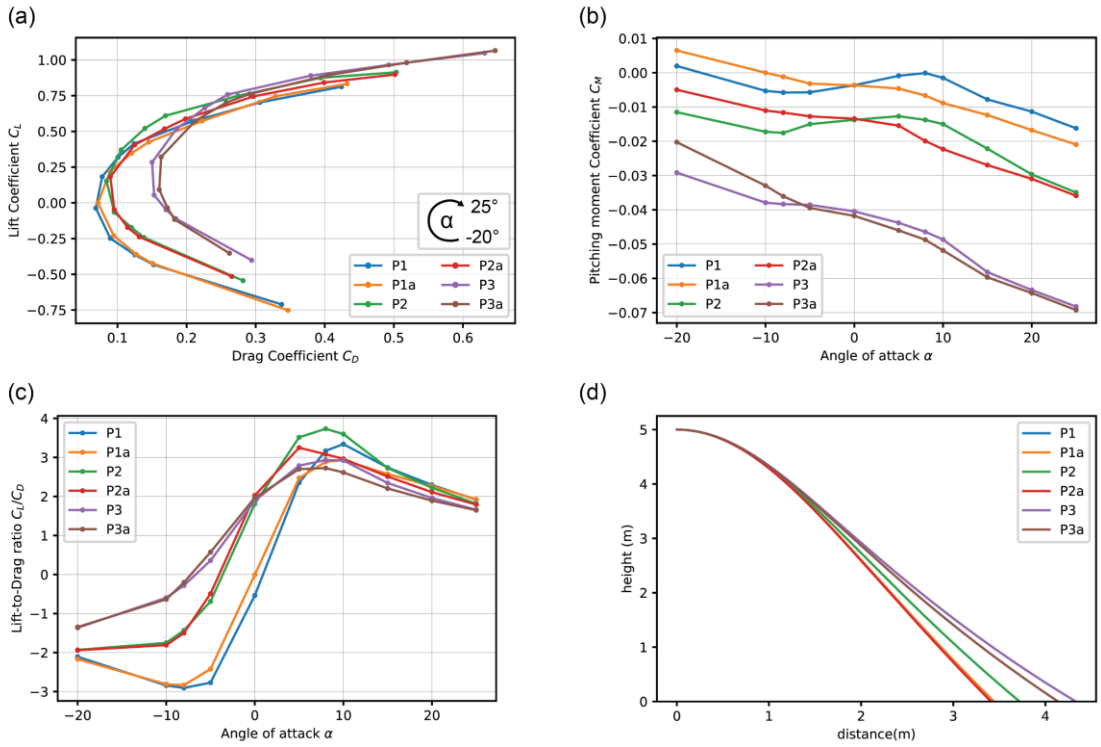

Figure 5-13: Aerodynamic and gliding performances for different *Draco* postural geometries: (**a**) lift and drag coefficients under varying angles of attack α; (**b**) pitching moment coefficient against angle of attack; (**c**) lift-do-drag ratio C_L/C_D against angle of attack; (**d**) Trajectory simulations, each geometry gliding at fixed angle of attack α which maximizes the lift-do-drag ratio C_L/C_D after jumping from an 5 m perch at an initial horizontal velocity $V_h(0)$ of 2.5 m/s.

As described above for P1, all gliding trajectories for a jump from 30 m can be divided into informal ballistic (1), mid-glide (2), and shallow descent (3) phases (Figure 14). P3 has the shortest phase (1) and thus falls for the shortest distance (< 10 m, Figure 14) before its horizontal acceleration overcomes its vertical one. However, P3 also has the shortest and steepest phase (2). As a result, the onset of phase (3) occurs earlier in P3, which explains why it covers

a shorter distance than P2. P2 shows a phase (1) that is only slightly longer than in P3 (< 15 m fall), but its phase (2) shows a nearly horizontal slope (Figure 14), meaning the horizontal acceleration of the animal is much stronger than its vertical one. As a result, the animal loses virtually no height for about 20 m of horizontal gliding. Thus, phase (3) starts from 10 m higher than for P1, which explains why this posture covers such a long distance.

C_M shows a marked decrease with camber (P1: -0.0036; P2: -0.0137; P3: -0.0405 at 0°), indicating more cambered geometries are less stable for the observed range of AoAs. As a result, P2 and P3 never show a C_M of 0 in the studies range of AoAs (-20° to 25°). These geometries thus do not show an AoA of no pitching moment in this range (Figure 13). Furthermore, the slope of C_M against AoA is similar for all cambers except in the range of low AoAs where an inversion in slope was noted above for P1. In this range, P2 also shows an inversion although its positive slope is shallower indicating less unstability, whereas there is no inversion noted for P3, which is stable in pitch for all AoAs.

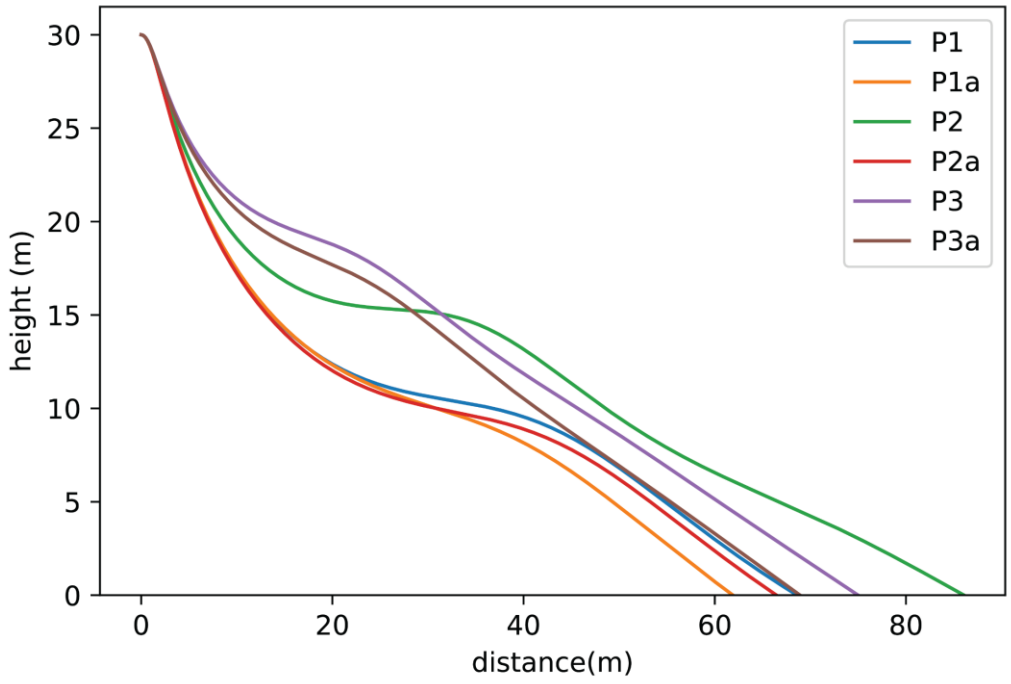

Figure 5-14: Trajectory simulations, each geometry gliding at fixed angle of attack α which maximizes the lift-do-drag ratio C_L/C_D after jumping from an 30 m perch at an initial horizontal velocity $V_h(0)$ of 2.5 m/s.

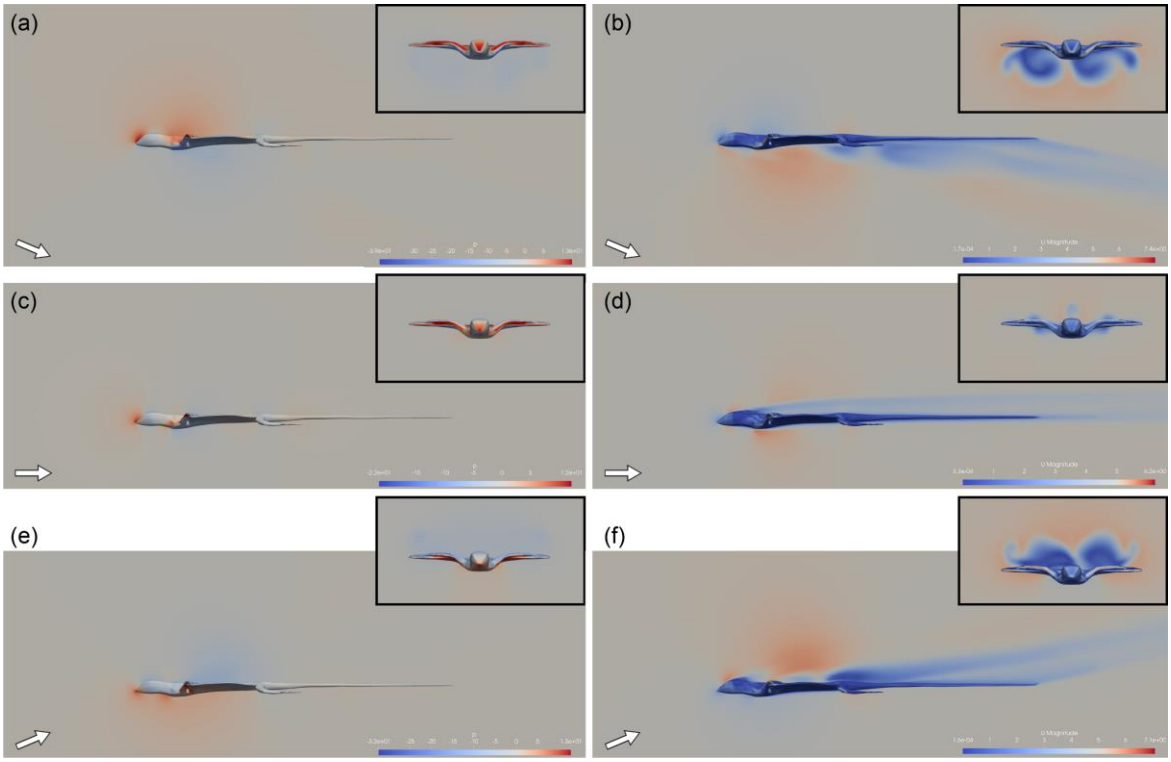

Figure 5-15: Pressure (**a**, **c**, **e**) and velocity (**b**, **d**, **f**) fields around a *Draco* P1a geometry in lateral (sagittal plane) and anterior views (transverse plane immediately behind the wings) for different angles of attack α: (**a**, **b**) α = -20°; (**c**, **d**) α = 0°; (**e**, **f**) α = 20°. Arrows indicate incoming airflow direction. Grey indicates initial value P = 0 Pa; U = 5 m/s), blue indicates lower values, red indicates higher values.

Forelimb position—The pressure and velocity fields behave mostly similarly between the P1a and P1 geometries with respect to AoA, although there are some significant differences that are best seen in the velocity field (Figure 15). Indeed, at 0°, the P1 geometry shows trails of lesser velocity along the lower surface of the flanks (Figure 8), but in P1a these trails have been displaced to the medial underside of the wings (best seen in anterior view, Figure 15d).

In a similar manner, the regions of lesser velocities are also slightly displaced posteriorly and less regular in the P1a then in the P1 geometry. For an AoA of 20°, the region of lesser velocity above the wings appear much smaller than in P1, but these regions are similar in size immediately after the wing (Figures 8, 15). This coincides with the formation of a pair of funnel-shaped vortices above each wing in P1a, contrasting with the more formless streamlines seen for P1 (Figures 8, 16).

Further supporting this point, for all degrees of camber, the vortices generated both above the wing for positive AoAs and below if for negative AoAs all appear to form circular whirls

and are much larger and slightly more posteriorly positioned in arms- transverse postures rather than in their arms-first counterparts (Figures 8, 11, 12,16).

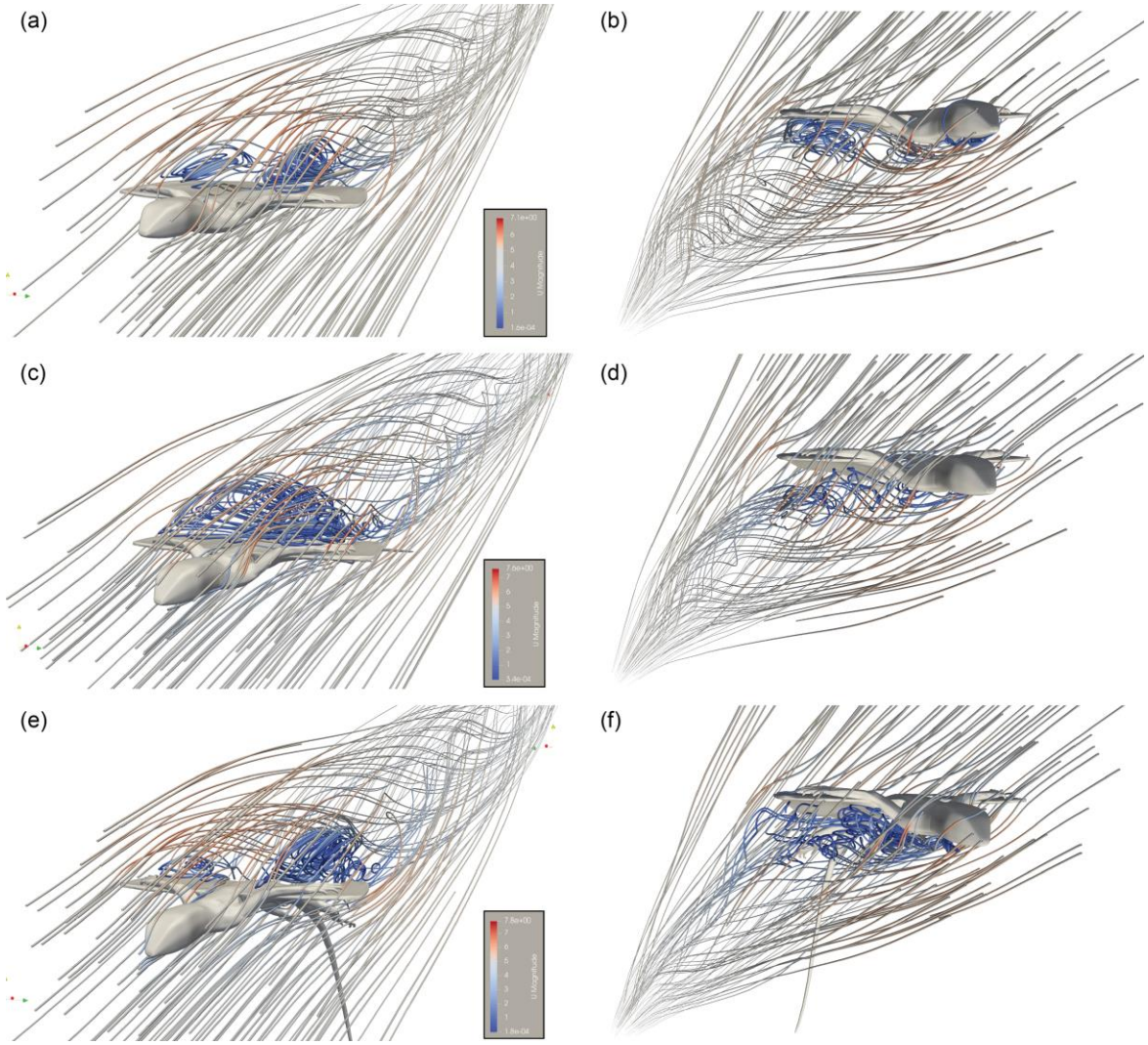

Figure 5-16: Oblique view of streamlines representing the velocity field around *Draco* P1a (top row), P2a (middle row) and P3a (bottom row) geometries for different angles of attack α: (**a**, **c**) α = 20°; (**b**, **d**) α = -20°. Grey indicates initial value P = 0 Pa; U = 5 m/s), blue indicates lower values, red indicates higher values.

It thus appears that the positioning of the arms along the leading edge of the wing has an impact on the shape and development of vortices, which are more posteriorly positioned, pushing the flow separation, and thus the generation of form drag more posteriorly along the animal.

The C_D and C_L coefficients are very similar between corresponding arms-first and arms-transverse postures (Figure 13a), and the difference in forelimb position does not seem to affect the

changes observed above for increasing camber. However, we note a significant increase in C_D for arms-transverse geometries at low positive AoAs (5° to 15°), which is most striking between the P2 and P2a geometries (0.14 and 0.17 resp. at 8°). Based on the ventral displacement of the frontal surface of the animal with increasing AoAs, we suggest the 5°-15° range is the range where the transverse position of the arm contributes most to the frontal surface, thus increasing drag.

The lift-to drag ratios are very similar for identical postures differing only in the position of the forelimbs except for AoAs between 5° and 15° where the postures with transverse arms show much lower $(C_L/C_D)_{max}$ values than their counterparts (e.g. P1: 3.34 ; P1a: 2.93) (Table 4; Figure 13c). For both P2a and P3a, this is obtained for slightly lower AoAs (5° and 8° resp.) than their counterparts P2 and P3 (8 and 10 resp.) (Table 4).

Given these differences in $(C_L/C_D)_{max}$, we expect the transverse positioning of the arms to have a negative impact on gliding distance for all geometries. This appears to be the case for a jump from a 5 m perch (Figure 13d). There is indeed hardly any difference in gliding distance between the P1 and P1a geometries (Table 4) but P2a and P3a cover markedly shorter distances (3.41 m and 4.14 m resp) than their counterparts P2 and P3 (3.72 m and 4.33 m resp.).

The gliding simulations starting from a 30 m perch yield very similar results (Figure 14). P1a indeed glides for a much shorter distance than P1 (61.90 m and 68.61 m resp.), similar to P3a and P3 (68.92 m and 74.99 m resp.) (Table 4). Lastly, P2a covers a much shorter distance and glides for a shorter time (66.46 m in 7.33 s) compared to P2 (86.07 m in 10.05 s).

Regarding informal gliding phases, all arms-transverse postures differ from their counterparts in their stronger slopes during mid-glide phase (phase (2)). Furthermore, P2a has a ballistic phase (phase (1)) that is much longer than that of P2, resulting in a fall of an additional 5 m, resulting in a much shorter glide (Figure 14).

The C_M values are also rather similar between corresponding geometries, showing an overall decrease in C_M with increased camber (Figure 13a). However, the slope of C_M against AoA differs slightly. All geometries show much higher C_M for high negative AoAs (P2: -0.0349; P2a: -0.0359 resp. at -20°), and lower C_M for low positive AoAs (P2: -0.0150; P2a: -0.0223, resp. at 10°). The C_M values for high positive AoAs are roughly identical for P2 and P2a, and

P3 and P3a but those of P1 are higher than those of P1a (-0.016 and -0.021 resp. at 25°). This indicates all geometries are less stable for high negative AoAs.

Interestingly, the decrease in negative sloping for low AoAs observed above for all arms-first geometries, and inversion in slope for P1 and P2, is almost entirely absent in arms-transverse geometries (Figure 13a). In fact, the slope of C_M appears nearly constant. Thus, it appears that positioning the arms transversely negates the region of instability observed for other geometries.

Discussion

Wing expansion and take-off

Our systematic examination of three postural changes, namely the extension of the wing, the degree of camber of the body, and the positioning of the forelimb confirms that all changes have a direct impact on the aerodynamic performances of *Draco volans*. This conforms to previous physical experiments and direct observations that indicated that *Draco* relies heavily on active control of its posture for gliding (Dehling, 2017; Khandelwal and Hedrick, 2022), which is confirmed here for the first time using Computational Fluid Dynamics.

During gliding, *Draco* is subject to several postural constraints. Among those, all reports indicate that the animal deploys its wing after take-off (Dehling, 2017; Khandelwal and Hendrick, 2020). Thus, there is a short time frame during which *Draco* is airborne with its wing only partially unfolded. A recorded take-off by Dehling (2017:fig. S2) shows the wing first fully extended 0.4 s after take-off, which incidentally corresponds to the mean duration for the take-off phase observed by Khandelwal and Hendrick (2020). It thus seems that *Draco* is constrained to a posture with partially folded wings for most of this phase, although we stress this assessment requires further quantification effort.

Our CFD analyses show that a posture with incompletely expanded wings (our P0 geometry) generates markedly more pitch-up moment (positive C_M coefficient) for high negative angles of attack (AoA) compared to a posture with completely unfolded wings (Figure 9b). In other words, a *Draco* individual gliding at a high negative AoA tends to passively reorient itself horizontally more when its wings are unfolden than folded. Given that all glide trajectories start

with a ballistic take-off phase (Khandelwal and Hendrick, 2020), it appears this constrained posture is actually well suited to passively enhance any active righting mechanism exerced by the animal during the unfolding of the wing.

In addition, the take-off phase allows the animal to gain the necessary speed to generate enough lift for gliding (Khandelwal and Hendrick, 2020). We note that the small time-frame in which the wing is unfolded is subject to less frictional drag as its frontal surface is smaller (Figure 7), thus maximizing speed gain. In short, despite resulting from a strict morphological constraint, we remark that an unfolded posture is actually well-suited for take-off in gliding lizards.

Are arms-first postures actually viable?

Draco has traditionally been represented in an arms-first posture (e.g. Colbert, 1967; Shine et al., 1998; McGuire, 2003; McGuire and Dudley, 2011). However, progress in motion capture technology recently demonstrated that flying lizards mostly glide with their arms in a transverse position along the leading edge of the wings (Dehling, 2017; Khandelwal and Hendrick, 2022), suggesting that this posture is favored by *Draco* for gliding.

Yet, our glide trajectory simulations show that a *Draco* individual adopting an arms-first posture should consistently outperform an identical lizard with an arms- transverse posture, resulting in a much longer maximal gliding distance, sometimes tens of meters longer (Figure 14). This result is in stark contrast with observed behavior for *Draco*, prompting the question of the viability of arms-first postures despite their theoretically greater gliding efficiency.

Our CFD results show that the maximal value of lift-to-drag ratio $(C_L/C_D)_{max}$ corresponds to an AoA between 5° and 10° for all arms-first postures depending on the degree of camber (Figure 13c). These conditions correspond to the maximal gliding efficiency described above. However, when taking into account pitching moment (Figure 13b), it becomes apparent that those AoAs correspond to an unstable region where the animal passively adds to its body angulation. In practical terms, keeping the constant angle of attack that maximizes the lift-to-drag ratio would require constant active adjustment. This seems very undesirable, as it would make *Draco* highly unstable against both passive perturbations (e.g. a gust of wind), or active ones (e.g. obstacle avoidance). Moreover, when taken in the context of a glide, transitioning from a

ballistic glide of high negative glide angle (and it is assumed high negative angle of attack), to an AoA of 5° to 10° would require constant control of body orientation while gliding at high velocities, which again seems undesirable.

Furthermore, by observing differences in the pressure and velocity fields around both arms-first and arms-transverse *Draco* geometries (Figures 8, 11, 12, 16), it appears that the latter postures generate much better-formed, whirl- or funnel-shaped vortices above the wing for positive AoAs (such as those that maximize the lift-to-drag ratio Figure 13c). These vortices are also more posteriorly positioned along the body. Given the difference in shape and location of the vortices, it appears that arms-transverse geometries push fluid separation backwards in the wake of the animal, thus reducing drag.

Lastly, the pressure field shows that the leading edge of the wing is always subject to a strong overpressure due to the incoming airflow (Figures 8, 11, 12, 15). Thus, we suspect that the trunk musculature of *Draco* alone might not be sufficient to entirely unfold the wings and keep them open during gliding to generate more lift. The appendicular musculoskeleton indeed appears much better-suited for this task, given its involvement in holding the patagium open in other tetrapod gliders, and its active role in all flyers (Norberg, 1990; Alexander, 2015). However, this assertion warrants further quantification. Given the evidence presented here, we suggest that several lines of argument, namely pitch stability, drag reduction and keeping the wings open, could explain why *Draco* nearly always operates under an arms-transverse posture despite an arms-first posture being theoretically more effective.

A cautionary note on the assessment of gliding performance

The discussion regarding the viability of the arms-first posture in *Draco* highlights the caveat of using only a single measure to quantify the aerodynamic performances of an animal.

Indeed, measures dependent on the lift coefficient C_L such as the maximum lift-to- drag ratio $(C_L/C_D)_{max}$ or the minimum airspeed U_{min} (the minimum velocity needed to generate enough lift to glide for a given AoA) are commonly used to assess the gliding efficiency of animals (Emerson and Koehl, 1990; Koehl et al., 2011). However, our study highlights the use of the pitching moment coefficient C_M which can help to determine the ranges of the previously mentionned measures that are actually viable. This is particularly important concerning taxa for

which direct observations are lacking, either due to difficulty in obtaining those data for extant organisms as was previously the case for *Draco*, or because the studied taxa are extinct (there are a variety of extinct gliding reptiles, dating as early as ca. 260 million years ago in the late Permian Period, McGuire and Dudley, 2011; Buffa et al., 2021, 2022; Pritchard et al., 2021).

Conclusion

The Computational Fluid Dynamics (CFD) analyses conducted here show that *Draco volans* generates large whirl-shaped vortices above its patagial wings during gliding that produce the lift necessary for gliding flight. Furthermore, our results confirm that posture has a direct impact on the aerodynamic performances in this animal, corroborating previous observations and physical experiments. In particular, our systematic description of wing extension, increased body camber, and forelimb positioning through the comparison of rigid-body models highlights the following points: (1) *Draco* generates large whirl-shaped vortices above and below their wings during gliding that produce the necessary pressure differences to generate lift; (2) the initial ballistic glide is subject to some passive nose-up pitching that tends to stabilize the animal, and can be supplemented by active reorientation; (3) stronger camber increases aerodynamic efficiency, but not necessarily gliding performance; (4) the traditionally represented arms-first posture is not aerodynamically viable, which conforms to its absence in recorded glides.

The present systematic description should serve as a detailed basis for further comparisons of gliding flight in *Draco* or other aerial animals. In addition, it should also be useful for the study of the aerodynamics of extinct gliding reptiles, for which modeling approaches represent the only methods to assess aerodynamic and gliding performance. Lastly, we stress the need to use different measures as a means to assess the aerodynamic and gliding performances of extant taxa, in particular through the study of pitching moment, which can help distinguishing between viable postures in gliding animals.

Chapter 6: Gliding performances of the World's first flying reptiles

> At the time of writing, the present chapter is very close to submission as a research article co-authored with P. Cinnella (IDA), E. Frey (SMNK), J.-S. Steyer (MNHN), and M. Laurin (MNHN).

Abstract—The gliding performances of the gliding reptile *Coelurosauravus elivensis* from the late Permian of Madagascar are studied here using a Computational Fluid Dynamics model. The comparison of gliding postures indicates *C. elivensis* generated lift through the creation of vortices above its wings during gliding in a manner convergent with other reptilian gliders. Trajectory simulations show that *C. elivensis* was capable of efficient gliding, bringing strong support to previous suggestions that weigeltisaurids represent the World's first gliding vertebrates. Surprisingly, *C. elivensis* appears capable of an oscillatory glide mode allowing for a passive climb-up while gliding between trees, contrary to the continuous descent shown by extant gliders. Lastly, the calculated gliding performance of *C. elivensis* are only reasonably efficient under the higher air density reconstructed for the Permian Period, suggesting the evolution of large size in weigeltisaurids may have been permitted by this hyperdense atmosphere.

Introduction

Major habitat transitions and the evolution of novel locomotor modes have shaped the evolutionary history of vertebrates, and are responsible for much of the past and present diversity of tetrapods (e.g. Laurin, 2010; Alexander, 2015; Vermeij and Motani, 2018; Gutarra and Rahman, 2020). Among such changes, the evolution of gliding flight, whereby an animal performs a controlled descent by converting potential energy to aerodynamic work, is a relatively common phenomenon in arboreal animals (Norberg, 1990; Dudley et al., 2007; Socha et al., 2015). More than thirty distinct lineages of arboreal tetrapods indeed show morphological specializations to lift generation, including several extinct groups (McGuire and Dudley, 2011; Dececchi et al., 2020; Martin-Silverstone et al., 2020).

Among those lineages, weigeltisaurid reptiles from the late Permian of Madagascar and Europe are the earliest known gliding vertebrates (Bulanov and Sennikov, 2006, 2010; Buffa et al., 2021, 2022; Pritchard et al., 2021). These small arboreal reptiles (ca. 20 cm in snout-vent length SVL, Buffa et al., 2022) show rows of long bony spars on either side of the body that supported a pair of broad membranous wings, enabling them to glide (Frey et al., 1997; Schaumberg et al., 2007; Pritchard et al., 2021; Buffa et al., 2022). Weigeltisaurids being the earliest known gliding vertebrates, their study is paramount to our understanding of the evolution of vertebrate flight. However, little is known of the actual aerodynamic performances and gliding behavior of these animals, and the only assessment to date suggests they might be better considered parachuters rather than true gliders because of their large size (McGuire and Dudley, 2011).

In the absence of direct observations, the study of the locomotion of extinct animals has to rely on other lines of evidence to produce inferences of performance and behavior. Biomechanical analyses provide quantitative measures to infer the locomotion of extinct organisms and have gained much attention from paleontologists in recent years (e.g. Rayfield, 2007; Bright, 2014; Rahman, 2017, 2020; Gibson et al., 2021), including for the study of extinct gliders (Stein et al., 2008; Koehl et al., 2011; Dyke et al., 2013; Dececchi et al., 2020). Computational Fluid Dynamics (CFD) provides numerical methods to simulate the flow of a fluid interacting with a solid surface, and has been recently applied in paleobiological studies of extinct marine organisms (Rahman, 2017, 2020; Gutarra et al., 2019; Gibson et al., 2021). However, it has yet to be applied to an extinct flying or gliding tetrapod.

We thus provide here the first quantitative study of gliding flight in the best known weigeltisaurid *Coelurosauravus elivensis* from the late Permian Sakamena Formation of Madagascar (Carroll, 1978; Buffa et al., 2021, 2022) using CFD. We make detailed comparisons to an extant analog to *C. elivensis*, the agamid flying lizard *Draco volans*, that was recently studied using similar methods (see Chapter 5 of this dissertation). The present CFD study thus relies on an actualistic approach to infer the gliding behavior of the world's first gliding reptiles.

Institutional abbreviations— IPS, Institute for Photon Science and Synchrotron Radiation, Karlsruhe, Germany; KIT, Karlsruhe Institute of Technology, Kalrsruhe, Germany; LSUMZ, Louisiana State Museum of Natural History, Bâton-Rouge, Lousiana, USA; SMNK, Staatliches Museum für Naturkunde Karlsruhe, Karlsruhe, Germany; TWCMS, Sunderland Museum, Tyne and Wear County Museums, Sunderland, U.K.

Materials and methods

Computational Fluid Dynamics (CFD) numerically simulates the flow of a fluid in a computational domain built to encompass the region understudy. Here, this region corresponds to a large volume surrounding the solid body, as is typical of external flows (Rahman, 2017, 2020; Hebdon et al., 2020; Gibson et al., 2021).

A typical CFD workflow can be divided in three main steps: (1) the construction of the 3D model of the object under study (hereafter 'geometry'); (2) the set up of the CFD calculations (computational domain, mesh generation, turbulence model, numerical solver, boundary and initial conditions); (3) the post-processing of the calculation results.

The geometries used for biomechanical studies of aquatic or aerial locomotion of tetrapods are generally much smoother than the real animal (e.g. excluding fur or squamation), but still provide a faithful reproduction of the body plan and soft tissue volume of the animal (e.g. Stein et al., 2008; Koehl et al., 2011; Dyke et al., 2013). This is typically the case in CFD analyses (e.g. Kogan et al., 2015; Liu et al., 2015; Dec, 2019; Gutarra et al., 2019, 2022; Troelsen et al., 2019; Zhao et al., 2019). However, producing such geometries can be challenging for extinct animals where no data on soft tissue is available (Rahman, 2017).

Geometry construction of *C. elivensis*

The production of a fleshed-out geometry of *Coelurosauravus elivensis* comes with several challenges. Based on all available specimens, and additional information from the well-preserved *Weigeltisaurus jaekeli* from Western Europe, Buffa et al. (2021, 2022) reconstructed *C. elivensis* as a moderate-sized animal (180 mm SVL), and provided reconstuctions in dorsal and lateral views, allowing for a three-dimensional perception of the animal for the first time. However, while the authors suggested that the patagial wing of *C. elivensis* originated from the ventral flanks of the animal contrary to modern reptilian gliders (e.g. *Draco*, Colbert, 1967; John, 1970; Russell and Dijkstra, 2001), they also stressed that this interpretation warranted further study (Buffa et al., 2022).

Skeletal reconstruction and wing anchoring—To palliate the uncertainty regarding the exact position of the wing relative to the body of the animal, we studied the best- preserved specimen of *W. jaekeli*, SMNK-PAL 2882 from the Late Permian of Germany using Computed Laminography (CL), a technique similar to Computed Tomography (CT) but designed to tackle flattened specimens (Zuber et al., 2017). This specimen was CL-scanned (voxel size 6.91 m) at the IPS Synchrotron facility in KIT. All vertical slices were converted from 32 bits to 8 bits using ImageJ v.2.1.0, and only the slices comprising the specimen (186 slices) were kept to save storage space. The slices were then imported into the 3D segmentation software Mimics v.21.0 (Materialise, Leuven, Belgium), and three-dimensional surface models of selected gastralia and patagials were generated in individual masks using the threshold tool for given grey levels.

The surface models derived from the CL-scan of specimen SMNK-PAL 2882 unambiguously show a one-to-one articulation between patagials and gastralia (Figure 1). A close articulation between both structures in this specimen had been tentatively proposed by Pritchard et al. (2021) but remained equivocal. Buffa et al. (2022) described a similar relationship in *C. elivensis*, and we thus suggest that all weigeltisaurids show such a one-to-one patagio-gastralial articulation.

Although the exact orientation of the gastralia relative to the transverse plane remains unclear, their orientation as preserved in SMNK-PAL 2882 is orthogonal with the main axis of the vertebral column, at least in the anterior trunk (Figure 1a). This does not appear to be the case in the posterior trunk where the gastralia appear more curved (Schaumberg, 1976; Pritchard, 2021),

but we suggest this would not have resulted in an inflated abdomen as the ribs in this region are shorter (Pritchard et al., 2021; Buffa et al., 2022).

Given that gastralia are small splint-like dermal bones found in the skin of the abdomen in reptiles (Claessens, 2004; Vickaryous and Hall, 2008), these observations provide the first unequivocal evidence that the patagial wing of weigeltisaurids extended from the ventral portion of the flanks, contrary to that of more recent reptilian gliders such as kuehneosaurids or *Draco* in which the patagium is more dorsally positioned and supported by the dorsal ribs (Robinson, 1962; Colbert, 1967, 1970; John, 1970; Russell and Dijkstra, 2001; Stein et al., 2008). Such a low-wing conformation had previously been proposed for weigeltisaurids (Pritchard et al., 2021; Buffa et al., 2022), which are thus confirmed here).

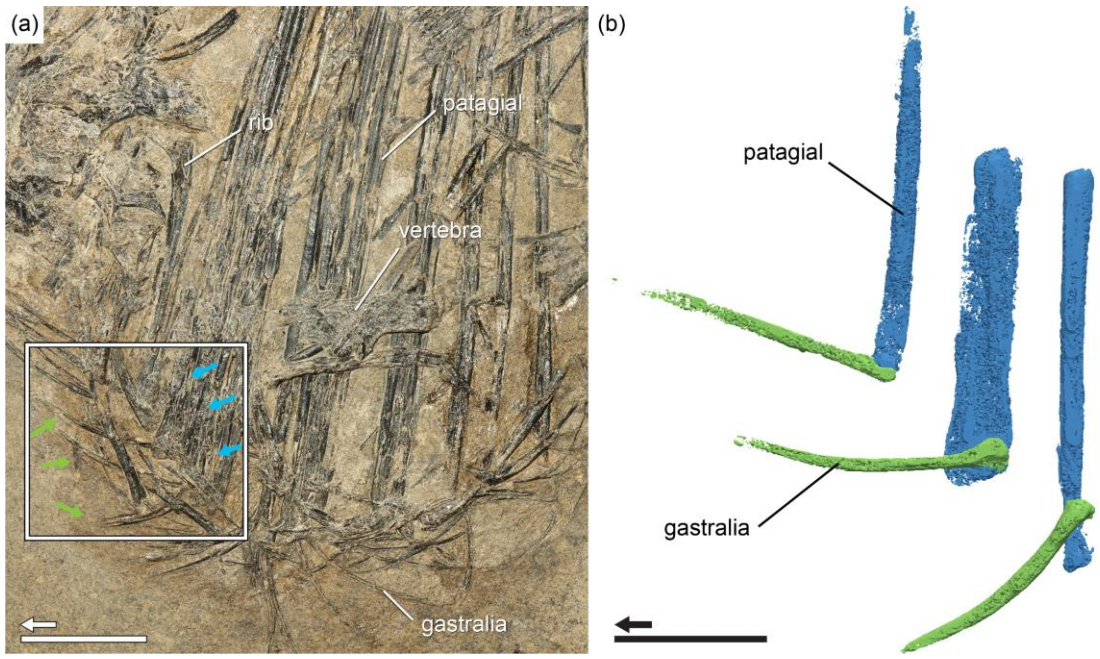

Figure 6-1: Patagium of *Weigeltisaurus jaekeli* SMNK-PAL 2882 (Late Permian, Germany) in medial view: (**a**) close-up view of the anterior half of the trunk showing gastralia and patagials; (**b**) segmented surface models of articulated gastralia and patagials indicated in rectangle in (**a**). Uncolored arrows indicate anterior direction. Scale bars equal 1 cm (**a**), 2 mm (**b**).

Fleshed-out reconstruction—At present, there does not appear to be a standard workflow to produce fleshed-out reconstructions of extinct animals for use in CFD analyses. For taxa with an external skeleton, such reconstructions can be obtained by digitizing the specimen and/or box-modeling (Rahman and Lautenschlager, 2016), but the amount of soft tissues and their distribution are much harder to assess in tetrapods for which the skeleton is internalized.

Some well-preserved aquatic taxa preserve the outline of soft tisses, and are known from enough specimens to show all necessary views for a 3D modelling (e.g. NURBS curves, Gutarra et al., 2019, 2022). However, such data are nearly always absent for terrestrial tetrapods. The latter are generally reconstructed either based on simple shapes in the context of mass estimation (Allen et al., 2009; Bishop et al., 2021), or in artistic life reconstructions (e.g. Steyer et al., 2010), neither of which produce the faithful (due to artistic license in the latter, Brassey, 2016; Lautenschlager, 2016), smooth reconstruction of the outline of the animal required for CFD analyses.

In this context, we provide here details of the major steps retracing our construction of a 3D geometry of *Coelurosauravus elivensis*. In essence, this workflow relies on an actualistic approach based on a modification of the methodology detailed in Chapter 5 of this dissertation using an original specimen of *Draco volans* (LSUMZ herp 81750, http://n2t.net/ark:/87602/m4/M77362).*D. volans* is indeed considered a good analogue to weigeltisaurids (Frey et al., 1997; Schaumberg et al., 2007; Buffa et al., 2022) and its similar body plan allows for an easier adaptation to the needs of our study:

(1) We imported the surface model of the skeleton of *D. volans* specimen LSUMZ herp 81750 segmented in Chapter 5 in Blender v.2.90.1, together with their geometry and armature used in CFD analyses (Figure 2a).

(2) We sightly modified the armature in prevision of future steps. First, we divided the bone parented to the skull region into two and manually adjusted the weight distribution on the meshes. Then, we added a 'Copy Scale' bone constraint applying changes in size of the leading edge row bones to the posterior rows in each wing and adjusted its influence to fit to the skeletal reconstructions of *C. elivensis* (influence 1, 0.9, and 0.1 for the median and lateral row two bones and row tree bone respectively). Note that the model constructed in Chapter 5 already included a 'Copy Rotation' bone constraint to the same bones to mimic the movement of the leading edge row with some degree of inertia, which were kept as is in the current study (influence 0.6, 0.1, and 0.3 respectively). Lastly, we added a 'Copy Location' constraint (influence 1) to the medial bones of the left wing, inverted along the transverse axis so that any manual displacement of the bones in the right right wing were automatically symmetrized on the left one.

(3) After scaling the 3D models and armature of *D. volans* to the size of *C. elivensis* based on snout-vent length, we deformed the skeleton and geometry by manipulating the armature in order to mimic the skeletal reconstruction of *C. elivensis* used as a background image (Figure

2b). This step also requires manual adjusting of weight distribution for each bone, especially in the wings and trunk, which can be very time-consuming.

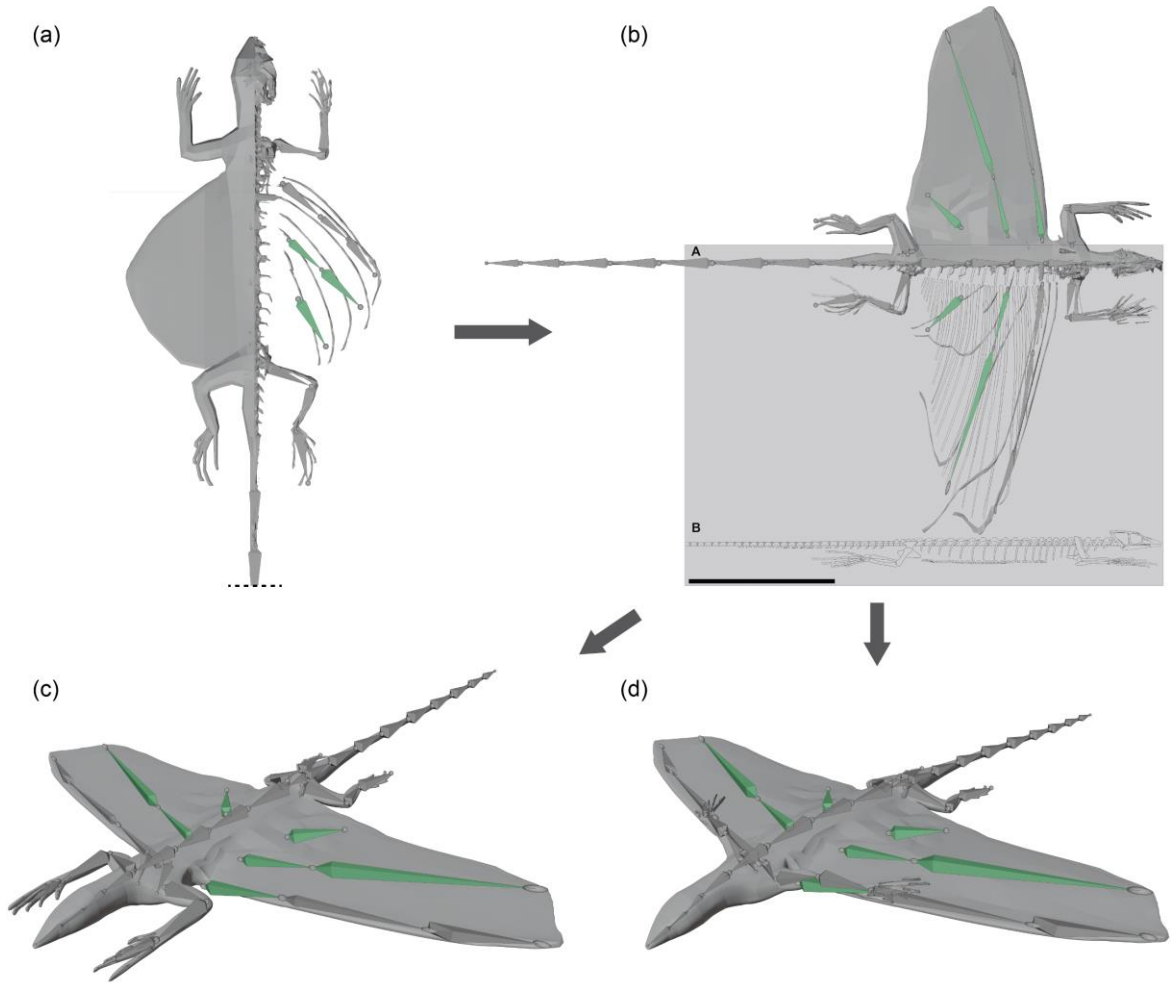

Figure 6-2: Main steps of the workflow employed to construct the 3D geometry of *Coelurosauravus elivensis* for use in CFD analyses: (**a**) imported *Draco volans* skeleton (LSUMZ herp 81750) and coarse geometry from Chapter 5 of this dissertation parented to a skeletal armature; (**b**) coarse geometry of *C. elivensis* obtained by moving the armature bones so that the deformed skeleton of *D. volans* mimics that of *C. elivensis* taken from skeletal reconstructions (from Buffa et al., 2022) used as background images (provisionally excluding ornamentation); (**c**) smooth P0 geometry with parented armature obtained by applying triangulate and subsurface modifiers; (**d**) P2 geometry obtained by moving the armature bones; Green bones indicate dependency on the vertical position of counterpart (medial bone in left leading edge row), or on the rotation and scale applied to the leading edge bones (posterior wing rows).

(4) Given the difference in size between *D. volans* and *C. elivensis*, we modified the 'SubSurface' modifier originally applied in Chapter 5 so that the number of faces was quadrupled from that of the coarse geometry rather than doubled. The 'Triangluate' modifier, however, was kept as in the latter study.

The resulting geometry is thus symmetrical, smooth and comprises only a single- layer outline of the specimen formed by numerous adjoined triangular faces (2 991 104 faces) that closely follows the morphology of the original specimen. It is also parented to a skeletal armature whose influence on the geometry was manually adjusted to allow for the repositioning of the model to mimic postures observed in living reptilian gliders, and previously inferred for *C. elivensis* (Buffa et al., 2022).

As a cautionary note, it was noted in Chapter 5 that while the integrity of the geometry is maintained when manipulating the armature, the volume is not constant for all postures. It is thus paramount that an estimation of the difference in volume be made as a sensitivity analysis. Lastly, since the original *D. volans* specimen was slightly asymmetrical even when retrodeformed by, some asymmetry in the calculation results might be expected.

Three-dimensional geometries

We generated six rigid-body postures derived from the newly constructed geometry (Figure 3). These postures mimic those constructed for *D. volans* in Chapter 5and were obtained by nearly identical rotations of the armature bones.

Posture P1 corresponds to the 'standard gliding posture' of Chapter 5 (Figure 3a), and is based on the most common representations of *C. elivensis* and other weigeltisaurids (Carroll, 1978; Steyer, 2009; Pritchard et al., 2021; Buffa et al., 2022). Postures P2 and P3 derive from posture P1 after angling the anterior and posterior trunk regions ca. 7 and 15 from the horizontal, creating camber (Figure 3b, c), with the tail of P3 being further angled at ca. 60 to mimic observed postures in *Draco* during gliding flight. In addition, we generated geometries P1a, P2a, and P3a (hereafter 'arms-tansverse' geometries), differing respectively from P1, P2, and P3 (hereafter 'arms-first' geometries) by the orientation of the forelimb along the leading edge of the wings (Figure 3e). This follows the suggestion by Buffa et al. (2022) that weigeltisaurids could form a composite wing by handling the leading edge of the wings with their claws, as in *Draco* (Dehling, 2017). Table 1 summarizes the morphological features of each postural geometry.

Table 6-1: Summary of the morphological features of the postural geometries ('PX', see text) used for CFD analyses.

	P1	P1a	P2	P2a	P3	P3a
Degree of body camber	none	none	low	low	high	high
Arms along the leading edge	no	yes	no	yes	no	yes

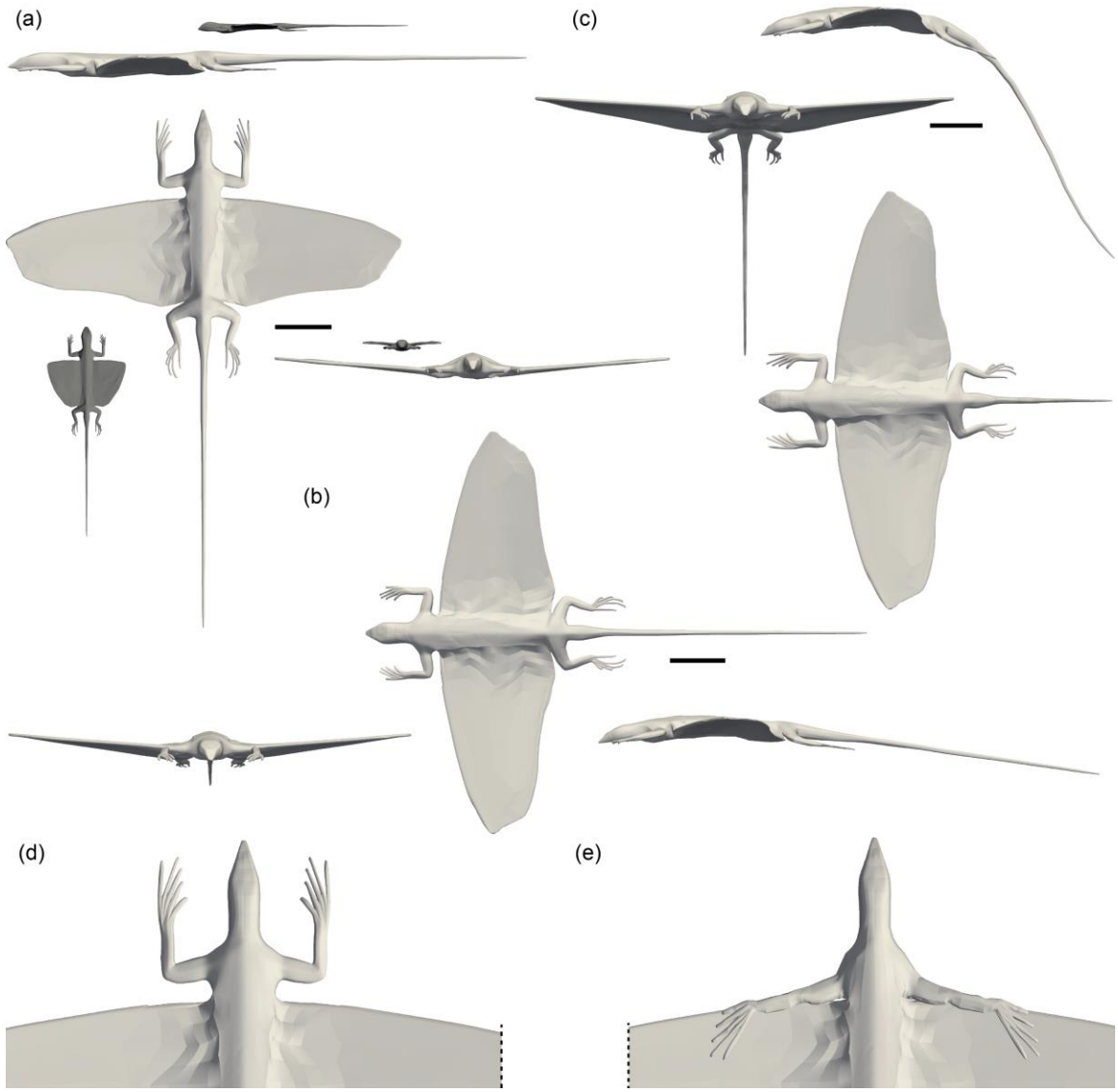

Figure 6-3: Selected geometries of *C. elivensis* used for CFD analyses in dorsal, anterior and left lateral views: (**a**) P1, no camber geometry, with similar geometry of *D. volans* (black) for comparison; (**b**) P2, low camber geometry; (**c**) P3, strong camber geometry; (**d**) close-up view of P1 geometry with arms flexed at the elbow and hands pointing anteriorly; (**e**) close-up view of arms oriented transversely and resting above the leading edge of the wing. Scale bars equal 5 cm.

All of these rigid-body posture geometries were exported in STL format. Key measurements of *D. volans* (from Chapter 5) and *C. elivensis* under a similar P1 posture are given in Table 2.

Table 6-2: Key measurements of *Draco volans* and *Coelurosauravus elivensis* P1 geometries. Abbreviations: *mc* is the mean value of 10 regularly spaced chords along the width of the wing, *rc* and *tc*; *R* taken at 25% of *mc*; *AR* equals s^2/A; *WL* equals m/A (kg/m^2) or mg/A (N/m^2) with *g* of 9.81 m/s^2. [1] From Chapter 5 of this dissertation; * indicates corrected measurement (see text).

	D. volans[1]	*C. elivensis*
Snout-vent length (mm)	75.7	177
Total length *l* (mm)	186	498
Wingspan *s* (mm)	70	352
Root chord *rc* (mm)	39.9	88.8
Tip chord *tc* (mm)	8.37	9.17
Mean chord *mc* (mm)	31.70	68.75
Reference point *R*–rostrum distance (mm)	38.7	99.8
Planform area *A* (cm^2)	23.87	246.07
Total area A_{tot} (cm^2)	31.05	625.89
Aspect ratio *AR*	2.05	5.04
Mass *m* (g)	7.25*	174.09
Wing loading *WL* (kg/m^2)	3.04	7.08
Wing loading *WL* (N/m^2)	29.80	69.40

Measurements—The mass *m* of geometry P1 of *C. elivensis* was estimated by measuring the volume of the geometry prior to smoothing (Figure 3b) and mutiplying it by a density value of 1000 g.cm^{-3}, as done in Chapter 5 based on a previously published mass estimation methodology (Bishop et al., 2021). The estimated mass for *C. elivensis* is 174.09 g (Table 2). This new estimation is much lower than that of 270 g by Evans (1982) for the Eppelton specimen (TWCMS B5937) of *W. jaekeli*, albeit based on a misinterpretation of the patagials as true dorsal ribs (as commonly accepted at the time) leading to an overestimation of the trunk length of the animal.

It was argued in Chapter 5 that posture P1 may overestimate the actual mass of the animal, but indicated that this difference was comprised in the error margin of the geometry construction. Thus, in the absence of possible direct measurements, we here retain this mass

estimation for *C. elivensis* even if that used for *D. volans* is based on a more faithful representation of specimen LSUMZ herp 81750 (the resting posture P0 of Chapter 5, Table 2).

We measured the planform area *A* (the area of the wings and trunk) of *C. elivensis* using the methodology described in Chapter 5, and use it as the reference area for all our geometries following common practice for airplane- like biological models (Koehl et al., 2011). We estimated an *A* of 246.07 cm^2 for *C. elivensis*, which is slightly less than the 279 cm^2 previously estimated by Evans (1982, but overestimated, see above).

The calculated aspect ratio *AR* (a dimensionless measurement of the slenderness of the wing) defined as the s^2/A ratio between the squared wingspan *s* and *A* is 5.04 for *C. elivensis* compared to 2.05 for *D. volans* (Table 2). The generation of induced drag, the component of the total drag force that is created through lift generation, is inversely proportional to *AR* (Anderson, 2017). Thus, we would expect a *C. elivensis* individual to be a more efficient glider than a *D. volans* one of identical mass and size. In other words, we expect the increased aspect ratio of *C. elivensis* to compensate, at least partially, its much greater weight.

Given our mass and planform area measurements, we estimate a wing loading *WL* of 69.40 N/m^2 (or 7.08 kg/m^2) for *C. elivensis* (Table 2). This is much less than the *WL* of 107.9 N/m^2 calculated by McGuire and Dudley (2011, based on a slight correction of Evans's, 1982 measurements), and conforms to the increased *AR*. This suggests that *C. elivensis* may have been a better glider than previously thought, as gliding performance decreases with *WL* in gliding reptiles (McGuire, 2003; McGuire and Dudley, 2005, 2011). The *m* and *WL* estimates for *C. elivensis* are similar to those of the northern flying squirrel *Glaucomys sabrinus* (mean: *m* = 140g; *WL* = 50 N/m^2, Thorington and Heaney, 1981). It is thus likely both taxa glided at similar speeds, which for *G. sabrinus* roughly range between 6 and 8 m/s (Scheibe et al., 2006). This is slightly more than the speeds recorded for *Draco* individuals of various species (McGuire and Dudley, 2005), which conforms to the expected higher airspeed for *C. elivensis* based on wing loading (McGuire and Dudley, 2011).

Computational Fluid Dynamics (CFD)

In the absence of direct observations of weigeltisaurids, we here make two assumptions. First, we assume that the gliding speed of *C. elivensis* is very small compared to the speed of

sound so that air is considered an incompressible fluid (Anderson, 2017). Second, we assume *C. elivensis* can reach equilibrium gliding during the mid-glide phase of a glide (sensu Khandelwal and Hendrick, 2020) provided there are no obstacles in its path and no changes in air velocity (see Chapter 5 for details on the applicability of this assumption in *Draco*). Equilibrium gliding occurs when the aerodynamic forces counteract weight so that the animal glides in a straight path at a fixed glide angle and velocity (Norberg, 1990; Koehl et al., 2011; Socha et al., 2015). This assumption thus allows for the use of steady-state aerodynamics to describe gliding in *C. elivensis*.

Lastly, given that the size, mass and wing loading of *C. elivensis* are similar to those of extant gliding mammals (Dececchi et al., 2020) it is expected *C. elivensis* glided in a 10^4 to 10^5 range of Reynolds number *Re*. This range is typical of vertebrate gliders and flyers and is indicative of transitional to turbulent flows (Norberg, 1990; Vogel, 1994; Anderson, 2017). These flows are best described using Reynolds Averaged Navier-Stokes (RANS) equations, a time-averaged approach that is both affordable and reasonably accurate.

CFD case setup—We thus conducted several CFD analyses (hereafter 'cases') of gliding flight in *C. elivensis* during mid-glide based on impressible steady-state RANS simulations. All cases were conducted using the open-source software OpenFOAM v.2012 on a Gnu/Linux Debian 9 workstation (Intel(R) Xeon(R) CPU X5650, 2.67GHz, 12 cores, 24 Go Ram), and were run in parallel on six processors.

The geometry of *C. elivensis* was immersed in a rectangular (7.8x6x6 m) computational domain obtained by scaling up that of Chapter 5. We then discretized the computational domain in a series of hexahedral and split-hexahedral cells (the 'mesh') using the snappyHexMesh immersed boundary mesh generation utility of OpenFOAM. All parameters were identical to the most refined mesh 'M3' computed in Chapter 5, except for the scaled-up refinement box. This refinement yielded dimensionless wall distance y^+ values around 3 for all cases at 5 m/s, indicating a rather good prediction of fluid flow in the boundary layer (typically attained for $y^+ \leq 5$, Wilcox, 2006).

All cases were run using a SIMPLE algorithm to solve the steady-state RANS equations in conjunction with a $k - \omega$ SST turbulence model (turbulence intensity 5%, turbulence length scale 7% of total length l), as done in Chapter 5.

The upstream and top faces of the domain were designated as the inlet where the freestream velocity and inflow angle are assigned according to the desired angle of attack for each case. The downstream and bottom faces were designated as the outlet and prescribed a zero-gradient condition, and a no-slip condition was assigned to our *C. elivensis* geometry to constraint velocity to zero at the boundary with the geometry. Lastly, we indicated a reference pressure *P* of 0, and the initial velocity and angle of attack are case-dependent.

We computed 66 cases of gliding flight in *C. elivensis*, one for each of the six postures (PP1, P1a, P2, P2a, P3, P3a) set at selected angles of attack (-20 , -10 , -8 , -5 , 0 , 5 , 8 , 10 , 15 , 20 and 25). Additional cases were set up for sensitivity analyses (detailed below). For all cases, the timeset was tailored to allow the calculations to converge over time, ranging from 160 to 800 steps.

Postprocessing—The open source software Paraview v.5.9.0 was used for visualization and postprocessing. The computation of streamlines relies of a point source forming a sphere of a 20 cm radius centered in the sagittal plane of the animal immediately behind the wing (18 cm from the rostrum) and at the mid-height of the animal (-7.5 mm from the coronal plane). The 200 computed streamlines all pass through this sphere, thus capturing the flow immediately around the geometry.

Trajectory simulations

Using the dimensionless aerodynamic coefficients of Lift C_L and Drag C_D returned by the CFD analyses, we compute 2D trajectory simulations by resolving equations of motion through time, following recent studies (Dyke et al., 2013; see Chapter 5 for equations). The velocity and location of *C. elivensis* are calculated for each time step (Δt = 0.01 s).

C. elivensis is associated with *Glossopteris* leaves (Buffa et al., 2021, 2022), and it has been suggested these seed ferns formed most of the arboreal strata in the forests of the late Permian Gondwanan Flora (Cúneo, 1996; Bernardi et al., 2017). It is thus likely that *C. elivensis* inhabited the canopy strata of *Glossopteris* woodlands. Gulbranson et al. (2012) estimated a height range of 20 to 30 m for in situ permineralized stumps of *Glossopteris* from the late Permian of Antarctica, and it is likely that forest canopies in Madagascar were slightly higher based on extant latitudinal gradients of tree heights (Moles et al., 2009; Zhang et al., 2016). Thus, we compute

gliding simulations starting from a height of 30 m. Conveniently, this height was also used by in Chapter 5 for gliding simulations of *Draco*. In the absence of data on initial jump speed in *C. elivensis*, all simulated glides started with an initial horizontal velocity $V_x(0)$ of 2.5 m/s and no vertical initial velocity (i.e., a strictly horizontal jump), as done in Chapter 5.

The air composition in the late Paleozoic has long been considered different than that of the present (Graham, 1995; Dudley, 1998). Various models and proxies suggest the Permian atmosphere was much more oxygenated that the present, with O_2 accounting for 25-35% of the composition of air throughout the period, although with a sharp decrease during the Lopingian (e.g. Berner, 2009; Clapham and Karr, 2012; Krause et al., 2018; although see e.g. Schachat et al., 2018; Brand et al., 2021 for lower estimates). The increased partial pressure of oxygen (and constant nitrogen levels, Dudley, 1998) is though to have led to an increase in total air density, which was proposed to be 1.56 kg/m^3 at the beginning of the Permian (Graham, 1995; Gans, 1999), and is taken here as an estimate for most of the Permian pending further quantification. As weigeltisaurids are generally considered Wuchiapingian in age (although a Capitanian to Changhsingian age cannot be excluded, Buffa et al., 2022), we conduct here two sets of trajectory simulations, one at the present-day air density ρ_{atm} of 1.125 kg/m^3, and one at $\rho_{P\,erm}$ of 1.5 kg/m^3.

All glide trajectories neglect the takeoff and landing phases to allow the application of steady-state conditions, and the animal is kept at a fixed angle of attack and posture throughout the glide, as done in Chapter 5. This allows for a systematic assessment of posture on gliding performance. For each posture, the initial angle of attack is the one which maximizes the lift-to-drag ratio C_L/C_D.

Results

Sensitivity analyses

Geometry construction—As noted above, it is necessary to assess the impact of the geometry construction on the aerodynamic coefficients. We thus automatically generated two additional P1 geometries, one slightly bulkier, the other slightly thinner (Figure 4a-c) using the Shrink/Fatten tool of Blender (offset ± 0.02 m along normal vectors), in a similar manner to

Chapter 5. This should provide a margin of error encompassing a possible overestimation of the overall volume of the geometry.

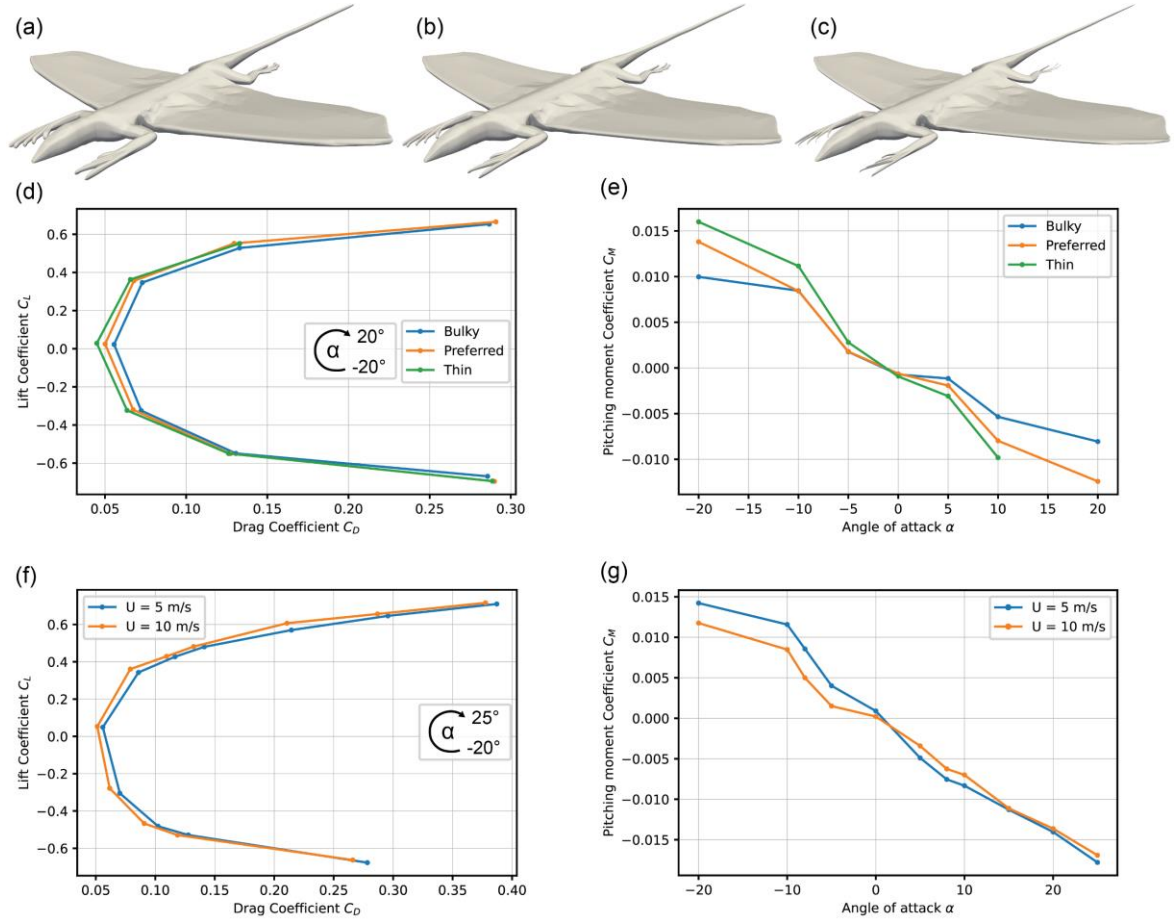

Figure 6-4: Geometries of varying thickness and results from sensitivity analyses: (**a**-**c**) bulkier, preferred and thinner P1 geometries; calculation results regarding the construction of the geometry based on P1 at velocity *U* of 5 m/s (**d**, **e**), and velocity *U* based on P1a (**f**, **g**). (**d**, **f**) lift and drag coefficients under varying angles of attack α; (**e**, **g**) pitching moment coefficient against α.

Whereas we see no significant difference in C_L (Figure 4d), C_D increases with overall thickness at low angles of attack (AoA) (thin: 0.045; peferred: 0.050; bulky: 0.056 resp. at 0°). In addition, the negative slope of the pitching moment coefficient C_M against AoA decreases with thickness, although all geometries retain a stable fixed point at ca. -2 (Figure 4e). As a result, all geometries show some pitch stability, but bulky ones appear more stable, as reported in Chapter 5 for *D. volans*. As expected, our preferred geometry always yielded intermediate values between the bulkier and thinner one for all aerodynamic coefficients (Figure 4d, e). Thus, all subsequent cases employ geometries derived from it.

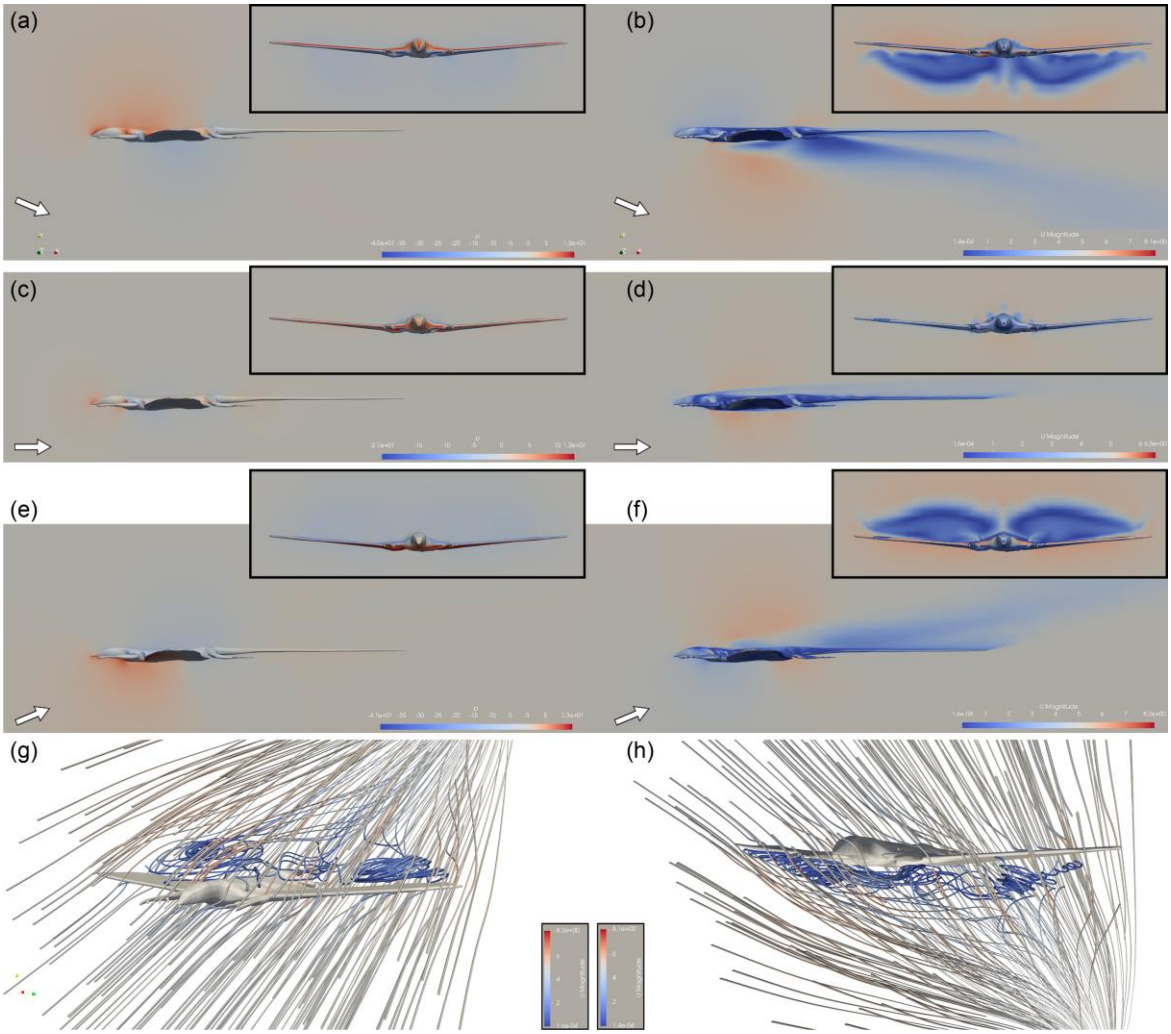

Figure 6-5: Pressure (**a**, **c**, **e**) and velocity (**b**, **d**, **f**-**h**) fields around a *Coelurosauravus elivensis* P1 geometry for different angles of attack α: (**a**-**f**) scalar fields in lateral (sagittal plane) and anterior views (transverse plane immediately behind the wings); (**g**, **h**) oblique view of streamlines representing the velocity field. (**a**, **b**, **h**) α = -20°; (**c**, **d**) α = 0°; (**e**-**g**) α = 20°. Arrows indicate incoming airflow direction. Grey indicates initial value P = 0 Pa; U = 5 m/s), blue indicates lower values, red indicates higher values.

Velocity—As estimated from the northern flying squirrel *Glaucomys sabrinus*, *C. elivensis* likely glided at speeds in a rough range of 5 m/s to 10 m/s. Given this uncertainty, we conducted preliminary analyses of the impact of velocity on calculation results by conducting cases at a characteristic velocity of either 5 m/s or 10 m/s (which corresponds to a doubling of the Reynolds number) based on a P1a geometry (Figure 4f, g).

The C_L values are nearly identical for cases of geometry P1a for velocities of 5 m/s or 10 m/s (Figure 4f). They differ very slightly in C_D values (5 m/s: 0.387; 10 m/s: 0.377 resp. at 25°), which is expected as drag decreases with flow speed (Anderson, 2017). The C_M values

are higher at high negative AoA for lower velocities (5 m/s: 0.0142; 10 m/s: 0.0117 resp. at -20°), indicating slightly lesser stability. All other C_M values are similar (Figure 4g).

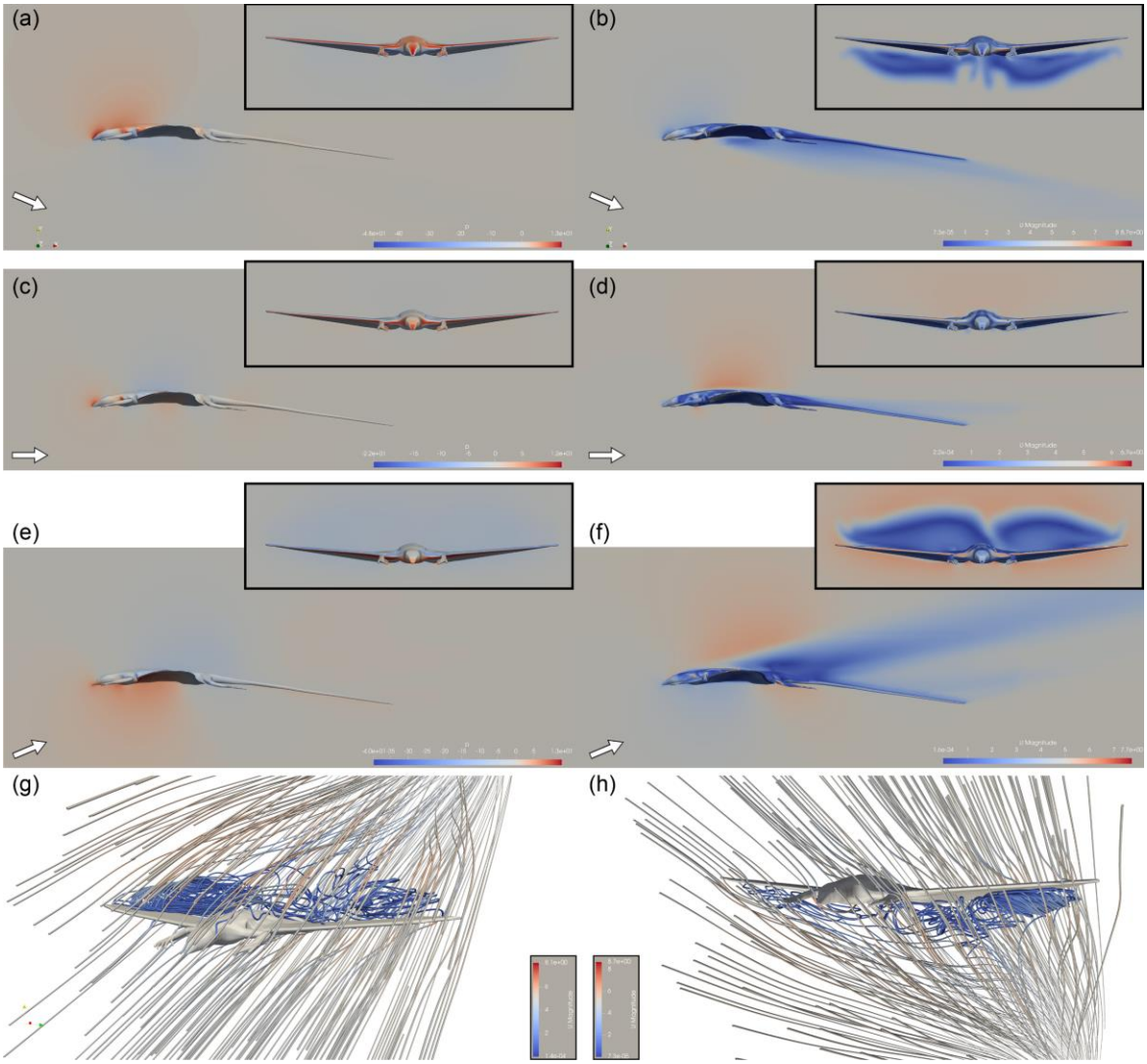

Figure 6-6: Pressure (**a**, **c**, **e**) and velocity (**b**, **d**, **f**-**h**) fields around a *Coelurosauravus elivensis* P2 geometry for different angles of attack α: (**a**-**f**) scalar fields in lateral (sagittal plane) and anterior views (transverse plane immediately behind the wings); (**g**, **h**) oblique view of streamlines representing the velocity field. (**a**, **b**, **h**) α = -20°; (**c**, **d**) α = 0°; (**e**-**g**) α = 20°. Arrows indicate incoming airflow direction. Grey indicates initial value P = 0 Pa; U = 5 m/s), blue indicates lower values, red indicates higher values.

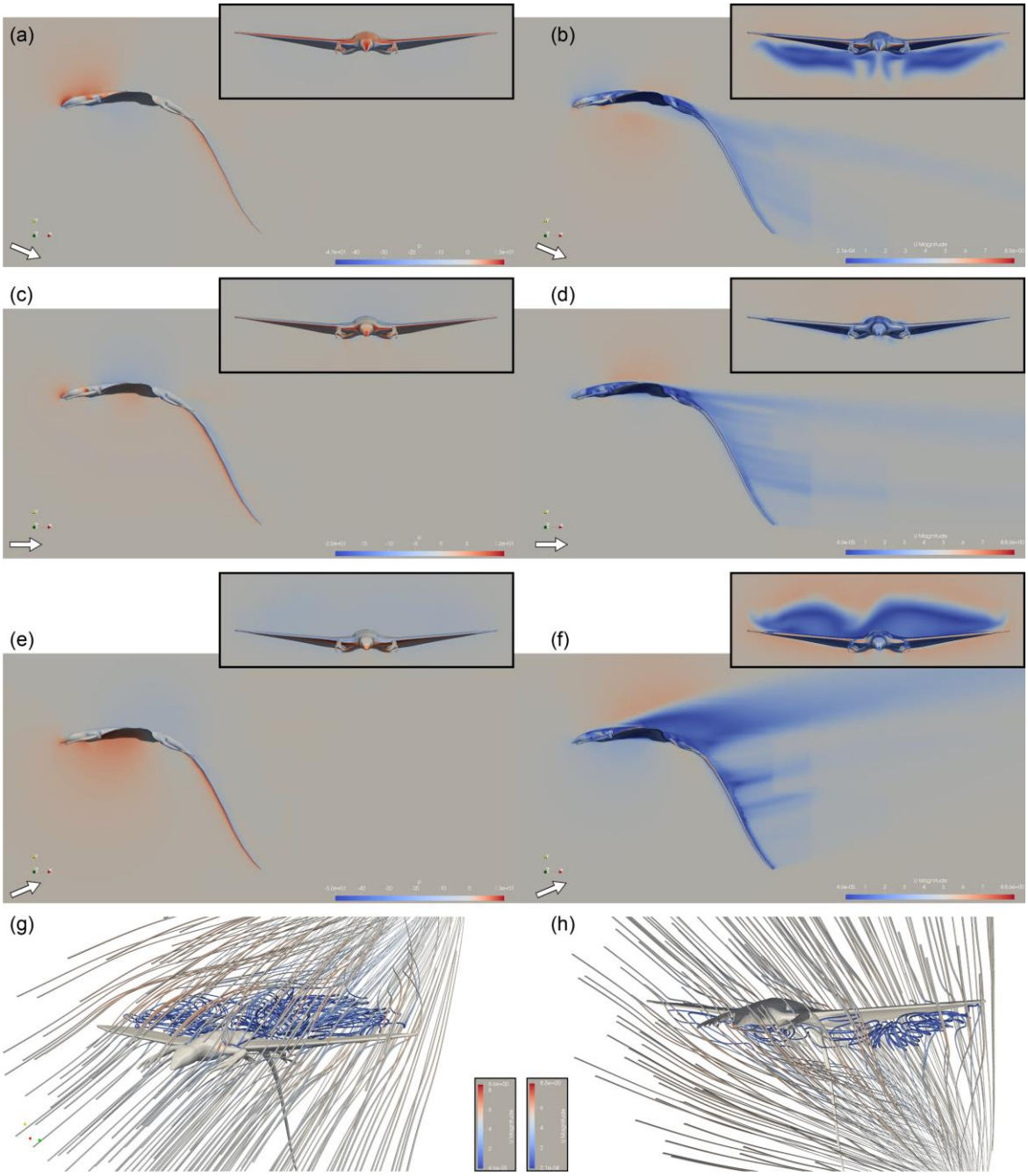

Figure 6-7: Pressure (**a**, **c**, **e**) and velocity (**b**, **d**, **f**-**h**) fields around a *Coelurosauravus elivensis* P3 geometry for different angles of attack α: (**a**-**f**) scalar fields in lateral (sagittal plane) and anterior views (transverse plane immediately behind the wings); (**g**, **h**) oblique view of streamlines representing the velocity field. (**a**, **b**, **h**) α = -20°; (**c**, **d**) α = 0°; (**e**-**g**) α = 20°. Arrows indicate incoming airflow direction. Grey indicates initial value P = 0 Pa; U = 5 m/s), blue indicates lower values, red indicates higher values.

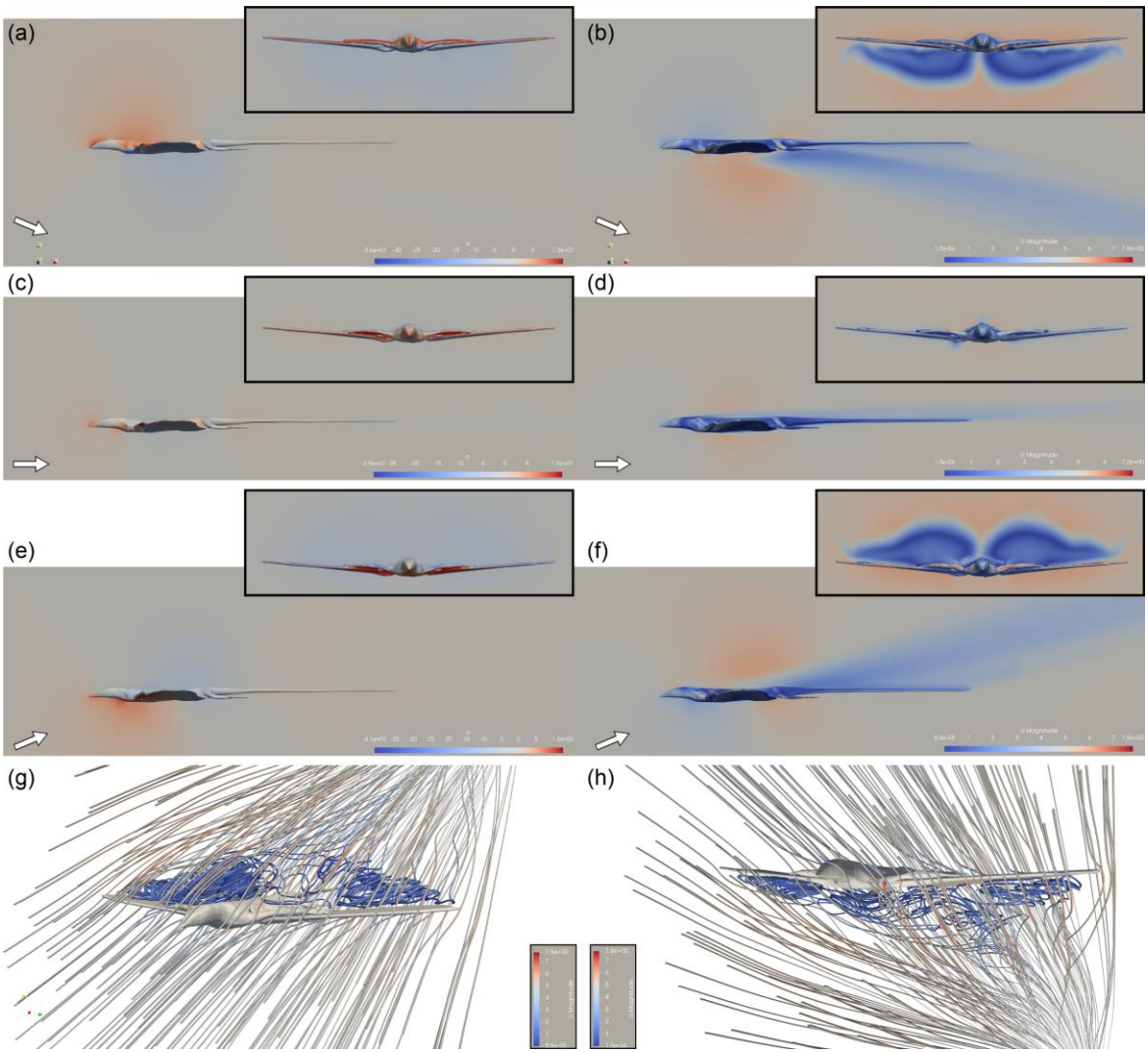

Figure 6-8: Pressure (**a**, **c**, **e**) and velocity (**b**, **d**, **f**-**h**) fields around a *Coelurosauravus elivensis* P1a geometry for different angles of attack α: (**a**-**f**) scalar fields in lateral (sagittal plane) and anterior views (transverse plane immediately behind the wings); (**g**, **h**) oblique view of streamlines representing the velocity field. (**a**, **b**, **h**) α = -20°; (**c**, **d**) α = 0°; (**e**-**g**) α = 20°. Arrows indicate incoming airflow direction. Grey indicates initial value P = 0 Pa; U = 5 m/s), blue indicates lower values, red indicates higher values.

Influence of posture

Scalar fields— As expected and described for extant gliders (see Chapter 5; Zhao et al., 2019), the frontal surface of *C. elivensis* always corresponds to a region of increased pressure due to the incoming airflow, and this overpressure is displaced dorsally with negative AoAs and ventrally for positive AoAs (Figures 5-8). More posteriorly, incipient underpressure and overpressure regions respectively above and under the wings are present for a geometry P1 at an AoA of 0 (Figures 5), and this pressure difference is exacerbated with increased camber (Figures 6, 7).

These pressure differences are mirrored by velocity differences, as seen in the velocity field for all geometries (Figures 5-8).

In addition, all geometries show an increase in the aforementioned pressure and velocity differences for high positive AoAs. Indeed, at 20°, all geometries show broad regions of lower pressure and velocited spanning the entire wingspan, and gradually decreasing gradients in the wake of the animal (Figures 5-8). In all cases, these regions correspond to regions of strong vorticity (Figure 9). In contrast, the pressure and velocity differences are reversed for high negative AoAs, with an overpressure above the wing and an underpressure under it, the latter again corresponding to a region of vorticity (Figures 5-9).

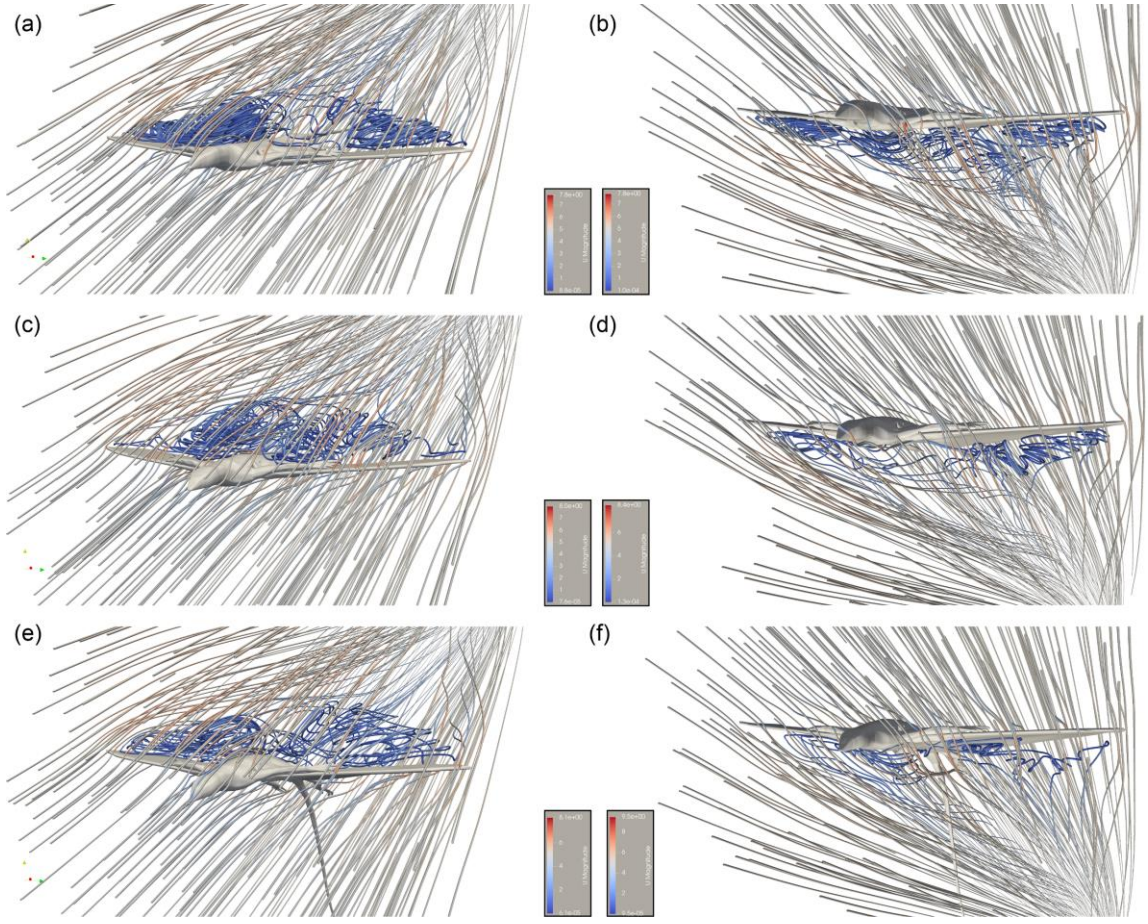

Figure 6-9: Oblique view of streamlines representing the velocity field around *Coelurosauravus elivensis* P1a (top row), P2a (middle row) and P3a (bottom row) geometries for different angles of attack α: (**a**, **c**) α = 20°; (**b**, **d**) α = -20°. Grey indicates initial value P = 0 Pa; U = 5 m/s), blue indicates lower values, red indicates higher values.

Table 6-3: Summary of the aerodynamic and gliding performances of *Draco volans* and *C. elivensis* for all postures. [1]from Chapter 5 of this dissertation.

	P0	P1	P1a	P2	P2a	P3	P3a
Draco volans[1] (ρ)							
$(CL/CD)_{max}$	2.96	3.34	2.93	3.73	3.25	2.93	2.73
AoA_{max}	10°	10°	10°	8°	5°	10°	8°
$Distance_{30m}$ (m)	62.61	68.61	61.90	86.07	66.46	74.99	68.92
$Time_{30m}$ (s)	7.17	7.56	7.10	10.05	7.33	10.69	9.66
Average $velocity_{30m}$ (m/s)	10.05	10.31	10.05	9.34	10.37	7.67	7.91
Coelurosauravus elivensis (ρ_{atm})							
$(CL/CD)max$	—	5.25	3.99	6.13	4.51	5.19	4.59
AoA_{max}	—	5	5	5	0	5	0
$Distance_{30m}$ (m)	—	17.46	16.68	91.71	16.78	87.11	24.84
$Time_{30m}$ (s)	—	2.79	2.79	8.14	2.78	8.36	3.13
Average $velocity_{30m}$ (m/s)	—	12.61	12.44	12.99	12.51	11.76	12.78
Coelurosauravus elivensis ($\rho_{P\,erm}$)							
$Distance_{30m}$ (m)	—	21.38	20.05	102.11	20.22	108.63	78.94
$Time_{30m}$ (s)	—	2.95	2.93	9.40	2.92	11.02	7.01
Average $velocity_{30m}$ (m/s)	—	12.74	12.50	12.11	12.59	10.69	13.12

Lift and Drag coefficients—C_L increases markedly with camber for all AoAs (Figure 10a). This increase is particularly strong for high negative AoAs (P1: -0.70; P3: -0.45 resp. at -20°) but is less marked for high positive ones (P1: 0.73; P3: 0.97 resp. at 25°). In addition, whereas C_D is lower for high camber at very high negative AoAs (P3: 0.24; P1: 0.29 resp. at -20°) and similar for all other negative and low positive AoAs, it markedly increases with camber at high positive AoAs (P1: 0.39; P3: 0.55 resp. at 25°). This conforms to the large regions of lesser pressure and velocity as well as the generation of large vortices in the wing regions observed for corresponding AoAs (Figures 5-8). Similar trends were noted for *D. volans* in Chapter 5. In addition, we note that the C_D and C_L coefficients are very similar between arms-first and arms-transverse counterparts for most AoAs, except for low positive ones (0° to 15°). In this range, all arms-first geometries show markedly higher C_L than arms-transverse ones (P3: 0.89; P3a: 0.77 resp. at 8°), with a similar increase in C_D as well (P3: 0.20; P3a: 0.22 resp. at 8°). A similar, although less marked, difference in *Draco* was attributed to the participation of the arms to lift and drag generation under arms-first postures in Chapter 5. This was certainly

also the case for *C. elivensis*, and is likely exacerbated compared to *D. volans* due to the absolute size of the animal as well as its relatively larger hands, which are held open in our geometries (Figure 3).

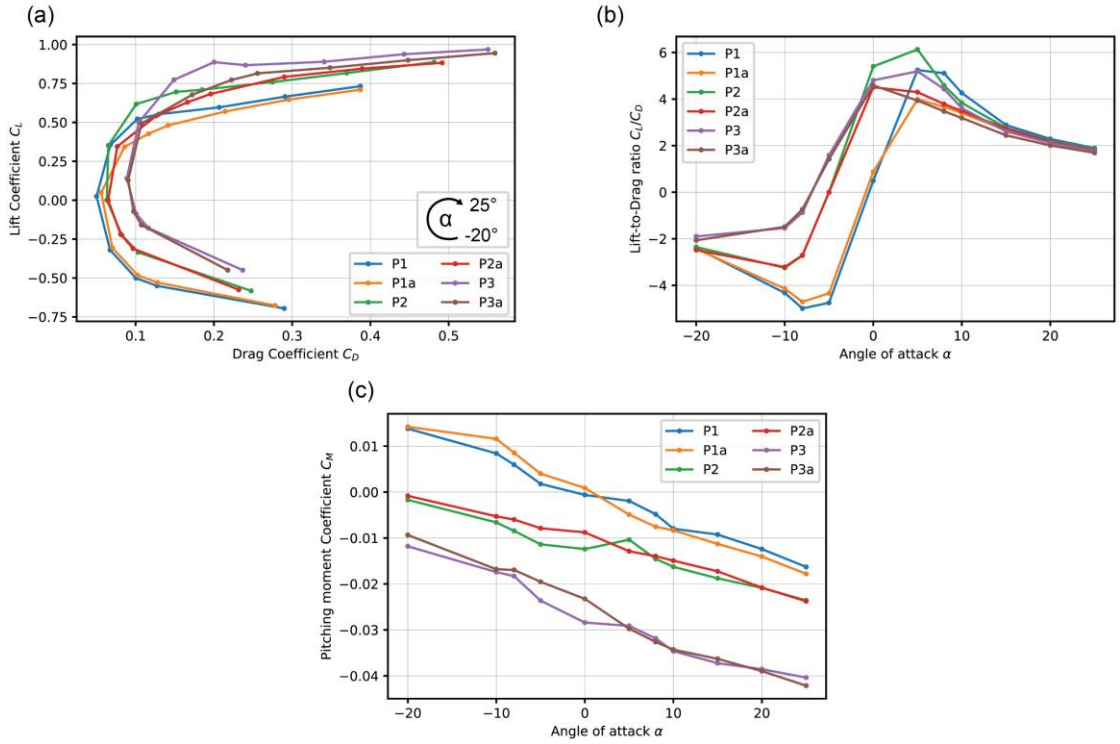

Figure 6-10: Aerodynamic performances for different *C. elivensis* postural geometries: (**a**) lift and drag coefficients under varying angles of attack α; (**b**) pitching moment coefficient against angle of attack; (**c**) lift-do-drag ratio C_L/C_D against angle of attack.

The lift-to-drag ratio C_L/C_D increases sharply with camber for negative AoAs whereas values for positive AoAs are more similar for all geometries (Figure 10b). All geometries reach their $(C_L/C_D)_{max}$ value for AoA between 0° and 5° (Table 3), indicating that the AoA for equilibrium glide was always shallower than that for *D. volans* (between 5° and 10°). Also, there appears to be a correlation between forelimb position and $(C_L/C_D)_{max}$ in *C. elivensis* contrary to the situation in *D. volans*. Indeed, for *C. elivensis*, all arms-first postures have higher $(C_L/C_D)_{max}$ than their arms-transverse counterparts (P2: 6.13; P2a: 4.51, Table 3), and at least for P2 and P3 this value is obtained for slightly higher AoA. As $(C_L/C_D)_{max}$ characterizes the glide angle (the angle between the animal and the ground) which maximizes horizontal distance (Emerson and Koehl, 1990; Koehl et al., 2011), we expect arms-first geometries to glide for longer

distances than their arms-transverse counterparts in *C. elivensis*, with P2 being the most efficient posture.

Pitching moment coefficient—All geometries show nearly identical negative slopes of C_M against AoA, indicating all postures offer some stability in pitch in *C. elivensis* (Figure 10c). However, C_M shows a marked decrease with camber (P1: -0.0006; P2: -0.0124; P3: -0.0284 at 0°), indicating stability decreases with camber for the observed range of AoAs. As a result, whereas a stable fixed point (i.e. an AoA of no pitching moment) is attained for ca. -1° and 1° for P1 ad P1 respectively, and can reasonably been inferred at ca. -22° for P2 and P2a, no such point can be seen for P3 and P3a in the observed range of AoA (Figure 10c). Lastly, for both P2 and P3, C_M is lower than their counterparts P2a and P3a for AoAs between -8° and 0° (P3a: -0.0195; P3: -0.0236 at -5°). As a result, it appears that arms-transverse postures are more stable at low negative AoAs for cambered postures.

Interestingly, in contrast to *D. volans*, there does not appear to be any marked inversion in the slope of C_M against AoA for any posture (except maybe for P2 at 5°, Figure 10c). As discussed in Chapter 5, the positive slope for low positive angles of attack for arms-first postures in *D. volans* as a region of instability and suggested that these postures were not viable in extant gliding reptiles. Given the lack of such slopes in *C. elivensis*, both arms-first and arms-transverse postures appear viable in *C. elivensis* with regards to pitching moment.

Gliding trajectory—When set at the AoA corresponding to their $(C_L/C_D)_{max}$, some postures (P1, P1a, P2a) perform a ballistic glide regardless of air density (full lines, Figure 11a). These ballistic glides are characterized by a sharp increase in glide angle to about 70° over nearly half of the glide (Figure 11c, d). The second half of the glide shows a decrease in glide angle, reaching about 30-40° at the end of the glide under present-day ρ_{atm} density (Figure 11c).

Despite covering more horizontal distance (24.84 m), P3a also performs a mostly straight descent under present-day air density ρ_{atm} when fixed at its $(C_L/C_D)_{max}$ AoA (full line, Figure 11a, c). However, it reaches a much longer distance (78.94 m) under the higher $\rho_{P\ erm}$ density. In the latter case, the glide trajectory can be roughly divided into informal phases: a ballistic phase where the animal accumulates speed while falling (1), a phugoid mid-glide phase where the animal accumulated enough speed to generate significant lift for forwards and upwards movement (as attested by a negative glide angle) (2), and a shallow descent phase (3) that ends at ground level (full line, Figure 11).

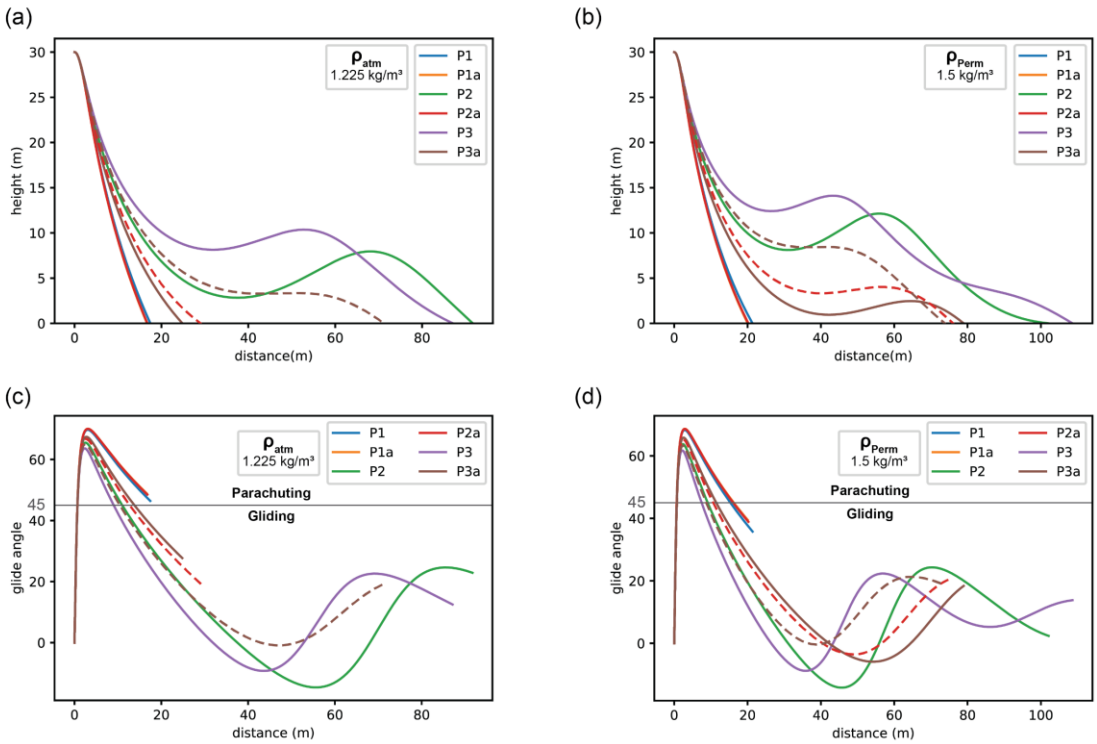

Figure 6-11: Trajectory simulations (**a**, **b**) and associated glide angles (**c**, **d**) during simulated glides at different air densities after jumping from a 30 m perch at an initial horizontal velocity $V_h(0)$ of 2.5 m/s: (filled lines) each postural geometry gliding at fixed angle of attack α which maximizes the lift-do-drag ratio C_L/C_D; (dotted lines) geometries P2a and P3a fixed at α = 5 in accordance all other postures (see Table 3). Parachuting and true gliding arbitrarily correspond to glide angles above and below 45°.

Postures P2 and P3 are the only ones to cover long gliding distances (> 80 m) under both air densities, but always reach longer distances under $\rho_{P\ erm}$ (Table 3). Their gliding trajectories are very similar to that described for P3a under $\rho_{P\ erm}$, with ballistic, phugoid mid-glide, and shallow descent phases (Figure 11). Under ρ_{atm} density, P2 shows a much longer ballistic phase (1) than P3 (falling ca 7 m more). However, its phugoid mid-glide phase (2) is much longer (over 30 m in horizontal distance), and its oscillation is much greater (gaining nearly 5 m in height), which explains its slightly longer total glide distance (91.71 m) compared to P3 (87.11 m). Interestingly, despite reaching a longer distance, P2 glides over a shorter time and at a higher average velocity (8.14 s; 12.99 m/s) than P3 (8.36 s; 11.76 m/s), indicating that gliding speed may not be correlated to gliding distance.

Under the higher $\rho_{P\ erm}$ density, postures P2, P3 and P3a show shorter falls during the ballistic phase (1) (e.g. ca. 16 m rather than 20 m for P3), such that the phugoid phase (2) occurs at a much greater height (Figure 11). As a result, the shallow descent phases of P2 and P3 cover

more horizontal and vertical distance under $\rho_{P\ erm}$ than ρ. For both geometries, the slope of descent decreases during gliding, and this occurs much earlier for P3 (height ca. 6 m) than P2 (ca. 3 m) (Figure 11), which explains its longer total glide distance (108.63 m) (Table 3).

Lastly, as P2a and P3a are the only postures that maximize $(C_L/C_D)_{max}$ at 0° rather than 5° in our study, we explored how these postures performed at a fixed AoA of 5° (dotted lines, Figure 11). This allows us to examine the glide performance of these two postures at an 'under-performing' AoA that does not maximize gliding distance.

As expected, for P3A under $\rho_{P\ erm}$ density, the animal covered slightly less distance under these conditions (73.80 m instead of 78.94 m at 0°). However, its ballistic phase is much shorter, covering only slightly more than 20m, and the mid-glide phase lacks the phugoid behavior described above, with the animal gliding horizontally (rather than climbing up) for about 20 m (dotted line, Figure 11b). Similarly, the ballistic phase of P3a under ρ_{Atm} is much shorter at 5° AoA rather than 0°, which allows it to glide effectively over nearly 40 additional meters (dotted line, Figure 11b).

However, the main change in performance concerns P2a, which yields a ballistic phase at 0° AoA for all densities, but yields an efficient gliding trajectory under $\rho_{P\ erm}$ at 5° AoA, showing the phugoid mid-glide phase at shallow glide angles described above and reaching a longer distance than P3a (76.06 m) (Figure 11).

Discussion

Weigeltisaurids, gliders or not?

Weigeltisaurid reptiles have long been recognized as the world's first gliding vertebrates (Huene, 1930; Carroll, 1978; Evans, 1982; Schaumberg, 1976, 1986; Frey et al., 1997). However, this assertion is solely based on the idea that if weigeltisaurids invest energy and resources in the formation of a patagial skeleton and wing membrane, then they must have been efficient gliders. Given the size of the weigeltisaurid patagia, this compelling argument has been followed in all recent studies (Schaumberg et al., 2007; Bulanov and Sennikov, 2010, 2015a, b; Buffa et al., 2021, 2022; Pritchard et al., 2021). Thus, there have been very few attempts to accurately quantify the gliding performances of these taxa. Incidentally, the only assessment of gliding flight

in weigeltisaurids to date argued that these reptiles would only be capable of steep descent at glide angles > 45° (at least for < 10 m high jumps, McGuire and Dudley, 2011). Such glide angles are typical of parachuting animals, which may be capable of controlling their descent, but cover very little horizontal ground while in air (Dudley et al., 2007). In contrast, true gliding animals are arbitrarily considered capable of gliding at angles < 45° relative to the horizontal (Oliver, 1951; Dudley et al., 2007). Prior to this study, it thus remained unclear whether weigeltisaurids were actual gliding reptiles, or are better considered as parachuters.

Our CFD analyses coupled with trajectory simulations indicate *C. elivensis* (and likely all weigeltisaurids) may have been capable of long glides with prolonged portions at glide angles lower than 45°, especially under a higher Permian air density (Figure 11). As such, our analyses support the hypothesis that weigeltisaurids were capable of true gliding.

Interestingly, we found no evidence of any impact of forelimb position on pitching moment (Figure 10). In contrast, *D. volans* appears unstable in pitching for low positive angles of attack (incidentally those corresponding to equilibrium gliding) when their forelimbs are anteriorly oriented. Thus, it appears that both arms-front and arms-transverse postures are viable for *C. elivensis* with regards to pitching moment. However, as discussed in Chapter 5, the increased air pressure on the leading edge of the wing for all angles of attack is expected to push back the wing in a folded position, especially at high speeds. Thus, it is likely that weigeltisaurids had a way of keeping the wing extended during gliding. This can be achieved either by strong and continuous contraction of the patagial and hypaxial musculature, or by holding the wings open with the forelimbs. We suggest that the second possibility is more likely as the forelimb appears well-suited to hold the patagium (as argued in Chapter 5 for *D. volans*). As a result, it is unlikely that weigeltisaurids glided under an arms-front posture (or at least not for a prolonged time).

Given these constraints, cambered arms-first postures appear impractical in *C. elivensis* despite their theoretical gliding efficiency during equilibrium gliding. However, we show that cambered arms-transverse postures also allowed for efficient gliding, although they all began with much longer starting ballistic phases. This is particularly true if the animal performs at slightly higher angle of attack for these postures, apparently maximizing rapid lift generation rather than horizontal distance. Lastly, given that these cases all show prolonged glide angles of less than 45° (Figures 11), our results strongly support the hypothesis that *C. elivensis*, and likely all weigeltisaurids, were true gliders.

Weigeltisaurid paleoecology and evolution

Our analyses indicate *C. elivensis* operated under a pseudo-phugoid mode during its mid-glide phase after a long ballistic fall (Figure 11d). Phugoid gliding is a flight dynamic mode whereby an aircraft passively oscillates between nose-up pitching and vertical climbing, and nose-down pitching and descent (Templin, 2000; Chatterjee and Templin, 2007). In the case of *C. elivensis*, this pseudo-phugoid mode could have allowed the animal to oscillate between trees by gaining speed during a long ballistic dive and then climbing back up a few meters and decelerating before landing. Similar gliding behaviors have been reported in extant birds (Templin, 2000) and sggested for extinct dinosaurs such as *Archaeopteryx* and *Microraptor* (Chatterjee and Templin, 2003, 2007). This cost-effective gliding mode could also have been supplemented by active righting. By comparison, *Draco* shows continuous descent during equilibrium gliding (see Chapter 5) and thus rely entirely on active righting to climb up during the landing phase of a glide (Dehling, 2017; Khandelwal and Hendrick, 2020, 2022).

Our trajectory simulations show that *C. elivensis* would have needed at least a 15-17 m drop (more likely 20m, P3a) to accumulate enough speed to generate lift and counteract weight. Provided a sufficiently high starting perch, the animal could then reach trees tens of meters away.

However, we stress that these simulations represent maximum glide performances obtained for a theoretical maximum of the lift-to-drag ratio $(C_L/C_D)_{max}$ in an unobstructed setup under still air. It may thus not be representative of the actual behavior of weigeltisaurids. As an example, *Draco* can reach equilibrium gliding in similar experimental settings, but never do so in natural conditions (Khandelwal and Hendrick, 2020, 2022). It is thus likely weigeltisaurids employed a large degree of active righting of the body angulation, camber control, and tail movement to navigate in their environment, as observed in extant gliders (Dehling, 2017; Khandelwal and Hendrick, 2020, 2022; Clark et al., 2021).

Moreover, it should also be noted that our CFD and trajectory analyses are all based on the reconstruction of *C. elivensis* as a moderate-sized animal (180 mm SVL, Buffa et al., 2022). It is likely that other weigeltisaurid specimens or species varied in overall size and mass, and possibly in planform area. While the examination of the gliding performances of all weigeltisaurids is out of the scope of this paper, we note that the very small Munk and Bahaus specimens of *W. jaekeli* (ca. 100 mm SVL, Schaumberg, 1976, 1986) would certainly have had

lower mass and wing loadings, and are expected to perform more efficient glides than *C. elivensis*.

On the matter of size, weigeltisaurids reached more than twice the linear dimensions of most *Draco* species, and their inferred mass and wing loadings are much larger (despite much higher aspect ratios of the wings). This led previous assessments to suggest weigeltisaurids were not efficient gliders (McGuire and Dudley, 2011). Whereas our analyses strongly support the capacity of weigeltisaurids for true gliding, it is clear that they may not have been efficient gliders, at least at present-day air density (ca. 30 m fall during the ballistic phase of P3a at AoA 5°, Figure 11a). However, our results indicate that the ballistic phase can be significantly shortened at higher air density (Figure 11b). It thus appears plausible that the large size of adult weigeltisaurids only allowed them to glide at such densities, despite their much higher wing aspect ratio counteracting part of this increase in weight. Assuming there were strong selective pressure towards controlled gliding between perches preventing falling to the ground, as in extant arboreal taxa (Cartmill, 1974, 1985), a corollary could be that the evolution of large size in weigeltisaurids was only permitted by the atmospheric condition of the Early-Middle Permian, highlighting a new line of evidence regarding the evolution of vertebrate gliders. Further supporting this point, similar hypotheses have been proposed to explain the evolution of gigantism in insects (Dudley, 1998; Clapham and Karr, 2012; Cannell, 2018).

However, in the case of weigeltisaurids, this hypothesis is first dependent on the actual air atmosphere at the time they lived, which is hampered by poor age constraints, except for *W. jaekeli* from the mid-Wuchiapingian Kupferschiefer Formation (Zechstein Group, Germany) (Ezcurra et al., 2014). Lastly, it also depends on the habitat in which weigeltisaurids lived, namely the density and mean height of the canopy strata, for which no data is currently available (all specimens having been transported by water).

Conversely, one may wonder whether weigeltisaurids can provide information to infer some aspects of the paleoenvironments they lived in since their glide performances appear dependent on environmental parameters such as air density or jumping height. This raises potential prospects regarding the use of gliding vertebrates as paleoenvironmental markers.

Conclusion

The detailed examination of several postures for weigeltisaurid reptiles, the first known aerial vertebrates, using Computational Fluid Dynamics confirms that these animals were capable of true gliding and not merely controlled steep aerial descent, corroborating previous informal suggestions. Our analyses show that weigeltisaurids generate sufficient lift to counteract weight through the creation of vortices, and thus regions of reduced pressure and velocity above their wings and in their wakes for positive angles of attack. This mechanism is nearly identical to that employed by extant gliders, indicating convergent adaptation for lift generation. Moreover, we show that changes in body posture have a direct impact on aerodynamic and gliding performance through the comparison of rigid-body models, as in extant gliders. Thus, weigeltisaurids were likely able to control the amount of lift and drag generated in air by adopting different postures. Our gliding trajectory analyses further show that weigeltisaurids required a long ballistic dive prior to horizontal movement, but would then have been able to generate enough lift to climb back up slightly, allowing them to oscillate between trees and decrease speed before landing. This 'phugoid' flight mode is unknown in known in extant and extinct birds and dinosaurs, but is otherwise unknown in extant gliders which are reliant on active righting to climb up while airborne. The flight mode of weigeltisaurids was thus very different from that of more recent gliders. However, such glides would only have been possible under the high air densities estimated for the Permian Period. It is thus likely weigeltisaurids originated and reached their large size under a hyperdense atmosphere, casting new light onto the early phases of weigeltisaurid evolution.

General conclusion

The new observations, hypotheses and calculations compiled in this thesis represent an attempt to improve our knowledge of the anatomy, evolution and paleobiology of the enigmatic Permo-Triassic diapsids that were weigeltisaurids and drepanosauromorphs. The various parts of this dissertation rely on different methodologies, namely comparative anatomy, cladistics, and fluid mechanics. They also cover a range of geological periods through the study of Permian, Triassic and extant taxa. Lastly, they all offer new implications and perspectives regarding early diapsid evolution and paleobiology.

As outlined in the title of this dissertation, the exquisitely preserved weigeltisaurid *Coelurosauravus elivensis* from the late Permian Lower Sakamena Formation of Madagascar is the main focus of this work. The detailed re-description of all specimens referred to this taxon thus serves as the basis for this dissertation, and reveals several hitherto unknown anatomical details. These new data allow for novel reconstructions of the entire skeleton and for morpho-functional inferences by analogy with extant and extinct reptiles that support the previously proposed insectivorous, arboreal and aerial lifestyle of this taxon. In particular, comparisons to recent analogues, namely *Draco* and chamaeleonids, suggest *C. elivensis* may have partaken in display behavior when on the ground, but was also an accomplished glider capable of controlling the extension and camber of its broad patagial wings with its forelimbs.

Among this new anatomical information, the observation that patagial spars – the patagial skeleton of weigeltisaurids – were closely articulated with the gastralia indicates that the wing of *C. elivensis* originated from the ventral margin of the flanks rather than their dorsal margins. This result is confirmed using Computational Laminography based on the Ellrich specimen from the Late Permian of Germany, which is congruent with previous suggestions. As a result, the dorsoventral position of the wing in weigeltisaurids, a key prerequisite for aerodynamical studies, can now be reliably reconstructed for the first time.

The wealth of novel anatomical data on weigeltisaurids prompted the detailed first-hand reexamination of most of the Late Triassic drepanosauromorph specimens from Italy. The most commonly accepted hypothesis when this work was undertaken united both taxa as sister-groups among stem-saurian diapsids inside the clade ‘Avicephala’. Surprisingly, this reexamination underlined many anatomical differences between drepanosauromorphs and

weigeltisaurids, and instead highlighted the presence of numerous characters typical of archosauromorphs in the former. Given those differences, all of these new anatomical observations were included into a novel phylogenetical dataset design to resolve the phylogenetic relationships of 'avicephalans' among Permo-Triassic reptiles.

The phylogenetic analyses presented here confirm that weigeltisaurids were non-saurian diapsids, but recover drepanosauromorphs as sister-taxa to pterosaurs in a hitherto unrecognized pterosauromorph clade or ornithodiran archosaurs. This latter result reduces the number of diapsid lineages that survived the Permo-Triassic Mass Extinction event, but more importantly, provides new insight on the evolution of powered flight in pterosaurs. Indeed, several characters previously thought to have evolved in the context of flight are in fact already present in drepanosauromorphs and are thus best reinterpreted as exaptations derived from an ancestral arboreal morphology. In other words, this new systematic position of drepanosauromorphs supports the arboreal hypothesis of the still debated origins of pterosaurs. In particular, it raises the possibility that a common arboreal ancestor to drepanosauromorphs and pterosaurs was capable of patagial gliding, highlighting the need for a better understanding of this peculiar locomotion in small reptiles.

The agamid squamate *Draco* is without contest the most accomplished extant reptilian glider. Yet, until recently, the cryptic and arboreal behavior of this animal prevented the detailed study of its aerodynamic and gliding performances. The detailed systematic examination of the aerodynamics of rigid-body models of *Draco volans* undertaken here using Computational Fluid Dynamics (CFD) highlights the importance of posture in this reptile, which conforms to observed behavior. Furthermore, this detailed description of modeled flight behavior allows for similar studies on extinct gliders.

The study of the aerodynamics and gliding performance in *C. elivensis* using CFD confirmed this reptile was – in theory – capable of true gliding flight. This animal was capable of creating vortices above its wings in flight, and thus generated lift in a convergent manner to *D. volans*. However, simulated gliding trajectories using rigid-body models were very different between both taxa, with *D. volans* showing continuous descent, whereas *C. elivensis* showing an oscillatory phugoid trajectory. This phugoid flight allows for a passive climb-up during gliding that compensates part of the initial ballistic glide, and seems particularly well-suited to larger animals such as *C. elivensis*. Yet, despite this passive adaptation, and the much larger

wings of weigeltisaurids compared to *D. volans*, our analyses indicate *C. elivensis* was likely a very poor glider at present-day air density. However, it was apparently capable of much more efficient gliding at the higher air density inferred for the Permian period, which suggests that past atmosphere allowed weigeltisaurids to reach much larger sizes than extant reptilian gliders.

In short, detailed anatomical reexaminations indicate the first two diapsid groups of arboreal specialists, the late Permian Weigeltisauridae, and the Late Triassic Drepanosauromorpha, are not closely related to each other. However, the results presented in this thesis highlight that the study of both taxa is intimately linked to the understanding of flight origins – plural emphasized – in reptiles. Weigeltisaurids were indeed accomplished gliders, while drepanosauromorphs are here recovered as the immediate sister-group to pterosaurs, the first vertebrates capable of powered flight, which suggests that pterosaurs evolved from arboreal, gliding ancestors. The systematic study of both extant and extinct reptilian gliders provided here should improve our understanding of the evolution of gliding flight, and opens numerous exciting prospects for future studies.

Perspectives and future directions

Weigeltisaurid wing anatomy

Much of the anatomy of weigeltisaurids was revised over the course of this thesis, adding to other recent works (Bulanov and Sennikov, 2010, 2015a-c; Pritchard et al., 2021). Sufficient data is now available to reliably reconstruct the wing of weigeltisaurids, enabling the aerodynamical studies presented here. However, just about anything else concerning these wings remains uncertain, including (1) inter-specific variation; (2) the range of movement of individual spars during gliding; (3) the folding and unfolding mechanism and resting posture; (4) the embryonic origin of the patagial spars themselves (see discussions in Frey et al., 1997; Schaumberg et al., 2007; Pritchard et al., 2021).

Given the one-to-one patagio-gastralial articulation described here, it is likely that a more detailed examination of these structures in well-preserved specimens could provide new data on the range of movement of this articulation and thus on wing expansion and camber. In addition, known specimens are preserved in articulation, and their 'death poses' could provide information on wing folding and resting posture – accounting for taphonomic biases. Lastly, further data gleaned from microanatomical and histological studies could provide additional information regarding the internal organization of the wing, specifically the presence of Sharpey's fibers indicating muscular, tendinous or ligamentous insertions. Such studies could also provide evidence with regards to the osteological nature of the patagials.

Indeed, an osteohistological study of the wing was initiated over the course of this project. Twenty-six thin sections were made from the *Weigeltisaurus* sp. specimen SMNK-PAL 34865 (an isolated wing including articulated patagials and gastralia, and a single anterior dorsal rib) including transverse and longitudinal sections of the ribs, gastralia and patagials. The best-preserved scrap of this specimen was then CT-scanned (MRI, Université de Montpellier), which was not possible to do for the entire slab. There is thus a wealth of data under study in the hopes of furthering our understanding of weigeltisaurid wing anatomy. However, this study could not be incorporated into this thesis due to time constraints.

Non-saurian diapsid phylogeny

The phylogenetic dataset built over the course of this thesis was initially designed with the study of stem-saurian diapsid relationships in mind since recent hypotheses placed 'Avicephala' at the base of the group. Yet, much of the work effort later glided over to Triassic archosauromorphs when it appeared that drepanosauromorphs were better interpreted as pterosaur relatives. Nevertheless, the new dataset presented here remains well-suited for future investigations on non-saurian diapsid phylogeny.

Several questions were indeed raised over the course of this work, and few concerning non-saurian diapsid relationships have been answered. Indeed, while the recovery of weigeltisaurids as the immediate sister-group to Sauria conforms to suggestions raised throughout the comparative description of *C. elivensis*, little has been said relative to other taxa. For example, the question of the monophyly of 'younginiforms' and of the systematic position of *Claudiosaurus* were raised here, but require in-depth studies of the material for further discussion (which are actually part of an ongoing MNHN project involving several Masters Theses, including my own, Buffa, 2019). Additionally, challenges to the 'traditional' composition of various amniote clades were raised while this Ph.D. project was underway (see Chapter 4; Ford and Benson, 2020; Simões et al., 2022), and the present dataset is also designed for future studies on non-saurian diapsids that would take those hypotheses under consideration.

Pterosaur origins

The phylogenetic analyses presented here recover a hitherto unrecognized clade uniting drepanosauromorphs and pterosaurs among ornithodiran archosaurs. These results have several outstanding implications, including further support for the arboreal hypotheses of pterosaur origins. However, there are actually two distinct arboreal hypotheses: the arboreal parachuting theory (Wild, 1978, 1984), and the arboreal leaping theory (Bennett, 1997). All things considered, both hypotheses differ mostly in the capacity of a 'proto-pterosaur' to launch itself in air rather than free-falling. Several muscular insertions were indicated during the re-description of drepanosauromorphs, and further study of the musculoskeletal system of drepanosauromorphs could provide insight into their jumping capacity.

Furthermore, it should also be noted that the topologies presented here rely on a dataset designed to resolve the phylogenetic relationships of 'avicephalans' among a wide array of Permo-Triassic reptiles. It would thus be worthwhile to include these new data into other matrices specifically designed to study pterosaur origins (e.g. Ezcurra et al., 2020; Foffa et al., 2022). Doing so could provide lines of evidence to tackle further outstanding questions, such as: (1) Are drepanosauromorphs monophyletic or do they form a grade leading to Pterosauria? (2) Is there any evidence of arboreality in lagerpetids? (3) What does this tell us about pterosaur origins from a biogeographical perspective?

Drepanosauromorph monophyly

This thesis could not run its course without discussing the several mentions of still undescribed subcomplete material of drepanosauromorphs from the Nugget Sandstone of northeastern Utah that share numerous characters with *Drepanosaurus,* such as the hypertrophied forelimb and manual claw II (Britt and Chure, 2016), but have "large maxillary and dentary teeth reminiscent of *Trilophosaurus*" (Chure et al., 2013; see also Engelmann, 2012; Chure et al., 2015). Given the uniqueness of *Trilophosaurus* teeth – with some species based solely on dental material (Mueller and Parker, 2006; Kligman et al., 2020) –, those of its sister-taxon *Teraterpeton* (Sues, 2003), and the clear absence of such morphology in the holotypes of *M. preonensis* and *V. cenensis*, this raises the question of drepanosauromorph monophyly. Indeed, some (alternatively all) drepanosauromorphs may be more closely related to trilophosaurids than to other drepanosauromorphs such as *M. preonensis* and *V. cenensis*. However, as this unpublished material was not observed here, these mentions are not further discussed here.

Weigeltisaurid paleoecology

The simulations conducted during this thesis confirm that weigeltisaurids were efficient gliders, at least under the relatively dense Permian atmosphere. However, these simulations were only conducted on geometries derived from the reconstruction of *C. elivensis*. Given the broad range of intra- and inter-specific gliding performances observed in extant *Draco* (McGuire and Dudley, 2005), this opens exciting prospects of comparative biomechanics

between known specimens. Indeed, it is expected that the very small Munk specimen of *W. jaekeli* had a much smaller mass and wing loading than any other known weigeltisaurid, and could thus glide more efficiently. However, it remains unclear whether this specimen represents a diminutive species or an immature individual, and thus whether this could suggest interspecific or ontogenetic differences – and eventually niche partitioning as suggested for *Draco* (Inger, 1983; McGuire, 2003).

Additionally, the interspecific differences in patagial spar organization noted between *C. elivensis* and *W. jaekeli*, the best-known weigeltisaurids, would undoubtedly include differences in active control during gliding, and thus result in different gliding efficiency. Lastly, much of the interspecific differences noted here between *C. elivensis* and *W. jaekeli* concern cranial ornamentation, with the latter being more ornamented than the former. It is expected that the spikes on the head of weigeltisaurids would break fluid flow and generate additional drag anterior to the wings, likely decreasing gliding efficiency. The comparison of both taxa could provide evidence of increased trade-off between flight efficiency and ornamentation – with the latter feature likely being used in display behavior.

Appendix 1: Taxon list for phylogenetical analyses

The present taxon list describes the 82 Operational Taxonomic Units (OTUs) employed in our dataset. Each entry comprises the material examined (if any), key references consulted, an approximate age range and a summary of the stratigraphic occurrences of each taxon. The age rages correspond to ICS stages (Cohen et al., 2022) equivalent to the stratigraphic occurrences described in each entry. For non-standard 'lower' or 'upper' designations for given ICS stages, each stage was arbitrarily divided in two equal 'lower' or 'upper' substages. Standard substages (ages based on Gradstein et al., 2020), were similarly divided (in two or three equal divisions following usual practice) when applicable.

Each OTU was scored primarily using direct observation of specimens, photographs and/or 3D models when available. All scorings were supplemented by published descriptions, which form the main source of information for all taxa where material was not studied. Lastly, scorings from previous matrices were studied as a third source of information, but were considered as reliable only when it was explicitly stated that the material was studied by the authors of these works, and when the formulation of given characters was similar to those of the present study. This is thus a more marginally used source of information.

All OTUs are scored at the species level with the exception of six OTUs taken at the generic level to increase scoring completeness or to palliate uncertain species-level discriminations: *Araeoscelis* spp., *Dimetrodon* spp., *Ophiacodon* spp., *Proterosuchus* spp., *Rautiania* sp., and *Seymouria* spp.

Institutional abbreviations—**BMNH**, British Museum of Natural History, London, England; **BP**, Bernard Price Institute, Johannesburg, South Africa; **MCSNB**, Museo "Caffi" di Scienze Naturali Bergamo, Bergamo, Italy; **MCZ**, Museum of Comparative Zoology, Harvard, USA; **MFSN**, Museo Friulano di Scienze Naturali, Udine, Italy; **MGM**, McGregor Museum, Kimberley, South Africa; **MNHN**, Muséum national d'Histoire naturelle, Paris, France; **MPUM**, Museo di Paleontologia Università degli Studi di Milano, Milano, Italy; **NMNH**, National Museum of Natural History, Smithsonian Institution, Washington, D. C., USA; **RM**, Redpath Museum, McGill University, Canada; **ROM**, Royal Ontario Museum, Toronto, Canada; **WMsN**, Westfälisches Museum für Naturkunde, Münster, Germany; **YPM**, Yale Peabody Museum, New Haven, Connecticut.

Outgroup taxa

Limnoscelis paludis Williston, 1911a

- Material examined: MNHN cast of YPM 811 (Holotype); photos of YPM 811 (Holotype)
- References: Williston, 1911b, 1912; Romer, 1946; Fracasso 1987; Sumida, 1990, 1997; Sumida et al., 1992; Berman and Henrici, 2003; Berman et al., 2010; Kennedy, 2010
- Age: Kasimovian-Gzhelian (ca. 307-298.9 Ma)
- Horizon and locality: lower part of El Cobre Canyon Formation, Rio Arriba County, New Mexico (Lucas and Krainer 2005; Berman et al., 2010), lower part of Culter Group, Late Pennsylvanian (Lucas and Krainer 2005; Lucas et al., 2010)

Seymouria spp. Broili, 1904

- References: Williston, 1911b; White, 1939; Berman et al., 1987, 2000a; Sumida, 1990, 1997; Sumida et al., 1992; Laurin, 1995, 1996; Klembara et al., 2005; Bazzana et al., 2019, 2020
- Age: Artinskian (ca. 290.1-283.5 Ma)
- Horizons and localities: Bromacker quarry, Tambach Formation, Germany (Artinskian, Menning et al., 2006; Schneider et al., 2020); various localities grouped under the Seymouran Land Vertebrate Faunachron (LVF) correlated with Artinskian Stage (Lucas, 2017; Schneider et al., 2020)

Ingroup taxa

Synapsida

Casea broilii Williston, 1910

- References: Williston, 1911b, 1913, 1914; Romer and Price, 1940; Olson, 1968; LeBlanc and Reisz, 2014
- Age: Kungurian (ca. 283.5-273.01 Ma)
- Horizon and locality: *Cacops* bonebed, Baylor County, Texas, Uppermost Arroyo Formation/lowermost Vale Formation, Clear Fork Group (LeBlanc and Reisz, 2014), Kungurian (Lucas, 2017; Schneider et al., 2020)

Dimetrodon spp. Cope, 1878

- References: Case, 1910a; Gilmore, 1911; Romer, 1927; Romer and Price, 1940; Reisz, 1986; Brink and Reisz, 2012
- Age: Asselian-early Roadian (ca. 298.9-270 Ma)

- Horizons and localities: Abo Formation, New Mexico (*D. occidentalis*), Asselian-Artinskian (Lucas et al., 2013; Lucas, 2017; Schneider et al., 2020); Putnam (*D. mirelli*), Admiral (*D. limbatus*, *D. natalis*) and Belle Plains (*D. booneorum*, *D. macrospondylus*) Formations, Wichita Group, Texas (Romer and Price, 1940), Sakmarian-Artinskian (Lucas, 2017; Schneider et al., 2020); Bromacker quarry, Tambach Formation, Germany (*D. teutonis*, Berman et al., 2001), Artinskian (Menning et al., 2006; Schneider et al., 2020); Arroyo Formation, Clear Fork Group, Texas (*D. grandis*, *D. loomisi*, *D. gigashomogenes*, *D. kempae*), Kungurian (Lucas, 2017; Schneider et al., 2020); San Angelo Formation, Pease River Group, Texas (*D. angelensis*), early Roadian (Laurin and Hook, 2022)

Eothyris parkeyi Romer, 1937

- Material examined: Photographs of MCZ 1161 (Holotype)
- References: Romer and Price, 1940; Reisz et al., 2009
- Age: Artinskian (ca. 290.1-283.5 Ma)
- Horizon and locality: Tit Mountain, near Dundee, Archer County, Texas, Petrolia Formation, Wichita Group (Reisz et al., 2009), Artinskian (Lucas, 2017; Schneider et al., 2020)

Haptodus garnettensis Currie, 1977

- References: Currie, 1977; Laurin, 1993
- Age: late Kasimovian (ca. 305.4-303.7 Ma)
- Horizon and locality: Charles A. Hardesty farm, near Garnett, Anderson County, Kansas, Rock Lake Shale Member, Santon Formation, Lansing Group (Laurin, 1993), late Kasimovian (Mazierski and Reisz, 2010)

Martensius bromackerensis Berman, Maddin, Henrici, Sumida, Scott and Reisz, 2020

- Reference: Berman et al., 2020
- Age: Artinskian (ca. 290.1-283.5 Ma)
- Horizon and locality: Bromacker quarry, Tambach Formation, Germany (Artinskian, Menning et al., 2006; Schneider et al., 2020)

Ophiacodon spp. Marsh, 1878

- References: Williston and Case, 1913; Romer and Price, 1940; Reisz, 1986
- Age: Kasimovian-Artinskian (ca. 307-283.5 Ma)
- Horizons and localities: El Cobre Canyon Formation, Rio Arriba County, New Mexico (*O. navajovicus*, Romer and Price, 1940), lower part of Culter Group, Late Pennsylvanian (Lucas and Krainer 2005; Lucas et al., 2010); Abo Formation, New Mexico (*O. mirus*), Asselian-Artinskian (Lucas, 2017; Schneider et al., 2020); Admiral (*O. retroversus*) and Clyde Formations, Wichita Group, Texas, Artinskian (Lucas, 2017; Schneider et al., 2020); Wildcat Canyon, near Winfield, Kansas, Fort Riley Limestone,

Chase Group (O. hili, Romer and Price, 1940), Artinskian (Sawin et al., 2008; Schneider et al., 2020)

Varanosaurus acutirostris Broili 1904

- References: Case, 1910b; Watson, 1914; Romer and Price, 1940; Berman et al., 1995; Sumida, 1989a, 1990
- Age: Kungurian (ca. 283.5-273.01 Ma)
- Horizon and locality: Arroyo Formation, Clear Fork Group, Texas, Kungurian (Lucas, 2017; Schneider et al., 2020);

Varanopidae

Aerosaurus wellesi Langston and Reisz, 1981

- Material examined: photographs of UCMP 40096 available on CalPhotos (https://calphotos.berkeley.edu/cgi/img_query?where-specimen_no=V40096&where-museum=UCMP)
- References: Langston and Reisz, 1981; Pelletier, 2014; Bazzana et al., 2022
- Age: Asselian-Sakmarian (ca. 298.9-290.1 Ma)
- Horizon and locality: Camp Quarry, Rio Arriba County, New Mexico, upper El Cobre Canyon Formation (Pelletier, 2014), Culter Group, lowermost Permian (Lucas and Krainer 2005), correlated with Asselian-Sakmarian (Lucas, 2017)

Archaeovenator hamiltonensis Reisz and Dilkes, 2003

- References: Reisz and Dilkes, 2003; LeBlanc and Reisz, 2014
- Age: late Gzhelian (ca. 301.3-298.9 Ma)
- Horizon and locality: Hamilton Quarry, Greenwood County, Kansas, Calhoum Shale, Shawnee Group, Virgilian regional stage equivalent to late Gzhelian (Wagner and Winkler Prins, 2016)

Mesenosaurus romeri Efremov, 1938

- References: Reisz and Berman, 2001; Spindler et al., 2019
- Age: late Kungurian-Wordian (ca. 278.3-264.28 Ma)
- Horizon and locality: Kimja River, Mezen River Basin, Arkhangel'sk Province, Russia (Romer and Price, 1940). Included in Mezen Assemblage (Golubev, 2000), correlated to late Ufimian-Urzhumian regional Stages (Cisularian-Biarmian Series), equivalent to late Kungurian-Wordian (Golubev, 2015; Sennikov and Golubev, 2017; Davidov et al., 2018)

Mycterosaurus longiceps Williston, 1915

- Material examined: FMNH UC 692 segmented CT data available on MorphoSource Repository (https://www.morphosource.org/concern/biological_specimens/000S12897)
- References: Vaughn, 1958; Berman and Reisz, 1982
- Age: Artinskian-early Kungurian (ca. 289-278.3 Ma)
- Horizons and localities: Dolese Brothers Limestone Quarry, near Richards Spur, Comanche County, Oklahoma, Artinskian (ca. 289-296 Ma, MacDougall et al., 2017); Mitchell Creek, Baylor County, Texas, Clyde Formation, Wichita Group (Berman and Reisz, 1982), late Artinskian-early Kungurian (Lucas, 2017)

Varanops brevirostris (Williston, 1911b)

- References: Williston, 1911b; Romer and Price, 1940; Maddin et al., 2006; Campione and Reisz, 2010, 2011
- Age: Artinskian- Kungurian (ca. 290.1-273.01 Ma)
- Horizons and localities: Dolese Brothers Limestone Quarry, near Richards Spur, Comanche County, Oklahoma, early Artinskian (ca. 289-296 Ma, MacDougall et al., 2017); *Cacops* bonebed, Baylor County, Texas, Kungurian (see *Casea* above); Mud Hill, Vale Formation, Clear Fork Group, Kungurian (Lucas, 2017; Schneider et al., 2020)

Parareptilia

Delorhynchus cifellii Reisz, MacDougall and Modesto, 2014

- References: Reisz et al., 2014; Haridy et al., 2016, 2018
- Age: middle Artinskian (ca. 289-286 Ma)
- Horizon and locality: Dolese Brothers Limestone Quarry, near Richards Spur, Comanche County, Oklahoma, Artinskian (ca. 289-296 Ma, MacDougall et al., 2017)

Deltavjatia rossicus (Hartmann-Weinberg 1937)

- Reference: Tsuji, 2013
- Age: late Capitanian-early Wuchiapingian (ca. 261.9-256.8 Ma)
- Horizon and locality: Vjatka River, Kotel'nich locality, Kirov Province, Russia (Tsuji, 2013). Included in Kotelnich Subassemblage and *Deltavjatia vjatkensis* Tetrapod Zone (Golubev, 2000; Sennikov and Golubev, 2017), correlated to Severodvinian regional Stage (Tatarian Series) and lower *Endothiodon* Assemblage Zone (*Lycosuchus* – *Eunotosaurus* Subzone), South Africa (Day and Smith, 2020), equivalent to late Capitanian-early Wuchiapingian (Golubev, 2015; Sennikov and Golubev, 2017; Davydov et al., 2020; Day and Smith, 2020)

Emeroleter levis Ivakhnenko, 1997

- Reference: Tsuji et al., 2012
- Age: late Capitanian-early Wuchiapingian (ca. 261.9-256.8 Ma)
- Horizon and locality: Vjatka River, Kotel'nich locality, Kirov Province, Russia (Tsuji et al., 2012), late Capitanian-early Wuchiapingian (see *Deltavjatia* above)

Macroleter poezicus Tverdokhlebova and Ivakhnenko, 1984

- Reference: Tsuji, 2006; Cisneros and Tsuji, 2009
- Age: late Kungurian-Wordian (ca. 278.3-264.28 Ma)
- Horizon and locality: Mezen River Basin, Arkhangel'sk Province, Russia, late Kungurian-Wordian (see *Mesenosaurus* above)

Mesosaurus tenuidens Gervais, 1865

- References: Huene, 1941; Modesto, 2006, 2010; Piñeiro et al., 2012a-b, 2016; Laurin and Piñeiro, 2017, 2018; MacDougall et al., 2018
- Age: Kungurian (ca. 283.5-273.01 Ma)
- Horizons and localities: Whitehill Formation, Ecca Group, South Africa, Kungurian (Schneider et al., 2020); correlated based on presence of *Mesosaurus* to Mangrullo Formation, Tacuarembo and Cerro Largo Counties, Uruguay and Irati Formation, Passa Dois Group, Brazil (Holz et al., 2010; Piñeiro et al., 2012), Kungurian (Santos et al., 2006)

Milleretta rubidgei (Broom, 1938)

- Material examined: Photos of BP/1/2040; BP/1/2610; BP/1/2614; BP/1/3818; BP/1/3821
- References: Broom, 1938, 1948; Watson, 1957; Gow, 1972, 1997; Thommasen and Carroll, 1981
- Age: late Wuchiapingian-early Changhsingian (ca. 256.7-253 Ma)
- Horizon and locality: several localities (listed in Gow, 1972) in the *Cistecephalus* Assemblage Zone, Wuchiapingian (ca. 256.6 +/- 0.1 - 255.24 +/- 0.06 Ma, Smith, 2020) and lower *Daptocephalus* Assemblage Zone (*Dicynodon* – *Theriognathus* Subzone), South Africa, late Wuchiapingian-early Changhsingian (ca. 255.2-253 Ma, Viglietti, 2020)

Procolophon trigoniceps Owen, 1876

- References: Kemp, 1974; Gow, 1977; Carroll and Lindsay, 1985; deBraga, 2003; Cisneros, 2008; Silva-Neves et al., 2020
- Age: Induan-Olenekian (ca. 251.902-247.2 Ma)
- Horizon and locality: several localities in the *Lystrosaurus declivis* Assemblage Zone, South Africa, Induan-early Olenekian (Botha and Smith, 2020); correlated to lower Fremouw Formation, Antartica and Sanga do Cabral Formation, Paraná Basin, Brazil (Botha and Smith, 2020)

Saurodektes kitchingorum (Reisz and Scott, 2002)

- Reference: Reisz and Scott, 2002; Hamley et al., 2021
- Age: Induan-Olenekian (ca. 251.902-247.2 Ma)
- Horizon and locality: Donovan's Kop, Tweefontein, South Africa (Reisz and Scott, 2002). Included in *Lystrosaurus declivis* Assemblage Zone, South Africa, Induan-early Olenekian (Botha and Smith, 2020)

Non-Diapsida Eureptilia

Captorhinomorpha

Captorhinus aguti (Cope, 1882)

- Material examined: MNHN uncatalogued specimen (subcomplete skull, presacral column and forelimbs) from Dolese Brothers Limestone Quarry, Oklahoma
- References: Price, 1935; Fox and Bowman, 1966; Vaughn, 1970; Holmes, 1977, 2003; Ricqlès and Bolt, 1983; Modesto, 1998; Sumida, 1990; LeBlanc and Reisz, 2015; Werneburg and Abel, 2022
- Age: Artinskian-early Kungurian (ca. 290.1-278.3 Ma)
- Horizons and localities: several localities of the Admiral, Belle Plains, Clyde, Arroyo and Vale Formations, Whichita and Clear Fork Groups, Texas (listed in Fox and Bowman, 1966, see also Olson, 1962), Artinskian-early Kungurian (Lucas, 2017; Schneider et al., 2020); Dolese Brothers Limestone Quarry, near Richards Spur, Comanche County, Oklahoma, Artinskian (ca. 289-296 Ma, MacDougall et al., 2017)
- Remarks: Fox and Bowman (1966) include one specimen from Poleo Creek, Rio Arriba County, New Mexico, Abo Formation, Asselian-Artinskian (Lucas et al., 2013; Lucas, 2017; Schneider et al., 2020), possibly pushing back the stratigraphic range of *C. aguti*, however this referral is not reported in later exhaustive taxonomic lists of the Abo Formation (Berman, 1993; Lucas et al., 2013), suggesting this specimen is indeterminate, and thus not considered here.

Labidosaurus hamatus (Cope, 1895)

- Material examined: MNHN cast of NMNH 17045
- References: Sumida, 1987, 1989b, 1990; Modesto et al., 2007
- Age: early Kungurian (ca. 283.5-278.3 Ma)
- Horizon and locality: Coffee Creek, Baylor County, Texas, USA, lowermost Clear Fork Group, early Kungurian (Lucas, 2017)

Thuringothyris mahlendorffae Boy and Martens, 1991

- References: Boy and Martens, 1991; Müller et al., 2006

- Age: Artinskian (ca. 290.1-283.5 Ma)
- Horizon and locality: Bromacker quarry, Tambach Formation, Germany (Artinskian, Menning et al., 2006; Schneider et al., 2020)

'Protorothyrididae'

Hylonomus lyelli Dawson, 1860

- Material examined: MNHN cast of RM 12016a
- References: Steen, 1934; Carroll, 1964; Meyer and Anderson, 2013
- Age: late Bashkirian (ca. 319.2-315.2 Ma)
- Horizons and localities: several localities (listed in Carroll, 1964), near Joggins, Nova Scotia, Canada, Joggins Formation, correlated to Langsettian and Westphalian A regional stages (summarized in Benton et al., 2015), equivalent to late Bahkirian (Rygel et al., 2015; Wagner and Winkler Prins, 2016), with Benton et al. (2015) giving a minimum age of 218 Ma.

Palaeothyris acadiana Carroll, 1969

- Material examined: MNHN cast of MCZ 3482
- References: Carroll, 1969
- Age: late Moscovian (ca. 311.1-307 Ma)
- Horizon and locality: Dominion Coal Co., near Florence, Cape Breton County, Nova Scotia, correlated to Westphalian C and D (Carroll, 1969), equivalent to late Moscovian (Wagner and Winkler Prins, 2016)

Non-Saurian Diapsida

Araeoscelidia

Araeoscelis spp. Williston 1910

- Material examined: Photographs of MCZ 4380; MCZ 8828
- References: Williston, 1913, 1914; Vaughn, 1955; Reisz et al., 1984; Zanon, 1990
- Age: Artinskian-early Kungurian (ca. 290.1-278.3 Ma)
- Horizons and localities: several localities in Admiral and Belle Plains Formations, Wichita Group (*A casei*, Vaughn, 1955; Reisz et al., 1984), Artinskian (Lucas, 2017; Schneider et al., 2020); Craddock bonebed, Craddock Ranch, Baylor County, Texas, Arroyo Formation, Clear Fork Group (*A. gracilis*), early Kungurian (Lucas, 2017; Schneider et al., 2020)
- Remarks: Vaughn (1955) found no significant anatomical difference between *A. gracilis* and *A. casei*, but elected to keep both species valid based on their stratigraphic

difference. Reisz et al. (1984) thus elect to consider *Araeoscelis* at the generic level in their subsequent description, a practice followed here.

Petrolacosaurus kansensis Lane, 1945

- Material examined: MNHN cast of ROM 29900
- References: Peabody, 1952; Reisz, 1981; Mazierski and Reisz, 2014
- Age: late Kasimovian (ca. 305.4-303.7 Ma)
- Horizon and locality: Garnett Quarry, Anderson County, Kansas, Rock Lake Shale Member, Santon Formation, Lansing Group, late Kasimovian (Mazierski and Reisz, 2010)

Neodiapsida

Acerosodontosaurus piveteaui Currie, 1980

- Material examined: MNHN.F.MAP359a-b (Holotype)
- References: Currie, 1980; Bickelmann et al., 2009
- Age: late Capitanian-Changhsingian (ca. 261.9-251.902 Ma)
- Horizon and locality: unrecorded locality, Lower Sakamena Formation, Madagascar, commonly correlated to Dzhulfian regional stage, and upper *Endothiodon* (*Tropidostoma-Gorgonops* Subzone) and *Cistecephalus* Assemblage Zones, South Africa, equivalent to Wuchiapingian (Piveteau, 1926; Currie, 1981a; Hankel, 1994; Lucas, 2017; Smith, 2000, 2020; Day and Smith, 2020). However, biostratigraphic correlations need to be revised, considering possible reidentifications of Malagasy material (Smith, 2020), and recent descriptions of Permian Malagasy reptiles or of their close relatives in older (see *Rautiania* below) and younger (see *Hovasaurus* below) strata. Thus, the Lower Sakamena Formation could be late Capitanian-Changhsingian (Buffa et al., in press).

Claudiosaurus germaini Carroll, 1981

- Material examined: MNHN.F.MAP1a-b (Holotype); MNHN.F.MAP362; MNHN.F.MAP 549; MNHN.F.MAP570; MNHN.F.MAP571; MNHN.F.MAP592; MNHN.F.MAP593; MNHN.F.MAP624; numerous unpublished MNHN specimens
- References: Brinkman, 1979; Carroll, 1981; Caldwell, 1995
- Age: late Capitanian-Changhsingian (ca. 261.9-251.902 Ma)
- Horizon and locality: near Leoposa Village, Lower Sakamena Formation, Madagascar, late Capitanian-Changhsingian (see *Acerosodontosaurus* above)

Coelurosauravus elivensis Piveteau, 1926

- Material examined: MNHN.F.MAP325a (Lectotype); MNHN.F.MAP317a-b (Paralectotype); MNHN.F.MAP327a

- References: Piveteau, 1926; Carroll, 1978; Evans, 1982; Evans and Haubold, 1987; Bulanov and Sennikov, 2015a; Buffa et al., 2021, in press
- Age: late Capitanian-Changhsingian (ca. 261.9-251.902 Ma)
- Horizon and locality: unrecorded locality, Lower Sakamena Formation, Madagascar, late Capitanian-Changhsingian (see *Acerosodontosaurus* above)

Hovasaurus boulei Piveteau, 1926

- Material examined: MNHN.F.MAP333 (Lectotype); MNHN.F.MAP316; MNHN.F.MAP333; MNHN.F.MAP352; MNHN.F.MAP373; cast of lost specimen from Piveteau (1926:pl. 14.1); numerous unpublished MNHN specimens.
- References: Brinkman, 1979; Currie, 1981a, b, 1982; Caldwell, 1995
- Age: late Capitanian-Changhsingian (ca. 261.9-249.2 Ma)
- Horizon and locality: near Mont Eliva, Lower Sakamena Formation, Madagascar, late Capitanian-Changhsingian (see *Acerosodontosaurus* above); unrecorded locality, likely in Diego Basin, Madagascar (Ketchum and Barrett, 2004), late Induan-early Olenekian (see Kogan and Romano, 2016; Laville et al., 2021)
- Remarks: Ketchum and Barrett (2004:2) only report that the Early Triassic material for *Hovasaurus* was collected from the "Middle Sakamena Formation of northwestern Madagascar". Given this limited information, we believe it possible the material was incorrectly provenanced, as suggested by Currie (1981a) for other specimens, but provisionally retain this occurrence.

Longisquama insignis Sharov, 1970

- Material examined: Photographs of PIN 2584/4
- References: Sharov, 1970; Haubold and Buffeteau, 1987; Jones et al., 2000; Unwin et al., 2000; Prum, 2001; Senter, 2004
- Age: Ladinian-Carnian (ca. 242-227 Ma)
- Horizon and locality: Dzailyau-Cho, Madygen area, Lyailyakskii district, Osh Province, Fergana, Kyrgyzstan, Ladinian-Carnian (Dobruskina 1995; Shcherbakov, 2008a)

Orovenator mayorum Reisz, Modesto and Scott, 2011

- Material examined: µCT segmentation data available on MorphoSource Repository
- References: Reisz et al., 2011; Ford and Benson, 2019
- Age: middle Artinskian (ca. 289-286 Ma)
- Horizon and locality: Dolese Brothers Limestone Quarry, near Richards Spur, Comanche County, Oklahoma, Artinskian (ca. 289-296 Ma, MacDougall et al., 2017)

Palaeagama vielhaueri Broom, 1926

- Material examined: MNHN cast of MGM 3707 (Holotype)
- References: Broom, 1926; Carroll, 1975
- Age: late Changhsingian-Olenekian (ca 253-247.2 Ma)

- Horizon and locality: Kinira, Mount Frere District, South Africa, either in upper *Daptocephalus* Assemblage Zone (*Lystrosaurus maccaigi-Moschorhinus* subzone, ca. 253-252 Ma, Viglietti, 2020) or *Lystrosaurus declivis* Assemblage Zone, Induan-early Olenekian (Botha and Smith, 2020) (Carroll, 1975)

Saurosternon bainii Huxley, 1868

- References: Carroll, 1975; Brinkman, 1979, 1980
- Age: late Wuchiapingian-early Changhsingian (ca. 255-253 Ma)
- Horizon and locality: Styl Krantz Sneeuwberg, South Africa, in lower *Daptocephalus* Assemblage Zone (*Dicynodon – Theriognathus* Subzone), South Africa (ca. 255-253 Ma, Viglietti, 2020)

Rautiania spp. Bulanov and Sennikov, 2006

- References: Bulanov and Sennikov, 2006, 2010, 2015a
- Age: late Capitanian-early Wuchiapingian (ca. 261.9-256.8 Ma)
- Horizon and locality: near Kul'chumovo, Orenburg Region, Russia, included in Sundyr Assemblage (Sennikov and Golubev, 2017), correlated to *Suchonica vladimiri* Tetrapod Zone, equivalent to early Wuchiapingian (Davydov et al., 2020), and to *Tapinocephalus* Assemblage Zone, South Africa, late Capitanian (~265-260 Ma, Day and Rubidge, 2020)

Weigeltisaurus jaekeli (Weigelt, 1930)

- Material examined: SMNK-PAL 34899a (cast of Holotype SSWG 113/7)
- References: Weigelt, 1930; Evans, 1982; Evans and Haubold, 1987; Bulanov and Sennikov, 2015c
- Age: Wuchiapingian (ca. 259.51-254.14 Ma)
- Horizon and locality: near Griefswald, Saxony-Anhalt, Germany, Kupferschiefer Formation, Zechstein Group, Wuchiapingian (Ezcurra et al., 2014; Schneider et al., 2020)
- Remarks: several additional specimens from various localities in the Kupferschiefer of Germany, as well as a headless specimen form the coeval Marl Slate Formation of England, have been referred to *W. jaekeli* (Evans, 1982; Evans and Haubold, 1987; Schaumberg et al., 2007). However, as noted by Buffa et al. (2021, in press), the alpha taxonomy of the weigeltisaurid material from Western Europe needs to be revised. We thus provisionally restrict this OTU to the holotype specimen of *W. jaekeli* (SSWG 113/7) while the better-preserved Ellrich specimen (SMNK-PAL 2882) is scored in a distinct OTU.

Youngina capensis Broom, 1914b

- Material examined: photos of BP/1/375; BP/1/2459; BP/1/2871; BP/1/3859

- References: Broom, 1921a-b, 1924; Olson, 1936; Goodrich, 1942; Watson, 1957; Gow, 1975; Carroll, 1981; Currie, 1981b; Evans, 1987; Evans and van de Heever, 1987; Smith and Evans, 1996; Reisz et al., 2000; Gardner et al., 2010
- Age: Wuchiapingian-early Changhsingian (ca. 258-253 Ma)
- Horizons and localities: several localities in upper *Endothiodon* (*Tropidostomoa-Grogonops* Subzone, ca. 258-256.8 Ma, Day and Smith, 2020), *Cistecephalus* ca. (256.6-255.25 Ma, Smith, 2020) and lower *Daptocephalus* (*Dicynodon-Theriognathus* Subzone, ca. 255-253 Ma, Viglietti, 2020) Assemblage Zones, South Africa,

Drepanosauromorpha

Avicranium renestoi Pritchard and Nesbitt, 2017

- References: Pritchard, 2015; Pritchard and Nesbitt, 2017
- Age: late Norian-Rhaetian (ca. 217.8-201.3 Ma)
- Horizon and locality: *Coelophysis* Quarry, Ghost Ranch, New Mexico, 'Siltstone Member, Chinle Formation, late Norian-Rhaetian (see Nesbitt and Sues, 2021)

Drepanosaurus unguicaudatus Pinna, 1980

- Material examined: MCNSB 5728 (Holotype)
- References: Pinna, 1980, 1984, 1986; Renesto, 1994a; Renesto and Fraser, 2003; Renesto et al., 2010; Pritchard et al., 2016
- Age: late middle-eary late Norian (ca. 215.2-211.9 Ma)
- Horizons and localities: Val Bruciata, near Zogno, Lombardy, Italy, Calcare di Zorzino Formation, Aralata Group, late middle-early late Norian (Alaunian 3-Sevatian 1, Dalla Vecchia, 2013, 2014, see also Pritchard et al., 2016 for a more conservative view); Hayden Quarry, Ghost Ranch, New Mexico, Petrified Forest Formation, Chinle Group, middle Norian (211.9 +/- 0.7 Ma, Irmis et al., 2011)
- We restrict *D. unguicaudatus* to the holotype specimen and the forelimb material referred by Pritchard et al. (2016), in agreement with the latter study. Thus, other previously referred fragmentary specimens are excluded, including an articulated pectoral girdle from the *Coelophysis* Quarry, Ghost Ranch, New Mexico, late Norian-Rhaetian (see Nesbitt and Sues, 2021) and a purported juvenile specimen from younger Lower Member of the Argillite di Riva di Solto Formation (Renesto and Paganoni, 1995; Renesto, 2006). Thus, we potentially restrict occurrences of *D. unguicaudatus* in the early Rhaetian.

Dolabrosaurus aquatilis Berman and Reisz, 1992

- References: Berman and Reisz, 1992; Renesto and Paganoni, 1995; Renesto et al., 2010
- Age: late Norian-early Rhaetian (ca. 213.1-207.8 Ma)
- Horizon and locality: UTM Zone 13, Rio Arriba County, New Mexico, lower Painted Desert Member, Petrified Forest Formation, Chinle Group (Renesto et al., 2009 contra

Berman and Reisz, 1992), equivalent to Petrified Forest Member, Chinle Formation, Arizona late Norian-early Rhaetian (ca. 213.1-207.8 Ma, Ramezani et al., 2011)

Hypuronector limnaios Colbert and Olsen, 2001

- References: Colbert and Olsen, 2001; Renesto et al., 2010
- Age: late early Norian (ca. 221.75-220.94 Ma)
- Horizons and localities: several localities in Nursery and Ewing Creek Members, Lockatong Formation, Newark Supergroup, New Jersey (Colbert and Olsen, 2001). Nursery and Ewing Creek Members estimated as respectively 221.35 Ma and 220.94 Ma through eccentricity cycles (Kent et al., 2017), conservative interval taken here using ages for underlying Princeton and overlying Byram Members (ca. 221.75 Ma and 220.54 Marespectively, Kent et al., 2017)

Megalancosaurus preonensis Calzavara, Muschio and Wild, 1980

- Material examined: MFSN 1769a-b; MFSN 1801; MFSN 18443; MPUM 6008; MPUM 8437
- References: Calzavara et al., 1980; Renesto, 1994b, 2000; Renesto and Fraser, 2003; Renesto and Dalla Vecchia, 2005; Renesto et al., 2010; Pritchard 2015; Castiello et al. 2016
- Age: late middle-eary late Norian (ca. 215.2-211.8 Ma)
- Horizons and localities: several localities in Calcare di Zorzino Formation, Aralata Group, Lombardy Italy (Renesto, 2006, Renesto et al., 2009), late middle-early late Norian (Alaunian 3-Sevatian 1, Dalla Vecchia, 2013, 2014, see also Pritchard et al., 2016 for a more conservative view); several localities in the Dolomia di Forni Formation, Friuli, Itay (see Dalla Vecchia, 2006), middle-late Norian (Alaunian 3-Sevatian 1, Dalla Vecchia, 2013, 2014, see also Pritchard et al., 2016 for a more conservative view).
- Remarks: we follow Pritchard (2015) in considering *M. endennae* as a junior synonym of *M. preonensis* and consequently referring MFSN 1801 and MFSN 18443 to the species level

Vallesaurus cenensis. Renesto and Binnelli, 2006

- Material examined: MCSNB 4751; MCSNB 4783
- References: Renesto and Binnelli, 2006; Renesto et al., 2010
- Age: late middle Norian (ca. 215.2-214.03 Ma)
- Horizons and localities: near Cene, Lombardy, Italy, Calcare di Zorzino Formation, Aralata Group, late middle Norian (Alaunian 3, Dalla Vecchia, 2013, 2014, see also Pritchard et al., 2016 for a more conservative view
- Remarks: we follow Pritchard (2015) in considering *V. zorzinensis* as a junior synonym of *V. cenensis* and consequently refer MCSNB 11342 to the latter taxon

Lepidosauromorpha

Icarosaurus siefkeri Colbert, 1966

- References: Colbert, 1966, 1970
- Age: late early Norian (ca. 221.35-220.54 Ma)
- Horizon and locality: Granton Quarry, Ewin Creek Member, Lockatong Formation, New Jersey, estimated as ca. 220.94 Ma through eccentricity cycles (Kent et al., 2017), conservative interval taken here using ages for underlying Nursery and overlying Byram Members (ca. 221.35 Ma and 220.54 Ma respectively, Kent et al., 2017)

Rhyncocephalia

Clevosaurus hudsoni Swinton, 1939

- References: Robinson, 1973; Fraser, 1988; Jenkins et al., 2017; O'Brien et al., 2018; Chambi-Trowell et al., 2019
- Age: Rhaetian (ca. 208.5-201.3 Ma)
- Horizons and localities: several localities in fissure fills, United Kingdom (listed in Whiteside and Marshall, 2008), Rhaetian (Whiteside and Marshall, 2008)

Gephyrosaurus bridensis Evans, 1980

- References: Evans, 1980, 1981a, 1985; Jenkins et al., 2017; Borsuk-Białynicka, 2018
- Age: Hettangian-Sinemurian (ca. 201.3-190.8 Ma)
- Horizons and localities: several localities in fissure fills, United Kingdom, Hettangian-Sinemurian (Evans and Kermack, 1994; Whiteside et al., 2016)

Planocephalosaurus robinsonae Fraser, 1982

- References: Fraser, 1982, Fraser and Walkden, 1984; Jenkins et al., 2017
- Age: Rhaetian (ca. 208.5-201.3 Ma)
- Horizons and localities: several localities in fissure fills, United Kingdom (listed in Whiteside and Marshall, 2008), Rhaetian (Whiteside and Marshall, 2008)

Squamata

Eichstaettisaurus schroederi (Broili, 1938)

- References: Evans et al. 2004; Simões et al., 2017; Conrad, 2018
- Age: early Tithonian (ca. 152.1-148.6 Ma)
- Horizon and locality: Wintershof, near Eichstätt, Germany, Solnhofen Limestone, early Tithonian (Villa et al., 2021)

Huehuecuetzpalli mixtecus Reynoso, 1998

- Reference: Reynoso, 1998

- Age: Late Albian (ca. 106.8-100.5 Ma)
- Horizon and locality: Tlayua Quarry, near Tepexi de Rodríguez, Puebla, Mexico, Middle Member, Tlayua Formation, late Albian (Benammi et al., 2006)

Megachirella wachtleri Renesto and Posenato, 2003

- References: Renesto and Posenato, 2003; Renesto and Bernardi 2014; Simões et al., 2018
- Age: lower Anisian (ca. 247-244.6 Ma)
- Horizon and locality: Monte Prà della Vacca/Kühwiesenkopf, Braies/Prags Dolomites, Italy, 'Plant Horizon', Dont Formation, Braies Group, lower Anisian (Pelsonian Substage) (Renesto and Bernardi, 2014)

Non-archosauriform Archosauromorpha

Prolacerta broomi Parrington, 1935

- Material examined: UCMP 37151 CT data available on DigiMorph archive (www.digimorph.org); Photos of BP/1/5375; BP/1/5880
- References: Camp, 1945a-b; Gow, 1975; Evans, 1986; Colbert, 1987; Modesto and Sues, 2004; Ezcurra, 2016; Spiekman, 2018
- Age: Induan-Olenekian (ca. 251.902-247.2 Ma)
- Horizon and locality: several localities in the *Lystrosaurus declivis* Assemblage Zone, South Africa, Induan-early Olenekian (Botha and Smith, 2020); correlated to lower Fremouw Formation, Antartica and Sanga do Cabral Formation, Paraná Basin, Brazil (Botha and Smith, 2020)

Protorosaurus speneri Meyer, 1830

- Material examined: SMNK cast of WMsN.P.47361
- Reference: Evans and King, 1993; Gottmann-Quesada and Sander, 2009
- Age: Wuchiapingian (ca. 259.51-254.14 Ma)
- Horizon and locality: several localities in, Kupferschiefer Formation, Germany (listed in Gottmann-Quesada and Sander), Zechstein Group, Wuchiapingian (Ezcurra et al., 2014; Schneider et al., 2020); Middridge and Quarrington quarries, near Durham, Marl Slate Formation, England, Wuchiapingian (Ezcurra et al., 2014)

Allokotosauria

Azendohsaurus madagaskarensis Flynn, Nesbitt, Parrish, Ranivoharimanana and Wyss, 2010

- References: Flynn et al., 2010; Nesbitt et al., 2015
- Age: late Ladinian-early Carnian (ca. 239.5-232 Ma)

- Horizon and locality: locality M-28, near Malio River, Makay Formation (‘Isalo II’), late Ladinian-early Carnian (Nesbitt et al., 2015)

Pamelaria dolichotrachela Sen, 2003

- Reference: Sen, 2003
- Age: Carnian (ca. 237-227 Ma)
- near Yerrapalli Village, Adilabad District, Andhra Pradesh, India, Yerrapalli Formation, Gondwana Supergroup, Pranhita-Godavari Basin, Anisian-early Ladinian (Ezcurra et al., 2021)

Teraterpeton hrynewichorum Sues, 2003

- References: Sues, 2003; Pritchard and Sues, 2019
- Age: Carnian (ca. 237-227 Ma)
- Horizon and locality: near Burntcoat Head Community Park, Burntcoat Head, Hants County, Nova Scotia, Canada, Evangeline Member, Wolfville Formation, Carnian (Sues and Olsen, 2015)

Trilophosaurus buettneri Case, 1928

- References: Gregory, 1945; Demar and Bolt, 1981; Spielmann et al., 2008; Nesbitt et al., 2015
- Age: late Carnian-middle Norian (ca. 232-217.8 Ma)
- Horizons and localities: several localities in Colorado City and Tecovas Formations, Dockum Group, Texas, and Bluewater Creek Formation and Blue Mesa Member of Petrified Forest Formation, Chinle Group, Arizona (see Spielmann et al., 2008), latest Carnian-middle Norian (Kligman et al., 2020).

Tanystropheidae

Langobardisaurus pandolfi Renesto, 1994b

- Material examined: MCSNB 2883; MCSNB 4860; MFSN 1921; MFSN 19235
- References: Renesto, 1994b; Muscio, 1997; Renesto and Dalla Vecchia, 2000; Renesto et al., 2002; Saller et al., 2013
- Age: Norian (ca. 227-208.5 Ma)
- Horizons and localities: near Cene, Lombardy, Italy, Calcare di Zorzino Formation, Aralata Group, early-middle Norian (Renesto, 2006; Renesto et al., 2009; Pritchard et al., 2016); near Preone, Friuli, Italy, Dolomia di Forni Formation (see Dalla Vecchia, 2006), middle-late Norian (Dalla Vecchia, 2006; Pritchard et al., 2016); near Seefeld, Tyrol, Austria, Seefeld Formation, middle-?late Norian (Alaunian-?Sevatian, see Saller et al., 2013)

Macrocnemus bassanii Nopcsa, 1930

- References: Peyer, 1937; Rieppel, 1989; Renesto and Avanzini, 2002; Saller, 2016; Jaquier et al., 2017; Miedema et al., 2020
- Age: late Anisian-early Ladinian (ca. 244.6-239.5 Ma)
- Horizons and localities: several localities (listed in Rieppel, 1989, Saller, 2016, see Spiekman et al., 2021) in Besano Formation and Meride Limestone, late Anisian-early Ladinian (Stockar, 2010)

Tanystropheus longobardicus (Bassani, 1886)

- References: Wild, 1973; Renesto, 2005; Nosotti, 2007; Spiekman and Scheyer, 2019; Spiekman et al., 2020a, b
- Age: late Anisian-early Ladinian (ca. 244.6-239.5 Ma)
- Horizons and localities: several localities (listed in Spiekman and Scheyer, 2019 as 'small morphotype') in Besano Formation and Meride Limestone, late Anisian-early Ladinian (Stockar, 2010)

Rhynchosauria

Howesia browni Broom, 1905a

- References: Broom, 1906; Carroll, 1976; Dilkes, 1995
- Age: early Anisian (ca. 247.2-244.6 Ma)
- Horizon and locality: unknown locality, near Aliwal North, Eastern Cape Province, South Africa, in middle *Cynognathus* Assemblage Zone (*Trirachodon-Kannemeyeria*, Subzone), early Anisian (Hancox et al., 2020)

Mesosuchus browni Watson, 1912

- References: Carroll, 1976; Dilkes, 1998; Sobral and Müller, 2019
- Age: early Anisian (ca. 247.2-244.6 Ma)
- Horizon and locality: unknown locality (identical to *Euparkeria*), between Aliwal North and Lady Crey, Eastern Cape Province, South Africa, in middle *Cynognathus* Assemblage Zone (*Trirachodon-Kannemeyeria*, Subzone), early Anisian (Hancox et al., 2020)

Rhynchosaurus articeps Owen, 1842

- References: Benton, 1990; Ezcurra et al., 2016
- Age: Anisian (ca. 247.2-242 Ma)
- Horizons and localities: several quarries, near Grinshill, England (listed in Benton, 1990), Tarporley Siltstone Formation, Mercia Mudstone Group, Anisian (Benton et al., 1994; Waters et al., 2007)

Non-archosaurian Archosauriformes

Erythrosuchus africanus Broom, 1905b

- References: Cruickshank, 1978; Gower, 1996, 1997, 2001, 2003
- Age: early Anisian (ca. 247.2-244.6 Ma)
- Horizon and locality: various localities, in particular near Aliwal North and Burgersdrop, Eastern Cape Province, and Rouxville, Free State Province, South Africa, in middle *Cynognathus* Assemblage Zone (*Trirachodon-Kannemeyeria*, Subzone), early Anisian (Hancox et al., 2020)

Euparkeria capensis Broom, 1913

- References: Ewer, 1965; Gow, 1970; Cruickshank, 1979; Clark et al., 1993; Gower and Weber, 1998; Senter, 2003; Sookias and Butler, 2013; Sobral et al., 2016; Demuth et al., 2020; Sookias et al., 2020
- Age: early Anisian (ca. 247.2-244.6 Ma)
- Horizon and locality: unknown locality (identical to *Mesosuchus*), between Aliwal North and Lady Grey, Eastern Cape Province, South Africa, in middle *Cynognathus* Assemblage Zone (*Trirachodon-Kannemeyeria*, Subzone), early Anisian (Hancox et al., 2020)

Proterochampsa barrionuevoi Reig, 1959

- References: Sill, 1967; Trotteyn, 2011; Trotteyn and Haro, 2011; Dilkes and Arcucci, 2012; Trotteyn et al., 2013
- Age: middle Carnian-early Norian (ca. 231.7-225 Ma)
- Horizon and locality: several localities in Ischigualasto Provincial Park, San Juan Province and near Cerro Las Lajas, La Rioja Province, Argentina, upper La Peña, Cancha de Bochas and lower Valle de la Luna members, Ischigualasto Formation, Agua de la Peña Group, in *Scaphonyx-Exaeretodon-Herrerasaurus* and lower *Exaeretodon* biozones (Martínez et al., 2013), middle Carnian-early Norian (231.4 +/- 0.3 Ma to 225.9 +/- 0.9 Ma, Martínez et al., 2011)

Proterosuchus spp. Broom, 1903

- References: Cruickshank, 1972, 1979; Gow, 1975; Gower, 1996; Welman, 1998; Clark et al., 1993; Klembara and Welman, 2009; Ezcurra et al., 2013; Ezcurra, 2016, 2017; Ezcurra and Butler, 2015a-b
- Age: Induan-Olenekian (ca. 251.902-247.2 Ma)
- Horizon and locality: several localities (listed in Ezcurra and Butler, 2015a) in the *Lystrosaurus declivis* Assemblage Zone, South Africa, Induan-early Olenekian (Botha and Smith, 2020)
- Remarks: The family Proterosuchidae and the genus *Proterosuchus* in particular have a complex taxonomic history (reviewed in Ezcurra and Butler, 2015a). Three species are

currently recognized in the genus: *P. fergusi* (type-species), *P. alexaderi* and *P. goweri*. At present, all comprehensive descriptions are based on material from all nominal species. Thus, we follow recent authors (e.g. Pritchard, 2015; Ford and Benson, 2020) in keeping a generic level OTU, pending a detailed redescription of *Proterosuchus* at the species level.

Pseudosuchia

Batrachotomus kupferzellensis Gower, 1999

- References: Gower, 1999, 2002; Gower and Schoch, 2009
- Age: late Ladinian (ca. 239.5-237)
- Horizon and locality: near Kupferzell, Hohenlohe region and Echenau, Vellberg municipality, Baden-Württemberg, Germany, layers 5b, 6a-c, Erfurt Formation, Lower Keuper, late Ladinian (Longobardian Substage) (Schoch, 2002)

Gracilisuchus stipanicicorum Romer, 1972

- References: Romer, 1972; Lecuona and Desojo, 2012; Lecuona, 2013; Butler et al., 2014; Lecuona et al., 2017, 2020
- Age: early Carnian (ca. 237-232 Ma)
- Horizons and localities: several localities (listed in Lecuona et al., 2020) in the Lower Member of the Chañares Formation, Agua de la Peña Group, Ischigualasto–Villa Unión Basin, Argentina, early Carnian (Ezcurra et al., 2017)

Parasuchus hislopi Lydekker, 1885

- References: Chatterjee, 1978; Kammerer et al., 2016
- Age: late Carnian (ca. 232-227 Ma)
- Horizon and locality: near Mutapuram, Pranhita–Godavari Valley, Telangana, India, Lower Maleri Formation, late Carnian (Datta et al., 2021)

Ornithodira

Ixalerpeton polesinensis Cabreira, Kellner, Dias-da-Silva, da Silva, Bronzati, de Almedia Marsola, Müller, Bittencourt, Batista, Raugust, Carrilho, Brodt, Langer, 2016

- Material examined: ULBRA-PVT059 segmented CT data available on MorphoSource Repository (https://www.morphosource.org/projects/0000C1095)
- References : Cabreira et al., 2016; Ezcurra et al., 2020
- Age : middle-late Carnian (233.9-227 Ma)

- Horizon and locality: Buriol ravine, São João Polêsine, Rio Grande do Sul, Brazil, Alemoa Member, Santa Maria Formation, Candelária Sequence, Paraná Basin, correlated to *Hyperodapedon* Assemblage Zone (Langer et al., 2007), middle Carnian (233.23 +/- 0.61 Ma dated for maximum depositional age, Langer et al., 2018)

Lagerpeton chanarensis Romer, 1971

- Material examined: PVL 4625 segmented CT data available on MorphoSource Repository (https://www.morphosource.org/projects/0000C1095)
- References: Romer, 1971, 1972; Arcucci, 1986; Sereno and Arcucci, 1994a; Ezcurra et al., 2020; McCabe and Nesbitt, 2021
- Age: early Carnian (ca. 237-232 Ma)
- Horizons and localities: Talampaya National Park, La Roja Province, Argenyina, Lower Member of the Chañares Formation, Agua de la Peña Group, Ischigualasto–Villa Unión Basin, early Carnian (Ezcurra et al., 2017)

Lagosuchus talampayensis Romer, 1971

- References: Romer, 1971, 1972; Bonaparte, 1975; Sereno and Arcucci, 1994b; Agnolin and Ezcurra, 2019
- Age: early Carnian (ca. 237-232 Ma)
- Horizons and localities: Talampaya National Park, La Roja Province, Argenyina, Lower Member of the Chañares Formation, Agua de la Peña Group, Ischigualasto–Villa Unión Basin, early Carnian (Ezcurra et al., 2017)

Scleromochlus taylori Woodward, 1907

- References: Padian, 1984; Sereno, 1991; Benton, 1999; Bennett, 2020
- Age: late Carnian-early Norian (ca. 232-217.8 Ma)
- Horizon: Lossiemouth East Quarry, Lossiemouth, Morayshire, Scotland, UK, Lossiemouth Sandstone Formation, considered late Carnian-early Norian based on faunal correlations (Benton and Walker, 2011)

Silesaurus opolensis Dzik, 2003

- References: Dzik, 2003; Dzik and Sulej, 2007; Piechowski and Dzik, 2010; Piechowski et al., 2014; Piechowski and Tałanda, 2020
- Age: Norian (227-208.5 Ma)
- Horizon and locality: Clay pit in Krasiejów, near Opole, Poland, Krasiejów, Norian (Szulc, 2005; Szulc et al., 2015; Jewuła et al., 2019)

Teleocrater rhadinus Nesbitt, Butler, Ezcurra, Barrett, Stocker, Angielczyk, Smith, Sidor, Niedźwiedzki, Sennikov and Charig, 2017

- Material examined: NMT RB843; NMT RB844; NMT RB845, segmented laser-scanned data from on MorphoSource Repository (http://n2t.net/ark:/87602/m4/408061; http://n2t.net/ark:/87602/m4/408066; http://n2t.net/ark:/87602/m4/408071)
- References: Nesbitt et al., 2017a, b
- Age: early Anisian (ca. 247.2-244.6 Ma)
- Horizon: near Mkongoleko and Rutikira rivers, Ruhu Basin, Tanzania, near base of Lifua Member, Manda Beds, correlated to middle *Cynognathus* Assemblage Zone (*Trirachodon-Kannemeyeria* Subzone) of South Africa (Nesbitt et al., 2017a, b), early Anisian (Hancox et al., 2020)
- Remarks: A braincase has been referred to *T. rhadinus* (Nesbitt et al., 2017a, b) and has been scored in phylogenetical matrices (e.g. Nesbitt et al., 2017a) but has yet to be described. Our codings for this element thus provisionally follows Ezcurra et al. (2020) for characters taken from the latter study. The surface-scanned femurs were referered by Pintore et al. (2021).

Pterosauria

Carniadactylus rosenfeldi (Dalla Vecchia, 1995)

- Material examined: MPUM 6009a, b
- References: Wild, 1979; Dalla Vecchia, 1995, 2009, 2013, 2014, 2018; Kellner, 2015
- Age: late middle Norian (ca. 215.2-214.03 Ma)
- Horizons and localities: Forchiar brook, Enemonzo, Udine Province, Friuli Venezia Giulia Region, Italy, Dolomia di Forni Formation, Friuli (see Dalla Vecchia, 2006), late middle Norian (Alaunian 3, Dalla Vecchia, 2013, 2014; near Cene, Lombardy, Italy, Calcare di Zorzino Formation, Aralata Group, late middle Norian (Alaunian 3, Dalla Vecchia, 2013, 2014, see also Pritchard et al., 2016 for a more conservative view)

Dimorphodon macronyx (Buckland, 1829)

- References: Padian, 1983; Unwin, 1988; Nesbitt and Hone, 2010; Bennett, 2015; Sangster, 2021
- Age: Hettangian- early Sinemurian (ca. 201.3-195.1 Ma)
- Horizon and locality: Lyme Regis, Dorset, England, ‘Blue Lias’, Lower Lias Group, Hettangian-early Sinemurian (Benton and Spencer, 1995)

Eudimorphodon ranzii Zambelli, 1973

- Material examined: MCSNB 2888
- Reference: Wild, 1979; Dalla Vecchia, 2013, 2014
- Age: middle-late Norian (ca. 227-212.6 Ma)
- Age: late middle Norian (ca. 215.2-214.03 Ma)

- Horizons and localities: near Cene, Lombardy, Italy, Calcare di Zorzino Formation, Aralata Group, late middle Norian (Alaunian 3, Dalla Vecchia, 2013, 2014, see also Pritchard et al., 2016 for a more conservative view)
- Remarks: We follow Dalla Vecchia (2014) is considering the holotype to be the only specimen unambiguously referable to *E. ranzii*.

Peteinosaurus zambelli Wild, 1979

- Material examined: MCSNB 2886 (Holotype), 3359, 3496
- References: Wild, 1979; Dalla Vecchia, 2003, 2013, 2014
- Age: late middle Norian (ca. 215.2-214.03 Ma)
- Horizons and localities: near Cene, Lombardy, Italy, Calcare di Zorzino Formation, Aralata Group, late middle Norian (Alaunian 3, Dalla Vecchia, 2013, 2014, see also Pritchard et al., 2016 for a more conservative view)

Raeticodactylus filisurensis Stecher, 2008

- References: Stecher, 2008; Dalla Vecchia, 2014; Bennett, 2015
- Age: late Norian (ca. 214.03-208.5 Ma)
- Horizon: near Tinzenhorn mountain, Mittelbünden, commune Filisur, Canton Grisons, Switzerland, lower part of Alpihorn Member, Kössen Formation, late Norian (Sevatian, Dalla Vecchia, 2013, 2014)

Rhamphorynchus muensteri (Goldfuss, 1831)

- Material examined: MNHN cast 1869-354; CM 11434 CT data available o DigiMorph archive (www.digimorph.org); MGUH 1891.738 CT data in Bonde and Leal, 2015
- References: Wellnhofer, 1975a-c, 1978; Bonde and Christiansen, 2003; Ősi et al., 2010; Hone, 2012; Hone et al., 2013, 2015; Bonde and Leal, 2015
- Age: early Tithonian (ca. 152.1-148.6 Ma)
- Horizon and locality: several localities in Solnhofen Limestone, Germany, early Tithonian (Villa et al., 2021)

Dinosauria

Eoraptor lunensis Sereno, Forster, Rogers and Moneta, 1993

- Material examined: PVSJ 512 CT data available on DigiMorph archive (www.digimorph.org)
- Reference: Sereno et al., 2013
- Age: middle-late Carnian (ca. 231.7-227 Ma)
- Horizons and Localities: several localities in the Cancha de Bochas region, Valle de la Luna, Argentina, Cancha de Bochas Member, Ischigualasto Formation, Agua de la Peña Group, in *Scaphonyx-Exaeretodon-Herrerasaurus* biozone (Martínez et al., 2013), middle-late Carnian (231.4 +/- 0.3 Ma dated at base, Martínez et al., 2011)

Herrerasaurus ischigualastensis Reig, 1963

- Material examined: PVSJ 407 CT data available o DigiMorph archive (www.digimorph.org)
- References: Novas, 1994; Sereno, 1994; Sereno and Novas, 1994; Ezcurra, 2010
- Age: middle-late Carnian (ca. 231.7-227 Ma)
- Horizons and Localities: several localities in the Cancha de Bochas Member, Ischigualasto Formation, Agua de la Peña Group, in *Scaphonyx-Exaeretodon-Herrerasaurus* biozone (Martínez et al., 2013), middle-late Carnian (231.4 +/- 0.3 Ma dated at base, Martínez et al., 2011)

Appendix 2: Character list for phylogenetical analyses

The present character list of 407 characters results from the compilation of 303 parsimony-informative characters published in previous phylogenetical analyses (74.45 %), 90 informative characters taken from publications that were modified to fit our dataset (22.13 %), as well as 14 new characters (3.44 %).

To reflect the broad panel of amniote taxa included in our analysis, we compiled characters from the following recent studies: Schoch and Sues (2018a); Ezcurra et al. (2020); Ford and Benson (2020); Griffiths et al. (2021); Pritchard et al. (2021); Spiekman et al. (2021); Simões et al. (2022). As some of the studies represent the last iterations of previous matrices, we refer the readers to detailed character lists and discussions in older publications: Ezcurra (2016) and Ezcurra and Butler (2018) for Ezcurra et al. (2020); Simões et al. (2018) for Griffiths et al. (2021); Pritchard (2015), Nesbitt et al. (2015), Pritchard et al. (2015, 2018); Pritchard and Nesbitt (2017), and Pritchard and Sues (2019) for Pritchard et al. (2021).

Previous matrices focusing on early amniotes (e.g. Gauthier et al., 1988; Laurin and Reisz, 1995; deBraga and Rieppel, 1997; Reisz et al., 2010; Bever et al., 2015), synapsids (e.g. Benson, 2012), parareptiles (e.g. Müller and Tsuji, 2007; MacDougall et al., 2019) sauropsids (e.g. Müller and Reisz, 2006; Modesto, 2018), early diapsids (e.g. Benton, 1985; Evans, 1988; Laurin, 1991; Müller, 2004; Senter, 2004; Ezcurra et al., 2014) and saurians (e.g. Dilkes, 1998; Nesbitt, 2011) were also consulted but are not refered to in the character list as they are themselves referenced in the selected studies listed above.

Each character is defined and followed by comments on the delimitation of character states and the coding for relevant taxa.

Of the following 396 characters, 84 multistate characters represent morphological series (20.64 %) whereby a given state is intermediate between the preceding and following one. Previous studies have shown that ordering such characters gives more reliable results than when not doing so, even if minor ordering errors are made (Rineau et al., 2015, 2018). These 84 characters are thus considered additive in our dataset.

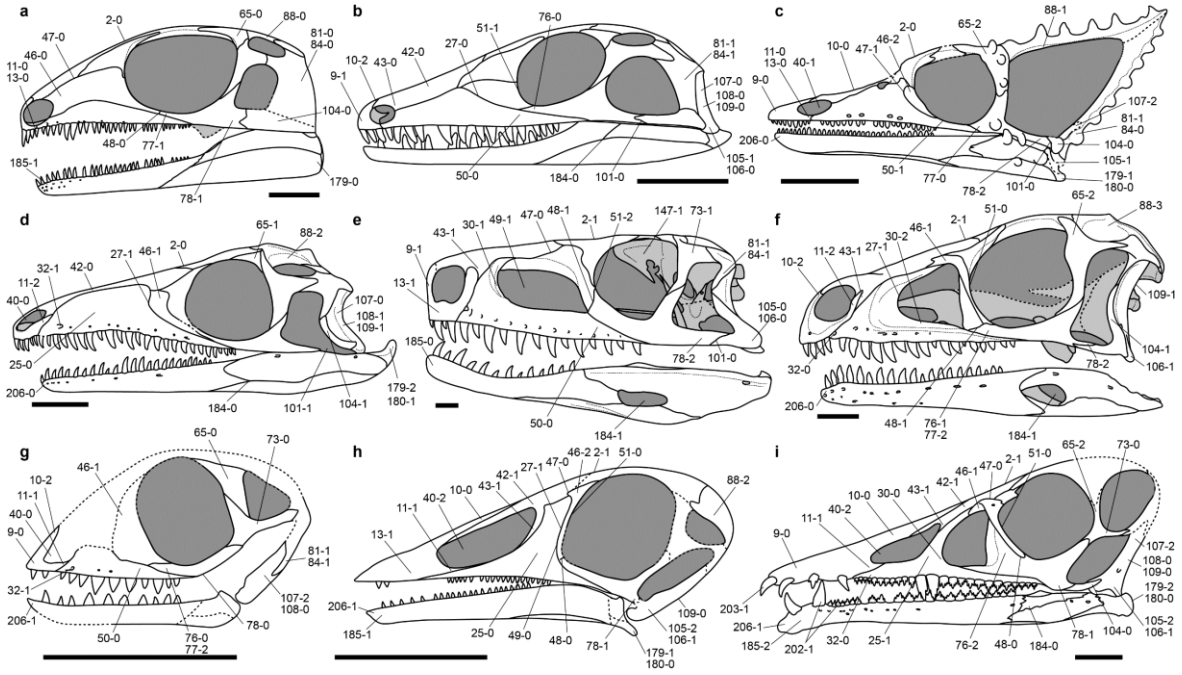

Figure A-S1: Reconstructions of the skull and lower jaws of neodiapsids in left lateral view. a, the araeoscelidian *Petrolacosaurus kansensis* (redrawn from Reisz, 1981). **b**, the neodiapsid *Youngina capensis* (redrawn from Carroll, 1981). **c**, the weigeltisaurid *Weigeltisaurus jaekeli* (redrawn and modified from Bulanov and Sennikov, 2015 and Buffa et al., 2021). **d**, the archosauromorph *Prolacerta broomi* (redrawn from Spiekman, 2018). **e**, the archosauriform *Euparkeria capensis* (redrawn from Sookias et al., 2020). **f**, the early dinosaur *Eoraptor lunensis* (redrawn from Sereno et al., 2013). **g**, the drepanosauromorph *Vallesaurus cenensis* (redrawn and modified from Renesto and Binelli). **h**, the drepanosaur *Megalancosaurus preonensis* (redrawn and modified from Renesto and Dalla Vecchia, 2005). **i**, the early pterosaur *Eudimorphodon ranzii* (redrawn from Wild, 1979). Numbers refer to character-character states. Scale bars, 1 cm.

Cranial characters (211 characters, 51.84 %)

1. **Skull, antorbital-postorbital length ratio: antorbital length (anterior tip of skull to anterior margin of orbit) equal to or longer than postorbital length (posterior margin of orbit to posterior end of skull) (0); postorbital length longer than antorbital length (1)**

From Ford and Benson (2020:k1)

Modified (removed state) from Schoch and Sues (2018a:k1); Griffiths et al. (2021:k348)

See comments in Ford and Benson (2020) and Griffits et al. (2021).

2. **Skull, shape of antorbital region: transversely broader than dorsoventrally tall or subequal (0); dorsoventrally taller than transversely broad (1)**

From Ezcurra et al. (2020:k22); Spiekman et al. (2021:k3)

See Fig. S1; Ezcurra (2016:fig. 16)

Previous studies have consistently recovered the presence of a dorsoventrally tall rostrum with a nearly vertical contribution of the nasal as an 'eupelycosaurian-grade' (i.e. excluding caseasaurs and therapsids) synapomorphy (e.g. Ford and Benson, 2020:k2 and references therein). However, we consider the contribution of the nasal to the rostrum and the shape of the latter as distinct characters. Consequently, we follow Ezcurra et al. (2020) and Spiekman et al. (2021) in conding only for the shape of the rostrum in the present character. The exposure of the nasal is scored in character 42 below.

3. **Skull, posterior margin in dorsal view: convex or roughly straight (0); concave, skull embayed medially (1)**

Modified (removed state) from Ford and Benson (2020:k5)

Previous studied described the presence and number of embayments in the posterior margin of the skull in a single multistate character (e.g. Ford and Benson, 2020 and references therein). However, we consider the presence of a double concavity as resulting from a sagittal posterior expansion of the skull, which can occur with or without a posterior concavity. Thus, we consider the presence of a concavity and an expansion in a pair of independent characters (see character 4 below).

4. **Skull, posterior margin in dorsal view, sagittal expansion: absent (0); present (1)**

Modified (removed state) from Ford and Benson (2020:k5)

See comments in character 3 above.

5. **Skull, dermal sculpturing: extensive, covering most bone surfaces (0); not extensive, restricted to regionalized areas of several circumorbital and temporal bones (1); absent (2)**

Modified (added state) from Schoch and Sues (2018a:k51); Ford and Benson (2020:k3)

See comments in Ford and Benson (2020). We include an additional state (state 1) to take into account the more localized ornamentation of weigeltisaurids and *Kuehneosaurus* (Robinson, 1962; Buffa et al., 2021). The presence of extensive ornamentation appears highly homoplasic but, as stated by Ezcurra (2016), might be informative at low phylogenetic levels.

6. **Skull, dermal sculpturing if extensive: composed of ridges and pits arranged in a honeycomb pattern (0); an irregular distribution of rounded pits (1); anastomosing narrow grooves and low ridges (2); deep pits with prominently raised knobs (3); inapplicable, sculpturing not extensive (-)**

From Ford and Benson (2020:k4)

Modified from Schoch and Sues (2018a:k52); Ezcurra et al. (2020:k5)

See Ezcurra (2016:fig. 16)

7. **Skull, circumorbital and temporal outgrowths: absent (0); numerous pointed ornamental outgrowths present (1)**

Modified (modified states) from Pritchard et al. (2021:k59)

Pritchard et al. (2021) used this character to describe the ornamentation of the parietosquamosal frill of weigeltisaurids. However, we apply this character to both the temporal and circumorbital bone series, following recent descriptions (Bulanov and Sennikov, 2015a, b; Buffa et al., 2021).

We also introduce several characters to further describe the ornamentation of weigeltisaurids (characters 80, 82, 93 below). The present binary character serves to discriminate between taxa with and without such ornamentation to avoid redundancy.

We consider this character as independent from character 5 above as taxa with a localized ornamentation can either have circumorbital and temporal outgrowths (e.g. *Coelurosauravus*, Buffa et al., 2021), or not (e.g. *Kuehneosaurus*¸ Evans, 2009). Lastly, as there is no basis to consider the outgrowths of weigeltisaurids and the tuberous ornamentation typical of some

varanopids as homologous, the latter ornamentation is considered in a separate character (character 81 below). Thus, all varanopids are scored as state 0 for the present character.

8. **Premaxillae: paired (0); single, fused (1)**

From Griffiths et al. (2021:k1); Pritchard et al. (2021:k2); Simões et al. (2022:k1)

See comments in Pritchard (2015:k295)

Figured in Simões et al. (2022:k1)

9. **Premaxilla, orientation of supranarial (dorsal) process with respect to marginal tooth row of premaxilla: slopes posterodorsally at an angle < 75° (0); subvertical at base, then slopes posterodorsally (1); slopes anterodorsally, overhanging tooth row ('rostral process' present) (2); inapplicable: supranarial process is absent (-). ORDERED**

Modified (ordered) from Ford and Benson (2020:k13)

See Fig. S1.

See comments in Ford and Benson (2020). We consider that the character states used by Ford and Benson (2020) form a morphological series describing the orientation of the base of the supranarial process of the premaxilla and consequently provide an ordered version of this character with state 1 being intermediate.

10. **Premaxilla, supranarial process: present, contributing to separation of external nares and extending posterior to midlength of nasals (0); present, contributing to separation of external nares and extending posteriorly at least to posterior margin of external nares (1); present, contributing to separation of external nares but failing to extend posteriorly beyond posterior margin of external nares (2); absent or incipient (3). ORDERED**

Modified (added states, ordered) from Ford and Benson (2020:k16); Pritchard et al. (2021:k5, 338); Simões et al. (2022:k1)

Modified from Ezcurra et al. (2020:k34); Spiekman et al. (2021:k7)

See Fig. S1; Ezcurra (2016:figs. 17, 21); figured in Simões et al. (2022:k1)

The supranarial process of the premaxilla has been subjected to various treatments. Previous studies have coded for its presence (Simões et al., 2018:k2; Pritchard et al., 2021:k5), or length relative to the posterior margin of the external naris (Ford and Benson, 2020:k16) or the alveolar portion of the bone (Ezcurra et al., 2020; Pritchard et al., 2021; Spiekman et al., 2021). We

consider that all morphologies described above form a morphological series describing the elongation of the supranarial process of the premaxilla and consequently include them in a single ordered character. Lastly, we consider the posterior extension of this process relative to the nasal and external naris rather than the alveolar portion of the bone as it could be scored more reliably in our dataset.

11. **Premaxilla, subnarial process: absent (0); short, ends well anterior to posterior margin of external naris (1); long, forms most of ventral margin of external naris or excludes maxilla from naris, but does not contact prefrontal (2); extremely long, forms most of ventral margin of external naris and contacts prerontal (3). ORDERED**

From Spiekman et al. (2021:k9)

Modified from Schoch and Sues (2018a:k5); Simões et al. (2018:k3); Ezcurra et al. (2020:k36, 40); Ford and Benson (2020:k14); Pritchard et al. (2021:k7); Simões et al. (2022:k3)

See Fig. S1; Ezcurra (2016:figs. 17, 19); figured in Simões et al. (2022:k3)

See comments in Spiekman et al. (2021) and references therein.

Previous studies have scored *Yougina* and/or *Protorosaurus* as possessing a short subnarial process of the premaxilla (e.g. Ezcurra et al., 2020; Spiekman et al., 2021). However, we consider this process as absent in *Youngina* (BP/1/2871) and *Protorosaurus* (as stated by Gottmann-Quesada and Sander, 2009:140), in agreement with Pritchard et al. (2021). Conversely, previous studies have scored drepanosaurs as lacking a subnarial process of the premaxilla (Pritchard et al., 2021). However, we consider that a short process is present (state 1) in both *Megalancosaurus* (MFSN 1769) and *Vallesaurus* (MCSNB 4751).

12. **Premaxilla, posterior knob fitting into anterior notch in maxilla: absent, premaxilla-maxilla suture roughly straight or with broad overlap from maxilla (0); present (1)**

From Schoch and Sues (2018a:k11); Ezcurra et al. (2020:k33)

Modified from Pritchard et al. (2021:k8); Spiekman et al. (2021:k17)

See Ezcurra (2016:fig. 20), Pritchard et al. (2018:fig. S1) and Spiekman et al. (2021:fig. 2)

Some recent studies have considered the presence of a posterior knob on the premaxilla and of an overlapping anterior flange of the maxilla as two states of a single multistate character (Pritchard et al., 2021; Spiekman et al., 2021). However, we consider both states to represent distinct structues and consequently score them in distinct binary characters. The presence of a broadly overlapping maxilla is considered in character 23 below. Spiekman et al. (2021) further

included the presence of a posterior medial peg on the premaxilla as another character state. However, as this state is only present in *Macrocnemus*, it is not included in our dataset.

13. **Premaxilla, main body, size: small, premaxillary body forms less than half of anteroposterior length of rostrum in front of posterior border of external nares (0); large, premaxillary body forms half or more than half of anteroposterior length of rostrum in front of posterior border of external nares (1)**

From Schoch and Sues (2018a:k1); Ezcurra et al. (2020:k27)

See Fig. S1; Ezcurra (2016:fig. 17)

This character is independent from the presence of a subnarial process of the premaxilla (character 11 above) as some taxa that lack such process have a relatively long premaxillary body (e.g. *Limnoscelis*, captorhinids; Modesto et al., 2007; Berman et al., 2010).

14. **Premaxilla, ventral slope of alveolar margin relative to ventral margin of maxilla: absent (0); slight, less than 10° from horizontal (1); moderate, 10-20° from horizontal (2); strong, 30-45° from horizontal (3); very strong > 45° from horizontal (4). ORDERED**

Modified (ordered) from Ford and Benson (2020:k18)

Modified from Ezcurra et al. (2020:k29); Pritchard et al. (2021:k4); Spiekman et al. (2021:k5)

See Ezcurra (2016:figs. 12, 18, 19)

As this character describes the angle of the alveolar margin of the premaxilla relative to that of the maxilla, we order the character states of Ford and Benson (2020) in agreement with previous iterations of this character (Ezcurra et al., 2020; Pritchard et al., 2021).

15. **Premaxilla, narial shelf: more or less sharp edge between lateral surface of skull and ventral wall of naris (0); rounded ventral narial shelf that transitions smoothly into ventral edge of skull (1); inapplicable: premaxilla does not participate in narial shelf (-)**

From Ford and Benson (2020:k19)

See comments in Ford and Benson (2020).

16. **Premaxilla, palatal process: absent (0); flattened process extends posteriorly no further than lateral surface of premaxilla (1); flattened process extends posteriorly beyond lateral surface of premaxilla (2). ORDERED**

Modified (added state, ordered) from Ezcurra (2016:k41); Pritchard et al. (2021:k10, 11); Spiekman et al. (2021:k11)

Modified from Simões et al. (2022:k8)

See Ezcurra (2016:figs. 20, 21); figured in Simões et al. (2022:k8)

Previous characters have treated the presence and elongation of the palatal process of the premaxilla in separate characters (e.g. Pritchard et al., 2021). However, we consider these morphologies to form a morphological series and consequently include them in a single ordered character.

17. **Premaxilla, tooth size compared to maxillary teeth: smaller or subequal to (non-caniniform) maxillary teeth (0); premaxillary teeth larger (1); inapplicable: premaxilla edentulous (-)**

From Ford and Benson (2020:k20)

Modified from Pritchard et al. (2021:k141)

We consider this character as independent from character 19 below following Ford and Benson (2020).

18. **Premaxilla, tooth size: isodont (0); anterior teeth larger than posterior teeth (1); inapplicable: premaxilla edentulous (-)**

From Ford and Benson (2020:k21)

We consider this character as independent from character 17 above following Ford and Benson (2020).

19. **Septomaxilla: present (0); absent as a distinct ossification (1)**

From Schoch and Sues (2018a:k16); Ezcurra et al. (2020:k45); Griffiths et al. (2021:k10); Spiekman et al. (2021:k18); Simões et al. (2022:k9)

See Ezcurra (2016:fig. 16)

See comments in Ezcurra (2016). We concur with previous studies that the ‘septomaxilla’ of phytosaurs is not homologous to the septomaxilla of early amniotes (Senter, 2002; Nesbitt, 2011; Ezcurra, 2016). Consequently, *Parasuchus* is scored with state 1 for the present character.

20. Septomaxilla, lateral exposure: absent or forming only small portion of external naris (0); extensive, septomaxilla forming ventral margin of external naris externally (1); inapplicable: septomaxilla is absent (-)

Modified (removed states) from Ford and Benson (2020:k22, in part)

In most early amniotes, the septomaxilla lies medial to the external surface of the skull, and may vary in overall morphology and superficial exposure (see character 21 below). However, the septomaxilla is mainly superficial in *Mesosaurus* and *Seymouria*, forming the entire ventral margin of the external naris (Modesto, 2006:fig. 5; Piñeiro et al., 2012:fig. 4). We consider this morphology as markedly different from that of other amniotes and consequently describe it in a separate character.

21. Septomaxilla, morphology in lateral view: transversely narrow, rectangular plate fully or partially partitioning naris but without external exposure (0); transversely broader, pillar-like bone partitioning naris and forming posterior margin of external naris externally (1); anterodorsally recurved rectangular sheet of bone, septomaxilla shaped as a conical funnel (2); inapplicable: septomaxilla is absent (-)

Modified (removed states) from Ford and Benson (2020:k22, in part)

See comments in character 20 above. The character states of the present character roughly correspond to states 1 to 3 of Ford and Benson's (2020:k22) iteration, however contrary to the latter, taxa coded with state 1 for the previous character can still be scored for the present character.

22. Premaxilla-maxilla, subnarial foramen between both elements: absent (0); present (1)

From Spiekman et al. (2021:k15)

Modified (reduced states) from Ezcurra et al. (2020:k25)

23. Maxilla, anterior lamina broadly overlapping posterior margin of premaxilla: absent (0); present (1)

Modified (removed state) from Pritchard et al. (2021:k8); Spiekman et al. (2021:k17)

See Pritchard et al. (2018:fig. S1)

See discussion in character 12 above.

24. Maxilla, preorbital (facial) ascending process, maximum dorsoventral height with respect to height of maxilla at anterior orbital margin: less than 1.5 times the height (0); between 1.5 and twice the height (1); greater than twice the height (2). ORDERED

Modified (ordered) from Ford and Benson (2020:k24)

Modified (added states) from Simões et al. (2022:k15)

Figured in Simões et al. (2022:k15)

We follow Ford and Benson (2020) in using a quantitative formulation of this character. As these character states form a series describing the elongation of the preorbital process of the maxilla, we order this character.

25. Maxilla, preorbital (facial) ascending process, anteroposterior width in lateral view: broad, with base occupying most of the length of the bone anterior to orbit (0); very thin, with base occupying less than a third of the bone anterior to orbit (1)

Modified (reworded states) from Ezcurra et al. (2020:k706)

See Fig. S1.

Ezcurra et al. (2020) considered the presence of a thin preorbital process of the maxilla (state 1) only in taxa that also possess an antorbital fenestra. However, some taxa in our dataset exhibit a very slender maxillary process despite lacking an antorbital fenestra, (e.g. *Claudiosaurus*, *Fraxinisaura*, *Marmoretta*, *Teraterpeton*, Carroll, 1981; Sues, 2003; Schoch and Sues, 2018b; Griffiths et al., 2021). Consequently, we reworded this character to make it applicable to a broader range of taxa.

26. Maxilla, position of apex of preorbital (facial) ascending process: anterior to external naris (0); immediately posterior to external naris (1); centrally between the orbit and external naris (2); tallest point located posteriorly, immediately anterior to the orbit (3). ORDERED

Modified (added state, ordered) from Ford and Benson (2020:k25)

We added state 3 to take into account the posteriorly located preorbital process of the maxilla of some early lepidosauromorphs (e.g. *Fraxinisaura*, *Gephyrosaurus*, *Marmoretta*, *Paliguana*, Evans, 1980; Schoch and Sues, 2018b; Ford et al., 2021; Griffiths et al., 2021). As the character states describe the position of the apex of the preorbital process of the maxilla along the rostrum, we order this character.

27. Maxilla, preorbital (facial) process, shape: gradual transition between dorsal and posterior margins (0); strongly concave posterior margin (1)

From Griffiths et al. (2021:k18); Pritchard et al. (2021:k17); Spiekman et al. (2021:k20)

Modified (removed states) from Ezcurra et al. (2020:k58)

See Fig. S1; Spiekman et al. (2021:fig. 3)

See comments in Spiekman et al. (2021).

28. Maxilla, apex of preorbital (facial) process: horizontal or smoothly curved (0); dorsal incisura framed by two small dorsal processes, preorbital fenestra (sensu Bulanov and Sennikov, 2015) present (1)

NEW CHARACTER

We erect this character to code for the small preorbital fenestra of all weigeltisaurids (e.g. Bulanov and Sennikov, 2006; 2015a, b; Buffa et al., 2021). Following Buffa et al. (2021), we do not consider this fenestra to be homologous with the antorbital fenestra of archausauriforms (described in character 49 below).

29. Maxilla, contact with anteroventral process of prefrontal anterior to lacrimal: absent, separated by anterior expansion of lacrimal (0); present (1)

From Schoch and Sues (2018a:k22); Ezcurra et al. (2020:k61); Ford and Benson (2020:k26)

See Ezcurra (2016:fig. 17)

This character describes the presence of a contact between the maxilla and the anteroventral process of the prefrontal only. It does not consider the presence of a contact between maxilla and prefrontal posterior to the lacrimal bone.

In most cases, state 1 is obtained through reduction of the anterior extent of the lacrimal which fails to reach the nasal, allowing for a maxilla-prefrontal contact. However, in the parareptile *Delorhynchus*, the maxilla overlaps the lacrimal and reaches the anteroventral portion of the prefrontal, but the anterior portion of the lacrimal remains in contact with the nasal (Reisz et al., 2014). Thus, the presence of a maxilla-prefrontal contact and of a lacrimal-nasal contact are not dependent, and both are considered in separate characters (see character 47 below).

30. Maxilla, lateral surface, antorbital fossa: absent (0); present on preorbital (facial) process only (1); present on preorbital and suborbital processes (2); inapplicable: antorbital fenestra absent (-). ORDERED

Modified (reduced states) from Ezcurra et al. (2020:k54)

Modified (added states) from Simões et al. (2022:k17)

See Fig. S1; Ezcurra (2016:figs. 13, 17-19, 22); figured in Simões et al. (2022:k17)

Simões et al. (2022:k17) recently figured *Euparkeria* as lacking an antorbital fossa on the maxilla, but we follow Sookias et al. (2020) in considering this taxon only has an antorbital fossa, but only on the preorbital fossa. Consequently, this taxon is scored with thates 1 here, in agreement with previous analyses (Ezcurra et al., 2020).

31. Maxilla, lateral (supralabial) maxillary foramina: absent (0); single anterior foramen (1); row of foramina (2)

Modified (added state) from Ford and Benson (2020:k27)

We consider the presence of a single anteriorly position lateral maxillary foramina in a separate state (state 1). This morphology occurs in most parareptiles (Tsuji and Müller, 2009), as well as kuehneosaurids (Evans, 2009). As this character describes the extent of external innervation and vascularisation above the tooth row, we suggest that this character could be ordered. However, we refrain from doing so in our analysis pending further work to clarify the homology of maxillary canals among early amniotes (e.g. Benoit et al., 2021).

32. Maxilla, anterior lateral (supralabial) maxillary foramen: equal in size to other maxillary foramina, if present (0); much larger than other foramina or a single large foramen (1); inapplicable, maxillary foramina absent (-)

From Schoch and Sues (2018a:k30); Ezcurra et al. (2020:k52); Ford and Benson (2020:k28); Griffiths et al. (2021:k16); Pritchard et al. (2021:k12); Spiekman et al. (2021:k19); Simões et al. (2022:k14)

See Fig. S1; Ezcurra (2016:fig. 17)

This character considers the presence of a relatively large anterior lateral maxillary foramen. Following previous studies (e.g. Ezcurra et al., 2020; Spiekman et al., 2021), it does not consider the presence of a subnarial foramen near the premaxilla-maxilla suture, scored in character 22 above.

33. Maxilla, suborbital (posterior) process, contact with quadratojugal externally: absent (0); present (1)

From Schoch and Sues (2018a:k26); Ford and Benson (2020:k78)

This character is identical to previous characters used to describe the presence of a contribution of the jugal to the ventral margin of the skull (e.g. Ford and Benson, 2020).

34. Maxilla, shape of ventral margin in lateral view: horizontal or weakly convex (0); pronounced ventral convexity (1)

From Ford and Benson (2020:k44); Pritchard et al. (2021:k15)

Modified (removed states) from Ezcurra et al. (2020:k68); Spiekman et al. (2021:k25)

See Ezcurra (2016:fig. 16) and Spiekman et al. (2021:fig. 5)

35. Maxilla, 'supracanine' buttress on medial surface: absent, alveolar shelf has uniform or gradually tapering dorsoventral height (0); present, subtriangular dorsal thickening of anterior alveolar shelf (1)

From Ford and Benson (2020:k37); Simões et al. (2022:k24)

See comments in Ford and Benson (2020).

36. Maxilla, multiple tooth rows (zahnreihen): absent, single row of marginal teeth only (0); present, at least two rows of marginal teeth (1); inapplicable: maxilla edentulous (-)

From Ezcurra et al. (2020:k73); Ford and Benson (2020:k29); Pritchard et al. (2021:k150); Spiekman et al. (2021:k164)

See comments in Ezcurra (2016).

37. Maxilla, caniniform region/teeth: absent, maxillary teeth approximately subequal in size, diminishing gradually posteriorly (0); caniniform region/teeth present (1); inapplicable: maxilla edentulous (-)

From Schoch and Sues (2018a:k170); Ezcurra et al. (2020:k301); Ford and Benson (2020:k31); Pritchard et al. (2021:k143)

See Ezcurra (2016:fig. 18)

See comments in Ford and Benson (2020).

38. External naris, posterodorsal expansion: absent (0); present (1)

From Ford and Benson (2020:k45)

See comments in Ford and Benson (2020).

39. External naris, position: marginal (minimal distance between nares ≥0.35 rostrum width at same level) (0); close to midline (1); confluent (2). ORDERED

Modified (added states, ordered) from Ezcurra et al. (2020:k9); Ford and Benson (2020:k47); Spiekman et al. (20201:k29)

See Ezcurra (2016:k16-17, 20)

As argued by Pritchard (2015:466), the absence of the supranarial process of the premaxilla is not correlated to the presence of confluent nares in some taxa (e.g. *Tanystropheus*). Thus, we consider the position of the external naris and the development of the supranarial process of the premaxilla (character 10 above) in independent characters. As such, we consider the presence of confluent nares as an extreme case of closely positioned nares, and consequently order this character. This follows previous iterations (e.g. Ezcurra et al., 2014:k20).

40. External naris, anteroposterior position: located close to anterior end of skull (0) separated from anterior end of skull by moderate expansion of premaxilla (1); posterior margin of naris closer to orbit than anterior end of skull, separated by large expansion of premaxilla (2). ORDERED

Modified (added state, ordered) from Spiekman et al. (2021:k31)

Modified from Schoch and Sues (2018a:k7); Ezcurra et al. (2020:k10)

See Fig. S1; Spiekman et al. (2021:fig. 6)

Spiekman et al. (2021) erected this character to describe the significant elongation of the rostrum anterior to the external nares in tanystropheids (state 1). We also consider this state to be present in weigeltisaurids (e.g. Buffa et al., 2021; Pritchard et al., 2021), the pterosaur *Dimorphodon* (Padian, 1983) and the squamate *Huehuecuetzpalli* (Reynoso, 1998). Further elongation of the anterior rostrum, resulting in posteriorly placed nares (state 2) can be foung in *Mesosaurus*, *Teraterpeton* (Sues, 2003; Modesto, 2006) and the pterosaur *Eudimorphodon* (MCSNB 2888).

As those character states describe the elongation of the rostrum anterior to the external nares, we order this character.

41. Nasal, midline length: distinctly shorter than frontal (0); approximately equal to frontal (1); longer than frontal (2). ORDERED

Modified (ordered) from Ford and Benson (2020:k48)

Modified from Schoch and Sues (2018a:k20)

Various studies have employed ratios between the midline length between the nasal and frontal bones (e.g. Ezcurra et al., 2020:k76). However, as the proposed threshold values have not been tested on our dataset, and as early amniote material is often disarticulated to some degree, making such measurements difficult, we elect to follow the broader designations used by other studies (e.g. Ford and Benson, 2020).

42. Nasal, exposure (excluding anterolateral process if present): largely dorsal element (1); nearly vertical contribution to rostrum (1)

From Ezcurra et al. (2020:k77)

See Fig. S1.

See comments in character 2 above.

43. Nasal, anterolateral process: absent (0); present, partially or totally excluding preorbital process of maxilla from external naris (1)

From Griffiths et al. (2021:k23); Simões et al. (2022:k27)

Modified (removed state) from Ezcurra et al. (2020:k81)

See Fig. S1; Ezcurra (2016:figs. 17, 23); figured in Simões et al. (2022:k27)

44. Nasal, prefrontal contact, orientation: parasagittal, at least in its caudal third (0); anterolateral (1)

From Ford and Benson (2020:k60); Pritchard et al. (2021:k22)

45. Lacrimal: present (0); absent as a distinct ossification (1)

From Griffiths et al. (2021:k27); Pritchard et al. (2021:k24); Simões et al. (2022:k30)

46. Lacrimal, facial contribution, anterior extent: forms a large portion of the lateral surface of the skull, reaching external naris or septomaxilla (0); forms a portion of

the lateral surface of the skull but does not reach the external naris (1); limited to orbital margin (2); inapplicable: lacrimal is absent (-). ORDERED

From Pritchard et al. (2021:k25)

Modified from Ezcurra (2016:k85); Ford and Benson (2020:k50); Spiekman et al. (2021:k35); Simões et al. (2022:k34)

See Fig. S1.

We follow Pritchard et al. (2021) in considering the anterior extent of the lacrimal over the rostrum in a single ordered character. However, our interpretation is slightly different from the latter study as it considers only the anterior extent of the bone, and not its vertical extent. As such, taxa with a very slender, tall lacrimal are coded as state 2 here, including the drepanosauromorph *Megalancosaurus*, the only one where this region is completely preserved (MFSN 1769), and the pterosaur *Dimorphodon* (Padian, 1983). We also score tanystropheids as possessing state 2 contrary to Pritchard et al. (2021) (Nosotti, 2007; Jaquier et al., 2010).

47. Lacrimal, facial contribution, dorsal portion: extends dorsally to reach ventral margin of nasal (0); lacrimal fails to reach nasal externally (1); inapplicable: lacrimal is absent (-)

From Pritchard et al. (2021:k26)

See Fig. S1.

See comments in character 29 above.

48. Lacrimal, suture with jugal in lateral view: small, less than 50% of minimum dorsoventral height of suborbital bar (0); well developed, greater than 50% of minimum dorsoventral height of suborbital bar (1); inapplicable: lacrimal-jugal lateral contact absent (-)

From Ford and Benson (2020:k55)

See Fig. S1.

49. Antorbital fenestra: absent (0); present (1)

From Schoch and Sues (2018a:k33); Ezcurra et al. (2020:k13); Pritchard et al. (2021:k27); Spiekman et al. (2021:k22)

See Fig. S1; Ezcurra (2016:fig. 17).

50. Orbit, participation of maxilla to anteroventral margin in lateral view: absent, jugal contacting lacrimal and/or prefrontal anteriorly, excluding maxilla from orbital margin (0); orbital exposure of maxilla present (1)

From Schoch and Sues (2018a:k25); Ford and Benson (2020:k54); Griffiths et al. (2021:k352)

See Fig. S1.

We use two independent characters to describe the bones forming the anteroventral margin of the orbit in early amniotes (see character 51 below). This margin can be formed by the maxilla, lacrimal, prefrontal and/or jugal. The present character described the participation of the maxilla to the orbital margin, which is allowed by the absence of contact between the jugal and the lacrimal and/or the prefrontal.

51. Orbit, participation of lacrimal to anteroventral margin in lateral view: large, at least half of orbit dorsoventral height (0); moderate, around 1/3 of orbit height (1); small, less than 1/4 of orbit height (2); absent, prefrontal contacts maxilla or jugal in lateral view (3); inapplicable: lacrimal is absent (-). ORDERED

Modified (added state, ordered) from Ford and Benson (2020:k52)

See Fig. S1.

This is the second character describing the bones forming the anteroventral orbital margin, concerning the participation of the lacrimal bone (see comments in character 50 above). Ford and Benson (2020) introduced qualitative criteria comparing the length of the lacrimal contribution to the orbit circumference, but we favor a simpler comparison to the dorsoventral height of the orbit to allow for an easier scoring in our dataset. Several taxa are indeed known from partial material, for which the orbit circumference cannot be confidently reconstructed.

We consider the exclusion of the lacrimal from the orbital margin as an extreme state of the reduction of the participation of this bone to the orbit, and consequently score for this morphology in state 3. This state is present in various diapsids, including *Claudiosaurus*, *Palaeagama* and kuehneosaurids (Carroll, 1975, 1981; Evans, 2009). As those character states describe the degree of participation of the lacrimal to the orbital margin, we order this character.

52. Orbit, laterally thickened orbital rim: absent or incipient (0); present, restricted to ascending process of jugal and ventral process of postorbital (1); present, well-developed along jugal, postorbital, frontal, prefrontal and lacrimal (2). ORDERED

From Ezcurra et al. (2020:k17); Spiekman et al. (2021:k48)

See Ezcurra (2016:figs. 16-17)

Ezcurra (2016:122) state that the orbital rim is not elevated in *Macrocnemus basanii*. However, a raised ridge is clearly visible in some specimens (e.g. PIMUZ T4822, Jaquier et al., 2017:fig.10), similar to that of *Tanystropheus* which was scored as state 1 by the latter study. Consequently, we consider that *M. basanii* has an elevated margin (state 1).

53. Nasolacrimal duct, posterior exit foramen/foramina: completely enclosed by lacrimal (0); enclosed by lacrimal and postfrontal (1)

From Ezcurra et al. (2020:k89)

See Ezcurra (2016:figs. 17, 19)

54. Prefrontal, sharp angle (~90°) between the dorsal and lateral surface: absent, dorsal surface grades smoothly into lateral surface (0); present (1)

From Ford and Benson (2020:k62)

55. Prefrontal, contact with counterpart on skull roof: absent (0); present (1)

From Ezcurra (2016:k107); Ford and Benson (2020:k57); Griffiths et al. (2021:k374)

See Ezcurra (2016:fig. 23)

56. Prefrontal, palatine contact: absent (0); narrow, forming less than 1/3 interorbital distance (1); broad, forming at least 1/2 interorbital distance (2). ORDERED

From Griffiths et al. (2021:k349)

Modified (added state, ordered) from Schoch and Sues (2018a:k39); Ford and Benson (2020:k58, 59)

We consider the presence of a narrow prefrontal-palatine contact as an intermediate state between a large contact and the absence of contact and consequently ordered this character.

57. Frontals: paired (suture patent) (0); single, fused (1)

From Schoch and Sues (2018a:k46); Ezcurra et al. (2020:k112); Griffiths et al. (2021:k67); Pritchard et al. (2021:k31); Spiekman et al. (2021:k54); Simões et al. (2022:k77)

58. Frontal, anteroposterior length at midline: less than 1.5 times parietal length (0); equal to or greater than 1.5 times parietal length (1); more than 2.5 times parietal length (2). ORDERED

Modified (ordered) from Ford and Benson (2020:k65)

As these character states form a morphological series describing the anteroposterior length of the frontal, we order this character.

59. Frontal, contribution to orbital margin: absent, frontal excluded from orbit by prefrontal-postfrontal contact (0); narrow (1); broad, >1/4 of maximum orbital length (2). ORDERED

Modified (added state, ordered) from Schoch and Sues (2018a:k47); Ezcurra (2016:k114); Ford and Benson (2020:k56, 63); Spiekman et al. (2021:k50)

We consider the lack of orbital contribution by the frontal as an extreme reduction of this exposure, and consequently consider the presence and breadth of the orbital contribution of the frontal in a single ordered character.

60. Frontal, contribution to orbital margin formed by lateral lappet: absent, no lateral extension of frontal at orbital level (0); present (1); inapplicable: frontal does not contribute to orbital margin (-)

From Schoch and Sues (2018a:k48); Ford and Benson (2020:k64)

61. Frontals, width of posterior region: frontal strongly tapers posteriorly (0); lateral margins subparallel, frontal maintains transverse width throughout length (1); frontal gradually widens throughout length (2); frontal abruptly widens at posteriormost margin (3). ORDERED

Modified (ordered) from Pritchard et al. (2021:k32)

Modified from Simões et al. (2022:k78)

Figured in Simões et al. (2022:k78)

We consider that the present character states represent a morphological series ranging from a posteriorly constricted frontal (state 0) to an expanded one (state 3) and consequently order this character.

In contrast to Pritchard et al. (2021), we score all allokotosaurians in our dataset as possessing a posteriorly tapered frontal (Sen, 2003; Sues, 2003; Spielmann et al., 2008; Flynn et al., 2010). In addition, we concur with the latter study that an abrupt posterior expansion of the frontal is

present in *Proterosuchus* and *Erythrosuchus*, but *Batrachotomus* and *Euparkeria* are here scored as presenting only a gradual expansion (state 2; Gower, 1999; Sookias et al., 2020). Lastly, we score weigeltisaurids as possessing a gradually expanded frontal as well based on *Coelurosauravus* (Buffa et al., 2021) and the Ellrich specimen (SMNK-PAL 2882), contrary to Pritchard et al. (2021).

62. **Frontal, posteromedial process: absent (0); short, separating anterior tip of parietals along midline (1); long, separating parietals for some distance anteriorly (2). ORDERED**

Modified from Ezcurra et al. (2020:k116)

See Ezcurra (2016:fig. 23)

We consider that the shape of the fontoparietal stuture can be summarized by the relative elongation of the posteromedial and posterolateral processes of the frontal, and consequently separate previously proposed character states in two distinct characters (see character 63 below).

63. **Frontal, posterolateral process: absent, frontoparietal suture forming anterolateral or right angle with parasagittal plane (0); short, only partially separating parietal from dorsolateral margin of postfrontal or forming obtuse posterolateral angle to parasagittal plane (1); long, narrow, 'U-shaped' frontoparietal suture forming acute posterolateral angle with parasagittal plane, substantially or fully separating parietal from dorsomedial margin of postfrontal (2). ORDERED**

Modified (ordered) from Ford and Benson (2020:k66)

Modified (added state, ordered) from Pritchard et al. (2021:k33); Spiekman et al. (2021:k56)

Modified from Ezcurra et al. (2020:k116)

See Ezcurra (2016:fig. 23)

This is the second character used to describe the morphology of the frontoparietal suture, which focuses on the elongation of the posterolateral process of the frontal (see character 62 above). As the character states forms a morphological series, we order this character, following previous iterations (e.g. Reisz et al., 2010:k27).

Our scoring broadly follows that of Ford and Benson (2020) for early amniotes and Pritchard et al. (2021) for early diapsids, with three notable exceptions. Pritchard et al. (2021) score *Avicranium* as possessing a U-shaped frontoparietal suture (equivalent to states 1 or 2 here), however, it appears that the posterolateral expansion of the frontal is covered by the parietal

externally, forming a transverse frontoparietal suture (Pritchard and Nesbitt, 2017). Consequently, this taxon is scored as possessing state 0 here. The same authors also score *Teraterpeton* and *Weigeltisaurus* as possessing a horizontal frontoparietal suture, however, *Weigeltisaurus* has a W-shaped suture formed by short posteromedial and posterolateral processes (Pritchard et al., 2021) while the frontoparietal suture of *Teraterpeton* is broadly convex (Sues, 2003). Consequently, *Teraterpeton* and *Weigeltisaurus* are scores as possessing state 2 and 1 respectively.

64. Frontal, anterior process length: short, not longer than posterior process (0); longer than posterior process (1); very long, forming at least 2/3 of anteroposterior length of bone (2). ORDERED

Modified (ordered) from Ford and Benson (2020:k67)

In most amniotes, the orbital margin of the frontal separates the anterior and posterior processes. For those taxa that lack an orbital contribution in our dataset, *Deltavjatia*, *Limnoscelis* and *Seymouria*, the frontal shows a slight expansion in its middle portion, which divides the bone in a similar way (Laurin, 1996; Berman et al., 2010; Tsuji, 2013). Thus, this character is applicable throughout our dataset. As the character states from a morphological series, we order this character.

65. Postfrontal: equivalent in size to postorbital (0); approximately less than half the size of postorbital (1); absent or fused with postorbital (2). ORDERED

From Ezcurra et al. (2020:k122)

Modified (added state, ordered) from Schoch and Sues (2018a:k54); Griffiths et al. (2021:k56); Pritchard et al. (2021:k36); Simões et al. (2022:k51)

See Ezcurra (2016:fig. 17); figured in Simões et al. (2022:k51)

As the distinction between the loss of the postfrontal and its fusion with the postorbital is difficult to make on fossil material, we consider both morphologies in a single character (contra Griffiths et al., 2021 who consider more recent taxa). Fusion between bones can indeed only be made out with certainty provided ontogenetic series are known or through the use of CT data or dedicated histological studies, all of which are uncommon in early amniote taxa.

66. Postfrontal, shape in dorsal view: forms a right triangle, with posterior margin oriented transversely (0); elongate, posterior margin inclined posteromedially or posteriorly (1); inapplicable: postfrontal absent (-)

From Griffiths et al. (2021:k60); Pritchard et al. (2021:k37)

See Pritchard (2015:fig. 6)

67. Postorbital, medial contact with frontal and/or parietal: present (0); absent (1)

From Schoch and Sues (2018a:k56); Ford and Benson (2020:k73); Pritchard et al. (2021:k49)

68. Postorbital, angle between ventral and posterior processes: approximately right angle (0); obtuse angle, both processes roughly aligned (1); inapplicable: posterior process of postorbital absent (-)

NEW CHARACTER

In most amniotes, the postorbital exhibits distinct ventral and posterior processes set at a right angle to each other. This is clearly marked in taxa with temporal fenestration in which the posteroventral margin of the postobital is embayed by the temporal opening. By contrast, in some taxa, both processes are set at a more obtuse angle (state 1). This occurs in the drepanosaurid *Vallesaurus* (MCSNB 4751), in allokotosaurian archosauromorphs (Spielmann et al., 2008; Flynn et al., 2010) and in most lepidosauromorphs in our dataset (Evans, 1980; Reynoso, 1998; Schoch and Sues, 2018b).

69. Postorbital, posterior process, anteroposterior length: absent (0); short, does not reach half of temporal region length (1); long, extending more than half of temporal length (2). ORDERED

Modified (added state, ordered) from Ford and Benson (2020:k70)

Modified from Ezcurra et al. (2020:k130); Pritchard et al. (2021:k52, k339); Spiekman et al. (2021:k60)

The lack of a posterior process of the postorbital was first proposed as a character by Pritchard et al. (2021) to describe the peculiar morphology of weigeltisaurids. However, we elect to consider this morphology as an extreme state in an ordered character describing the elongation of the posterior process of the postorbital. As argued by Ford and Benson (2020), this character is independent from the presence/absence of a postorbital-supratemporal contact (treated in character 71 below).

70. Postorbital, posterior process, dorsoventral height at midlength: broad, at least 25% of dorsoventral height of temporal region (0); narrow, no more than 20% of dorsoventral height of temporal region (1); inapplicable: posterior process of postorbital absent (-)

From Ford and Benson (2020:k71)

71. Postorbital, posterior process, contact with supratemporal: absent (0); present (1); inapplicable: supratemporal is absent (-)

From Schoch and Sues (2018a:k61); Ford and Benson (2020:k69)

72. Postorbital, posterodorsal margin, contribution to supratemporal fenestra: absent (0); present, at least at one point (1)

From Ford and Benson (2020:k75)

See comments in Ford and Benson (2020:k75).

73. Supratemporal bar, position in lateral view: positioned distinctly ventral to dorsal border of orbit, broadly exposing supratemporal fenestra in lateral view (0); approximately aligned to dorsal border of orbit, supratemporal fenestra barely exposed in lateral view (1); inapplicable: supratemporal bar absent (-)

From Ezcurra et al. (2020:k126)

See Fig. S1; Ezcurra (2016:figs. 17, 19)

74. Infratemporal bar dorsoventral height (if complete or partially complete): tall, occupying more than 20% of skull height in temporal region (0); narrow, less than 20% of skull height (1); inapplicable: infratemporal bar absent (-)

From Ford and Benson (2020:k74)

Modified (reworded states) from Schoch and Sues (2018a:k79)

This character describes the height of the inferior temporal bar regardless of which bone it comprises (jugal and/or quadratojugal), following previous iterations (e.g. Ford and Benson, 2020).

75. Jugal, posterior margin, contribution to lower temporal fenestra or emargination: absent (0); present, at least at one point (1)

From Ford and Benson (2020:k76)

See comments in Ford and Benson (2020:k76).

76. Jugal, anterior process, shape in lateral view: lower than suborbital process of maxilla (0); higher than suborbital process of maxilla (1); higher than suborbital process of maxilla and with an ascending subprocess (2)

Modified (reduced states) from Ezcurra et al. (2020:k92)

Modified (added states) from Spiekman et al. (2021:k38); Pritchard et al. (2021:k54)

See Fig. S1; Ezcurra (2016:figs. 17, 19); Spiekman et al. (2021:fig. 8)

We revert to previous iterations of this character (e.g. Ezcurra, 2016:k92) as the elongation of the ascending subprocess of the jugal is not informative for our dataset. We consider it unclear whether state 1 constitutes a morphological intermediate state between states 0 and 2 and consequently refrain from odering this character, in agreement with previous iterations (Ezcurra, 2016; Ezcurra et al., 2020).

77. Jugal, anterior process, extension: posterior to midpoint of the orbit (0); does not extend to anterior orbital margin (1); extends at least to anterior orbital margin (2). ORDERED

Modified (added state, ordered) from Ford and Benson (2020:k80); Griffiths et al. (2021:k367)

Modified from Schoch and Sues (2018a:k76)

See Fig. S1.

78. Jugal, posterior process: absent (0); short, failing to extend to posterior half of temporal region (1); elongate, extending to posterior half of temporal region or further (2). ORDERED

Modified from Pritchard et al. (2021:k58)

Modified (added state, ordered) from Schoch and Sues (2018a:k77, 78); Ford and Benson (2020:k82); Griffiths et al. (2021:k36, 371); Spiekman et al. (2021:k42); Simões et al. (2022:k42)

See Fig. S1; Spiekman et al. (2021:fig. 9); figured in Simões et al. (2022:k42)

Pritchard et al. (2021) considered the elongation of the posterior process of the jugal and the presence of a jugal-quadratojugal contact in a single ordered character. In contrast, we consider the length of this process and the presence of such a contact in two independent characters (se character 104 below).

79. Jugal, dorsal process, anteroposterior width: broad, temporal fenestra only weakly emarginates jugal, if present (0); narrow (1)

From Ford and Benson (2020:k81)

Ford and Benson (2020) scored this character as inapplicable for all taxa that lack a temporal fenestration emarginating the jugal. However, the jugal of *Limnoscelis* has a slender dorsal process compared to other unfenestrated taxa (e.g. captorhinids, Heaton, 1979; Modesto et al., 2007), or some taxa with a secondarily closed lower temporal fenestra (*Trilophosaurus*, Spielmann et al., 2008). Thus, this character can be scored in the absence of temporal fenestration.

80. Jugal, tuberous striations on lateral surface: absent (0); present (1)

From Ford and Benson (2020:k83)

This character describes the ornamentation typical of varanopids (Ford and Benson, 2020), which we consider non-homologous to that of weigeltisaurids (see characters 7 and 80 above).

81. Squamosal, lateral flange: anteroposteriorly broad, largely covering quadrate and quadratojugal in lateral view (0); anteroposteriorly narrow, bracing the lateral margin of the quadrate (1); absent, quadrate is not braced laterally (2). ORDERED

From Pritchard et al. (2021:k60).

Modified (added state, ordered) from Ezcurra et al. (2020:k135); Griffiths et al. (2021:k50); Spiekman et al. (2021:k66, 69).

See Fig. S1; Spiekman et al. (2021:fig. 13)

Our scoring for this character differs somewhat from that of Pritchard et al. (2021). Most notably, we do not score state 0 for any neodiapsids in our dataset, in agreement with other studies (e.g. Spiekman et al., 2021). In particular, the quadrate of weigeltisaurids remains visible behind the squamosal and quadratojugal, and these taxa are consequently scored with state 1 (Bulanov and Sennikov, 2010; Buffa et al., 2021). *Avicranium* and *Claudiosaurus* both show tall, vertically oriented squamosals, which are reconstructed as covering the quadrate in lateral view (Carroll, 1981; Pritchard and Nesbitt, 2017). However, this morphology is clearly different from the anteroposteriorly broad lamina of non-neodiapsid taxa such as *Petrolacosaurus* (Reisz, 1981). As both taxa are in need of a detailed re-description, we provisionally score them as possessing both states 0 or 1 to highlight this uncertainty. In addition, Pritchard et al. (2021) score both *Teraterpeton* and *Trilophosaurus* as displaying state 0. However, both taxa appear to lack a lateral flange of the squamosal entirely as the entire

quadrate is clearly visible in lateral view (Sues, 2003; Spielmann et al., 2008). Consequently, both taxa are scores as having state 2 herein.

82. Squamosal, anteroventral process (lateral flange) contact with posterodorsal margin of jugal: present (0); absent (1)

Ford and Benson (2020:k89); Pritchard et al. (2020:k57)

Ford and Benson (2020) consider that taxa with a jugal-squamosal contact lack a lateral temporal fenestra. However, as a squamosal-jugal contact is common among rhychocephalians (Evans, 1980; Fraser, 1988) and trilophosaurids (Sues, 2003; Spielmann et al., 2008), we consider this character independently of the presence of temporal emargination.

83. Squamosal, anteroventral process (lateral flange) contact with posteroventral margin of jugal: present (0); absent (1)

From Ford and Benson (2020:k90)

Modified from Simões et al. (2022:k45)

84. Squamosal, occipital (posterior) lamina: present, covering much of posterior aspect of quadrate (0); absent, posterior aspect of quadrate exposed in occipital view (1)

From Schoch and Sues (2018a:k82); Griffiths et al. (2021:k53); Pritchard et al. (2021:k61); Simões et al. (2022:k60)

Modified from Ford and Benson (2020:k92)

See Fig. S1; Figured in Simões et al. (2022:k60)

We favor here the character-state delimitation traditionally used in diapsid-focused matrices rather than the states used by Ford and Benson (2020) because we found it difficult to reliably score taxa for which the occipital flange was ‘broad’ or ‘very narrow’ as this structure is often poorly described in the literature.

85. Squamosal, contribution to the posttemporal fenestra: absent (0); present (1)

From Schoch and Sues (2018a:k81); Ford and Benson (2020:k94)

86. Parietals: paired (suture patent) (0); single, fused (1)

From Schoch and Sues (2018a:k69); Ezcurra et al. (2020:k159); Griffiths et al. (2021:k72); Pritchard et al. (2021:k39); Spiekman et al. (2021:k74); Simões et al. (2022:k82)

See Ezcurra (2016:fig. 16)

87. Parietal, lateral margin, contribution to supratemporal fenestra: absent (0); present (1)

From Ford and Benson (2020:k95)

88. Parietal, lateral embayment: absent, parietal dorsoventrally flat (0); dorsoventrally narrow flange extending ventrally from lateral margin (ventrolateral flange) (1); broad lateral embayments and elevated parietal dorsal exposure (2); parietal forms blade-like sagittal crest (3); inapplicable: lateral margin of parietal is not free (-). ORDERED

Modified (added states, ordered) Ford and Benson (2020:k98); Pritchard et al. (2021:k40); Spiekman et al. (2021:k83); Simões et al. (2022:k94)

See Spiekman et al. (2021:fig. 14); figured in Simões et al. (2022:k94)

Previous characters considered either the presence of a narrow ventrolateral flange (Ford and Benson, 2020) or of dorsolateral embayments of the parietal (Pritchard et al., 2021). However, as both characters describe progressively hypertrophied attachment of the jaw adductor musculature, we grouped them into a single, ordered, character.

89. Parietal, posterolateral process, height: dorsoventrally low, considerably lower than supraoccipital (0); dorsoventrally tall, plate-like in posterior view and subequal in height to supraoccipital (1); inapplicable: lateral margin of parietal is not free (-)

From Ezcurra et al. (2020:k168); Spiekman et al. (2021:k80)

See Ezcurra (2016:fig. 27)

We consider posterolateral processes to result from the lateral emargination of the parietal by the temporal fenestration. Consequently, state 1 is applicable only to those taxa in which the parietal contributes to the temporal fenestration (scored 1 for character 89 above). This excludes some anapsid or synapsid taxa (e.g. *Dimetrodon*, *Ophiacodon*, Romer and Price, 1940) that show posterolateral exapansions of the parietal bone because their parietal is bordered laterally by other bones.

90. Parietal, posterolateral process: perpendicular to sagittal plane (0); angled posterolaterally (~45° angle from midline) (1); parallel to sagittal plane, forming a crest prolonging skull table (2); inapplicable: lateral margin of parietal is not free (-). ORDERED

Modified (added state) from Ezcurra et al. (2020:k634); Pritchard et al. (2021:k41); Spiekman et al. (2021:k79)

See Spiekman et al. (2021:fig. 14)

We added state 2 to describe the parasagittal posterolateral process of weigeltisaurids (e.g. Bulanov and Sennikov, 2015, a-c). See character 91 above for an explanation of the inapplicability criterion.

91. Pineal foramen, diameter: pineal foramen absent (0); small, less than 25% of inter-parietal length (1); large, more than 25% of inter-parietal length (2). ORDERED

From Spiekman et al. (2021:k77)

Modified (ordered) from Ezcurra et al. (2020:k164) and Ford and Benson (2020:k96)

Modified from Simões et al. (2022:k83)

These character states form a morphological series describing the diameter of the pineal foramen with state 1 as intermediate between the absence of pineal foramen and a relatively large pineal foramen. Consequently, we ordered this character following previous iterations (e.g. Reisz et al., 2010:k31).

92. Pineal foramen, position on parietal midline suture: posterior rim within posterior third of suture (0); close to midlength (1); anterior rim within anterior third of suture (2); situated within the frontoparietal suture (3); inapplicable: pineal foramen absent (-). ORDERED

From Spiekman et al. (2021:k78)

Modified (added state, ordered) Schoch and Sues (2018a:k67); Ezcurra (2016k165); Ford and Benson (2020:k97) Pritchard et al. (2021:k45)

We consider a pineal foramen enclosed by both frontals and parietals as a very anteriorly positioned foramen. Consequently, we follow Spiekman et al. (2021) in considering this morphology and the position of the pineal foramen along the parietal midline suture in a single ordered character.

93. Postparietals: present (0); absent as distinct ossifications (1)

From Schoch and Sues (2018a:k70); Ford and Benson (2020:k108); Griffiths et al. (2021:k65); Pritchard et al. (2021:k46); Simões et al. (2022:k75)

Modified (reduced states) from Ezcurra et al. (2020:k171)

Figured in Simões et al. (2022:k75)

94. Postparietals: paired (0), median, fused (1); inapplicable: postparietals are absent (-)

From Schoch and Sues (2018a:k71); Ezcurra et al. (2020:k172); Ford and Benson (2020:k109); Griffiths et al. (2021:k66); Pritchard et al. (2021:k47); Spiekman et al. (2021:k85); Simões et al. (2022:k76)

95. Postparietals, contralateral contact: postparietals in contact along median height (0); postparietals separated from midline ventrally by supraoccipital (1); inapplicable, postparietals absent (-)

From Ford and Benson (2020:k110)

96. Tabulars: present (0); absent as a distinct ossification (1)

From Schoch and Sues (2018a:k74); Ezcurra et al. (2020:k173); Ford and Benson (2020:k103); Griffiths et al. (2021:k64); Pritchard et al. (2021:k65); Spiekman et al. (2021:k86); Simões et al. (2022:k72)

97. Tabular, morphology: broad sub-rectangular sheet (0); large L-shaped bone (1); long and slender (2); small and wedge-shaped (3); inapplicable: tabular absent (-)

Modified from Ford and Benson (2020:k104)

The morphology of the tabular is highly variable in early amniotes, and previous studies have struggled to provide characters to describe potential homologies (see comments in Ford and Benson, 2020). Owing to this uncertainty, we provisionnaly restrict this character to the description of the overall shape of the bone, extracted from Ford and Benson's (2020) character states. Additional characters could be added, following further studies of the homologies of the tabular bone. As it is unclear whether the present character states form a morpocline, we refrain from ordering this character.

98. Supratemporal: broad element of the skull table, width greater than 30% of that of posterior skull table (measured from its lateral to midline margins) (0); slender, width approximately 15% (1); absent (2). ORDERED

Modified (added states, ordered) from Schoch and Sues (2018a:k59, 60); Ford and Benson (2020:k99, 100); Simões et al. (2022:k70)

Modified (reworded states) from Ezcurra et al. (2020:k157); Spiekman et al. (2021:k73)

See Ezcurra (2016:fig. 16)

We follow recent iterations of a similar character (Ezcurra et al., 2020; Spiekman et al., 2021) in considering that the character states form a morphocline and ordering this character.

99. Supratemporal, posteroventral extent: equal to or less than that of tabular (0); greatly exceeds that of tabular (1); inapplicable: supratemporal or tabular absent (-)

From Ford and Benson (2020:k101)

100. Quadratojugals: present (0); absent or fused to quadrate (1)

From Schoch and Sues (2018a:k83); Ezcurra et al. (2020:k150); Griffiths et al. (2021:k38); Pritchard et al. (2021:k66); Spiekman et al. (2021:k87); Simões et al. (2022:k47)

See Ezcurra (2016:fig. 24)

101. Quadratojugal, contact with posteroventral margin of jugal: present (0); absent (1)

From Ford and Benson (2020:k85); Griffiths et al. (2021:k372)

Modified from Simões et al. (2022:k45)

See Fig. S1.

Ford and Benson (2020) argued that the presence of an anterior process of the quadratojugal is synonymous to the presence of a jugal-quadratojugal contact. This is not the case in our dataset, as some taxa lack an anterior process of the quadratojugal, but nevertheless exhibit a jugal-quadratojugal contact (e.g. weigeltisaurids, Buffa et al., 2021). Consequently, we include both characters in our analysis (see character 105 below). Since it can prove impossible to determine whether the quadratojugal is fused to the quadrate or entirely absent in some taxa, we refrain from considering the lack of a distinct quadratojugal bone as an inapplicability criterion for this

character. Nevertheless, all taxa scored as 1 for character 103 above are also scored with state 1 for the present character.

102. Quadratojugal, anterior process: present (0); absent (1); inapplicable: quadratojugal is absent (-)

From Schoch and Sues (2018a:k84); Griffiths et al. (2021:k39); Pritchard et al. (2021:k67); Simões et al. (2022:k48)

See comments in character 104 above.

103. Quadratojugal, shape of anterior process: blunt, parallel dorsal and ventral margins (0); tapering to a point, dorsal and ventral margins converge anteriorly (1); inapplicable: quadratojugal absent or without anterior process (-)

From Ford and Benson (2020:k87); Pritchard et al. (2021:k68)

104. Quadratojugal, extention of dorsal process on lateral surface: absent or dorsoventrally short, limited to posteroventral corner of skull (0); dorsoventrally tall, at least 1/3 of the skull height in the temporal region (1); inapplicable: quadratojugal is absent (-)

Modified (reworded states) from Pritchard et al. (2021:k69)

See Fig. S1.

As argued by Pritchard and Nesbitt (2017), the extent of the quadratojugal is hard to evaluate for taxa with a broad anteroventral flange of the squamosal covering the quadrae and quadratojugal externally. Various studies have tried scoring the external extent of the dorsal process of the quadratojugal relative to the dorsal margin of the infratemporal fenestra (e.g. Pritchard et al., 2021), or the ventral margin of the orbit (e.g. MacDougall et al., 2019), but both are difficult to apply throughout our dataset. We thus measure the height of the quadratojugal externally relative to the temporal region of the skull instead.

105. Quadrate, jaw articulation position: posterior to occiput (0); approximately level with occiput (1); anterior to occiput (2). ORDERED

Modified (ordered) from Schoch and Sues (2018a:k155); Ezcurra et al. (2020:k228); Ford and Benson (2020:k155)

See Fig. S1; Ezcurra (2016:fig. 26)

We consider that the character states represent a morphological series and consequently ordered this character.

106. Quadrate, jaw articulation height: level with alveolar margin of maxilla (0); quadrate projects ventral to alveolar margin of maxilla (1)

From Ford and Benson (2020:k156)

See Fig. S1.

107. Quadrate, orientation in lateral or medial view: inclined anteriorly (<90° with respect to transverse plane of skull) (0); vertical or subvertical (90-110°) (1); inclined posteriorly (>110°) (2). ORDERED

Modified (ordered) from Ezcurra et al. (2020:k720)

Modified (reworded states, ordered) from Ford and Benson (2020:k158)

See Fig. S1.

108. Quadrate, lateral flange (tympanic crest): absent (0); present as a lateral expansion of bone (1); present as deep concavity on posterior surface of crest (tympanic conch) (2). ORDERED

Modified (added states, ordered) from Schoch and Sues (2018a:k129); Griffiths et al. (2021:k121); Pritchard et al. (2019:k71, 72); Simões et al. (2022:k125)

Modified (reworded states) from Ezcurra et al. (2020:k176)

See Fig. S1; Ezcurra (2016:figs. 17, 24)

Previous studies have scored the presence of posterior emargination, tympanic crest and tympanic conch in various ways. Some have elected to consider the presence of a tympanic crest and the presence of a posteriorly concave quadrate as dependent characters (e.g. Ezcurra et al., 2020). However, as argued by Pritchard (2015:497), we refrain from doing so as it is unclear whether some taxa that lack a tympanic crest really have a straight quadrate (e.g. *Erythrosuchus*, Gower, 2003). We thus follow Griffiths et al. (2021, see Simões et al., 2018:k121) and Pritchard et al. (2021) in considering the presence of posterior emargination and lateral expansion in separate characters (see character 112 below).

In addition, it is clear that the tympanic conch of lepidosaurs is homologous to the tympanic crest of other saurians. Thus, we elect to consider the presence of a tympanic crest as intermediate between the lack of lateral expansion of the quadrate and the presence of a

tympanic conch. Consequently, we include these states in a single, ordered character similar to Ezcurra et al. (2020).

109. Quadrate, posterior emargination: absent, quadrate straight posteriorly (0); present, quadrate concave posteriorly (1)

From Schoch and Sues (2018a:k127); Ford and Benson (2020:k159); Griffith et al. (2021:k120); Pritchard et al. (2021:k74); Simões et al. (2022:k124)

Modified (reworded states) from Ezcurra et al. (2020:k176)

See Fig. S1; Ezcurra (2016:figs. 17, 24)

See comments in character 111 above.

110. Quadrate, posterior margin, ventral half: flat or slightly concave (0); convex (1)

From Ezcurra et al. (2020:k182); Pritchard et al. (2019:k75)

See Ezcurra (2016:fig. 24)

111. Quadrate, proximal posterior margin in lateral view: continuous with shaft (0); expanded and hooked (1)

From Ezcurra et al. (2021:k180); Pritchard et al. (2021:k76); Spiekman et al. (2021:k91)

See Ezcurra (2016:fig. 24)

112. Quadrate, dorsalmost portion: tapering dorsally (0); dorsally expanded into prominent convexity (cephalic condyle) (1)

From Pritchard et al. (2021:k63)

We follow Pritchard et al. (2018) who consider that the convex dorsal head of the quadrate of several archosaurs is homologous the long recognized convex cephalic condyle of lepidosauromorphs.

113. Internal naris, posterior expansion on palatine: palatine not incised (0); short to moderate incisure on palatine (1); extensive incisure on palatine, anteroposterior length of incisure more than 2/3 of palatine width (2). ORDERED

Modified (reworded states, ordered) from Ford and Benson (2020:k139)

We modified this character to include a threshold to distinguish between states 1 and 2. This character describes the extent of the incision of the palatine, with state 1 being intermediate. Consequently, we ordered this character.

114. Vomer, teeth: present (0); absent (1)

From Schoch and Sues (2018a:k124); Ezcurra et al. (2020:k187); Ford and Benson (2020:k132); Griffiths et al. (2021:k89); Pritchard et al. (2021:k78); Spiekman et al. (2021:k95); Simões et al. (2022:k98)

115. Vomer, teeth, height and diameter: small, considerably smaller than those of marginal dentition (0); relatively large, similar to those of marginal dentition (1); inapplicable: vomerine dentition absent (-)

From Spiekman et al. (2021:k97)

See Spiekman et al. (2021:fig. 16)

116. Vomer, shape: broad, plate-like bone, at least as transversely broad as the choanas (0); stick-like bone, transversely narrower than the choanas (1)

From Ezcurra et al. (2020:k185)

117. Vomer, asymmetric bifurcated anterior processes: present, vomer terminates anteriorly in short lateral and elongate medial projections (0); absent, vomer not bifurcate anteriorly (1)

From Ford and Benson (2020:k134)

118. Vomer, medial contact with pterygoid: extensive, more than 1/2 of vomerian median margin (0) short (1); absent (2). ORDERED

Modified (added states, ordered) from Ford and Benson (2020:k135, 136)

We consider state 1 as intermediate between the absence of pterygoid incision on the vomer and an elongate vomer-pterygoid median contact and consequently order this character.

119. Vomer, anterolateral contact with maxilla: absent, vomer only contacts premaxilla (0); present, vomer-premaxilla contact extends to maxilla (1)

From Schoch and Sues (2018a:k27); Ezcurra et al. (2020:k186); Griffiths et al. (2021:k373); Pritchard et al. (2021:k79)

120. Suborbital opening: absent (0); present as a small foramen (1); present as an elongate fenestra (2). ORDERED

Modified (added state, ordered) from Schoch and Sues (2018a:k120, 121); Ford and Benson (2020:k153, 154)

We consider the presence of a small suborbital foramen to be intermediate between the absence of suborbital opening and the presence of a homologous elongate fenestra and consequently order this character.

121. Palatine, teeth: present (0); absent (1)

From Schoch and Sues (2018a:k123); Ford and Benson (2020:k137); Griffiths et al. (2021:k97); Pritchard et al. (2021:k80); Simões et al. (2022:k104)

122. Palatine, teeth, height and diameter: small, considerably smaller than those of marginal dentition (0); relatively large, similar to those of marginal dentition (1); inapplicable: palatine dentition absent (-)

From Pritchard et al. (2021:k83); Spiekman et al. (2021:k101)

Modified from Ezcurra et al. (2020:k189); Griffiths et al. (2021:k362)

See Ezcurra (2016:figs. 25, 26), Spiekman et al. (2021:fig. 16)

123. Palatine: anterior transverse expansion: absent, producing anteriorly curved suborbital fenestra (0); present, producing anteriorly tapered suborbital fenestra (1); inapplicable: suborbital fenestra absent (-)

From Pritchard et al. (2021:k81)

124. Pterygoid, palatal process, teeth, medial row (row T3 of Welman, 1998): absent (0); present as a single row (1); subdivided (rows T3a and T3b of Ezcurra, 2016) (2)

Modified (added state) from Pritchard et al. (2021:k84)

Modified from Ezcurra et al. (2020:k195); Spiekman et al. (2021:k102)

See Ezcurra (2016:figs. 25, 26)

The palatal dentition of most amniotes can be divided into distinct palatal tooth rows when present, which Welman (1998) called T1 (posterior transverse flange row), T2 (lateral palatal process row), T3 (medial palatal process row) and T4 (medial edge palatal process row). Rows T1 and T4 are easy to identify when present and are treated in characters 131, 137 and 138 below. The present character and characters 128 and 129 below consider the morphology of rows T3 and T2 respectively.

Ezcurra (2016) introduced a 6-state character to describe the various repartitions of rows T2 and T3 in archosauromorphs, including potential subdivisions of these rows. In contrast, other studies (e.g. Pritchard et al., 2021) consider the presence of both processes independently, but do not take into account the subdivisions of those rows. We elect to score each row independently (similar to e.g. Pritchard et al., 2021) as either absent, present as a single row, or subdivided (see also character 128 below). This scoring captures the morphologies of 5 of the six states introduced by Ezcurra (2016).

The last state of Ezcurra (2016), whereby the palatal process of the pterygoid is mostly covered by a continuous shagreen of palatal teeth is scored in character 129 below. As there is no identifiable subdivision, and as the teeth of those taxa cover the given areas of both rows T2 and T3 (e.g. *Claudiosaurus*, *Kuehneosaurus*, Carroll, 1981; Evans, 2009), all taxa scored with state 1 for character 129 below are scored with state 1 for the present character and character 128 as well.

125. Pterygoid, palatal process, teeth, lateral row (row T2 of Welman, 1998): absent (0); present as a single row (1); subdivided (rows T2a and T2b of Ezcurra, 2016) (2)

Modified (added state) from Pritchard et al., (2021:k85)

Modified from Ezcurra et al. (2020:k195); Spiekman et al. (2021:k102)

See Ezcurra (2016:figs. 25, 26)

See comments character 127 above.

126. Pterygoid, palatal teeth if present: distinct tooth rows (0); shagreen of teeth covering most of palatal process of the pterygoid (1); inapplicable: pterygoid palatal process dentition absent (-)

Modified from Ezcurra et al. (2020:k195); Spiekman et al. (2021:k102)

See comments in character 127 above. This character is inapplicable to taxa that lack dentition on the palatal process of the pterygoid to avoid redundant scoring between this character and characters 127 and 128 above.

127. Pterygoid, palatal process, teeth, height and diameter: small, considerably smaller than those of marginal dentition (0); relatively large, similar to those of marginal dentition (1); inapplicable: pterygoid palatal process dentition absent (-)

From Spiekman et al. (2021:k105)

Modified from Ezcurra et al. (2021:k189)

See Ezcurra (2016:figs. 25, 26), Spiekman et al. (2021:fig. 16)

This character only considers the morphology of the teeth on the ventral surface of the palatal process of the pterygoid (rows T2 and T3 of Welman, 1998). It should not consider the morphology of the teeth on the medial edge of this process if present (row T4 of Welman, 1998) nor the dentition on other regions of the pterygoid.

128. Pterygoid, palatal process, medial edge, row of fang-like teeth (row T4 of Welman, 1998): absent (0); present (1)

From Ezcurra et al. (2020:k199)

See Ezcurra (2016:figs. 25, 26)

See comments character 127 above.

129. Pterygoid, palatal process, anterior extent: terminates anteriorly level with or posterior to anterior margin of palatine (0); extends anterior to palatine (1)

From Ford and Benson (2020:k144)

Modified (reduced state) from Ezcurra et al. (2020:k193)

See Ezcurra (2016:fig. 26)

130. Pterygoid, palatal process, midline contact with contralateral pterygoid: absent (0); present, small median contact anteriorly (1); present, broad median contact along >50% of anteroposterior length (2). ORDERED

From Pritchard et al. (2021:k88)

Modified (added state, ordered) from Ezcurra et al. (2020:k192); Ford and Benson (2020:k145)

See Ezcurra (2016:fig. 26)

131. Pterygoid, palatal process, ascending lamina: absent or low (0); tall (1)

From Ford and Benson (2020:k148)

132. Pterygoid, orientation of transverse flange in ventral view: directed laterally or sligthly posterolaterally, forming obtuse angle with palatal process (0); directed anterolaterally, forming acute angle with palatal process (1)

From Schoch and Sues (2018a:k107); Ford and Benson (2020:k143); Griffiths et al. (2021:k356); Pritchard et al. (2021:k89)

Modified (reworded states) from Ezcurra et al. (2020:k200)

See Ezcurra (2016:25, 26)

133. Pterygoid, transverse flange, lateral margin: rectangular, forming acute corner (0); merges smoothly into anterolateral margin, forming smoothly convex lateral outline (1)

From Ezcurra et al. (2020:k201)

See Ezcurra (2016:figs. 25, 26)

134. Pterygoid, transverse flange, teeth: present (0); absent (1)

From Schoch and Sues (2018a:k108); Ford and Benson (2020:k141); Griffiths et al. (2021:k109); Pritchard et al. (2021:k86); Spiekman et al. (2021:k106); Simões et al. (2022:k112)

Modified (reduced states) from Ezcurra et al. (2020:k202)

See Ezcurra (2016:figs. 25, 26)

See comments character 127 above.

135. Pterygoid, transverse flange, arrangement of dentition: shagreen of teeth covering ventral surface of flange (0); additional teeth anterior to a single tooth row on ventral rim of flange (1); single tooth row on ventral rim of flange (row T1 of Welman, 1998) (2); inapplicable: pterygoid transverse flange teeth absent (-)

From Ford and Benson (2020:k142)

Modified (added states) from Schoch and Sues (2018a:k109); Pritchard et al. (2021:k87); Spiekman et al. (2021:k107)

Modified from Ezcurra et al. (2020:k202)

See Ezcurra (2016:figs. 25, 26)

See comments character 127 above.

136. Pterygoid, quadrate ramus, teeth: absent (0); present (1)

From Ford and Benson (2020:k147); Simões et al. (2022:k116)

137. Pterygoid, quadrate ramus, median shelf (= 'posteromedian flange', 'tympanic flange', 'arcuate flange'): absent (0); present (1)

From Schoch and Sues (2018a:k112); Ford and Benson (2020:k146); Griffiths et al. (2021:k111)

138. Ectopterygoid: present (0); absent (1)

From Schoch and Sues (2018a:k116); Griffiths et al. (2021:k113); Simões et al. (2022:k117)

139. Ectopterygoid teeth: present (0); absent (1); inapplicable: ectopterygoid absent (-)

From Schoch and Sues (2018a:k117); Ford and Benson (2020:k151); Simões et al. (2022:k118)

140. Ectopterygoid, articulation with pterygoid: ectopterygoid overlaps pterygoid ventrally (0); interlaced articulation between ectopterygoid and pterygoid (1); inapplicable: ectopterygoid absent (-)

From Ezcurra et al. (2020:k204); Spiekman et al. (2021:k111)

See Ezcurra (2016:fig. 26)

141. Ectopterygoid, suture with pterygoid: does not reach posterolateral corner of transverse flange of pterygoid (0); reaches posterolateral corner of transverse flange of pterygoid (1); inapplicable: ectopterygoid absent (-)

From Ezcurra et al. (2020:k205); Spiekman et al. (2021:k112)

See Ezcurra (2016:fig. 26)

142. Ectopterygoid, lateral process, posterior expansion: absent (0); present (1)

Modified (reworded states) from Ezcurra et al. (2020:k207)

Modified (reduced states) from Spiekman et al. (2021:k110)

See Ezcurra (2016:fig. 26), Spiekman et al. (2021:fig. 16)

We follow Spiekman et al. (2021) in describing the presence of a posterior expansion on the lateral process independently from its relationships to the skull roof bones. However, we found it hard to reliably score between a 'curved but unexpanded' and a 'curved and expanded' lateral process (states 1 and 2 of Spiekman et al., 2021) and reverted to previous binary iterations of this character.

143. Ectopterygoid, contact with maxilla: present (0); absent (1); inapplicable, ectopterygoid absent (-)

From Schoch and Sues (2018a:k28); Ezcurra et al. (2020:k206); Ford and Benson (2020:k152); Griffiths et al. (2021:k364)

See Ezcurra (2016:fig. 26)

144. Supraoccipital, posterior surface: smooth (0); distinct dorsoventrally running crest in the midline (1)

From Schoch and Sues (2018a:k139); Ezcurra et al. (2020:k210); Ford and Benson (2020:k106); Griffiths et al. (2021:k128); Pritchard et al. (2021:k92); Simões et al. (2022:k132)

See Ezcurra (2016:fig. 26)

145. Supraoccipital, shape: consists of a flattened posterior lamina (0); pillar-like or U-shaped in posterior view (1)

From Ezcurra et al. (2020:k208); Pritchard et al. (2021:k93)

146. Supraoccipital, lateral expansion providing dorsal margin of posttemporal fenestra: absent (0); present (1)

From Ford and Benson (2020:k107)

We follow Ford and Benson (2012) in coding state 1 as present only when a prominent process is present and well visible in posterior view. Several taxa such as captorhinids exhibit a broad contribution of the supraoccipital to the posttemporal fenestea, but lack a distinct lateral process (different from the 'lateral ascending process' of some taxa) (Price, 1935; Heaton, 1979).

147. Laterosphenoid: absent (0); present (1)

From Schoch and Sues (2018a:k153); Ezcurra et al. (2020:k258); Griffiths et al. (2021:k157); Simões et al. (2022:k160)

Modified from Pritchard et al. (2021:k113)

See Fig. S1; Ezcurra (2016:fig. 28)

148. Prootic, crista prootica: absent, lateral surface continuous and slightly convex (0); present (1)

From Ezcurra et al. (2020:k254); Ford and Benson (2020:k117); Pritchard et al. (2021:k114); Spiekman et al. (2021:k137); Simões et al. (2022:k145)

See Ezcurra (2016:fig. 28), Spiekman et al. (2021:fig. 18)

149. Prootic, anterior inferior process: absent or developed as a small peg-like projection, trigeminal foramen unframed anteriorly (0); well-developed, framing anterior margin of trigeminal foramen (1)

From Ezcurra et al. (2020:k255); Pritchard et al. (2021:k116); Simões et al. (2022:k148)

Modified (reworded states) from Ford and Benson (2020:k118); Griffiths et al. (2021:k144)

See Ezcurra (2016:fig. 28)

150. Prootic, contribution to paroccipital process: absent (0); present, contributes laterally tapering lamina to anterior surface of process (1)

From Pritchard et al. (2021:k117); Spiekman et al. (2021:k139)

See Spiekman et al. (2021:fig. 18)

151. Opisthotic, paroccipital process, contact with skull laterally: present (0); absent, process ends freely (1)

From Schoch and Sues (2018a:k142); Ford and Benson (2020:k115); Pritchard et al. (2021:k96); Spiekman et al. (2021:k131)

Modified (reduced states) from Ezcurra et al. (2020:k214)

As argued by Pritchard (2015:508), the paroccipital process of the opisthotic can articulate with different bones in early amniotes, but the homologies between different contacts can be hard to formulate. Thus, we follow recent studies in provisionally coding for the presence of a contact between the paroccipital process and the other skull bones regardless of which bones it is in contact with. This character is supplemented by character 155 below, which considers the presence of a contact with the tabular.

152. Opisthotic, paroccipital process, contact with tabular: present (0); absent (1); inapplicable: paroccipital process ends freely or tabular is absent (-)

From Ford and Benson (2020:k116)

153. Opisthotic, paroccipital process, morphology: slender and rod-like (0); dorsoventrally broad sheet (1)

Modified (reduced states) from Ford and Benson (2020:k114)

Ford and Benson (2020) employ a 4-state character to describe the overall shape, expansion and orientation of the paroccipital process in early amniotes. However, this formulation encompasses various morphological aspects. Consequently, we restrain the present character to the overall shape of the paroccipital process of the opisthotic, which can be provisionnaly divided into a rod-like shape (states 0 and 1 of Ford and Benson, 2020), and a dorsoventrally broad sheet (states 2 and 3 of Ford and Benson, 2020). The distal expansion of the paroccipital process is considered in character 157 below, as typically done for Permo-Triassic diapsids (e.g. Ezcurra et al., 2020).

154. Opisthotic, paroccipital process, distal morphology if rod-like: unflattened and tapered (0); anteroposteriorly flattened distally (1); inapplicable: paroccipital process forms dorsoventrally broad sheet (-)

From Ezcurra et al. (2020:k215); Pritchard et al. (2021:k95)

See Ezcurra (2016:fig. 30)

See comments in character 156 above.

155. Opisthotic, ventral ramus, distal expansion: absent, forms anteroposteriorly narrow plate or is pyramidal with a tapered distal end (0); columnar with anteroposteriorly expanded but not bulbous distal head (1); club-shaped with large bulbous distal head (2). ORDERED

Modified (added state, ordered) from Pritchard et al. (2021:k94)

Modified from Ezcurra et al. (2020:k217); Spiekman et al. (2021:k133)

See Spiekman et al. (2021:fig. 18)

Recent studies (e.g. Ezcurra et al., 2020; Spiekman et al., 2021) have employed a multistate character to describe the various morphologies of the ventral ramus of the opisthotic in archosauromorphs (see comments in Ezcurra, 2016:k217). However, none of these states correspond to the anteroposteriorly narrow plate-like process typical of other early amniotes such as non-therapsid synapids (Romer and Price, 1940) or captorhinids (Price, 1935; Heaton, 1979). As the homology between the various morphologies of the ventral ramus of the opisthotic in early amniotes are hard to assess, we provisionnally refrain from employing a categorical character to describe the overall morphology of this process. Instead, we follow Pritchard et al. (2021) in scoring only for presence of a distal expansion of this process, and follow Spiekman et al. (2021) in considering that some taxa show a clear, yet not club-like, expansion of this process. As the latter morphology appears intermediate between a narrow or tapering end, and a club-shaped one, we elect to order this character.

156. Parabasisphenoid, orientation of long axis: horizontal (0); anterodorsal (1)

From Ezcurra et al. (2020:k235); Pritchard et al. (2021:k103); Spiekman et al. (2021:k120)

See comments in Pritchard (2015:593)

See Ezcurra (2016:figs. 27, 28)

157. Parabasisphenoid, body shape from basipterygoid processes to posterior end: transversely broad, width greater than length (0); transversely narrow, length greater than width (1)

From Ford and Benson (2020:k128)

158. Parabasisphenoid, dentition on ventral surface of parasphenoidal plate: absent (0); present (1)

From Ford and Benson (2020:k124)

In a similar manner to the pterygoid dentition, and in agreement with Ford and Benson (2020), we elect to consider the presence of dentition on the parasphenoidal plate and cultriform process in distinct characters (character 162 below). We further consider presence of teeth on the cultriform process of the parasphenoid and its repartition, either trougout the length of the process or clustered at its base, in distinct characters (characters 162 and 163 below) following Pritchard et al. (2021), as it is unclear if both states form a morphological series.

159. Parabasisphenoid, dentition on ventral surface of cultriform process: absent (0); present (1)

From Ezcurra et al. (2020:k244); Ford and Benson (2020:k125); Pritchard et al. (2021:k104); Spiekman et al. (2021:k113)

See comments in character 161 above.

160. Parabasisphenoid, dentition on the cultriform process if present: teeth run anteroposteriorly on process (0); teeth clustered at base of process (1); inapplicable: cultriform process edentulous (-)

From Pritchard et al. (2021:k105)

See comments in character 161 above.

161. Parabasisphenoid, orientation of the basipterygoid process in the transverse plane: anterolateral (0); lateral (1); posterolateral (2). ORDERED

Modified (added states, ordered) from Schoch and Sues (2018a:k113); Ezcurra et al. (2020:k248); Pritchard et al. (2021:k111)

Modified from Ford and Benson (2020:k123)

See Ezcurra (2016:fig. 28)

162. Parabasisphenoid, basipterygoid processes, length: moderately short, finger-like and with short articular facets (0); long, with hemispherical articular facets (1); extremely long and rod-like, longer than body of parabasisphenoid (2). ORDERED

Modified (reduced states, ordered) from Ezcurra et al. (2020:k247)

We did not include state 2 of Ezcurra et al. (2020) which described the very shord basipterygoid processes of choristoderans, which are not included in our dataset. In addition, as the present

states form a continuum describing the elongation of the basipterygoid process of the parabasisphenoid, we order this character.

163. Parabasisphenoid, basal articulation position: anterior to posterior rim of transverse flange of pterygoid (0); level with rim of transverse flange (1); posterior to rim of transverse flange (2). ORDERED

Modified (ordered) from Ford and Benson (2020:k122)

164. Parabasisphenoid, entry foramen for pathway of internal carotid arteries: ventral, medial to the basipterygoid processes (0); lateral, dorsal to the basipterygoid processes (1)

From Ford and Benson (2020:k126); Griffiths et al. (2021:k124); Simões et al. (2022:k128)

Modified (reduced states) from Ezcurra et al. (2020:k240); Pritchard et al. (2021:k107)

See Ezcurra (2016:fig. 28)

165. Parabasisphenoid, parasphenoid crests: present as prominent ventrolateral extensions framing ventromedial floor of vidian canal (0); absent such that there is no ventral floor for the vidian canal (1); inapplicable, entry foramen is located on the lateral surface of the parabasisphenoid (-)

From Ezcurra et al. (2020:k246); Ford and Benson (2020:k127); Pritchard and Sues (2019:k106)

166. Parabasisphenoid, posterodorsal portion: incompletely ossified (0); completely ossified (1)

From Ezcurra et al. (2020:k236); Spiekman et al. (2021:k116)

167. Parabasisphenoid, semilunar depression on lateral surface of basal tubera: absent (0); present (1); inapplicable: posterodorsal portion of parabasispenoid incompletely ossified (-)

From Ezcurra et al. (2020:k238); Pritchard et al. (2021:k108); Spiekman et al. (2021:k119)

See Ezcurra (2016:fig. 28)

168. Parabasisphenoid, median concavity between cristae ventrolaterales ('pharyngeal recess'): absent, ventral surface flat (0); present as a shallow depression (1); present as a deep excavation (2). ORDERED

From Spiekman et al. (2021:k118)

Modified (ordered) from Ford and Benson (2020:k130)

Modified from Ezcurra et al. (2020:k239); Simões et al. (2022:k142)

See Ezcurra (2016:fig. 27)

See comments in Spiekman et al. (2021). The pharyngeal recess of archosauriforms was recently homologized with the shallow median depression of the parabasisphenoid in some archosauromorphs (Sobral et al., 2016; Sobral and Müller, 2019). As similar depressions can be seen in various early amniotes (Ford and Benson, 2020), we further extend the application of this character to our dataset.

169. Parabasisphenoid, ventral plate, median longitudinal ridge: absent (0); present (1)

From Ford and Benson (2020:k131)

170. Exoccipital, fusion with opisthotic: absent (0); present (1)

From Ezcurra et al. (2020:k211); Spiekman et al. (2021:k127)

Modified (reduced states) from Griffiths et al. (2021:k151); Pritchard et al. (2021:k99); Simões et al. (2022:k155)

See Ezcurra (2016:fig. 27)

Pritchard et al. (2021) employ a multistate character to describe the fusion of the exoccipital to either the opisthotic or the basioccipital. However, as these describe distinct sutural relationships, we elect to score the fusion of the exoccipital to each bone in separate binary characters (see character 174 below). A similar division was also advocated by Simões et al. (2022) based on the diversity of fusion patterns in squamates.

171. Exoccipital, fusion with basioccipital: absent (0); present (1)

From Griffiths et al. (2021:k132); Simões et al. (2022:k134)

Modified (reduced states) from Pritchard et al. (2021:k99)

See comments in character 173 above.

172. Exoccipital, dorsomedial process: absent or incipient, exoccipital columnar, forming transversely narrow contact with dorsal occiput elements (0); dorsomedially inclined processes do not meet in the midline (1); dorsomedial processes meet dorsally excluding supraoccipital from foramen magnum (2); inapplicable: exoccipital fused to opisthotic (-). ORDERED

From Pritchard et al. (2021:k97); Spiekman et al. (2021:k128)

Modified (added states, ordered) from Ezcurra et al. (2020:k209, k219)

See Spiekman et al. (2021:fig. 17)

173. Exoccipital, ventral contact with contralateral exoccipital: absent, basioccipital contributes to floor of foramen magnum (0); present, excluding basioccipital from foramen magnum (1)

From Schoch and Sues (2018a:k143); Ford and Benson (2020:k120); Pritchard et al. (2021:k98); Spiekman et al. (2021:k129)

Modified (reduced states) from Ezcurra et al. (2020:k221)

See Ezcurra (2016:fig. 27)

174. Basioccipital, basal tubera: absent or poorly developed, not extending ventral to the occipital condyle (0); well developed, extending ventral to the occipital condyle (1)

From Pritchard et al. (2021:k101)

Modified from Ezcurra et al. (2020:k226) ; Spiekman et al. (2021:k122)

See Ezcurra (2016:fig. 27)

See comments in Pritchard and Nesbitt (2017:k64). Pritchard and Nesbitt (2017) describe the basioccipital of the drepanosauromorph *Avicranium* as lacking well-developed basal tubera extending ventral to the occipital condyle. While it is true that the basal tubera hardly extend ventrally beyond the ventral margin of the condyle in this taxon, they expand markedly laterally so that the bone is overall three times as wide as the occipital condyle. This differs markedly from the morphology of other taxa showing poorly developed basal tubera such as captorhinids or non-saurian diapsids (Price, 1935; Vaughn, 1955; Gardner et al., 2010) and we argue that this taxon thus does exhibit well-developed basal tubera. Consequently, *Avicranium* is score as state 1 herein.

175. Basioccipital, occipital condyle, posterior surface: elliptocal notochordal depression occupying most of posterior surface of condyle (0); narrow "prinpick" notochordal pit within posterior surface (1); condyle smoothly convex (2). ORDERED

From Pritchard et al. (2021:k100)

Modified from Ezcurra et al. (2020:k230)

See Ezcurra (2016:fig. 27)

Pritchard and Nesbitt (2017) describe a large, elliptical notochordal pit on the posterior surface of the occipital condyle of *Avicranium*. There is indeed an unequivocal pit marking the passage of the notochord. However, we suggest that the notochordal pit of *Avicranium* is not as large as that of *Captorhinus* or *Youngina* (Price 1935, Gardner et al., 2010). In fact, its size is more reminiscent of a variety of saurian taxa such as *Trilophosaurus* (Spielmann et al., 2008) or proterochampsian archosauriforms (Ezcurra, 2016:fig. 27). Given this uncertainty, we score *Avicranium* with both states 0 and 1 for uncertainty pending a more quantitative character state delimitation.

176. Stapes, stapedial shaft, robustness: robust with thick shaft, similar or greater in breadth to paroccipital process of opisthotic (0); slender with rod-like shaft, much slenderer than paroccipital process (1)

From Ezcurra et al. (2021:k296); Pritchard et al. (2021:k118); Spiekman et al. (2021:k141)

Modified (reduced states) from Schoch and Sues (2018a:k135)

177. Stapes, foramen for stapedial artery: present (0); absent (1)

From Ezcurra et al. (2020:k297); Ford and Benson (2020:k161); Griffiths et al. (2021:k156); Pritchard et al. (2021:k120); Spiekman et al. (2021:k142); Simões et al. (2022:k158)

178. Stapes, dorsal process: present (0); absent (1)

From Schoch and Sues (2018a:k136); Ford and Benson (2020:k162); Griffiths et al. (2021:k155); Pritchard et al. (2021:k119); Simões et al. (2022:k159)

179. Mandible, retroarticular process, shape in lateral view: absent, no extension posterior to quadrate articulation (0); present, dorsoventrally shallow, dorsal margin posteroventral to quadrate articulation (1); present, dorsoventrally deep, dorsal margin level with quadrate articulation (2). ORDERED

From Ezcurra et al. (2020:k283); Spiekman et al. (2021:k162)

Modified (added states, ordered) from Ford and Benson (2020:k170, 171); Pritchard et al. (2021:k137, 139); Simões et al. (2022:k193)

See Fig. S1; Ezcurra (2016:figs. 17, 29)

180. Mandible, retroarticular process, orientation: anteroposteriorly straight or downturned (0); dorsally upturned (1); inapplicable: retroarticular process is absent (-)

From Schoch and Sues (2018a:k169); Ezcurra et al. (2020:k284); Pritchard et al. (2021:k140); Spiekman et al. (2021:k163)

Modified (reduced states) from Ford and Benson (2020:k173)

See Fig. S1; Ezcurra (2016:figs. 17, 29)

181. Mandible, retroarticular process, composition: composite, articular with participation of angular and/or surangular (0); formed only by articular (eventually fused to prearticular) (1); inapplicable: retroarticular process is absent (-)

From Ford and Benson (2020:k172)

182. Mandible, coronoid process, height: absent or low, dorsal margin of mandible flat or only slightly convex behind alveolar portion (0); dorsoventrally shorter than anterior process of jugal (1); dorsoventrally tall, equivalent or taller than anterior process of jugal (2). ORDERED

From Spiekman et al. (2021:k153)

Modified from Schoch and Sues (2018a:k156); Ezcurra et al. (2020:k261); Ford and Benson (2020:k168); Pritchard et al. (2021:k126, 127)

See Ezcurra (2016:fig. 29)

We follow Spiekman et al. (2021) in considering the dorsal extent of the coronoid process in a single ordered character and scoring the character states relative to the height of the anterior process of the jugal, as introduced by Pritchard et al. (2018:k319). We have not included state 2 of Ford and Benson (2020) describing the lack of coronoid eminence as we found it hard to differenciate between this morphology and the presence of a shallow eminence (state 0 herein). Taxa scored as lacking a coronoid eminence by Ford and Benson (2020) are thus scored with state 0 here (e.g. *Varanops*).

183. Mandible, coronoid eminence (process), contribution of dentary: absent (0); present (1)

From Ford and Benson (2020:k169); Simões et al. (2022:k173)

184. Mandible, external mandibular fenestra between dentary, surangular and angular: absent (0); present (1)

From Ezcurra et al. (2020:k262); Ford and Benson (2020:k174); Pritchard et al. (2021:k133); Spiekman et al. (2021:k152); Simões et al. (2022:k188)

See Fig. S1; Ezcurra (2016:figs. 17, 29)

185. Dentary, anterior portion: upturned, positioned dorsal to anteroposterior middle portion of dentary (0); in same horizontal plane as midde portion of dentary (1); dorwnturned, positioned ventral to middle portion of dentary (2). ORDERED

Modified (ordered) from Ezcurra et al. (2020:k267); Spiekman et al. (2021:k145)

Modified (added state, ordered) from Ford and Benson (2020:k165); Pritchard et al. (2021:k121)

See Ezcurra (2016:figs. 17, 29)

We consider that an anteroposterorly straight dentary represents an intermediate state between an anteriorly upturned and denturned one, and consenquently order this character.

186. Coronoids, number in mandible: three (0); two (1); one (2); zero (3). ORDERED

Modified (added states, ordered) from Schoch and Sues (2015:k157); Ford and Benson (2020:k188); Spiekman et al. (2021:k154)

187. Coronoid(s), teeth: present (0); absent (1); inapplicable: coronoid bones are absent (-)

From Ford and Benson (2020:k189)

188. Splenial: present (0); absent as a distinct ossification (1)

From Schoch and Sues (2018a:k163); Griffiths et al. (2021:k176); Pritchard et al. (2021:k134); Spiekman et al. (2021:k143); Simões et al. (2022:k178)

189. Splenial, contact with posterior coronoid: absent (0); present (1); inapplicable: coronoid or splenial absent (-)

From Ford and Benson (2020:k186)

190. Symphysis, height: dorsoventrally low, mandible tapers anteriorly (0); dorsoventrally high, symphysis almost as deep as mandible at midlength of tooth row (1); dorsally expanded, symphysis deeper than mandible at midlength of tooth row (2). ORDERED

Modified (added state, ordered) from Ezcurra et al. (2020:k271); Ford and Benson (2020:k179)

See Ezcurra (2016:figs. 18, 19, 29)

We consider a relatively highy symphysis, whereby the dorsal and ventral margins of the mandible are subparallel (state 1) as intermediate between anteriorly tapering and expanded mandibles, and consequently order this character.

191. Symphysis, composition: formed by dentary and splenial (0); formed solely by dentary (1)

From Schoch and Sues (2018a:k164); Pritchard et al. (2021:k135); Ford and Benson (2020:k183); Simões et al. (2022:k179)

192. Angular, exposure on lateral surface of mandible: dorsoventrally deep (0); dorsoventrally shallow, limited to less than 1/3 of mandible height (1)

From Ezcurra et al. (2020:k290); Griffiths et al. (2021:k351); Pritchard et al. (2021:k131)

Modified (reduced states) from Schoch and Sues (2018a:k166); Spiekman et al. (2021:k159)

See Ezcurra (2016:fig. 29)

193. Surangular, anterior extension in lateral view: extends anteriorly beyond coronoid eminence (0); terminates posterior to or level with anterior border of coronoid eminence (1)

From Schoch and Sues (2018a:k160); Ezcurra et al. (2020:k285); Ford and Benson (2020:k191)

See Ezcurra (2016:fig. 29)

194. Surangular, anterodorsal process preventing contact between dentary and posterior coronoid: absent (0); narrow splint-like process present (1); dorsoventrally broad, at least posteriorly (2); inapplicable: coronoid absent (-). ORDERED

Modified (added state, ordered) from Ford and Benson (2020:k196, 197)

We consider that the present character states form a morphological series and consequently fuse characters 196 and 197 of Ford and Benson (2020) into a single ordred character.

195. Surangular, anterior surangular foramen on lateral surface, near surangular-dentary contact: absent (0); present (1)

From Ezcurra et al. (2020:k288); Ford and Benson (2020:k192); Griffith et al. (2021:k184); Pritchard et al. (2021:k129); Spiekman et al. (2021:k156); Simões et al. (2022:k186)

See Ezcurra (2016:fig. 29)

196. Surangular, posterior surangular foramen on lateral surface, directly anterolateral to glenoid fossa: absent (0); present (1)

From Ezcurra et al. (2020:k289); Ford and Benson (2020:k193); Griffith et al. (2021:k185); Pritchard et al. (2021:k130); Spiekman et al. (2021:k157); Simões et al. (2022:k187)

See Ezcurra (2016:fig. 29)

197. Surangular, dorsolateral surface: transversely narrow (0); exhibits transversely wide shelf (1)

From Schoch and Sues (2018a:k161); Ford and Benson (2020:k195); Griffiths et al. (2021:k183); Pritchard et al. (2021:k128); Simões et al. (2022:k184)

Modified (reduced states) from Ezcurra et al. (2020:k286); Spiekman et al. (2021:k155)

See Ezcurra (2016:fig. 18, 29)

198. Marginal dentition, implantation: mediolateral tooth-bone contact (=pleurodonty or thecodonty) (0); on tooth-bearing element without mediolateral tooth-bone contact (=acrodonty) (1)

Modified (reduced states) from Pritchard et al. (2021:k152); Simões et al. (2022:k213)

Figured in Simões et al. (2022:k213)

From a strictly geometrical perspective, tooth implantation can be described by the presence of mediolateral tooth-bone contact, and when present, by the extent of the lingual tooth wall that describes the symmetry of this contact (Bertin et al., 2018, see also Simões et al., 2022 for similar character formulations). As such, we describe the tooth implantation geometry using two hierarchical characters (see character 202 below). This conforms with the character sampling of Pritchard et al. (2021), but contrast with other recent studies that employ a single multistate character describing both tooth implantation, and to some extent tooth attachment, considered here in character 204 below (e.g. Ezcurra, 2016:k299; Spiekman et al., 2021:k169).

The present character considers the presence of mediolateral tooth-bone contact, thus differentiating between acrodont and non-acrodont taxa. Following Bertin et al. (2018:4) acrodonty can be defined as follows: "the apex of the tooth is set at the top [...] of the tooth-bearing element, without any mediolateral tooth-bone contact. The tooth is neither set in a groove nor in alveoli because no bony wall is present on any side of the tooth".

Note that Pritchard et al. (2021) employed an ordered multistate character describing an "intermediate" state for acrodonty. However, as their states 1 and 2 can only be differenciated based on histological sections or CT-scan data (see comments in Pritchard and Nesbitt, 2017:k94), we revert to a previous binary iteration of this character (see Pritchard, 2015:k93).

199. Marginal dentition, implantation, height of lingual wall: lingual wall absent or forming only basal contact with tooth, tooth mainly attached on labial side (=pleurodonty) (0); low lingual wall, lower than labial wall, forming asymmetrical attachment for tooth (=subthecodonty) (1); high lingual wall, forming symmetrical attachment for tooth (=thecodonty) (2); inapplicable: mediolateral tooth-bone contact absent (=acrodonty) (-). ORDERED

Modified (added state, ordered) from Pritchard et al. (2021:k153)

Modified (reduced states) from Simões et al. (2022:k215)

Modified from Schoch and Sues (2018a:k172); Ezcurra et al. (2020:k299); Spiekman et al. (2021:k169)

See Ezcurra (2016:14, 22); Bertin et al. (2018:fig. 3); figured in Simões et al. (2022:k215)

From a geometrical perspective, tooth implantation in non-acrodont taxa can be defined according to the extent of the lingual wall of the tooth bearing bone (see comments in character 201 above).

The extent of the lingual tooth wall can be discretized into three states, defined by Bertin et al. (2018:4-6): pleurodonty ("the labial surface of the tooth is set against the labial side [...] of the

tooth-bearing element"); subthecodonty ("the tooth is set in an asymmetrical and shallow socket. Asymmetry is created by differences in height between the lingual and labial walls of jaw bones, the labial wall being higher than the lingual wall."); thecodonty ("the tooth is set in a deep and symmetrical alveolus. The depth of the alveolus is at least equal to the height of the crown.").

As the present character states from a morphological series, state 1 being intermediate, we elect to order this character.

200. Marginal dentition, interdental plates: absent, teeth walled only by lingual wall (0); present (1); inapplicable: mediolateral tooth-bone contact absent (=acrodonty) (-)

From Pritchard et al. (2021:k154)

Modified (reduced states) from Ezcurra et al. (2020:k1)

See Ezcurra (2016:fig. 14)

We follow Bertin et al. (2018, see also Ezcurra et al., 2020) in considering the presence of interdental plates independently from implantation geometry (contrary to Pritchard et al., 2021).

201. Marginal dentition, attachment: tooth crowns not attached to dentigerous bone (=gomphosis) (0); ankylosed to bone of attachment (=ankylosis) (1)

From Ezcurra et al. (2020:k754); Griffiths et al. (2021:k211); Pritchard et al. (2021:k155); Simões et al. (2022:k214)

See Bertin et al. (2018:fig. 2); figured in Simões et al. (2022:k214)

We follow Bertin et al. (2018) in considering tooth implantation and attachment independently (see comments in character 201 above, also Simões et al., 2018:k210-211). The present character thus describes tooth attachment, or the connection between the tooth and the tooth-bearing element.

Tooth attachment can be descritized into two states, recently defined by Bertin et al. (2018:6): gomphosis ("the tooth is attached to the bone through a non-mineralized ligament that links the cementum to the alveolar bone") and ankylosis ("the tooth is fused to the tooth-bearing element through mineralized tissues").

202. Marginal dentition, heterodonty: teeth generally homodont (0); markedly heterodont (clear shift in morphology) (1)

From Ezcurra et al. (2020:k300)

Modified from Pritchard et al. (2021:k157)

See Fig. S1; Ezcurra (2016:fig. 14)

Previous studies have scored either for the presence of marked heterodonty (e.g. Ezcurra et al. 2020) or regionalization (e.g. Pritchard et al., 2021), both of which are grouped into state 1 here. We indeed consider the marked regionalization of *Clevosaurus* (Fraser, 1988) as a form of heterodonty and consequently score this taxon with state 1 pending further studies on heterodonty in early saurians. Note that taxa with caniniform teeth should not be considered heterodont if all other teeth ave the same morphology.

203. Marginal teeth, procumbency: absent, anteriormost marginal teeth have similar apicobasal orientation to posterior teeth (0); anteriormost teeth are procumbent (1); inapplicable: premaxilla and anterior portion of dentary edentulous (-)

From Ezcurra et al. (2020:k763); Pritchard et al. (2021:k158)

See Fig. S1.

204. Marginal dentition, distal recurvature of teeth: teeth straight throughout length (0); slightly recurved (1); strongly recurved, apex approximately 80-90 degrees from vertical (2). ORDERED

Modified (added state, ordered) from Ford and Benson (2020:k6, 7); Spiekman et al. (2021:k171)

Modified from Ezcurra et al. (2020:k303); Pritchard et al. (2021:k147)

Following Ford and Benson (2020), teeth are recurved when the apex is situated distal to the distal margin of the crown base.

205. Marginal dentition, serrations on tooth crown: absent (0); present (1)

From Ford and Benson (2020:k9); Griffiths et al. (2021:k203); Pritchard et al. (2021:k145); Simões et al. (2022:k205)

Modified (reduced states) from Ezcurra et al. (2020:k304); Spiekman et al. (2021:k172)

See Ezcurra (2016:fig. 14)

206. Marginal dentition on anterior portion of dentary: present (0); absent (1)

From Ezcurra et al. (2020:k278); Simões et al. (2022:k216)

Modified from Schoch and Sues (2018a:k12); Griffiths et al. (2021:k4); Pritchard et al. (2021:k142)

See Fig. S1; Ezcurra (2016:fig. 29)

207. Marginal dentition, crown height of upper dentition compared to lower dentition: lower dentition shorter relative to higher dentition (0); similar tooth crown height (1); upper dentition shorter relative to lower dentition (2)

Modified (added state) from Ezcurra et al. (2020:k679); Pritchard et al. (2021:k144)

Pritchard et al. (2021) considered the presence of a relatively larger lower marginal dentition in azendohsaurid archosauromorphs. However, they did not consider the presence of a larger higher marginal dentition, which is seen in some eupelycosaurs (e.g. *Dimetrodon*, *Ophiacodon*, Reisz, 1986) and archosauriforms (e.g. *Euparkeria*, Sookias et al., 2020) and archosaurs (*Dimorphodon*, *Herrerasaurus*, Sereno and Novas, 1994; Nesbitt and Hone, 2010). We have thus included this morphology in a new character state.

As it is unclear, for instance, if the presence of a larger upper dentition results from an increase in its size, from a reduction of the lower dentition, or from both, we refrain from ordering this character.

208. Marginal dentition, tooth shape at crown base on maxilla or mid-posterior portion of dentary: subcircular (0); labiolingually compressed (1); labiolingually wider than mesiodistally long (2)

From Pritchard et al. (2021:k156); Spiekman et al. (2021:k174)

Modified from Ezcurra et al. (2020:k305); Ford and Benson (2020:k10)

See Ezcurra (2016:fig. 14); Spiekman et al. (2021:fig. 20)

209. Marginal dentition, middle-posterior portion: crown tapers apically from tooth-crown junction (0); crown expands mesiodistally apical to root-crown junction (1)

From Ezcurra et al. (2020:k308); Pritchard and Sues (2019:k148); Spiekman et al. (2021:k308)

See Ezcurra (2016:fig. 14)

210. Marginal dentition, crown morphology, mesiodistally arranged cusps: absent (0); present (1)

From Ford and Benson (2020:k11); Griffiths et al. (2021:k204)

Modified (reduced states) from Ezcurra et al. (2020:k680); Schoch and Sues (2018a:k173); Pritchard et al. (2021:k151); Simões et al. (2022:k208)

We follow Griffiths et al. (2021) and Simões et al. (2022) in considering the presence of mesiodistally and labiolingually arranged tooth cusps in separate characters due to their marked topological difference (see character 214 below and comments in Simões et al., 2018:k204).

211. Marginal dentition, crown morphology: all single pointed apex or with mesiodistally arranged cusps (0); flattened platform with pointed cusps (1)

From Griffiths et al. (2021:k205); Simões et al. (2022:k209)

Modified (reduced states) from Ezcurra et al. (2020:k680); Pritchard et al. (2021:k151)

See comments in character 213 above.

Postcranial characters (196 characters, 48.16 %)

212. Vertebrae, notochordal canal: present throughout ontogeny (0); absent in adults (1)

From Schoch and Sues (2018a:k177); Ezcurra et al. (2020:k310); Ford and Benson (2020:k199); Griffiths et al. (2021:k229); Pritchard et al. (2021:k159); Spiekman et al. (2021:k176); Simões et al. (2022:k230)

See Ezcurra (2016:fig. 31)

213. Presacral vertebrae, anterior centrodiapophyseal lamina or paradiapophyseal lamina: absent (0); present (1)

From Ezcurra et al. (2020:k315); Ford and Benson (2020:k222); Griffiths et al. (2021:k365)

See Ezcurra (2016:figs. 31, 32, 34)

The anterior centrodiapophyseal lamina extends anteroventrally from the base of the diaphysis to the anterodorsal corner of the centrum while the paradiapophyseal lamina links the diapophysis to the parapophysis (Wilson, 1999). See Ezcurra (2016) for comments on the homology of the anterior centrodiapophyseal lamina and the paradiapophyseal lamina.

214. Presacral vertebrae, posterior centrodiapophyseal lamina: absent (0); present (1)

From Ezcurra et al. (2020:k316)

See Ezcurra (2016:figs. 31, 34)

The posterior centrodiapophyseal lamina extends posteroventrally from the base of the diaphysis to the posterodorsal corner of the (Wilson, 1999).

215. Presacral vertebrae, prezygodiapophyseal lamina in posterior cervicals and anterior-middle dorsals: absent (0); present (1)

From Ezcurra et al. (2020:k317); Griffiths et al. (2021:k366)

See Ezcurra (2016:fig. 34)

The prezygodiapophyseal lamina extends anterodorsally from the base of the diaphysis to the lateral margin of the prezygapophysis (Wilson, 1999).

216. Presacral vertebrae, postzygodiapophyseal lamina in posterior cervicals and anterior-middle dorsals: absent (0); present (1)

From Ezcurra et al. (2020:k318)

See Ezcurra (2016:fig. 34)

The postzygodiapophyseal lamina extends posterodorsally from the base of the diaphysis to the lateral margin of the postzygapophysis (Wilson, 1999).

217. Presacral vertebrae, posterodorsally projecting processes (= mammillary processes) on dorsolateral surface of posterior cervical and anterior dorsal neural spines: absent (0); present (1)

From Ford and Benson (2020:k212); Griffiths et al. (2021:k257); Pritchard et al. (2021:k199); Spiekman et al. (2021:k201); Simões et al. (2022:k258)

Modified (removed states) from Ezcurra et al. (2020:k320)

See Ezcurra (2016:figs. 31, 34)

See description of mammillary processes in Spiekman et al. (2021:k201). We concur with Ford and Benson (2020) tha the ‘mammillary processes’ of *Mesosaurus* (Modesto, 2010) are not

homologous to that of other amniotes (see character 238 below for another interpretation as epipophyses). *Mesosaurus* is therefore scored with state 0 for the present character.

218. Presacral vertebrae, at least one vertebra with parallelogram-shaped centra in lateral view, with anterior surface higher than posterior one: absent (0); present (1)

From Ezcurra et al. (2020:k313); Spiekman et al. (2021:k177)

See Ezcurra (2016:fig. 33)

A parallelogram-shaped centrum (state 1) has typically been described in archosauromorphs (Ezcurra et al., 2014; Ezcurra, 2016). A similar morphology can also be found in araeoscelidians (Vaughn, 1955; Reisz, 1981) and *Claudiosaurus* (MNHN.F.MAP1a, b), as scored by Spiekman et al. (2021), but also in *Coelurosauravus* (MNHN.F.MAP317a, b). In all cases, this morphology is highlighted by a significant anterodorsal angulation of the anterior and posterior surfaces of the centra in lateral view.

219. Atlas, atlantal ribs: present (0); absent (1)

From Schoch and Sues (2018a:k180); Ford and Benson (2020:k201); Griffiths et al. (2021:k222); Simões et al. (2022:k224)

220. Axis, neural spine, shape in lateral view: dorsal margin horizontal or inclined anteroventrally (0); dorsal margin extends anterodorsally (1)

From Ezcurra et al. (2020:k329); Pritchard et al. (2020:k165); Spiekman et al. (2021:k186)

See Ezcurra (2016:fig. 30)

221. Cervical vertebrae, number of vertebrae in neck: less than eight (0); eight or nine (1); ten or more (2). ORDERED

From Ezcurra et al. (2020:k324)

Modified from Spiekman et al. (2021:k195)

When a cervical region can be confidently differenciated, most early amniotes have less than eight cervicals, including early synapsids (Reisz, 1986), parareptiles (Reisz and Scott, 2002; Modesto et al., 2015) and the early diapsids *Petrolacosaurus*, *Youngina* and tangasaurids (Gow, 1975; Currie, 1981a; Reisz, 1981). In contrast, most other Permo-Triassic diapsids have between eight and nine cervical vertebrae (Ezcurra, 2016). A further increase in cervical

number occurs in long-necked taxa such as *Mesosaurus* or *Tanystropheus* (Nosotti, 2007; Modesto, 2010).

Cervical count ranges from five (e.g. *Petrolacosaurus*, Reisz, 1981) to 13 (*Tanystropheus*, Nosotti, 2007) in our dataset. However, given the rather clear demarcation between taxa with fewer than eight cervical vertebrae, those with eight or nine, and those with at least 10, we refrain from employing separate character states for each cervical count to avoid overpondering this character. Lastly, given that our dataset is not focused on tanystropheids contrary to Spiekman et al. (2021), we follow the character states used by Ezcurra et al. (2021).

222. Cervical vertebrae, morphology of intervertebral articulations: circular or ovoid articular surfaces appressed to one another directly (0); saddle-shaped articular surfaces (= heterocoely) (1)

From Pritchard et al. (2021:k167)

223. Cervical vertebrae, posterior articular surface: concave (0); planar (1); convex (2)

Modified from Ezcurra et al. (2020:k681); Griffiths et al. (2021:k228); Pritchard et al. (2021:k160); Spiekman et al. (2021:k181); Simões et al. (2022:k229)

We follow Pritchard et al. (2021) in describing the intervertebral articulations through the morphology of the posterior articular surface of the centrum rather than in a single multistate character (as done in e.g. Griffiths et al., 2021; Spiekman et al., 2021; Simões et al. 2022).

The posterior surface of the centrum is typically concave in amphicoelous or opistocoelous articulations (state 0), planar in platicoelous articulations (state 1), and convex in procoelous articulations (state 2) (Romer, 1956; Hoffstetter and Gasc, 1969). Additional morphologies could be considered by describing the morphology of the anterior surface of the centrum, but this is not relevant to our dataset which lacks taxa with opisthocoelous articulations.

In addition, previous studies have typically used a single character to described all presacral intervertebral articulations (e.g. Griffiths et al., 2021; Pritchard et al., 2021). However, some taxa are known to exhibit different morphologies between the cervical and dorsal centra (e.g. drepanosaromorphs, *Trilophosaurus*, Renesto et al., 2010; Spielmann et al., 2008). We thus consider cervical articulations in the present character, and dorsal articulations in character 247 below.

As a result, our scoring for drepanosauromorphs differs from that of Pritchard et al. (2021) who scored all drepanosauromorphs as possessing a concave posterior surface, likely based on their dorsal vertebral column. However, the anterior and posterior articular surfaces of drepanosauromorph cervicals have been described as a cotyle and a condyle respectively, and

are broadly respectively concave and convex (e.g. Renesto and Fraser, 2003). Consequently, all drepanosauromorphs where the cervical vertebrae are known are scores as state 2 for the present character.

224. Cervical vertebrae, post-axial intercentra: present (0); absent (1)

From Schoch and Sues (2018a:k182); Ezcurra et al. (2020:k346); Griffiths et al. (2021:k237); Pritchard et al. (2021:k184); Simões et al. (2022:k237)

225. Cervical vertebrae, centra length: shorter than or subequal to anterior and mid-dorsal centra (0); longer than anterior dorsal centra (1)

From Ford and Benson (2020:k206)

226. Cervical vertebrae, posterior extent of centrum in lateral view: anterior or level with posterior margin of postzygapophysis (0); extends markedly beyond posterior margin of postzygapophysis (1)

NEW CHARACTER

We introduce this character to describe the marked posterior extension of the centrum in drepanosauromorphs and early pterosaurs (Renesto and Fraser, 2003; Dalla Vecchia, 2014; Dalla Vecchia and Cau, 2015). In all other taxa in our dataset, the centrum barely extends posterior to the postzygapophysis, if at all.

227. Cervical vertebrae, centrum, shape in ventral view: rectangular, lateral margins subparallel (0); tapering posteriorly, anterior surface much wider than posterior one (1)

NEW CHARACTER

We introduce this character to describe the strongly tapering cervical centra of drepanosauromorphs and early pterosaurs (Renesto and Fraser, 2003; Dalla Vecchia, 2014; Dalla Vecchia and Cau, 2015).

228. Cervical vertebrae, hypapophyses: absent, ventral surface of centrum unexpanded posteroventrally (0); present, posteroventral surface of centrum with massive posteroventrally projecting crest (1)

From Pritchard et al. (2021:k171)

229. Cervical vertebrae, centrum, ventral surface: rounded (0); bearing a low longitudinal median ridge or keel (1)

From Schoch and Sues (2018a:k181); Ford and Benson (2020:k207); Griffiths et al. (2021:k231); Pritchard et al. (2021:k169); Simões et al. (2022:k233)

Modified (reduced states) from Ezcurra et al. (2020:k327)

230. Cervical vertebrae, number of costal facets: one (0); two closely appressed facets with little finished bone separation (1) two facets distinctly offset from each other (2); inapplicable: cervical ribs absent or fused to costal facets (-)

Modified from Ezcurra et al. (2020:k332); Spiekman et al. (2021:k188)

Modified (added state) from Pritchard et al. (2021:k172, 174)

See Ezcurra (2016:fig. 30)

We follow Pritchard et al. (2021) in considering only the number of costal facets, contrary to Ezcurra et al. (2020) or Spiekman et al. (2021) whose formulation considers also the number of processes bearing those surfaces. Note that this character is very similar to previously proposed characters describing the number of cervical rib heads (e.g. Ford and Benson, 2020:k211), which have thus not been included in our study to avoid oversampling.

We included both characters 172 and 174 of Pritchard et al. (2021) in a single character as the presence of closely appressed costal facets could be considered as intermediate between the presence of two distinctly offset facets and a single one, implying a fusion of both facets. However, as the presence of only one facet could also result from the lack of contact between one of the rib heads and the vertebra, we refrain from ordering this character.

231. Cervical vertebrae, position of diapophysis or dorsal margin of synapophysis in anterior postaxial cervicals: at or near dorsoventral level of pedicels (0); near the dorsoventral mid-point of the centrum (1); inapplicable: cervical ribs absent (-)

From Ezcurra et al. (2020:k333); Pritchard et al. (2021:k173)

232. Cervical vertebrae, neural arch, transverse breadth (excluding transverse processes) at anteroposterior midpoint relative to centrum: subequal (0); substantially broader (1)

From Pritchard et al. (2021:k175)

233. Cervical vertebrae, neural arch excavation lateral to base of neural spine: absent (0); present (1)

From Ford and Benson (2020:k208)

Modified (reduced states) from Ezcurra et al. (2020:k337)

See Ezcurra (2016:figs. 33, 34)

We merged states 1 and 2 of Ezcurra et al. (2020) describing a shallow and deep excavation respectively as it proved hard to distinguish between both states in our dataset.

234. Cervical vertebrae, prezygapophysis, orientation of articular surface: facing medially (0); subvertical (1)

NEW CHARACTER

We introduce this character to describe the subvertical angulation of the cervical zygapophyses of drepanosauromorphs and early pterosaurs (Renesto and Fraser, 2003; Dalla Vecchia, 2014; Dalla Vecchia and Cau, 2015).

235. Cervical vertebrae, postzygapophysis, epipophyses: absent, dorsal surface of postzygapophyses smooth and rounded (0); present as vertical expansion of bone above postzygapophyseal facet (1); present and extending markedly posteriorly beyond postzygapophysis (2). ORDERED

Modified (added states, ordered) from Spiekman (2021:k190, 191)

Modified from Ezcurra et al. (2020:k336); Pritchard et al. (2021:k182, 183)

See Ezcurra (2016:figs. 30, 33); Spiekman et al. (2021:fig. 24)

We concur with Spiekman et al. (2021) that a binary delimitation of the posterior extent of the epipophyses is more reliably scored for compared to Pritchard et al.'s (2021) multistate delimitation. In addition, we consider that the presence of shallow vertical epipophyses is intermediate between the absence of epipophyses and that of posteriorly extended ones and consequently order this character.

Lastly, we concur with Ford and Benson (2020) that the 'mammillary processes' of *Mesosaurus*, that "project posterodorsally directly above the postzygapophyses" (Modesto, 2010:1380) are better described as epipophyses than true mammillary processes. Thus, *Mesosaurus* is scored as 0 for character 220 above and as 1 for the present character.

236. Cervical vertebrae, neural spine, outline in lateral view: sub-triangular, with anterior margin strongly posterodorsally oriented (0); sub-rectangular, with anterior margin roughly vertical (1)

From Ezcurra et al. (2020:k339); Ford and Benson (2020:k209)

This character describes the overall shape of the neural spines. We consider the shape and height of the neural spines independently (see character 240 below) as some taxa with rectangular neural spines can have either low spines (e.g. *Coelurosauravus*, MNHN.F.MAP317a, b) or high ones (e.g. *Acerosodontosaurus* MNHN.F.MAP359a, b). In addition, this character may be linked to previously proposed characters describing the shape of the base of cervical neural spines (e.g. Pritchard et al., 2021:k176), which are thus not included in our dataset to avoid oversampling.

As some taxa show marked differences between their cervical and dorsal neural spines (e.g. drepanosauromorphs, Renesto et al., 2010), we consider both regions in distinct characters (see characters 263 and 264 below).

237. Cervical vertebrae, neural spine height: tall, higher than length at base (0); short, lower than long (1)

From Ezcurra et al. (2020:k342)

See comments in character 239 above.

238. Cervical vertebrae, anterior post-axial cervicals, neural spine, inclination of anterior margin: dorsal or posterodorsal (0); anterodorsal (1)

From Pritchard et al. (2021:k179)

Pritchard et al. (2021) employ two characters to describe the presence of an anterodorsal overhang of the neural spines and their overall inclination independently. Spiekman et al. (2021) recently opted to fuse both characters, however, we refrain from following this formuation as both morphologies do not seem homologous. For example, the seventh cervical of *Prolacerta* presents a marked overhang (captioned as character 343 on Ezcurra, 2016:fig. 33D) but lacks any inclination. In other words, the presence of an anterodorsal process forming an overhang does not imply that the neural spine is inclined anteriorly. Thus, we employ two independent characters to describe the morphology of the neural spines of the postaxial cervicals (see character 242 below) in agreement with Pritchard et al. (2021). We further suggest that this character is independent from the overall shape of the neural spines (see character 239 above) as an anterior inclination is present in taxa with both rectangular (e.g. *Azendohsaurus*, Nesbitt et al., 2015) and triangular (e.g. drepanosauromorphs, Renesto et al., 2010) neural spines.

239. Cervical vertebrae, anterior post-axial cervicals, neural spine, anterodrosal process forming anterior overhang: absent (0); present (1)

From Ezcurra et al. (2020:k343); Pritchard et al. (2021:k178)

See Ezcurra (2016:figs. 30, 33)

See comments in character 241 above.

240. Cervical vertebrae, ribs: present (0); absent (1)

From Griffiths et al. (2021:k260); Pritchard et al. (2021:k186); Simões et al. (2022:k263)

Contrary to Pritchard et al. (2021), we consider cervical ribs as present even when fused to the associated vertebrae (scored as state 1 in the following character).

241. Cervical vertebrae, ribs, fusion to costal facets: absent (0); present (1); inapplicable: cervical ribs are absent (-)

NEW CHARACTER

This character was created to take into account the fused cervical ribs of *Avicranium*, *Teraterpeton* and *Trilophosaurus* (Pritchard and Sues, 2019).

242. Cervical vertebrae, rib shape: tapering rapidly, roughly triangular in lateral view (0); tapering gradually, elongate and spint-like in lateral view (1); inapplicable: cervical ribs are absent (-)

From Ford and Benson (2020:k205); Pritchard et al. (2021:k187)

Modified (reduced states) from Ezcurra et al. (2020:k349); Spiekman et al. (2021:k199)

See Spiekman et al. (2021:fig. 27)

243. Cervical ribs, accessory process on anterolateral surface: absent (0); present (1); inapplicable: cervical ribs are absent (-)

From Schoch and Sues (2018a:k183); Ezcurra et al. (2020:k350); Ford and Benson (2020:k210); Griffiths et al. (2021:k261); Pritchard et al. (2021:k188); Simões et al. (2022:k264)

Modified (reduced states) from Spiekman et al. (2021:k200)

See Ezcurra (2016:fig. 30); Spiekman et al. (2021:fig. 27); figured in Simões et al. (2022:k264)

244. Dorsal vertebrae, posterior surface of centrum: concave (0); planar (1); convex (2)

Modified from Ezcurra et al. (2020:k681); Griffiths et al. (2021:k228); Pritchard and Sues (2021:k160); Spiekman et al. (2021:k181); Simões et al. (2022:k229)

See character 226 above for a discussion on a similar character.

245. Dorsal vertebrae, intercentra: present (0); absent (1)

From Schoch and Sues (2018a:k185); Ezcurra et al. (2020:k366); Griffiths et al. (2021:k239); Pritchard et al. (2021:k208); Simões et al. (2022:k239)

246. Dorsal vertebrae, hyposphene-hypantrum accessory articulation: absent (0); present (1)

From Ezcurra et al. (2020:k359); Spiekman et al. (2021:k208); Simões et al. (2022:k250)

Modified from Pritchard et al. (2021:k331)

See Ezcurra (2016:figs. 31 , 32)

The present character describes the presence of an hyposphene-hypantrum articulation, as defined by Stefanic and Nesbitt (2018:22): “a bony projection, the hyposphene, on the posterior portion of the vertebra that fits into a complementary space, the hypantrum, on the anterior portion of the subsequent vertebra within a vertebral series”

247. Dorsal vertebrae, zygosphene-zygantrum accessory articulation: absent (0); present (1)

From Ezcurra et al. (2020:k360); Griffiths et al. (2021:k248); Pritchard et al. (2021:k202); Simões et al. (2022:k249)

See Ezcurra (2016:fig. 31)

The present character describes the presence of a zygopshene-zygantrum articulation, as defined by Hoffstetter and Gasc (1966:207): “The surfaces form a tenon (zygosphene) set into a mortise (zygantrum) excavated in the posterior face of the neural arch of the preceding vertebra.”

248. Dorsal vertebrae, ventral surface of centra: rounded (0); bearing a low longitudinal median ridge or keel (1); bearing a longitudinal median groove bordered by two longitudinal lateral ridges or keels (2)

Modified (reduced states) from Ezcurra et al. (2020:k353); Ford and Benson (2020:k214)

Modified (added state) from Griffiths et al. (2021:k232); Simões et al. (2022:k234)

The ventral surface of the centrum shows various morphologies in early amniotes. Most early eureptiles and non-saurian diapsids only show a low ventromedian ridge (e.g. *Youngina*, BP/1/3859). We thus consider this low ridge as a distinct state from a rounded centrum (e.g. *Coelurosauravus*, MNHN.F.MAP317a, b) in agreement with Ford and Benson (2020) but contrary to other studies who consider only the presence of conspicuous keels (e.g. Ezcurra et al., 2020; Griffiths et al., 2021).

Our character states thus mostly follow Ford and Benson (2020). However, this study further considers the presence of a median keel, or of a median groove framed by paramedian ridges. We consider the number or ridges or keels and their extent (low for ridges, deep for keels) independently. The present character thus describes the number of ridges or keels. We did not include a character distinguishing between ridges and keels as both terminologies have been used interchangingly in the literature, making it difficult to score accurately without direct observation of specimens.

249. Dorsal vertebrae, anterior dorsals, pedicel, dorsoventral height: shorter or subequal to respective centra (0); substantially taller than respective centra (1)

From Pritchard et al. (2021:k194)

All rhyncocephalians included in our dataset exhibit relatively tall pedicels relative to associated centra, at least in the posterior dorsal vertebrae (Evans, 1981; Fraser and Walkden, 1984; Fraser, 1988). They are consequently scored as state 1 herein, contrary to Pritchard et al. (2021).

250. Dorsal vertebrae, neural arches: swollen with heavy postzygapophyseal buttress, neural arch more than twice as broad as associated centrum (0); swollen with conspicuous postzygapophyseal buttress, neural arch up to twice as wide as associated centrum (1); narrow, neural arch without postzygapophyseal buttress, no extension of neural arch beyond centrum lateral margin (2). ORDERED

Modified from Ford and Benson (2020:k223)

Following Sumida and Modesto (2001), the neural arch is considered swollen if its dorsal surface is conspicuously convex in anterior or posterior view, typically through development of postzygapophyseal buttresses. Swollen neural arches (state 1) are present in several Permo-

Carboniferous taxa, such as caprorhinids, parareptiles or araeoscelidians, and to a stronger degree (state 0) in stem-amniotes and pareiasaurs. Most synapsids, ‘protorothyridids’ and neodiapsids exhibit narrow neural arches lacking the swollen morphology described above (state 2). As the present character states form a morphological series, we ave ordered this character.

Contrary to Ford and Benson (2020), we elect to consider the swelling of the neural arch independently from the presence of excavations at the base of the neural spines. Those excavations (scored in character 256 below) are indeed present in taxa with both swollen (e.g. *Petrolacosaurus*, Reisz, 1981) and narrow (e.g. *Protorosaurus*, Gottmann-Quesada and Sander, 2009) neural arches. In addition, we suggest that the swelling of the neural arch is also linked to the spacing of the postzygapophyses, whereby taxa with swollen taxa have more widely spaced postzygapophyses than taxa with narrow neural arches. Consequently, we did not include such characters in our dataset (e.g. Ford and Benson, 2020:k224).

251. Dorsal vertebrae, neural arch excavation lateral to base of neural spine: absent (0); present (1)

From Pritchard et al. (2021:k195); Simões et al. (2022:k251)

Modified (reduced states) from Ford and Benson (2020:k223); Ezcurra et al. (2020:k361); Spiekman et al. (2021:k209)

See Ezcurra (2016:fig. 34); Simões et al. (2022:k251)

See character 255 above, and character 236 above for comments on a similar character.

252. Dorsal vertebrae, transverse processes: short, projecting equal with or only slightly beyond the lateral surface of the neural arch (0); moderately long, projecting beyond the lateral surface of the neural arch (1); extremely long, twice the width of the neural arch (2). ORDERED

Modified (reworded states, ordered) from Ezcurra et al. (2020:k358)

Modified (added states, ordered) from Schoch and Sues (2018a:k186); Ford and Benson (2020:k215); Griffiths et al. (2021:k355); Spiekman et al. (2021:k207)

See Ezcurra (2016:fig. 32)

Previous studies have described the elongation of the transverse process through a binary character describing short or moderately long processes (e.g. Ford and Benson, 2020; Spiekman et al., 2021). Ezcurra et al. (2020) employ an additional character state describing extremely long processes, which we have reworded to compare to the neural arch width. This state is only

present in kuehneosaurids in our dataset (Colbert, 1970; Evans, 2009). As the present character states from a morphological series, we order this character.

253. Anterior dorsal vertebrae, pectoral region, number of costal facets: one (= holocephaly) (0); two (= dichocephaly) (1); three (=tricephaly) (2). ORDERED

From Pritchard et al. (2021:k191); Spiekman et al. (2021:k213)

Modified (added states, ordered) from Ezcurra et al. (2020:k314); Simões et al. (2022:k252)

See Ezcurra (2016:fig. 31); figured in Simões et al. (2022:k252)

See character 233 above for comments on a similar character. Note that this character is very similar to previously proposed characters describing the number of dorsal rib heads (e.g. Ezcurra et al., 2020:k368; Ford and Benson, 2020:k225), which have not been included in our study to avoid oversampling.

254. Posterior dorsal vertebrae, costal facets: one, ovoid (0); one, inverse L-shaped (1) two facets distinctly offset from eachother (2). ORDERED

From Pritchard et al. (2021:k192)

See characters 233 and 258 above for comments on similar characters.

Our scoring mostly conforms to that of Pritchard et al. (2021), except regarding ‘younginiforms’, which were scored as state 0 by the latter study. Our observations indicate that the diapohyseal and parapophyseal portion of the rib facet of *Acerosodontosaurus*, *Hovasaurus* and *Thadeosaurus* remain clearly distinguishable in the posterior dorsals (MNHN.F.MAP359a, b, MNHN.F.MAP360a, b; Currie, 1981a, b), and similar morphologies have been reported in *Kenyasaurus* and *Youngina* (Currie, 1981b). This is most similar to the inverted L-shaped facet of *Claudiosaurus* (Carroll, 1981), consequently, these taxa are scored as state 1 herein.

255. Dorsal vertebrae, anteroposterior position of diapophysis: on anterior portion of neural arch or centrum (0); near anteroposterior midpoint of neural arch or centrum (1)

From Ezcurra et al. (2020:k660); Pritchard et al. (2021:k193)

256. Anterior dorsal vertebrae, position of parapophysis or ventral portion of synapophysis: partially on lateral margin of centrum or intercentrum (0); entirely on neural arch (1)

From Pritchard et al. (2021:k189)

Our scoring mostly conforms to that of Pritchard et al. (2021). However, our re-examination of drepanosauromorphs suggest that the costal facets are located entirely on the neural arch of the anterior vertebrae in *Megalancosaurus* (MPUM 6008) and *Vallesaurus* (MCSNB 4751), contrary to the scoring of Pritchard et al. (2021). In addition, this character cannot be confidently assessed in *Drepanosaurus* as the anterior vertebrae are partially obscured (MCSNB 5728). This taxon is thus scored as uncertain.

257. Posterior dorsal vertebrae, position of parapophysis or ventral portion of synapophysis: partially on lateral margin of centrum or intercentrum (0); entirely on neural arch (1)

From Ezcurra et al. (2020:k659); Pritchard and Sues (2019:k190); Spiekman et al. (2021:k212)

Our scoring mostly conforms to that of Pritchard et al. (2021). However, our re-examination of drepanosauromorphs suggest that the costal facets are located entirely on the neural arch of the posterior vertebrae in *Megalancosaurus* (MCSNB 8437; MPUM 6008) and *Vallesaurus* (MCSNB 4751), contrary to the scoring of Pritchard et al. (2021).

258. Dorsal vertebrae, outline of anterior and middle dorsal neural spines in lateral view: sub-triangular, with anterior margin strongly posterodorsally oriented (0); sub-rectangular, with anterior margin rougly vertical (1)

From Ezcurra et al. (2020:k362); Ford and Benson (2020:k216)

This character does not describe spine height, which is described by character 264 below (see character 239 above for the discussion of a similar character).

259. Dorsal vertebrae, neural spine height: tall, dorsoventrally higher than length at base (0); short, lower than long (1)

From Pritchard et al. (2021:k201); Spiekman et al. (2021:k211)

Modified (reduced states) from Ford and Benson (2020:k219)

See comments in character 263 above. We removed state 2 of Ford and Benson (2020, “very tall”) as it is a synapomophy of sphenacodont synapsids and therefore not relevant to our dataset. In case of taxa showing alternations of neural spine eight along the dorsal column (e.g. *Captorhinus*, *Limnoscelis*, Sumida, 1990), this character should be applied to the higer neural spine type.

260. Dorsal vertebrae, neural spine, distal anteroposterior expansion: similar or shorter than anteroposterior length at base (0); anteroposteriorly broader than base (1)

Modified (reworded) from Ezcurra et al. (2020:k363); Spiekman et al. (2021:k210)

Modified from Pritchard et al. (2021:k196)

Pritchard et al. (2021) employ a multistate ordered character to describe the distal expansion of dorsal neural spines in drepanosauromorphs and tanystropheids. However, this expansion is present throughout most of the vertebral column in tanystropheids (Pritchard et al., 2015) while it is restricted to the fist three to five dorsals in drepanosauromorphs (Renesto et al., 2010). Thus, we suggest that the distal expansions of the neural spines in tanystropheids and drepanosauromorphs are not homologous, and consequently separated both morphologies in separate characters (see character 266 below).

The present character thus describes the distal expansion typical of tanystropheids (Pritchard et al., 2015), which we also report in *Claudiosaurus* and *Kuehneosaurus* (Carroll, 1981; Evans, 2009). As stated above, drepanosauromorphs are scored with state 0 for this character.

261. Dorsal vertebrae 1 to 5, neural spine, distal anteroposterior expansion: similar to following vertebrae (0) anteroposteriorly expanded relative to following vertebrae (1); third dorsal spine anteroposteriorly expanded and hatchet-shaped, contacting neighboring neural spines (2)

Modified from Pritchard et al. (2021:k196)

See comments in character 265 above.

262. Dorsal vertebrae, neural spine, distal transverse expansion (excluding mammillary processes): absent, similar or thinner than width at base (0); present, gradual transverse expansion over distal half of neural spine (1); present, rapid transverse expansion restricted to distal end of neural spine (2)

From Spiekman et al. (2021:k203)

Modified (added state) from Griffiths et al. (2021:k258); Pritchard et al. (2021:k197); Simões et al. (2022:k259)

Modified from Ezcurra et al. (2020:k320, 321)

See Ezcurra (2016:figs. 31, 32, 34) ; Spiekman et al. (2021:fig. 28)

See comments in Spiekman et al. (2021). As it is unclear whether the present character states form a morphological series, we refrain from ordering this character following Spiekman et al. (2021).

263. Dorsal vertebrae, neural spine, dorsal tip, texturing: smooth (0); transverse striations forming crenulated surface (1)

From Pritchard et al. (2021:k200)

264. Dorsal vertebrae, ribs, orientation: ribs strongly arched proximally and curved thougout length, trunk barrell-shaped (0); ribs slightly curved, framing trunk (1); ribs splay laterally, forming patagial skeleton (2)

Modified (added state) from Ezcurra et al. (2020:k367); Ford and Benson (2020:k226); Pritchard et al. (2021:k203)

The barrel-shaped trunk of caseid synapsids has often been considered in phylogenetic analyses (Ford and Benson, 2020 and references therein). Among diapsids, a similar morphology has been reported in drepanosauromorphs (Renesto et al., 2010) and is also present in *Tereaterpeton* (Sues, 2003).

In addition, Pritchard et al. (2021) employ a separate character to describe the very long dorsal ribs of kuehneosaurids. As both morphologies pertain to the morphology of the rib shafts, we elect to consider them in a single character. However, as it is unclear if these states from a morphological series, we refrain from ordering this character.

265. Dorsal vertebrae, ribs, fusion to costal facets: absent (0); present in posterior dorsal vertebrae (1); present in mid- and posterior dorsals (2). ORDERED

Modified (added states, ordered) from Ezcurra et al. (2020:k661); Griffiths et al. (2021:k266); Pritchard et al. (2021:k205, 206); Simões et al. (2022:k265)

Pritchard et al. (2021) employ two character to describe the fusion of the ribs to the vertebrae in the posterior and mid-posteror dorsal column respectively. However, we consider that fusion in the mid-posterior dorsals always occurs in conjuction with fusion in the posterior dorsals (e.g. *Megalancosaurus*, MPUM 6008). Thus, we consider that both morphologies form a continuum and consequently fuse both characters from Pritchard et al. (2021) in a single ordered character.

266. Sacral vertebrae, count: two or fewer (0); three (1); four or more (2). ORDERED

From Ezcurra et al. (2020:k370)

Modified (added state, ordered) from Schoch and Sues (2018a:k187); Ford and Benson (2020:k230)

Modified (redced states, ordered) from Griffiths et al. (2021:k235); Simões et al. (2022:k235)

267. Sacral vertebrae, first sacral rib: distinctly enlarged compared to second sacral rib (0); subequal or slightly larger than second sacral rib (1); inapplicable: only one sacral vertebra present (-)

From Ezcurra et al. (2020:372); Ford and Benson (2020:k228); Pritchard et al. (2021:k209); Spiekman et al. (2021:k215)

268. Sacral vertebrae, second sacral rib: not bifurcate, rib as a single unit (0); bifurcates distally into anterior and posterior processes (1); inapplicable: only one sacral vertebra present (-)

From Ezcurra et al. (2020:k373); Ford and Benson (2020:k229); Pritchard et al. (2021:k210); Spiekman et al. (2021:k216)

See Ezcurra (2016:fig. 35)

269. Sacral vertebrae, second sacral rib, posterior process: terminally blunted (0); sharp distally (1); inapplicable: second sacral rib not bifurcate or only one sacral vertebra present (-)

From Ezcurra et al. (2021:k374) ; Pritchard et al. (2021:k211); Spiekman et al. (2021:k217)

See Ezcurra (2016:fig. 35)

270. Anterior caudal vertebrae, shape of transverse processes in dorsal view: L-shaped, strongly curved (0); straight or smoothly curved (1)

From Schoch and Sues (2018a:k189)

We consider that the slightly anterolaterally or posterolaterally curved, but still mostly straight caudal transverse processes of some neodiapsids represent a distinct morphology compared to the L-shaped processes of other amniotes. Consequently, we consider both morphologies in distinct characters (see character 276 below).

271. Anterior caudal vertebrae, shape of transverse processes in dorsal view: curved posterolaterally (0); straight, extending strictly laterally (1); curved anterolaterally (2): inapplicable: caudal ribs L-shaped. ORDERED

Modified (ordered) from Pritchard et al. (2021:k213)

See comments character 275 above.

272. Anterior caudal vertebrae, transverse processes, orientation of base: angled posterolaterally (0); perpendicular to long axis of vertebra (1)

From Pritchard et al. (2021:k214); Spiekman et al. (2021:k221)

273. Posterior caudal vertebrae, prezygapophyses: not elongated (0); elongated, more than a quarter of associated centrum (1)

From Ezcurra et al. (2020:k381)

See Ezcurra (2016:fig. 35)

274. Caudal vertebrae, neural spine, distal anteroposterior expansion: similar or shorter than anteroposterior length at base (0); slightly expanded, anteroposteriorly broader than base (1); strongly expanded, neural spine T-shaped, with slender anterior and posterior projections (1). ORDERED

Modified (added state, ordered) from Pritchard et al. (2021:k216)

Pritchard et al. (2021) employ this character to describe the T-shaped caudal neural spines of the drepanosauromorphs *Dolabrosaurus*, *Drepanosaurus* and *Megalancosaurus*, which are absent in *Hypuronector* and *Vallesaurus*n the other drepanosauromorphs for which caudal material is known. However, these taxa actually exhibit a gradual anteroposterior expansion of the caudal neural spines (MCSNB 4751; Colbert and Olsen, 2001), which we consider in an additional, intermediate state. We consider the present character states to form a morphological series and consequently order this character.

275. Chevrons, proximal articular morphology: chevrons remain separated from centra (0); chevrons fused to centra (1)

From Griffiths et al. (2021:k244); Pritchard et al. (2021:k221)

This character was defined by Pritchard et al. (2016) to describe the peculiar morphology of the chevrons in drepanosauromorphs.

276. Chevrons, haemal spine, anterior process: absent, haemal spine plate-like in lateral view (0); present, haemal spine inverted T-shaped in lateral view (1)

Modified (reduced states) from Pritchard et al. (2021:k129)

Pritchard et al. (2021) considered the presence of an anterior projection of the haemal spine as a character state describing the distal anteroposterior expansion of the haemal spines. This type of character has typically been used to describe the presence of a distal expansion of the haemal spine (see character 284 below). However, among taxa which have an anterior process of the haemal spine, the posterior process is slender and tapering in weigeltisaurids and pterosaurs (Wellnhofer, 1978; Evans, 1982), while it is much broader in *Trilophosaurus* where the chevron is markedly T-shaped (Spielmann et al., 2008). Consequently, we elect to score the presence of an anterior process of the haemal spine in a separate character.

277. Chevrons, haemal spine, distal width in lateral view: tapering along proximodistal length (0); equivalent to proximal width (1); gradually wider than proximal width (2). ORDERED

Modified (ordered) from Ezcurra et al., (2020:k382); Ford and Benson (2020:k232)

Modified from Pritchard et al. (2021:k219); Spiekman et al. (2021:k223)

As discussed in character 283 above, this character only considers the width formed by the posterior process of the haemal spine and not the contribution of the anterior process if present.

278. Chevrons, haemal spine curvature in lateral view: spine roughly straight (0); spine concave anteriorly (1)

From Pritchard et al. (2021:k222)

279. Terminal caudal vertebra(e): similar in morphology to other posterior caudal vertebrae (0); modified into claw-like element (1)

From Pritchard et al. (2021:k226)

280. Gastralia: present, forming extensive gastral basket with closely packed elements (0); present, well separated (1); absent (2). ORDERED

Modified (ordered) from Ezcurra et al. (2020:k383)

Modified (added states, ordered) from Schoch and Sues (2018a:k246); Griffiths et al. (2018:k342); Pritchard et al. (2021:k327); Simões et al. (2022:k343)

See Ezcurra (2016:fig. 15)

281. Patagial spars: absent (0); present (1)

From Pritchard et al. (2021:k204)

Modified from Griffiths et al. (2021:k274)

282. Osteoderms: absent (0); present, one row (1); present, two rows (2). ORDERED

Modified (reduced states) from Ezcurra et al. (2020:k588)

Modified (added states) from Ford and Benson (2020:k227); Griffiths et al. (2021:k343); Pritchard et al. (2021:k328); Simões et al. (2022:k344)

Modified from Schoch and Sues (2018a:k243)

See Ezcurra (2016:fig. 47)

283. Cleithrum: present (0); absent (1)

From Schoch and Sues (2018:k191); Ezcurra et al. (2020:k404); Griffiths et al. (2021:k295); Pritchard et al. (2021:k228); Spiekman et al. (2021:k233); Simões et al. (2022:k297)

Simões et al. (2022:k297) recently figured a cleithrum apposed to the scaplar blade of *Protorosaurus*, but this bone was Gottmann-Quesada and Sander (2009:fig. 20B). As the pectoral grirdle of this specimen is partially disarticulated, we conseider the identification of this element as equivocal.

284. Clavicle, anteroposterior breadth of ventromedian portion compared to mid-height of distal portion: broader (0); subequal (1); inapplicable: clavicle absent as a distinct ossification (-)

From Ezcurra et al. (2020:k686); Pritchard et al. (2021:k229)

Modified from Schoch and Sues (2018a:k192); Ford and Benson (2020:k234)

285. Interclavicle: present (0); absent (1)

From Ezcurra et al. (2020:k405); Spiekman et al., (2021:k234)

See Ezcurra (2016:fig. 15)

286. Interclavicle, anterior process: present (0); absent (1); inapplicable: interclavicle absent (-)

From Ezcurra et al. (2020:k406); Griffiths et al. (2021:k293); Spiekman et al. (2021:k235); Simões et al. (2022:k294)

Modified from Ford and Benson (2020:k238); Pritchard et al. (2021:k230)

See Ezcurra (2016:fig. 38)

287. Interclavicle, lateral processes: short, head roughly as long as wide (0); long, head twice wider than long (1); inapplicable: interclavicle absent (-)

From Ezcurra et al. (2020:k408)

Modified from Schoch and Sues (2018a:k194); Ford and Benson (2020:k237)

See Ezcurra (2016:fig. 38)

288. Interclavicle, anterior margin: smoothly convex (0); notch between clavicles (1); inapplicable: interclavicle absent (-)

From Ezcurra et al. (2020:k407); Ford and Benson (2020:k235); Griffiths et al. (2021:k375); Pritchard et al. (2021:k231); Spiekman et al. (2021:k236)

See Ezcurra (2016:fig. 38)

289. Scapulocoracoid, both bones fuse with each other in mature individuals: present (0); absent (1)

From Ezcurra et al. (2020:k384); Spiekman et al. (2021:k226)

See Ezcurra (2016:fig. 36)

290. Scapulocoracoid, notch on anterior margin at level of suture between both bones: absent (0); present (1)

From Ezcurra et al. (2021:k385)

Modified (reduced states) from Spiekman et al. (2021:k227)

See Ezcurra (2016:fig. 36); Spiekman et al. (2021:fig. 31)

Spiekman et al. (2021) consider the presence of a fenestra anteriorly between the scapula and coracoid as a character state of this character. However, we find it unclear if the presence of a notch and fenestra are homologous and consequently retain Ezcurra et al.'s (2021) formulation. As this fenestra is typical for tanystropheids, whose interrelationships are out of the scope of this study, we provisionally do not consider it in our analysis pending further examination of this structure.

291. Scapulocoracoid, glenoid fossa, orientation: mainly lateral, facing more laterally than posteriorly and without posteriorly prominent supraglenoid lip in lateral view (0); slightly posterolateral facing more posteriorly than laterally, with prominent supraglenoid lip in lateral view (1); posteroventral (2). ORDERED

From Ezcurra et al. (2020:k386)

See Ezcurra (2016:figs. 36, 37)

292. Scapula, scapular blade, height compared to anteroposterior length at base: height less than 1.5 times length at base (0); between 1.5 and 2.5 times length at base (1); between 2.5 and 4 times length at base (2); more than 4 times length at base (3). ORDERED

Modified (added state) from Pritchard et al. (2021:k233)

Pritchard et al. (2021) employ a similar ordered character to describe the height of the scapular blade in archosauromorphs. However, we include an additional state (state 0) to differenciate between taxa with the moderaterly tall blade of most archosauromorphs (state 1) and the extremely short blades of tanystropheids (*Langobardisaurus*, MCSNB 2883; Rieppel, 1989; Nosotti, 2007), 'younginiforms' (Carroll, 1981; Currie, 1981a) and araeoscelidians (Reisz, 1981) (state 0).

293. Scapula, supraglenoid buttress: present (0); absent (1)

From Schoch and Sues (2018a:k197); Griffiths et al. (2021:k276); Simões et al. (2022:k276)

294. Scapula, supraglenoid foramen: present (0); absent (1)

From Ezcurra et al. (2020:k392); Ford and Benson (2020:k239); Griffiths et al. (2021:k275); Spiekman et al. (2021:k231); Simões et al. (2022:k275)

Figured in Simões et al. (2022:k275)

295. Scapula, orientation: posterodorsally inclined, deep posterior concavity present (0); directed dorsally, posterior margin vertical or slightly concave (1); anterodorsally curved (2). ORDERED

Modified (ordered) from Pritchard et al. (2019:k234)

Modified from Griffiths et al. (2021:k280)

We consider a subvertical scapular blade as an intermediate state between posterodorsally and anterodorsally slanted ones and consequently order this character.

296. Scapula, scapular blade shape: mostly dorsally oriented with rectangular outline (0); convex along entire length, slanted posteriorly with continuously curved anterior and dorsal margins (1)

From Ford and Benson (2020:k241); Spiekman et al. (2021:k228)

Modified from et al. Ezcurra (2021:k389)

See Ezcurra (2016:fig. 36); Spiekman et al. (2021:fig. 31)

297. Scapula, scapular blade, anterior margin, maked concavity: absent (0); present (1)

From Ezcurra et al. (2020:k390); Pritchard et al. (2021:k235); Spiekman et al. (2021:k229); Simões et al. (2022:k281)

See Ezcurra (2016:fig. 36)

Contrary to Pritchard et al. (2021), we score drepanosauromorphs with the exception of *Hypuronector* (Colbert and Olsen, 2001) as possessing a markedly concave scapular blade, as shown in *Drepanosaurus* (MCSNB 5728), *Megalancosaurus* (MCSNB 6008; MFSN 1769), and *Vallesaurus* (MCSNB 4751).

298. Scapula, acromion process: in about same plane as ventral edge of scapula (0); distinctly raised above ventral edge of scapula (1)

From Ezcurra et al. (2020:k395)

See Ezcurra (2016:figs. 36, 37)

299. Scapula, acromion process: gently raised from anterior margin of scapular blade (0); sharply raised from anterior margin of scapular blade (1)

From Ezcurra (2021:k396)

300. Coracoids, number: one (0); two (1)

From Schoch and Sues (2018a:k198); Ford and Benson (2020:k244); Griffiths et al. (2021:k285); Pritchard et al. (2021:k239); Simões et al. (2022:k286)

301. Coracoid, posterior border in lateral view: unexpanded posteriorly (0), moderately expanded posteriorly (1); strongly expanded posteriorly, resulting in L-shaped scapulocoracoid in lateral view (2). ORDERED

From Ezcurra et al. (2020:k398); Spiekman et al. (2021:k232)

Modified (added state, ordered) fromPritchard et al. (2021:k240)

See Ezcurra (2016:fig. 37)

302. Coracoid, biceps process on lateral surface: absent or small (0); large (1)

From Ezcurra et al. (2020:k401)

See Ezcurra (2016 :figs. 36, 37)

303. Coracoid, postglenoid process separated from glenoid fossa by notch: absent (0); present (1)

From Ezcurra et al. (2020:k402)

See Ezcurra (2016 :fig. 36)

304. Coracoid, process for triceps muscle: small or absent (0); large, extending posterodorsally from coracoid plate (1)

From Ford and Benson (2020:k245)

305. Sternum (presternum), ossification of sternal plates: absent (0); present (1)

From Schoch and Sues (2018a:k195); Ezcurra et al. (2020:k413); Ford and Benson (2020:k246); Pritchard et al. (2021:k241); Simões et al. (2022:k272)

306. Humerus, diaphysis: absent, distal and proximal heads merge and lack discrete shaft (0); distinct shaft present (1)

From Ford and Benson (2020:k249)

307. Humerus, torsion between proximal and distal ends: approximately 45° or more (0); 35° or less (1)

From Schoch and Sues (2018a:k201); Ezcurra et al. (2020:k415); Griffiths et al. (2021:k357); Spiekman et al. (2021:k241)

See Ezcurra (2016:fig. 39)

308. Humerus, shape in lateral view: roughly straight (0); sigmoid (1)

From Ezcurra et al. (2020:k774)

309. Humerus, proximal end in dorsal (anterior) view: approximately symmetric (0); medially expanded and asymmetric (1)

From Ezcurra (2020:k419)

See Ezcurra (2016:fig. 39)

310. Humerus, conical process on proximal surface immediately adjacent to base of deltopectoral crest: absent (0); present (1)

From Ezcurra et al. (2020:k420); Spiekman et al. (2021:k243)

See Ezcurra (2016:fig. 39)

311. Humerus, internal tuberosity: continuous with humeral shaft or absent (0); prominent projection offset from humeral shaft (1)

From Ezcurra et al. (2020:k421); Pritchard et al. (2021:k242)

See Ezcurra (2016:fig. 39)

312. Humerus, deltopectoral crest, size: scarcely or moderately developed (0); hypertrophied with proximal apex close to the level of the humeral head (1)

From Ezcurra et al. (2020:k775)

313. Humerus, capitellum and trochlea: strongly developed as distinct ball-shaped structures (0); poorly developed but distinct from the ectepicondyle and entepicondyle (1); indistinct from the ectepicondyle and entepicondyle (2). ORDERED

Modified (ordered) from Ford and Benson (2020:k247)

Modified (added state, ordered) from Schoch and Sues (2018a:k203); Ezcurra et al. (2020:k428); Pritchard et al. (2021:k254); Simões et al. (2022:k311)

See Ezcurra (2016:fig. 39); figured in Simões et al. (2022:k311)

We consider that the present character states form a morphological series and consequently order this character.

314. Humerus, ectepicondyle, radial nerve groove: present (0); absent (1)

From Pritchard et al. (2021:k245)

Modified (reduced states) from Ezcurra et al. (2021:k427)

See Ezcurra (2016:fig. 39)

315. Humerus, ectepicondylar foramen: absent, supinator process very low or absent (0); short supinator process fails to enclose ectepicondylar groove (1); present, enclosed by well developed supinator process (2). ORDERED

Modified (ordered) from Schoch and Sues (2018a:k205); Ezcurra et al. (2020:k427); Spiekman et al. (2021:k427)

Modified from Ford and Benson (2020:k253); Griffiths et al. (2021:k307); Pritchard et al. (2021:k246); Simões et al. (2022:k308)

See Ezcurra (2016:fig. 39); figured in Simões et al. (2022:k308)

The enclosing of the entepicondylar foramen is synonymous with the elongation of the supinator process. As the present character states describe a morphological series, we order this character.

316. Humerus, supinator process: transversely broad and extends laterally or anterolaterally (0); transversely narrow and almost confluent with humeral shaft (1); inapplicable: supinator process absent (-)

From Schoch and Sues (2018a:k204); Ford and Benson (2020:k254)

317. Humerus, entepicondylar foramen: present (0); absent (1)

From Schoch and Sues (2018a:k206); Ezcurra et al. (2020:k426); Ford and Benson (2020:k251); Griffiths et al. (2021:k309); Pritchard et al. (2021:k249); Spiekman et al. (2021:k246)

See Ezcurra (2016:fig. 39)

318. Humerus, entepicondyle, transverse width: small, barely expanded beyond posterior margin of diaphysis (0); moderate, roughly half of distal transverse width (1); large, more than 2/3 of distal transverse width (2). ORDERED

Modified (ordered) from Ford and Benson (2020:k252)

Modified (added states, ordered) from Ezcurra et al. (2020:k425); Pritchard et al. (2021:k243); Spiekman et al. (2021:k245); Simões et al. (2022:k310)

See Ezcurra (2016:fig. 39)

As the present character states form a morphological series we order this character.

319. Humerus, entepicondyle proximal margin, angle relative to main axis of bone: obtuse angle, entepicondyle curves smoothly into diaphysis (0); roughly perpendicular, resulting in angular entepicondyle (1)

From Ezcurra et al. (2020:k687); Pritchard et al. (2021:k251)

320. Humerus, entepicondyle, distal extension: terminates proximal to distal margin of trochlea (0); extends distally relative to trochlea (1)

From Pritchard et al. (2021:k252)

321. Radius, shape in anterior view: straight (0); distinctly twisted in lateral view (1)

From Ezcurra et al. (2020:k437); Ford and Benson (2020:k257)

322. Ulna, olecranon process: absent or very low (0); prominent but lower than transverse depth at base (1); strongly developed, higher than transverse depth at base (2). ORDERED

From Ezcurra et al. (2020:k430)

Modified (ordered) from Ford and Benson (2020:k258)

Modified (added state, ordered) from Schoch and Sues (2018a:k208); Pritchard et al. (2021:k258); Griffiths et al. (2021:k318); Spiekman et al. (2021:k249); Simões et al. (2022:k320)

See Ezcurra (2016:fig. 40)

323. Carpus, maximum width (excluding pisiform): subequal to or greater than length of 4th metacarpal (0); less than length of 4th metacarpal (1)

From Ford and Benson (2020:k261)

324. Carpus, proximal carpals: ulnare and radiale as distinct ossifications (0); single proximal carpal ossification (= proximal syncarpal) (1)

From Ezcurra et al. (2021:k778)

325. Carpus, ulnare, elongation: longer than wide (0); short, width equal to or greater legth (1); inapplicable: proximal fused into syncarpal (-)

From Pritchard et al. (2021:k260)

Modified (reworded states) from Ford and Benson (2020:k260)

326. Carpus, intermedium: present (0); absent (1)

From Ezcurra et al. (2021:k439) ; Grifiths et al. (2021:k321)

See Ezcurra (2016:fig. 40)

327. Carpus, perforating foramen between ulnare and intermedium: present (0); absent (1); inapplicable: intermedium is absent (-)

From Schoch and Sues (2018a:k209); Ezcurra et al. (2020:k440); Griffiths et al. (2021:k320); Pritchard et al. (2021:k261); Spiekman et al. (2021:k252)

Modified (reduced states) from Simões et al. (2022:k321)

328. Carpus, medial centrale: present (0); absent (1)

From Ezcurra (2016:k441); Pritchard et al. (2019:k262)

Modified (reduced states) from Spiekman et al. (2021:k253)

329. Carpus, pisiform: present (0); absent (1)

From Ezcurra et al. (2020:k443); Griffiths et al. (2021:k322); Spiekman et al. (2021:k254); Simões et al. (2022:k322)

See Ezcurra (2016:fig. 40); figured in Simões et al. (2022:k322)

330. Carpus, pteroid bone: absent (0); present (1)

From Ezcurra et al. (2021:k776)

331. Carpus, distal carpal 1: present (0); absent (1)

From Griffiths et al. (2021:k324); Spiekman et al. (2021:k255); Simões et al. (2022:k324)

332. Carpus, distal carpal 5: present (0); absent (1)

From Ezcurra et al. (2020:k444); Griffiths et al. (2021:k325) Pritchard et al. (2021:k263); Spiekman et al. (2021:k256); Simões et al. (2022:k325)

333. Metacarpal IV, length: less than half of radius length (0); more than half of radius length (1)

Modified (reworded states) from Ford and Benson (2020:k263)

334. Metacarpal IV, length: longer than metacarpal III (0); subequal or shorter than metacarpal III (1)

From Schoch and Sues (2018a:k210); Ezcurra et al. (2020:k450); Spiekman et al. (2021:k260)

Modified (reduced states) from Griffiths et al. (2021:k359)

See Ezcurra (2016:k450)

335. Manus, digit II, phalangeal formula: three (0); two (1)

NEW CHARACTER

We introduce this character to take into account the reduced phalangeal formula of digit II in the drepanosauromorphs *Megalancosaurus* (MFSN 1769) and *Drepanosaurus* (MCSNB 5728).

336. Manus, digit III, phalangeal formula: four (0); three (1); two (2). ORDERED

Modified from Pritchard et al., (2021:k265)

We expand on Pritchard et al.'s (2021) iteration of this character to take into account the intermediate phalangeal formula of digit III of the pareiasaurs *Deltavjatia* (Tsuji, 2013) and the extreme reduction in the drepanosauromorps *Megalancosaurus* (MFSN 1769) and *Drepanosaurus* (MCSNB 5728). As the present character states form a morphological series, we order this character.

337. Manus, digit IV, phalangeal formula: five (0); four (1); three (2); two (3); one (4). ORDERED

Modified (added states) from Ezcurra et al. (2020:k454)

Modified (added state, ordered) from Pritchard et al. (2021:k266); Spiekman et al. (2021:k263)

We expand on Ezcurra et al.'s (2020) iteration of this character to take into account the strong reduction of the phalangeal formula of digit IV in drepanosauromorphs (e.g. two phalanges in *Drepanosaurus*, MCSNB 5728) and dinosaurs (Sereno, 1994).

338. Manus, digit V, phalangeal formula: four (0); three (1); two (2); one or zero (3). ORDERED

NEW CHARACTER

We introduce this character to describe variations in the phalangeal formula of digit V. All weigeltisaurids have an additional phalanx on this digit (*Coelurosauravus*, MNHN.F.MAP317a, b; *Weigeltisaurus* SMNK-PAL 2882; *Rautiania*, Bulanov and Sennikov, 2010). In contrast, several archosaurs show a distinct reduction of phalangeal number (Wellnhofer, 1978; Sereno, 1994). A reduction of the number of phalanges is also present in *Drepanosaurus* (MCSNB 5728).

339. Manus, penultimate phalanx, proximodistal length: shorter than preceding phalanx (or metacarpal) (0); significantly longer than preceding phalanx (or metacarpal) (1)

From Griffiths et al. (2021:k370)

We elect to code the elongation of the penultimate phalanges of the manus and pes independently (see character 406 below) as some taxa are known from the manus or pes only (e.g. *Rautiania*, Bulanov and Sennikov, 2010).

340. Manus, penultimate phalanx, distal contralateral facets: absent or subtle and facing distolaterally (0); well-developed, subcircular and expanded dorsoventrally relative to bone shaft, forming laterally oriented facets and distal gynglymus (1)

NEW CHARACTER

We introduce this character to take into account the highly developed disal contralateral facets of drepanosauromorphs such as *Drepanosaurus* (MCSNB 5728). We also report this morphology in some pterosaurs, such as *Eudimorphodon* (MCNSB 2888).

341. Manus, unguals, shape: bluntly spaded or hoof-like, with no ventral curvature (0); tapering distally and ventrally curved (1)

From Ford and Benson (2020:k266)

342. Manus, unguals, length: subequal or shorter than preceding phalanx (0); significantly longer than preceding phalanx (1)

From Ezcurra et al. (2020:k451); Pritchard et al. (2021:k267); Spiekman et al. (2021:k262)

We elect to code the elongation of the ungual phalanges of the manus and pes independently (see character 407 below) as some taxa are known from the manus or pes only (e.g. *Rautiania*, Bulanov and Sennikov, 2010).

343. Pelvis, puboischiatic plate, ventral emargination (thyroid fenestra): absent, continuous contact between pubis and ischium (0); present, small fenestra bordered ventrally by a strong pubis-ischium suture (1); present, large fenestra between pubis and ischium that is opened ventrally in lateral view, strictly dorsal pubis-ischium contact (2)

Modified (added state) from Schoch and Sues (2018a:k211); Ezcurra et al. (2020:k471); Pritchard et al. (2021:k268); Spiekman et al. (2021:k273)

See Ezcurra (2016:fig. 41)

As noted by Müller (2004), the thyroid fenestra of drepanosauromorphs and kuehneosaurids differs from that of other diapsids as it is ventrally bounded by a broad ischium-pubis contact. We thus expand on previous iterations of this character to take into account this morphology. However, it is unclear whether the paired thyroid fenestrae of drepanosauromorphs and kuehneosaurids form an intermediate state being an unfenestrated pelvis and one with a large median thyroid fenestra. Thus, we refrain from ordering this character.

344. Pelvis, acetabulum shape: irregular, marked by posterodorsal invasion of finished bone (0); roughly circular articular surface (1)

From Schoch and Sues (2018a:k215); Ezcurra et al. (2021:k469); Ford and Benson (2020:k267); Pritchard et al., (2021:k272); Simões et al. (2022:k298)

345. Ilium, anteroventral process (pubic flange) extending from anterior margin of pubic peduncle: absent (0); present, process draping across anterior surface of pubis (1)

From Griffiths et al. (2021:k298); Pritchard et al. (2021:k269); Spiekman et al. (2021:k272); Simões et al. (2022:k300)

346. Ilium, iliac blade, mediolateral expansion on dorsal surface: absent, ilium is plate-like with no mediolateral expansion along the dorsal surface (0); present, forming a shelf along the dorsal surface (1)

Modified from Ford and Benson (2020:k273)

Ford and Benson (2020) considered the mediolateral expansion of the iliac blade and the presence of a trough or fossa along its dorsal surface in a single character. However, we suggest both morphologies are best considered separately and consequently describe them in a pair of hierarchical characters.

The present character describes the presence of a mediolaterally expanded iliac blade while character 349 below describes the presence of a dorsal fossa. Outside this difference in character formulation, our scorings conform to that of Ford and Benson (2020).

347. Ilium, iliac blade, shelf: without discernable fossa (0); forms a trough or well-defined fossa (1); inapplicable: ilium plate-like without mediolateral expansion along dorsal surface (-)

Modified from Ford and Benson (2020:k273)

See comments in character 348 above.

348. Ilium, iliac blade, maximum anteroposterior length: less than 3 times maximul dorsoventral height (0): more than three times dorsoventral height (1)

From Pritchard et al. (2021:k275)

349. Ilium, iliac blade, preacetabular process: absent or incipient (0); present, anteroposteriorly shorter than 2/3 of dorsoventrally high (1); present, anteroposteriorly long but not extending beyond anterior margin of pubic peduncle (2); present, anteroposteriorly long and extending beyond anterior margin of pubic peduncle (3). ORDERED

From Ezcurra et al. (2021:k460)

Modified (added states) from Griffiths et al. (2021:k299); Spiekman et al. (2021:k264); Simões et al. (2022:k301)

See Ezcurra (2016:fig. 41)

350. Ilium, iliac blade, postacetabular process: absent or incipient (0) present but not extending beyond posterior margin of ischiatic peduncle (1); present, extending beyond posterior margin of ischiatic peduncle (2). ORDERED

Modified (added states, ordered) from Pritchard et al. (2021:k280)

We modified the formulation of the character states based on character 351 above to fit our dataset. As the charcter states form a morphological series, we order this character.

351. Ilium, iliac blade, main axis of postacetabular process: posterodorsally oriented (0); mainly posteriorly oriented (1); inapplicable: postacetabular process of ilium absent (-)

From Ezcurra et al. (2021:k464); Spiekman et al. (2021:k268)

Modified from Pritchard et al. (2021:k274)

See Ezcurra (2016:figs. 9, 41)

352. Ilium, supra-acetabular buttressing: absent (0); prominent anterodorsal bony lamina frames anterodorsal margin of acetabulum (1); bulbous rugosity on crest, dorsal to acetabulum (2). ORDERED

Modified (added state, ordered) from Ezcurra et al., (2020:k667); Griffiths et al. (2021:k297); Pritchard et al. (2021:k270, 271); Spiekman et al. (2021:k270, 271); Simões et al. (2022:k299)

353. Pubis, pubic apron: absent, symphysis mostly in coronal plane and visible in lateral view (0); present, symphysis downturned anteroventrally and not visible in lateral view (1)

From Ezcurra et al. (2020:k477); Ford and Benson (2020:k269); Pritchard et al., (2021:k282); Spiekman et al. (2021:k275)

See Ezcurra (2016:fig. 41)

354. Pubis, tuberosity for attachment of ambiens muscle: absent or incipient (0); prominent (1)

From Ezcurra et al. (2020:k474); Spiekman et al. (2021:k274)

Modified (removed state) from Pritchard et al. (2021:k284)

As proposed by Pritchard and Nesbitt (2017), the lateral pubic tubercle (sensu Vaughn, 1955) present in *Paleothyris* and araeoseclidian diapsids (Reisz, 1981) may be homologous to the tuberosity for the attachment of the ambiens muscle of later diapsids. We thus score these taxa with state 1, in agreement with previous studies (Ezcurra et al., 2020).

355. Ischium, posterior margin: vertical and flattened (0); posterior process extends from posterodorsal margin of bone (1)

From Ezcurra et al. (2020:k488); Pritchard et al. (2021:k286); Spiekman et al. (2021:k278)

See Ezcurra (2016:fig. 41)

We concur with Pritchard (2015) that the posterodorsal process of the ischium in some lepidosauromorphs and archosauromorphs is homologous to the spina ischia of (El-Toubi, 1949). As described by Spiekman et al. (2021), this process is formed by a distinct concavity or constriction of the ventral margin of the ischium.

356. Femur, proportions: short and broad, maximum length less than three times distal width (0); long and slender, maximum length more than three times distal width (1)

From Ford and Benson (2020:k278)

357. Femur, proximal surface: well-ossified, convex (0); markedly concave surface with central groove (1)

From Ezcurra et al. (2021:k491); Pritchard et al. (2021:k288); Spiekman et al. (2021:k279)

See Ezcurra (2016:fig. 42)

358. Femur, proximal head: not distinctly offset from shaft (0); distinctly offset from shaft (1)

From Ezcurra et al. (2020:k492)

359. Femur, proximal head, profile in medial or lateral view if offset from shaft: rounded (0); hook-shaped (1); inapplicable: proximal head of femur not offset from shaft (-)

From Ezcurra et al. (2020:k800)

360. Femur, anterior trochanter (iliofemoralis cranialis insertion, = lesser or minor trochanter): absent (0); present (1)

From Pritchard et al; (2021:k290)

Modified (reduced states) from Ezcurra et al. (2020:k502)

361. Femur, trochanteric shelf (iliofemoralis externus insertion): absent (0); present (1)

From Ezcurra et al. (2020:k503)

362. Femur, attachment of the caudifemoralis musculature on ventral (or posterior) surface of bone: crest-like, with intertrochanteric fossa (= internal trochanter), and convergent with proximal end (0); crest like, with intertrochanter fossa (= internal trochanter) but not convergent with proximal end (1); crest-like but without intertrochanteric fossa and not convergent with proximal end (= 'fourth trochanter' of archosauriforms) (2). ORDERED

From Ezurra et al. (2020:k504)

Modified (ordered) from Spiekman et al. (2021:k280)

Modified from Pritchard et al. (2021:k291, 292); Simões et al. (2022:k326, 328)

See Ezcurra (2016:figs. 42, 43)

We follow Ezcurra (2016), building upon previous studies (e.g. Hutchinson, 2001; Nesbitt et al., 2009; Nesbitt, 2011) in considering the internal trochanter of early reptiles and lepidosaurs as homologous to the 'fourth trochanter' of extinct archosauriforms as both structures invariably serve as the insertion of the M. caudifemoralis. Note that the 'fourth trochanter' of archosauriforms is analogous, and not homologous to the fourth trochanter of tetrapods and early amniotes (Romer, 1956; Hutchinson, 2001), the presence of which is considered in character 361 below. See Ezcurra (2016:247-248) for further details.

We concur with Ezcurra et al. (2020) that the present character states form a morphological series and order this character contra Spiekman et al. (2021).

363. Femur, 4th trochanter: present as a raised ridge on the ventral surface of the femoral shaft (0); absent (1)

From Schoch and Sues (2018a:k218); Ford and Benson (2020:k279); Griffiths et al. (2021:k328); Simões et al. (2022:k327)

See comments in character 367 above.

364. Femur, distal adductor crest on ventral surface: prominent (0); low and feebly developed (1); absent or reduced to a rugosity on the surface of the bone (2). ORDERED

Modified (ordered) from Ford and Benson (2020:k280)

365. Femur, distal condyles: uneven, posterior (fibular) condyle larger and projecting distinctly beyond anterior (tibial) condyle (0); both condyles subequal and extend distally to approximately same level (1)

From Schoch and Sues (2018a:k222); Ford and Benson (2020:k276); Pritchard et al. (2021:k293)

Modified (reduced states) from Ezcurra et al. (2020:k512); Spiekman et al. (2021:k282)

See Ezcurra (2016:k512)

366. Femur, distal condyles, dimensions relative to femoral shaft: distinct expansion beyond circumference of femoral shaft (0); limited expansion beyond circumference of femoral shaft (1)

From Schoch and Sues (2018a:k221); Ezcurra et al. (2020:k511); Pritchard et al. (2021:k294); Spiekman et al. (2021:k281)

See Ezcurra (2016:fig. 43)

367. Femur, tibial condyle, medial surface: rounded and mound-like (0); triangular and sharply pointed (1)

From Ezcurra et al. (2020:k673); Pritchard et al. (2019:k295)

368. Femur, fibular condyle, lateral surface: rounded and mound-like (0); triangular and sharply pointed (1)

From Ezcurra et al. (2020:k515); Spiekman et al. (2021:k284)

See Ezcurra (2016:fig. 42)

369. Femur, fibular condyle, ventral surface: flattened and planar (0); rounded and mound-like (1)

From Pitchard et al. (2021:k296)

370. Tibia, length: shorter or subequal to femur (0); markedly longer than femur (1)

From Spiekman et al. (2021:k285)

Modified from Ezcurra et al. (2020:k516)

See Ezcurra (2016:fig. 15)

Ezcurra et al. (2020) employ a discretised caracter with several character states based on a cluster analysis. However, as such character states has been computed for a markedly different taxon sample, and as an exhaustive resampling of limb bone lengths is out of the scope of this paper, we revert to previous binary iterations of this character (e.g. Nesbitt, 2011:k299)

371. Tibia, cnemial crest: absent (0); prominent and distinct (1)

From Ford and Benson (2020:k282)

Modified (reduced states) from Ezcurra et al. (2020:k517)

See Ezcurra (2016:fig. 44)

372. Fibula, curvature: arcuate, bowing away from tibia or straight (0); distinctly sigmoidal (1)

NEW CHARACTER

373. Tarsus, transverse width across tarsus at widest point: subequal to or greater than 4th metatarsal (0); less than 4th metatarsal (1)

From Ford and Benson (2020:k285)

374. Tarsus, astragalus: absent (0); present (1)

From Schoch and Sues (2018a:k226); Ford and Benson (2020:k286)

375. Tarsus, astragalus, proximal neck region: short (0); long, at least 40% of proximodistal length of astragalus (1); inapplicable: astragalus is absent or fused to tibiofibula (-)

From Ford and Benson (2020:k287)

376. Tarsus, tibio-astragalar joint: flat or slightly concave (0); low tibial ridge fits into shallow astragalar groove (1); tibial surface of astragalus divided into distinct posteromedial and anterolateral basins (2); inapplicable: astragalus is absent or fused to tibiofibula (-)

From Ezcurra et al. (2020:k536); Ford and Benson (2020:k284)

The tibial surface of the astragalus is generally flat in early amniotes (e.g. *Captorhinus*, Holmes, 2003), but more complex articulations have been reported in various taxa. Previous studies focusing on early amniotes (e.g. Ford and Benson, 2020) have indeed described the tibio-astragalar joint of diapsids (mainly based on araeoscelidians; Vaughn, 1955; Reisz, 1981) to comprise of a low tibial ridge fitting into a shallow astragalar groove (state 1). In addition, much attention has been fiven to the tibio-astragalar articulation of archosaurs, and previous studies on the latter taxa (e.g. Nesbitt, 2011; Ezcurra et al., 2020) have differenciated the 'saddle-shaped' articulation of pseudosuchians in which he tibial surface of the astragalus is divided (state 2) from that of other saurians.

We elect to consider all morphologies of the tibial surface of the astragalus in the present character. However, it is unclear whether the character states form a morphological series, so we refrain from ordering this character.

377. Tarsus, posterior groove: present (0); absent (1); inapplicable: astragalus is absent (-)

From Ezcurra et al. (2020:k539); Spiekman et al. (2021:k290)

378. Tarsus, astragalus and calcaneum: unfused, present as distinct ossifications (0); fused, astragalocalcaneum present (1); inapplicable: astragalus is absent (-)

From Ezcurra et al. (2020:k606); Griffiths et al. (2021:k331); Pritchard et al. (2021:k298); Simões et al. (2022:k330)

Modified (reduced states) from Schoch and Sues (2018a:k227)

Figured in Simões et al. (2022:k330)

Ezcurra et al. (2020) considered the morphology of the astragalocalcaneal articulation and the fusion between astragalus and calcaneum in a single character. However, we revert to previous iterations (e.g. Nesbitt, 2011) in considering coosification in a separate character. The morphology of the astragalocananeal articulation is treated in character 384 below.

379. Tarsus, astragalus and calcaneum, articulation: roughly flat (0); concavoconvex with concavity on calcaneum (1); concavoconvex with concavity on astragalus (2); inapplicable: astragalaus and calcaneum fused (-)

Modified (reduced states) from Ezcurra et al. (2020:k532)

Modified from Spiekman et al. (2021:k289); Simões et al. (2022:k331)

See Ezcurra (2016:fig. 45)

See discussion in character 383 above. As discussed in other studies (e.g. Sereno, 1991; Nesbitt, 2011), state 1 describes the traditional ‘crocodile-normal’ articulation while state 2 describes the ‘crocodile-reverse’ one.

380. Tarsus, perforating foramen between astragalus and calcaneum: present (0); absent (1); inapplicable: astragalus is absent (-)

From Schoch and Sues (2018a:k224); Ezcurra et al. (2020:k533); Pritchard et al. (2021:k299); Spiekman et al. (2021:k295) ; Simões et al. (2022:k333)

See Ezcurra (2016:fig. 45); figured in Simões et al. (2022:k333)

381. Astragalus, tibial and fibular facets facets: separated by non-articular surface (0); continuous (1); inapplicable: astragalus is absent (-)

From Ezcurra et al. (2020:k534); Pritchard et al. (2021:k301)

382. Astragalus, margin between tibial and fibular facets: grades smoothly into anterior hollow (0); separated by prominent ridge from anterior hollow (1); inapplicable: astragalus is absent or with continuous tibial and fibular facets (-)

From Ezcurra et al. (2020:k535); Pritchard et al. (2021:k302)

383. Tarsus, calcaneum, lateral tuber: absent or incipient (0); prominent (1)

From Schoch and Sues (2018a:k229); Ezcurra et al. (2020:k545); Griffiths et al. (2021:k333); Pritchard et al. (2021:k306); Simões et al. (2022:k332)

See Ezcurra (2016:figs. 45, 46)

384. Tarsus, calcaneum, lateral tuber, proportions at midshaft: proximodistally taller than anteroposteriorly broad (0); roughly as tall as broad (1); markedly broader than tall (2); inapplicable: calcaneal tuber is absent (-). ORDERED

From Ezcurra et al. (2020:k547)

Modified (added states, ordered) from Pritchard et al. (2021:k308)

See Ezcurra (2016:fig. 45)

385. Tarsus, calcaneum, ventral notch between main body and calcaneal tuber: absent (0); present (1); inapplicable: calcaneal tuber is absent (-)

From Ezcurra et al. (2021:k551)

See Ezcurra (2016:fig. 45)

386. Tarsus, number of centralia: two or more (0); one (1); zero (2)

From Schoch and Sues (2018a:k236)

Modified (added state) from Ford and Benson (2020:k291); Griffiths et al. (2021:k335); Pritchard et al. (2021:k297); Spiekman et al. (2021:k291); Simões et al. (2022:k335, 336)

Modified from Ezcurra et al. (2020:k557)

See Ezcurra (2016:figs. 45, 46)

The number of distinct centralia is variable among amniotes. 'Pelycosaur-grade' synapsids typically show both a medial and a lateral centrale (state 0, Romer and Price, 1940), although there is confusion as to the number of centralia in early caseasaurs (Ford and Benson, 2020). Two centralia have also been scored as present in the parareptile *Emeroleter* (e.g. Tsuji et al., 2012; Ford and Benson, 2020). However, we were unable to confirm the presence of two centralia based on the description and figures of Tsuji et al. (2012). *Emeroleter* is thus scored with states 0 or 1 for uncertainty. The medial centrale is otherwise absent as a distinct ossification in sauropsids. In addition, some saurians lack distinct centralia altogether (state 2, e.g. *Azendohsaurus*, *Erythrosuchus*, Gower, 1996; Nesbitt et al., 2015). However, it is unclear in each case if a centrale is entirely lost or fuses to a neighboring element (and which element it fuses to). We thus provisionally score for the number of distinct centralial ossifications in this character. Given this confusion, we also refrain from ordering this character.

387. Tarsus (lateral) centrale, contact with tibia: absent (0); present (1); inapplicable: (lateral) centrale absent as discrete element (-)

From Pritchard et al. (2021:k312); Grifiths et al. (2021:k376)

Modified from Ezcurra et al. (2020:k557)

See Ezcurra (2016:figs. 45, 46)

388. Tarsus, distal tarsal 1: present (0); absent (1)

From Schoch and Sues (2018a:k230); Ezcurra et al. (2020:k558); Griffiths et al. (2021:k336); Pritchard et al. (2021:k313); Simões et al. (2022:k337)

Figured in Simões et al. (2022:k337)

389. Tarsus, distal tarsal 2: present (0); absent (1)

From Ezcurra et al. (2020:k559); Griffiths et al. (2021:k337); Pritchard et al. (2021:k314); Simões et al. (2022:k338)

Figured in Simões et al. (2022:k338)

390. Tarsus, distal tarsal 4, morphology of proximal contact: smooth surface for proximal tarsals (0); prominent proximomedial process that fits under the astragalus medial to the calcaneal-distal tarsal 4 articulation (= lepidosauromorph ankle joint) (1)

From Griffiths et al. (2021:k338); Pritchard et al. (2021:k311); Simões et al. (2022:k339)

Figured in Simões et al. (2022:k339)

391. Distal tarsal 4, transverse width: broader than distal tarsal 3 (0); subequal to distal tarsal 3 (1)

From Ezcurra et al. (2020:k560)

392. Tarsus, distal tarsal 5: present (0); absent (1)

From Schoch and Sues (2018a:k231); Ezcurra et al. (2020:k563); Ford and Benson (2020:k290); Griffiths et al. (2021:k339); Pritchard et al. (2021:k315); Spiekman et al. (2021:k293); Simões et al. (2022:k340)

393. Metatarsus, configuration: metatarsals diverge from ankle (0); compact, metatarsals I-IV tightly bunched (1)

From Ezcurra et al. (2020:k565); Spiekman et al. (2021:k296)

See Ezcurra (2016:fig. 46)

The present character describes the tighly bunched metatarsus of tanystropheids and ornithodiran archosaurs. Following previous studies (e.g. Ezcurra et al., 2020), we consider this morphology independently from the presence of a proximal overlap between the metatarsals

(see character 396 below) as some taxa (e.g. *Silesaurus*, Dzik, 2003) show a tightly bunched metatarsus with no overlapping of the metatarsals.

394. Metatarsus, metapodials overlapping proximally: absent (0); present (1)

From Schoch and Sues (2018a:k238); Ford and Benson (2020:k293); Ezcurra et al. (2020:k566); Spiekman et al. (2021:k296)

See Ezcurra (2016:fig. 46)

See comments in character 395 above.

395. Metatarsus, longest metatarsal: equal to or shorter than half of tibia (0); longer than half of tibia (1)

Modified from Ezcurra et al. (2020:k567)

Ezcurra et al. (2020) employ a discretised caracter with several character states based on a cluster analysis. However, as such character states has been computed for a markedly different taxon sample, and as an exhaustive resampling of bone lengths is out of the scope of this paper, we revert to previous binary iterations of this character (e.g. Nesbitt, 2011:k383)

Previous studies have employed characters to describe both the length of the longest digit and that of the longest metatarsal relative to the tibia (e.g. Ezcurra et al., 2020:k564, 567). However, we suggest both characters could be related. Given the fragmentary nature of several taxa in our dataset, we favor the use of the present character over a measurement of the longest digit, which is more liable to be incompletely preserved.

396. Metatarsal IV, proximodistal length: longer than metatarsal III (0); subequal or shorter than metatarsal III (1)

From Pritchard et al. (2021:k317)

Modified from Ezcurra et al. (2020:k574)

See Ezcurra (2016:fig. 46)

397. Metatarsal V, proximodistal length: equal to or longer than half of metatarsal III (0); shorter than half of metatarsal III (1)

From Ezcurra et al. (2020:k823)

398. Metatarsal V, shape of proximolateral margin: smooth, curved margin (0); prominent, pointed process (outer process sensu Robinson, 1975) (1)

From Ezcurra et al. (2020:k578); Pritchard et al. (2021:k318); Spiekman et al. (2021:k302)

399. Metatarsal V, proximal end hook-shaped: absent, straight metatarsal V (0); present, proximal process gradually curves medially (1); present, proximal process abruptly flexed medially, metatarsal V L-shaped in dorsal view (2)

From Ezcurra et al. (2020:k577); Spiekman et al. (2021:k300)

Modified (added state) from Griffiths et al. (2021:k340); Pritchard et al. (2021:k319); Simões et al. (2022:k341)

See Ezcurra (2016:fig. 46); figured in Simões et al. (2022:k341)

As it is unclear whether the present character states form a morphological series, we refrain from ordering this character in accordance with Ezcurra et al. (2020) and Spiekman et al. (2021).

400. Metatarsal V, dorsiflexion: absent, metatarsal V straight along proximodistal length (0); present, metatarsal V angles dorsally near proximodistal midpoint (1)

Modified (reworded) from Pritchard et al. (2021:k332)

401. Pes, digit III, phalangeal formula: four (0); three (1)

From Pritchard et al. (2021:k324)

402. Pes, digit IV, phalangeal formula: five (0); four (1); three (2). ORDERED

NEW CHARACTER

403. Pes, digit V, phalangeal formula: four (0); three (1); two (2); one or zero (3). ORDERED

NEW CHARACTER

404. Pes, distal non-ungual phalanges, distal articular portion: lateral and medial sides subparallel (0); lateral and medial sides converging anterodorsally (1)

From Ezcurra et al. (2020:k585); Pritchard et al. (2021:k322)

405. Pes, penultimate phalanx, proximodistal length: shorter than preceding phalanx (0); significantly longer than preceding phalanx (1)

From Ezcurra et al. (2020:k689); Pritchard et al. (2021:k323)

See character 346 above.

406. Pes, unguals, length: subequal or shorter than preceding phalanx (0); significantly longer than preceding phalanx (1)

NEW CHARACTER

See character 349 above.

407. Pes, unguals, ventral tubercle: absent or small (0); well-developped and extended ventral to proximal articular facet (1)

From Ezcurra et al. (2020:k587); Pritchard et al. (2021:k326); Spiekman et al. (2021:k307)

Appendix 3: Expanded comparative anatomy of drepanosauromorphs

Much of the uncertainty on the systematic position of drepanosauromorphs stems from their unique and highly specialized body plan, and is exacerbated by the nature of preservation of the Italian specimens that underwent severe diagenetic compression. Furthermore, despite the inclusion of several drepanosauromorphs in some recent broad-scale phylogenetic analyses (Pritchard and Nesbitt, 2017; Bennett, 2020; Sobral et al. 2020; Ford et al., 2021; Griffiths et al., 2021; Martínez et al., 2021; Simões et al., 2022), no consensus on their systematic position has been reached. Thus, a detailed statement of comparative anatomy is needed to reexamine previously proposed hypotheses on the systematic position of this enigmatic group.

Skull

The drepanosauromorph skull remains particularly poorly understood despite several rigorous descriptions (Renesto, 2000; Renesto and Dalla Vecchia, 2005; Renesto and Binelli, 2006; Pritchard and Nesbitt, 2017). We provide here a detailed reexamination and new interpretations of all cranial remains referred to *Megalancosaurus* and *Vallesaurus* based on direct observation and Reflectance Transformation Imaging (RTI), a method well-suited to palliate the preservation state of these specimens (see Methods), as well as a restudy of the three-dimensional surface models of the holotype specimen of *Avicranium* (Fig. S2). Excluding the mandibular elements referred to *Hypuronector* (Colbert and Olsen, 2001), we thus provide a comprehensive revision of nearly all cranial material currently attributed to drepanosauromorphs.

MFSN 1769 (*M. preonensis*, holotype)—The skull of the holotype of *M. preonensis* was last described in detail by Renesto and Dalla Vecchia (2005). Our identification of most bones and structures are nearly identical to the latter study, with slight differences in the identified outlines of the bones stemming from the poor preservation of the specimen (Fig. S2). The holotype indeed underwent strong diagenetic compression, and the block broke through the skull along the sagittal plane, thus hampering delimitation of individual structures.

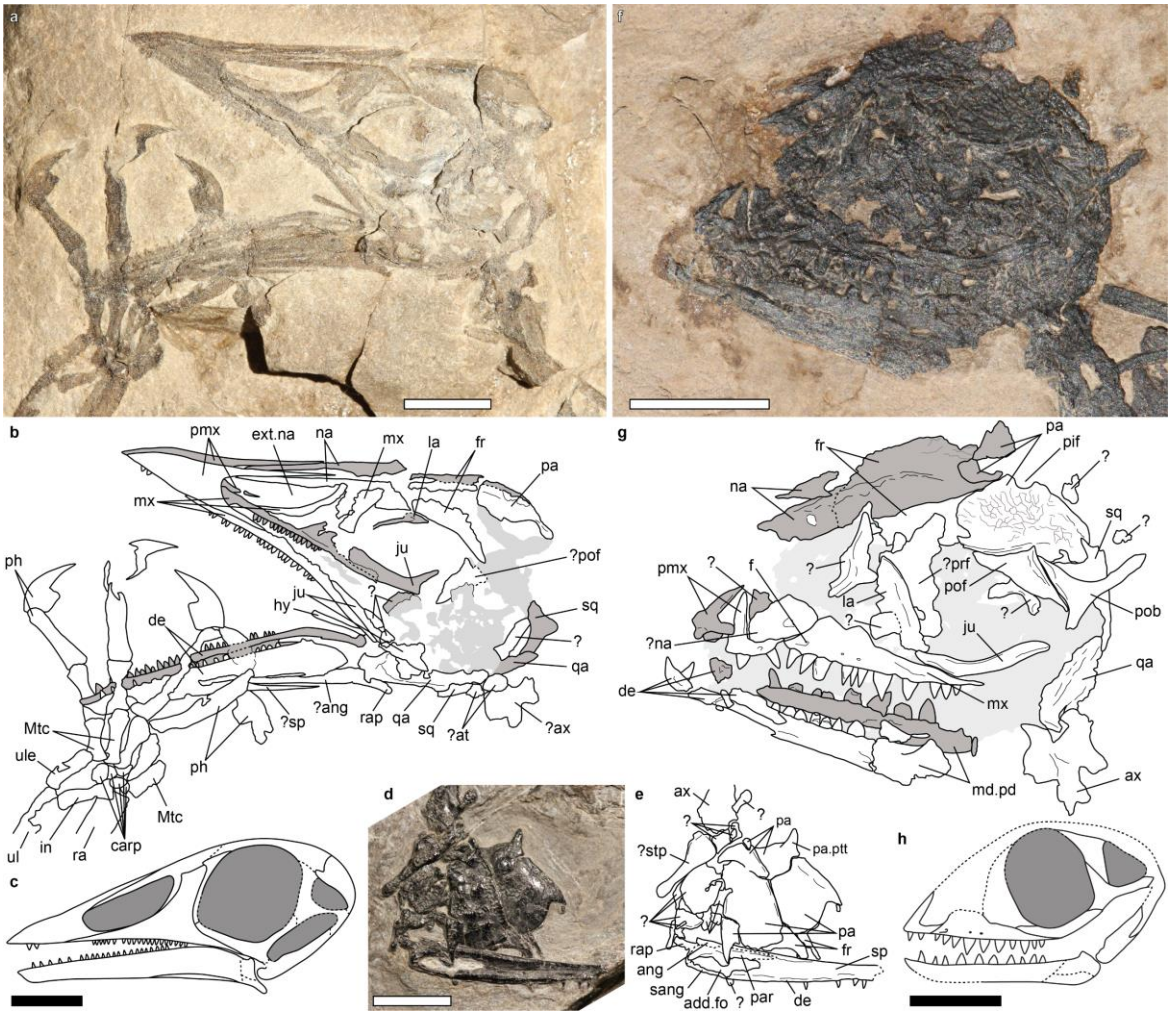

Figure A-S2: Cranial anatomy and reconstructions of *Megalancosaurus preonensis* and *Vallesaurus cenensis* (Norian, Italy). **a**, subcomplete skull of *M. preonensis* (holotype MFSN 1769b) in left lateral view. **b**, interpretative drawing of **a**. **c**, cranial reconstruction of *M. preonensis* (modified from Renesto and Dalla Vecchia, 2005). **d**, skull and jaw fragments of *M. preonensis* (MPUM 8437a) in mostly dorsal view. **e**, interpretative drawing of **d**. **f**, subcomplete skull of *V. cenensis* (MCSNB 4751) in left lateral view. **g**, interpretative drawing of **f**. **h**, cranial reconstruction of *V. cenensis* (modified from Renesto and Binelli, 2006). **add.fo**, adductor fossa; **ang**, angular; **at**, atlas; **ax**, axis; **carp**, carpal bones; **de**, dentary; **ext.na**, external naris; **f**, foramen; **fr**, frontal; **hy**, hyoid; **in**, intermedium; **ju**, jugal; **la**, lacrimal; **md.pd**, mandibular postdentary complex; **Mtc**, metacarpal; **mx**, maxilla; **na**, nasal; **pa**, parietal; **pa.ptt**, posttemporal process of parietal; **par**, prearticular; **ph**, phalanx; **prf**, prefrontal; **pob**, postorbital; **pof**, postfrontal; **pmx**, premaxilla; **qa**, quadrate; **ra**, radius; **rap**, retroarticular process; **rid**, ridge; **sang**, surangular; **sp**, splenial; **sq**, squamosal; **stp**, stapes; **ul**, ulna; **ule**, ulnare. Light grey shading in **b**, **f** indicates bony matter of unclear shape and identification; dark grey shading in **b**, **f** indicates bones from the right side of the specimen. Scale bars, 5 mm.

As described by Renesto and Dalla Vecchia (2005), the skull of *M. preonensis* is high and triangular, much taller than transversely broad, and with its rostrum tapering to a point anteriorly (Fig. S2). Such a sharply pointed rostrum, whereby the supranarial process of the premaxilla is strongly angled relative to the vertical, is also present in weigeltisaurids (Bulanov

and Sennikov, 2010, 2015) and tanystropheids (Spiekman et al., 2021). However, no non-archosauriform diapsids shows such a high skull (except *Trilophosaurus*, Spielmann et al., 2008). In fact, the conjunction of a tall skull and sharply tapering rostrum is only present in pterosaurs among Permo-Triassic reptiles (Wild, 1979; Dalla Vecchia, 2014). Given that our interpretation of the skull bones of the holotype mostly conforms to previous studies, we do not provide a detailed redescription of this specimen, focusing instead on selected areas where our interpretations differ from, or add to that of Renesto and Dalla Vecchia (2005).

We identify a subrectangular lamina overlying the anterolateral process of the left nasal anterior to the lacrimal in MFSN 1769b as a part of the dorsal process of the left maxilla (Fig. S2). However, it seems this lamina was slightly posteroventrally displaced from the anterior half of the dorsal process of the maxilla which lies slightly anteriorly (as identified also by Renesto and Dalla Vecchia, 2005). This displacement conforms to that of the alveolar portion of the maxilla and the nasal, whose anterolateral process now lies posterior to the anterior portion of the dorsal process of the maxilla instead of anterior to it (Fig. S2). The distance seen between both parts of the dorsal process of the maxilla thus likely does not reflect its actual width. Once reconstructed (Fig. S2c), the dorsal process of the maxilla thus appears slightly larger than the subtriangular process reconstructed by Renesto and Dalla Vecchia (2005) and has a more concave posterior margin than previously thought.

The rostral region of the skull of *M. preonensis* shows several apomorphies that suggest archosauromorph or even pterosaur affinities. First, the premaxilla of this specimen is large, occupying more than half of the rostrum, with its bulk anterior to the external naris, and has a short but distinct subnarial process separating the anterior-most portion of the maxilla from the external naris, two characters that are considered synapomorphies of all archosauromorphs crownward to the early-diverging *Protorosaurus* (Ezcurra, 2016). Second, the supranarial process of the premaxilla of *M. preonensis* is extremely long, extending to the posterior half of the nasal (Fig. S2a, b), a morphology that is only reported in weigeltisaurids (Buffa, 2021; Pritchard et al., 2021) and pterosaurs (Dalla Vecchia, 2014) among Permo-Triassic taxa. Third, the external naris is posteriorly displaced by the long beak-like rostral portion of the premaxilla (Fig. S2a-c). Such a marked displacement is only known in the allokotosaur *Teraterpaton* (Sues, 2003), phytosaurs (Stocker and Butler, 2013) and pterosaurs (Dalla Vecchia, 2014) among Triassic diapsids, although a less marked posterior displacement is also present in tanystropheids (Spiekman et al., 2021) and weigeltisaurids (Buffa et al., 2021; Pritchard et al.,

2021). Fourth, the nasal is mostly exposed laterally, with little dorsal exposure in *M. preonensis*, contrary to the dorsally exposed nasal of most other Permo-Triassic neodiapsids, but as in the allokotosaur *Trilophosaurus* (Spielmann et al., 2008) and pterosaurs (Dalla Vecchia, 2014). Fifth, *M. preonensis* exhibits a long anterolateral process of the nasal that excludes the maxilla from the posteroventral margin of the external naris (Fig. S2a-c). This process is typical in non-proterosuchid archosauriforms among Triassic taxa (Ezcurra, 2016). Lastly, the dorsal process of the maxilla of *M. preonensis* appears to have a markedly concave posterior margin, a synapomorphy of tanystropheids and crocopodan archosauromorphs (Nesbitt et al., 2015; Spiekman et al., 2021).

Despite minor differences in our identification of the bones anterior to the orbit in the holotype of *M. preonensis*, we concur with Renesto and Dalla Vecchia's (2005) identification of the lacrimal (Fig. S2a-c). We also agree that this bone was displaced due to diagenetic compression, and would have been in close contact with the dorsal process of the maxilla, likely precluding the presence of an antorbital fenestra. Thus, this taxon had a very tall lacrimal that extended dorsally to reach the nasal, contrary to most Permo-Triassic neodiapsids, but as in *Prolacerta* (Modesto and Sues, 2004) and most archosauriforms (Nesbitt, 2011; Nesbitt et al., 2013). As reconstructed (Fig. S2c, see also Renesto and Dalla Vecchia, 2005), this bone also formed nearly the entire anterior orbital margin in *M. preonensis*. Such a large participation of the lacrimal to the orbit is known in araeoscelidians diapsids, but contrasts sharply with nearly all other neodiapsids (e.g. *Claudiosaurus*, *Youngina*, weigeltisaurids, Gow, 1975; Carroll, 1981; Buffa et al., 2021) and non-archosaur saurians (lepidosauromorphs, Evans, 2003; archosauromorphs, Ezcurra, 2016; archosauriforms, Ezcurra et al., 2013; Sookias and Butler, 2013; Trotteyn et al., 2013) in which the lacrimal has only much shorter orbital contribution, if any. However, a large contribution of the lacrimal to the orbit is common among archosaurs (Nesbitt, 2011; Nesbitt et al., 2013), especially pterosaurs (Dalla Vecchia, 2013, 2014) with which *Megalancosaurus* also shares a slight anteroposterior dorsal expansion of the lacrimal (as noted by Renesto and Dalla Vecchia, 2005). The lacrimal of *M. preonensis* thus suggests archosauriform affinities for this taxon, yet the absence of an antorbital fenestra, a long-recognized synapomorphy of this group (Benton, 1985; Gauthier et al., 1988; Juul, 1994; Pinheiro et al., 2016, 2020) contradicts this view. However, reduction of the antorbital fenestra has been noted among crocodilians and ornithischian dinosaurs (Witmer, 1997), and is also

present in proterochampsids among Triassic archosauriforms (Trotteyn et al., 2013), culminating in *Vancleavea* where this opening is entirely absent (Nesbitt et al., 2009).

Contrary to previous studies (Renesto, 2000; Renesto and Dalla Vecchia, 2005), the parietal is nearly completely preserved in MFSN 1769b (Fig. S2a-c, 'Slab B' of Renesto and Dalla Vecchia, 2005) and is very similar to the complete parietal table of MPUM 8437a (described below). Most of the interparietal suture is broken on the specimen, so it is unclear if a pineal foramen was present. Laterally, the parietal bears short and dorsoventrally narrow posterolateral processes (Fig. S2a-c). Similarly shallow processes are present in non-saurian diapsids (araeoscelidians, Reisz, 1981; weigeltisaurids, Buffa et al., 2021; 'younginifoms', Gow, 1975, Currie, 1981) and lepidosauromorphs (O'Brien et al., 2018: Ford et al., 2021; Griffiths et al., 2021), but these processes are much taller dorsoventrally in crocopodan archosauromorphs, except rhynchosaurids (Ezcurra, 2016). However, shallow posterolateral processes of the parietal have also been noted in some ornithodirans (e.g. lagerpetids, some dinosaurs and pterosaurs, scored in Ezcurra et al., 2020).

Lastly, Renesto and Dalla Vecchia (2005) and Renesto et al. (2010) described a splint-like external mandibular fenestra in the holotype while Renesto (1994a, 2000) considered it absent in this specimen. There indeed appears to be a narrow opening immediately ventral to the coronoid eminence in the left lower jaw of this specimen. However, this interpretation would make for a very posteriorly positioned and anteroposteriorly long fenestra, whereas the external mandibular fenestra is more ovoid and located around the junction between the dentary and postdentary bones in archosauriforms (Nesbitt, 2011). Furthermore, we suggest that the opening observed by Renesto and Dalla Vecchia (2005) could result from the ventral displacement of some of the lower jaw bones, as seen on the other hemimandible and as argued by Pinheiro et al. (2020) for some Triassic tanystropheids. However, given its state of preservation and the superposition of both hemimandibles, the presence of an external mandibular fenestra in the mandible of the holotype of *M. preonensis* cannot be excluded unequivocally.

MPUM 8437 (*M. preonensis*, referred)—Specimen MPUM 8437a preserves a portion of the skull roof, left lower jaw and unidentified fragments (Fig. S2d, e). This specimen was described by Renesto (2000), Renesto and Dalla Vecchia (2005) and Pritchard (2015), but our interpretation differs in some ways from each study.

We concur with Pritchard (2015) that the preserved skull roof portion corresponds to the nearly complete (but transversely broken) parietals and posterior portion of the frontals, with no trace of the supraoccipital or other occipital bones, contrary to the interpretation of Renesto (2000) and Renesto and Dalla Vecchia (2005). The parietal portion of the skull roof is thus inflated in *Megalancosaurus*, as can also be seen in the less well-preserved holotype (Fig. S2a-c), and in *Avicranium* (Pritchard and Nesbitt, 2017). As noted by previous studies (Renesto and Dalla Vecchia, 2005; Pritchard and Nesbitt (2017), an inflation of the parietal skull roof is prevalent in birds, but is only present in pterosaurs among Triassic taxa. Anteriorly, the suture with the frontal is W-shaped, indicating the presence of both medial and lateral processes of the frontals that incise the parietals (Fig. S2d, e), a morphology that is shared with weigeltisaurids (Buffa et al., 2021; Pritchard et al., 2021). Laterally, the parietal bears a shallow but broad embayment for the jaw adductor musculature (Fig. S2d, e), and a similar morphology is present in *Avicranium* (Pritchard and Nesbitt, 2017). Interestingly, such a broad adductor surface is absent in most neodiapsids (araeoscelidians, Reisz, 1981; weigeltisaurids, Buffa et al., 2021; 'younginiformes', Gow, 1975; Currie, 1981; but not *Claudiosaurus*, Carroll, 1981), but is prevalent in saurian diapsids (Spiekman et al., 2021). Lastly, there is no trace of a pineal foramen along the interparietal suture.

We consider that the subcomplete hemimandible is the left one visible in lingual view, and not in labial view as described by Renesto (2000). The splenial, prearticular, surangular and angular can indeed be identified although the sutures between those bones are only tentatively followed (Fig. S2d, e). There is no trace of a distinct coronoid bone, which we interpret as absent in this taxon given the lack of marked coronoid eminence and preservation of all other mandibular bones. The coronoid is present in all diapsids ancestrally and is convergently lost in several saurians (Benton, 1985; Spiekman et al., 2021), including pterosaurs and some pseudosuchians among Triassic taxa (Bona et al., 2021).

Given this lower jaw is preserved in lingual view, the large hole in its posterior half cannot be interpreted as an external mandibular fenestra (contra Pritchard, 2015), and the presence of this opening is equivocal as the labial wall of the mandible cannot be seen. As the ventral margin of this opening is genuine (but the dorsal margin is clearly broken, unfinished bone), it likely corresponds to the adductor fossa, which has a large exposure in medial view, as suggested by Renesto (2000). As we were unable to unequivocally attest to the presence or absence of an external mandibular fenestra in the holotype as well (see above), the presence of

this fenestra in *M. preonensis* is equivocal. The presence of this fenestra has long been considered as a synapomorphy of archosauriformes (Juul, 1994; Nesbitt, 2011) and their immediate sister-group (Pinheiro et al., 2016, 2020), but this fenestra is also interpreted as subsequently lost in the proterchampian *Doswellia* (Dilkes and Sues, 2009) and most pterosaurs (Nesbitt and Hone, 2010; Bennett, 2015) among Triassic taxa. This fenestra is also very small in other taxa such as *Proterosuchus* (Welman, 1998), and we suggest such a small fenestra, if present, would not be detectable in the holotype (Fig. S2a-c).

Finally, although we were unable to anatomically identify any of the other cranial fragments in MPUM 8437a, a long fragment with a very expanded extremity conforms well with the stapes of *Avicranium* (Pritchard and Nesbitt, 2017) and is tentatively identified as the right stapes lying near its anatomical position.

MCSNB 4751 (*V. cenensis*, holotype)—The skull of the holotype and only known specimen of *V. cenensis* was last described in detail by Renesto and Binelli (2006). This specimen underwent severe diagenetic compression, making the individual bones hard to identify. Our interpretation of the premaxillae, left jugal, postorbital and parietal is identical to that of Renesto and Binelli (2006). However, our reexamination of the specimen led to different interpretations in the rest of the skull. We thus do not provide a complete redescription of this specimen, focusing instead first on the skull roof, which forms the basis of most of our rationale for a new interpretation, before describing other differences with the interpretation of Renesto and Binelli (2006).

The main difference of our new interpretation is the location of the sagittal suture of the skull. Renesto and Binelli (2006) tentatively followed this suture anterior to the medial margin of the left parietal, curving at the level of the third maxillary tooth. This region appears to represent a marked ridge in the holotype (Fig. S2f-h). Alternatively, we interpret a relatively straight fracture running anteriorly from the medial margin of the parietal as the sagittal suture of the skull. We argue that a suture would have likely broken or separated under diagenetic compression and slight posteroventral displacement of the left half of the skull rather than form a ridge, which supports our interpretation.

If this interpretation is correct, portions of both frontals can be identified, visible in dorsal view (Fig. S2f, g). The right frontal is nearly complete and much wider than previously recognized, similar to that of *Avicranium* (Pritchard and Nesbitt, 2017). However, the posterior

portion of both frontals is poorly preserved and obscured by the parietal. The left parietal appears to be incised by the frontal laterally, but the overall shape of the frontoparietal suture remains unclear. As tentatively identified by Renesto and Binelli (2006), a semicircular notch on the medial margin of the parietal framed by a slightly elevated ridge likely corresponds to the pineal foramen, which is absent in *M. preonensis* (see above) and *A. renestoi* (see below). A pineal foramen is common in Permo-Triassic diapsids but has been considered absent in all archosauriforms (Nesbitt, 2011). However, this structure was subsequently shown to be apparently retained in some archosauriforms (Stocker et al., 2016) and phythosaurs (Stocker and Butler, 2013), suggesting a more complex evolutionary history. More anteriorly, we tentatively identify a slightly anteromedially oriented separation line in the skull of *V. cenensis* as the suture between the right frontal and nasal. Only fragments of both nasals can be identified with some degree of certainty, and the very long anterolateral process of the left nasal figured by Renesto and Binelli (2006) cannot be seen. As such, the presence of the very large external nares reconstructed for this taxon by Renesto and Binelli (2006) is unclear.

The skull fragments immediately anterior to the orbit are very difficult to identify. We suggest that the very tall lamina lying just anterodorsal to the jugal is the lacrimal with a surimposed rectangular fragment, possibly corresponding to a fragment of the dorsal process of the maxilla. This interpretation contrasts with Renesto and Binelli's (2006), whereby both fragments make up a wide triangular dorsal process of the maxilla, but conforms well to the height of the lacrimal identified in *Megalancosaurus* (Fig. S2). In addition, the area on the dorsal margin of the maxilla where the dorsal and posterior processes meet can be reliably identified on the specimen as the entire dorsal margin of the posterior process, despite some breakage, shows a linear margin of finished bone (Fig. S2f, g). We thus cannot find evidence for a very wide dorsal process of the maxilla as reconstructed by Renesto and Binelli (2006), which we describe as rather narrow relative to the overall length of the bone. Given our interpretation of the lacrimal, we suggest that the badly crushed lamina partially overlain by the latter may correspond to the left prefrontal, although it is too poorly preserved to be anatomically described. The lateral margin of the maxilla above the alveolar region bears at least three supra-alveolar foramina, the most anterior of which is significantly larger and linked to a short anteriorly directed groove.

Renesto and Binelli (2006) only identified the left jugal and postorbital bones in the temporal region. We additionally recognize the left postfrontal and squamosal bones lying

respectively anterior and posterior to the postorbital. The postfrontal is broad and triangular, with a straight posterior margin, and conforms well with that of *Avicranium* (described below). The squamosal of *Vallesaurus* is triradiate, with no posterior lamina and a narrow lateral lamina that provides little lateral covering to the quadrate, as is also the case in *Megalancosaurus* (Fig. S2f-h; Renesto and Dalla Vecchia, 2005). A triradiate squamosal only partially covering the quadrate laterally has long been recognized as a synapomorphy of neodiapsids (Benton, 1985; Laurin, 1991), although it is absent in weigeltisaurids which have a broad lateral lamina largely covering the quadrate laterally as in other early amniotes (Bulanov and Sennikov, 2010; Buffa et al., 2021; Pritchard et al., 2021).

Renesto and Binelli (2006) figured the left quadrate of *Vallesaurus*, but we are unable to identify this structure during our examination of the holotype. Instead, we identify the left quadrate as a tall columnar bone with the articular condyles lying between the centrum and prezygapophyses of the axis, and the dorsal extremity partially covered by the ventral process of the squamosal (Fig. S2f-h). Renesto and Binelli (2006) figured this element and tentatively identified it as part of the opisthotic.

The quadrate of *Vallesaurus* is thus very tall, extending ventrally well beyond the level of the alveolar margin of the maxilla, and is strongly oriented posterodorsally so that the articular condyles lie much anterior to its dorsal head and the jaw articulation lies anterior to the occiput (Fig. S2f-h). In all of these characters, the quadrate of *Vallesaurus* conforms well with the more poorly preserved bone in *Megalancosaurus* (Fig. S2a-c). The quadrate is typically subvertical in Permo-Triassic diapsids (non-saurian diapsids, Currie, 1980; Reisz, 1981; lepidosauromorphs, Fraser, 1988; Griffiths et al., 2021), or markedly anterodorsally oriented so that the jaw articulation lies posterior to the occiput as in most crocopodan archosauromorphs (Nesbitt, 2011; Nesbitt et al., 2013; Ezcurra, 2016). A strongly posterodorsally angled quadrate so that the lower jaw articulation lies ventral to the upper alveolar margin and anterior to the occiput is prevalent in weigeltisaurids (Bulanov and Sennikov, 2015; Buffa et al., 2021), aetosaurs (Desojo et al., 2013) and pterosaurs (Dalla Vecchia, 2013, 2014) among Permo-Triassic taxa. At its dorsal extremity, the quadrate of *Vallesaurus* appears to lack a cephalic condyle, unlike in most saurian diapsids (Pritchard et al., 2018). However, a cephalic condyle is also absent in a few saurian taxa, such as some pterosaurs (e.g. *Carniadactylus*, *Rhamphorhynchus*, Prondvai and Ősi, 2011; Dalla Vecchia, 2018).

A slender lamina with unregular margins lies posterior to the quadrate shaft in the *Vallesaurus* holotype (Fig. S2). Owing to its position, it is likely a part of the quadrate complex, although we are unable to say whether it is a broken-off tympanic crest, a structure prevalent in Permo-Triassic saurians (Evans, 2016; Sobral and Müller, 2016) and currently unreported in drepanosauromphs (Pritchard and Nesbitt, 2017), or a slender quadratojugal with a long dorsal process as is typical in archosauromorphs (Nesbitt, 2011; Nesbitt et al., 2013; Ezcurra, 2016). Alternatively, this lamina could pertain to a portion of the occiput, though we suggest this is unlikely given its close relationship with the lateral surface of the quadrate. While we are unable to identify this lamina unequivocally, both of our interpretations would support a placement of drepanosauromophs among the crown-group.

Lastly, we identify a few bone fragments lying in the region of the anterior mandible in *Vallesaurus* as portions of the symphyseal region of the dentaries (Fig. S2). As best seen on the left side, the anterior tip of the dentary is edentulous, as in *Megalancosaurus*. Teeth are present throughout the dentary in most Permo-Triassic diapsids, although the most anterior part of the bone is also edentulous in the tanystropheid *Langobardisaurus*, (Saller et al., 2013) some allokotosaurians (Sues, 2003; Spielmann et al., 2008), rhynchosaurids (Ezcurra et al., 2016), aetosaurs (Desojo et al., 2013) and silesaurids (Langer et al., 2013), and pterosauromorphs, (Ezcurra et al., 2020). As the anterior portions of both hemimandibles in the *Vallesaurus* holotype are broken and somewhat displaced, it is unclear whether they tapered anteriorly, or if the anterior portion of the dentary was upturned or downturned (Fig. S2).

AMNH FARB 30834 (*A. renestoi*, holotype)—The holotype and only known specimen of *Avicranium* was recently µCT-scanned and described by Pritchard (2015) and Pritchard and Nesbitt (2017) and comprises a subcomplete skull and four cervical vertebrae. Based on our examination of the surface models segmented from the µCT data of this specimen (courtesy A. Pritchard), we concur with previous interpretations of the skull roof and dorsal temporal regions. However, we propose alternative interpretations for several structures in the cheek, palate and braincase (Fig. S3). As the detailed description of this specimen is underway elsewhere (A. Pritchard, pers. comm. 2022), we do not provide a detailed redescription nor a reconstruction of this specimen here, but only provide a statement of comparative anatomy in an effort to further our understanding of the phylogenetic position of drepanosauromorphs. Thus, after commenting on the maturity of this specimen, we provide first our comments on the

palate, which form the basis of most of our rationale for new interpretations, before describing selected circumorbital bones and braincase elements.

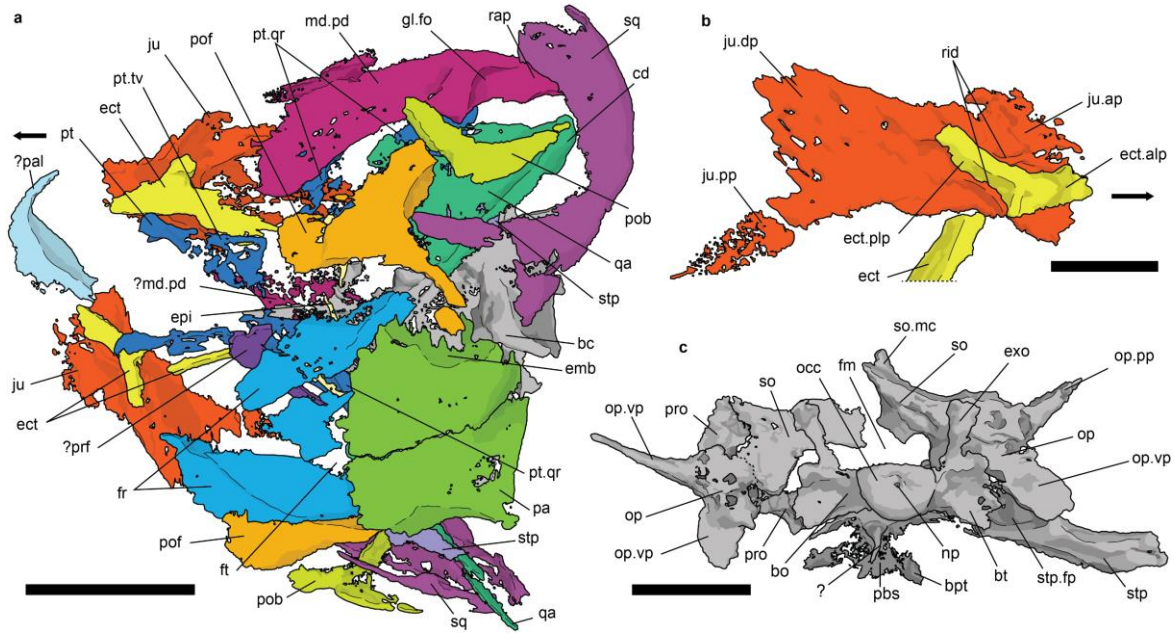

Figure A-S3: Cranial anatomy of *Avicranium renestoi* (Norian, New Mexico, USA). Interpretative drawings of STL files of holotype (AMNH FARB 30834) from µCT data (STL files courtesy A. Pritchard). **a**, subcomplete skull (lacking rostrum) in dorsal view. **b**, left jugal and ectopterygoid in medial view. **c**, subcomplete braincase in posterior view. Arrows indicate anterior direction. **bc**, braincase; **bo**, basioccipital; **bpt**, basipterygoid process; **bt**, basal tuberosities; **cd**, condyle; **ect**, ectopterygoid; **ect.alp**, anterolateral process of ectopterygoid; **ect.plp**, posterolateral process of ectopterygoid; **emb**, embayment; **exo**, exoccipital; **fm**, foramen magnum; **fr**, frontal; **ft**, fontanelle; **gl.fo**, glenoid fossa; **md.pd**, mandibular postdentary complex; **ju**, jugal; **ju.ap**, anterior process of jugal; **ju.dp**, dorsal process of jugal; **ju.pp**, posterior process of jugal; **np**, notochordal pit; **occ**, occipital condyle; **op**, opisthotic; **op.pp**, paroccipital process of opisthotic; **op.vp**, ventral process of opisthotic; **pa**, parietal; **pal**, palatine; **pbs**, parabasisphenoid; **pob**, postorbital; **pof**, postfrontal; **prf**, prefrontal; **pro**, prootic; **pt**, pterygoid; **pt.qr**, quadrate ramus of pterygoid; **pt.tv**, transverse flange of pterygoid; **qa**, quadrate; **rap**, retroarticular process; **so**, supraoccipital; **so.mc**, median crest of supraoccipital; **sq**, squamosal; **stp**, sapes; **stp.fp**, stapedial footplate. Scale bars, 1 cm (**a**); 5 mm (**b**, **c**).

Maturity assessment—Given the three-dimensional preservation of this specimen compared to the flattened specimens from Italy, we think it possible to assess the degree of maturity of the skull of *Avicranium* through the degree of ossification of the skull bones, a commonly used size-independent character to estimate morphological maturity in fossil diapsid reptiles (Griffin et al., 2021). There indeed appears to be a large triangular fontanelle between both frontals and parietals (Fig. S3), suggesting the bones of the dermal skull roof might be incompletely ossified. A similar, although much larger fontanelle has been used to suggest a juvenile ontogenetic stage in the Triassic rhynchocephalian *Colobops* (Pritchard et al., 2018;

Scheyer et al., 2020), and is also a common criterion of immaturity for extant reptiles (Rieppel, 1992; Maisano, 2002; Hoffman and Rowe, 2018). Alternatively, this could be an artefact of the resolution of the µCT scan, and contrast level of the slices (see Pritchard, 2015). Given this uncertainty, this maturity character is thus here considered equivocal, but raises doubt regarding the identification of this individual as morphologically mature.

Beyond this putative fontanelle, it is very hard to assess the morphological maturity of this specimen given (1) previously noted limitations of the µCT scan data; (2) the lack of phylogenetic bracket to reliably interpret size-independent characters if drepanosauromorphs are indeed non-saurian diapsids; (3) the inherent subjectivity in interpreting an incompletely immature structure as a plesiomorphy or evidence for morphological immaturity. Points (1) and (2) result directly from the studied material and are not discussed further. In contrast, point (3) has important bearing to our understanding of *A renestoi*. Indeed, Pritchard (2015) and Pritchard and Nesbitt (2017) interpreted the short and slender paroccipital process, large notochordal pit on the basioccipital, poorly developed basal tuberosities and large oval foramen as plesiomorphies supporting an identification of drepanosauromorphs as stem-saurians (discussed below). However, all of these characters have also been noted as evidence of morphological immaturity in both extant (Rieppel, 1993; Evans, 2008; Bhullar, 2012; Dufeau and Witmer, 2015) and extinct (Bullar et al., 2019) reptiles. Given this uncertainty, we remain cautious in several interpretations of the cranial anatomy of this specimen.

Palate—The skull of *Avicranium* appears slightly compressed so that the skull roof and temporal regions have been pushed to the left and slightly posteriorly whereas the braincase and palate remain mostly in their anatomical position (Fig. S3). Both epipterygoids indeed remain articulated with the pterygoids, indicating that the basicranial articulation is only slightly anteromedially displaced relative to the basipterygoid processes. Posterior to the basicranial articulation, the pterygoid extends as a long and wide quadrate ramus bearing distinct dorsal and arcuate flanges. A roughly rectangular fragment lying lateral of the right epipterygoid could be interpreted as the posterolateral corner of the transverse flange, but we concur with Pritchard (2015) that it is most likely a portion of the very wide quadrate ramus as it lies in the same plane as the more posterior portion, lacking the typical ventral angulation of the transverse flange (Fig. S3).

More anteriorly, both pterygoids are closely associated with Y-shaped bones (Fig. S3). Given the very close proximity to the quadrate ramus we suggest that these bones represent ectopterygoids, and not palatines as suggested by previous studies (Pritchard, 2015; Pritchard and Nesbitt, 2017). As such, the small preserved portion of the pterygoid anterior to the basicranial articulation likely corresponds to the transverse flange and not the palatal process.

Both ectopterygoids apparently met the entire lateral margin of the transverse flange of the pterygoid medially. Laterally, they expand rapidly into anterolateral and posterolateral processes, both of which clearly articulate with a large neighboring bone on both sides of the holotype (Fig. S3). Given the presence of an unequivocal articular surface on a ridge on the medial side on the latter bone, it is clear that it lies in its anatomical position relative to the palate. Owing to its large extension posterior to its articulation with the ectopterygoid, we thus identify this bone as the jugal, and not the maxilla contrary to previous interpretations (Pritchard, 2015; Pritchard and Nesbitt, 2017).

Lastly, the small fragment lying anterior to the ectopterygoid, identified as the premaxilla by previous studies, is of unclear attribution. Given its location, we suggest it might be a portion of the left palatine, however this cannot be ascertained and we are unable to anatomically orient and describe this element.

Circumorbital bones—As best seen on the left side, the jugal of *Avicranium* is much larger than that of *Vallesaurus*, extending beyond the anterior margin of the orbit and expanding dorsoventrally anterior and posterior to its contribution to the ventral orbital margin (Fig. S3). A jugal with an anterior process extending at least to the anterior orbital margin is typical in archosauromorphs, excluding the maxilla from the orbit (Nesbitt, 2011; Nesbitt et al., 2013; Ezcurra, 2016), but contrasts with the condition in other Permo-Triassic diapsids where this process is shorter, especially in weigeltisaurids (Bulanov and Sennikov, 2015; Buffa, 2021) and rhyncocephalians (Chambi-Trowell et al., 2019) where the very short anterior process of the jugals does not reach the midpoint of the orbit diameter. In addition, while the jugal of most Permo-Triassic diapsids tapers anteriorly, including in *Megalancosaurus* and *Vallesaurus* (Fig. S2), that of some archosauriforms and most archosaurs has a more rectangular anterior process (Nesbitt, 2011; Ezcurra, 2016). Furthermore, a marked dorsoverntral expansion of the jugal anterior to the orbit as seen in *Avicranium* is otherwise common in erythrosuchids and eucrocopodan archosauriforms (Nesbitt et al., 2009).

More posteriorly, the jugal bears a rather wide dorsal process for the postorbital, and a narrow and long posterior process that likely extended to the level of the squamosal, possibly reaching the posterior margin of the skull (Fig. S3). However, it is unclear if a contact between the jugal and squamosal was present, closing the inftratemporal bar or simply approaching the latter bone, similar to the condition in *Prolacerta* and early rhynchosaurs (Modesto and Sues, 2004; Ezcurra et al., 2016). As discussed by Buffa et al. (2021), such a large contribution of the posterior process of the jugal to the infratemporal bar contrasts with its more modest contribution in non-saurian diapsids and is suggestive of a secondarily reacquisition of this bar, which has only been attested in some saurian clades (especially archosauriforms; Müller, 2003) and suggested in weigeltisaurids (Buffa et al., 2021). Lastly, the posterior portion of the jugal of *Avicranium* is clearly posteroventrally inclined relative to the main axis of the articular surface for the ectopterygoid (Fig. S3). Thus, if the jugal-ectopterygoid articulation is oriented horizontally and taken as a reference for the main axes of the palate and alveolar margin as is typical in most Triassic reptiles (e.g. Borsuk-Białynicka and Evans, 2009a, b; Evans and Borsuk-Białynicka, 2009), then the jugal extends markedly posteroventral to this level. This would suggest the jaw articulation lied markedly ventral to the alveolar margin of the maxilla, as in other drepanosauromorphs, weigeltisaurids, aetosaurs and pterosaurs (discussed for *Vallesaurus* above).

The slender curved bone identified as the jugal in previous studies (Pritchard 2015; Pritchard and Nesbitt, 2017), lies in a mostly dorsoventral orientation between the palate and skull roof near the expected location of the anterior orbital margin (Fig. S3). We thus tentatively identify it as the prefrontal given its height and close position to the forntal, although it could also be identified as the lacrimal given the high lacrimal present *Megalancosaurus* and *Vallesaurus* (Fig. S2).

Pritchard and Nesbitt (2017) describe *Avicranium* with a broad squamosal extensively covering the quadrate externally through well-developed lateral and posterior laminae, a condition that has long been considered typical of early amniotes, araeoscelidians and weigeltisaurids (Heaton, 1979; Reisz, 1981; Bulanov and Sennikov, 2010; Buffa et al., 2021) and plesiomorphic for all other diapsids (Benton, 1985; Laurin, 1991). We concur that the squamosal of this taxon bears a prominent posterior lamina (Fig. S3). However, the lateral lamina of *Avicranium* is rather narrow, only comprising a short anterior ventral projection that likely did not cover all of the quadrate laterally (as was reconstructed by Pritchard and Nesbitt,

2017:fig. 3), giving the squamosal a strongly concave anterior margin (Fig. S3). In contrast, the lateral lamina of the squamosal of other early amniotes is broad throughout its length, even when temporal fenestrae are present (e.g. *Petrolacosaurus*, Reisz, 1981). However, it is possible that the relatively thin lateral lamina of *Avicranium* is due to limited resolution and contrast of the µCT scan, or to an immature stage of ossification (see above). We thus suggest that the presence of an anteroposteriorly broad lateral lamina is equivocal in this taxon. Further supporting this point, the squamosal of both *Megalancosaurus* and *Vallesaurus* clearly show only a narrow lateral lamina and lack all traces of a posterior lamina (Fig. S2). Owing to these observations and the apical position in which Pritchard and Nesbitt (2017) recover *Avicranium* among drepanosauromorphs, it is possible the peculiar squamosal morphology of *Avicranium* is apomorphic.

Braincase—The braincase of *Avicranium* is nearly complete, with most portions lying in anatomical position (Fig. S3). Interestingly, Pritchard (2015) and Pritchard and Nesbitt (2017) appear to use the left portion of the braincase as the basis for both their anatomical description and reconstruction. However, we suggest that the right half of the braincase is much better preserved. The presence of the right stapes still in anatomical position (Fig. S3) whereas the left has been displaced further supports this interpretation. As described by Pritchard and Nesbitt (2017), the main axis of the parasphenoid is dorsally oriented so that the basipterygoid processes lie ventral to the basal tuberosities (Fig. S3), a condition that is commonly present in non-proterosuchid archosauriforms (Gower and Sennikov, 1996; Nesbitt, 2011; Ezcurra, 2016) as well as allokotosaurian archosauromorphs (Spielmann et al., 2008; Flynn et al., 2010). However, we concur with Pritchard and Nesbitt (2017) that there is no trace of a laterosphenoid in the surface models, the presence of which has long been considered a synapomorphy of archosauriforms (Clark et al., 1993; Nesbitt, 2011).

As preserved, the roof of the braincase bears a sharp dorsal crest in the sagittal plane directly above the occipital condyle (Fig. S3). This is the expected location of the medial crest of the supraoccipital which is common in Permo-Triassic saurians (Ezcurra, 2016), but is absent in most other neaodiaspids (Carroll, 1981; Gardner et al., 2010; Buffa, et al., 2021). The fragment identified as the supraoccipital by (Pritchard, 2015) is indeed part of this bone, but ought to be reoriented dorsally to conform to what is preserved on the right side. The large foramen magnum is thus mostly preserved, framed by the supraoccipital, exoccipital and basioccipital (Fig. S3).

The right opisthotic appears undistinguishably fused to the supraoccipital in the surface models of the *Avicranium* holotype, and we remain cautious regarding the demarcation between the supraoccipital and left opisthotic made by previous studies as both structures seem largely continuous (Fig. S3). We concur with Pritchard's (2015) identification of the very slender paroccipital process that apparently failed to reach the dermal skull bones. Such a short paroccipital process is uncommon among early diapsids, being present in the araeoscelidian *Petrolacosaurus* but not *Araeoscelis* (Vaughn, 1955; Reisz, 1981), in some non-saurian neodiapsids (*Claudiosaurus*, *Hovasaurus*, Carroll, 1981; Currie, 1981, but not *Youngina*, Gardner et al., 2010). In contrast, a longer process that reaches the dermal skull roof laterally is prevalent throughout Permo-Triassic saurians (Laurin, 1991). As stated above, the paroccipital process expands laterally and increases in thickness during ontogeny in both extant and extinct saurians (Bhullar, 2012; Bullar et al., 2019), so it is possible the short paroccipital process results from an immature ontogenetic stage. However, this is unlikely as we are unaware of any taxon where a contact between the paroccipital process and dermal skull is achieved during postnatal ontogeny.

While we concur with the identification of the basioccipital-exoccipital complex of previous studies, we interpret several structures differently. First, Pritchard and Nesbitt (2017) describe the basioccipital of *Avicranium* as lacking well-developed basal tuberosities extending ventral to the occipital condyle. While it is true that the basal tuberosities do not expand markedly ventrally, they actually extend a very short distance beyond the ventral margin of the condyle once the floor of the foramen magnum is oriented horizontally (Fig. S3). In addition, they expand markedly laterally so that the bone is overall three times as wide as the occipital condyle. This differs markedly from the morphology of other taxa showing poorly developed basal tuberosities such as captorhinids or non-saurian diapsids in which the basal tuberosities are only incipient (Price, 1935; Vaughn, 1955; Gardner et al., 2010). In fact, transversely broad but dorsoventrally short basal tuberosities seem to be indicative of an immature ontogenetic stage, as it can be seen in juveniles of some extant (Evans, 2008) and extinct (Bhullar et al., 2019) reptiles in which the adult has ventrally expanded basal tuberostities.

Second, Pritchard and Nesbitt (2017) describe a large, elliptical notochordal pit on the posterior surface of the occipital condyle of *Avicranium*. There is indeed an unequivocal pit marking the passage of the notochord (Fig. S3). However, we argue that the notochordal pit of *Avicranium* is much less extensive than that of other early amniotes such as captorhinids or

non-saurian diapsids (Gardner et al., 2010; deBraga et al., 2019). In fact, we find it rather similar to the smaller notochordal scar of proterochampsian archosauriforms (Dilkes and Sues, 2009; Trotteyn and Haro, 2011), and to that of the enigmatic eucrocopod *Polymorphodon* (Sues et al., 2020). Furthermore, as some extinct taxa close the notochordal pit during postnatal ontogeny (see Dufeau and Witmer, 2015), it is possible that the depth of this notochordal pit is accentuated by an immature degree of ossification (see above).

We concur with Pritchard and Nesbitt (2017) that *Avicranium* has an exceptionally robust stapes for a Triassic diapsid (Fig. S3). The stapes is indeed much more slender and rod-like than in *Youngina* (Gardner et al., 2010), weigeltisaurids (SMNK-PAL 2882, VB pers. obs.) and saurians (Sobral et al., 2016), and such a robust stapes is only found in earlier amniotes and non-neodiapsid disapsids (Price, 1935; Reisz, 1981). However, as also noted by Pritchard and Nesbitt (2017), the stapes of *Avicrnaium* lacks the dorsal process typical of non-neodiapsid reptiles (Price, 1935; Reisz, 1981) and the stapedial foramen that is prevalent in the latter taxa and is also present in *Youngina* (Gardner et al., 2010).

Mandible—Parts of both mandibles are preserved in the holotype of *Avicranium*. The right postdentary process is the best-preserved portion and shows a deep glenoid fossa prolonged by a robust retroarticular process (Fig. S3), contrary to the much dorsoventrally shorter retroarticular process of other drepanosauromorphs (Fig. S2; Colbert and Olsen, 2001; Renesto and Dalla Vecchia, 2005). A strong retroarticular process has long been considered a synapomorphy of saurians, contrasting with the shorter, spur-like process of non-saurian neodiapsids (Laurin, 1991), however, the elongation is variable among saurians, especially archosauromorphs, with several taxa such as some pseudosuchians or pterosaurs also having short retroarticular processes (Dalla Vecchia, 2014; Bona et al., 2022).

Pritchard and Nesbitt (2017) identified a very large structure composed of numerous bone fragments as the anterior portion of the right lower jaw. However, we suggest this structure comprises the right jugal (which lies in articulation with the ectopterygoid) and actual fragments of the lower jaw (Fig. S3). The latter, however, are too poorly preserved to be anatomically described. Lastly, we concur with Pritchard (2015) that the presence of an external mandibular fenestra is equivocal in this specimen.

Comments on skull reconstruction—We do not attempt a new reconstruction of the skull of *Avicranium* for the following reasons: (1) such endeavor would require a detailed

redescription of the entire skull, which is out of the scope of this paper; (2) some surface models should be slightly resegmented (e.g. to separate the right jugal from possible mandibular fragments, see above), which is not attempted here; (3) a detailed redescription of *Avicranium* is currently underway (A. Pritchard, pers. comm. 2022) which will likely provide more detailed data of the relationship between the skull bones. Nevertheless, our rationale for new interpretations of some bones has implications on the reconstruction of the skull, which warrants discussion.

First, *Avicranium* has been reconstructed with a long, tapering and edentulous rostrum, one of the most striking 'bird-like' characters of this taxon (Pritchard and Nesbitt, 2017). However, our reinterpretation of the 'premaxilla' 'left maxilla', and 'right dentary' of previous studies (Pritchard, 2015; Pritchard and Nesbitt, 2017) as a possible fragment of palatine, left jugal, and right jugal (and possible right lower jaw fragments) respectively suggest that all bones of the rostrum are actually absent in this specimen (Fig. S3). Thus, owing to our interpretation nothing can be said of the rostrum or marginal dentition of *Avicranium*.

Second, the newly identified jugals of *Avicranium* are very large. In fact, simply replacing the 'jugal' identified by previous study by this bone on Pritchard and Nesbitt's (2017:fig. 3) reconstruction would form an extremely small, dorsoventrally constricted orbit, contrasting with the morphology of most Permo-Triassic taxa (e.g. Lautenschlager, 2022). This is also the case if the jugal is oriented slightly posteroventrally so that the jugal-ectopterygoid joint is horizontal (as discussed above). Thus, our interpretation of the jugal suggests that the arrangement of the temporal bones needs to be revised, which is out of the scope of the present paper as it would require a detailed redescription of the other temporal bones and their articular surfaces. However, we note that while the dorsal portion of postorbital bar (i.e. postfrontal and postorbital) appears continuous in Pritchard and Nesbitt's (2017:fig. 3C) reconstruction, the supratemporal fossa is not and would be interrupted laterally by the postorbital bar. This likely suggests that the postorbital and squamosal (and possibly postfrontal) may have to be more ventrally positioned and reoriented posteroventrally relative to the skull roof. This would lead to a morphology similar to that of other drepanosaurs and pterosaurs, with a more inflated skull roof and anteroventrally sloping posterior skull margin. However, we stress again that no reconstruction was attempted here so this remarks on the reconstruction of the skull of *Avicranium* should be considered preliminary pending a detailed revision of the anatomy of this

specimen. None of these considerations are thus included in our phylogenetical dataset at present.

Lastly, *Avicranium* has also been described with an edentulous palate (Pritchard, 2015; Pritchard and Nesbitt, 2017). However, as for the rostrum and anterior mandible, our reinterpretations of the purported 'palatines' and 'anterior processes of the pterygoids' as ectopterygoids and transverse flanges of the pterygoids indicate nothing of the palate anterior to the transverse flange of the pterygoid is preserved (Fig. S3). No neodiapsids shows ectopterygoid teeth, and the dentition of the transverse flange of the pterygoid is absent in nearly all Permo-Triassic saurians (Matsumoto and Evans, 2017). However, palatal dentition is otherwise prevalent in lepidosauromorphs and non-archosaurian archosauromorphs (Matsumoto and Evans, 2047), and it is still present in some early archosaurs (e.g. *Eoraptor*, Sereno et al., 2013). Thus, given our reinterpretation of the palate of *Avicranium*, the lack of dentition on its preserved portions do not indicate that the palate was entirely edentulous.

As a result, our reinterpretation of the skull of *Avicranium* differs significantly from previous reconstructions. While some of the 'bird-like' traits of this taxon are undoubtedly present, such as the inflated skull roof, others such as the lack of marginal or palatal teeth cannot be assessed are the respective bones are not preserved in the specimen. Based on preliminary remarks, it is likely the temporal region was higher and slightly anteroventrally angled as in other drepanosauromorphs (described above).

Postcranial skeleton

The drepanosauromorph postcranium has been subject to several detailed descriptions (Pinna, 1984; Berman and Reisz, 1992; Renesto, 1994a, b; Renesto and Paganoni, 1995; Colbert and Olsen, 2001; Harris and Downs, 2002; Renesto and Fraser, 2003; Fraser and Renesto, 2005; Renesto and Binnelli, 2006; Renesto et al., 2009, 2010; Dalla Vecchia and Cau, 2015; Castiello et al., 2016; Pritchard et al., 2016), which need not be repeated here. Instead, we provide only new anatomical details resulting from our direct observations of the specimens in an effort to further our understanding of the phylogenetic relationships of drepanosauromorphs.

Figure A-S4: Presacral vertebrae of *Megalancosaurus preonensis* and *Vallesaurus cenensis* (Norian, Italy). **a**, cervical and anterior dorsal vertebrae of *M. preonensis* (MPUM 6008) in mostly left lateral view. **b**, posterior dorsal vertebrae of *M. preonensis* (MPUM 6008) in posterior view. **c**, cervical vertebrae of *V. cenensis* (MCSNB 4751) in mostly ventral view. **d**, anterior dorsal vertebrae of *V. cenensis* (MCSNB 4751) in left lateral view. Arrows indicate anterior direction. **ax**, axis; **cd**, condyle; **ce**, centrum; **ct**, cotyle; **cv**, cervical vertebra; **dv**, dorsal vertebra; **hpp**, hypapophysis; **hpc**, hyposphene; **il**, ilium; **nc**, neural canal; **ns**, neural spine; **para**, parapophysis; **poz**, postzygapophysis; **prz**, prezygapophysis; **sc**, scapula; **snb**, supraneural bone; **sv**, sacral vertebra; **syn**, synapophysis. Scale bars, 5 mm (**a**, **b**); 2 mm (**c**, **d**).

Cervical vertebrae—The drepanosauromorph cervical vertebrae were extensively described and discussed by Renesto and Fraser (2003) Renesto et al. (2009) and Dalla Vecchia and Cau (2015) so their anatomy will only be summarized here. As seen in *Megalancosaurus* and *Vallesaurus* (Fig. S4), as well as *Hypuronector* (Colbert and Olsen, 2001), the cervical vertebrae are much longer than the anterior dorsals in drepanosauromorphs. A similar elongation is present in araeoscelidians (Reisz, 1981; Reisz et al., 1984) and weigeltisaurids (Pritchard et al., 2021; Buffa et al., 2022) among non-saurian diapsids, and is also prevalent in non-archosauriform archosauromorphs (except rhynchosaurs) and ornithodirans (Nesbitt, 2011). There is no trace of cervical intercentra, as in weigeltisaurids (Buffa et al., 2022), which Pritchard et al. (2021) recovered as a synapomorphy of Avicephala. However, the absence of

cervical intercentra is also typical for non-archosauriform archosauromorphs (except *Prolacerta*) and archosaurs (Nesbitt, 2011).

The cervical vertebrae of drepanosauromophs have been described as both procoelous and heterocoelous, with a kidney-shaped anterior cotyle and posterior condyle (Fig. S4; Renesto and Fraser, 2003; Renesto et al., 2009; Dalla Vecchia and Cau, 2015). Few Permo-Triassic diapsids exhibit procoelous cervical vertebrae, namely some tanystropheids (*L. pandolfii*, *T. ahynis*, Pritchard et al., 2015), *Trilophosaurus* (Spielmann et al., 2008), and pterosaurs (Dalla Vecchia, 2013, 2014). However, heterocoely, whereby the intervertebral articular surfaces are kidney- or saddle-shaped has otherwise only been reported in some pterosaurs (e.g. *Carniadactylus*, *Rhaeticodactylus*; Dalla Vecchia, 2009, 2014).

The cervical centrum of drepanosauromorphs is posteriorly displaced relative to the zygapophyses so that the posterior condyle lies markedly posterior to the postzygapophyses (Fig. S4). As a result, the intercentral and interzygapophyseal articulations do not lie in the same plane vertically. In addition, the centrum tapers markedly posteriorly, so that its anterior width is much broader than its posterior, giving it a Y-shaped outline in ventral view (Fig. S4). Lastly, all drepanosauromorphs show a long, keel-like hypapophyses that extends posteroventrally beyond the level of the posterior condyle (Fig. S4). As noted by Renesto and Fraser (2003) and Dalla Vecchia and Cau (2015), in all of these characters, the cervical centra of drepanosauromorphs sharply contrast to those of all Permo-Triassic diapsids in which the roughly cylindrical centrum extends to the same anteroposterior level as the zygapophyses, but conform well to that of Triassic pterosaurs which only differs in a having more incipient hypapophyses.

The cervical neural arch is robust in all drepanosauromorphs, extending some distance beyond the lateral margins of the centrum (especially posteriorly) and giving the vertebrae an overall quadrangular shape in ventral view (Fig. S4) similar to that of Triassic pterosaurs (Dalla Vecchia and Cau, 2015). As seen in the isolated drepanosauromophs vertebrae from Cromhall Quarry (Renesto and Fraser, 2003; Dalla Vecchia and Cau, 2015), the cervicals bore robust and distinct diapophyses and parapophyses, and this was likely the case in other drepanosauromorphs as well given the similarities in their parapophyses (the diapophyses could not be unequivocally identified in the cervicals of any of the MCSNB, MPUM and MFSN specimens given their state of preservation, VB pers. obs.). The zygapophyses are very robust

and bear subvertical articular surfaces (Fig. S4), as in Triassic pterosaurs but contrary to the more medially oriented surfaces of all other Permo-Triassic reptiles (Dalla Vecchia and Cau, 2015).

Interestingly, Dalla Vecchia and Cau (2015) report small foramina on the neural arch of isolated drepanosauromorph cervical vertebrae that lie in the same position as the pneumatic foramina of pterosaurs (e.g. Butler et al., 2009). We were unable to confirm the presence of similar foramina in any of the MCSNB, MPUM and MFSN specimens (VB, pers. obs.), but they would have likely been obliterated by diagenetic compression, making their presence of absence equivocal in these specimens. Lastly, the cervical neural spines of drepanosauromoprhs are triangular, short and strongly anterodorsally oriented. Anterodorsally oriented cervical neural spines are common in archosauromorphs (Pritchard et al., 2015), and are also present in the weigeltisaurid *Coelurosauravus* (Buffa et al., 2022), in contrast to the more vertical spines of other diapsids (Hofstetter and Gasc, 1969; Carroll, 1981; Reisz, 1981).

Lastly, cervical ribs appear absent in both *Megalancosaurus* and *Vallesaurus* (Fig. S4), contrary to the situation in other Permo-Triassic diapsids. Conversely, we concur with Pritchard and Sues (2019:1747) that the cervical ribs of *Avicranium* are present appear fused to the associated neural arches, as in trilophosaurid archosauromorphs and some pterosaurs (Dalla Vecchia, 2014; Pritchard and Sues, 2019).

Dorsal vertebrae—The drepanosauromorph dorsal vertebrae have been subject to detailed descriptions, in particular the most anterior ones which show unique notarium-like adaptations in relation to the front limb (Renesto, 1994a; Colbert and Olsen, 2001; Fraser and Renesto, 2005; Renesto and Binelli, 2006). The dorsal centra of drepanosauromorphs are amphicoelous (Pinna, 1984; Fraser and Renesto, 2005; Renesto et al., 2009) except in *Megalancosaurus* where they are procoelous (Fig. S4, Renesto, 2000). Procoelous dorsal vertebrae are only present in some tanystropheids (e.g. *Langobardisaurus*, *Tanytrachelos*; Pritchard et al., 2015), tilophosaurids (but only in the anterior dorsals, Spielmann et al., 2008) and some pterosaurs (Dalla Vecchia, 2013, 2014) among Permo-Triassic taxa.

None of the presacral vertebrae of *Megalancosaurus* and *Drepanosaurus* show any trace of a notochordal canal, and this also appears to be the case in *Vallesaurus* although the preservation of the specimens precludes a definite statement (Fig. S4; Renesto et al., 2010). Renesto et al. (2010) similarly suggested the presacral centra of *Hypuronector* were not

notochordal (contra Colbert and Olsen, 2001). Conversely, Berman and Reisz (1982) report notochordal centra in *Dolabrosaurus*, but we suggest the presence of a notochordal canal is equivocal based on published photographs (Renesto et al., 2010:figs. 16-17). Further supporting this point, no notochordal canal has been described in the several three-dimensional isolated presacral vertebrae referred to drepanosauromorphs (Fraser and Renesto, 2005; Renesto et al., 2009, 2010). A notochordal persisting in mature individuals is typical in Permo-Triassic non-archosauromorph diapsids, but all archosauromorphs show a completely closed notochordal canal with the exception of the early-diverging *Aenigmastropheus* (Ezcurra et al., 2014; Ezcurra, 2016).

The dorsal neural arches of drepanosauromorphs are very tall, with pedicels markedly exceeding the height of the centrum, especially in the more anterior vertebrae (Fig. S4). A similar, though less extreme pedicel height is also seen in rhyncocephalians (Evans, 1981; Fraser and Walkden, 1984; O'Brien et al., 2018). As seen in *Megalancosaurus* and *Vallesaurus* (Fig. S4), and likely also in *Drepanosaurus* given its unicephalous ribs, the dorsal vertebrae only bore a single costal facet throughout the column. While most non-archosaurian diapsids also have a single costal facet in the posterior dorsals, the presence of a single costal facets in the anterior dorsals is typical of 'younginiforms' (Gow, 1975; Currie, 1980) and lepidosauromorphs (Fraser and Walkden, 1984; O'Brien et al., 2018).

The dorsal neural spines of drepanosauromorphs are much higher than broad in lateral view, as in most 'younginiforms' (Currie, 1981b) and archosauromorphs except tanystropheids (Ezcurra, 2016) but contrary to the much lower neural spines of weigeltisaurids (Buffa et al., 2022) and Triassic lepidosauromorphs (O'Brien et al., 2018; Simões et al., 2018). As seen in *Drepanosaurus*, *Megalancosaurus* and *Vallesaurus*, but not *Hypuronector*, the most anterior dorsals show a very strong anteroposterior expansion of the neural spines, some of which fuse together in *Drepanosaurus* and *Megalancosaurus*, and this region is reinforced by a 'supraneural bone' of uncertain osteological nature (Renesto et al., 2010). While this structure is reminiscent of the notarium pterodactyloid pterosaurs (as well as birds), it is unlikely that they are homologous given the lack of notarium in the early diverging rhamphorhynchoid pterosaurs (Dalla Vecchia, 2013, 2014).

An accessory intervertebral articulation has been described in both *Dolabrosaurus* (Berman and Reisz, 1992) and *Megalancosaurus* (Renesto, 1994, 2000). As seen in posterior

view in *Megalancosaurus* (e.g. MPUM 6008, Fig. S4), the postzygapophyses are reduced and unidentifiable in the posterior dorsals. According to Renesto (2000), the prezygapophyses instead fit into a pair of excavations on the posterior surface of the neural arch. Both depressions frame a sharp postpinal lamina that runs dorsoventrally from the ventral half of the neural spine to the dorsal margin of the neural canal. In its most ventral part, this lamina transitions into a more robust posterior process that likely fitted into a corresponding cavity on the anterior margin of the preceding vertebra (Fig. S4). Such a cavity has been described in the dorsals of *Dolabrosaurus*, preserved in anterior view, suggesting both taxa share this accessory intervertebral articulation (Berman and Reisz, 1992). We were unable to confirm the presence of this structure in any of the other drepanosauromorph MCSNB, MFSN and MPUM specimens, but this is most likely due to their nature of preservation as most vertebrae are either not exposed in anterior or posterior view, badly crushed, or both.

Previous studies have not addressed the homology of the accessory intervertebral articulation of drepanosauromorphs (Berman and Reisz, 1992; Renesto, 1994, 2000). As the prezygapophyses apparently fit into the excavations framing the postspinal lamina, it is possible they likely represent the expected position of the postzygapophyses, which have been used as a landmark to define other accessory intervertebral articulations in amniotes. The posterior process indeed lies roughly at the same level as the cavities, or slightly more ventral (Fig. S4). This position contrasts with the zygosphene-zygantrum articulation typical of some lepidosaurians (as defined by Hoffstetter and Gasc, 1966) or the intervertebral articulation described in 'younginiforms' (Currie, 1981a, b) as both lie dorsal to the zygapophyseal surfaces. The more ventral position of the posterior process of drepanosauromorphs is thus more consistent with an hyposphene-hypantrum articulation of archosaurs as defined by Stefanic and Nesbitt (2018, 2019), and its slender, dorsoventrally oriented shaped also conforms well with this type of articulation. However, it is unclear if the hyposphene-like structure of drepanosauromorphs bore actual articular surfaces given the preservation of the specimens. In addition, the lack of unequivocal hyposphene-hypantrum in any small-sized archosaur suggests it is only present in large-sized taxa (> 130 mm in femur length, Stefanic and Nesbitt, 2019). Given the small size of all known drepanosauromorphs, the presence of an hyposphene-hypantrum articulation in these taxa would represent the first known occurrence in a small-sized reptile. We thus think the presence of an hyposphene-hypantrum articulation in drepanosauromoprhs is unlikely. Alternatively, the posterior process of drepanosauromorphs

could result from a reduction and fusion of both postzygapophyses into a single, median process. However, we are unaware of the presence of such fusion in the dorsal column of any other diapsid.

The dorsal ribs of all drepanosauromorphs except *Megalancosaurus* are strongly curved proximally, giving the animal a barrel-shaped trunk (Renesto et al., 2010), a morphology that is only shared with the allokotosaurian *Teraterpeton* (Sues, 2003) and to a stronger degree in doswelliid archosauriforms (Dilkes and Sues, 2009; Schoch and Sues, 2014) among Permo-Triassic diapsids. Lastly, *Hypuronector*, *Megalancosaurus* and *Drepanosaurus* all have the posterior ribs fused to their associated neural arches, which extends roughly to the middle of the column in *Hypuronector* and *Megalancosaurus* (Fig. S4). Such fusion has been reported in some tanystropheids (e.g. *Langobardisaurus*, *Tanystropheus*; Pritchard et al., 2015) and allokotosaurians (*Azendohsaurus*, *Trilophosaurus*; Spielmann et al., 2008; Nesbitt et al., 2015), although it is restricted to the posterior dorsals.

Sacral vertebrae—Various number of sacral vertebrae have been reported in drepanosauromorphs. The sacral series is best preserved in specimen MBSN 25 of *M. edennae*, which clearly show three sacrals (Renesto, 2000; Renesto et al., 2010, although four sacrals were initially identified by Renesto, 1994a). In this specimen, the three sacrals follow a vertebra whose ribs are obscured (the 'first sacral' of Renesto, 1994a), itself following the last vertebra with long and curved ribs. In specimen MPUM 8437b of *M. preonensis*, the last vertebra with long curved ribs is followed by one with half as long ribs that extend strictly laterally (Fig. S5). However, as this rib tapers to a point and ends rather far from the iliac blade (even taking into account a slight postmortem displacement), we do not consider it as the first sacral vertebra, contrary to previous studies (Renesto, 1994a, 2000; Renesto et al., 2010). The two following vertebrae show short, curved ribs lying near the iliac blade, which we identify as the first and second sacrals (Fig. S5). The vertebra following the second sacral is badly preserved, but bears a rib that is mostly obscured by the iliac blade (Fig. S5), we thus identify this vertebra as the third sacral, leading to a count of three sacral vertebrae in both *Megalancosaurus* species. Three sacral ribs were also identified in *Dolabrosaurus* (Berman and Reisz, 1992 contra Renesto et al., 2010 who identify the first caudal as a fourth sacral).

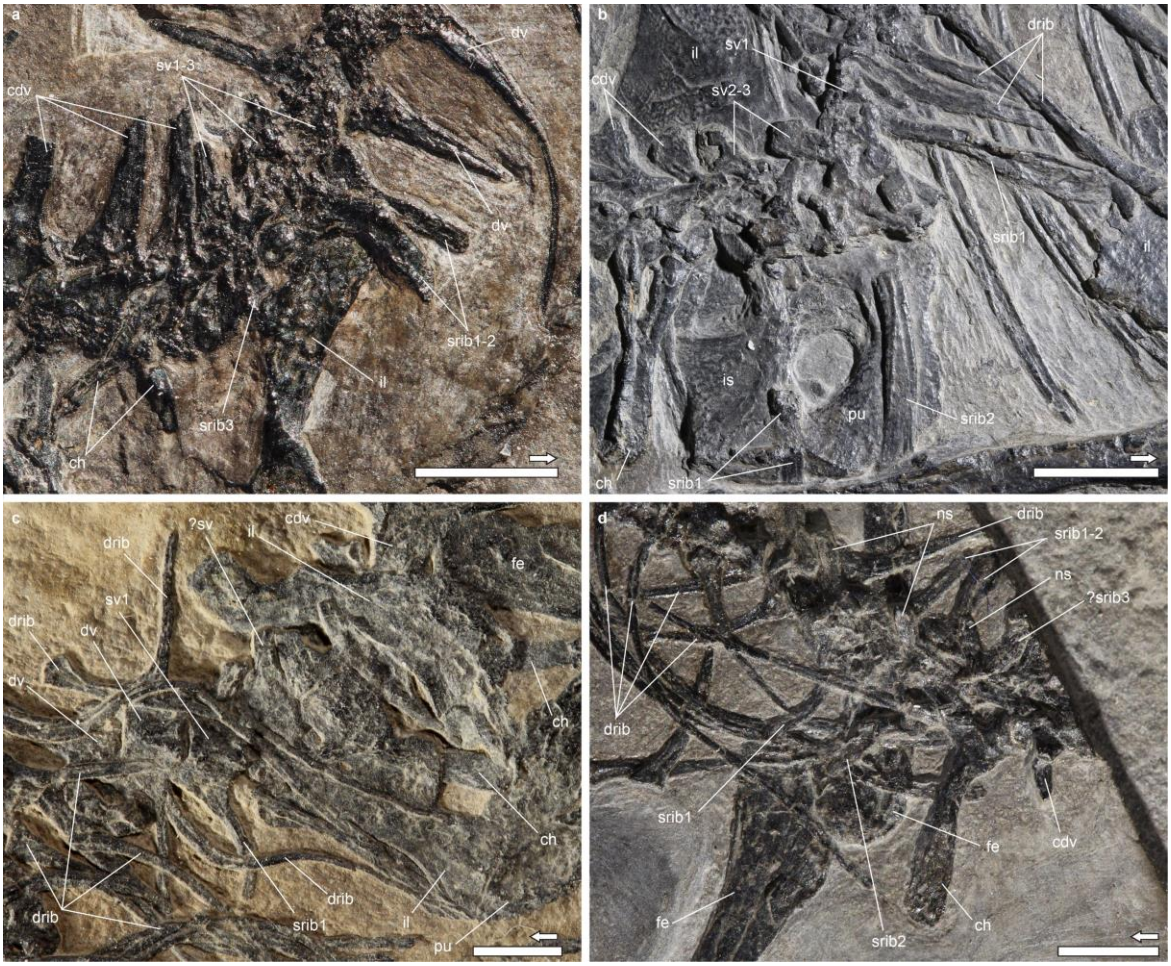

Figure A-S5: Sacral vertebrae of Italian drepanosauromorphs (Norian). **a**, sacral vertebrae of *M. preonensis* (MPUM 8473b) in mostly posterior view. **b**, sacral vertebrae of *D. unguicaudatus* (MCSNB 5728) in mostly left lateral view. **c**, sacral vertebrae of *V. cenensis* (MCSNB 4751) in mostly ventral view. **d**, sacral vertebrae of *V. zorzinensis* (MCSNB 11342) in dorsal view. Arrows indicate anterior direction. **cdv**, caudal vertebra; **ch**, chevron; **dri**, dorsal rib; **dv**, dorsal vertebra; **fe**, femur; **il**, ilium; **is**, ischium; **ns**, neural spine; **pu**, pubis; **srib**, sacral rib; **sv**, sacral vertebra. Scale bars, 5 mm (**a**); 10 mm (**b**); 2 mm (**c**, **d**).

Two sacral vertebrae have been identified in *V. cenensis* but three in *V. zorzinensis* (Renesto and Binelli, 2006; Renesto et al., 2010). Based on the sacral and posterior dorsal series of *Megalancosaurus*, we identify the last dorsal with a shorter, tapering rib as the last dorsal, and the two following ribs as that of the first and second sacrals (Fig. S5). There appears to be a short rib posterior to that of the second sacral on the right side, but the left rib cannot be seen as the rest of this vertebra and the first caudals are badly preserved. Thus, we tentatively follow Renesto et al. (2010) in identifying three sacral vertebrae in *V. zorzinensis*. The number of sacral vertebrae cannot be determined in the holotype of *V. cenensis* because of the disarticulation of the posterior region of the presacral column, and several vertebrae are hidden by the left pelvis

(Fig. S5). Nevertheless, two closely articulated vertebrae lie immediately anterior to the left ilium, the first which bears straight and tapering ribs and the second which bears ventrally curved ribs which conform well to the last dorsal and first sacral of both *Megalancosaurus* and *V. zorzinensis* (Fig. S5). Whether additional sacral vertebrae were present in *V. cenensis* is unclear.

Pinna (1980, 1984, 1986) and Renesto et al. (2010) report two sacrals in *Drepanosaurus*. We concur that the two vertebrae lying medial to the right pelvis bear long, robust, ventrally oriented ribs and can be confidently identified as sacrals (Fig. S5). However, the preceding vertebra bears a rib of similar length that is more horizontal, but ends is a blunt terminus suggesting it articulated with the nearby right iliac blade (Fig. S5). This indicates *Drepanosaurus* also had three sacral vertebrae. Three sacrals were similarly reported in a putative juvenile *Drepanosaurus* specimen (Renesto and Paganoni, 1995). Lastly, only two sacrals have been reported in *Hypuronector* (Colbert and Olsen, 2001; Renesto et al., 2010). However, since the vertebrae immediately anterior to the first recognized sacral is unpreserved in the holotype, the only specimen with an articulated sacral series, we consider the presence of additional sacral vertebrae equivocal in this taxon.

Thus, all drepanosauromorphs have three sacral vertebrae (with the possible exception of *Hypuronector*). Most Permo-Triassic diapsids only have two sacral vertebrae, the plesiomorphic amniote condition (Romer, 1956). However, a similar increase in the number of sacral vertebrae has been reported in weigeltisaurids (Bulanov and Sennikov, 2010; Buffa et al, 2022) and in some archosaur groups such as dinosaurs and pterosaurs (Wellnhofer, 1978; Langer and Benton, 2006; Nesbitt, 2011).

Caudal vertebrae—The bizarre caudal vertebrae of drepanosauromorphs have been subject to extensive descriptions (Pinna, 1984; Berman and Reisz, 1992; Renesto, 1994a; Colbert and Olsen, 2001; Fraser and Renesto, 2005; Renesto and Binelli, 2006; Renesto et al., 2010), that are only summarized here. The drepanosauromorph caudals have been considered apomorphic in the presence of well-developed chevrons that fuse to the posteroventral margin of the associated centra (Berman and Reisz, 1992; Renesto, 2000; Fraser and Renesto, 2005; Renesto and Binelli, 2006). The haemal spines of drepanosauromorphs are either exceptionally long as in *Hypuronector* (Colbert and Olsen, 2001), or anteriorly concave and anteroposteriorly wide distally as in other drepanosauromorphs (Berman and Reisz, 1992; Renesto and Binelli,

2006), possibly bifid as in *Drepanosaurus* (Pinna, 1984; Renesto and Paganoni, 1995) or encasing a large foramen in *Megalancosaurus* (Renesto, 1994a). In all cases, the drepanosauromorph chevrons are highly apomorphic. Furthermore, the tail ends in an apomorphic claw-shaped element in *Drepanosaurus* and *Megalancosaurus* (Pinna, 1984; Fraser and Renesto, 2005).

The caudal neural spines of drepanosauromorphs have a marked distal anteroposterior expansion in all drepanosauromorphs, which is highly developed in *Drepanosaurus*, *Dolabrosaurus* and *Megalancosaurus*, forming T-shaped spines in lateral view, contrary to other Permo-Triassic diapsids (Pinna, 1984; Berman and Reisz, 1992; Renesto, 1994a). In addition, all drepanosauromorphs have elongated prezygapophyses in the anterior caudals, that extend halfway over the lateral margins of the preceding centra (Pinna, 1984; Berman and Reisz, 1992; Fraser and Renesto, 200; Renesto and Binelli, 20065). This morphology is absent in other Permo-Triassic diapsids, although several archosaurs show a similar elongation of the prezygapophyses, but in the posterior caudals (Nesbitt, 2011). Lastly, all drepanosauromorphs have short transverse processes (Pinna, 1984; Berman and Reisz, 1992; Colbert and Olsen, 2001) that contrast with the L-shaped transverse processes of early amniotes and araeoscelidians (Carroll, 1969; Reisz, 1981; deBraga, 2003), but conform to the transverse processes of all neodiapsids (Gow, 1975; Carroll, 1981).

Gastralia—Gastralia have not been reported in any drepanosauromorph. A reduction of the gastral basket is present in several groups such as allokotosaurian archosauromorphs and some pterosaurs (Dalla Vecchia, 2014; Nesbitt et al., 2015), but a complete reduction is rare in Permo-Triassic taxa (Nesbitt, 2011).

Pectoral girdle—The drepanosauromorph pectoral girdle has been subject to detailed descriptions, especially in relation to the highly modified forelimb of *Drepanosaurus* (Renesto, 1994b; Harris and Downs, 2002; Renesto et al., 2010; Castiello et al., 2016; Pritchard et al., 2016). However, our reexamination of the well-preserved material of *M. preonensis* revealed novel anatomical details which shed light on the homology of the less modified girdles of non-*Drepanosaurus* drepanosauromorphs.

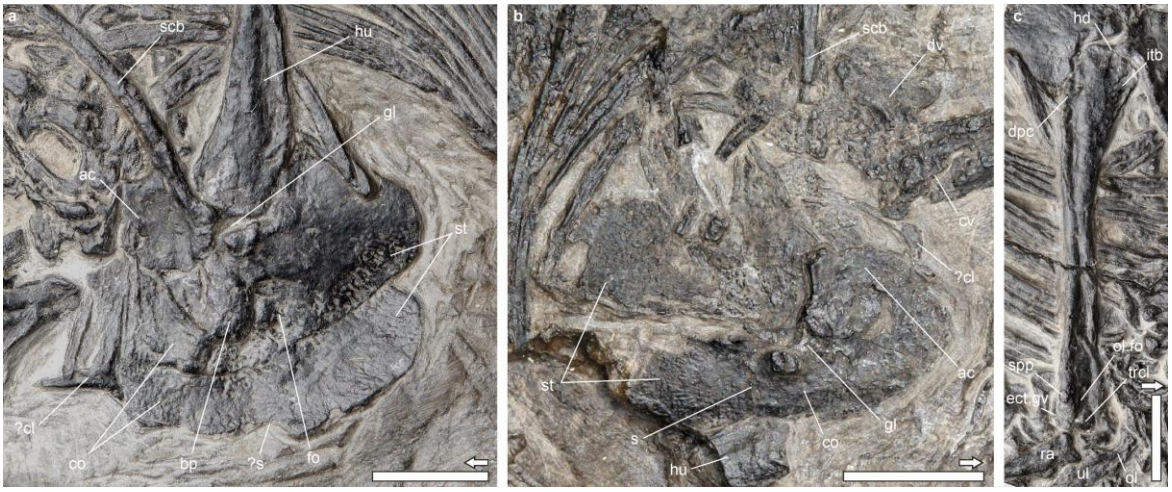

Figure A-S6: Pectoral girdle and humerus of *Megalancosaurus preonensis* (Norian, Italy). **a**, MPUM 6008, pectoral girdle in left lateral view. **b**, MPUM 8437a, pectoral girdle in right lateral view; **c**, MPUM 6008, humerus in oblique anterodorsal view. Arrows indicate anterior direction. **ac**, acromion process; **bt**, tubercle for biceps muscle; **cl**, clavicle; **co**, coracoid; **cv**, cervical vertebra; **dpc**, deltopectoral crest; **dv**, dorsal vertebra; **ect**, ectepicondyle; **fo**, fossa; **gl**, glenoid fossa; **hd**, proximal head of humerus; **hu**, humerus; **itb**, internal tuberosity; **ol**, olecranon; **ol.fo**, olecranon fossa; **ra**, radius; **s**, suture; **scb**, scapular blade; **st**, sternum; **trcl**, trochlea; **ul**, ulna. Scale bars, 5 mm.

Castiello et al. (2016) identified a Y-shaped bone lying just anterior to the pectoral girdle of MPUM 6008 as fused clavicles, similar to the avian furcula. In light of this interpretation, we suggest the single clavicle identified by Renesto (2000) in the more poorly-preserved MPUM 8437a could represent the same element (Fig. S6). We note that the avian furcula is now generally considered homologous to the interclavicle rather than the clavicles (Vickaryous and Hall, 2010; Hall and Vickaryous, 2015; Cau et al., 2021), but given the presence of paired clavicles but lack of distinct interclavicle in *Hypuronector* (Colbert and Olsen, 2001) and *Drepanosaurus* (Harris and Downs, 2002), which bracket *Megalancosaurus* in most phylogenies (Renesto et al., 2010; Pritchard and Nesbitt, 2017), we provisionally consider the lack of interclavicle as plesiomorphic for drepanosauromorphs and thus concur with Castiello et al. (2016) that the median element of the pectoral girdle of *M. preonensis* represents fused clavicles. However, we stress that this requires further study in light of the long debate around the homology of the similarly-shaped avian furcula (summarized in Hall and Vickaryous, 2015). Most Permo-Triassic diapsids retain distinct clavicles and interclavicle, and such reduction and fusion of the dermal elements of the pectoral girdle only occurs in ornithodiran archosaurs among Permo-Triassic taxa (Nesbitt, 2011).

The scapula and coracoid are indistinguishably fused into a scapulocoracoid in *Drepanosaurus* (Renesto, 1994b; Harris and Downs, 2002), and the fusion between both bones cannot be reliable assessed in the heavily crushed pectoral girdles of *Hypuronector* and *Vallesaurus* (Colbert and Olsen, 2001; Renesto and Binelli, 2006). In *Megalancosaurus*, both bones appear fused in MPUM 8437a but not in the larger (and thus possibly more morphologically mature) MPUM 6008 (Fig. S6). We suggest this might result from an incomplete fusion between both bones, which would have broken in MPUM 6008 and been obliterated in MPUM 8437a due to different degrees of diagenetic compression. Partial or complete fusion between scapula and coracoid is plesiomorphic for diapsids, and occurs in most saurians except non-archosaurian archosauromorphs and archosauriforms in which both bones are generally distinct (Ezcurra, 2016).

The scapular blade is extremely tall and thin in drepanosauromorphs, its length reaching nearly 20 times its width in *Megalancosaurus* (Renesto, 2000). The scapular blades are much shorter relative to their width in all other Permo-Triassic diapsids, with only some archosaurs showing relatively high scapular blades, such as erpetosuchid pseudosuchians (Benton and Walker (2002) or some ornithodirans (Langer et al., 2013), including pterosaurs (Dalla Vecchia, 2014). The scapular blade of all drepanosauromorphs except *Hypuronector* bears a markedly concave anterior margin (Fig. S6), as in most crocopodan archosauromorphs except pterosaurs (Ezcurra, 2016). The anterior ventral portion of the scapula extends as a strong acromion process distinctly raised above the level of the glenoid fossa in all drepanosauromorphs (Fig. S6; Colbert and Olsen, 2001; Renesto and Binelli, 2006). This morphology is reminiscent of the dorsally positioned acromion process of archosaurs and some eucropodan archosauriforms but contrasts with the condition of other Permo-Triassic diapsids where the anterior margin of the scapula only bears a shallow acromion process, or no distinct process at all (Nesbitt, 2011; Ezcurra, 2016).

Previous studies have suggested that the large ventral portion of the scapulocoracoid of drepanosauromorphs comprises fused coracoid and sternal plates (Renesto, 2000; Renesto and Binelli, 2006; Renesto et al., 2010; Castiello et al., 2016), with the only unequivocal evidence of sternal plates coming from an isolated pectoral girdle referred to *Drepanosaurus* sp. (Harris and Downs, 2002). In addition, a straight break can be seen on the left lateral surface of the pectoral girdle of MPUM 8437a, located just posterior to the subglenoid lib of the glenoid fossa (Fig. S6). This is the expected location of the coracosternal suture based on the unequivocal

Drepanosaurus sp. specimen (Harris and Downs, 2002). Further supporting this point, the ventral plate of the pectoral girdle expands markedly dorsally relative to the subglenoid lib in both MPUM 8437a and MPUM 6008 (Fig. S6), giving the putative sternal plate the same triangular outline seen in other diapsids that have an ossified sternum such as 'younginiforms' (Carroll, 1981; Currie, 1981). The sternum also extends dorsal to the glenoid in the isolated pectoral girdle attributed to *Drepanosaurus* sp. (Harris and Downs, 2002). We were unable to unambiguously identify a coracosternal suture in the *V. cenensis* holotype (MCSNB 4751, VB, pers. obs.) because this specimen underwent severe diagenetic compression, but it likely formed the portion of the coracosternal plate posterior to the glenoid as it extends slightly dorsally posterior to the subglenoid lip, as in *Megalancosaurus* (as suggested by Renesto and Binelli, 2006). We also suggest the presence of sternal plates is possible, though equivocal, in the crushed pectoral girdles of *Hypuronector* (Colbert and Olsen, 2001). It is this possible that all drepanosauromorphs had an ossified sternum (confirmed at least in *Drepanosaurus* and *Megalancosaurus*), as previously suggested (Harris and Downs, 2002; Renesto et al., 2010; Castiello et al., 2016).

Given the recognition of the sternum in *Megalancosaurus*, it is clear the coracoid extended only slightly posterior to the glenoid fossa, as is typical in archosauromorphs but contrary to the long coracoid plate of non-saurian neodiapsids (Carroll, 1981; Currie, 1981; Buffa et al., 2022), lepidosauromorphs (Evans, 1981; Fraser, 1988; Simões et al., 2018) and pterosaurs (Dalla Vecchia, 2014). In addition, the left coracoid plate of MPUM 6008 (*M. preonensis*), is very well preserved in lateral view, showing a very strong tubercle lying ventral to the subglenoid lip, with a rather deep fossa immediately posterior to it (Fig. S6). Given the position of this tubercle, we suggest it is homologous to the marked, tuber-like process for the biceps musculature that is typical of archosaurs but absent in all other Permo-Triassic reptiles (Nesbitt, 2011; Ezcurra, 2016). Further supporting this identification, Castiello et al. (2016:fig. 5) reconstructed the origin of the m. biceps in a similar position, but made no reference to this tubercle. Given this identification, we suggest the fossa immediately posterior to the biceps process could be homologous to the postglenoid notch or archosaurs (Nesbitt, 2011), although this requires further scrutiny.

Humerus—The humerus of drepanosauromorphs was described in detail in previous studies (Renesto, 1994b; Castiello et al., 2016; Pritchard et al., 2016). All drepanosauromorphs have a long and slender humerus, although that of *Drepanosaurus* has markedly larger

epiphyses, in relation to its highly modified forelimb (Pritchard et al., 2016). The left humerus of MPUM 6008 (*M. preonensis*), seen in anterodorsal view, is the only reasonably uncrushed humerus in a non-*Drepanosaurus* drepanosauromorph (Fig S6), and warrants further attention.

Both epiphyses of the humerus of MPUM 6008 are slightly enlarged relative to the diaphysis, and their main axes are set at a rather low angle to each other (likely < 45°, but the preservation precludes a direct measurement). Such a low degree of humeral torsion is typical of archosauromorphs (Ezcurra, 2016), but is absent in most other Permo-Triassic diapsids where the humeral heads are set roughly at right angle to each other, the plesiomorphic amniote condition (Romer, 1956). Although somewhat crushed, both humeri of the *D. unguicaudatus* holotype also appear to lack a strong torsion (MCSNB 5287, VB, pers. obs.; Renesto, 1994b). We were unable to assess the degree of humeral torsion in any other MCSNB, MFSN or MPUM specimens, nor in *Hypuronector* (Colbert and Olsen, 2001) due to the nature of preservation of the material.

The proximal epiphysis of the humerus of MPUM 6008 is angled medially so that the proximal epiphysis is asymmetric in ventral view and the articular head is slightly offset form the main axis of the bone (Fig S6), as is typical in proterochampsians and archosaurs, but contrary to the more symmetrical epiphysis of other Permo-Triassic reptiles (Ezcurra, 2016). The deltopectoral crest and internal tuberosity are low in MPUM 6008, hardly expanding beyond the margins of the bone (Fig S6). While the proximal epiphyses of the humeri of all other non-*Drepanosaurus* are poorly preserved, their outline conforms to that of the humerus of MPUM 6008, suggesting its morphology could be typical for drepanosauromorphs.

As noted by Renesto (1994a), the distal epiphysis of the humerus of MPUM 6008 bears a deep olecranon fossa on its dorsal surface. This fossa is framed ventrally by a rounded condylar structure, which we interpret as the dorsal surface of an hypertrophied trochela, similar to the condition in *Drepanosaurus* (Renesto, 1994b; Pritchard et al., 2016). A strong development of the articular surfaces for the lower arms is the plesiomorphic state in diapsids whereas most saurians show only reduced surfaces, which are entirely reduced in most archosauromorphs (Ezcurra, 2016). However, pterosaurs also show a very well-developed capitellum and trochlea (Wellnhofer, 1978; Dalla Vecchia, 2014).

The ectepicondyle is visible in MPUM 6008 and bears a clear ectepicondylar groove but there is no ectepicondylar foramen as the supinator process is short (Fig. S6). It is unclear

whether the ectepicondylar groove or foramen and the supinator process were present in any other drepanosauromorph (Renesto, 1994b; Renesto and Binelli, 2006; Casitello et al., 2016; Pritchard et al., 2016). The entepicondyle is relatively undamaged in MPUM 8437a and apparently lacks an entepicondylar foramen. There is also no trace of this foramen in the *M. preonensis* holotype, although the nature of preservation of this specimen precludes a definite statement. Furthermore, we concur with Renesto (1994b) and Renesto and Binelli (2006) that an entepicodylar foramen was also likely absent in *Drepanosaurus* and *Vallesaurus*. The absence of an entepicondylar foramen has long been considered a synapomorphy of archosauromorphs (Benton, 1985; Laurin, 1991).

Figure A-S7: Forelimb elements of *Megalancosaurus preonensis* and *Drepanosaurus unguicaudatus* (Norian, Italy). **a**, *M. preonensis* (MPUM 8437a), forelimb in mostly ventral view; **b**, *M. preonensis* (MPUM 8437a), interpretive drawing carpus in ventral view; **c**, *Drepanosaurus unguicaudatus* (MCSNB 5728), non-ungual phalanx of digit IV in lateral view. Arrow indicates distal direction. **carp**, carpus; **clf**, contralateral facet; **dc**, distal carpal; **ent**, entepicondyle; **gy**, ginglymus; **hu**, humerus; **in**, intermedium; **lc**, lateral centrale; **mc**, medial centrale; **Mtc**, metacarlal; **ol**, olecranon; **pf.f**, perforating foramen; **ph**, phalanx; **ra**, radius; **rae**, radiale; **sw**, swelling; **ul**, ulna; **ule**, ulnare; **uph**, ungual phalanx; **tb**, tubercle. Scale bars, 5 mm (**a**), 2 mm (**b**, **c**).

Lower arm—The lower arm of *Drepanosaurus* has been subjected to detailed descriptions because of its highly modified morphology (Pinna, 1984; Renesto, 1994b; Pritchard et al., 2016), and needs not be discussed here. The radius and ulna of non-

Drepanosaurus drepanosauromorphs were described in previous studies (Colbert and Olsen, 2001; Renesto and Binelli, 2006; Renesto et al., 2010; Castiello et al., 2016) and consist of slender, straight bones (Fig. S7). Of note is the presence of a very strong olecranon process of the ulna, as in araeoscelidians (Vaughn, 1955; Reisz, 1981), weigeltisaurids (Buffa et al., 2022) and various saurians (Ezcurra, 2016).

Manus—The proximal carpal series of *Drepanosaurus*, *Megalancosaurus* and *Vallesaurus*, the only drepanosauromorphs with a preserved carpus, comprise the radiale, ulnare and intermedium (Renesto et al., 2010; Castiello et al., 2016; Pritchard et al., 2016). The ulnare and intermedium of drepanosauromorphs are proximodistally very long (Fig. S7), reminiscent of the condition of araeoscelidians (Vaughn, 1955; Reisz, 1981) but contrary to the much shorter proximal carpals of all Permo-Triassic neodiapsids (Pritchard et al., 2016). Conversely, the proximal carpals of *Vallesaurus* are much shorter (Renesto and Binelli, 2006; Renesto et al., 2010), and its position as a non-drepanosaurid drepanosauromorph (Renesto et al., 2010; Pritchard et al., 2016; Pritchard and Nesbitt, 2017) suggests the elongate proximal carpals of *Drepanosaurus* and *Megalancosaurus* could be apomorphic.

The more distal carpals are only known in *Megalancosaurus* among drepanosauromorphs, and comprise two centralia and five distal carpals. As evidenced by the carpi of the *M. preonensis* holotype (Fig. S2) and MPUM 8437 (Fig. S7), there is no trace of a pisiform, which was almost certainly absent in *Megalancosaurus*. The presence of a pisiform is plesiomorphic in amniotes (Romer, 1956), and is prevalent among non-archosauromorph diapsids (Currie, 1980, 1981; Reisz, 1981; Buffa et al., 2022), but is generally absent in Triassic archosauromorphs (Nosotti, 2007; Gottmann-Quesada and Sander, 2009; Nesbitt et al., 2015; Sereno, 1994) except *Trilophosaurus* (Nesbitt et al., 2015). However, this bone is present in later archosaurs (e.g. *Heterodontosaurus*, Galton, 2014) and the fossil record for archosauriforms is extremely poor, suggesting a more complex evolutionary history.

Regarding the distal carpal series, whereas distal carpal 5 is prevalent in non-saurian diapsids (Currie, 1980, 1981; Reisz, 1981; Currie and Carroll, 1981; Caldwell, 1995; Buffa et al., 2022), it is generally considered absent in archosauromorphs (Dilkes, 1998; Nosotti, 2007; Gottmann-Quesada and Sander, 2009; Nesbitt et al., 2015). However, both the pisiform and distal carpal 5 are present in dinosaurs (Ezcurra 2010; Botelho et al., 2014; Galton, 2014; Barta

et al., 2018), indicating again that the evolutionary history of the carpus is poorly understood in archosauromorphs.

Drepanosauromorphs show much interspecific variability in their manual phalangeal formula (Renesto et al., 2010). *Vallesaurus* has the plesiomorphic 2-3-4-5-3 formula prevalent in early amniotes (Romer, 1956), while *Megalancosaurus* (2-2-2-3-3) and *Drepanosaurus* (?2-2-2-2-2) show strongly reduced formulas (Renesto et al., 2010). A similar reduction appears to have been present in *Hypuronector* as well, although the manus is not entirely preserved in this taxon (Colbert and Olsen, 2001). Among Permo-Triassic amniotes, divergences from the plesiomorphic condition are rare, with weigeltisaurids having an additional phalanx in digit V (Bulanov and Sennikov, 2010; Pritchard et al., 2021; Buffa et al., 2022) while most ornithodirans show a reduction of digit V, and dinosaurs of digit IV as well (Barta et al., 2018). All drepanosauromorphs with the exception of *Hypuronector* have longer penultimate manual phalanges than antepenultimate ones, as in weigeltisaurids (Pritchard et al., 2021; Buffa et al., 2022), *Trilophosaurus* (Spielmann et al., 2008) and pterosaurs (Dalla Vecchia, 2014) but in contrast to most other Permo-Triassic diapsids (Gow, 1975; Dilkes, 1998; Nesbitt et al., 2015; O'Brien et al., 2018). The distal phalanges of drepanosauromorphs all show highly-developed subcircular distal contralateral facets that form a distal ginglymus, a characteristic also seen in pterosaurs and which is particularly visible in the alar metacarpal (Dalla Vecchia and Cau, 2015).

Pelvic girdle—Whereas our interpretation of most drepanosauromorph pelvic girdles conforms to previous studies (e.g. Renesto et al., 2010), we suggest the right pelvis of the holotype of *V. cenensis* is seen in anterior view (Fig. S8), and not in medial view as described by Renesto and Binelli (2006). However, little information can be reliably described from this pelvis due to strong diagenetic compression.

As seen in *Drepanosaurus*, the pelvic girdle of drepanosauromophs bears a deep subcircular acetabulum (Fig. S8), contrasting with the more irregularly-shaped acetabulum of non-saurian diapsids (Currie, 1980, 1981; Reisz, 1981). There does not appear to be any evidence of a supraacetabular buttress, contrary to most Permo-Triassic diapsids (Pritchard and Sues, 2019), but as in pterosaurs (Dalla Vecchia, 2014). More ventrally, each puboischiatic plate of *Drepanosaurus* is pierced by an ovoid thyroid fenestra (Fig. S8), contrasting with the wider, single thyroid fenestra of early saurians or the entirely closed puboischiatic plate of non-

saurian diapsids and archosaurs (Pritchard and Nesbitt, 2019), but in a manner similar to the pelvis of kuehneosaurids (Müller, 2004). There is also no trace of a pubic apron that is common to most archosauriforms (Ezcurra, 2016) except pterosaurs (Wellnhofer, 1978).

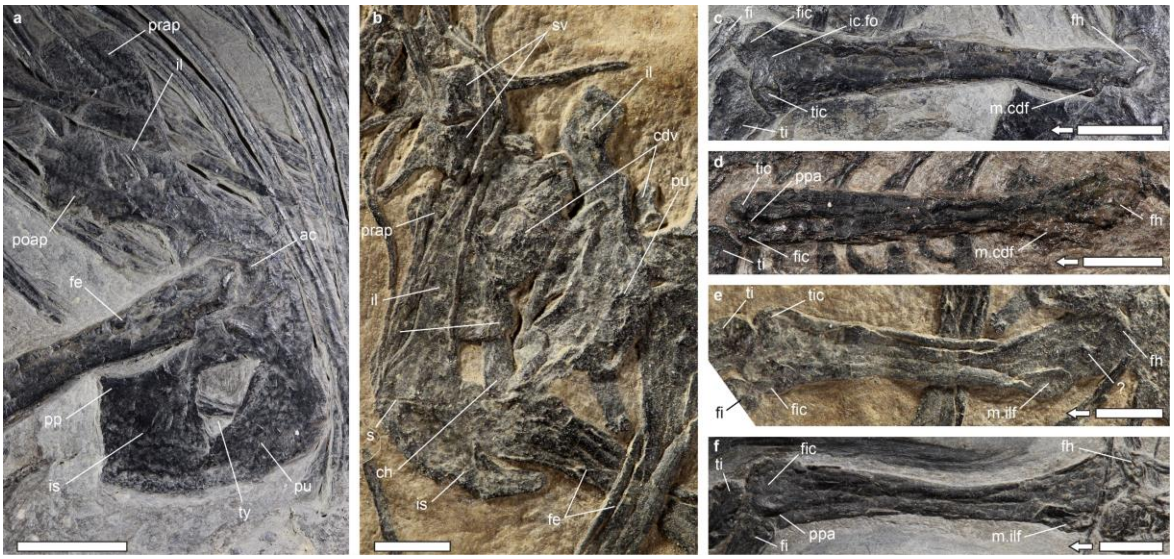

Figure A-S8: Pelvic girdle and femur of Italian drepanosauromorphs (Norian). **a**, *Drepanosaurus unguicaudatus* (MCSNB 5728), right pelvis in lateral view. **b**, *Vallesaurus cenensis* (MCSNB 4751) pelvic girdle in mostly left lateral view. **c**, *Drepanosaurus unguicaudatus* (MCSNB 5728), right femur in anterodorsal view. **d**, *Megalancosaurus preonensis* (MPUM 8437a), left femur in anteroventral view (reversed). **e**, *Vallesaurus cenensis* (MCSNB 4751), left femur in posterodorsal view. **f**, *Vallesaurus zorzinensis* (MCSNB 11342) in posterior view. Arrows indicate distal direction. **ac**, acetabulum; **cdv**, caudal vertebra; **ch**, chevron; **fe**, femur; **fh**, proximal head of femur; **fi**, fibula; **fic**, fibular condyle; **ic.fo**, intercondylar fossa; **il**, ilium; **is**, ischium; **m.cdf**, insertion for m. caudofemoralis; **m.ilf**, insertion for m. iliofemoralis; **poap**, postacetabular process; **pp**, posterior process; **prap**, preacetabular process; **pu**, pubis; **s**, suture; **sv**, sacral vertebra; **ti**, tibia; **tic**, tibial condyle; **ty**, tyroid fenestra. Scale bars, 10 mm (**a**, **c**), 2 mm (**b**, **e**, **f**), 5 mm (**d**).

The ilium of all drepanosauromorphs bears a very tall triangular iliac blade formed by a strong preacetabular process and a slightly less expanded postacetabular process (Fig. S8). The iliac blade of most non-archosauromorph diapsids lacks a strong development of the preacetabular process (Pritchard and Sues, 2019), although it is present as a large expansion in weigeltisaurids (Buffa et al., 2022) and most archosaurs (Nesbitt, 2011). The pubis and ischium are broad rectangular bones bordering the thyroid fenestra. As seen in *Drepanosaurus*, *Hypuronector* and *Megalancosaurus*, the ischium bears a pointed posterodorsal process. A similar process is also found in non-crocopodan archosauromorphs and *Prolacerta* (Ezcurra, 2016), as well as in some lepidosaurians (Evans, 1981; Fraser and Walkden, 1984; Simões et al., 2017).

Femur—Although it has been described several times (see Renesto et al., 2010), the femur of drepanosauromorphs warrants further discussion based on our reexamination of the Italian specimens. All drepanosauromorphs have long and slender femora, with slightly enlarged epiphyses relative to the diaphysis (Fig. S8).

The proximal epiphysis is rounded and well-ossified in all drepanosaurormophs, as in most Permo-Triassic diapsids except non-eucocopodan archosauromorphs where the proximal epiphysis is less well-ossified (Pritchard et al., 2015). As best seen in *Vallesaurus* (Fig. S8), the proximal epiphysis is markedly upturned, giving the bone its sigmoid shape. This sigmoid shape is apparently absent in *Drepanosaurus* and is less marked in *Megalancosaurus* (Fig. S8), although it may be accentuated because the bone is not preserved in anterior or posterior views.

A large trochanter has been described in the holotypes of both *Vallesaurus* species (Renesto and Binelli, 2006; Renesto et al., 2010), however, it is unclear to which trochanter previous authors refer to. These trochanters are indeed very robust and are located on the posterior margin of the femur in both specimens (Fig. S8E, F). Given their position, these trochanters cannot correspond to the insertion of the m. caudofemoralis, namely the internal or archosaurian fourth trochanters, as this muscle inserts on the anterior margin of the femur (in a transverse position) in reptiles (Hutchinson, 2001). Owing to the posterior location of the identified trochanter in *Vallesaurus*, we suggest it marks the insertion of the m. iliofemoralis (Hutchinson, 2001), although we are unable to equivocally identify which branch (caudalis or externus). Among Permo-Triassic diapsids, the insertion of the m. iliofemoralis is only developed into trochanteric expansions (the anterior trochanter and trochanteric shelf) in archosaurs (Hutchinson, 2001). Given the numerous similarities noted above with archosaur-line taxa, we suggest the trochanters seen on the posterior margin of the femur of *Vallesaurus* could be homologous to the trochanteric shelf of archosaurs as no other Triassic reptiles show such prominent muscular insertions. We are unable to assess the presence of this structure in other drepanosauromorphs, in which the femur is not preserved in posterior view.

As seen in *Drepanosaurus* and *Megalancosaurus*, the anterior margin of the femur also bears a marked trochanter. Given this trochanter is anteriorly positioned, is likely served as the insertion of the m. caudofemoralis, as in other reptiles (Hutchinson, 2001). Given the proximal position of this process, it would conform well with that of the internal trochanter of early amniotes and lepidosaurs (Hutchinson, 2001; Nesbitt et al., 2009). However, as the ventral

surface of the proximal epiphysis is not exposed in any drepanosauromorph, it is unclear if an intertrochanteric fossa was present, and thus the identification of this structure as the internal or archosaurian fourth trochanter remains equivocal.

The distal epiphysis of the femur is robust in all drepanosauromorphs and bears distinct tibial and fibular condyles. As best seen in the holotypes of *D. unguicaudatus* and *V. cenensis*, the distal condyles are uneven, with the fibular condyle extending markedly posterior to the tibial one (Fig. S8), as in araeoscelidians and some non-archosauriform archosauromorphs and pseudosuchians, but contrary to the more even distal condyles of other Permo-Triassic diapsids (Ezcurra, 2016). Little can be said of the distal condyles themselves because of crushing, but the well-preserved tibial condyle of *D. unguicaudatus* has a rounded medial margin (Fig. S8C), as in most Permo-Triassic diapsids, but contrary to the triangular-shaped tibial condyle of crocopodan archosauromorphs and some early archosauriforms (Pritchard et al., 2015).

Figure A-S9: Pes of Italian drepanosauromorphs (Norian). **a**, *Drepanosaurus unguicaudatus* (MCSNB 5728), left pes in ventral view. **b**, *Megalancosaurus preonensis* (MCSNB 8437a), right pes in mostly dorsal view. **c**, *Megalancosaurus preonensis* (MCSNB 8437a), left pes in mostly dorsal view. **ast**, astragalus; **cal**, calcaneus; **clf**, contralateral facet; **ctb**, calcaneal tuber; **dt**, distal tarsal; **fi**, fibula; **gy**, ginglymus; **Mtt**, metatarsal; **nav**, navicular; **nt**, notch; **pf.f**, perforating foramen; **ph**, pahalanx; **tb**, tubercle; **ti**, tibia; **uph**, ungual phalanx. Scale bars, 5 mm.

Lower leg—The lower leg bones are significantly shorter than the femur in drepanosauromorphs (Renesto, 1994a), as in most Permo-Triassic diapsids but in contrast to the very elongate tibia and fibula of most ornithodirans (Nesbitt, 2011). An incipient cnemial crest is present in most drepanosauromorphs and is rather prominent in *D unguicaudatus* (MCSNB 5728, VB pers. obs).

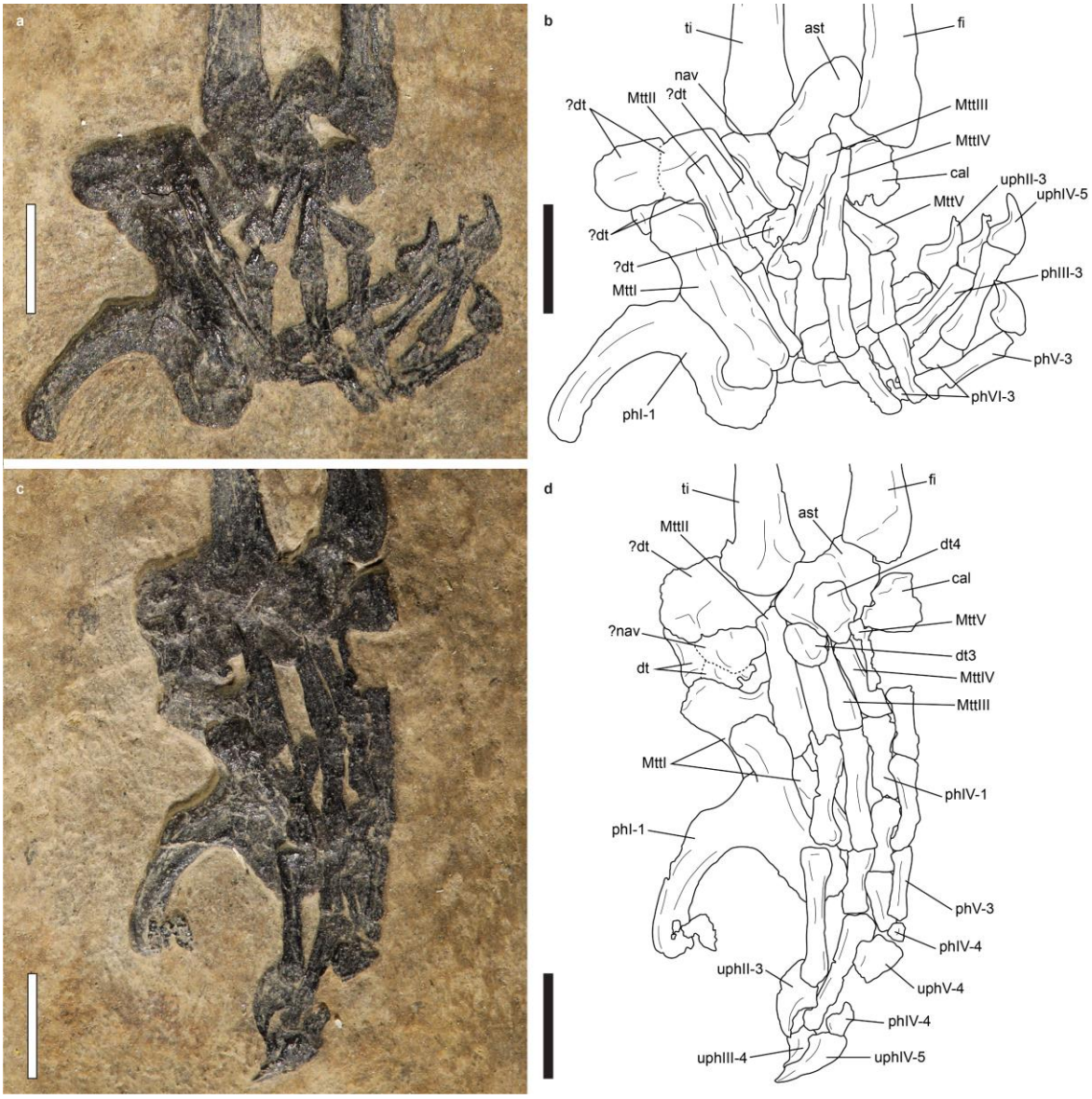

Figure A-S10: Pes of *Vallesaurus cenensis* holotype MCSNB 4751 (Norian, Italy). **a**, left pest in mostly dorsal view. **b**, interpretive drawing of **a**. **c**, right pes in ventral view. **d**, interpretive drawing of **c**. **ast**, astragalus; **cal**, calcaneus; **dt**, distal tarsal; **fi**, fibula; **Mtt**, metatarsal; **nav**, navicular; **ph**, pahalanx; **ti**, tibia; **uph**, ungual phalanx. Scale bars, 2 mm.

Pes—The proximal tarsals are tall in all drepanosauromorphs (Figs. S9, S10; Renesto and Paganoni, 1995), much taller than in other Permo-Triassic diapsids except araeoscelidians (Reisz, 1981) and the allokotosaurian *Trilophosaurus* (Spielmann et al., 2008). As a result, the astragalar articular surfaces for the tibia and fibula are widely spaced, as in most Permo-Triassic diapsids, but in contrast to the continuous crural articular surfaces of eythrosuchids and eucrocopodan archosauriforms (Nesbitt, 2011). The astragalus and calcaneus are best-preserved in the holotype of *D. unguicaudatus* where they appear partially fused (Fig. S9), contrary to other drepanosauromorphs (Figs. S9, S10; Renesto et al., 2010) and most Permo-Triassic saurians, but as in pterosauromorphs (Ezcurra et al., 2020). As seen in this specimen and in those of *Dolabrosaurus* and *Megalancosaurus*, the articulation between the two proximal tarsals is mostly flat (Fig. S9), contrary to the concavoconvex articulations of most crocopodan archosauromorphs (Sereno, 1991; Nesbitt, 2011). Lastly, a large perforating foramen is present between the astragalus and calcaneus, contrary to some lepidosaurians and all eytrhosuchid and eucrocopodan archosauriforms where this foramen is absent (Nesbitt, 2011).

The calcaneus of *Drepanosaurus* (Fig. S9), *Dolabrosaurus* and *Megalancosaurus* (Renesto and Paganoni, 1995; Renesto et al., 2010), but not *Vallesaurus* (Fig. S10, Renesto and Binelli, 2006; Renesto et al., 2010), bears a robust calcaneal tuber, which has long been considered a synapomorphy of archosauromorphs (Benton, 1985; Laurin, 1991) although it is absent in pterosauromorphs among Triassic taxa (Nesbitt, 2011). The ventral margin of the calcaneal tuber is strongly concave in all drepanosauromorphs in which it is present, as in allokotosaurians (Nesbitt et al., 2015) and several archosauriforms (Ezcurra, 2016).

More distally, the tarsus of drepanosauromorphs comprises several bones, which are very well preserved in the *D. unguicaudatus* holotype and some *Megalancosaurus* specimens (Fig. S9), but very hard to identify in *Vallesaurus* specimens due to their small size, slight disarticulation, and diagenetic compression. As seen in the better-preserved left tarsus of the *Vallesaurus* holotype (Fig. S10a, b), a large rectangular bone lying immediately distomedial to the astragalus is preserved in articulation with the tibia, and can thus be confidently identified as the navicular in agreement with previous studies (Renesto and Binelli, 2006; Renesto et al., 2010). We could not identify a similar bone in the more poorly-preserved right tarsus of the same specimen (Fig. S10c, d). All other drepanosauromorphs also have a navicular bone in the pes (Fig. S9, Renesto and Paganoni, 1995). This bone is present ancestrally in diapsids, but is lost as a distinct ossification in most lepidosaurians and archosauriforms (Nesbitt, 2011). The

navicular of *V. cenensis* also lies in close contact with the tibia, as in *Dolabrosaurus* and some *Megalancosaurus* specimens (Renesto and Paganoni, 1995), suggesting both bones articulated in drepanosauromorphs. Such an articulation is typical in archosauromorphs (Rieppel, 1989; Carroll, 1976; Gower, 1996) but is absent in other Permo-Triassic diapsids that have a distinct navicular bone (Currie, 1981a; Reisz, 1981).

The distal tarsal series is complete in the *D. unguicaudatus* holotype, comprising distal tarsals 1 through 5 (Fig. S9a), similar to the distal series of *Megalancosaurus* (Fig. S9b, c). The elements of the distal tarsal series are hard to identify in the holotype of *V. cenensis*, but the two elements lying immediately proximal to metacarpals III and IV may be identified as distal tarsals 3 and 4 (Fig. S10). The medial elements of the distal tarsal series are unidentifiable but likely compose the large structure proximal to the similarly enlarged metatarsal I (Fig. S10). The complete distal tarsal series attested by *Drepanosaurus* and *Megalancosaurus* is also present in araeoscelidians, *Youngina* and weigeltisaurids (Goodrich, 1942; Reisz, 1981; Buffa et al., 2022) but is highly unusual for a Triassic reptile. Distal tarsals 1 and 2 are indeed present in most Permo-Triassic diapsids, but are absent in some tanystropheids, erythrosuchids and eucrocopodan archosauriforms (Nesbitt, 2011). Distal tarsal 5 is apparently lost as a distinct ossification in most 'younginiforms' (Harris and Carroll, 1977; Currie, 1981a) and as long been considered absent in saurians (Benton, 1985; Laurin, 1991).

Similar to the manus, drepanosauromorphs show much interspecific variability in their pedal phalangeal formula (Renesto et al., 2010). The phalangeal formula of *V. cenensis* is 1-3-4-5-4, very similar to the plesiomorphic diapsid formula except in the reduction of the number of phalanges in the highly modified digit I (Fig. S10; Renesto and Binelli, 2006; Renesto et al., 2010). In contrast, both *Drepanosaurus* and *Megalancosaurus* show a reduced phalangeal formula of 2-3-3-3-3 (Fig. S9; Renesto et al., 2010). Such reduction of the number of phalanges in digits III and IV is rare among Permo-Triassic diapsids, but a strong reduction of the phalangeal formula of digit V is also present in ornithodirans (Nesbitt, 2011). As seen in all drepanosauromorphs, metatarsal V is straight, as in non-saurian diapsids (Reisz, 1981; Currie, 1981; Buffa et al., 2022) but in contrast to the hook-shaped metatarsal V that has long been considered a synapomorphy of Sauria (Borsuk-Białynicka, 2018). However, we note that proterochampsids (*Chanaresuchus*, *Pseudochampsa*; Romer, 1972; Trotteynand Ezcurra, 2014) and several early ornithodirans (*Lagerpeton*, *Lagosuchus*, *Silesaurus*; Sereno and

Arcucci, 1994a, b; Dzik, 2003) and most dinosaurs (Sereno, 1991) lack a hooked fifth metatarsal.

The penultimate phalanges of all digits are very long in drepanosauromorphs, much longer than the preceding phalanges or metacarpals, as in the allokotosaurian *Trilophosaurus* (Spielmann et al., 2008) and pterosaurs (Dalla Vecchia, 2014) among Permo-Triassic taxa. Lastly, all pedal ungual phalanges bear a strong ventral flexor tubercle, as in weigeltisaurids (Pritchard et al., 2021), allokotosaurians (Spielmann et al., 2008; Nesbitt et al., 2015) and pterosaurs (Dalla Vecchia, 2014).

Appendix 4: Extended topology descriptions

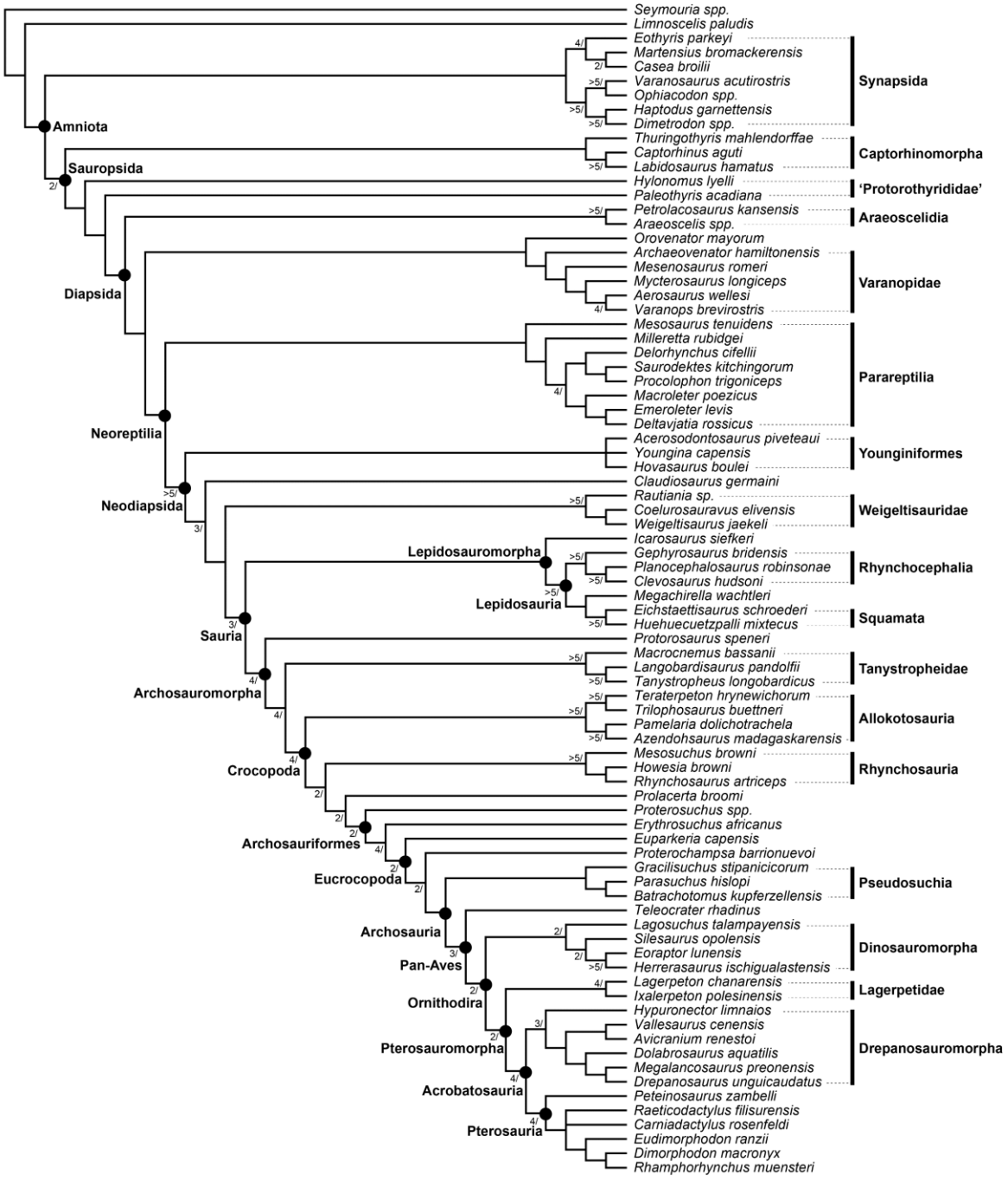

Figure A-S11: Strict consensus tree (12 MPTs of 2698 steps; L = 2700; CI = 0.1965; RI = 0.6181) of Analysis 1. Node label: Bremer value (when > 1)/Bootstrap (when > 50%).

Analysis 1

Our first phylogenetic analysis recovered 4 most parsimonious trees (MPTs) of a length of 2698 steps. The strict consensus tree is highly resolved, with a length of 2700 steps, a consistency index (CI) of 0.1965 and a retention index (RI) of 0.6181. The topology (Fig. S11) detailed below is broadly congruent with that of Ford and Benson (2020) regarding early amniotes (i.e. with Varanopidae and Parareptilia inside Diapsida), while our topology of Sauria, in particular archosauromorphs, is congruent with that of Ezcurra et al. (2020) and Pritchard et al. (2021), especially in the recovery of a monophyletic clade comprising lagerpetids and pterosaurs. This result was expected since our character sample is mostly based on these three studies.

Regarding non-diapsid taxa, our topology conforms to most previous studies on early amniotes (Fig. S11). First, we recover *Seymouria* (the designated outgroup) and *Limnoscelis* as successive sister-groups to a monophyletic Amniota comprising the dichotomy between Synapsida and Sauropsida, as recovered by most cladistic analyses (e.g. Gauthier et al., 1988; Laurin and Reisz, 1995; deBraga and Rieppel, 1997, but see Berman, 2013; Klembara et al., 2020 for an inclusion of diadectomorphs within Synapsida). Second, we recover a monophyletic Synapsida with Caseasauria as sister-group to an 'eupelycosaurian' clade composed of Ophiacodontidae and Sphenacodontidae congruent with previous studies (Reisz, 1986; Benson, 2012), but excluding Varanopidae as in several recent analyses (Laurin and Piñeiro, 2018; MacDougall et al., 2018; Ford and Benson, 2019, 2020, but see Simões et al., 2022 for a re-inclusion of varanopids among eupelycosaurian synapsids). Third, among sauropsids, Captorhinomorpha, *Hylonomus* and *Paleothyris* are recovered as successive sister-groups to Diapsida, supporting the paraphyly of 'protorothyridids' as first suggested by Müller and Reisz (2006).

Support values are very low in this region of the tree, except in less inclusive clades (e.g. synapsid interrelationships) but this is expected regarding current debates on the position of various early amniote taxa (varanopids as discussed above, but also parareptiles, see below), the possible synapsid affinities of diadectomorphs (Berman, 2013; Klembara et al., 2020), and the very recent suggestion that these taxa, as well as araeoscelidians, could be stem-amniotes, and that parareptiles are paraphyletic (Simões et al., 2022).

Our topology recovers an expanded concept of Diapida which conforms to the topology of Ford and Benson (2020, echoing other recent studies, Laurin and Piñeiro, 2017, 2018;

MacDougall et al., 2018; Ford and Benson, 2019) whereby Araeoscelidia and a clade comprising Varanopidae and the 'varanopid-like' diapsid *Orovenator* form successive sister-groups to Neoreptilia, the clade containing the dichotomy between Parareptilia and Neodiapsida (Fig. S11). This contrasts with the traditional view of early amniote relationships, whereby varanopids are eupelycosaurian synapsids (Romer and Price, 1940; Reisz, 1986; Benson, 2012; Simões et al., 2022) and parareptiles form a dichotomy with Eureptilia at the base of Sauropsida (e.g. Gauthier et al., 1988; Laurin and Reisz, 1995; deBraga and Rieppel, 1997; Müller and Reisz, 2006). However, this result was expected as our taxon-character sample is heavily based on that of Ford and Benson (2020) regarding non-diapsid amniotes. We note that these results are incongruent with the recent analysis of Simões et al. (2022). However, a detailed reexamination of early amniote relationships is out of the scope of this paper so this portion of our topology will not be discussed further here.

Regarding non-saurian diapsids, our topology differs significantly from previous studies. First, we recover a monophyletic Younginiformes at the base of Neodiapsida (Fig. S11), as in older studies (Currie, 1982; Benton, 1985; Evans, 1988; Laurin, 1991) but contrary to recent studies that support the paraphyly of this clade (Bickelmann et al., 2009; Reisz et al., 2011, but see Simões et al., 2022). This clade is here supported by three unambiguous synapomorphies (see Supplementary Material), but very low support values. Given only three taxa are included in our analysis (*Acerosodontosaurus*, *Hovasaurus*, *Youngina*), support for a monophyletic Younginiformes remains equivocal and further studies may recover this clade as paraphyletic.

Second, we recover the enigmatic *Claudiosaurus* immediately crownward to Younginiformes (Fig. S11). This result is highly supported by 10 unambiguous synapomorphies (see Supplementary Material) and relatively high support values, and conforms to some previous studies (Müller, 2004; Reisz et al., 2011, but see Pritchard et al., 2021). However, a revision of this taxon is necessary to better assess its phylogenetic position.

Lastly, we recover Weigeltisauridae as sister-group to Sauria, the reptilian crown-group (Fig. S11), as supported by eight unambiguous synapomorphies (see Supplementary Material), but rather low support values. This very crownward position is in stark contrast to most previous published analyses which recover younginiforms crownward to weigeltisaurids (Evans, 1988; Laurin, 1991; Ezcurra et al., 2014; Senter, 2004; Pritchard et al., 2021, but see Müller, 2004).

However, Buffa et al. (2021, 2022) argued that some aspects of weigeltisaurid anatomy could suggest a more crownward position for this clade. In addition, our analysis does not recover a monophyletic Avicephala containing Weigeltisauridae and Drepanosauromorpha, with the latter not being recovered inside the crown-group, contrary to recent studies (Fig. S11; Müller, 2004; Senter, 2004; Pritchard et al., 2016; Pritchard and Nesbitt, 2017; Pritchard et al., 2021).

Sauria, the reptilian crown-group, comprises the dichotomy between Lepidosauromorpha and Archosauromorpha (Fig. S11). The former clade is composed in our analysis by the kuehneosaurid *Icarosaurus* as sister-group to Lepidosauria, itself composed of Rhyncocephalia and Squamata. The recovery of *Icarosaurus* as sister-group to Lepidosauria is supported by three unambiguous synapomorphies (see Supplementary Material) but very low support values. This topology conforms well with some previous studies (Evans, 2009), but contrasts with recent analyses that support archosauromorphs affinities for kuehneosaurids (Pritchard and Sues, 2019). Lepidosauria comprises the well-supported clades Rhyncocephalia and Squamata, and we recover *Megachirella* as a stem-squamate, in agreement with Simões et al. (2018).

Regarding archosauromorphs, our topology is broadly consistent with recent studies in the placement of *Protorosaurus*, Tanystropheidae, Allokotosauria, Rhynchosauria and *Prolacerta* as successive sister-groups to Archosauriformes (Fig. S11; Nesbitt et al., 2015; Ezcurra, 2016; Pritchard and Sues, 2019, but see Spiekman et al., 2021 for a more stemward placement of *Prolacerta*, and Simões et al., 2018, 2022 for markedly different topologies). *Proterosuchus*, *Erythrosuchus*, *Euparkeria* and *Proterochampsa* form an archosauriform grade leading to Archosauria, in agreement with previous studies (Nesbitt, 2011; Ezcurra, 2016), the latter which is divided into Pseudosuchia and Pan-Aves. Support values in this region of the tree are relatively low compared to recent studies (e.g. Ezcurra et al., 2020) except for a few nodes (Fig. S11), but this likely stems from conflicting hypotheses on archosauromorphs interrelationships (e.g. Simoes et al., 2018; Spiekman et al., 2021) and a reduced taxon sampling of archosauriforms and early archosaurs, whose interrelationships are out of the scope of this paper.

Among Pan-Aves, our topology conforms to previous studies (e.g. Nesbitt et al., 2017; Ezcurra et al., 2020) in recovering the aphanosaur *Teleocrater* as sister-group to Ornithodora, itself comprising a dichotomy between Dinosauromorpha and Pterosauromorpha, the latter of

which includes Lagerpetidae and Pterosauria (Fig. S11). Support values in this region of the tree are among the highest recovered (Fig. S11). This is likely due to a broader taxon sample compared to archosauriforms and pseudosuchians, especially regarding pterosaurs (as advocated by Baron, 2021), as well as an history of well documented characters, especially in the ankle (e.g. Sereno, 1991; Juul, 1994; Nesbitt, 2011) that significantly improve tree resolution.

The most striking result of our analysis is undoubtedly the recovery of Drepanosauromorpha apical to Lagerpetidae, as sister group to Pterosauria. We propose the name Acrobatosauria clade nov. for this hitherto unnamed clade. Acrobatosauria is supported in our analysis by 12 unambigous synamoporphies (discussed below, see Systematic Paleontology above). This topology echoes the analysis of Renesto and Binelli (2006), the only other study to recovered drepanosauromorhs and pterosaurs (represented by *Eudimorphodon* in their dataset) as sister-groups, but outside Archosauria. Our study is thus the first to recover a clade comprising Drepanosauromorpha and Pterosauria among Ornithodira.

Finally, the interrelationships of drepanosauromorphs are entirely congruent with that of Renesto et al. (2010) with Elyrosauria, Drepanosauridae and Megalancosaurinae being recovered as successively less inclusive clades. However, we recover *Avicranium* and *Vallesaurus* as sister taxa among non-drepanosaurid elyrosaurs, contrary to Pritchard and Nesbitt (2017) who recover this taxon closer to the megalancosaurine *Drepanosaurus*. However, this clade is only supported by a single unambiguous synapomorphy, and is rather poorly supported in our analysis. This is likely due to the little postcranial material available for *Avicranium*.

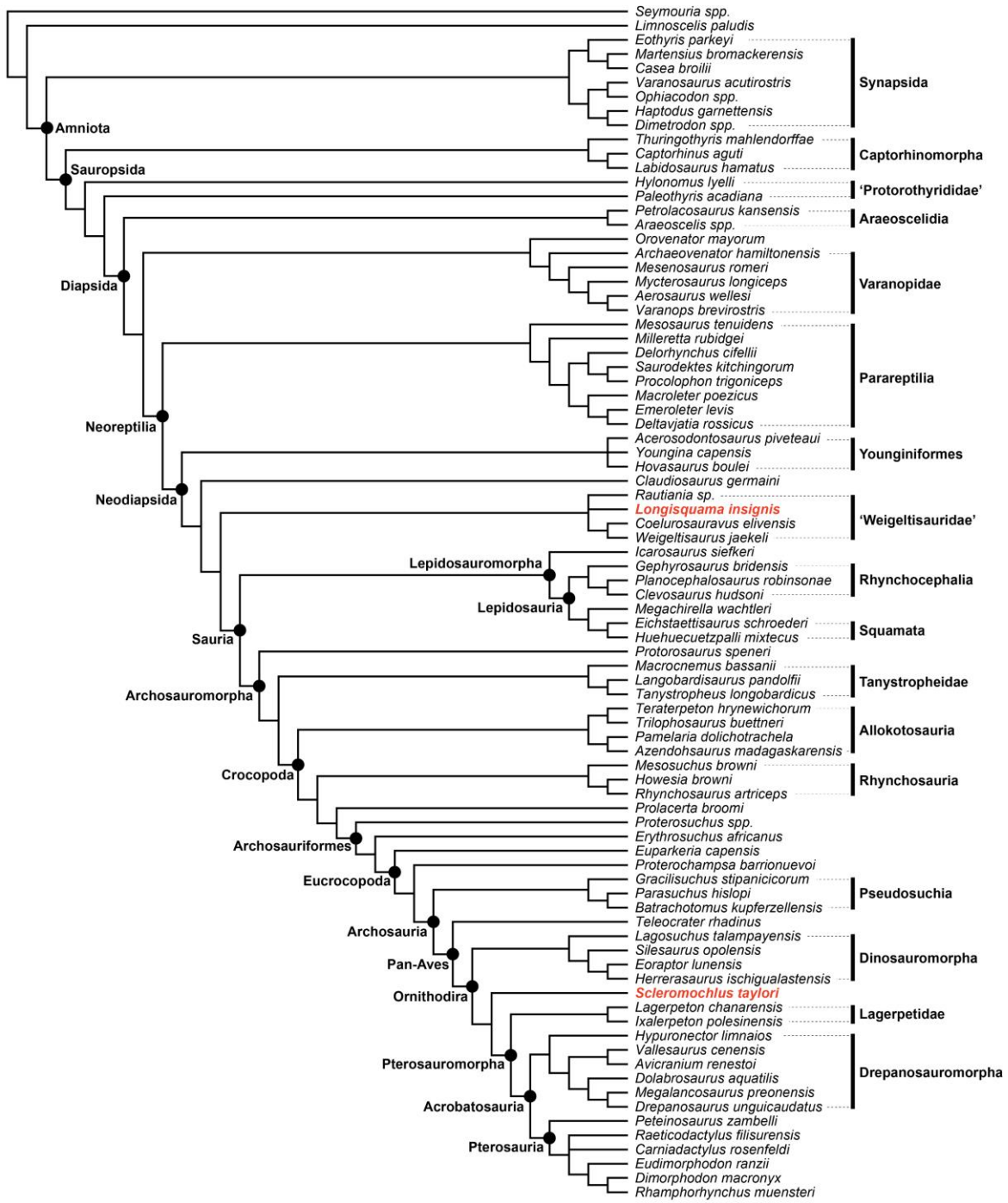

Figure A-S12: Strict consensus tree (12 MPTs of 2708 steps; L = 2710; CI = 0.1967; RI = 0.6187) of Analysis 2. Newly added OTUs *Longisquama insignis* and *Scleromochlus taylori* in red.

Analysis 2

Our second phylogenetic analysis including the enigmatic taxa *L. insignis* and *S. taylori* recovered 12 MPTs of a length of 2708 steps. The strict consensus tree has a length of 2710 steps, a consistency index (CI) of 0.1967 and a retention index (RI) of 0.6187. The resulting topology is fully congruent with the present analysis, while recovering *L. insignis* in a polytomy with weigeltisaurids and *S. taylori* as the sister-group to pterosauromorphs (Fig. S12).

The conjunction of the position of *L. insignis* together with weigeltisaurids while drepanosauromorphs are included among archosauromorphs echoes the analysis of Renesto and Binelli (2006). However, the authors noted several similarities between *L. insignis* and drepanosauromorphs in the neck and forelimb that could support drepanosauromorphs affinities for this taxon, provided it is redescribed in detail. This identification appears to have been accepted by some authors (Alifanov and Kurochkin, 2011). We did not study the material first-hand, but concur with the similarities showed by Renesto and Binelli (2006) based on photographs and published descriptions. Consequently, support for weigeltisaurid affinities for *L. insignis* is low, pending the redescription of the skeleton of the holotype.

The recovery of *S. taylori* among ornithodiran archosaurs in our analysis conforms to the view expressed by most studies (Padian, 1984; Sereno, 1991; Benton, 1999; Nesbitt et al., 2017; Ezcurra et al., 2020; Foffa et al., 2022; see Bennett, 1996, 2013, 2020 for a stem-archosaur hypothesis). There have also been debate regarding the position of *S. taylori* among ornithodirans (see Foffa et al., 2022 for an historical overview), but recent studies (e.g. Ezcurra et al., 2020; Kammerer et al., 2020; Foffa et al., 2022) recover it as closely related to pterosauromorphs. Whereas Foffa et al. (2022), in their very recent revision of the taxon, recover better support for a lagerpetid affinity, our results conform to those of Ezcurra et al. (2020) who recovered it as the sister-group to all other pterosauromorphs. However, since Foffa et al. (2022) came out after our sampling campaign, rescoring *S. taylori* based on their novel anatomical data may result in a similar topology.

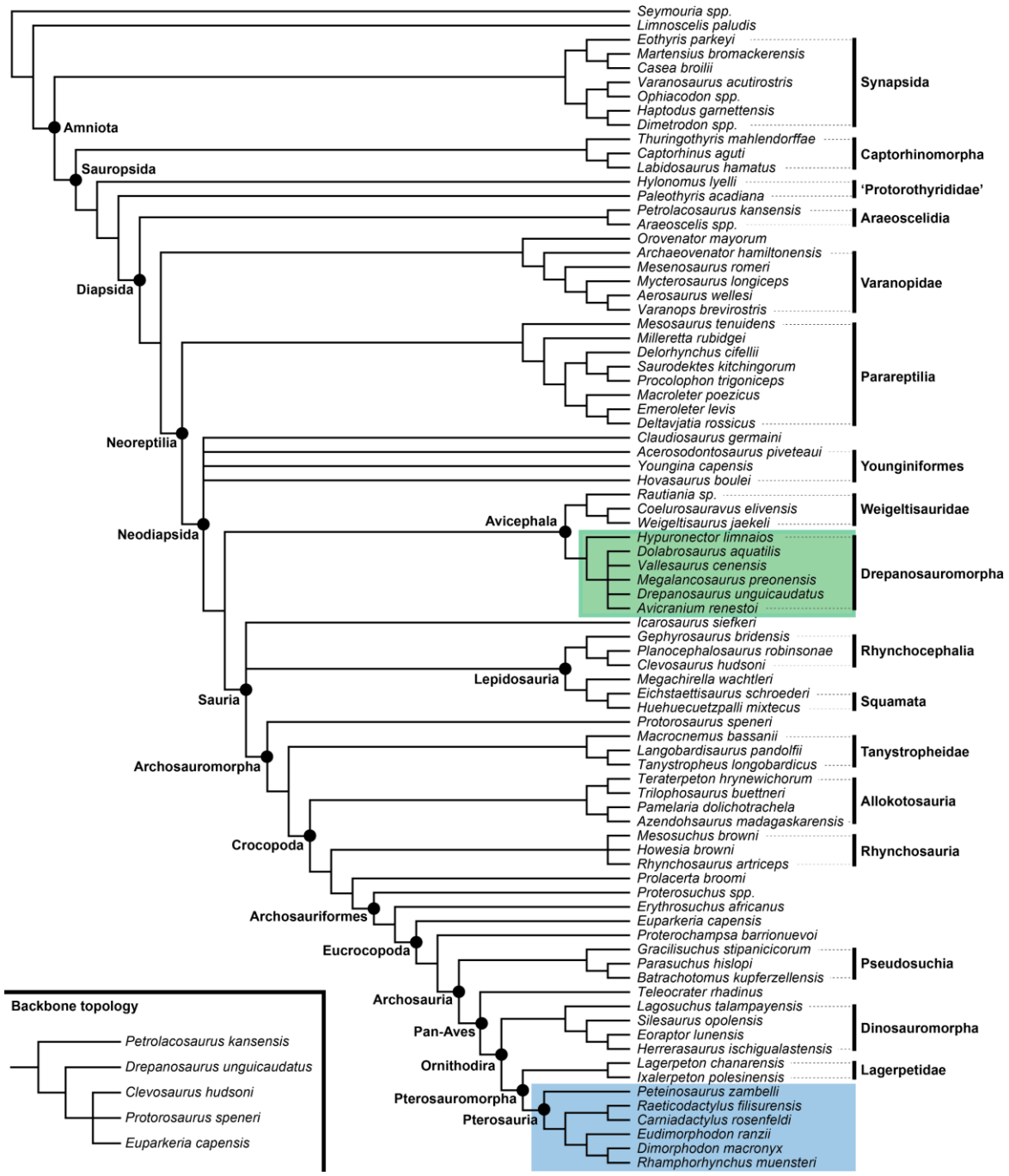

Figure A-S13: Strict consensus tree (42 MPTs of 2703 steps; L = 2740; CI = 0.1945; RI = 0.6110) of Analysis C1. Reduced phylogeny used as backbone for analysis in bottom left. Green box indicates Drepanosauromorpha, blue box indicates Pterosauria.

Analysis C1

C1 = (*Petrolacosaurus kansensis*, (*Drepanosaurus unguicaudatus*, (*Clevosaurus hudsoni*, *Protorosaurus speneri*, *Euparkeria capensis*)))

Our first constrained phylogenetic analysis forcing the recovery of drepanosauromorphs among non-archosauromorph diapsids recovered 42 MPTs of a length of 2703 steps. The strict consensus tree has a length of 2740 steps, a CI of 0.1945 and a RI of 0.6110.

The topology is broadly congruent to that of Analysis 1, although 'younginiforms' and *Claudiosaurus* form an unresolved polytomy at the base of Neodiapsida, and *Icarosaurus* is recovered in a trichotomy with Lepidosauria and Archosauromorpha (Fig. S13). None of these irresolutions are surprising given ongoing debates regarding the monophyly of 'younginiforms' and the position of kuehneosaurids among Sauria (see above).

As expected under this constraint, drepanosauromorphs are recovered together with weigeltisaurids, forming the clade Avicephala (Fig. S13). However, drepanosauromorphs are mostly unresolved, with only elyurosaurs forming a clade in this analysis.

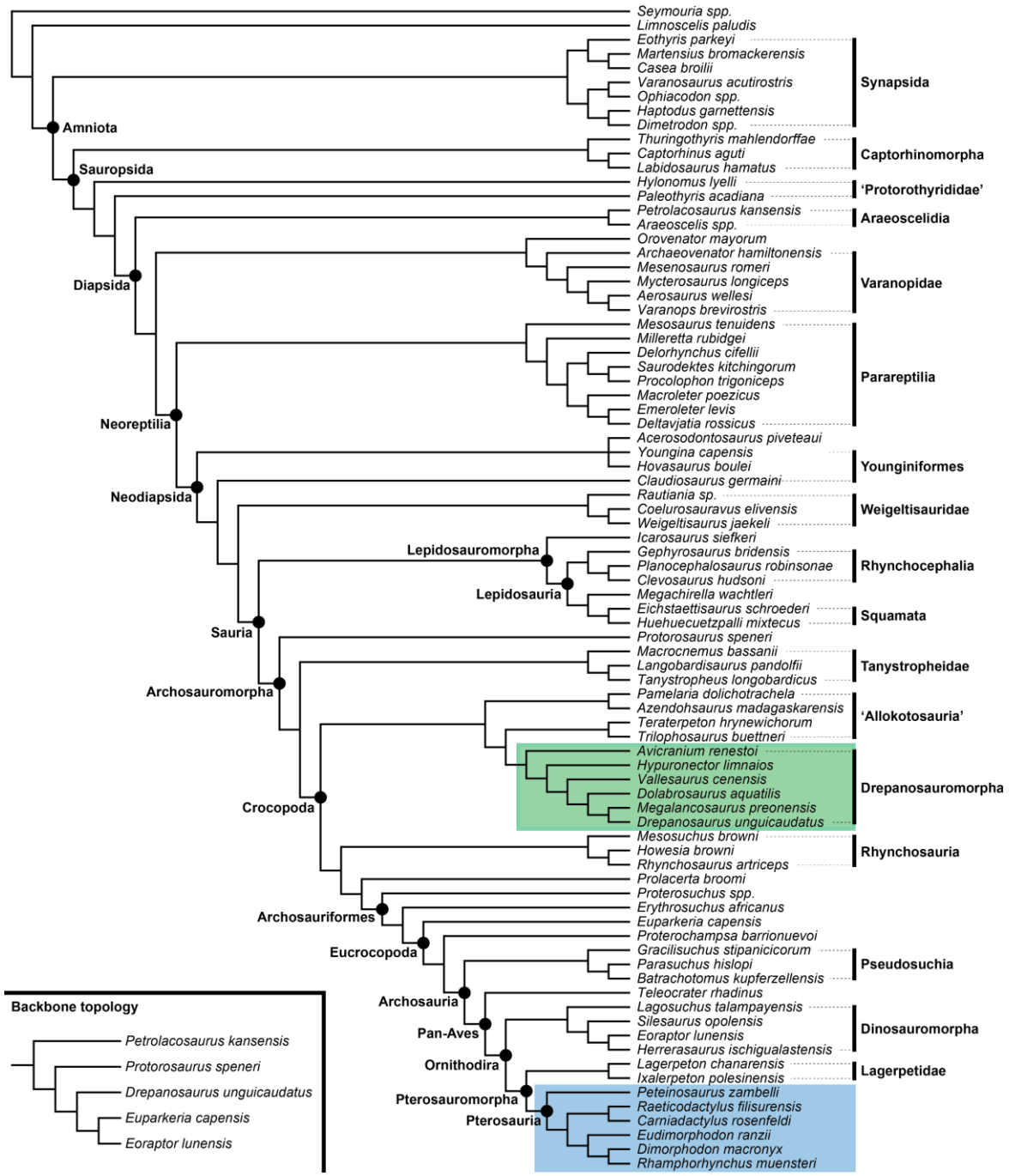

Figure A-S14: Strict consensus tree (2 MPTs of 2704 steps; L = 2705; CI = 0.1970; RI =0.6172) of Analysis C2. Reduced phylogeny used as backbone for analysis in bottom left. Green box indicates Drepanosauromorpha, blue box indicates Pterosauria.

Analysis C2

C2 = (*Petrolacosaurus kansensis*, (*Protorosaurus speneri*, (*Drepanosaurus unguicaudatus*, (*Euparkeria capensis*, *Eoraptor lunensis*))))

Our second constrained phylogenetic analysis forcing the recovery of drepanosauromorphs among Triassic non-archosauriform archosauromorphs (i.e. crownward to *Protorosaurus*) recovered 2 MPTs of a length of 2704 steps. The strict consensus tree has a length of 205 steps, a CI of 0.1970 and a RI of 0.6172.

The topology recovered is nearly fully congruent with that of Analysis 1 except in the position of drepanosauromorphs (Fig. 14). Indeed, we recover an ‘allokotosaurian’ grade with azendohsaurids and trilophosurids forming successive sister-groups to drepanosauromorphs. Given *Trilophosaurus* is the only non-acrobatosaur Triassic saurian to show unequivocal arboreal adaptations (Spielmann et al., 2005, 2008), this result likely portrays convergent adaptations to an arboreal lifestyle, as proposed by Renesto and Binelli (2006) regarding Avicephala.

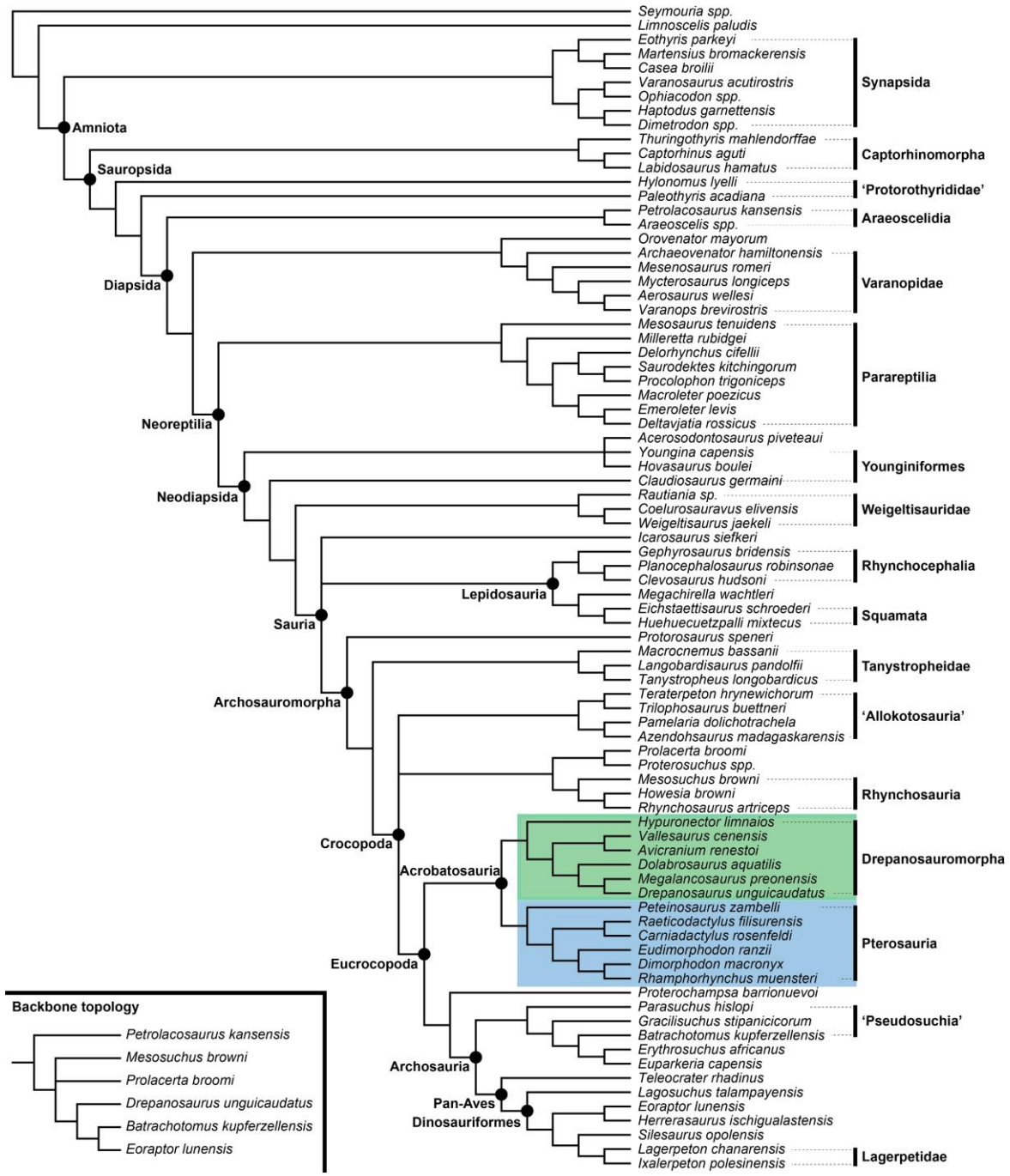

Figure A-S15: Strict consensus tree (6 MPTs of 2706 steps; L = 2714; CI = 0.1955; RI = 0.6156) of Analysis C3. Reduced phylogeny used as backbone for analysis in bottom left. Green box indicates Drepanosauromorpha, blue box indicates Pterosauria.

Analysis C3

C3 = (*Petrolacosaurus kansensis*, (*Mesosuchus browni*, *Prolacerta broomi*, (*Drepanosaurus unguicaudatus*, (*Batrachotomus kupferzellensis*, *Eoraptor lunensis*))))

Our first constrained phylogenetic analysis forcing the recovery of drepanosauromorphs among non-archosaurian archosauriforms recovered 6 MPTs of a length of 2706 steps. The strict consensus tree has a length of 2714 steps, a CI of 0.1955 and a RI of 0.6156.

The topology recovered is mostly congruent with Analysis 1 regarding non-crocopodan amniotes except that *Icarosaurus* is recovered in a trichotomy with Lepidosauria and Archosauromorpha (Fig. S15). Among crocopodans, first, we fail to recover an archosauriform clade, with *Proterosuchus* formin a clade with *Prolacerta* and rhynchosaurs. Second, we recover an Acrobatosaurian clade as sister-taxon to the clade comprising *Proterochampsa* and Archosauria, somewhat similar to the analyses of Bennett (2013, 2020). Third, we recover an expanded concept of Archosauria (following the phylogenetic definition of Gauthier and Padian, 2020), including *Erythrosuchus* and *Euparkeria*, taxa recovered as non-archosaurian archosauriforms in Analysis 1, apical to a ‘pseudosuchian’ grade. We suggest this topology caused by the applied constraint might be subject to change if the taxon sample of non-ornithodiran archosauriforms was increased. Last, we recover lagerpetids deeply-nested among dinosauromorphs.

Appendix 5: Synapomorphies for selected clades recovered in Analysis 1

Despite being key outputs for all phylogenetical analyses, lists of synapomorphies are just that –outputs. An effort was made here to make it more intelligible than the raw PAUP* results, as is often done in published articles, but no original discourse was added. As such, it was ultimately decided that this Appendix would be made available together with the Supplemental Data to avoid unnecessary lengthening of the manuscript, especially when considering several copies will be printed.

As for the rest of the Supplemental Data, Appendix 5 is thus available at Zenodo Archive.

Summary of Supplemental Data

Several of the data underlying the work presented in this thesis could not be printed, and are instead available online at Zenodo Archive.

The data for chapters 2 and 3 are already published and freely accessible:

Chapter 2—https://zenodo.org/record/4300212#.Y1LV9-c69PY

Chapter 3—https://zenodo.org/record/6078599#.Y1LWQ-c69PY

The data for all other chapters is available at (ZIP file, 2.98 Go):

http://doi.org/10.5281/zenodo.7236388

Temporary link available for Ph.D. defense committee (open until 31/12/2022):

https://zenodo.org/record/7236388?token=eyJhbGciOiJIUzUxMiIsImV4cCI6MTY3MjQzNzU5OSwiaWF0IjoxNjY2Mzc4MzA3fQ.eyJkYXRhIjp7InJlY2lkIjo3MjM2Mzg4fSwiaWQiOjI3MDQzLCJybmQiOiJiMzliZmE2YSJ9.Rt_WjwJpQk4cwFg788vncLTU4iFeoigqfkJp3JtRq4lPIvraLLSgWK8wQcSsYnNN7YRMDc-OQzlsqR41ksJzEQ

Short summary of contents:

Chapter 4—Appendix 5 of chapter; RTI photographs of regions of interest of Ialian drepanosauromorphs; matrices and backbone topologies used in phylogenetic analyses.

Chapters 5 and 6—Geometries used for CFD analyses; Empty but fully parametered case files for *D. volans* (posture P0) and *C. elivensis* (posture P1) at velocity U = 5 m/s and Angla of attack 0°; files compiling calucation results form each case; Python script to compute trajectory simulations.

Chapter 6—STL models of the patagials and gastralia segmented from Computed Laminography data, as shown in Fig. 6-1b.

References

Abdala, V., and S. Moro. 2003. A cladistic analysis of ten lizard families (Reptilia: Squamata) based on cranial musculature. Russian Journal of Herpetology 10:53–78.

Agnolin, F. L., and M. D. Ezcurra. 2019. The validity of *Lagosuchus talampayensis* Romer, 1971 (Archosauria, Dinosauriformes), from the Late Triassic of Argentina. Breviora 565:1.

Aires, A. S., L. M. Reichert, R. T. Müller, and M. B. Andrade. 2022. Review of morphology, development, and evolution of the notarium in birds. The Anatomical Record 305:2079–2098.

Aires, A. S., L. M. Reichert, R. T. Müller, F. L. Pinheiro, and M. B. Andrade. 2021. Development and evolution of the notarium in Pterosauria. Journal of Anatomy 238:400–415.

Alexander, D. E. 2015. On the Wing: Insects, Pterosaurs, Birds, Bats and the Evolution of Animal Flight. Oxford University Press, Oxford, UK, 210 pp.

Alexander, R. M. 2013. Principles of Animal Locomotion. Princeton University Press, Prinston, NJ, 384 pp.

Alifanov, V. R., and E. N. Kurochkin. 2011. *Kyrgyzsaurus bukhanchenkoi* gen. et sp. nov., a new reptile from the triassic of southwestern Kyrgyzstan. Paleontological Journal 45:639–647.

Allen, V., H. Paxton, and J. R. Hutchinson. 2009. Variation in center of mass estimates for extant sauropsids and its importance for reconstructing inertial properties of extinct archosaurs. The Anatomical Record 292:1442–1461.

Anderson, C. V., and T. E. Higham. 2013. Chameleon anatomy; pp. 7–55 in K. A. Tolley and A. Herrel (eds.), The Biology of Chameleons. University of California Press, Berkley, CA.

Anderson, J. D. 2017. Fundamentals of Aerodynamics, Sixth edition. McGraw Hill Education, New York, NY, 1130 pp.

Andres, B., and K. Padian. 2020. Pterosauromorpha; pp. 1195–1198 in K. De Queiroz, P. Cantino, and J. A. Gauthier (eds.), Phylonyms: A Companion to the PhyloCode. CRC Press, Boca Raton.

Angielczyk, K. D., and C. F. Kammerer. 2018. Non-mammalian synapsids: the deep roots of the mammalian family tree; pp. 117–198 in F. E. Zachos and R. J. Asher (eds.), Mammalian evolution, diversity and systematics., . Handbook of Zoology de Gruyter, Berlin.

Anzai, W., A. Omura, A. C. Diaz, M. Kawata, and H. Endo. 2014. Functional morphology and comparative anatomy of appendicular musculature in Cuban *Anolis* lizards with different locomotor habits. Zoological Science 31:454–463.

Arcucci, A. 1986. New materials and reinterpretation of *Lagerpeton chanarensis* Romer (Thecodontia, Lagerpetonidae nov.) from the Middle Triassic of La Rioja, Argentina. Ameghinianna 23:233–242.

Arnold, E. N. 1998. Structural niche, limb morphology and locomotion in lacertid lizards (Squamata, Lacertidae); a preliminary survey. Bulletin of the Natural History Museum (Zoology Series) 64:63–89.

Baron, M. G. 2021. The origin of Pterosaurs. Earth-Science Reviews 221:103777.

Barrett, P. M., R. J. Butler, N. P. Edwards, and A. R. Milner. 2008. Pterosaur distribution in time and space: an atlas. Zitteliana 61–107.

Barrick, R. E., M. K. Stoskopf, J. D. Marcot, D. A. Russell, and W. J. Showers. 1998. The thermoregulatory functions of the *Triceratops* frill and horns: heat flow measured with oxygen isotopes. Journal of Vertebrate Paleontology 18:746–750.

Barta, D. E., S. J. Nesbitt, and M. A. Norell. 2018. The evolution of the manus of early theropod dinosaurs is characterized by high inter- and intraspecific variation. Journal of Anatomy 232:80–104.

Bassani, F. 1886. Sui fossili e sull'età degli scisti bituminosi triasici di Besano in Lombardia. Comunicazione preliminare. Atti Della Societa Italiana Di Scienze Naturali e Del Museo Civico Di Storia Naturale Di Milano 29:15–72.

Bazzana, K. D., B. M. Gee, J. J. Bevitt, and R. R. Reisz. 2019. Neurocranial anatomy of *Seymouria* from Richards Spur, Oklahoma. Journal of Vertebrate Paleontology 39:e1694535.

Bazzana, K. D., B. M. Gee, J. J. Bevitt, and R. R. Reisz. 2020. Postcranial anatomy and histology of *Seymouria*, and the terrestriality of seymouriamorphs. PeerJ 8:e8698.

Bazzana, K. D., D. C. Evans, J. J. Bevitt, and R. R. Reisz. 2022. Neurosensory anatomy of Varanopidae and its implications for early synapsid evolution. Journal of Anatomy 240:833–849.

Bels, V., A.-S. Paindavoine, L.-N. Zghikh, E. Paulet, J.-P. Pallandre, and S. J. Montuelle. 2019. Feeding in lizards: form–function and complex multifunctional system; pp. 469–525 in V. Bels and I. Q. Whishaw (eds.), Feeding in Vertebrates: Evolution, Morphology, Behavior, Biomechanics. Springer International Publishing, Cham, Switzerland.

Benammi, M., J. Alvarado-Ortega, and J. Urrutia-Fucugauchi. 2006. Magnetostratigraphy of the lower Cretaceous strata in Tlayúa Quarry, Tepexi de Rodriguez, State of Puebla, Mexico. Earth, Planets and Space 58:1295–1302.

Bennett, S. C. 1996. The phylogenetic position of the Pterosauria within the Archosauromorpha. Zoological Journal of the Linnean Society 118:261–308.

Bennett, S. C. 1997. The arboreal leaping theory of the origin of pterosaur flight. Historical Biology 12:265–290.

Bennett, S. C. 2013. The phylogenetic position of the Pterosauria within the Archosauromorpha re-examined. Historical Biology 25:545–563.

Bennett, S. C. 2015. An external mandibular fenestra and other archosauriform characters in basal pterosaurs re-examined. Historical Biology 27:796–814.

Bennett, S. C. 2020. Reassessment of the Triassic archosauriform *Scleromochlus taylori*: neither runner nor biped, but hopper. PeerJ 8:e8418.

Benoit, J., D. P. Ford, J. A. Miyamae, and I. Ruf. 2021. Can maxillary canal morphology inform varanopid phylogenetic affinities? Acta Palaeontologica Polonica 66:389–393.

Benson, R. B. J. 2012. Interrelationships of basal synapsids: cranial and postcranial morphological partitions suggest different topologies. Journal of Systematic Palaeontology 10:601–624.

Benton, M. J. 1985. Classification and phylogeny of the diapsid reptiles. Zoological Journal of the Linnean Society 84:97–164.

Benton, M. J. 1990. The species of *Rhyncosaurus*, a rhynchosaur (Reptilia, Diapsida) from the Middle Triassic of England. Philosophical Transactions of the Royal Society of London. B, Biological Sciences 328:213–306.

Benton, M. J. 1999. *Scleromochlus taylori* and the origin of dinosaurs and pterosaurs. Philosophical Transactions of the Royal Society of London. Series B: Biological Sciences 354:1423–1446.

Benton, M. J. 2003. When Life Nearly Died: The Greatest Mass Extinction of All Time. Thames & Hudson, London, UK, 352 pp.

Benton, M. J. 2010. Studying function and behavior in the fossil record. PLoS Biology 8:e1000321.

Benton, M. J. 2016. The Triassic. Current Biology 26:R1214–R1218.

Benton, M. J., and P. S. Spencer. 1995. Fossil Reptiles of Great Britain. Chapman and Hall, London, UK, 386 pp.

Benton, M. J., and J. L. Allen. 1997. *Boreopricea* from the Lower Triassic of Russia, and the relationships of the prolacertiform reptiles. Palaeontology 40:931–954.

Benton, M. J., and A. D. Walker. 2002. *Erpetosuchus*, a crocodile-like basal archosaur from the Late Triassic of Elgin, Scotland. Zoological Journal of the Linnean Society 136:25–47.

Benton, M. J., and R. J. Twitchett. 2003. How to kill (almost) all life: the end-Permian extinction event. Trends in Ecology & Evolution 18:358–365.

Benton, M. J., and A. D. Walker. 2010. *Saltopus*, a dinosauriform from the Upper Triassic of Scotland. Earth and Environmental Science Transactions of the Royal Society of Edinburgh 101:285–299.

Benton, M. J., G. Warrington, A. J. Newell, and P. S. Spencer. 1994. A review of the British Middle Triassic tetrapod assemblages; pp. 131–160 in N. C. Fraser and H.-D. Sues (eds.), In the shadow of the dinosaurs: Early Mesozoic tetrapods. Cambridge University Press, Cambridge, UK.

Benton, M. J., P. C. J. Donoghue, R. J. Asher, M. Friedman, T. J. Near, and J. Vinther. 2015. Constraints on the timescale of animal evolutionary history. Palaeontologia Electronica 18:1–106.

Bergmann, P. J., and C. P. Berk. 2012. The evolution of positive allometry of weaponry in horned lizards (*Phrynosoma*). Evolutionary Biology 39:311–323.

Berman, D. S. 2013. Diadectomorphs: amniotes or not. New Mexico Museum of Natural History and Science Bulletin 60:22–35.

Berman, D. S., and R. R. Reisz. 1982. Restudy of *Mycterosaurus longiceps* (Reptilia, Pelycosauria) from the Lower Permian of Texas. 51:423–453.

Berman, D. S., and R. R. Reisz. 1992. *Dolabrosaurus aquatilis*, a small lepidosauromorph reptile from the Upper Triassic Chinle Formation of north-central New Mexico. Journal of Paleontology 66:1001–1009.

Berman, D. S., and A. C. Henrici. 2003. Homology of the astragalus and structure and function of the tarsus of Diadectidae. Journal of Paleontology 77:172–188.

Berman, D. S., R. R. Reisz, and D. A. Eberth. 1987. *Seymouria sanjuanensis* (Amphibia, Batrachosauria) from the Lower Permian Cutler Formation of north-central New Mexico and the occurrence of sexual dimorphism in that genus questioned. Canadian Journal of Earth Sciences 24:1769–1784.

Berman, D. S., S. G. Lucas, and J. Zidek. 1993. Lower Permian vertebrate localities of New Mexico and their assemblages. New Mexico Museum of Natural History and Science Bulletin 2:11–21.

Berman, D. S., R. R. Reisz, and D. M. Scott. 2010. Redescription of the skull of *Limnoscelis paludis* Williston (Diadectomorpha: Limnoscelidae) from the Pennsylvanian of Canon del Cobre, northern New Mexico. New Mexico Museum of Natural History and Science Bulletin 49:185–210.

Berman, D. S., R. R. Reisz, J. R. Bolt, and D. Scott. 1995. The cranial anatomy and relationships of the synapsid *Varanosaurus* (Eupelycosauria: Ophiacodontidae) from the Early Permian of Texas and Oklahoma. Annals of the Carnegie Museum 64:99–133.

Berman, D. S., A. C. Henrici, S. S. Sumida, and T. Martens. 2000. Redescription of *Seymouria sanjuanensis* (Seymouriamorpha) from the Lower Permian of Germany based on complete, mature specimens with a discussion of paleoecology of the Bromacker locality assemblage. Journal of Vertebrate Paleontology 20:253–268.

Berman, D. S., H. C. Maddin, A. C. Henrici, S. S. Sumida, D. Scott, and R. R. Reisz. 2020. New primitive caseid (Synapsida, Caseasauria) from the Early Permian of Germany. Annals of Carnegie Museum 86:43–75.

Berman, D. S., S. S. Sumida, A. C. Henrici, D. Scott, R. R. Reisz, and T. Martens. 2021. The Early Permian bolosaurid *Eudibamus cursoris*: Earliest reptile to combine parasagittal stride and digitigrade posture during quadrupedal and bipedal locomotion. Frontiers in Ecology and Evolution 9:674173.

Bernardi, M., H. Klein, F. M. Petti, and M. D. Ezcurra. 2015. The origin and early radiation of archosauriforms: Integrating the skeletal and footprint record. PLoS ONE 10:e0128449.

Bernardi, M., F. M. Petti, E. Kustatscher, M. Franz, C. Hartkopf-Fröder, C. C. Labandeira, T. Wappler, J. H. A. van Konijnenburg-van Cittert, B. R. Peecook, and K. D. Angielczyk. 2017. Late Permian (Lopingian) terrestrial ecosystems: A global comparison with new data from the low-latitude Bletterbach Biota. Earth-Science Reviews 175:18–43.

Berner, R. A. 2009. Phanerozoic atmospheric oxygen: New results using the GEOCARBSULF model. American Journal of Science 309:603–606.

Bertin, T. J. C., B. Thivichon-Prince, A. R. H. LeBlanc, M. W. Caldwell, and L. Viriot. 2018. Current perspectives on tooth implantation, attachment, and replacement in Amniota. Frontiers in Physiology 9:1630.

Besairie, H. 1972. Géologie de Madagascar. I. Les terrains sédimentaires. Annales Géologiques de Madagascar 35:1–465.

Besairie, H. 1973. Précis de géologie malgache. Annales Géologiques de Madagascar 36:1–141.

Béthoux, O., A. Llamosi, and S. Toussaint. 2016. Reinvestigation of *Protelytron permianum* (Insecta; Early Permian; USA) as an example for applying reflectance transformation imaging to insect imprint fossils. Fossil Record 20:1–7.

Bever, G. S., T. R. Lyson, D. J. Field, and B.-A. S. Bhullar. 2015. Evolutionary origin of the turtle skull. Nature 525:239–242.

Bhullar, B.-A. S. 2012. A phylogenetic approach to ontogeny and heterochrony in the fossil record: cranial evolution and development in anguimorphan lizards (Reptilia: Squamata). Journal of Experimental Zoology Part B: Molecular and Developmental Evolution 318:521–530.

Bickel, R., and J. B. Losos. 2002. Patterns of morphological variation and correlates of habitat use in Chameleons. Biological Journal of the Linnean Society 76:91–103.

Bickelmann, C., J. Müller, and R. R. Reisz. 2009. The enigmatic diapsid *Acerosodontosaurus piveteaui* (Reptilia: Neodiapsida) from the Upper Permian of Madagascar and the paraphyly of "younginiform" reptiles. Canadian Journal of Earth Sciences 46:651–661.

Birn-Jeffery, A. V., C. E. Miller, D. Naish, E. J. Rayfield, and D. W. E. Hone. 2012. Pedal claw curvature in birds, lizards and Mesozoic dinosaurs – complicated categories and compensating for mass-specific and phylogenetic control. PLoS ONE 7:e50555.

Bishop, P. J., A. R. Cuff, and J. R. Hutchinson. 2021. How to build a dinosaur: Musculoskeletal modeling and simulation of locomotor biomechanics in extinct animals. Paleobiology 47:1–38.

Bona, P., M. V. Fernandez Blanco, M. D. Ezcurra, M. B. von Baczko, J. B. Desojo, and D. Pol. 2022. On the homology of crocodylian post-dentary bones and their macroevolution throughout Pseudosuchia. The Anatomical Record 305:2980–3001.

Bonaparte, J. F. 1975. Nuevos materiales de *Lagosuchus talampayensis* Romer (Thecodontia-Pseudosuchia) y su significade en el origende los Sauriscia. Acta Geologica Lilloana 13:5–90.

Bonde, N., and P. Christiansen. 2003. The detailed anatomy of *Rhamphorhynchus*: axial pneumaticity and its implications. Geological Society, London, Special Publications 217:217–232.

Bonde, N., and M. E. C. Leal. 2015. The detailed anatomy of *Rhamphorhynchus* II: braincase, pneumatics and jaws. Historical Biology 27:755–770.

Borsuk-Białynicka, M. 2008. Evolution of the iliosacral joint in diapsid phylogeny. Neues Jahrbuch Für Geologie Und Paläontologie - Abhandlungen 249:297–311.

Borsuk-Białynicka, M. 2018. Diversity of diapsid fifth metatarsals from the Lower Triassic karst deposits of Czatkowice, southern Poland—functional and phylogenetic implications. Acta Palaeontologica Polonica 63:417–434.

Borsuk-Białynicka, M., and S. E. Evans. 2009a. A long-necked archosauromorph from the Early Triassic of Poland. Palaeontologia Polonica 65:203–234.

Borsuk-Białynicka, M., and S. E. Evans. 2009b. Cranial and mandibular osteology of the Early Triassic archosauriform *Osmolskina czatkowicensis* from Poland. Paleontologia Polonica 65:235–281.

Botelho, J. F., L. Ossa-Fuentes, S. Soto-Acuña, D. Smith-Paredes, D. Nuñez-León, M. Salinas-Saavedra, M. Ruiz-Flores, and A. O. Vargas. 2014. New developmental evidence clarifies the evolution of wrist bones in the dinosaur–bird transition. PLoS Biology 12:e1001957.

Botha, J., and R. M. H. Smith. 2020. Biostratigraphy of the *Lystrosaurus declivis* Assemblage Zone (Beaufort Group, Karoo Supergroup), South Africa. South African Journal of Geology 123:207–216.

Botha, J., S. P. Modesto, and R. M. H. Smith. 2007. Extended procolophonoid reptile survivorship after the end-Permian extinction. South African Journal of Science 103:54–56.

Boule, M. 1910. Sur le Permien de Madagascar. Bulletin de la Société Géologique de France 10:314–316.

Boy, J. A., and T. Martens. 1991. Ein neues captorhinomorphes Reptil aus dem thüringischen Rotliegend (Unter-Perm; Ost-Deutschland). Paläontologische Zeitschrift 65:363–389.

Bradley, A. B., S. H. Burch, A. H. Turner, N. D. Smith, R. B. Irmis, and S. J. Nesbitt. 2019. Sternal elements of early dinosaurs fill a critical gap in the evolution of the sternum in Avemetatarsalia (Reptilia: Archosauria). Journal of Vertebrate Paleontology 39:e1700992.

Brand, U., A. M. Davis, K. K. Shaver, N. J. F. Blamey, M. Heizler, and C. Lécuyer. 2021. Atmospheric oxygen of the Paleozoic. Earth-Science Reviews 216:103560.

Brassey, C. A. 2016. Body-mass estimation in paleontology: a review of volumetric techniques. The Paleontological Society Papers 22:133–156.

Bright, J. A. 2014. A review of paleontological finite element models and their validity. Journal of Paleontology 88:760–769.

Brink, K. S., and R. R. Reisz. 2012. Morphology of the palate and braincase of *Dimetrodon milleri*. Historical Biology 24:453–459.

Brinkman, D. 1979. The structural and functional evolution of the diapsid tarsus. Ph.D. dissertation, McGill University, Montreal, Canada, 328 pp.

Brinkman, D. 1988. A weigeltisaurid reptile from the Lower Triassic of British Columbia. Palaeontology 31:951–956.

Britt, B., and D. Chure. 2016. Rise of the Erg—Paleontology and paleoenvironments of the Triassic-Jurassic transition in Northeastern Utah. Geology of the Intermountain West 3:1–32.

Brocklehurst, N. 2017. Rates of morphological evolution in Captorhinidae: an adaptive radiation of Permian herbivores. PeerJ 5:e3200.

Brocklehurst, N. 2020. Olson's Gap or Olson's Extinction? A Bayesian tip-dating approach to resolving stratigraphic uncertainty. Proceedings of the Royal Society B: Biological Sciences 287:20200154.

Brocklehurst, N. 2021. The First Age of Reptiles? Comparing Reptile and Synapsid Diversity, and the Influence of Lagerstätten, During the Carboniferous and Early Permian. Frontiers in Ecology and Evolution 9:669765.

Brocklehurst, N., and R. J. Benson. 2021. Multiple paths to morphological diversification during the origin of amniotes. Nature Ecology & Evolution 5:1243–1249.

Brocklehurst, N., M. Ruta, J. Müller, and J. Fröbisch. 2015. Elevated Extinction Rates as a Trigger for Diversification Rate Shifts: Early Amniotes as a Case Study. Scientific Reports 5:17104.

Brocklehurst, N., M. O. Day, B. S. Rubidge, and J. Fröbisch. 2017. Olson's Extinction and the latitudinal biodiversity gradient of tetrapods in the Permian. Proceedings of the Royal Society B: Biological Sciences 284:20170231.

Brocklehurst, N., E. M. Dunne, D. D. Cashmore, and J. Fröbisch. 2018. Physical and environmental drivers of Paleozoic tetrapod dispersal across Pangaea. Nature Communications 9:5216.

Broili, F. 1904. Permische Stegocephalen und Reptilien aus Texas. Palaeontographica 1–48.

Broili, F. 1938. Ein neuer fund von ?*Ardeosaurus* H. von Meyer. Sitzungsberichte Der Mathematisch-Naturwissenschaftlichen Abteilung 1938:97–114.

Broom, R. 1903. On a new reptile (*Proterosuchus fergusi*) from the Karoo beds of Tarkastad, South Africa. Annals of the South African Museum 4:159–163.

Broom, R. 1905a. Notice of some new fossil reptiles from the Karroo beds of South Africa. Records of the Albany Museum 1:331–337.

Broom, R. 1905b. Preliminary notice of some new fossil reptiles collected by Mr. Alfred Brown at Aliwal North, South Africa. Records of the Albany Museum 1:269–275.

Broom, R. 1906. On the South African diaptosaurian reptile *Howesia*. Proceedings of the Zoological Society of London 1906:591–600.

Broom, R. 1913. On the South-African pseudosuchian *Euparkeria* and allied genera. Proceedings of the Zoological Society of London 83:619–633.

Broom, R. 1914. A new thecodont reptile. Proceedings of the Zoological Society of London 1914:1072–1077.

Broom, R. 1921. On the structure of the reptilian tarsus. Proceedings of the Zoological Society of London 91:143–156.

Broom, R. 1922. An imperfect skeleton of *Youngia capensis*, Broom, in the collection of the Transvaal Museum. Annals of the Transvaal Museum 8:273–276.

Broom, R. 1924. Further evidence on the structure of the Eosuchia. Bulletin of the American Museum of Natural History 51:67/76.

Broom, R. 1938. On a new type of primitive fossil reptile from the Upper Permian of South Africa. Proceedings of the Zoological Society of London 108:535–542.

Broom, R. 1947. A contribution to our knowledge of the vertebrates of the Karroo Beds of South Africa. Transactions of the Royal Society of Edinburgh 61:577–629.

Brusatte, S. L., M. J. Benton, G. T. Lloyd, M. Ruta, and S. C. Wang. 2011. Macroevolutionary patterns in the evolutionary radiation of archosaurs (Tetrapoda: Diapsida). Earth and Environmental Science Transactions of The Royal Society of Edinburgh 101:367–382.

Bryant, H. N., and K. L. Seymour. 1990. Observations and comments on the reliability of muscle reconstruction in fossil vertebrates. Journal of Morphology 206:109–117.

Buckland, W. 1829. On the discovery of a new species of pterodactyle in the Lias at Lyme Regis. Transactions of the Geological Society of London 3:217–222.

Buffa, V. 2019. Réévaluation d'un ensemble de vertébrés fossiles du Permien de Madagascar conservés sous le nom de genre *Datheosaurus* dans les collections du MNHN : anatomie, systématique et phylogénie. M.Sc. dissertation, Muséum national d'Histoire Naturelle, Paris, France, 42 pp.

Buffa, V., E. Frey, J.-S. Steyer, and M. Laurin. 2021. A new cranial reconstruction of *Coelurosauravus elivensis* Piveteau, 1926 (Diapsida, Weigeltisauridae) and its implications on the paleoecology of the first gliding vertebrates. Journal of Vertebrate Paleontology 41:e1930020.

Buffa, V., E. Frey, J.-S. Steyer, and M. Laurin. 2022. The postcranial skeleton of the gliding reptile *Coelurosauravus elivensis* Piveteau, 1926 (Diapsida, Weigeltisauridae) from the late Permian of Madagascar. Journal of Vertebrate Paleontology e2108713.

Buffrénil, V. de, F. Clarac, A. Canoville, and M. Laurin. 2016. Comparative data on the differentiation and growth of bone ornamentation in gnathostomes (Chordata: Vertebrata). Journal of Morphology 277:634–670.

Buffrénil, V. de, F. Clarac, M. Fau, S. Martin, B. Martin, E. Pellé, and M. Laurin. 2015. Differentiation and Growth of Bone Ornamentation in Vertebrates: A Comparative Histological Study Among the Crocodylomorpha. Journal of Morphology 276:425–445.

Bulanov, V. V., and A. G. Sennikov. 2006. The first gliding reptiles from the Upper Permian of Russia. Paleontological Journal 40:S567–S570.

Bulanov, V. V., and A. G. Sennikov. 2010. New data on the morphology of Permian gliding weigeltisaurid reptiles of Eastern Europe. Paleontological Journal 44:682–694.

Bulanov, V. V., and A. G. Sennikov. 2014. New localities of the Upper Permian gliding diapsids (Weigeltisauridae) in European Russia. Journal of Vertebrate Paleontology 74A:100.

Bulanov, V. V., and A. G. Sennikov. 2015a. New data on the morphology of the Late Permian gliding reptile *Coelurosauravus elivensis* Piveteau. Paleontological Journal 49:413–423.

Bulanov, V. V., and A. G. Sennikov. 2015b. *Glaurung schneideri* gen. et sp. nov., a new weigeltisaurid (Reptilia) from the Kupfershiefer (Upper Permian) of Germany. Paleontological Journal 49:1353–1364.

Bulanov, V. V., and A. G. Sennikov. 2015c. Substantiation of validity of the Late Permian genus *Weigeltisaurus* Kuhn, 1939 (Reptilia, Weigeltisauridae). Paleontological Journal 49:1101–1111.

Bullar, C. M., Q. Zhao, M. J. Benton, and M. J. Ryan. 2019. Ontogenetic braincase development in *Psittacosaurus lujiatunensis* (Dinosauria: Ceratopsia) using micro-computed tomography. PeerJ 7:e7217.

Butler, R. J., P. M. Barrett, and D. J. Gower. 2009. Postcranial skeletal pneumaticity and air-sacs in the earliest pterosaurs. Biology Letters 5:557–560.

Butler, R. J., C. Sullivan, M. D. Ezcurra, J. Liu, A. Lecuona, and R. B. Sookias. 2014. New clade of enigmatic early archosaurs yields insights into early pseudosuchian phylogeny and the biogeography of the archosaur radiation. BMC Evolutionary Biology 14:128.

Byrnes, G., and B. C. Jayne. 2012. The effects of three-dimensional gap orientation on bridging performance and behavior of brown tree snakes (*Boiga irregularis*). Journal of Experimental Biology 215:2611–2620.

Cabreira, S. F., A. W. A. Kellner, S. Dias-da-Silva, L. R. da Silva, M. Bronzati, J. C. de A. Marsola, R. T. Müller, J. de S. Bittencourt, B. J. Batista, T. Raugust, R. Carrilho, A. Brodt, and M. C. Langer. 2016. A unique Late Triassic dinosauromorph assemblage reveals dinosaur ancestral anatomy and diet. Current Biology 26:3090–3095.

Caldwell, M. W. 1995. Developmental constraints and limb evolution in Permian and extant lepidosauromorph diapsids. Journal of Vertebrate Paleontology 14:459–471.

Calzavara, M., G. Muscio, and R. Wild. 1980. *Megalancosaurus preonensis* ng, n. sp., a new reptile from the Norian of Friuli, Italy. Gortiana 2:49–64.

Camp, C. L. 1945a. *Prolacerta* and the protorosaurian reptiles. Part I. American Journal of Science 243:17–32.

Camp, C. L. 1945b. *Prolacerta* and the protorosaurian reptiles. Part II. American Journal of Science 243:84–101.

Campione, N. E., and R. R. Reisz. 2010. *Varanops brevirostris* (Eupelycosauria: Varanopidae) from the Lower Permian of Texas, with discussion of varanopid morphology and interrelationships. Journal of Vertebrate Paleontology 30:724–746.

Campione, N. E., and R. R. Reisz. 2011. Morphology and evolutionary significance of the atlas-axis complex in varanopid synapsids. Acta Palaeontologica Polonica 56:739–748.

Cannell, A. E. R. 2018. The engineering of the giant dragonflies of the Permian: revised body mass, power, air supply, thermoregulation and the role of air density. Journal of Experimental Biology 221:jeb185405.

Carrano, M. T. 1998. Locomotion in non-avian dinosaurs: integrating data from hindlimb kinematics, in vivo strains, and bone morphology. Paleobiology 24:450–469.

Carroll, R. L. 1964. The earliest reptiles. Journal of the Linnean Society of London, Zoology 45:61–83.

Carroll, R. L. 1969a. A Middle Pennsylvanian captorhinomorph, and the interrelationships of primitive reptiles. Journal of Paleontology 151–170.

Carroll, R. L. 1969b. Problems of the Origin of Reptiles. Biological Reviews 44:393–431.

Carroll, R. L. 1975. Permo-Triassic “lizards” from the Karroo. Paleontologia Africana 18:71–87.

Carroll, R. L. 1976. *Noteosuchus*, the oldest known rhynchosaur. Annals of the South African Museum 72:37–57.

Carroll, R. L. 1977. The origin of lizards; pp. 359–396 in S. M. Andrews, R. S. Miles, and A. D. Walker (eds.), Problems in Vertebrate Evolution. Academic Press, London.

Carroll, R. L. 1978. Permo-Triassic “lizards” from the Karoo System. Part II. A gliding reptile from the Upper Permian of Madagascar. Paleontologia Africana 21:143–159.

Carroll, R. L. 1981. Plesiosaur ancestors from the Upper Permian of Madagascar. Philosophical Transactions of the Royal Society of London. Series B, Biological Sciences 293:315–383.

Carroll, R. L. 1988. Vertebrate Paleontology and Evolution. W.H. Freeman and Company, New York, pp.

Carroll, R. L., and D. Baird. 1972. Carboniferous stem-reptiles of the family Romeriidae. Bulletin of the Museum of Comparative Zoology 143:321–364.

Carroll, R. L., and W. Lindsay. 1985. Cranial anatomy of the primitive reptile *Procolophon*. Canadian Journal of Earth Sciences 22:1571–1587.

Cartmill, M. 1974. Pads and claws in arboreal locomotion. Primate Locomotion 1:43–83.

Cartmill, M. 1985. Climbing; pp. 73–88 in M. Hildebrand, D. M. Bramble, K. F. Liem, and D. B. Wake (eds.), Functional Vertebrate Morphology. Harvard University Press, Cambridge, MS.

Case, E. C. 1910a. Description of a skeleton of *Dimetrodon incisivus* Cope. Bulletin of the American Museum of Natural History 28:198–196.

Case, E. C. 1910b. The skeleton of *Poecilospondylus francisi*, a new genus and species of Pelycosauria. Bulletin of the American Museum of Natural History 28:183–188.

Case, E. C. 1928. A cotylosaur from the Upper Triassic of western Texas. Journal of the Washington Academy of Sciences 18:177–178.

Castiello, M., S. Renesto, and S. C. Bennett. 2016. The role of the forelimb in prey capture in the Late Triassic reptile *Megalancosaurus* (Diapsida, Drepanosauromorpha). Historical Biology 28:1090–1100.

Cau, A., V. Beyrand, R. Barsbold, K. Tsogtbaatar, and P. Godefroit. 2021. Unusual pectoral apparatus in a predatory dinosaur resolves avian wishbone homology. Scientific Reports 11:14722.

Cavicchini, I., M. Zaher, and M. J. Benton. 2020. An enigmatic neodiapsid reptile from the Middle Triassic of England. Journal of Vertebrate Paleontology 40:e1781143.

Chambi-Trowell, S. A., D. I. Whiteside, and M. J. Benton. 2019. Diversity in rhynchocephalian *Clevosaurus* skulls based on CT reconstruction of two Late Triassic species from Great Britain. Acta Palaeontologica Polonica 64.

Chatterjee, S. 1978. A primitive parasuchid (phytosaur) reptile from the Upper Triassic Maleri Formation of India. Palaeontology 21:83–127.

Chatterjee, S., and R. J. Templin. 2003. The flight of *Archaeopteryx*. Naturwissenschaften 90:27–32.

Chatterjee, S., and R. J. Templin. 2004. Posture, locomotion, and paleoecology of pterosaurs. Geological Society of America Special Papers 376:1–64.

Chatterjee, S., and R. J. Templin. 2007. Biplane wing planform and flight performance of the feathered dinosaur *Microraptor gui*. Proceedings of the National Academy of Sciences 104:1576–1580.

Chen, Z.-Q., and M. J. Benton. 2012. The timing and pattern of biotic recovery following the end-Permian mass extinction. Nature Geoscience 5:375–383.

Chun, L., O. Rieppel, C. Long, and N. C. Fraser. 2016. The earliest herbivorous marine reptile and its remarkable jaw apparatus. Science Advances 2:e1501659.

Chure, D. C., B. B. Britt, M. S. Engel, A. S. Andrus, and R. D. Scheetz. 2013. Drepanosaurs in the desert: multiple skeletons of a new drepanosaurid from the eolian Nugget Sandstone (?Late Triassic- Early Jurassic), Saints and Sinners Quarry, Utah: morphology, relationships, and biostratigraphic implications. Journal of Vertebrate Paleontology 33:106.

Chure, D. C., A. S. Andrus, B. B. Britt, G. F. Engelmann, A. C. Pritchard, R. D. Scheetz, and M. Chambers. 2015. Micro CT imagery reveals a unique manus morphology with digging/scratching adaptations in the Saints and Sinners Quarry (SSQ) drepanosaur, Nugget Sandstone (Late Triassic), Northeastern Utah. Journal of Vertebrate Paleontology, Program with Abstracts 1:408.

Cisneros, J. C. 2008. Taxonomic status of the reptile genus *Procolophon* from the Gondwanan Triassic. Palaeontologia Africana 43:7–17.

Cisneros, J. C., and L. A. Tsuji. 2009. Nycteroleter affinities of a Permian parareptile from the South African Karoo Basin. Acta Palaeontologica Polonica 54:165–169.

Cisneros, J. C., and M. Ruta. 2010. Morphological diversity and biogeography of procolophonids (Amniota: Parareptilia). Journal of Systematic Palaeontology 8:607–625.

Cisneros, J. C., K. Angielczyk, C. F. Kammerer, R. M. H. Smith, J. Fröbisch, C. A. Marsicano, and M. Richter. 2020. Captorhinid reptiles from the lower Permian Pedra de Fogo Formation, Piauí, Brazil: the earliest herbivorous tetrapods in Gondwana. PeerJ 8:e8719.

Cisneros, J. C., C. F. Kammerer, K. D. Angielczyk, J. Fröbisch, C. Marsicano, R. M. H. Smith, and M. Richter. 2021. A new reptile from the lower Permian of Brazil (*Karutia fortunata* gen. et sp. nov.) and the interrelationships of Parareptilia. Journal of Systematic Palaeontology 1–23.

Claessens, L. P. A. M. 2004. Dinosaur gastralia; origin, morphology, and function. Journal of Vertebrate Paleontology 24:89–106.

Claessens, L. P. A. M., P. M. O'Connor, and D. M. Unwin. 2009. Respiratory evolution facilitated the origin of pterosaur flight and aerial gigantism. PLoS ONE 4:e4497.

Clapham, M. E., and J. A. Karr. 2012. Environmental and biotic controls on the evolutionary history of insect body size. Proceedings of the National Academy of Sciences 109:10927–10930.

Clark, J., and R. L. Carroll. 1973. Romeriid reptiles from the Lower Permian. Bulletin of the Museum of Comparative Zoology 144:353–407.

Clark, J., C. Clark, and T. E. Higham. 2021. Tail control enhances gliding in arboreal lizards: an integrative study using a 3D geometric model and numerical simulation. Integrative and Comparative Biology 61:579–588.

Clark, J. M., J. Welman, J. A. Gauthier, and J. M. Parrish. 1993. The laterosphenoid bone of early archosauriforms. Journal of Vertebrate Paleontology 13:48–57.

Clark, J. M., J. A. Hopson, R. Hernández R., D. E. Fastovsky, and M. Montellano. 1998. Foot posture in a primitive pterosaur. Nature 391:886–889.

Cohen, K. M., S. C. Finney, P. L. Gibbard, and J.-X. Fan. 2020. (2013; updated). The ICS international chronostratigraphic chart. Episodes 36:199–204.

Cohen, K. M., S. C. Finney, P. L. Gibbard, and J.-X. Fan. 2022. (2013; updated). The ICS international chronostratigraphic chart. Episodes 36:199–204.

Colbert, E. H. 1966. A gliding reptile from the Triassic of New Jersey. American Museum Novitates 2246:1–24.

Colbert, E. H. 1967. Adaptations for gliding in the lizard *Draco*. American Museum Novitates 2283:1–20.

Colbert, E. H. 1970. The Triassic gliding reptile *Icarosaurus*. Bulletin of the American Museum of Natural History 143:87–142.

Colbert, E. H. 1987. The Triassic Reptile *Prolacerta* in Antarctica. American Museum Novitates 2882:1–19.

Colbert, E. H., and P. E. Olsen. 2001. A new and unusual aquatic reptile from the Lockatong Formation of New Jersey (Late Triassic, Newark Supergroup). American Museum Novitates 2001:1–24.

Conrad, J. L. 2008. Phylogeny and systematics of Squamata (Reptilia) based on morphology. Bulletin of the American Museum of Natural History 310:1–182.

Conrad, J. L. 2018. A new lizard (Squamata) was the last meal of *Compsognathus* (Theropoda: Dinosauria) and is a holotype in a holotype. Zoological Journal of the Linnean Society 183:584–634.

Cope, E. D. 1869. Synopsis of the extinct Batrachia, Reptilia and Aves of North America. Part I. Transactions of the American Philosophical Society, New Series 14:1–104.

Cope, E. D. 1878. Descriptions of extinct Batrachia and Reptilia from the Permian formation of Texas. Proceedings of the American Philosophical Society 17:505–530.

Cope, E. D. 1882. Third contribution to the history of the Vertebrata of the Permian formation of Texas. Proceedings of the American Philosophical Society 20:447–461.

Cope, E. D. 1895. The reptilian order Cotylosauria. Proceedings of the American Philosophical Society 34:436–457.

Cruickshank, A. R. I. 1972. The proterosuchian thecodonts; pp. 89–119 in K. A. Josey and T. S. Kemp (eds.), Studies in vertebrate evolution. Winchester Press, New York, NY.

Cruickshank, A. R. I. 1979. The ankle joint in some early archosaurs. South African Journal of Science 75:168–178.

Cui, Y., S. Toussaint, and O. Béthoux. 2018. The systematic position of the stonefly †*culonga* Sinitshenkova, 2011 (Plecoptera: Leuctrida) reassessed using Reflectance Transforming Imaging and cladistic analysis. Arthropod Systematics & Phylogeny 72:173–178.

Cúneo, N. R. 1996. Permian phytogeography in Gondwana. Palaeogeography, Palaeoclimatology, Palaeoecology 125:75–104.

Currie, P. J. 1977. A new haptodontine sphenacodont (Reptilia: Pelycosauria) from the Upper Pennsylvanian of North America. Journal of Paleontology 51:927–942.

Currie, P. J. 1980. A new younginid (Reptilia: Eosuchia) from the Upper Permian of Madagascar. Canadian Journal of Earth Sciences 17:500–511.

Currie, P. J. 1981a. *Hovasaurus boulei*, an aquatic eosuchian from the Upper Permian of Madagascar. Paleontologia Africana 24:99–168.

Currie, P. J. 1981b. The vertebrae of *Youngina* (Reptilia: Eosuchia). Canadian Journal of Earth Sciences 18:815–818.

Currie, P. J. 1982. The osteology and relationships of *Tangasaurus mennelli* Haughton (Reptilia, Eosuchia). Annals of the South African Museum 86:247–265.

Currie, P. J., and R. L. Carroll. 1984. Ontogenetic changes in the eosuchian reptile *Thadeosaurus*. Journal of Vertebrate Paleontology 4:68–84.

Curtis, N., M. E. H. Jones, J. Shi, P. O'Higgins, S. E. Evans, and M. J. Fagan. 2011. Functional relationship between skull form and feeding mechanics in *Sphenodon*, and implications for diapsid skull development. PLoS ONE 6:e29804.

Cuthill, I. C. 2019. Camouflage. Journal of Zoology 308:75–92.

Dalla Vecchia, F. M. 1995. A new pterosaur (Reptilia, Pterosauria) from the Norian (Late Triassic) of Friuli (Northeastern Italy). Preliminary note. Gortiana 16:59–66.

Dalla Vecchia, F. M. 2003. New morphological observations on Triassic pterosaurs. Geological Society, London, Special Publications 217:23–44.

Dalla Vecchia, F. M. 2006. The tetrapod fossil record from the Norian-Rhaetian of Friuli (northeastern Italy). New Mexico Museum of Natural History and Science Bulletin 37:432–444.

Dalla Vecchia, F. M. 2009. Anatomy and systematics of the pterosaur *Carniadactylus gen. n. rosenfeldi* (Dalla Vecchia, 1995). Rivista Italiana Di Paleontologia e Stratigrafia 115:159–186.

Dalla Vecchia, F. M. 2013. Triassic pterosaurs. Geological Society, London, Special Publications 379:119–155.

Dalla Vecchia, F. M. 2014. Gli Pterosauri Triassici. Edizioni del Museo Friulano di Storia Naturale, Udine, Italy, 320 pp.

Dalla Vecchia, F. M. 2018. Comments on Triassic pterosaurs with a commentary on the "ontogenetic stages" of Kellner (2015) and the validity of *Bergamodactylus wildi*. Rivista Italiana Di Paleontologia e Stratigrafia 124.

Dalla Vecchia, F. M., and A. Cau. 2015. Re-examination of the purported pterosaur wing metacarpals from the Upper Triassic of England. Historical Biology 27:684–696.

D'Amore, D. C., S. Clulow, J. S. Doody, D. Rhind, and C. R. McHenry. 2018. Claw morphometrics in monitor lizards: variable substrate and habitat use correlate to shape diversity within a predator guild. Ecology and Evolution 8:6766–6778.

Datta, D., S. Ray, and S. Bandyopadhyay. 2021. Cranial morphology of a new phytosaur (Diapsida, Archosauria) from the Upper Triassic of India: implications for phytosaur phylogeny and biostratigraphy. Papers in Palaeontology 7:675–708.

Davydov, V. I., A. S. Biakov, M. D. Schmitz, and V. V. Silantiev. 2018. Radioisotopic calibration of the Guadalupian (middle Permian) series: Review and updates. Earth-Science Reviews 176:222–240.

Davydov, V. I., M. P. Arefiev, V. K. Golubev, E. V. Karasev, M. A. Naumcheva, M. D. Schmitz, V. V. Silantiev, and V. V. Zharinova. 2020. Radioisotopic and biostratigraphic constraints on the classical Middle–Upper Permian succession and tetrapod fauna of the Moscow syneclise, Russia. Geology 48:742–747.

Day, M. O., and B. S. Rubidge. 2020. Biostratigraphy of the *Tapinocephalus* Assemblage Zone (Beaufort Group, Karoo Supergroup), South Africa. South African Journal of Geology 123:149–164.

Day, M. O., and R. M. H. Smith. 2020. Biostratigraphy of the *Endothiodon* Assemblage Zone (Beaufort Group, Karoo Supergroup), South Africa. South African Journal of Geology 123:165–180.

Day, M. O., and B. S. Rubidge. 2021. The Late Capitanian Mass Extinction of Terrestrial Vertebrates in the Karoo Basin of South Africa. Frontiers in Earth Science 9:631198.

deBraga, M. 2003. The postcranial skeleton, phylogenetic position, and probable lifestyle of the Early Triassic reptile *Procolophon trigoniceps*. Canadian Journal of Earth Sciences 40:527–556.

deBraga, M., and R. R. Reisz. 1995. A new diapsid reptile from the uppermost Carboniferous (Stephanian) of Kansas. Palaeontology 38:199–212.

deBraga, M., and O. Rieppel. 1997. Reptile phylogeny and the interrelationships of turtles. Zoological Journal of the Linnean Society 120:281–354.

deBraga, M., J. J. Bevitt, and R. R. Reisz. 2019. A new captorhinid from the Permian cave system near Richards Spur, Oklahoma, and the taxic diversity of Captorhinus at this locality. Frontiers in Earth Science 7:112.

Dec, M. 2019. Hydrodynamic performance of psammosteids: New insights from computational fluid dynamics simulations. Acta Palaeontologica Polonica 64.

Dececchi, T. A., and H. C. E. Larsson. 2011. Assessing arboreal adaptations of bird antecedents: testing the ecological setting of the origin of the avian flight stroke. PLoS ONE 6:e22292.

Dececchi, T. A., A. Roy, M. Pittman, T. G. Kaye, X. Xu, M. B. Habib, H. C. E. Larsson, X. Wang, and X. Zheng. 2020. Aerodynamics show membrane-winged theropods were a poor gliding dead-end. IScience 101574.

Dehling, J. M. 2017. How lizards fly: a novel type of wing in animals. PLoS ONE 12:e0189573.

Demar, R., and J. R. Bolt. 1981. Dentitional organization and function in a Triassic reptile. Journal of Paleontology 55:967–984.

Demuth, O. E., E. J. Rayfield, and J. R. Hutchinson. 2020. 3D hindlimb joint mobility of the stem-archosaur *Euparkeria capensis* with implications for postural evolution within Archosauria. Scientific Reports 10:15357.

Desojo, J. B., A. B. Heckert, J. W. Martz, W. G. Parker, R. R. Schoch, B. J. Small, and T. Sulej. 2013. Aetosauria: a clade of armoured pseudosuchians from the Upper Triassic continental beds. Geological Society, London, Special Publications 379:203–239.

DeVries, R. P., P. C. Sereno, D. Vidal, and S. L. Baumgart. 2022. Reproducible digital restoration of fossils using blender. Frontiers in Earth Science 10:833379.

Diaz, R. E., and P. A. Trainor. 2015. Hand/foot splitting and the 're-evolution' of mesopodial skeletal elements during the evolution and radiation of chameleons. BMC Evolutionary Biology 15:184.

Didier, G., and M. Laurin. 2020. Exact Distribution of Divergence Times from Fossil Ages and Tree Topologies. Systematic Biology 69.

Didier, G., and M. Laurin. 2021. Distributions of extinction times from fossil ages and tree topologies: the example of some mid-Permian synapsid extinctions. BioRxiv 2021.06.11.448028.

Dilkes, D. W. 1995. The rhynchosaur *Howesia browni* from the Lower Triassic of South Africa. Palaeontology 38:665–686.

Dilkes, D. W. 1998. The early Triassic rhynchosaur *Mesosuchus browni* and the interrelationships of basal archosauromorph reptiles. Philosophical Transactions of the Royal Society of London. Series B, Biological Sciences 353:501–541.

Dilkes, D. W., and H.-D. Sues. 2009. Redescription and phylogenetic relationships of *Doswellia kaltenbachi* (Diapsida: Archosauriformes) from the Upper Triassic of Virginia. Journal of Vertebrate Paleontology 29:58–79.

Dilkes, D. W., and A. Arcucci. 2012. *Proterochampsa barrionuevoi* (Archosauriformes: Proterochampsia) from the Late Triassic (Carnian) of Argentina and a phylogenetic analysis of Proterochampsia. Palaeontology 55:853–885.

DiMichele, W. A., and H. J. Falcon-Lang. 2011. Pennsylvanian 'fossil forests' in growth position (T0 assemblages): origin, taphonomic bias and palaeoecological insights. Journal of the Geological Society 168:585–605.

Diogo, R., J. M. Ziermann, J. Molnar, N. Siomava, and V. Abdala. 2018. Muscles of Chordates: Development, Homologies, and Evolution. CRC Press, 664 pp.

Dobruskina, I. A. 1995. Keuper (Triassic) flora from Middle Asia (Madygen, Southern Fergana). New Mexico Museum of Natural History and Science Bulletin 5:1–35.

Dodick, J. T., and S. P. Modesto. 1995. The cranial anatomy of the captorhinid reptile *Labidosaurikos meachami* from the Lower Permian of Oklahoma. Palaeontology 38:687.

Dodson, P., C. A. Forster, and S. D. Sampson. 2007. Ceratopsidae; pp. 494–513 in D. B. Weishampel, P. Dodson, and H. Osmólska (eds.), The Dinosauria. University of California Press, Berkley, CA.

Dollion, A. Y., G. J. Measey, R. Cornette, L. Carne, K. A. Tolley, J. M. da Silva, R. Boistel, A.-C. Fabre, and A. Herrel. 2017. Does diet drive the evolution of head shape and bite force in chameleons of the genus *Bradypodion*? Functional Ecology 31:671–684.

Druckenmiller, P. S., N. P. Kelley, E. T. Metz, and J. Baichtal. 2020. An articulated Late Triassic (Norian) thalattosauroid from Alaska and ecomorphology and extinction of Thalattosauria. Scientific Reports 10:1746.

Dudley, R. 1998. Atmospheric oxygen, giant Paleozoic insects and the evolution of aerial locomotor performance. Journal of Experimental Biology 201:1043–1050.

Dudley, R., and P. DeVries. 1990. Tropical rain forest structure and the geographical distribution of gliding vertebrates. Biotropica 22:432–434.

Dudley, R., G. Byrnes, S. P. Yanoviak, B. Borrell, R. M. Brown, and J. A. McGuire. 2007. Gliding and the functional origins of flight: biomechanical novelty or necessity? Annual Review of Ecology, Evolution, and Systematics 38:179–201.

Dufeau, D. L., and L. M. Witmer. 2015. Ontogeny of the Middle-Ear Air-Sinus System in *Alligator mississippiensis* (Archosauria: Crocodylia). PLOS ONE 10:e0137060.

Dunne, E. M., R. A. Close, D. J. Button, N. Brocklehurst, D. D. Cashmore, G. T. Lloyd, and R. J. Butler. 2018. Diversity change during the rise of tetrapods and the impact of the 'Carboniferous rainforest collapse.' Proceedings of the Royal Society B: Biological Sciences 285:20172730.

Dyke, G., R. de Kat, C. Palmer, J. van der Kindere, D. Naish, and B. Ganapathisubramani. 2013. Aerodynamic performance of the feathered dinosaur *Microraptor* and the evolution of feathered flight. Nature Communications 4:2489.

Dzik, J. 2003. A beaked herbivorous archosaur with dinosaur affinities from the early Late Triassic of Poland. Journal of Vertebrate Paleontology 23:556–574.

Dzik, J., and T. Sulej. 2007. A review of the early Late Triassic Krasiejów biota from Silesia, Poland. Paleontologia Polonica 64:3–27.

Edinger, T. 1955. The size of parietal foramen and organ in reptiles: a rectification. Bulletin of the Museum of Comparative Zoology, Harvard College 114:1–34.

Efremov, J. A. 1938. Some new Permian reptiles of the USSR. Comptes Rendus (Doklady) de l'Académie Des Sciences de l'URSS 19:771–776.

El-Toubi, M. R. 1949. The post-cranial osteology of the lizard, *Uromastyx aegyptia* (Forskål). Journal of Morphology 84:281–292.

Emerson, S. B., and M. a. R. Koehl. 1990. The interaction of behavioral and morphological change in the evolution of a novel locomotor type: "flying" frogs. Evolution 44:1931–1946.

Engelmann, G. F., D. J. Chure, B. B. Britt, and A. S. Andrus. 2012. The biostratigraphic and paleoecological significance of a new drepanosaur from the Triassic-?Jurassic Nugget

Sandstone of Northeasern Utah. Geological Society of America, Abstracts with Programs 44:604.

Erwin, D. H. 1990. The end-Permian mass extinction. Annual Review of Ecology and Systematics 21:69–91.

Evans, A. R., and G. D. Sanson. 1998. The effect of tooth shape on the breakdown of insects. Journal of Zoology 246:391–400.

Evans, S. E. 1980. The skull of a new eosuchian reptile from the Lower Jurassic of South Wales. Zoological Journal of the Linnean Society 70:203–264.

Evans, S. E. 1981. The postcranial skeleton of the Lower Jurassic eosuchian *Gephyrosaurus bridensis*. Zoological Journal of the Linnean Society 73:81–116.

Evans, S. E. 1982. The gliding reptiles of the Upper Permian. Zoological Journal of the Linnean Society 76:97–123.

Evans, S. E. 1985. Tooth replacement in the Lower Jurassic lepidosaur *Gephyrosaurus bridensis*. Neues Jahrbuch Für Geologie Und Paläontologie. Monatshefte 411–420.

Evans, S. E. 1986. The braincase of *Prolacerta broomi* (Reptilia, Triassic). Neues Jahrbuch Für Geologie Und Paläontologie. Abhandlungen 173:181–200.

Evans, S. E. 1987. The braincase of *Youngina capensis* (Reptilia: Diapsida; Permian). Neues Jahrbuch Für Geologie Und Paläontologie. Monatshefte 1987:193–203.

Evans, S. E. 1988. The early history and relationships of the Diapsida; pp. 221–260 in M. J. Benton (ed.), The phylogeny and classification of the tetrapods. Clarendon Press, Oxford.

Evans, S. E. 1991. A new lizard-like reptile (Diapsida: Lepidosauromorpha) from the Middle Jurassic of England. Zoological Journal of the Linnean Society 103:391–412.

Evans, S. E. 2003. At the feet of the dinosaurs: the early history and radiation of lizards. Biological Reviews 78:513–551.

Evans, S. E. 2008. The skull of lizards and tuatara; pp. 1–347 in C. Gans, A. S. Gaunt, and K. Adler (eds.), Biology of the Reptilia, Volume 20, Morphology H. The Skull of Lepidosauria. Society for the Study of Amphibians and Reptiles, Ithaca, New York.

Evans, S. E. 2009. An early kuehneosaurid reptile from the Early Triassic of Poland. Palaeontologia Polonica 65:145–178.

Evans, S. E. 2016. The lepidosaurian ear: variations on a theme; pp. 245–284 in J. A. Clack, R. R. Fay, and A. N. Popper (eds.), Evolution of the Vertebrate Ear: Evidence from the Fossil Record. Springer International Publishing, Cham.

Evans, S. E., and H. Haubold. 1987. A review of the Upper Permian genera *Coelurosauravus*, *Weigeltisaurus* and *Gracilisaurus* (Reptilia: Diapsida). Zoological Journal of the Linnean Society 90:275–303.

Evans, S. E., and J. A. van den Heever. 1987. A new reptile (Reptilia: Diapsida) from the Upper Permian *Daptocephalus* zone of South Africa. South African Journal of Science 83:724–730.

Evans, S. E., and M. S. King. 1993. A new specimen of *Protorosaurus* (Reptilia: Diapsida) from the Marl Slate (late Permian) of Britain. Proceedings of the Yorkshire Geological Society 49:229–234.

Evans, S. E., and K. A. Kermack. 1994. Assemblages of small tetrapods from the Early Jurassic of Britain; pp. 271–283 in N. C. Fraser and H.-D. Sues (eds.), In the shadow of the dinosaurs: Early Mesozoic tetrapods. Cambridge University Press, Cambridge, UK.

Evans, S. E., and L. J. Barbadillo. 1998. An unusual lizard (Reptilia: Squamata) from the Early Cretaceous of Las Hoyas, Spain. Zoological Journal of the Linnean Society 124:235–265.

Evans, S. E., and M. Borsuk-Białynicka. 2009. A small lepidosauromorph reptile from the Early Triassic of Poland. Palaeontologia Polonica 65:179–202.

Evans, S. E., and M. E. H. Jones. 2010. The origin, early history and diversification of lepidosauromorph reptiles; pp. 27–44 in S. Bandyopadhyay (ed.), New Aspects of Mesozoic Biodiversity. vol. 132. Springer Berlin Heidelberg, Berlin, Heidelberg.

Evans, S. E., P. Raia, and C. Barbera. 2004. New lizards and rhynchocephalians from the Lower Cretaceous of southern Italy. Acta Palaeontologica Polonica 49:393–408.

Ewer, R. F. 1965. The anatomy of the thecodont reptile *Euparkeria capensis* Broom. Philosophical Transactions of the Royal Society of London. Series B, Biological Sciences 248:379–435.

Ezcurra, M. D. 2010. A new early dinosaur (Saurischia: Sauropodomorpha) from the Late Triassic of Argentina: a reassessment of dinosaur origin and phylogeny. Journal of Systematic Palaeontology 8:371–425.

Ezcurra, M. D. 2016. The phylogenetic relationships of basal archosauromorphs, with an emphasis on the systematics of proterosuchian archosauriforms. PeerJ 4:e1778.

Ezcurra, M. D. 2017. Can social and sexual selection explain the bizarre snout of proterosuchid archosauriforms? Historical Biology 29:348–358.

Ezcurra, M. D., and R. J. Butler. 2015a. Taxonomy of the proterosuchid archosauriforms (Diapsida: Archosauromorpha) from the earliest Triassic of South Africa, and implications for the early archosauriform radiation. Palaeontology 58:141–170.

Ezcurra, M. D., and R. J. Butler. 2015b. Post-hatchling cranial ontogeny in the Early Triassic diapsid reptile *Proterosuchus fergusi*. Journal of Anatomy 226:387–402.

Ezcurra, M. D., and R. J. Butler. 2018. The rise of the ruling reptiles and ecosystem recovery from the Permo-Triassic mass extinction. Proceedings of the Royal Society B: Biological Sciences 285:20180361.

Ezcurra, M. D., R. J. Butler, and D. J. Gower. 2013. 'Proterosuchia': The Origin and Early History of Archosauriformes. Geological Society, London, Special Publications 379:9–33.

Ezcurra, M. D., T. M. Scheyer, and R. J. Butler. 2014a. Correction: The origin and early evolution of Sauria:rReassessing the Permian eaurian eossil record and the timing of the crocodile-lizard divergence. PLoS ONE 9:e89165.

Ezcurra, M. D., T. M. Scheyer, and R. J. Butler. 2014b. The origin and early evolution of Sauria: reassessing the Permian saurian fossil record and the timing of the crocodile-lizard divergence. PLoS ONE 9:e89165.

Ezcurra, M. D., F. Montefeltro, and R. J. Butler. 2016. The early evolution of rhynchosaurs. Frontiers in Ecology and Evolution 3:142.

Ezcurra, M. D., F. C. Montefeltro, F. L. Pinheiro, M. J. Trotteyn, A. R. Gentil, O. E. R. Lehmann, and L. A. Pradelli. 2021. The stem-archosaur evolutionary radiation in South America. Journal of South American Earth Sciences 105:102935.

Ezcurra, M. D., L. E. Fiorelli, A. G. Martinelli, S. Rocher, M. B. von Baczko, M. Ezpeleta, J. R. A. Taborda, E. M. Hechenleitner, M. J. Trotteyn, and J. B. Desojo. 2017. Deep faunistic turnovers preceded the rise of dinosaurs in southwestern Pangaea. Nature Ecology & Evolution 1:1477–1483.

Ezcurra, M. D., S. J. Nesbitt, M. Bronzati, F. M. Dalla Vecchia, F. L. Agnolin, R. B. J. Benson, F. Brissón Egli, S. F. Cabreira, S. W. Evers, A. R. Gentil, R. B. Irmis, A. G. Martinelli, F. E. Novas, L. Roberto da Silva, N. D. Smith, M. R. Stocker, A. H. Turner, and M. C. Langer. 2020. Enigmatic dinosaur precursors bridge the gap to the origin of Pterosauria. Nature 588:445–449.

Fabbri, M., N. Mongiardino Koch, A. C. Pritchard, M. Hanson, E. Hoffman, G. S. Bever, A. M. Balanoff, Z. S. Morris, D. J. Field, J. Camacho, T. B. Rowe, M. A. Norell, R. M. Smith, A. Abzhanov, and B.-A. S. Bhullar. 2017. The skull roof tracks the brain during the evolution and development of reptiles including birds. Nature Ecology & Evolution 1:1543–1550.

Falconnet, J. 2012. First evidence of a bolosaurid parareptile in France (latest Carboniferous-earliest Permian of the Autun basin) and the spatiotemporal distribution of the Bolosauridae. Bulletin de La Société Géologique de France 183:495–508.

Falconnet, J. 2014. An evaluation of French amniote diversity through the Pennsylvanian-Cisuralian boundary. Annales de Paléontologie 100:119–130.

Farke, A. A. 2004. Horn use in *Triceratops* (Dinosauria: Ceratopsidae): testing behavioral hypotheses using scale models. Palaeontologia Electronica 7:1–10.

Farke, A. A. 2014. Evaluating combat in ornithischian dinosaurs. Journal of Zoology 292:242–249.

Farke, A. A., E. D. S. Wolff, and D. H. Tanke. 2009. Evidence of combat in *Triceratops*. PLoS ONE 4:e4252.

Farke, A. A., R. E. Chapman, and A. Andersen. 2010. Modeling structural properties of the frill of *Triceratops*; pp. 264–270 in M. J. Ryan, B. J. Chinnery-Allgeier, and D. A. Eberth (eds.), New Perspectives on Horned Dinosaurs: The Royal Tyrrell Museum Ceratopsian Symposium. Indiana University Press.

Farlow, J. O., and P. Dodson. 1975. The behavioral significance of frill and horn morphology in ceratopsian dinosaurs. Evolution 353–361.

Fedak, T. J., and B. K. Hall. 2004. Perspectives on hyperphalangy: patterns and processes. Journal of Anatomy 204:151–163.

Feduccia, A. 1993. Evidence from claw geometry indicating arboreal habits of *Archaeopteryx*. Science 259:790–793.

Feduccia, A., and R. Wild. 1993. Birdlike characters in the Triassic archosaur *Megalancosaurus*. Naturwissenschaften 80:564–566.

Fischer, M. S., C. Krause, and K. E. Lilje. 2010. Evolution of chameleon locomotion, or how to become arboreal as a reptile. Zoology 113:67–74.

Fleming, P. A., and P. W. Bateman. 2012. Autotomy, tail regeneration and jumping ability in Cape dwarf geckos (*Lygodactylus capensis*) (Gekkonidae). African Zoology 47:55–59.

Flynn, J. J., S. J. Nesbitt, J. M. Parrish, L. Ranivoharimanana, and A. R. Wyss. 2010. A new species of *Azendohsaurus* (Diapsida: Archosauromorpha) from the Triassic Isalo Group of southwestern Madagascar: cranium and mandible. Palaeontology 53:669–688.

Foffa, D., E. M. Dunne, S. J. Nesbitt, R. J. Butler, N. C. Fraser, S. L. Brusatte, A. Farnsworth, D. J. Lunt, P. J. Valdes, S. Walsh, and P. M. Barrett. 2022. *Scleromochlus* and the early evolution of Pterosauromorpha. Nature 610:313–318.

Ford, D. P., and R. B. J. Benson. 2019. A redescription of *Orovenator mayorum* (Sauropsida, Diapsida) using high-resolution μCT, and the consequences for early amniote phylogeny. Papers in Palaeontology 5:197–239.

Ford, D. P., and R. B. J. Benson. 2020. The phylogeny of early amniotes and the affinities of Parareptilia and Varanopidae. Nature Ecology & Evolution 4:57–65.

Ford, D. P., S. E. Evans, J. N. Choiniere, V. Fernandez, and R. B. J. Benson. 2021. A reassessment of the enigmatic diapsid *Paliguana whitei* and the early history of Lepidosauromorpha. Proceedings of the Royal Society B: Biological Sciences 288:20211084.

Foth, C., R. B. Sookias, and M. D. Ezcurra. 2021. Rapid initial morphospace expansion and delayed morphological disparity peak in the first 100 million years of the archosauromorph evolutionary radiation. Frontiers in Earth Science 9:723973.

Foth, C., M. D. Ezcurra, R. B. Sookias, S. L. Brusatte, and R. J. Butler. 2016. Unappreciated diversification of stem archosaurs during the Middle Triassic predated the dominance of dinosaurs. BMC Evolutionary Biology 16:188.

Fox, R. C., and M. C. Bowman. 1966. Osteology and relationships of *Captorhinus aguti* (Cope) (Reptilia: Captorhinomorpha). University of Kansas Paleontological Contributions, Vertebrata 11:1–80.

Fracasso, M. A. 1987. Braincase of *Limnoscelis paludis* Williston. Postilla 201:1–22.

Fraser, N. C. 1982. A new rhynchocephalian from the British Upper Trias. Palaeontology 25:710–725.

Fraser, N. C. 1988. The osteology and relationships of *Clevosaurus* (Reptilia: Sphenodontida). Philosophical Transactions of the Royal Society of London. B, Biological Sciences 321:125–178.

Fraser, N. C., and G. M. Walkden. 1984. The postcranial skeleton of the upper Triassic Sphenodontid *Planocephalosaurus robinsonae*. Palaeontology 27:575–595.

Fraser, N. C., and H.-D. Sues. 1997. In the Shadow of the Dinosaurs: Early Mesozoic Tetrapods. Cambridge University Press, Cambridge, UK, 448 pp.

Fraser, N. C., and S. Renesto. 2005. Additional drepanosaur elements from the Triassic fissure infills of Cromhall Quarry, England. Jeffersoniana 15:1–16.

Fraser, N. C., and H.-D. Sues. 2010. The beginning of the 'Age of Dinosaurs': a brief overview of terrestrial biotic changes during the Triassic. Earth and Environmental Science Transactions of The Royal Society of Edinburgh 101:189–200.

Frey, E., H.-D. Sues, and W. Munk. 1997. Gliding mechanism in the Late Permian reptile *Coelurosauravus*. Science 275:1450–1452.

Frey, E., M.-C. Buchy, and D. M. Martill. 2003. Middle- and bottom-decker Cretaceous pterosaurs: unique designs in active flying vertebrates. Geological Society Special Publications 217:267–274.

Fröbisch, J., and R. R. Reisz. 2009. The Late Permian herbivore *Suminia* and the early evolution of arboreality in terrestrial vertebrate ecosystems. Proceedings of the Royal Society B: Biological Sciences 276:3611–3618.

Galton, P. 2014. Notes on the postcranial anatomy of the heterodontosaurid dinosaur *Heterodontosaurus tucki*, a basal ornithischian from the Lower Jurassic of South Africa. Revue de Paleobiologie 33:97–141.

Gans, C., R. Dudley, N. M. Aguilar, and J. B. Graham. 1999. Late paleozoic atmospheres and biotic evolution. Historical Biology 13:199–219.

Gardner, N. M., C. M. Holliday, and F. R. O'Keefe. 2010. The braincase of *Youngina capensis* (Reptilia, Diapsida): new insights from high-resolution CT scanning of the holotype. Palaeontologia Electronica 13:19A.

Garwood, R., and J. Dunlop. 2014. The walking dead: Blender as a tool for paleontologists with a case study on extinct arachnids. Journal of Paleontology 88:735–746.

Gauthier, J. A., and K. de Queiroz. 2020a. Diapsida; pp. 1033–1040 in K. de Queiroz, P. Cantino, and J. A. Gauthier (eds.), Phylonyms: A Companion to the PhyloCode. CRC Press, Boca Raton.

Gauthier, J. A., and K. de Queiroz. 2020b. Sauria; pp. 1065–1073 in K. de Queiroz, P. Cantino, and J. A. Gauthier (eds.), Phylonyms: A Companion to the PhyloCode. CRC Press, Boca Raton.

Gauthier, J. A., and K. Padian. 2020. Archosauria; pp. 1187–1193 in K. De Queiroz, P. D. Cantino, and J. A. Gauthier (eds.), Phylonyms: A Companion to the PhyloCode. CRC Press.

Gauthier, J. A., A. G. Kluge, and T. Rowe. 1988a. The early evolution of the Amniota; pp. 103–155 in M. J. Benton (ed.), The phylogeny and classification of the tetrapods. Clarendon Press, Oxford.

Gauthier, J. A., A. G. Kluge, and T. Rowe. 1988b. Amniote Phylogeny and the Importance of Fossils. Cladistics 4:105–209.

Gauthier, J. A., M. Kearney, J. A. Maisano, O. Rieppel, and A. D. Behlke. 2012. Assembling the squamate Tree of Life: perspectives from the phenotype and the fossil record. Bulletin of the Peabody Museum of Natural History 53:3–308.

Geist, N. R., and A. Feduccia. 2000. Gravity-defying behaviors: identifying models for protoaves. American Zoologist 40:664–675.

Gervais, P. 1865. Description du *Mesosaurus tenuidens*: reptile fossile de l'Afrique australe. Académie Des Sciences et Lettres de Montpellier. Mémoires de La Section Des Sciences 6:169–175.

Gibson, B. M., D. J. Furbish, I. A. Rahman, M. W. Schmeeckle, M. Laflamme, and S. A. F. Darroch. 2021. Ancient life and moving fluids. Biological Reviews 96:129–152.

Gillis, G. B., and T. E. Higham. 2016. Consequences of lost endings: caudal autotomy as a lens for focusing attention on tail function during locomotion. Journal of Experimental Biology 219:2416–2422.

Gillis, G. B., L. A. Bonvini, and D. J. Irschick. 2009. Losing stability: tail loss and jumping in the arboreal lizard *Anolis carolinensis*. Journal of Experimental Biology 212:604–609.

Gilmore, C. W. 1911. A mounted skeleton of *Dimetrodon gigas* in the United States National Museum, with notes on the skeletal anatomy. Proceedings of the United States National Museum 56:525–539.

Glynne, E., J. D. Daza, and A. M. Bauer. 2020. Surface sculpturing in the skull of gecko lizards (Squamata: Gekkota). Biological Journal of the Linnean Society 131:801–813.

Goldfuss, G. A. 1831. Beiträge zur kenntnis verschiedener Reptilien der Vorwelt. Nova Acta Physico-Medica Academiae Caesareae Leopoldino-Carolinae Naturae Curiosorum 11:61–128.

Golubev, V. K. 2000. The faunal assemblages of Permian terrestrial vertebrates from Eastern Europe. Paleontological Journal 34:S211–S224.

Golubev, V. K. 2015. Dinocephalian stage in the history of the Permian tetrapod fauna of Eastern Europe. Paleontological Journal 49:1346–1352.

Gonçalves, G. S., and C. A. Sidor. 2019. A new drepanosauromorph, *Ancistronychus paradoxus* n. gen. et sp., from the Chinle Formation of Petrified Forest National Park, Arizona, USA. PaleoBios 36.

Goodrich, E. S. 1916. On the classification of the Reptilia. Proceedings of the Royal Society of London. Series B, Containing Papers of a Biological Character 89:261–276.

Goodrich, E. S. 1942. The hind foot of *Youngina* and fifth metatarsal in Reptilia. Journal of Anatomy 76:308–312.

Goodwin, M. B., and D. C. Evans. 2016. The early expression of squamosal horns and parietal ornamentation confirmed by new end-stage juvenile *Pachycephalosaurus* fossils from the Upper Cretaceous Hell Creek Formation, Montana. Journal of Vertebrate Paleontology 36:e1078343.

Goodwin, M. B., W. A. Clemens, J. R. Horner, and K. Padian. 2006. The smallest known *Triceratops* skull: new observations on ceratopsid cranial anatomy and ontogeny. Journal of Vertebrate Paleontology 26:103–112.

Gottmann-Quesada, A., and P. M. Sander. 2009. A redescription of the early archosauromorph *Protorosaurus speneri* Meyer, 1832, and its phylogenetic relationships. Palaeontographica Abteilung A 287:123–220.

Gould, S. J. 1974. The origin and function of "bizarre" structures: antler size and skull size in the "Irish Elk," *Megaloceros giganteus*. Evolution 28:191–220.

Gow, C. E. 1970. The anterior of the palate in *Euparkeria*. Paleontologia Africana 13:61–62.

Gow, C. E. 1972. The osteology and relationships of the Millerettidae (Reptilia: Cotylosauria). Journal of Zoology 167:219–264.

Gow, C. E. 1975. The morphology and relationships of *Youngina capensis* Broom and *Prolacerta broomi* Parrington. Paleontologia Africana 89–131.

Gow, C. E. 1977. Tooth function and succession in the Triassic reptile *Procolophon trigoniceps*. Palaeontology 20:695–704.

Gow, C. E. 1997. A note on the postcranial skeleton of *Milleretta* (Amniota: Parareptilia). Paleontologia Africana 55–57.

Gower, D. J. 1996. The tarsus of erythrosuchid archosaurs, and implications for early diapsid phylogeny. Zoological Journal of the Linnean Society 116:347–375.

Gower, D. J. 1997. The braincase of the early archosaurian reptile *Erythrosuchus africanus*. Journal of Zoology 242:557–576.

Gower, D. J. 1999. The cranial and mandibular osteology of a new rauisuchian archosaur from the Middle Triassic of southern Germany. Stuttgarter Beiträge Zur Naturkunde. Serie B (Geologie Und Paläontologie) 280:1–49.

Gower, D. J. 2001. Possible postcranial pneumaticity in the last common ancestor of birds and crocodilians: evidence from *Erythrosuchus* and other Mesozoic archosaurs. Naturwissenschaften 88:119–122.

Gower, D. J. 2002. Braincase evolution in suchian archosaurs (Reptilia: Diapsida): evidence from the rauisuchian *Batrachotomus kupferzellensis*. Zoological Journal of the Linnean Society 136:49–76.

Gower, D. J. 2003. Osteology of the early archosaurian reptile *Erythrosuchus africanus*, Broom. Annals of the South African Museum 110:1–88.

Gower, D. J., and A. G. Sennikov. 1996. Morphology and phylogenetic informativeness of early archosaur braincases. Palaeontology 39:883–906.

Gower, D. J., and E. Weber. 1998. The braincase of *Euparkeria*, and the evolutionary relationships of birds and crocodilians. Biological Reviews 73:367–411.

Gower, D. J., and R. R. Schoch. 2009. Postcranial anatomy of the rauisuchian archosaur *Batrachotomus kupferzellensis*. Journal of Vertebrate Paleontology 29:103–122.

Gradstein, F. M., J. G. Ogg, M. D. Schmitz, and G. M. Ogg. 2020. Geologic Time Scale 2020. Elsevier, Amsterdam, Netherlands, 1390 pp.

Graham, J. B., N. M. Aguilar, R. Dudley, and C. Gans. 1995. Implications of the late Palaeozoic oxygen pulse for physiology and evolution. Nature 375:117–120.

Graham, M., and J. J. Socha. 2020. Going the distance: the biomechanics of gap-crossing behaviors. Journal of Experimental Zoology Part A: Ecological and Integrative Physiology 333:60–73.

Green, D. M. 1981. Adhesion and the toe-pads of treefrogs. Copeia 1981:790–796.

Greene, H. W. 1987. Antipredator mechanisms in reptiles; pp. 1–152 in C. Gans and R. B. Huey (eds.), Biology of the Reptilia, Volume 16, Ecology B. Defense and Life History. vol. 16. Alan R. Liss, inc., New York, NYS.

Greer, A. E. 1992. Hyperphalangy in squamates: insight on the reacquisition of primitive character states in limb-reduced lineages. Journal of Herpetology 26:327–329.

Gregory, J. T. 1945. Osteology and relationships of *Trilophosaurus*. University of Texas Publication 4401:273–359.

Griffin, C. T., M. R. Stocker, C. Colleary, C. M. Stefanic, E. J. Lessner, M. Riegler, K. Formoso, K. Koeller, and S. J. Nesbitt. 2021. Assessing ontogenetic maturity in extinct saurian reptiles. Biological Reviews 96:470–525.

Griffiths, E. F., D. P. Ford, R. B. J. Benson, and S. E. Evans. 2021. New information on the Jurassic lepidosauromorph *Marmoretta oxoniensis*. Papers in Palaeontology 7:2255–2278.

Grinham, L. R., and D. B. Norman. 2020. The pelvis as an anatomical indicator for facultative bipedality and substrate use in lepidosaurs. Biological Journal of the Linnean Society 129:398–413.

Grinham, L. R., C. S. VanBuren, and D. B. Norman. 2019. Testing for a facultative locomotor mode in the acquisition of archosaur bipedality. Royal Society Open Science 6:190569.

Gulbranson, E. L., J. L. Isbell, E. L. Taylor, P. E. Ryberg, T. N. Taylor, and P. P. Flaig. 2012. Permian polar forests: deciduousness and environmental variation. Geobiology 10:479–495.

Gundy, G. C., and G. Z. Wurst. 1976. Parietal eye-pineal morphology in lizards and its physiological implications. The Anatomical Record 185:419–431.

Günther, A. 1867. Contribution to the anatomy of *Hatteria* (*Rhynchocephalus*, Owen). Philosophical Transactions of the Royal Society of London 157:595–629.

Gutarra, S., and I. A. Rahman. 2020. The locomotion of extinct secondarily aquatic tetrapods. Biological Reviews 97:67–98.

Gutarra, S., T. L. Stubbs, B. C. Moon, C. Palmer, and M. J. Benton. 2022. Large size in aquatic tetrapods compensates for high drag caused by extreme body proportions. Communications Biology 5:1–12.

Gutarra, S., B. C. Moon, I. A. Rahman, C. Palmer, S. Lautenschlager, A. J. Brimacombe, and M. J. Benton. 2019. Effects of body plan evolution on the hydrodynamic drag and energy requirements of swimming in ichthyosaurs. Proceedings of the Royal Society B: Biological Sciences 286:20182786.

Haas, G. 1955. The jaw musculature in *Protoceratops* and in other ceratopsians. American Museum Novitates 1–24.

Haas, G. 1973. Muscles of the jaws and associated structures in the Rhynchocephalia and Squamata; pp. 285–490 in C. Gans and T. S. Parsons (eds.), Biology of the Reptilia, Volume 4, Morphology D. vol. 4. Academic Press, London and New York.

Hall, B., and M. K. Vickaryous. 2015. Merrythoughts; Homology of the furcula; pp. 439–454 in O. R. P. Bininda-Emonds, G. L. Powell, H. A. Jamniczky, A. M. Bauer, and J. Theodor (eds.), All Animals are Interesting: A Festschrift in Honour of Anthony P. Russell, Bis-Verlag der Carl von Ossietzky Universität Oldenburg. Oldenburg, Germay.

Hamley, T., J. C. Cisneros, and R. Damiani. 2021. A procolophonid reptile from the Lower Triassic of Australia. Zoological Journal of the Linnean Society 192:554–609.

Hammer, Ø., S. Bengtson, T. Malzbender, and D. Gelb. 2002. Imaging fossils using reflectance transforation and interactive manipulation of virtual light sources. Palaeontologia Electronica 5:1–9.

Hancox, P. J., J. Neveling, and B. S. Rubidge. 2020. Biostratigraphy of the *Cynognathus* Assemblage Zone (Beaufort Group, Karoo Supergroup), South Africa. South African Journal of Geology 123:217–238.

Hankel, O. 1994. Early Permian to Middle Jurassic rifting and sedimentation in East Africa and Madagascar. Geologische Rundschau 83:703–710.

Haridy, Y., M. J. Macdougall, and R. R. Reisz. 2018. The lower jaw of the Early Permian parareptile *Delorhynchus*, first evidence of multiple denticulate coronoids in a reptile. Zoological Journal of the Linnean Society 184:791–803.

Haridy, Y., M. J. Macdougall, D. Scott, and R. R. Reisz. 2016. Ontogenetic change in the temporal region of the Early Permian parareptile *Delorhynchus cifellii* and the implications for closure of the temporal fenestra in amniotes. PLOS ONE 11:e0166819.

Harris, J. D., and A. Downs. 2002. A drepanosaurid pectoral girdle from the Ghost Ranch (Whitaker) *Coelophysis* Quarry (Chinle Group, Rock Point Formation, Rhaetian), New Mexico. Journal of Vertebrate Paleontology 22:70–75.

Harris, J. M., and R. L. Carroll. 1977. *Kenyasaurus*, a new eosuchian reptile from the Early Triassic of Kenya. Journal of Paleontology 51:139–149.

Hartmann-Weinberg, A. P. 1937. Pareiasauriden als Leitfossilien. Problems in Paleontology 2–3:649–712.

Haubold, H., and G. Schaumberg. 1985. Die Fossilien Des Kupferschiefers. A. Ziemsen Verlag, Wittenberg, 223 pp.

Haubold, H., and E. Buffetaut. 1987. Une nouvelle interprétation de *Longisquama insignis*, reptile énigmatique du Trias supérieur d'Asie centrale. Comptes Rendus de l'Académie Des Sciences. Série 2, Mécanique, Physique, Chimie, Sciences de l'univers, Sciences de La Terre 305:65–70.

Heaton, M. J. 1979. Cranial anatomy of primitive captorhinid reptiles from the Late Pennsylvanian and Early Permian, Oklahoma and Texas. Bulletin of the Oklahoma Geological Survey 127:1–84.

Heaton, M. J., and R. R. Reisz. 1986. Phylogenetic relationships of captorhinomorph reptiles. Canadian Journal of Earth Sciences 23:402–418.

Hebdon, N., K. Ritterbush, and Y. Choi. 2020. Computational fluid dynamics modeling of fossil ammonoid shells. Palaeontologia Electronica 23:a21.

Henderson, D. M. 1999. Estimating the masses and centers of mass of extinct animals by 3-D mathematical slicing. Paleobiology 25:88–106.

Herrel, A., L. Spithoven, R. V. Damme, and F. D. Vree. 1999. Sexual dimorphism of head size in *Gallotia galloti*: testing the niche divergence hypothesis by functional analyses. Functional Ecology 13:289–297.

Herrel, A., J. J. Meyers, P. Aerts, and K. C. Nishikawa. 2000. The mechanics of prey prehension in chameleons. Journal of Experimental Biology 203:3255–3263.

Herrel, A., R. V. Damme, B. Vanhooydonck, and F. D. Vree. 2001. The implications of bite performance for diet in two species of lacertid lizards. Canadian Journal of Zoology 79:662–670.

Higham, T. E., and B. C. Jayne. 2004. Locomotion of lizards on inclines and perches: hindlimb kinematics of an arboreal specialist and a terrestrial generalist. Journal of Experimental Biology 207:233–248.

Higham, T. E., M. S. Davenport, and B. C. Jayne. 2001. Maneuvering in an arboreal habitat: the effects of turning angle on the locomotion of three sympatric ecomorphs of *Anolis* lizards. Journal of Experimental Biology 204:4141–4155.

Hildebrand, M., and G. E. Goslow. 2001. Analysis of Vertebrate Structure, 5th ed. John Wiley & Sons, New York, NY, 656 pp.

Hoffman, E. A., and T. B. Rowe. 2018. Jurassic stem-mammal perinates and the origin of mammalian reproduction and growth. Nature 561:104–108.

Hoffstetter, R., and J.-P. Gasc. 1969. Vertebrae and ribs of modern reptiles; pp. 201–310 in C. Gans, A. d'A. Bellairs, and T. S. Parsons (eds.), Biology of the Reptilia. Volume 1. Morphology A. Academic Press, New York, NY.

Holliday, C. M. 2009. New insights into dinosaur jaw muscle anatomy. The Anatomical Record 292:1246–1265.

Holliday, C. M., and L. M. Witmer. 2007. Archosaur adductor chamber evolution: integration of musculoskeletal and topological criteria in jaw muscle homology. Journal of Morphology 268:457–484.

Holmes, R. 1977. The osteology and musculature of the pectoral limb of small captorhinids. Journal of Morphology 152:101–140.

Holmes, R. B. 2003. The hind limb of *Captorhinus aguti* and the step cycle of basal amniotes. Canadian Journal of Earth Sciences 40:515–526.

Holz, M., A. B. França, P. A. Souza, R. Iannuzzi, and R. Rohn. 2010. A stratigraphic chart of the Late Carboniferous/Permian succession of the eastern border of the Paraná Basin, Brazil, South America. Journal of South American Earth Sciences 29:381–399.

Hone, D., D. M. Henderson, F. Therrien, and M. B. Habib. 2015. A specimen of *Rhamphorhynchus* with soft tissue preservation, stomach contents and a putative coprolite. PeerJ 3:e1191.

Hone, D. W. E. 2012. A new specimen of the pterosaur *Rhamphorhynchus*. Historical Biology 24:581–585.

Hone, D. W. E., and M. J. Benton. 2007. An evaluation of the phylogenetic relationships of the pterosaurs among archosauromorph reptiles. Journal of Systematic Palaeontology 5:465–469.

Hone, D. W. E., and D. Naish. 2013. The 'species recognition hypothesis' does not explain the presence and evolution of exaggerated structures in non-avialan dinosaurs. Journal of Zoology 290:172–180.

Hone, D. W. E., and C. G. Faulkes. 2014. A proposed framework for establishing and evaluating hypotheses about the behaviour of extinct organisms. Journal of Zoology 292:260–267.

Hone, D. W. E., D. Naish, and I. C. Cuthill. 2012. Does mutual sexual selection explain the evolution of head crests in pterosaurs and dinosaurs? Lethaia 45:139–156.

Hone, D. W. E., M. B. Habib, and M. C. Lamanna. 2013. An annotated and illustrated catalogue of Solnhofen (Upper Jurassic, Germany) pterosaur specimens at Carnegie Museum of Natural History. Annals of Carnegie Museum 82:165–191.

Horner, J. R., and M. B. Goodwin. 2006. Major cranial changes during *Triceratops* ontogeny. Proceedings of the Royal Society B: Biological Sciences 273:2757–2761.

Horner, J. R., and M. B. Goodwin. 2008. Ontogeny of cranial epi-ossifications in *Triceratops*. Journal of Vertebrate Paleontology 28:134–144.

Howes, G. B., and H. H. Swinnerton. 1901. On the development of the skeleton of the tuatara, *Sphenodon punctatus*; with remarks on the egg, on the hatching, and on the hatched young. Transactions of the Zoological Society of London 16:1–84.

Huene, F. R. von. 1930. *Palaeochameleo* und *Coelurosauravus*. Centralblatt Für Geologie Und Paläontologie (B) 440–441.

Huene, F. R. von. 1941. Osteologie und systematische Stellung von *Mesosaurus*. Palaeontographica Abteilung A 92:45–58.

Huene, F. R. von. 1956. Paläontologie und Phylogenie der Niederen Tetrapoden. VEB Gustav Fischer Verlag, Jena, 716 pp.

Hutchinson, J. 2001a. The evolution of femoral osteology and soft tissues on the line to extant birds (Neornithes). Zoological Journal of The Linnean Society - ZOOL J LINN SOC 131:169–197.

Hutchinson, J. R. 2001b. The evolution of pelvic osteology and soft tissues on the line to extant birds (Neornithes). Zoological Journal of the Linnean Society 131:123–168.

Hutchinson, J. R., K. T. Bates, J. Molnar, V. Allen, and P. J. Makovicky. 2011. A computational analysis of limb and body dimensions in *Tyrannosaurus rex* with implications for locomotion, ontogeny, and growth. PLOS ONE 6:e26037.

Huyghe, K., A. Herrel, D. Adriaens, Z. Tadić, and R. Van Damme. 2009. It is all in the head: morphological basis for differences in bite force among colour morphs of the Dalmatian wall lizard. Biological Journal of the Linnean Society 96:13–22.

ICZN. 1999. International Code of Zoological Nomenclature. Fourth Edition. The International Trust for Zoological Nomenclature, London, UK, 306 pp.

Inger, R. F. 1983. Morphological and ecological variation in the flying lizards (genus *Draco*). Fieldiana Zoology 18:1–35.

Inthavong, K., J. Wen, J. Tu, and Z. Tian. 2009. From CT scans to CFD modelling – Fluid and heat transfer in a realistic human nasal cavity. Engineering Applications of Computational Fluid Mechanics 3:321–335.

Irmis, R. B., R. Mundil, J. W. Martz, and W. G. Parker. 2011. High-resolution U–Pb ages from the Upper Triassic Chinle Formation (New Mexico, USA) support a diachronous rise of dinosaurs. Earth and Planetary Science Letters 309:258–267.

Ivakhnenko, M. F., V. K. Golubev, Y. M. Gubin, N. N. Kalandadze, I. V. Novikov, A. G. Sennikov, and A. S. Rautian. 1997. Permian and Triassic Tetrapods of Eastern Europe. Moscow, Russia, 216 pp.

Jaquier, V. P., N. C. Fraser, H. Furrer, and T. M. Scheyer. 2017. Osteology of a new specimen of *Macrocnemus* aff. *M. fuyuanensis* (Archosauromorpha, Protorosauria) from the Middle Triassic of Europe: Potential implications for species recognition and paleogeography of tanystropheid protorosaurs. Frontiers in Earth Science 5:91.

Jenkins, F. A., N. H. Shubin, S. M. Gatesy, and K. Padian. 2001. A diminutive pterosaur (Pterosauria: Eudimorphodontidae) from the Greenlandic Triassic. Bulletin of the Museum of Comparative Zoology at Harvard College 156:151–170.

Jenkins, K. M., M. E. H. Jones, T. Zikmund, A. Boyde, and J. D. Daza. 2017. A review of tooth implantation among rhynchocephalians (Lepidosauria). Journal of Herpetology 51:300–306.

Jenkins, R., and W. Tanner. 1968. Osteology and myology of *Phrynosoma p. platyrhinos* Girard and *Phrynosoma d. hernandesi* Girard. Brigham Young University Science Bulletin, Biological Series 9:1–35.

Jenkins, X. A., A. C. Pritchard, A. D. Marsh, B. T. Kligman, C. A. Sidor, and K. E. Reed. 2020. Using manual ungual morphology to predict substrate use in the Drepanosauromorpha and the description of a new species. Journal of Vertebrate Paleontology 40:e1810058.

Jewuła, K., M. Matysik, M. Paszkowski, and J. Szulc. 2019. The late Triassic development of playa, gilgai floodplain, and fluvial environments from Upper Silesia, southern Poland. Sedimentary Geology 379:25–45.

John, K. O. 1970. On the 'patagial musculature' of the South Indian flying lizard *Draco dussumieri* Dum and Bib. British Journal of Herpetology 4:161–168.

John, K. O. 1971. Caudal musculature of the South Indian flying lizard *Draco dussumieri* Dum. and Bibr. Acta Zoologica 52:249–255.

Jones, T. D., J. A. Ruben, L. D. Martin, E. N. Kurochkin, A. Feduccia, P. F. A. Maderson, W. J. Hillenius, N. R. Geist, and V. Alifanov. 2000. Nonavian Feathers in a Late Triassic Archosaur. Science 288:2202–2205.

Joyce, W. G., I. Werneburg, and T. R. Lyson. 2013. The hooked element in the pes of turtles (Testudines): a global approach to exploring primary and secondary homology. Journal of Anatomy 223:421–441.

Jusufi, A., D. I. Goldman, S. Revzen, and R. J. Full. 2008. Active tails enhance arboreal acrobatics in geckos. Proceedings of the National Academy of Sciences 105:4215–4219.

Jusufi, A., D. T. Kawano, T. Libby, and R. J. Full. 2010. Righting and turning in mid-air using appendage inertia: reptile tails, analytical models and bio-inspired robots. Bioinspiration & Biomimetics 5:045001.

Jusufi, A., Y. Zeng, R. J. Full, and R. Dudley. 2011. Aerial righting reflexes in flightless animals. Integrative and Comparative Biology 51:937–943.

Juul, L. 1994. The phylogeny of basal archosaurs. Paleontologia Africana 31:1–38.

Kammerer, C. F., R. J. Butler, S. Bandyopadhyay, and M. R. Stocker. 2016. Relationships of the Indian phytosaur *Parasuchus hislopi* Lydekker, 1885. Papers in Palaeontology 2:1–23.

Kammerer, C. F., S. J. Nesbitt, J. J. Flynn, L. Ranivoharimanana, and A. R. Wyss. 2020. A tiny ornithodiran archosaur from the Triassic of Madagascar and the role of miniaturization in dinosaur and pterosaur ancestry. Proceedings of the National Academy of Sciences 117:17932–17936.

Kellner, A. W. 2015. Comments on Triassic pterosaurs with discussion about ontogeny and description of new taxa. Anais Da Academia Brasileira de Ciências 87:669–689.

Kellner, A. W. A., B. Holgado, O. Grillo, F. A. Pretto, L. Kerber, F. L. Pinheiro, M. B. Soares, C. L. Schultz, R. T. Lopes, O. Araújo, and R. T. Müller. 2022. Reassessment of *Faxinalipterus minimus*, a purported Triassic pterosaur from southern Brazil with the description of a new taxon. PeerJ 10:e13276.

Kelso, E. C., and P. A. Verrell. 2002. Do male veiled chameleons, *Chamaeleo calyptratus*, adjust their courtship displays in response to female reproductive status? Ethology 108:495–512.

Kemp, T. S. 1974. The braincase and associated structures of the cotylosaur reptile *Procolophon trigoniceps*. Annals of the South African Museum 64:11–26.

Kennedy, N. K. 2010. Redescription of the postcranial skeleton of *Limnoscelis paludis* Williston Diadectomorpha, Limnoscelidae from the Upper Pennsylvanian of El Cobre Canyon, northern New Mexico. New Mexico Museum of Natural History and Science Bulletin 49:211–220.

Kent, D. V., P. E. Olsen, and G. Muttoni. 2017. Astrochronostratigraphic polarity time scale (APTS) for the Late Triassic and Early Jurassic from continental sediments and correlation with standard marine stages. Earth-Science Reviews 166:153–180.

Ketchum, H. F., and P. M. Barrett. 2004. New reptile material from the Lower Triassic of Madagascar: implications for the Permian–Triassic extinction event. Canadian Journal of Earth Sciences 41:1–8.

Khandelwal, P. C., and T. L. Hedrick. 2020. How biomechanics, path planning and sensing enable gliding flight in a natural environment. Proceedings of the Royal Society B: Biological Sciences 287:20192888.

Khandelwal, P. C., and T. L. Hedrick. 2022. Combined effects of body posture and three-dimensional wing shape enable efficient gliding in flying lizards. Scientific Reports 12:1793.

Klembara, J., and J. Welman. 2009. The anatomy of the palatoquadrate in the Lower Triassic *Proterosuchus fergusi* (Reptilia, Archosauromorpha) and its morphological transformation within the archosauriform clade. Acta Zoologica 90:275–284.

Klembara, J., D. S. Berman, A. C. Henrici, and A. Cernanský. 2005. New structures and reconstructions of the skull of the seymouriamorph *Seymouria sanjuanensis* Vaughn. Annals of Carnegie Museum 74:217–224.

Klembara, J., M. Hain, M. Ruta, D. S. Berman, S. E. Pierce, and A. C. Henrici. 2020. Inner ear morphology of diadectomorphs and seymouriamorphs (Tetrapoda) uncovered by high-resolution x-ray microcomputed tomography, and the origin of the amniote crown group. Palaeontology 63:131–154.

Kligman, B. T., A. D. Marsh, S. J. Nesbitt, W. G. Parker, and M. R. Stocker. 2020. New trilophosaurid species demonstrates a decline in allokotosaur diversity across the Adamanian-Revueltian boundary in the Late Triassic of western North America. Palaeodiversity 13:25–37.

Knell, R. J., and S. Sampson. 2011. Bizarre structures in dinosaurs: species recognition or sexual selection? A response to Padian and Horner: Bizarre structures in dinosaurs. Journal of Zoology 283:18–22.

Koehl, M. A. R., D. Evangelista, and K. Yang. 2011. Using physical models to study the gliding performance of extinct animals. Integrative and Comparative Biology 51:1002–1018.

Kogan, I., and C. Romano. 2016. Redescription of *Saurichthys madagascariensis* Piveteau, 1945 (Actinopterygii, Early Triassic), with implications for the early saurichthyid morphotype. Journal of Vertebrate Paleontology 36:e1151886.

Kogan, I., S. Pacholak, M. Licht, J. W. Schneider, C. Brücker, and S. Brandt. 2015. The invisible fish: hydrodynamic constraints for predator-prey interaction in fossil fish *Saurichthys* compared to recent actinopterygians. Biology Open 4:1715–1726.

Koroljov, A. V. 2017. Pterosaur flight. Biology Bulletin Reviews 7:179–228.

Krause, A. J., B. J. W. Mills, S. Zhang, N. J. Planavsky, T. M. Lenton, and S. W. Poulton. 2018. Stepwise oxygenation of the Paleozoic atmosphere. Nature Communications 9:4081.

Krauss, D., A. N. Pezon, P. E. Nguyen, I. S. Salame, and S. Rywkin. 2010. Evolutionary interactions between horn and frill morphology in chasmosaurine ceratopsians; pp. 282–292 in M. J. Ryan, Chinnery-Allgeier, and D. A. Eberth (eds.), New Perspectives on Horned Dinosaurs: The Royal Tyrrell Museum Ceratopsian Symposium. Indiana University Press.

Kuhlmann, K., C. Sinn, J. M. U. Siebert, G. Wehinger, J. Thöming, and G. R. Pesch. 2022. From μCT data to CFD: an open-source workflow for engineering applications. Engineering Applications of Computational Fluid Mechanics 16:1706–1723.

Kuhn, O. 1939. Schädelbau und systematische Stellung von *Weigeltisaurus*. Paläontologische Zeitschrift 21:163–167.

Kuhn-Schmyder, E., and H. Rieber. 1986. Handbook of Paleozoology. Johns Hopkins University Press, Baltimore, MD, 408 pp.

Kuo, C.-Y., G. B. Gillis, and D. J. Irschick. 2012. Take this broken tail and learn to jump: the ability to recover from reduced in-air stability in tailless green anole lizards [*Anolis carolinensis* (Squamata: Dactyloidae)]. Biological Journal of the Linnean Society 107:583–592.

Labonte, D., C. J. Clemente, A. Dittrich, C.-Y. Kuo, A. J. Crosby, D. J. Irschick, and W. Federle. 2016. Extreme positive allometry of animal adhesive pads and the size limits of adhesion-based climbing. Proceedings of the National Academy of Sciences 113:1297–1302.

Lammers, A., and U. Zurcher. 2011. Stability During Arboreal Locomotion; pp. 319–334 in V. Klika (ed.), Theoretical Biomechanics. IntechOpen Limited, London.

Lane, H. H. 1945. New mid-Pennsylvanian reptiles from Kansas. Transactions of the Kansas Academy of Science 47:381–390.

Langer, M. C., and M. J. Benton. 2006. Early dinosaurs: A phylogenetic study. Journal of Systematic Palaeontology 4:309–358.

Langer, M. C., A. M. Ribeiro, C. L. Schultz, and J. Ferigolo. 2007. The continental tetrapod-bearing Triassic of South Brazil. 18.

Langer, M. C., S. J. Nesbitt, J. S. Bittencourt, and R. B. Irmis. 2013. Non-dinosaurian Dinosauromorpha. Geological Society, London, Special Publications 379:157–186.

Langston, W., Jr., and R. R. Reisz. 1981. *Aerosaurus wellesi*, new species, a varanopseid mammal-like reptile (Synapsida : Pelycosauria) from the Lower Permian of New Mexico. Journal of Vertebrate Paleontology 1:73–96.

Larson, S. G., and J. T. Stern. 2006. Maintenance of above-branch balance during primate arboreal quadrupedalism: Coordinated use of forearm rotators and tail motion. American Journal of Physical Anthropology 129:71–81.

Laurin, M. 1991. The osteology of a Lower Permian eosuchian from Texas and a review of diapsid phylogeny. Zoological Journal of the Linnean Society 101:59–95.

Laurin, M. 1993. Anatomy and relationships of *Haptodus garnettensis*, a Pennsylvanian synapsid from Kansas. Journal of Vertebrate Paleontology 13:200–229.

Laurin, M. 1995. Comparative cranial anatomy of *Seymouria sanjuanensis* (Tetrapoda: Batrachosauria) from the lower Permian of Utah and new Mexico. PaleoBios 16:1–8.

Laurin, M. 1996. A redescription of the cranial anatomy of *Seymouria baylorensis*, the best known seymouriamorph (Vertebrata: Seymouriamorpha). PaleoBios 17:1–16.

Laurin, M. 2010. How Vertebrates Left the Water. Univ of California Press, Berkeley, CA, 216 pp.
Laurin, M., and R. R. Reisz. 1995. A reevaluation of early amniote phylogeny. Zoological Journal of the Linnean Society 113:165–223.
Laurin, M., and G. H. Piñeiro. 2017. A reassessment of the taxonomic position of mesosaurs, and a surprising phylogeny of early amniotes. Frontiers in Earth Science 5:88.
Laurin, M., and G. H. Piñeiro. 2018. Response: Commentary: A reassessment of the taxonomic position of mesosaurs, and a surprising phylogeny of early amniotes. Frontiers in Earth Science 6:220.
Laurin, M., and R. R. Reisz. 2020. Reptilia; pp. 1027–1031 in K. de Queiroz, P. D. Cantino, and J. A. Gauthier (eds.), Phylonyms: A Companion to the PhyloCode. CRC Press, Boca Raton.
Laurin, M., and R. W. Hook. 2022. The age of North America's youngest Paleozoic continental vertebrates: a review of data from the Middle Permian Pease River (Texas) and El Reno (Oklahoma) Groups. BSGF - Earth Sciences Bulletin 193:10.
Lautenschlager, S. 2016a. Digital reconstruction of soft-tissue structures in fossils. The Paleontological Society Papers 22:101–117.
Lautenschlager, S. 2016b. Reconstructing the past: methods and techniques for the digital restoration of fossils. Royal Society Open Science 3:160342.
Lautenschlager, S. 2022. Functional and ecomorphological evolution of orbit shape in mesozoic archosaurs is driven by body size and diet. Communications Biology 5:1–11.
Laville, T., C. P. A. Smith, M.-B. Forel, A. Brayard, and S. Charbonnier. 2021. Review of Early Triassic Thylacocephala. Rivista Italiana Di Paleontologia e Stratigrafia 127:73–101.
LeBlanc, A. R. H., and R. R. Reisz. 2014. New postcranial material of the early caseid *Casea broilii* Williston, 1910 (Synapsida: Caseidae) with a review of the evolution of the sacrum in Paleozoic non-mammalian synapsids. PLOS ONE 9:e115734.
LeBlanc, A. R. H., and R. R. Reisz. 2015. Patterns of tooth development and replacement in captorhinid reptiles: a comparative approach for understanding the origin of multiple tooth rows. Journal of Vertebrate Paleontology 35:e919928.
LeBlanc, A. R. H., I. Paparella, D. O. Lamoureux, M. R. Doschak, and M. W. Caldwell. 2021. Tooth attachment and pleurodont implantation in lizards: histology, development, and evolution. Journal of Anatomy 238:8.
Lecuona, A. 2013. Anatomía y relaciones filogenéticas de *Gracilisuchus stipanicicorum* y sus implicancias en el origen de Crocodylomorpha. Ph.D. dissertation, Universidad de Buenos Aires. Facultad de Ciencias Exactas y Naturales, 758 pp.
Lecuona, A., and J. B. Desojo. 2012. Hind limb osteology of *Gracilisuchus stipanicicorum* (Archosauria: Pseudosuchia). Earth and Environmental Science Transactions of The Royal Society of Edinburgh 102:105–128.
Lecuona, A., J. B. Desojo, and D. Pol. 2017. New information on the postcranial skeleton of *Gracilisuchus stipanicicorum* (Archosauria: Suchia) and reappraisal of its phylogenetic position. Zoological Journal of the Linnean Society 181:638–677.
Lecuona, A., J. B. Desojo, and I. A. Cerda. 2020. New information on the anatomy and histology of *Gracilisuchus stipanicicorum* (Archosauria: Pseudosuchia) from the Chañares Formation (early Carnian), Argentina. Comptes Rendus Palevol 19:40–62.

Lee, M. S. Y. 1995. Historical burden in systematics and the interrelationships of "parareptiles." Biological Reviews 70:459–547.

Lee, M. S. Y. 1997a. A taxonomic revision of pareiasaurian reptiles: implications for Permian terrestrial palaeoecology. Modern Geology 21:231–298.

Lee, M. S. Y. 1997b. The evolution of the reptilian hindfoot and the homology of the hooked fifth metatarsal. Journal of Evolutionary Biology 10:253–263.

Libby, T., T. Y. Moore, E. Chang-Siu, D. Li, D. J. Cohen, A. Jusufi, and R. J. Full. 2012. Tail-assisted pitch control in lizards, robots and dinosaurs. Nature 481:181–184.

Lichtig, A., and S. Lucas. 2021. *Chinlechelys* from the Upper Triassic of New Mexico, USA, and the origin of turtles. Palaeontologia Electronica 24:a13.

Liu, S., A. S. Smith, Y. Gu, J. Tan, C. K. Liu, and G. Turk. 2015. Computer simulations imply forelimb-dominated underwater flight in plesiosaurs. PLOS Computational Biology 11:e1004605.

Longrich, N. 2006. Structure and function of hindlimb feathers in *Archaeopteryx lithographica*. Paleobiology 32:417–431.

Losos, J. B., D. A. Creer, and J. A. Schulte II. 2002. Cautionary comments on the measurement of maximum locomotor capabilities. Journal of Zoology 258:57–61.

Lucas, S. G. 2017. Permian tetrapod biochronology, correlation and evolutionary events. Geological Society, London, Special Publications 450:405–444.

Lucas, S. G., and K. Krainer. 2005. Stratigraphy and correlation of the Permo-Carboniferous Cutler Group, Chama Basin, New Mexico. New Mexico Geological Society, 56th Field Conference Guidebook 1:145–159.

Lucas, S. G., J. Spielmann, and K. Krainer. 2010. Summary of geology of Cañon del Cobre, Rio Arriba County, New Mexico. New Mexico Museum of Natural History and Science 49:15–24.

Lucas, S. G., K. Krainer, D. S. Chaney, W. A. DiMichele, S. Voigt, D. S. Berman, and A. C. Henrici. 2013. The Lower Permian Abo Formation in Central New Mexico. New Mexico Museum of Natural History and Science Bulletin 59:161–180.

Luthardt, L., R. Rößler, and J. W. Schneider. 2016. Palaeoclimatic and site-specific conditions in the early Permian fossil forest of Chemnitz—sedimentological, geochemical and palaeobotanical evidence. Palaeogeography, Palaeoclimatology, Palaeoecology 441:627–652.

Lydekker, R. 1885. The Reptilia and Amphibia of the Maleri and Denwa groups. Palaeontologia Indica, Series 1 1:1–38.

Lyson, T. R., and G. S. Bever. 2020. Origin and Evolution of the Turtle Body Plan. Annual Review of Ecology, Evolution, and Systematics 51:143–166.

MacDougall, M. J., N. Brocklehurst, and J. Fröbisch. 2019a. Species richness and disparity of parareptiles across the end-Permian mass extinction. Proceedings of the Royal Society B: Biological Sciences 286:20182572.

MacDougall, M. J., D. Scott, S. P. Modesto, S. A. Williams, and R. R. Reisz. 2017a. New material of the reptile *Colobomycter pholeter* (Parareptilia: Lanthanosuchoidea) and the diversity of reptiles during the Early Permian (Cisuralian). Zoological Journal of the Linnean Society 180:661–671.

MacDougall, M. J., N. J. Tabor, J. Woodhead, A. R. Daoust, and R. R. Reisz. 2017b. The unique preservational environment of the Early Permian (Cisuralian) fossiliferous cave deposits of the Richards Spur locality, Oklahoma. Palaeogeography, Palaeoclimatology, Palaeoecology 475:1–11.

MacDougall, M. J., S. P. Modesto, N. Brocklehurst, A. Verrière, R. R. Reisz, and J. Fröbisch. 2018. Commentary: A reassessment of the taxonomic position of mesosaurs, and a surprising phylogeny of early amniotes. Frontiers in Earth Science 6:99.

MacDougall, M. J., A. Winge, J. Ponstein, M. Jansen, R. R. Reisz, and J. Fröbisch. 2019b. New information on the early Permian lanthanosuchoid *Feeserpeton oklahomensis* based on computed tomography. PeerJ 7:e7753.

Maddin, H. C., D. C. Evans, and R. R. Reisz. 2006. An Early Permian varanodontine varanopid (Synapsida: Eupelycosauria) from the Richards Spur locality, Oklahoma. Journal of Vertebrate Paleontology 26:957–966.

Maddin, H. C., A. Mann, and B. Hebert. 2020. Varanopid from the Carboniferous of Nova Scotia reveals evidence of parental care in amniotes. Nature Ecology & Evolution 4:50–56.

Maiorino, L., A. A. Farke, T. Kotsakis, and P. Piras. 2017. Macroevolutionary patterns in cranial and lower jaw shape of ceratopsian dinosaurs (Dinosauria, Ornithischia): phylogeny, morphological integration, and evolutionary rates. Evolutionary Ecology Research 18:123–167.

Maisano, J. A. 2002. Postnatal skeletal ontogeny in five Xantusiids (Squamata: Scleroglossa). Journal of Morphology 254:1–38.

Mann, A., E. J. McDaniel, E. R. McColville, and H. C. Maddin. 2019. *Carbonodraco lundi* gen et sp. nov., the oldest parareptile, from Linton, Ohio, and new insights into the early radiation of reptiles. Royal Society Open Science 6:191191.

Mann, A., T. W. Dudgeon, A. C. Henrici, D. S. Berman, and S. E. Pierce. 2021. Digit and ungual morphology suggest adaptations for scansoriality in the Late Carboniferous eureptile *Anthracodromeus longipes*. Frontiers in Earth Science 9:675337.

Manzano, A. S., M. Fabrezi, and M. Vences. 2007. Intercalary elements, treefrogs, and the early differentiation of a complex system in the Neobatrachia. The Anatomical Record 290:1551–1567.

Marchetti, L., S. Voigt, S. G. Lucas, M. R. Stimson, O. A. King, and J. H. Calder. 2020. Footprints of the earliest reptiles: *Notalacerta missouriensis* – Ichnotaxonomy, potential trackmakers, biostratigraphy, palaeobiogeography and palaeoecology. Annales Societatis Geologorum Poloniae 90:271–290, doi: 10.14241/asgp.2020.13.

Marsh, O. C. 1878. Notice of new fossil reptiles. American Journal of Science 15:409–411.

Martínez, R. N., T. R. Simões, G. Sobral, and S. Apesteguía. 2021. A Triassic stem lepidosaur illuminates the origin of lizard-like reptiles. Nature 597:235–238.

Martínez, R. N., B. Andres, C. Apaldetti, and I. A. Cerda. 2022. The dawn of the flying reptiles: first Triassic record in the southern hemisphere. Papers in Palaeontology 8:e1424.

Martinez, R. N., P. C. Sereno, O. A. Alcober, C. E. Colombi, P. R. Renne, I. P. Montañez, and B. S. Currie. 2011. A basal dinosaur from the Dawn of the Dinosaur Era in Southwestern Pangaea. Science 331:206–210.

Martínez, R. N., C. Apaldetti, O. A. Alcober, C. E. Colombi, P. C. Sereno, E. Fernandez, P. S. Malnis, G. A. Correa, and D. Abelin. 2012. Vertebrate succession in the Ischigualasto Formation. Journal of Vertebrate Paleontology 32:10–30.

Martin-Silverstone, E., M. B. Habib, and D. W. E. Hone. 2020. Volant fossil vertebrates: potential for bioinspired flight technology. Trends in Ecology & Evolution 35:618–629.

Matsumoto, R., and S. E. Evans. 2017. The palatal dentition of tetrapods and its functional significance. Journal of Anatomy 230:47–65.

Mazierski, D. M., and R. R. Reisz. 2010. Description of a new specimen of *Ianthasaurus hardestiorum* (Eupelycosauria: Edaphosauridae) and a re-evaluation of edaphosaurid phylogeny. Canadian Journal of Earth Sciences 47:901–912.

Mazierski, D. M., and R. R. Reisz. 2014. New materials of *Petrolacosaurus kansensis* (Diapsida: Araeoscelidae), the earliest known diapsid from the Upper Pennsylvanian of Kansas, provide insight into early tetrapod morphology and locomotion. Journal of Vertebrate Paleontology, Program with Abstracts 74:183.

Mazin, J.-M., and J. Pouech. 2020. The first non-pterodactyloid pterosaurian trackways and the terrestrial ability of non-pterodactyloid pterosaurs. Geobios 58:39–53.

McCabe, M. B., and S. J. Nesbitt. 2021. The first pectoral and forelimb material assigned to the lagerpetid *Lagerpeton chanarensis* (Archosauria: Dinosauromorpha) from the upper portion of the Chañares Formation, Late Triassic. Palaeodiversity 14:121–131.

McGuire, J. A. 2003. Allometric prediction of locomotor performance: an example from Southeast Asian flying lizards. The American Naturalist 161:337–349.

McGuire, J. A., and K. B. Heang. 2001. Phylogenetic systematics of Southeast Asian flying lizards (Iguania: Agamidae: *Draco*) as inferred from mitochondrial DNA sequence data. Biological Journal of the Linnean Society 72:203–229.

McGuire, J. A., and R. Dudley. 2005. The cost of living large: comparative gliding performance in flying lizards (Agamidae: *Draco*). The American Naturalist 166:93–106.

McGuire, J. A., and R. Dudley. 2011. The biology of gliding in flying lizards (genus *Draco*) and their fossil and extant analogs. Integrative and Comparative Biology 51:983–990.

Measey, G. J., K. Hopkins, and K. A. Tolley. 2009. Morphology, ornaments and performance in two chameleon ecomorphs: is the casque bigger than the bite? Zoology 112:217–226.

Measey, G. J., A. Raselimanana, and A. Herrel. 2013. Ecology and life history of chameleons; pp. 85–113 in K. A. Tolley and A. Herrel (eds.), The Biology of Chameleons. University of California Press, Berkley, CA.

Measey, G. J., A. D. Rebelo, A. Herrel, B. Vanhooydonck, and K. A. Tolley. 2011. Diet, morphology and performance in two chameleon morphs: do harder bites equate with harder prey? Journal of Zoology 285:247–255.

Mendelson, T. C., and K. L. Shaw. 2012. The (mis)concept of species recognition. Trends in Ecology & Evolution 27:421–427.

Mendelson, T. C., and K. L. Shaw. 2013. Further misconceptions about species recognition: a reply to Padian and Horner. Trends in Ecology & Evolution 28:252–253.

Menning, M., A. S. Alekseev, B. I. Chuvashov, V. I. Davydov, F.-X. Devuyst, H. C. Forke, T. A. Grunt, L. Hance, P. H. Heckel, N. G. Izokh, Y.-G. Jin, P. J. Jones, G. V. Kotlyar, H. W.

Kozur, T. I. Nemyrovska, J. W. Schneider, X.-D. Wang, K. Weddige, D. Weyer, and D. M. Work. 2006. Global time scale and regional stratigraphic reference scales of Central and West Europe, East Europe, Tethys, South China, and North America as used in the Devonian–Carboniferous–Permian Correlation Chart 2003 (DCP 2003). Palaeogeography, Palaeoclimatology, Palaeoecology 240:318–372.

Menter, F. R. 1994. Two-equation eddy-viscosity turbulence models for engineering applications. AIAA Journal 32:1598–1605.

Merck, J. 2003. An arboreal radiation of non-saurian diapsids. Journal of Vertebrate Paleontology 23:78A.

Meyer, H. v. 1832. Palaeologica Zur Geschichte Der Erde Und Ihrer Geschöpfe. Verlag von Siegmund Schmerber, Frankfurt, Germany, 560 pp.

Meyer, T. E., and J. S. Anderson. 2013. Tarsal fusion and the formation of the astragalus in *Hylonomus lyelli*, the earliest amniote, and other early tetrapods. Journal of Vertebrate Paleontology 33:488–492.

Miedema, F., S. N. F. Spiekman, V. Fernandez, J. W. F. Reumer, and T. M. Scheyer. 2020. Cranial morphology of the tanystropheid *Macrocnemus bassanii* unveiled using synchrotron microtomography. Scientific Reports 10:12412.

de Miguel Chaves, C., F. Ortega, and A. Pérez-García. 2018. New highly pachyostotic nothosauroid interpreted as a filter-feeding Triassic marine reptile. Biology Letters 14:20180130.

Miller, A. H., J. T. Stroud, and J. B. Losos. 2022. The ecology and evolution of key innovations. Trends in Ecology & Evolution S0169534722002257.

Modesto, S. P. 1995. The skull of the herbivorous synapsid *Edaphosaurus boanerges* from the Lower Permian of Texas. Palaeontology 38:213.

Modesto, S. P. 1998. New information on the skull of the Early Permian reptile *Captorhinus aguti*. 18:16.

Modesto, S. P. 2006. The cranial skeleton of the Early Permian aquatic reptile *Mesosaurus tenuidens*: implications for relationships and palaeobiology. Zoological Journal of the Linnean Society 146:345–368.

Modesto, S. P. 2010. The postcranial skeleton of the aquatic parareptile *Mesosaurus tenuidens* from the Gondwanan Permian. Journal of Vertebrate Paleontology 30:1378–1395.

Modesto, S. P., and R. R. Reisz. 2003. An enigmatic new diapsid reptile from the Upper Permian of eastern Europe. Journal of Vertebrate Paleontology 22:851–855.

Modesto, S. P., and H.-D. Sues. 2004. The skull of the Early Triassic archosauromorph reptile *Prolacerta broomi* and its phylogenetic significance. Zoological Journal of the Linnean Society 140:335–351.

Modesto, S. P., C. D. Richards, O. Ide, and C. A. Sidor. 2018. The vertebrate fauna of the Upper Permian of Niger—X. The mandible of the captorhinid reptile *Moradisaurus grandis*. Journal of Vertebrate Paleontology 38:e1531877.

Modesto, S. P., D. M. Scott, D. S. Berman, J. Müller, and R. R. Reisz. 2007. The skull and the palaeoecological significance of *Labidosaurus hamatus*, a captorhinid reptile from the Lower Permian of Texas. Zoological Journal of the Linnean Society 149:237–262.

Modesto, S. P., D. M. Scott, M. J. MacDougall, H.-D. Sues, D. C. Evans, and R. R. Reisz. 2015. The oldest parareptile and the early diversification of reptiles. Proceedings of the Royal Society B: Biological Sciences 282:20141912.

Moles, A. T., D. I. Warton, L. Warman, N. G. Swenson, S. W. Laffan, A. E. Zanne, A. Pitman, F. A. Hemmings, and M. R. Leishman. 2009. Global patterns in plant height. Journal of Ecology 97:923–932.

Mori, A., and T. Hikida. 1994. Field observations on the social behavior of the flying lizard, *Draco volans sumatranus*, in Borneo. Copeia 1994:124–130.

Motani, R. 2009. The evolution of marine reptiles. Evolution: Education and Outreach 2:224–235.

Mueller, B., and W. Parker. 2006. A new species of *Trilophosaurus* (Diapsida: Archosauromorpha) from the Sonsela Member (Chine Formation) of Petrified Forest National Park, Arizona. Museum of Northern Arizona Bulletin 62:119–125.

Müller, J. 2003. Early loss and multiple return of the lower temporal arcade in diapsid reptiles. Naturwissenschaften 90:473–476.

Müller, J. 2004. The relationships among diapsid reptiles and the influence of taxon selection; pp. 379–408 in M. V. H. Arratia and R. Cloutier (eds.), Recent Advances in the Origin and Early Radiation of Vertebrates. Dr. Friedrich Pfeil, München.

Müller, J., and R. R. Reisz. 2005. An early captorhinid reptile (Amniota, Eureptilia) from the Upper Carboniferous of Hamilton, Kansas. Journal of Vertebrate Paleontology 25:561–568.

Müller, J., and R. R. Reisz. 2006. The phylogeny of early eureptiles: comparing parsimony and bayesian approaches in the investigation of a basal fossil clade. Systematic Biology 55:503–511.

Müller, J., and L. A. Tsuji. 2007. Impedance-matching hearing in Paleozoic reptiles: evidence of advanced sensory perception at an early stage of amniote evolution. PLoS ONE 2:e889.

Müller, J., J. Sterli, and J. Anquetin. 2011. Carotid circulation in amniotes and its implications for turtle relationships. Neues Jahrbuch Für Geologie Und Paläontologie. Abhandlungen 261:289–297.

Müller, J., D. S. Berman, A. C. Henrici, T. Martens, and S. S. Sumida. 2006. The basal reptile *Thuringothyris mahlendorffae* (Amniota: Eureptilia) from the Lower Permian of Germany. Journal of Paleontology 80:726–739.

Müller, J., T. M. Scheyer, J. J. Head, P. M. Barrett, I. Werneburg, P. G. P. Ericson, D. Pol, and M. R. Sánchez-Villagra. 2010. Homeotic effects, somitogenesis and the evolution of vertebral numbers in recent and fossil amniotes. Proceedings of the National Academy of Sciences 107:2118–2123.

Müller, R. T., and M. S. Garcia. 2020. A paraphyletic ‘Silesauridae’ as an alternative hypothesis for the initial radiation of ornithischian dinosaurs. Biology Letters 16:20200417.

Müller, R. T., M. C. Langer, and S. Dias-Da-Silva. 2018. Ingroup relationships of Lagerpetidae (Avemetatarsalia: Dinosauromorpha): a further phylogenetic investigation on the understanding of dinosaur relatives. Zootaxa 4392:149–158.

Muscio, G. 1996. Preliminary note on a specimen of Prolacertiformes (Reptilia) from the Norian (Late Triassic) of Preone (Udine, north-eastern Italy). Gortania 18:33–40.

Musters, C. J. M. 1983. Taxonomy of the genus *Draco* L. (Agamidae, Lacertilia, Reptilia). Zoologische Verhandelingen 199:1–120.

Myhrvold, N. P., E. Baldridge, B. Chan, D. Sivam, D. L. Freeman, and S. K. M. Ernest. 2015. An amniote life-history database to perform comparative analyses with birds, mammals, and reptiles. Ecology 96:3109–3109.

Nesbitt, S. J. 2011. The early evolution of archosaurs: relationships and the origin of major clades. Bulletin of the American Museum of Natural History 352:1–292.

Nesbitt, S. J., and D. W. E. Hone. 2010. An external mandibular fenestra and other archosauriform character states in basal pterosaurs. Palaeodiversity 3:225–233.

Nesbitt, S. J., and H.-D. Sues. 2021. The osteology of the early-diverging dinosaur *Daemonosaurus chauliodus* (Archosauria: Dinosauria) from the *Coelophysis* Quarry (Triassic: Rhaetian) of New Mexico and its relationships to other early dinosaurs. Zoological Journal of the Linnean Society 191:150–179.

Nesbitt, S. J., J. B. Desojo, and R. B. Irmis. 2013. Anatomy, Phylogeny and Palaeobiology of Early Archosaurs and Their Kin. Geological Society of London, London, UK, 624 pp.

Nesbitt, S. J., M. R. Stocker, B. J. Small, and A. Downs. 2009. The osteology and relationships of *Vancleavea campi* (Reptilia: Archosauriformes). Zoological Journal of the Linnean Society 157:814–864.

Nesbitt, S. J., R. J. Butler, M. D. Ezcurra, A. J. Charig, and P. M. Barrett. 2017a. The anatomy of *Teleocrater rhadinus*, an early avemetatarsalian from the lower portion of the Lifua Member of the Manda Beds (Middle Triassic). Journal of Vertebrate Paleontology 37:142–177.

Nesbitt, S. J., C. A. Sidor, R. B. Irmis, K. D. Angielczyk, R. M. H. Smith, and L. A. Tsuji. 2010. Ecologically distinct dinosaurian sister group shows early diversification of Ornithodira. Nature 464:95–98.

Nesbitt, S. J., J. J. Flynn, A. C. Pritchard, J. M. Parrish, L. Ranivoharimanana, and A. R. Wyss. 2015. Postcranial osteology of *Azendohsaurus madagaskarensis* (?Middle to Upper Triassic, Isalo Group, Madagascar) and its systematic position among stem archosaur reptiles. Bulletin of the American Museum of Natural History 398:1–126.

Nesbitt, S. J., R. J. Butler, M. D. Ezcurra, P. M. Barrett, M. R. Stocker, K. D. Angielczyk, R. M. H. Smith, C. A. Sidor, G. Niedźwiedzki, A. G. Sennikov, and A. J. Charig. 2017b. The earliest bird-line archosaurs and the assembly of the dinosaur body plan. Nature 544:484–487.

Nopcsa, F. B. 1930. Notizen über *Macrochemus Bassanii* nov. gen. et spec. Centralblatt Für Mineralogie, Geologie Und Paläontologie B 7:252–255.

Norberg, U. M. 1990. Vertebrate Flight: Mechanics, Physiology, Morphology, Ecology and Evolution. Springer Science & Business Media, Berlin, Germany, 291 pp.

Norman, D. B., FLS, M. G. Baron, M. S. Garcia, and R. T. Müller. 2022. Taxonomic, palaeobiological and evolutionary implications of a phylogenetic hypothesis for Ornithischia (Archosauria: Dinosauria). Zoological Journal of the Linnean Society 196:1273–1309.

Nosotti, S. 2007. *Tanystropheus Longobardicus* (Reptilia, Protorosauria): re-interpretations of the anatomy based on new specimens from the Middle Triassic of Besano (Lombardy, Northern Italy). Memorie Della Società Italiana Di Scienze Naturali e Del Museo Civico Di Storia Naturale Di Milano 35:1–88.

Novas, F. E. 1994. New information on the systematics and postcranial skeleton of *Herrerasaurus ischigualastensis* (Theropoda: Herrerasauridae) from the Ischigualasto Formation (Upper Triassic) of Argentina. Journal of Vertebrate Paleontology 13:400–423.

O'Brien, A., D. I. Whiteside, and J. E. A. Marshall. 2018. Anatomical study of two previously undescribed specimens of *Clevosaurus hudsoni* (Lepidosauria: Rhynchocephalia) from Cromhall Quarry, UK, aided by computed tomography, yields additional information on the skeleton and hitherto undescribed bones. Zoological Journal of the Linnean Society 183:163–195.

Oliver, J. A. 1951. "Gliding" in amphibians and reptiles, with a remark on an arboreal adaptation in the lizard, *Anolis carolinensis carolinensis* Voigt. The American Naturalist 85:171–176.

Olroyd, S. L., and C. A. Sidor. 2017. A review of the Guadalupian (middle Permian) global tetrapod fossil record. Earth-Science Reviews 171:583–597.

Olson, E. C. 1936. Notes on the Skull of *Youngina Capensis* Broom. The Journal of Geology 44:523–533.

Olson, E. C. 1968. The family Caseidae. Fieldiana: Geology 17:225–349.

Olson, E. C., and H. Barghusen. 1962. Permian vertebrates from Oklahoma and Texas. Oklahoma Geological Survey 59:1–68.

Opluštil, S., J. Pšenička, M. Libertín, A. R. Bashforth, Z. Šimůnek, J. Drábková, and J. Dašková. 2009. A Middle Pennsylvanian (Bolsovian) peat-forming forest preserved in situ in volcanic ash of the Whetstone Horizon in the Radnice Basin, Czech Republic. Review of Palaeobotany and Palynology 155:234–274.

Opluštil, S., J. Pšenička, J. Bek, J. Wang, Z. Feng, M. Libertin, Z. Šimůnek, J. Bureš, and J. Drábková. 2014. T0 peat-forming plant assemblage preserved in growth position by volcanic ash-fall: a case study from the Middle Pennsylvanian of the Czech Republic. Bulletin of Geosciences 89.

Opluštil, S., J. Wang, H. W. Pfefferkorn, J. Pšenička, J. Bek, M. Libertín, J. Wang, M. Wan, X. He, M. Yan, H. Wei, and J. Votočková Frojdová. 2021. T0 Early Permian coal-forest preserved in situ in volcanic ash bed in the Wuda Coalfield, Inner Mongolia, China. Review of Palaeobotany and Palynology 294:104347.

Osborn, H. F. 1903. On the primary division of the Reptilia into two sub-classes, Synapsida and Diapsida. Science 17:275–276.

Ősi, A., E. Prondvai, E. Frey, and B. Pohl. 2010. New interpretation of the palate of pterosaurs. The Anatomical Record 293:243–258.

Ostrom, J. H. 1964. A functional analysis of jaw mechanics in the dinosaur *Triceratops*. Postilla 88:1–35.

Ostrom, J. H. 1966. Functional morphology and evolution of the ceratopsian dinosaurs. Evolution 20:290–308.

Owen, R. 1842. Description of an extinct lacertian reptile, *Rhynchosaurus articeps* Owen of which the bones and foot-prints characterize the Upper New Red Sandstone at Grinsill, near Shrewsbury. Transactions of the Cambridge Philosophical Society 7:355–369.

Owen, R. 1876. Descriptive and illustrated catalogue of the fossil reptilia of South Africa in the collection of the British Museum. Order of the Trustees, London, UK, 88 pp.

Padian, K. 1983a. A functional analysis of flying and walking in pterosaurs. Paleobiology 9:218–239.

Padian, K. 1983b. Osteology and functional morphology of *Dimorphodon macronyx* (Buckland) (Pterosauria: Rhamphorhynchoidea) based on new material in the Yale Peabody Museum. Postilla 189:1–44.

Padian, K. 1984. The origin of pterosaurs. Symposium on Mesozoic Terrestrial Ecosystems. 3 163–168.

Padian, K. 1985. The origins and aerodynamics of flight in extinct vertebrates. Palaeontology 28:413–433.

Padian, K. 1986. The Beginning of the Age of Dinosaurs: Faunal Change across the Triassic-Jurassic Boundary. Cambridge University Press, Cambridge, UK, 404 pp.

Padian, K., and K. P. Dial. 2005. Could 'four-winged' dinosaurs fly? Nature 438:E3.

Padian, K., and J. R. Horner. 2011. The evolution of 'bizarre structures' in dinosaurs: biomechanics, sexual selection, social selection or species recognition? Journal of Zoology 283:3–17.

Padian, K., and J. R. Horner. 2014. The species recognition hypothesis explains exaggerated structures in non-avialan dinosaurs better than sexual selection does. Comptes Rendus Palevol 13:97–107.

Paparella, I., A. R. H. LeBlanc, M. R. Doschak, and M. W. Caldwell. 2020. The iliosacral joint in lizards: an osteological and histological analysis. Journal of Anatomy 236:668–687.

Parrington, F. R. 1935. On *Prolacerta broomi*, gen. et sp. n., and the origin of lizards. Annals and Magazine of Natural History 16:197–205.

Patankar, S. 1980. Numerical Heat Transfer and Fluid Flow. CRC Press, Boca Raton, 214 pp.

Paukstis, G. L., and L. E. Brown. 1990. Evolutionary trends in the morphology of the intercalary phalanx of anuran amphibians. Canadian Journal of Zoology 69:1297–1301.

Pawley, K. A. T., and A. Warren. 2006. The appendicular skeleton of *Eryops megacephalus* Cope, 1877 (Temnospondyli: Eryopoidea) from the lower Permian of North America. Journal of Paleontology 80:561–580.

Peabody, F. E. 1952. *Petrolacosaurus kansensis* Lane, a Pennsylvanian reptile from Kansas. University of Kansas Paleontological Contributions, Vertebrata 1:1–41.

Pelletier, V. 2014. Postcranial description and reconstruction of the varanodontine varanopid *Aerosaurus wellesi* (Synapsida: Eupelycosauria); pp. 53–68 in C. F. Kammerer, K. D. Angielczyk, and J. Fröbisch (eds.), Early Evolutionary History of the Synapsida. Springer Netherlands, Dordrecht.

Persons, S. W. IV., and P. J. Currie. 2012. Dragon tails: convergent caudal morphology in winged archosaurs. Acta Geologica Sinica (English Edition) 86:1402–1412.

Persons, S. W. IV., P. J. Currie, and M. A. Norell. 2013. Oviraptorosaur tail forms and functions. Acta Palaeontologica Polonica 59:553–567.

Peyer, B. 1937. Die Triasfauna der Tessiner Kalkalpen, XII: *Macrocnemus bassanii* Nopcsa. Abhandlungen der Schweizierischen Palaeontologischen Gesellschaft 59:1–140.

Piechowski, R., and J. Dzik. 2010. The axial skeleton of *Silesaurus opolensis*. Journal of Vertebrate Paleontology 30:1127–1141.

Piechowski, R., and M. Tałanda. 2020. The locomotor musculature and posture of the early dinosauriform *Silesaurus opolensis* provides a new look into the evolution of Dinosauromorpha. Journal of Anatomy 236:1044–1100.

Piechowski, R., M. Tałanda, and J. Dzik. 2014. Skeletal variation and ontogeny of the Late Triassic dinosauriform *Silesaurus opolensis*. Journal of Vertebrate Paleontology 34:1383–1393.

Piñeiro, G., P. Núñez Demarco, and M. D. Meneghel. 2016. The ontogenetic transformation of the mesosaurid tarsus: a contribution to the origin of the primitive amniotic astragalus. PeerJ 4:e2036.

Piñeiro, G., J. Ferigolo, A. Ramos, and M. Laurin. 2012a. Cranial morphology of the Early Permian mesosaurid *Mesosaurus tenuidens* and the evolution of the lower temporal fenestration reassessed. Comptes Rendus Palevol 11:379–391.

Piñeiro, G., A. Ramos, C. Goso, F. Scarabino, and M. Laurin. 2012b. Unusual environmental conditions preserve a Permian mesosaur-bearing Konservat-Lagerstätte from Uruguay. Acta Palaeontologica Polonica 57:299–318.

Pinheiro, F. L., D. De Simão-Oliveira, and R. J. Butler. 2020. Osteology of the archosauromorph *Teyujagua paradoxa* and the early evolution of the archosauriform skull. Zoological Journal of the Linnean Society 189:378–417.

Pinheiro, F. L., M. A. G. França, M. B. Lacerda, R. J. Butler, and C. L. Schultz. 2016. An exceptional fossil skull from South America and the origins of the archosauriform radiation. Scientific Reports 6:22817.

Pinna, G. 1980. *Drepanosaurus unguicaudatus*, nuovo genere e nuova specie di lepidosauro del Trias alpino. Atti Della Societa Italiana Di Scienze Naturali e Del Museo Civico Di Storia Naturale Di Milano 121:181–192.

Pinna, G. 1984. Osteologia di *Drepanosaurus unguicaudatus*, lepidosauro triassico del sottordine Lacertilia. Memorie Della Società Italiana Di Scienze Naturali e Del Museo Civico Di Storia Naturale Di Milano 24:1–28.

Pinna, G. 1986. On *Drepanosaurus unguicaudatus* , an Upper Triassic lepidosaurian from the Italian Alps. Journal of Paleontology 60:1127–1132.

Pintore, R., A. Houssaye, S. J. Nesbitt, and J. R. Hutchinson. 2022. Femoral specializations to locomotor habits in early archosauriforms. Journal of Anatomy 240:867–892.

Pittman, M., S. M. Gatesy, P. Upchurch, A. Goswami, and J. R. Hutchinson. 2013. Shake a tail feather: the evolution of the theropod tail into a stiff aerodynamic surface. PLoS ONE 8:e63115.

Piveteau, J. 1926. Paléontologie de Madagascar: XII. amphibiens et reptiles Permiens. Annales de Paléontologie 1–151.

Powell, G. L., A. P. Russell, H. A. Jamniczky, and B. Hallgrímsson. 2017. Shape variation in the dermatocranium of the greater short-horned lizard *Phrynosoma hernandesi* (Reptilia: Squamata: Phrynosomatidae). Evolutionary Biology 44:240–260.

Presch, W. 1969. Evolutionary osteology and relationships of the horned lizard genus *Phrynosoma* (family Iguanidae). Copeia 1969:250–275.

Preuschoft, H. 2002. What does" arboreal locomotion" mean exactly and what are the relationships between" climbing", environment and morphology? Zeitschrift Für Morphologie Und Anthropologie 83:171–188.

Price, L. I. 1935. Notes on the brain case of *Captorhinus*. Proceedings of the Boston Society of Natural History 40:377–386.

Pritchard, A. C. 2015. The early evolution of diapsid reptiles and the origin of Sauria. Ph.D. dissertation, Stony Brook University, Stony Brook, NY, 791 pp.

Pritchard, A. C., and S. J. Nesbitt. 2017. A bird-like skull in a Triassic diapsid reptile increases heterogeneity of the morphological and phylogenetic radiation of Diapsida. Royal Society Open Science 4:170499.

Pritchard, A. C., and H.-D. Sues. 2019. Postcranial remains of *Teraterpeton hrynewichorum* (Reptilia: Archosauromorpha) and the mosaic evolution of the saurian postcranial skeleton. Journal of Systematic Palaeontology 17:1745–1765.

Pritchard, A. C., H.-D. Sues, D. Scott, and R. R. Reisz. 2021. Osteology, relationships and functional morphology of *Weigeltisaurus jaekeli* (Diapsida, Weigeltisauridae) based on a complete skeleton from the Upper Permian Kupferschiefer of Germany. PeerJ 9:e11413.

Pritchard, A. C., A. H. Turner, S. J. Nesbitt, R. B. Irmis, and N. D. Smith. 2015. Late Triassic tanystropheids (Reptilia, Archosauromorpha) from northern New Mexico (Petrified Forest Member, Chinle Formation) and the biogeography, functional morphology, and evolution of Tanystropheidae. Journal of Vertebrate Paleontology 35:e911186.

Pritchard, A. C., A. H. Turner, R. B. Irmis, S. J. Nesbitt, and N. D. Smith. 2016. Extreme modification of the tetrapod forelimb in a Triassic diapsid reptile. Current Biology 26:2779–2786.

Pritchard, A. C., J. A. Gauthier, M. Hanson, G. S. Bever, and B.-A. S. Bhullar. 2018. A tiny Triassic saurian from Connecticut and the early evolution of the diapsid feeding apparatus. Nature Communications 9:1213.

Prondvai, E., and A. Ősi. 2011. Potential for intracranial movements in pterosaurs. The Anatomical Record 294:813–830.

Prötzel, D., M. Heß, M. D. Scherz, M. Schwager, A. van't Padje, and F. Glaw. 2018. Widespread bone-based fluorescence in chameleons. Scientific Reports 8:698.

Provini, P., and S. Van Wassenbergh. 2018. Hydrodynamic performance of suction feeding is virtually unaffected by variation in the shape of the posterior region of the pharynx in fish. Royal Society Open Science 5:181249.

Prum, R. O. 2001. *Longisquama* Fossil and Feather Morphology. Science 291:1899–1902.

Rahman, I. A. 2017. Computational fluid dynamics as a tool for testing functional and ecological hypotheses in fossil taxa. Palaeontology 60:451–459.

Rahman, I. A. 2020. Computational Fluid Dynamics and Its Applications in Echinoderm Palaeobiology. Cambridge University Press, Cambridge, UK, 21 pp.

Rahman, I. A., and S. Lautenschlager. 2016. Applications of three-dimensional box modeling to paleontological functional analysis. The Paleontological Society Papers 22:119–132.

Ramezani, J., D. E. Fastovsky, and S. A. Bowring. 2014. Revised chronostratigraphy of the Lower Chinle Formation strata in Arizona and New Mexico (USA): High-precision U-Pb

geochronological constraints on the Late Triassic evolution of dinosaurs. American Journal of Science 314:981–1008.

Rayfield, E. J. 2007. Finite element analysis and understanding the biomechanics and evolution of living and fossil organisms. Annual Review of Earth and Planetary Sciences 35:541–576.

Reig, O. A. 1958. Primeros datos descriptivos sobre nuevos reptiles arcosaurios del Triásico de Ischigualasto (San Juan, Argentina). Revista de la Asociación Geológica Argentina 13:257–270.

Reig, O. A. 1963. La presencia de dinosaurios saurisquios en los estratos de Ischigualasto (mesotriasico superior) de las provincias de San Juan y La Rioja (Republica Argentina). Ameghiniana 3:3–20.

Reisz, R. R. 1981. A diapsid reptile from the Pennsylvanian of Kansas. Special Publication of the Museum of Natural History, University of Kansas 7:1–74.

Reisz, R. R. 1986. Encyclopedia of Paleoherpetology. Part 17A. Pelycosauria. Gustav Fischer Verlag, Stuttgart, 102 pp.

Reisz, R. R., and D. S. Berman. 2001. The skull of *Mesenosaurus romeri*, a small varanopseid (Synanpsida: Eupelycosauria) from the Upper Permian of the Mezen River Basin, northern Russia. Annals of Carnegie Museum 70:113–132.

Reisz, R. R., and D. Scott. 2002. *Owenetta kitchingorum*, sp. nov., a small parareptile (Procolophonia: Owenettidae) from the Lower Triassic of South Africa. Journal of Vertebrate Paleontology 22:244–256.

Reisz, R. R., and D. W. Dilkes. 2003. *Archaeovenator hamiltonensis*, a new varanopid (Synapsida: Eupelycosauria) from the Upper Carboniferous of Kansas. Canadian Journal of Earth Sciences 40:667–678.

Reisz, R. R., D. S. Berman, and D. Scott. 1984. The anatomy and relationships of the Lower Permian reptile *Araeoscelis*. Journal of Vertebrate Paleontology 4:57–67.

Reisz, R. R., S. P. Modesto, and D. M. Scott. 2000. *Acanthotoposaurus bremneri* and the origin of the Triassic archosauromorph reptile fauna of South Africa. South African Journal of Science 96:443–445.

Reisz, R. R., S. J. Godfrey, and D. Scott. 2009. *Eothyris* and *Oedaleops*: do these Early Permian synapsids from Texas and New Mexico form a clade? Journal of Vertebrate Paleontology 29:39–47.

Reisz, R. R., M. Laurin, and D. Marjanović. 2010. *Apsisaurus witteri* from the Lower Permian of Texas: yet another small varanopid synapsid, not a diapsid. Journal of Vertebrate Paleontology 30:1628–1631.

Reisz, R. R., S. P. Modesto, and D. M. Scott. 2011a. A new Early Permian reptile and its significance in early diapsid evolution. Proceedings of the Royal Society B: Biological Sciences 278:3731–3737.

Reisz, R. R., M. J. Macdougall, and S. P. Modesto. 2014. A new species of the parareptile genus *Delorhynchus*, based on articulated skeletal remains from Richards Spur, Lower Permian of Oklahoma. Journal of Vertebrate Paleontology 34:1033–1043.

Reisz, R. R., H. C. Maddin, J. Fröbisch, and J. Falconnet. 2011b. A new large caseid (Synapsida, Caseasauria) from the Permian of Rodez (France), including a reappraisal of "*Casea*" *rutena* Sigogneau-Russell & Russell, 1974. Geodiversitas 33:227–246.

Renesto, S. 1994a. A new prolacertiform reptile from the Late Triassic of Northern Italy. Rivista Italiana Di Paleontologia e Stratigrafia 100:285–306.

Renesto, S. 1994b. *Megalancosaurus*, a possibly arboreal archosauromorph (Reptilia) from the Upper Triassic of northern Italy. Journal of Vertebrate Paleontology 14:38–52.

Renesto, S. 1994c. The shoulder girdle and anterior limb of *Drepanosaurus unguicaudatus* (Reptilia, Neodiapsida) from the upper Triassic (Norian) of Northern Italy. Zoological Journal of the Linnean Society 111:247–264.

Renesto, S. 2000. Bird-like head on a chameleon body: new specimens of the enigmatic diapsid reptile *Megalancosaurus* from the Late Triassic of Northern Italy. Rivista Italiana Di Paleontologia e Stratigrafia 106:152–180.

Renesto, S. 2005. A new specimen of *Tanystropheus* (Reptilia, Protorosauria) from the Middle Triassic of Switzerland and the ecology of the genus. Rivista Italiana Di Paleontologia e Stratigrafia 111:377–394.

Renesto, S. 2006. A reappraisal of the diversity and biogeographic significance of the Norian (Late Triassic) reptiles from the Calcare di Zorzino. New Mexico Museum of Natural History and Science Bulletin 37:445–456.

Renesto, S., and A. Paganoni. 1995. A new *Drepanosaurus* (Reptilia, Neodiapsida) from the Upper Triassic of Northern Italy. Neues Jahrbuch Für Geologie Und Paläontologie - Abhandlungen 87–99.

Renesto, S., and F. M. Dalla Vecchia. 2000. The unusual dentition and feeding habits of the prolacertiform reptile *Langobardisaurus* (Late Triassic, northern Italy). Journal of Vertebrate Paleontology 20:622–627.

Renesto, S., and M. Avanzini. 2002. Skin remains in a juvenile *Macrocnemus bassanii* Nopcsa (Reptilia, Prolacertiformes) from the Middle Triassic of Northern Italy. Neues Jahrbuch Für Geologie Und Paläontologie - Abhandlungen 224:31–48.

Renesto, S., and N. C. Fraser. 2003. Drepanosaurid (Reptilia: Diapsida) remains from a Late Triassic fissure infilling at Cromhall Quarry (Avon, Great Britain). Journal of Vertebrate Paleontology 23:703–705.

Renesto, S., and R. Posenato. 2003. A new lepidosauromorph reptile from the Middle Triassic of the Dolomites (Northern Italy). Rivista Italiana Di Paleontologia e Stratigrafia 109:463–474.

Renesto, S., and F. M. Dalla Vecchia. 2005. The skull and lower jaw of the holotype of *Megalancosaurus preonensis* (Diapsida, Drepanosauridae) from the Upper Triassic of Northern Italy. Rivista Italiana Di Paleontologia e Stratigrafia 111:247–257.

Renesto, S., and G. Binelli. 2006. *Vallesaurus cenensis* Wild, 1991, a drepanosaurid (Reptilia Diapsida) from the late Triassic of northern Italy. Rivista Italiana Di Paleontologia e Stratigrafia 112:77–94.

Renesto, S., and M. Bernardi. 2014. Redescription and phylogenetic relationships of *Megachirella wachtleri* Renesto et Posenato, 2003 (Reptilia, Diapsida). Paläontologische Zeitschrift 88:197–210.

Renesto, S., F. M. Dalla Vecchia, and D. Peters. 2002. Morphological evidence for bipedalism in the Late Triassic prolacertiform reptile *Langobardisaurus*. Senckenbergiana Lethaea 82:95–106.

Renesto, S., J. A. Spielmann, and S. G. Lucas. 2009. The oldest record of drepanosaurids (Reptilia, Diapsida) from the Late Triassic (Adamanian *Placerias* Quarry, Arizona, USA) and the stratigraphic range of the Drepanosauridae. Neues Jahrbuch Für Geologie Und Paläontologie - Abhandlungen 252:315–325.

Renesto, S., J. A. Spielmann, S. G. Lucas, and G. T. Spagnoli. 2010. The taxonomy and paleobiology of the Late Triassic (Carnian-Norian: Adamanian-Apachean) drepanosaurs (Diapsida: Archosauromorpha: Drepanosauromorpha). New Mexico Museum of Natural History and Science Bulletin 46:1–81.

Reynoso, V.-H. 1998. *Huehuecuetzpalli mixtecus* gen. et sp. nov: a basal squamate (Reptilia) from the Early Cretaceous of Tepexi de Rodríguez, Central México. Philosophical Transactions of the Royal Society of London. Series B: Biological Sciences 353:477–500.

de Ricqlès, A., and J. R. Bolt. 1983. Jaw growth and tooth replacement in *Captorhinus aguti* (Reptilia: Captorhinomorpha): a morphological and histological analysis. Journal of Vertebrate Paleontology 3:7–24.

Rieppel, O. 1981. The skull and jaw adductor musculature in chamaeleons. Revue Suisse de Zoologie 88:433–445.

Rieppel, O. 1984a. The upper temporal arcade of lizards: an ontogenetic problem. Revue Suisse de Zoologie 91:475–482.

Rieppel, O. 1984b. The structure of the skull and jaw adductor musculature in the Gekkota, with comments on the phylogenetic relationships of the Xantusiidae (Reptilia: Lacertilia). Zoological Journal of the Linnean Society 82:291–318.

Rieppel, O. 1987. The phylogenetic relationships within the Chamaeleonidae, with comments on some aspects of cladistic analysis. Zoological Journal of the Linnean Society 89:41–62.

Rieppel, O. 1989. The hind limb of *Macrocnemus bassanii* (Nopcsa) (Reptilia, Diapsida): development and functional anatomy. Journal of Vertebrate Paleontology 9:373–387.

Rieppel, O. 1992. The skull in a hatchling of *Sphenodon punctatus*. Journal of Herpetology 26:80–84.

Rieppel, O. 1993a. Patterns of diversity in the reptilian skull; pp. 344–390 in J. Hanken and B. K. Hall (eds.), The Skull, Volume 2: Patterns of Structural and Systematic Diversity. University of Chicago Press, Chicago, IL.

Rieppel, O. 1993b. Studies on skeleton formation in reptiles. II. *Chamaeleo hoehnelii* (Squamata: Chamaeleoninae), with comments on the homology of carpal and tarsal bones. Herpetologica 49:66–78.

Rieppel, O. 1993c. Studies on skeleton formation in reptiles. v. Patterns of ossification in the skeleton of *Alligator mississippiensis* Daudin (Reptilia, Crocodylia). Zoological Journal of the Linnean Society 109:301–325.

Rieppel, O., and R. W. Gronowski. 1981. The loss of the lower temporal arcade in diapsid reptiles. Zoological Journal of the Linnean Society 72:203–217.

Rieppel, O., and C. Crumly. 1997. Paedomorphosis and skull structure in Malagasy chamaeleons (Reptilia: Chamaeleoninae). Journal of Zoology 243:351–380.

Rieppel, O., N. C. Fraser, and S. Nosotti. 2003. The monophyly of Protorosauria (Reptilia, Archosauromorpha): a preliminary analysis. Atti Della Società Italiana Di Scienze Naturali e Del Museo Civico Di Storia Naturale Di Milano 144:359–382.

Rieppel, O., J. Müller, and J. Liu. 2005. Rostral structure in Thalattosauria (Reptilia, Diapsida). Canadian Journal of Earth Sciences 42:2081–2086.

Rineau, V., R. Zaragüeta i Bagils, and M. Laurin. 2018. Impact of errors on cladistic inference: simulation-based comparison between parsimony and three-taxon analysis. Contributions to Zoology 87:25–40.

Rineau, V., A. Grand, R. Zaragüeta i Bagils, and M. Laurin. 2015. Experimental systematics: sensitivity of cladistic methods to polarization and character ordering schemes. Contributions to Zoology 84:129–148.

Robinson, P. L. 1962. Gliding lizards from the Upper Keuper of Great Britain. Proceedings of the Geological Society of London 1601:137–146.

Robinson, P. L. 1973. A problematic reptile from the British Upper Trias. Journal of the Geological Society 129:457–479.

Robinson, P. L. 1975. The functions of the hooked fifth metatarsal in lepidosaurian reptiles. Colloques Internationaux Du Centre National de La Recherche Scientifique 218:461–483.

Romer, A. S. 1922. The locomotor apparatus of certain primitive and mammal-like reptiles. Bulletin of the American Museum of Natural History 40:517–606.

Romer, A. S. 1927. Notes on the Permo-Carboniferous reptile *Dimetrodon*. The Journal of Geology 35:673–689.

Romer, A. S. 1937. New genera and species of pelycosaurian reptiles. Proceedings of the New England Zoölogical Club 16:89–96.

Romer, A. S. 1946. The primitive reptile *Limnoscelis* restudied. American Journal of Science 244:149–188.

Romer, A. S. 1956. Osteology of the Reptiles, 3rd ed. University of Chicago Press, Chicago, IL, 772 pp.

Romer, A. S. 1971. The Chañares (Argentina) Triassic reptile fauna. X. Two new but incompletely known long-limbed pseudosuchians. Breviora. 378:1–10.

Romer, A. S. 1972a. The Chañares (Argentina) Triassic reptile fauna. XII. The postcranial skeleton of the thecodont *Chanaresuchus*. Breviora 385:1–21.

Romer, A. S. 1972b. The Chañares (Argentina) Triassic reptile fauna. XIII. An early ornithosuchid pseudosuchian, *Gracilisuchus stipanicicorum*, gen. et sp. nov. Breviora. 389:1–24.

Romer, A. S. 1972c. The Chañares (Argentina) Triassic reptile fauna. XV. Further remains of the thecodonts *Lagerpeton* and *Lagosuchus*. .

Romer, A. S., and L. I. Price. 1940. Review of the Pelycosauria. Geological Society of America, Special Papers 28:1–538.

Ruben, R. R. 1998. Gliding adaptations in the Triassic archosaur *Megalancosaurus*. Journal of Vertebrate Paleontology 18:73A.

Russell, A. P., and A. M. Bauer. 1990. Digit I in pad-bearing gekkonine geckos: alternate designs and the potential constraints of phalangeal number. Memoirs of the Queensland Museum 29:453–472.

Russell, A. P., and L. D. Dijkstra. 2001. Patagial morphology of *Draco volans* (Reptilia: Agamidae) and the origin of glissant locomotion in flying dragons. Journal of Zoology 253:457–471.

Russell, A. P., and A. M. Bauer. 2008. The appendicular locomotor apparatus of *Sphenodon* and Normal-limbed Squamates; pp. 1–465 in C. Gans, A. S. Gaunt, and K. Adler (eds.), Biology of the Reptilia, Volume 21, Morphology I. The Skull and Appendicular Locomotor Apparatus of Lepidosauria. Society for the Study of Amphibians and Reptiles, Ithaca, New York.

Russell, A. P., A. Y. Stark, and T. E. Higham. 2019. The integrative biology of gecko adhesion: historical review, current understanding, and grand challenges. Integrative and Comparative Biology 59:101–116.

Rygel, M. C., C. Lally, M. R. Gibling, A. Ielpi, J. H. Calder, and A. R. Bashforth. 2015. Sedimentology and stratigraphy of the type section of the Pennsylvanian Boss Point Formation, Joggins Fossil Cliffs, Nova Scotia, Canada. Atlantic Geology 51:001–043.

Sahney, S., M. J. Benton, and P. A. Ferry. 2010. Links between global taxonomic diversity, ecological diversity and the expansion of vertebrates on land. Biology Letters 6:544–547.

Saller, F. 2016. Anatomia, paleobiologia e filogenesi di *Macrocnemus bassanii* Nopcsa 1930 (Reptilia, Protorosauria). Ph.D. dissertation, Università di Bologna, 206 pp.

Saller, F., S. Renesto, and F. M. Dalla Vecchia. 2013. First record of *Langobardisaurus* (Diapsida, Protorosauria) from the Norian (Late Triassic) of Austria, and a revision of the genus. Neues Jahrbuch Für Geologie Und Paläontologie - Abhandlungen 268:83–95.

Sampson, S. D., M. J. Ryan, and D. H. Tanke. 1997. Craniofacial ontogeny in centrosaurine dinosaurs (Ornithischia: Ceratopsidae): taxonomic and behavioral implications. Zoological Journal of the Linnean Society 121:293–337.

Sangster, S. 2021. The Osteology of *Dimorphodon macronyx*, a Non-Pterodactyloid Pterosaur from the Lower Jurassic of Dorset, England. Monographs of the Palaeontographical Society 175:1–48.

Santos, R. V., P. A. Souza, C. J. S. de Alvarenga, E. L. Dantas, M. M. Pimentel, C. G. de Oliveira, and L. M. de Araújo. 2006. Shrimp U–Pb zircon dating and palynology of bentonitic layers from the Permian Irati Formation, Paraná Basin, Brazil. Gondwana Research 9:456–463.

Sawin, R. S., E. K. Franseen, R. R. West, G. A. Ludvigson, and W. L. Watney. 2008. Clarification and changes in Permian stratigraphic nomenclature in Kansas. Current Research in Earth Sciences 254:1–4.

Schachat, S. R., C. C. Labandeira, M. R. Saltzman, B. D. Cramer, J. L. Payne, and C. K. Boyce. 2018. Phanerozoic pO2 and the early evolution of terrestrial animals. Proceedings of the Royal Society B: Biological Sciences 285:20172631.

Schaumberg, G. 1976. Zwei Reptilneufunde (*Weigeltisaurus* Kuhn [?], Lepidosauria [?], Reptilia) aus dem Kupferschiefer von Richelsdorf (Perm, Hessen). Philippia 3:3–8.

Schaumberg, G. 1982. Paläozoische Reptilien in Nordhessen. Philippia 5:3–10.

Schaumberg, G. 1986. Bemerkungen zu einem Neufund von *Weigeltisaurus jaekeli* (Weigelt) im nordhessischen Kupferschiefer. Paläontologische Zeitschrift 60:319–327.

Schaumberg, G., D. M. Unwin, and S. Brandt. 2007. New information on the anatomy of the Late Permian gliding reptile *Coelurosauravus*. Paläontologische Zeitschrift 81:160–173.

Scheyer, T. M., S. N. F. Spiekman, H.-D. Sues, M. D. Ezcurra, R. J. Butler, and M. E. H. Jones. 2020. *Colobops*: a juvenile rhynchocephalian reptile (Lepidosauromorpha), not a diminutive archosauromorph with an unusually strong bite. Royal Society Open Science 7:192179.

Schmidt, A., and M. S. Fischer. 2011. The kinematic consequences of locomotion on sloped arboreal substrates in a generalized (*Rattus norvegicus*) and a specialized (*Sciurus vulgaris*) rodent. Journal of Experimental Biology 214:2544–2559.

Schneider, J. W., S. G. Lucas, F. Scholze, S. Voigt, L. Marchetti, H. Klein, S. Opluštil, R. Werneburg, V. K. Golubev, J. E. Barrick, T. Nemyrovska, A. Ronchi, M. O. Day, V. V. Silantiev, R. Rößler, H. Saber, U. Linnemann, V. Zharinova, and S.-Z. Shen. 2020. Late Paleozoic–early Mesozoic continental biostratigraphy — Links to the Standard Global Chronostratigraphic Scale. Palaeoworld 29:186–238.

Schoch, R. 2002. Stratigraphie und Taphonomie wirbeltierreicher Schichten im Unterkeuper (Mitteltrias) von Vellberg (SW-Deutschland). Stuttgarter Beiträge Zur Naturkunde Serie B (Geologie Und Paläontologie) 318:1–30.

Schoch, R. R., and H.-D. Sues. 2014. A new archosauriform reptile from the Middle Triassic (Ladinian) of Germany. Journal of Systematic Palaeontology 12:113–131.

Schoch, R. R., and H.-D. Sues. 2018a. A new lepidosauromorph reptile from the Middle Triassic (Ladinian) of Germany and its phylogenetic relationships. Journal of Vertebrate Paleontology 38:e1444619.

Schoch, R. R., and H.-D. Sues. 2018b. Osteology of the Middle Triassic stem-turtle *Pappochelys rosinae* and the early evolution of the turtle skeleton. Journal of Systematic Palaeontology 16:927–965.

Schumacher, G.-H. 1973. The head muscles and hyolaryngeal skeleton of turtles and crocodilians; pp. 101–194 in C. Gans and T. S. Parsons (eds.), Biology of the Reptilia, Volume 4, Morphology D. vol. 4. Academic Press, London and New York.

Sen, K. 2003. *Pamelaria dolichotrachela*, a new prolacertid reptile from the Middle Triassic of India. Journal of Asian Earth Sciences 21:663–681.

Sennikov, A. G., and V. K. Golubev. 2017. Sequence of Permian tetrapod faunas of Eastern Europe and the Permian–Triassic ecological crisis. Paleontological Journal 51:600–611.

Senter, P. 2002. Lack of a pheromonal sense in phytosaurs and other archosaurs, and its implications for reproductive communication. Paleobiology 28:544–550.

Senter, P. 2003. New information on cranial and dental features of the Triassic archosauriform reptile *Euparkeria capensis*. Palaeontology 46:613–621.

Senter, P. 2004. Phylogeny of Drepanosauridae (Reptilia: Diapsida). Journal of Systematic Palaeontology 2:257–268.

Sereno, P. C. 1991. Basal archosaurs: phylogenetic relationships and functional implications. Memoir (Society of Vertebrate Paleontology) 2:1–53.

Sereno, P. C. 1994. The pectoral girdle and forelimb of the basal theropod *Herrerasaurus ischigualastensis*. Journal of Vertebrate Paleontology 13:425–450.

Sereno, P. C., and A. B. Arcucci. 1994a. Dinosaurian precursors from the Middle Triassic of Argentina: *Lagerpeton chanarensis*. Journal of Vertebrate Paleontology 13:385–399.

Sereno, P. C., and A. B. Arcucci. 1994b. Dinosaurian precursors from the Middle Triassic of Argentina: *Marasuchus lilloensis*, gen. nov. Journal of Vertebrate Paleontology 14:53–73.

Sereno, P. C., and F. E. Novas. 1994. The skull and neck of the basal theropod *Herrerasaurus ischigualastensis*. Journal of Vertebrate Paleontology 13:451–476.

Sereno, P. C., R. N. Martínez, and O. A. Alcober. 2013. Osteology of *Eoraptor lunensis* (Dinosauria, Sauropodomorpha). Journal of Vertebrate Paleontology 32:83–179.

Sereno, P. C., C. A. Forster, R. R. Rogers, and A. M. Monetta. 1993. Primitive dinosaur skeleton from Argentina and the early evolution of Dinosauria. Nature 361:64–66.

Sharov, A. G. 1970. A peculiar reptile from the Lower Triassic of Fergana. Paleontological Journal 1:127–130.

Shcherbakov, D. E. 2008. Madygen, Triassic Lagerstätte number one, before and after Sharov. Alavesia 2:12.

Shine, R., S. Keogh, P. Doughty, and H. Giragossyan. 1998. Costs of reproduction and the evolution of sexual dimorphism in a 'flying lizard' *Draco melanopogon* (Agamidae). Journal of Zoology 246:203–213.

Sill, W. D. 1967. *Proterochampsa barrionuevoi* and the early evolution of the Crocodilia. Bulletin of the Museum of Comparative Zoology 135:415–446.

da Silva, J. M., and K. A. Tolley. 2013. Ecomorphological variation and sexual dimorphism in a recent radiation of dwarf chameleons (*Bradypodion*). Biological Journal of the Linnean Society 109:113–130.

da Silva, J. M., L. Carne, G. John Measey, A. Herrel, and K. A. Tolley. 2016. The relationship between cranial morphology, bite performance, diet and habitat in a radiation of dwarf chameleon (*Bradypodion*). Biological Journal of the Linnean Society 119:52–67.

Silva-Neves, E., S. P. Modesto, and S. Dias-da-Silva. 2020. A new, nearly complete skull of *Procolophon trigoniceps* Owen, 1876 from the Sanga do Cabral Supersequence, Lower Triassic of Southern Brazil, with phylogenetic remarks. Historical Biology 32:574–582.

Simões, T. R., M. W. Caldwell, and A. W. A. Kellner. 2015. A new Early Cretaceous lizard species from Brazil, and the phylogenetic position of the oldest known South American squamates. Journal of Systematic Palaeontology 13:601–614.

Simões, T. R., M. W. Caldwell, R. L. Nydam, and P. Jiménez-Huidobro. 2017. Osteology, phylogeny, and functional morphology of two Jurassic lizard species and the early evolution of scansoriality in geckoes. Zoological Journal of the Linnean Society 180:216–241.

Simões, T. R., C. F. Kammerer, M. W. Caldwell, and S. E. Pierce. 2022. Successive climate crises in the deep past drove the early evolution and radiation of reptiles. Science Advances 8:eabq1898.

Simões, T. R., G. F. Funston, B. Vafaeian, R. L. Nydam, M. R. Doschak, and M. W. Caldwell. 2016. Reacquisition of the lower temporal bar in sexually dimorphic fossil lizards provides a rare case of convergent evolution. Scientific Reports 6:24087.

Simões, T. R., M. W. Caldwell, M. Tałanda, M. Bernardi, A. Palci, O. Vernygora, F. Bernardini, L. Mancini, and R. L. Nydam. 2018. The origin of squamates revealed by a Middle Triassic lizard from the Italian Alps. Nature 557:706–709.

Smith, R. M. H. 2000. Sedimentology and taphonomy of Late Permian vertebrate fossil localities in Southwestern Madagascar. Paleontologia Africana 36:25–41.

Smith, R. M. H. 2020. Biostratigraphy of the *Cistecephalus* Assemblage Zone (Beaufort Group, Karoo Supergroup), South Africa. South African Journal of Geology 123:181–190.

Smith, R. M. H., and S. E. Evans. 1996. New material of *Youngina*: evidence of juvenile aggregation in Permian diapsid reptiles. Palaeontology 39:289–304.

Sobral, G., and J. Müller. 2016. Archosaurs and their kin: the ruling reptiles; pp. 285–326 in J. A. Clack, R. R. Fay, and A. N. Popper (eds.), Evolution of the Vertebrate Ear: Evidence from the Fossil Record. Springer International Publishing, Cham.

Sobral, G., and J. Müller. 2019. The braincase of *Mesosuchus browni* (Reptilia, Archosauromorpha) with information on the inner ear and description of a pneumatic sinus. PeerJ 7:e6798.

Sobral, G., T. R. Simões, and R. R. Schoch. 2020. A tiny new Middle Triassic stem-lepidosauromorph from Germany: implications for the early evolution of lepidosauromorphs and the Vellberg fauna. Scientific Reports 10:2273.

Sobral, G., R. B. Sookias, B.-A. S. Bhullar, R. Smith, R. J. Butler, and J. Müller. 2016. New information on the braincase and inner ear of *Euparkeria capensis* Broom: implications for diapsid and archosaur evolution. Royal Society Open Science 3:160072.

Socha, J. J., F. Jafari, Y. Munk, and G. Byrnes. 2015. How animals glide: from trajectory to morphology. Canadian Journal of Zoology 93:901–924.

Soemmerring, S. T. v. 1812. Über einen *Ornithocephalus*. Denkschriften Der Königlichen Akademie Der Wissenschaften Zu München 3:89–158.

Sookias, R. B., and R. J. Butler. 2013. Euparkeriidae. Geological Society, London, Special Publications 379:35–48.

Sookias, R. B., R. J. Butler, and R. B. J. Benson. 2012. Rise of dinosaurs reveals major body-size transitions are driven by passive processes of trait evolution. Proceedings of the Royal Society B: Biological Sciences 279:2180–2187.

Sookias, R. B., D. Dilkes, G. Sobral, R. M. H. Smith, F. P. Wolvaardt, A. B. Arcucci, B.-A. S. Bhullar, and I. Werneburg. 2020. The craniomandibular anatomy of the early archosauriform *Euparkeria capensis* and the dawn of the archosaur skull. Royal Society Open Science 7:200116.

Spiekman, S. N. F. 2018. A new specimen of *Prolacerta broomi* from the lower Fremouw Formation (Early Triassic) of Antarctica, its biogeographical implications and a taxonomic revision. Scientific Reports 8:17996.

Spiekman, S. N. F., and T. Scheyer. 2019. A taxonomic revision of the genus *Tanystropheus* (Archosauromorpha, Tanystropheidae). Palaeontologia Electronica 22.3.80:1–46.

Spiekman, S. N. F., N. C. Fraser, and T. M. Scheyer. 2021. A new phylogenetic hypothesis of Tanystropheidae (Diapsida, Archosauromorpha) and other “protorosaurs”, and its implications for the early evolution of stem archosaurs. PeerJ 9:e11143.

Spiekman, S. N. F., J. M. Neenan, N. C. Fraser, V. Fernandez, O. Rieppel, S. Nosotti, and T. M. Scheyer. 2020a. Aquatic habits and niche partitioning in the extraordinarily long-necked Triassic reptile *Tanystropheus*. Current Biology 30:1–7.

Spiekman, S. N. F., J. M. Neenan, N. C. Fraser, V. Fernandez, O. Rieppel, S. Nosotti, and T. M. Scheyer. 2020b. The cranial morphology of *Tanystropheus hydroides* (Tanystropheidae, Archosauromorpha) as revealed by synchrotron microtomography. PeerJ 8:e10299.

Spielmann, J. A., A. B. Heckert, and S. G. Lucas. 2005. The Late Triassic archosauromorph *Trilophosaurus* as an arboreal climber. Rivista Italiana Di Paleontologia e Stratigrafia 111:395–412.

Spielmann, J. A., S. Renesto, and S. G. Lucas. 2006. The utility of claw curvature in assessing the arboreality of fossil reptiles. New Mexico Museum of Natural History and Science Bulletin 37:365–368.

Spielmann, J. A., S. G. Lucas, L. F. Rhinehart, and A. B. Heckert. 2008. The Late Triassic archosauromorph *Trilophosaurus*. New Mexico Museum of Natural History and Science Bulletin 43:1–177.

Spindler, F., R. Werneburg, and J. W. Schneider. 2019. A new mesenosaurine from the lower Permian of Germany and the postcrania of *Mesenosaurus*: implications for early amniote comparative osteology. PalZ 93:303–344.

Spindler, F., R. Werneburg, J. W. Schneider, L. Luthardt, V. Annacker, and R. Rößler. 2018. First arboreal “pelycosaurs” (Synapsida: Varanopidae) from the early Permian Chemnitz Fossil Lagerstätte, SE Germany, with a review of varanopid phylogeny. PalZ 92:315–364.

Stecher, R. 2008. A new Triassic pterosaur from Switzerland (Central Austroalpine, Grisons), *Raeticodactylus filisurensis* gen. et sp. nov. Swiss Journal of Geosciences 101:185–201.

Steen, M. C. 1934. The amphibian fauna from the South Joggins, Nova Scotia. Proceedings of the Zoological Society of London 104:465–504.

Stefanic, C. M., and S. J. Nesbitt. 2018. The axial skeleton of *Poposaurus langstoni* (Pseudosuchia: Poposauroidea) and its implications for accessory intervertebral articulation evolution in pseudosuchian archosaurs. PeerJ 6:e4235.

Stefanic, C. M., and S. J. Nesbitt. 2019. The evolution and role of the hyposphene-hypantrum articulation in Archosauria: phylogeny, size and/or mechanics? Royal Society Open Science 6:190258.

Stein, K., C. Palmer, P. G. Gill, and M. J. Benton. 2008. The aerodynamics of the British Late Triassic Kuehneosauridae. Palaeontology 51:967–981.

Stevens, M., and S. Merilaita. 2009. Animal camouflage: current issues and new perspectives. Philosophical Transactions of the Royal Society B: Biological Sciences 364:423–427.

Steyer, J. S., M. Boulay, and S. Lorrain. 2010. 3D external restorations of stegocephalian skulls using ZBrush: The renaissance of fossil amphibians. Comptes Rendus Palevol 9:463–470.

Stockar, R. 2010. Facies, depositional environment, and palaeoecology of the Middle Triassic Cassina beds (Meride Limestone, Monte San Giorgio, Switzerland). Swiss Journal of Geosciences 103:101–119.

Stocker, M. R., and R. J. Butler. 2013. Phytosauria. Geological Society, London, Special Publications 379:91–117.

Stocker, M. R., S. J. Nesbitt, K. E. Criswell, W. G. Parker, L. M. Witmer, T. B. Rowe, R. Ridgely, and M. A. Brown. 2016. A dome-headed stem archosaur exemplifies convergence among dinosaurs and their distant relatives. Current Biology 26:2674–2680.

Stuart-Fox, D. 2013. Chameleon behavior and color change; pp. 115–130 in K. A. Tolley and A. Herrel (eds.), The Biology of Chameleons. University of California Press, Berkley, CA.

Stuart-Fox, D. M., D. Firth, A. Moussalli, and M. J. Whiting. 2006. Multiple signals in chameleon contests: designing and analysing animal contests as a tournament. Animal Behaviour 71:1263–1271.

Sues, H.-D. 2003. An unusual new archosauromorph reptile from the Upper Triassic Wolfville Formation of Nova Scotia. Canadian Journal of Earth Sciences 40:635–649.

Sues, H.-D. 2019. The Rise of Reptiles: 320 Million Years of Evolution. Johns Hopkins University Press, Baltimore, MD, 401 pp.

Sues, H.-D., and N. C. Fraser. 2010. Triassic Life on Land: The Great Transition. Columbia University Press, New York, NY, 224 pp.

Sues, H.-D., and P. E. Olsen. 2015. Stratigraphic and temporal context and faunal diversity of Permian-Jurassic continental tetrapod assemblages from the Fundy rift basin, eastern Canada. Atlantic Geology 51:139–205.

Sues, H.-D., R. R. Schoch, G. Sobral, and R. B. Irmis. 2020. A new archosauriform reptile with distinctive teeth from the Middle Triassic (Ladinian) of Germany. Journal of Vertebrate Paleontology 40:e1764968.

Sumida, S. S. 1987. Two different vertebral forms in the axial column of *Labidosaurus* (Captorhinomorpha: Captorhinidae). Journal of Paleontology 61:155–167.

Sumida, S. S. 1989a. The appendicular skeleton of the Early Permian genus *Labidosaurus* (Reptilia, Captorhinomorpha, Captorhinidae) and the hind limb musculature of captorhinid reptiles. Journal of Vertebrate Paleontology 9:295–313.

Sumida, S. S. 1989b. Reinterpretation of vertebral structure in the Early Permian pelycosaur *Varanosaurus acutirostris* (Amniota, Synapsida). Journal of Vertebrate Paleontology 9:451–458.

Sumida, S. S. 1990. Vertebral morphology, alternation of neural spine height, and structure in Permo-Carboniferous tetrapods, and a reappraisal of primitive modes of terrestrial locomotion. University of California Publications, Zoology 122:1–129.

Sumida, S. S. 1997. Locomotor features of taxa spanning the origin of amniotes; pp. 353–398 in S. S. Sumida and K. L. M. Martin (eds.), Amniote origins: completing the transition to land. Academic Press San Diego, California.

Sumida, S. S., and S. Modesto. 2001. A phylogenetic perspective on locomotory strategies in early amniotes. Integrative and Comparative Biology 41:586–597.

Sumida, S. S., R. E. Lombard, and D. S. Berman. 1992. Morphology of the atlas-axis complex of the late Palaeozoic tetrapod suborders Diadectomorpha and Seymouriamorpha. Philosophical Transactions of the Royal Society of London. Series B, Biological Sciences 336:259–273.

Sustaita, D., E. Pouydebat, A. Manzano, V. Abdala, F. Hertel, and A. Herrel. 2013. Getting a grip on tetrapod grasping: form, function, and evolution. Biological Reviews 88:380–405.

Swinton, W. E. 1939. A new Triassic Rhynchocephalian from Gloucestershire. Annals and Magazine of Natural History 4:591–594.

Swofford, D. L. 2003. PAUP*. Phylogenetic Analysis Using Parsimony (*and Other Methods). Version 4. Sinauer Associates, Sunderland, Massachusetts.

Szulc, J. 2005. Sedimentary environments of the vertebrate-bearing Norian deposits from Krasiejow, Upper Silesia (Poland). Hallesches Jahrbuch Für Geowissenschaften. Reihe B 19:161–170.

Szulc, J., G. Racki, K. Jewuła, and J. Środoń. 2015. How many Upper Triassic bone-bearing levels are there in Upper Silesia (southern Poland)? A critical overview of stratigraphy and facies. Annales Societatis Geologorum Poloniae 85:587–626.

Tanke, D. H., and B. M. Rothschild. 2010. Paleopathologies in Albertan ceratopsids and their behavioral significance; pp. 355–384 in M. J. Ryan, B. J. Chinnery-Allgeier, and D. A. Eberth (eds.), New Perspectives on Horned Dinosaurs: The Royal Tyrrell Museum Ceratopsian Symposium. Indiana University Press.

Thommasen, H., and R. L. Carroll. 1981. *Broomia*, the oldest known millerettid reptile. Palaeontology 24:379–390.

Tinius, A., A. P. Russell, H. A. Jamniczky, and J. S. Anderson. 2018. What is bred in the bone: ecomorphological associations of pelvic girdle form in greater Antillean *Anolis* lizards. Journal of Morphology 279:1016–1030.

Troelsen, P. V., D. M. Wilkinson, M. Seddighi, D. R. Allanson, and P. L. Falkingham. 2019. Functional morphology and hydrodynamics of plesiosaur necks: does size matter? Journal of Vertebrate Paleontology 39:e1594850.

Trotteyn, M. J. 2011. Material Postcraneano de *Proterochampsa barrionuevoi* Reig 1959 (Diapsida: Archosauriformes) del Triásico Superior del Centro-oeste de Argentina. Ameghiniana 48:424–446.

Trotteyn, M. J., and J. A. Haro. 2011. The braincase of a specimen of *Proterochampsa* Reig (Archosauriformes: Proterochampsidae) from the Late Triassic of Argentina. Paläontologische Zeitschrift 85:1–17.

Trotteyn, M. J., and M. D. Ezcurra. 2014. Osteology of *Pseudochampsa ischigualastensis* gen. et comb. nov. (Archosauriformes: Proterochampsidae) from the Early Late Triassic Ischigualasto Formation of Northwestern Argentina. PLoS ONE 9:e111388.

Trotteyn, M. J., A. B. Arcucci, and T. Raugust. 2013. Proterochampsia: an endemic archosauriform clade from South America. Geological Society, London, Special Publications 379:59–90.

Tschopp, E., and O. Mateus. 2013. Clavicles, interclavicles, gastralia, and sternal ribs in sauropod dinosaurs: new reports from Diplodocidae and their morphological, functional and evolutionary implications. Journal of Anatomy 222:321–340.

Tsuji, L. A. 2006. Cranial anatomy and phylogenetic affinities of the Permian parareptile *Macroleter poezicus*. Journal of Vertebrate Paleontology 26:849–865.

Tsuji, L. A. 2013. Anatomy, cranial ontogeny and phylogenetic relationships of the pareiasaur *Deltavjatia rossicus* from the Late Permian of central Russia. Earth and Environmental Science Transactions of The Royal Society of Edinburgh 104:81–122.

Tsuji, L. A., and J. Müller. 2009. Assembling the history of the Parareptilia: phylogeny, diversification, and a new definition of the clade. Fossil Record 12:71–81.

Tsuji, L. A., J. Müller, and R. R. Reisz. 2012. Anatomy of *Emeroleter levis* and the phylogeny of the nycteroleter parareptiles. Journal of Vertebrate Paleontology 32:45–67.

Tulli, M. J., F. B. Cruz, A. Herrel, B. Vanhooydonck, and V. Abdala. 2009. The interplay between claw morphology and microhabitat use in neotropical iguanian lizards. Zoology 112:379–392.

Tverdokhlebova, G. I., and M. F. Ivakhnenko. 1984. Nykteroleterids from the Upper Permian of Eastern Europe. Paleontological Journal 1984:98–111.

Unwin, D. 1988. New remains of the pterosaur *Dimorphodon* (Pterosauria: Rhamphorhynchoidea) and the terrestrial ability of early pterosaurs. Modern Geology 13:57–68.

Unwin, D. M., V. R. Alifanov, and M. J. Benton. 2000. Enigmatic small reptiles from the Middle-Late Triassic of Kirgizstan; pp. 177–186 in M. J. Benton, M. A. Shishkin, D. M. Unwin, and E. N. Kurochkin (eds.), The age of dinosaurs in Russia and Mongolia. Cambridge University Press, Cambridge, UK.

Vanhooydonck, B., A. Herrel, and R. Van Damme. 2007. Interactions between habitat use, behavior, and the trophic niche of lacertid lizards; pp. 427–449 in D. B. Miles, L. B. McBrayer, and S. M. Reilly (eds.), Lizard Ecology. Cambridge University Press, Cambridge.

Vaughn, P. P. 1955. The Permian reptile *Araeoscelis* restudied. Bulletin of the Museum of Comparative Zoology 113:1–467.

Vaughn, P. P. 1958. A pelycosaur with subsphenoidal teeth from the lower Permian of Oklahoma. Journal of the Washington Academy of Sciences 48:44–47.

Vaughn, P. P. 1970. Alteration of neural spine height in certain Early Permian tetrapods. Bulletin of the Southern California Academy of Sciences 69:80–86.

Vermeij, G. J., and R. Motani. 2018. Land to sea transitions in vertebrates: the dynamics of colonization. Paleobiology 44:237–250.

Verwaijen, D., R. V. Damme, and A. Herrel. 2002. Relationships between head size, bite force, prey handling efficiency and diet in two sympatric lacertid lizards. Functional Ecology 16:842–850.

Vickaryous, M. K., and B. K. Hall. 2008. Development of the dermal skeleton in *Alligator mississippiensis* (Archosauria, Crocodylia) with comments on the homology of osteoderms. Journal of Morphology 269:398–422.

Vickaryous, M. K., and J.-Y. Sire. 2009. The integumentary skeleton of tetrapods: origin, evolution, and development. Journal of Anatomy 214:441–464.

Vickaryous, M. K., and B. K. Hall. 2010. Comparative development of the crocodylian interclavicle and avian furcula, with comments on the homology of dermal elements in the pectoral apparatus. Journal of Experimental Zoology Part B: Molecular and Developmental Evolution 314B:196–207.

Viglietti, P. A. 2020. Biostratigraphy of the *Daptocephalus* Assemblage Zone (Beaufort Group, Karoo Supergroup), South Africa. South African Journal of Geology 123:191–206.

Villa, A., R. Montie, M. Röper, M. Rothgaenger, and O. W. M. Rauhut. 2021. *Sphenofontis velserae* gen. et sp. nov., a new rhynchocephalian from the Late Jurassic of Brunn (Solnhofen Archipelago, southern Germany). PeerJ 9:e11363.

Vogel, S. 1996. Life in Moving Fluids: The Physical Biology of Flow. Revised and Expanded Second Edition. Princeton University Press, Princeton, NJ, 488 pp.

Vorobyeva, E. I. 2007. The morphofunctional approach in paleontology. Paleontological Journal 41:347–359.

Wagner, R. H., and C. F. Winkler Prins. 2016. History and current status of the Pennsylvanian chronostratigraphic units: problems of definition and interregional correlation. Newsletters on Stratigraphy 49:281–320.

Waldman, M., and S. E. Evans. 1994. Lepidosauromorph reptiles from the Middle Jurassic of Skye. Zoological Journal of the Linnean Society 112:135–150.

Wang, J., H. W. Pfefferkorn, Y. Zhang, and Z. Feng. 2012. Permian vegetational Pompeii from Inner Mongolia and its implications for landscape paleoecology and paleobiogeography of Cathaysia. Proceedings of the National Academy of Sciences 109:4927–4932.

Waters, C. N., K. Smith, P. M. Hopson, D. Wilson, D. M. Bridge, J. N. Carney, A. H. Cooper, R. G. Crofts, R. A. Ellison, S. J. Mathers, B. S. P. Moorlock, R. C. Scrivener, A. A. McMillan, K. Ambrose, W. J. Barclay, and A. J. M. Barron. 2008. Stratigraphical chart of the United Kingdom: Southern Britain. British Geological Survey.

Watson, D. M. S. 1912. *Mesosuchus browni*, gen. et spec. nov. Records of the Albany Museum 2:298–299.

Watson, D. M. S. 1914. Notes on *Varanosaurus acutirostris*, Broili. Annals and Magazine of Natural History 13:297–310.

Watson, D. M. S. 1957. On *Millerosaurus* and the early history of the sauropsid reptiles. Philosophical Transactions of the Royal Society of London. Series B, Biological Sciences 240:325–398.

Weigelt, J. 1930a. *Palaeochamaeleo jaekeli* nov. gen. nov. sp. Ein neuer Rhynchocephale aus dem Mansfelder Kupfer schiefer. Leopoldina 6:625–642.

Weigelt, J. 1930b. Über die vermutliche Nahrung von *Protorosaurus* und über einen körperlich erhaltenen Fruchtstand von *Archaeopodocarpus germanicus* aut. Leopoldina 6:269–280.

Weishampel, D. B., P. Dodson, and H. Osmólska. 2007. The Dinosauria. University of California Press, Berkley, CA, 880 pp.

Wellnhofer, P. 1975a. Die Rhamphorhynchoidea (Pterosauria) der Oberjura-Plattenkalke Süddeutschlands. Teil I: Allgemeine Skelettmorphologie. Palaeontographica Abteilung A 148:1–33.

Wellnhofer, P. 1975b. Die Rhamphorhynchoidea (Pterosauria) der Oberjura-Plattenkalke Süddeutschlands. Teil II: Systematische Beschreibung. Palaeontographica Abteilung A 148:132–186.

Wellnhofer, P. 1975c. Die Rhamphorhynchoidea (Pterosauria) der Oberjura-Plattenkalke Süddeutschlands. Teil III: Palökologie und Stammesgeschichte. Palaeontographica Abteilung A 149:1–30.

Wellnhofer, P. 1978. Handbuch Der Palaoherpetologie. Teil 19. Pterosauria. Gustav Fischer Verlag, 82 pp.

Welman, J. 1998. The taxonomy of the South African proterosuchids (Reptilia, Archosauromorpha). Journal of Vertebrate Paleontology 18:340–347.

Werneburg, I. 2019. Morphofunctional categories and ontogenetic origin of temporal skull openings in amniotes. Frontiers in Earth Science 7:1–7.

Werneburg, I., and P. Abel. 2022. Modeling skull network integrity at the dawn of amniote diversification with considerations on functional morphology and fossil jaw muscle reconstructions. Frontiers in Ecology and Evolution 9:799637.

Wescott, W. A., and J. N. Diggens. 1998. Depositional history and stratigraphical evolution of the Sakamena group (Middle Karoo Supergroup) in the southern Morondava Basin, Madagascar. Journal of African Earth Sciences 27:461–479.

White, T. E. 1939. Osteology of *Seymouria baylorensis* Broili. Bulletin of the Museum of Comparative Zoology 85:325–409.

Whiteside, D. I. 1986. The head skeleton of the Rhaetian sphenodontid *Diphydontosaurus avonis* gen. et sp.nov. and the modernizing of a living fossil. Philosophical Transactions of the Royal Society of London. B, Biological Sciences 312:379–430.

Whiteside, D. I., and J. E. A. Marshall. 2008. The age, fauna and palaeoenvironment of the Late Triassic fissure deposits of Tytherington, South Gloucestershire, UK. Geological Magazine 145:105–147.

Whiteside, D. I., C. J. Duffin, P. G. Gill, J. E. A. Marshall, and M. J. Benton. 2016. The Late Triassic and Early Jurassic fissure faunas from Bristol and South Wales: stratigraphic setting. Paleontologia Polonica 97:257–287.

Wilcox, D. C. 2006. Turbulence Modeling for CFD. DCW industries, La Cañada, CA, 522 pp.

Wild, R. 1973. Die TriasFauna der Tessiner Kalkalpen. XXII. *Tanystropheus longobardicus* (Bassani). Schweizerische Palaeontologische Abhandlungen 95:1–162.

Wild, R. 1978. Die Flugsaurier (Reptilia, Pterosauria) aus der Oberen Trias von Cene bei Bergamo, Italien. Bollettino Della Società Paleontologica Italiana 17:176–256.

Wild, R. 1984. Flugsaurier aus der Obertrias von Italien. Naturwissenschaften 71:1–11.

Wild, R. 1993. A juvenile specimen of *Eudimorphodon ranzii* Zambelli (Reptilia, Pterosauria) from the upper Triassic (Norian) of Bergamo. Rivista Del Museo Civico Di Scienze Naturali 16:95–120.

Williston, S. W. 1910. New Permian reptiles: rhachitomous vertebrae. The Journal of Geology 18:585–600.

Williston, S. W. 1911a. A new family of reptiles from the Permian of New Mexico. American Journal of Science 378–398.

Williston, S. W. 1911b. American Permian Vertebrates. University of Chicago Press, Chicago, IL, 145 pp.

Williston, S. W. 1912. Restoration of *Limnoscelis*, a cotylosaur reptile from New Mexico. American Journal of Science 457–468.

Williston, S. W. 1913. The skulls of *Araeoscelis* and *Casea*, Permian reptiles. The Journal of Geology 21:743–747.

Williston, S. W. 1914. The osteology of some American Permian vertebrates. The Journal of Geology 22:364–419.

Williston, S. W. 1915. A new genus and species of American Theromorpha: *Mycterosaurus longiceps*. The Journal of Geology 23:554–559.

Williston, S. W., and E. C. Case. 1913. Description of a nearly complete skeleton of *Ophiacodon* Marsh. Carnegie Institution of Washington Publication 181:37–59.

Wilson, J. A. 1999. A nomenclature for vertebral laminae in sauropods and other saurischian dinosaurs. Journal of Vertebrate Paleontology 19:639–653.

Witmer, L. M. 1995. Homology of facial structures in extant archosaurs (birds and crocodilians), with special reference to paranasal pneumaticity and nasal conchae. Journal of Morphology 225:269–327.

Witmer, L. M. 1997. The evolution of the antorbital cavity of archosaurs: a study in soft-tissue reconstruction in the fossil record with an analysis of the function of pneumaticity. Journal of Vertebrate Paleontology 17:1–76.

Witmer, L. M., S. Chatterjee, J. Franzosa, and T. Rowe. 2003. Neuroanatomy of flying reptiles and implications for flight, posture and behaviour. Nature 425:950–953.

Witton, M. P. 2013. Pterosaurs: Natural History, Evolution, Anatomy. Princeton University Press, Princeton, NJ, 304 pp.

Witton, M. P. 2015. Were early pterosaurs inept terrestrial locomotors? PeerJ 3:e1018.

Witzmann, F. 2007. The evolution of the scalation pattern in temnospondyl amphibians. Zoological Journal of the Linnean Society 150:815–834.

Witzmann, F., H. Scholz, J. Müller, and N. Kardjilov. 2010. Sculpture and vascularization of dermal bones, and the implications for the physiology of basal tetrapods. Zoological Journal of the Linnean Society 160:302–340.

Wood Jones, F. 1953. Some readaptations of the mammalian pes in response to arboreal habits. Proceedings of the Zoological Society of London 123:33–41.

Woodward, A. S. 1907. On a new dinosaurian reptile (*Scleromochlus taylori*, gen. et sp. nov.) from the Trias of Lossiemouth, Elgin. Quarterly Journal of the Geological Society 63:140–144.

Zaaf, A., A. Herrel, P. Aerts, and F. De Vree. 1999. Morphology and morphometrics of the appendicular musculature in geckoes with different locomotor habits (Lepidosauria). Zoomorphology 119:9–22.

Zambelli, R. 1973. *Eudimorphodon ranzii* gen. nov., sp. nov., uno pterosauro triassico. Rendiconti Scienze Di Instituto Lombardo, B 107:27–32.

Zani, P. A. 2000. The comparative evolution of lizard claw and toe morphology and clinging performance. Journal of Evolutionary Biology 13:316–325.

Zanon, R. T. 1990. The sternum of *Araeoscelis* and its implications for basal diapsid phylogeny. Journal of Vertebrate Paleontology 10:51A.

Zhang, J., S. E. Nielsen, L. Mao, S. Chen, and J.-C. Svenning. 2016. Regional and historical factors supplement current climate in shaping global forest canopy height. Journal of Ecology 104:469–478.

Zhao, F., W. Wang, J. Zhang, J. Wyrwa, and F. Sun. 2019. Aerodynamic characteristics and pitching adjusting mechanism of the flying squirrel with deployed patagium. IEEE Access 7:185554–185564.

Zuber, M., M. Laaß, E. Hamann, S. Kretschmer, N. Hauschke, T. van de Kamp, T. Baumbach, and T. Koenig. 2017. Augmented laminography, a correlative 3D imaging method for revealing the inner structure of compressed fossils. Scientific Reports 7:41413.

Abstract

Diapsid reptiles, represented today by their crown-group Sauria, form the most diverse group of extant amniotes and were also the most conspicuous tetrapods of the Mesozoic Era. Despite their much sparser Permo-Triassic fossil record, stem-saurian diapsids show a surprising large morphological and ecological disparity, including arboreal and aerial taxa. Among those, the late Permian Weigeltisauridae, the oldest known gliding vertebrates, and the chameleon-like Drepanosauromorpha from the Late Triassic show some of the most extreme specializations in tetrapods linked to an arboreal habitat. Both groups have been proposed to form the clade 'Avicephala', the earliest diapsid group of arboreal specialists, and one of the few to survive the Permo-Triassic Mass Extinction (PTME). Yet, the monophyly of 'Avicephala' remains controversial. Furthermore, given that weigeltisaurids are the earliest known gliding vertebrates, their study is paramount to the understanding the evolution of vertebrate flight. Yet, few studies have examined the actual gliding capabilities of these reptiles.

In this work, I first redescribe and provide novel anatomical data on both weigeltisaurids and drepanosauromorphs using several imaging techniques, with a particular focus of the weigeltisaurid *Coelurosauravus elivensis* from the late Permian of Madagascar. These new data are then included in a novel phylogenetic dataset designed to examine the phylogenetic relationships of these reptiles among Permo-Triassic diapsids. Lastly, I examine the aerodynamic performances of *C. elivensis* through Computational Fluid Dynamics (CFD) simulations of gliding flight.

My phylogenetic analyses recover a paraphyletic 'Avicephala', with weigeltisaurids closer to the saurian crown-group than previously suggested, and drepanosauromorphs as sister-group to Pterosauria in a new, well-supported clade of ornithodiran archosaurs. The implications of the latter result are two-fold. First, it drastically reduces the ghost lineage at the base of Drepanosauromorpha, and reduces the number of diapsid lineages that survive the PTME. Second, it illuminates the sequence of acquisition of character states prior to the acquisition of powered flight in pterosaurs, supports the hypothesis that the latter evolved from arboreal ancestors, and suggests that this habitat played a role in the origin of flight.

Weigeltisaurids thus represent the only arboreal specialists among stem-saurian diapsids. I show that the patagial wings of these reptiles are anchored to the gastral basket, and thus emerge from the ventral flanks, contrary to the more dorsal wings of extant gliders such as *Draco volans* in which the wings derive from the dorsal ribs. CFD analyses of gliding flight in both *D. volans* and *C. elivensis* demonstrate both taxa show convergent adaptation to lift generation during gliding by generating a strong underpressure and vortices above the wings at high angle of attack. Like *D. volans*, *C. elivensis* and other weigeltisaurids may have been able to control lift and drag generation by adopting different postures in air, enabling them to maneuver better and to glide over longer distances.

This work thus improves our understanding of the morphological and ecological evolution of the first arboreal diapsids, and provides ground work for future numerical paleobiological studies of gliding or flying vertebrates.

Résumé

Les reptiles diapsides, représentés aujourd'hui par leur groupe apical Sauria, constituent actuellement le groupe d'amniotes le plus diversifié et furent également les tétrapodes les plus remarquables durant l'Ère Mésozoïque. Malgré un registre fossile épars concernant le Permien-Trias, les diapsides non-sauriens montrent une étonnante disparité morphologique et écologique, incluant notamment des taxons arboricoles et aériens. Parmi eux, les Weigeltisauridae du Permien tardif, premiers vertébrés planeurs connus, et les Drepanosauromorpha du Trias Supérieur, ressemblant à des caméléons, présentent parmi les plus extrêmes spécialisations liées à un habitat arboricole chez les tétrapodes. Ces deux groupes ont été suggérés comme formant le clade 'Avicephala', le plus ancien groupe de diapsides arboricoles, et l'un des rares à avoir survécu à l'Extinction Permo-Triasique (EPT). Néanmoins, la monophylie des 'Avicephala' reste controversée. De plus, les weigeltisauridés étant les premiers vertébrés planeurs, leur étude est primordiale pour comprendre l'évolution du vol chez les vertébrés. Pourtant, peu d'études se sont intéressées aux capacités de vol plané de ces reptiles.

Dans ce travail, j'ai tout d'abord redécrit et apporté de nouvelles données sur l'anatomie des weigeltisauridés et drépanosauromorphes à l'aide de plusieurs techniques d'imagerie, en me concentrant particulièrement sur le weigeltisauridé *Coelurosauravus elivensis* du Permien supérieur de Madagascar. J'ai ensuite inclus ces informations dans une nouvelle matrice phylogénétique conçue pour examiner les relations de parenté de ces reptiles au sein des diapsides du Permo-Trias. Enfin, j'ai examiné les performances aérodynamiques de *C. elivensis* au travers de simulations de vol plané à l'aide de la Dynamique des Fluides Numérique (CFD).

Mes analyses phylogénétiques retrouvent les 'Avicephala' paraphylétiques, les weigeltisauridés étant plus proches du groupe couronne des sauriens que précédemment supposé, et les drépanosauromorphes étant groupe-frère des Pterosauria, formant un clade robuste d'archosaures ornithodires jusqu'ici inconnu. Ce dernier résultat a deux principales implications. Premièrement, il réduit la lignée fantôme à la base des Drepanosauromorpha, et réduit le nombre de lignées diapsides qui survivent à l'EPT. Deuxièmement, il met en lumière la séquence d'acquisition des états de caractère précédant l'acquisition du vol battu chez les ptérosaures, soutient l'hypothèse que les ptérosaures ont évolué à partir d'ancêtres arboricoles, et suggère que ce milieu de vie a joué un rôle dans l'origine du vol.

Les weigeltisauridés représentent donc les seuls diapsides non-sauriens arboricoles. J'ai montré également que les ailes patagiales de ces reptiles étaient ancrées aux gastralia et émergeaient donc du bord ventral des flancs, contrairement aux ailes plus dorsales des planeurs actuels comme *Draco volans* qui sont portées par les côtes dorsales. L'étude CFD du vol plané chez *D. volans* et *C. elivensis* montre que ces deux taxons génèrent leur portance d'une manière convergente en créant une forte sous-pression et des tourbillons d'air au-dessus des ailes à un angle d'attaque élevé. Comme *D. volans, C. elivensis* et les autres weigeltisauridés contrôlaient vraisemblablement leur portance et leur traînée en adoptant différentes postures dans les airs, ce qui leur aurait permis de mieux manœuvrer et de planer sur de plus grandes distances.

Ce travail a donc permis d’approfondir notre compréhension de l'évolution morphologique et écologique des premiers diapsides arboricoles, et fournit une base pour de futures études numériques sur la paléobiologie des vertébrés planeurs ou volants.

Abstract

Despite their very sparse record, Permo-Triassic diapsids – those not closely related to extant reptiles – were surprisingly diverse. They included the earliest-known gliding vertebrates, the Weigeltisauridae from the Late Permian, and the Drepanosauromorpha, chameleon-like reptiles from the Late Triassic. Both have been proposed to form the 'Avicephala', a group of arboreal specialists, but this remains controversial. Also, the gliding capabilities of weigeltisaurids remain to be assessed. Based on new anatomical data, I conduct phylogenetic analyses that recover drepanosauromorphs not as sister-group to weigeltisaurids, but to pterosaurs, thus shedding new light on the evolutionary history of the acquisition of powered flight in the latter. Based on numerical simulations, I also demonstrate that weigeltisaurids were convergent with extant reptilian gliders such as the flying lizard *Draco* in their generation of lift and postural changes.

Key words: Weigeltisauridae, Drepanosauromorpha, Pterosauria, phylogeny, Permo-Triassic, gliding flight, Computational Fluid Dynamics, paleobiology

Résumé

Malgré un registre fossile très épars, les diapsides du Permo-Trias – ceux n'étant pas proches parents des reptiles actuels – étaient étonnamment diversifiés. Ils incluaient les Weigeltisauridés du Permien tardif, premiers vertébrés planeurs connus, et les Drepanosauromorpha du Trias Supérieur ressemblant à des caméléons. Ces deux taxons formeraient les 'Avicephala', le plus ancien groupe de diapsides arboricoles, mais cela reste controversé. De plus, la capacité de vol plané des weigeltisauridés reste à examiner. Sur la base de nouvelles données anatomiques, j'ai effectué une analyse phylogénétique qui retrouve les drépanosauromorphes groupe-frère non pas des weigeltisauridés, mais des ptérosaures, ce qui éclaire l'origine du vol battu chez ces derniers. Grâce à des simulations numériques, j'ai aussi montré que les weigeltisauridés et les reptiles planeurs actuels comme le lézard volant *Draco* étaient convergents dans leur génération de portance et leurs changements de posture en vol.

Mots clés : Weigeltisauridae, Drepanosauromorpha, Pterosauria, phylogénie, Permien-Trias, vol plané, Computational Fluid Dynamics, paléobiologie